TITLE PAGE

Report Title:	Innovative SOFC Technologies
Type of Report:	Final Technical Report
Reporting Period:	October 1, 2015 to September 30, 2019
Principal Investigator:	Hossein Ghezel-Ayagh
Date Report Issued:	December 31, 2019
Report Prepared for:	U. S. Department of Energy (DOE) – National Energy Technology Laboratory (NETL)
DOE Award No.:	DE-FE0026093
Report Prepared by:	FuelCell Energy, Inc. 3 Great Pasture Road Danbury, CT 06810
Subcontractors:	Versa Power Systems, Ltd 4852 - 52nd Street SE Calgary, AB T2B 3R2

DISCLAIMER

This Final Technical Report was prepared with the support of the U.S. Department of Energy, under Award No. DE-FE0026093. However, any opinions, findings, conclusions, or recommendations expressed herein are those of the author(s) and do not necessarily reflect the views of the DOE.

ABSTRACT

The overarching goal of this project is to advance the reliability, robustness and endurance of low-cost SOFC technology that will ultimately be deployed in coal power systems with greater than 60% percent efficiency based on Higher Heating Value (HHV) of fuel and capability for ≥97% CO_2 capture at a cost-of-electricity that is approximately 40 percent below presently available Integrated Gasification Combined Cycle (IGCC) systems.

The main objective of the research and development is to reduce the SOFC stack cost to the extent which undercuts DOE's cost targets by 50%. The pathways in reaching the project's objective consist of novel materials development, transformational manufacturing processes, high performance cell components, and innovative robust and reliable stack designs leveraging advancements that have occurred in the DOE SOFC Program. To verify the advances in developing the proposed innovations, the project will culminate in a 5 kW-scale stack test for at least 1000 hours using full-size cells, operating on natural gas at self-sustained Normal Operating Conditions (NOC) that would be envisioned in a commercial system.

TABLE OF CONTENTS

LIST OF FIGURES

LIST OF TABLES

EXECUTIVE SUMMARY

This final technical report presents the results of the work completed under the U.S. Department of Energy (DOE) cooperative agreement DE-FE0026093.

Single cell testing was carried out on 18 candidate materials that offer low firing temperature. Several of the candidate sub-1300 °C fired cells demonstrated good performance and good degradation results to the limits of testing. The overall goal of demonstrating feasibility of low temperature firing has been met. Some candidate materials were prepared for sub 1,250 °C firing trials.

Automated screen printing was explored for cell component production. An automated screen printer along with supporting equipment was purchased, installed, commissioned, and underwent trial for cell production. The automated screen printing demonstrated a 67% reduction in cycle time per print while meeting all quality requirements. The system was incorporated into the production process for manufacturing of the cells in this project and enabled the collection of cell fabrication cost data for the CSA stacks. The line is composed entirely of off-the-shelf equipment from the printed circuit board industry and can easily be extended and replicated when production volumes are required.

Cell production processes were demonstrated and ramped up to full production capacity including incorporation of an automated manufacturing cell. Seal application technology including dispensing and stenciling were evaluated and found to require future development if they are to be considered for incorporation in the cell production process.

Reactive Spray Deposition Technology (RSDT) and Atomic Layer Deposition (ALD) methods were explored in cell fabrication processes. Progress was made in achieving uniform and dense coatings, but not yet to the level that allows full sized cell testing. More lab scale development work is needed before the processes can be considered for demonstration at the stack level.

Testing of the 225-cell stack (22.3 cm^2 cell active area) as initial trial of a new cell/stack geometry was conducted through 5,000 h at 291 mA/cm^2, 68% fuel utilization, 36% in-stack reforming level and 40% (higher than the typical 20%) air utilization, demonstrating an average performance degradation rate of 0.72%/1,000h. This first-ever test of this stack platform at these test conditions showed a degradation rate in-line with what would be expected from the baseline large area stack.

This performance gave confidence in the operability of the next generation stack design at the operating conditions. Also, it showed that despite an order of magnitude reduction in material content and a simplification to the structure, there are no indications of compromised stack capability. Based on the results of the test, several improvements (including oxidant flow configuration and fuel manifold sizing) were implemented for the CSA stack design to improve the thermal conditions within and around the stack.

The reported fuel bypass weakness observed in stack tests triggered a redesign and a process change in the manufacture of the centre post. The revised design underwent brazing and installation trials and was incorporated into subsequent stacks.

The next generation of full-sized stack design, Compact SOFC Architecture (CSA) stack platform based on a cell active area of 81 cm^2 and a full height of 350 cells per stack, offers a roughly 10x reduction in material content in the stack (for cost savings) as compared to the legacy Large-Area Stack (LAS) design. A 145-cell CSA stack was successfully tested for 1,000 hours under simulated reformate (system) conditions and demonstrated a degradation rate of 0.7% /khr, exceeding the program target of 1% /khr. This stack served as a confirmation of the design that culminated in build of a full height stack.

Final activities for the project were the build and test of a full height 350-cell CSA stack and demonstration of both the manufacturing approach and the overall stack design capability, as well as the completion of the factory cost model. These two activities completed the final milestones for the project and close it on a positive note.

Stack GT060081-0001, with 340 cells, (considered the effective 350-cell height equivalent) validated the manufacturing processes and exceeded the final program performance and degradation milestones. It has shown relatively good stability over the 2,000+ hours of testing and the performance and degradation profiles across the stack that illustrate a good uniformity across the 340 repeat units (cells, interconnects, and seals) within the stack.

The CSA Stack Factory Cost Estimate forecasts a CSA stack cost of $889 (Year 2011 USD) which translates to 105 $/kW DC at 1,000 MW/year volume production. This CSA stack cost is 61% lower (per kW) compared to the Large Area Stack reported cost of $5,316 (Year 2011 USD) equivalent to 270 $/kW DC at the same production rate of 1,000 MW per year and at the same operational power density of 298 mW/cm^2. Additionally, if the Net AC to Gross DC ratio is equal to x 1.272, which is the same as that for LAS-SOFC stack, the converted CSA Stack cost at $/kW AC will be $83/kW AC which is significantly lower than the DOE cost target of $225/kW AC (2011 USD). The reduction of $/kW AC from $/kW DC is due to the presence of a bottoming cycle and thus greater overall power generation within the combined system. This CSA stack achievement is realized via the minimization of stack material content, simplified unit cell design and design for automation and assembly.

INTRODUCTION AND OBJECTIVES

This project focuses on developing cell and stack technologies that have the potential to undercut current DOE SOFC cost targets by 50%. The pathways in reaching the project's objective consist of novel materials development, transformational manufacturing processes, high performance cell components, and innovative, robust and reliable stack designs leveraging advancements that have occurred in the DOE SOFC Program. To verify the advances in developing the proposed innovations, the project will culminate in a 5 kW-scale stack test for at least 1000 hours using full-size cells, operating on natural gas and under a thermally self-sustained environment.

This project is focused on multidisciplinary research and development of technologies that are anticipated to achieve substantial reduction in the SOFC cell and stack factory costs. Additionally, the results of the project have far reaching implications in lowering the system capital cost as well as the operating and maintenance (O&M) costs.

The Factory Cost of the SOFC stack is dependent on many parameters that by themselves have cause-and-effect interplays. To highlight this point, the stack cost dependencies on key parameters are shown in Figure I-1. There are two levels of dependencies. The primary level consists of the fundamental parameters, including cell materials, cell fabrication processes, stack design architecture and stack manufacturing processes. However, as shown in Figure 1, there are secondary factors resulting from the interplay of the primary parameters which also influence the cost of the stack. These include cell performance and endurance. As an example, if two different cell-material sets have equivalent costs but different performance or decay rates, obviously, the cell-material set that offers the highest performance (power density) and/or the lowest decay rate is the preferred one for use in the fuel cell stack. This points to the fact that considerations given only to one or a few primary factors does not necessarily lead to the most cost-effective SOFC stack solution.

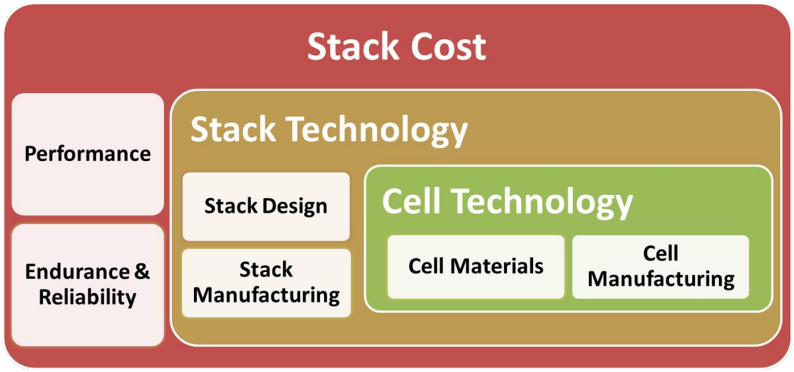

Figure I-1 Factors Influencing Manufactured SOFC Stack Cost

Fuel Cell Energy, Inc. (FCE) has performed a thorough cost analysis of the state-of-the-art SOFC stack under the currently active DOE project DE-FE0011691. At a high volume production level of about 1 GW per year, the stack is projected to cost $241 per kW gross stack dc (Year 2011 USD) equivalent to $189 per kW net ac, in line with DOE's SOFC stack and system cost targets.

Figure I-2 shows how the overall stack cost is distributed. Materials account for 82% of the total cost. The Repeat stack components including the metallic cell holder, shims, flow fields, and interconnect represent the largest proportion of stack cost at 55%. The cell and seal materials account for an additional 25%. The Non-repeat stack parts include two current-collecting end

plates and tie-rods, accounting for only 2% of cost. The labor and other costs account for the remaining 18%.

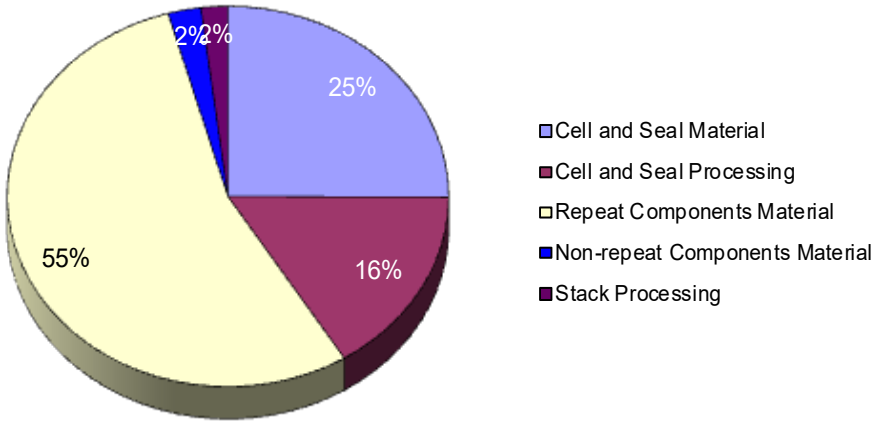

Figure I-2 SOFC Stack Cost Breakdown by Categories

The low labor content is due in part to the fact that the cells and seals are fabricated in-house. As there are several components for each cell in a stack, at high annual production volumes, there can be tens of millions of pieces per year for stack assembly which justifies the investment in automation. An automated stack assembly factory would be equipped with carts or trays with individual pieces or subassemblies which would be automatically fed in sequence.

The main goal of this project is to reduce the stack cost per kW further by 50% while maintaining the same functional materials developed and demonstrated over the course of the DOE's SOFC Program. The cost reductions will be attributable to intensive R&D in three key areas:

- Stack Performance Increase - Peak power increase through cell/stack scale-up and improved thermal management.
- Material Reduction - Thinner cells and stack components, interconnect material reduction, and elimination of certain repeat stack hardware.
- Manufacturing Process Changes and Optimization - Interconnect manufacturing development, improved material utilization, automation and elimination of process steps.

The project is centered on comprehensive multi-prong approaches covering the rudimentary primary parameters, shown in Figure I-1, while building on the advancements that have occurred in the DOE SOFC Program and advanced cell manufacturing techniques developed in prior years.

The scope of work is designed to focus on SOFC stack cost competitiveness to the extent of undercutting the DOE's cost targets for the SOFC systems. The scope of work includes research and development efforts to reduce the cell and stack factory costs while advancing the performance and durability of the technology beyond the state-of-the-art SOFC technology. In support of the aforementioned goals and project objectives, activities to be conducted during this project are as follows:

- Develop low-cost manufacturing of the anode support layer by reduction of the sintering temperature to less than 1300°C.

- Conduct R&D activities related to manufacturing of the cell components using advanced Roll-to-Roll fabrication process.
- Explore the applicability of the Atomic Layer Deposition (ALD) technique in reducing the thickness of the barrier layer and decreasing the imperfections which are prevalent with the wet methods
- Investigate fabrication of dense electrolyte/barrier compound layer using Reactive Spray Deposition Technology (RSDT) in order to reduce the number of manufacturing process steps and lower the sintering cost in fabrication of the SOFC.
- Design and Develop an innovative stack technology with two-pass flow geometry, de-integrated manifold structure, horizontal mounting orientation, scaled-up thin anode (<0.45 mm), and thin interconnect and flow fields for better thermal management, material reduction, better packaging within stack modules, and ease of installation.
- Design and fabricate a nominal 5 kW-scale stack using full-size 550 cm^2 cells to be tested for at least 1000 hours at Normal Operating Conditions (NOC) fueled by natural gas.
- Estimate the factory cost of SOFC cell and stack technologies, innovated as an outcome of this project, based on high volume manufacturing and operating conditions expected in commercial SOFC products.

The outcome of this project will result in reduction of cell and stack costs below current DOE targets, as shown in Figure I-3, by impacting the four cost drivers consisting of: 1) materials, 2) cell manufacturing, 3) stack design and durability, and 4) improvements in the cell and stack performance.

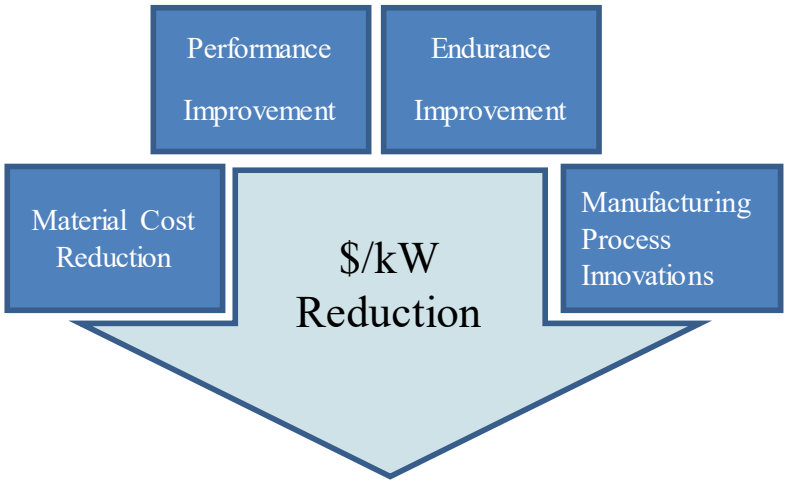

Figure I-3 Multiple Paths to SOFC Cost Reduction

RESULTS AND DISCUSSIONS

1.0 Task 1.0 – Project Management

FCE managed the project in accordance with a Project Management Plan (PMP) to meet all technical, schedule and budget objectives and requirements. The project activities were coordinated in order to effectively accomplish the work. The project milestones listed in Table 1.1 were all met.

Table 1-1 Project Milestones List

Id.	Task /Subtask No.	Milestone Description	Actual Completion
1	1.1	Updated Project Management Plan	11/27/15
2	1.1	Project Kickoff Meeting	12/3/15
3	2.1	Verify <0.45 mm Anode Thickness in 1000 hours Tests	3/20/16
4	2.2.1	Demonstrate Role-to-Role Technology Development in Single Cells	9/28/16
5	2.2.2	Complete Evaluation of ADL for Fabrication of Barrier Layer	12/29/17
6	2.2.3	Complete Evaluation of RSDT for Fabrication of Electrolyte Bi-Layer	12/29/17
7	3.1.1	Complete Advanced Stack Design	4/4/17
8	4.3	Complete >1000 hrs. Tests of the 5 kW Stack with <1% per 1000 hrs. Degradation	10/30/19
9	5.2	Complete Validation of SOFC Stack Cost Reduction	9/30/19

2.0 Task 2.0 – Cell Technology & Manufacturing Development

2.1 Task 2.1 Low-Cost Anode

Objective:

- Reduce cost of anode through firing temperature reduction

Approach:

This subtask will target reducing FCE's baseline TSC3 anode supported SOFC cell cost by 40% through materials reduction and sintering temperature reduction. This work will involve optimizing materials formulations and particle size distribution of nickel oxide to have the anode substrate sintered at ~1,300°C with equivalent shrinkage as compared to the current baseline cell. This task will also focus on development of anode structures with reduced thickness as low as 0.45 mm resulting in diminished amount of materials used in fabrication of the anode support.

The performance and stability of the resulting cell technology will be tested in conjunction with the anode substrate developments and evaluated as a lower cost cell, including testing in both single-cell (10 cm x 10 cm) and large area stack platforms. After meeting cell performance and

endurance criteria, a sufficient number of cells will be produced for assembly for the technology stacks and the 5-kW validation stack.

Results & Discussion:

Previous work in an electrolysis project showed that the performance of thin cells at high current density (during electrolysis testing) is sensitive to the anode functional layer (AFL) thickness. For ease of processing, it is preferable to decrease the AFL thickness when using thin anode substrates. However, thicker AFL offers higher performance in electrolysis testing. The effect of AFL thickness on performance degradation rate has been studied for thin cells (~0.3 mm thickness). It was also noted that these cells have relatively high density of 5.61g/cm^3 and so new cells were fabricated with lower density while still meeting the leak rate target. This is similar to the 0.6 mm cells previously built using increased nickel oxide content in the anode substrate. One challenge in doing this is to keep the firing temperature low enough for reasonable processing. In order to do this, finer nickel oxide needs to be blended with the coarse particle size nickel oxide typically used to produce VPS anode-supported cells. A range has been found offering the optimum performance and density. Figure 2-1 shows the cell performance characteristics and power curves for one of these cells, GLOB 101993 (10 cm x 10 cm), in the temperature range of 600–800°C and up to a current density of 0.74 A/cm^2. The cell performance is slightly higher than that of previous 0.3 mm cells.

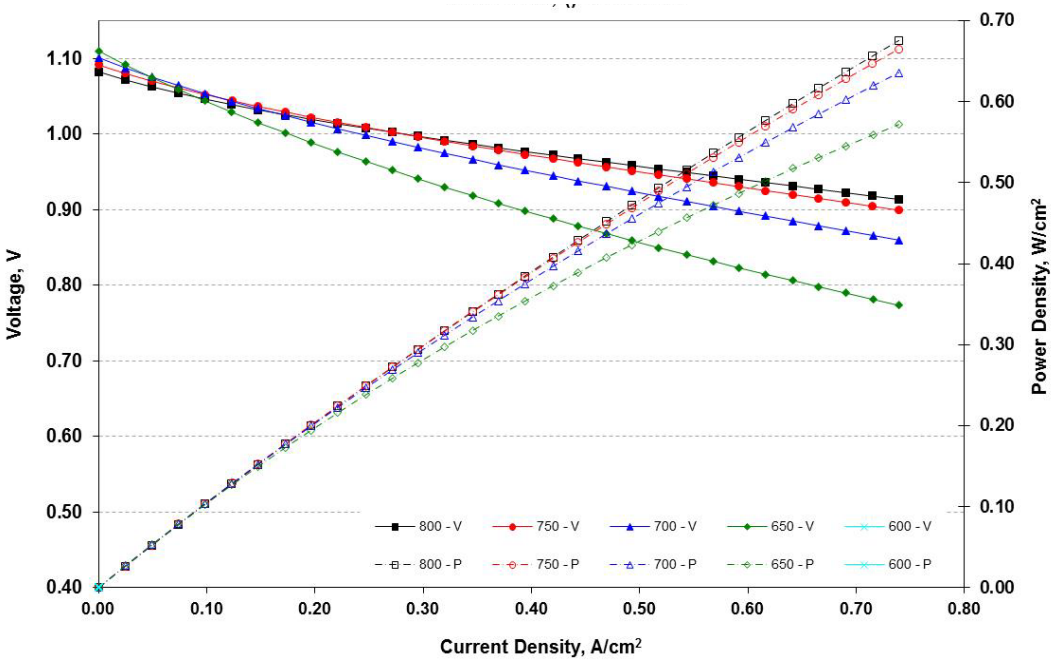

Figure 2-1 Performance Characteristics and Power curves for Thin Cell GLOB 101993 (in temperature range 600-800°C)

Figure 2-2 shows the cell performance at 40.5 A (0.5 A/cm^2) and 25% air utilization (Ua) during 2-hour steady-state holds with fuel utilizations (Uf) of 50, 60, 70, 80, 85 and 90%. Cell voltages are remarkably high at high fuel utilization, based on the significantly higher porosity of the reduced anode (the cell has 65% w/w NiO in the anode substrate compared with the usual 57% w/w). The plot shows the performance before (TC0) and after (TC1) thermal cycle. This cell with lower density anode showed higher Uf performance than previous tests. The cell voltage dropped below 0.6 V limit at 95% Uf.

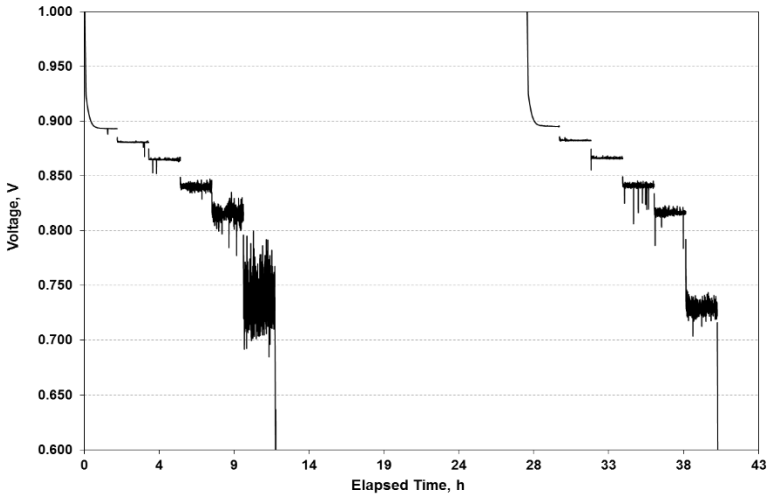

Figure 2-2 Performance of Thin Cell GLOB 101993 at 0.5 A/cm^2 (25% Ua) During Constant Fuel Utilization Holds at 50, 60, 70, 80, 85 and 90% Before and After Thermal Cycle

It was decided to examine the performance at high current density since previous tests had failed due to diffusional limitations (thought to be on the anode side).

Figure 2-3 presents the cell performance characteristics and power curves for a 5 cm x 5 cm cell (built for testing at high current density) in the temperature range of 600 to 800°C showing peak power density of 2.34 W/cm^2 at 4.6 A/cm^2 and 800°C. This is the highest power density recorded at this temperature at Versa Power Systems due to no noticeable diffusional overpotential loss. This is a significant technical development and will contribute to the baseline of next generation TSC4 cell technology.

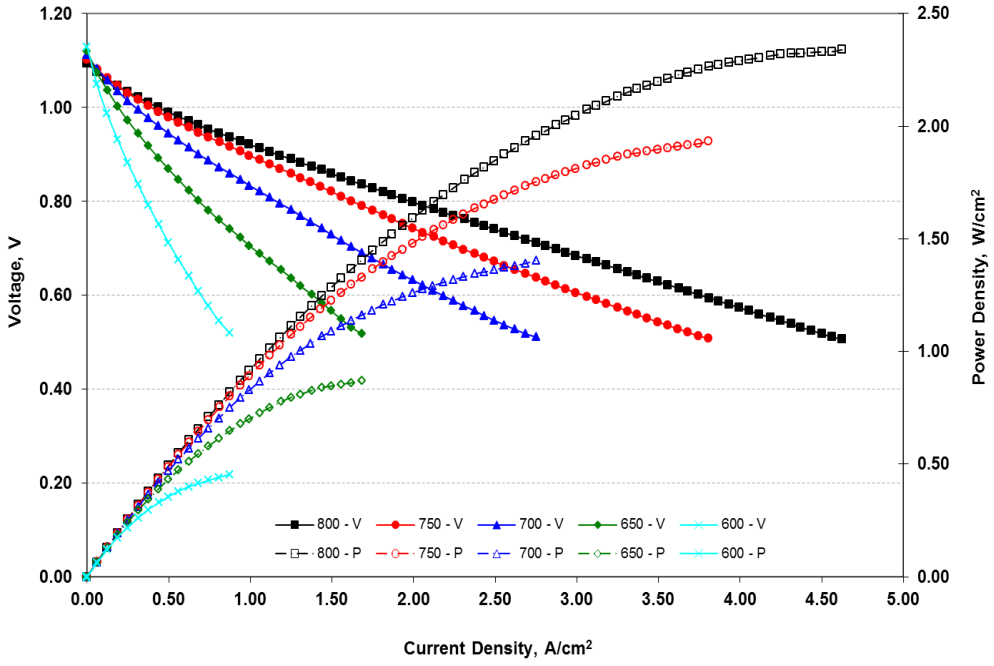

Figure 2-3. Performance Characteristics and Power curves for Thin Cell GLOB 5111 (in temperature range 600-800°C)

Another 10 cm x 10 cm cell was prepared with this same composition and 286 µm thickness and long-term testing was initiated. Figure 2-4 shows the power curves indicating good performance.

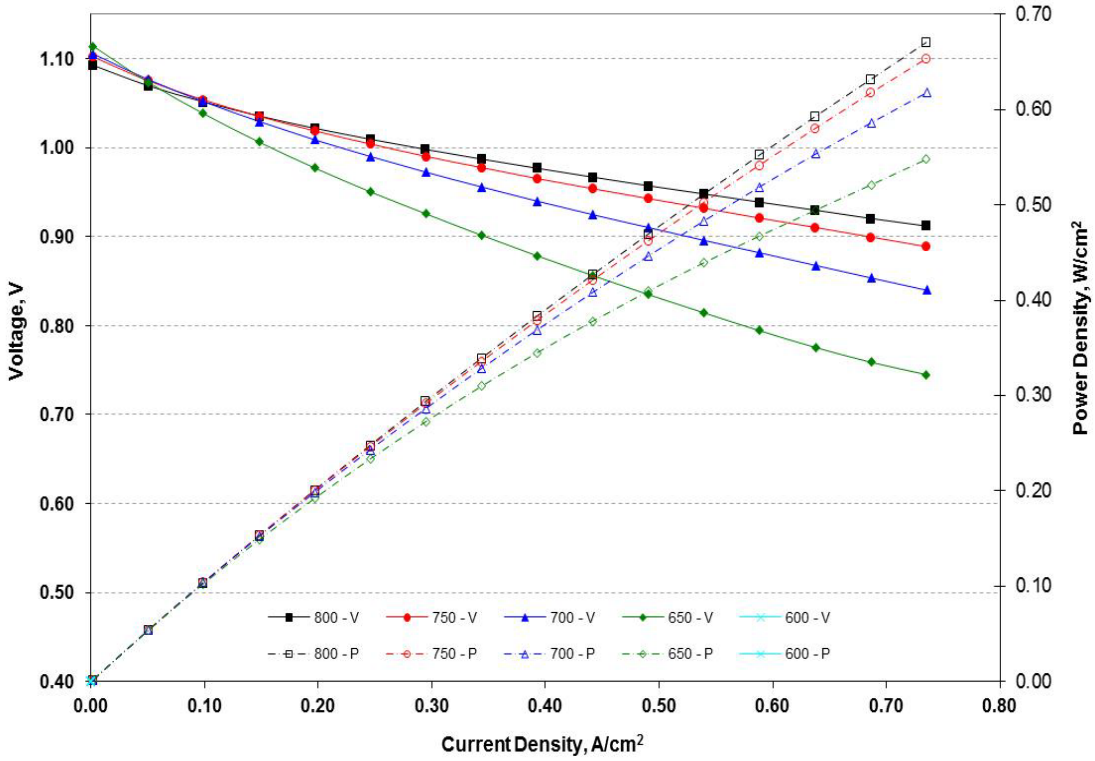

Figure 2-4. Performance Characteristics and Power curves for thin cell (286 µm, 5.17 g/cm^3) GLOB 101991 (in temperature range 600-800°C)

Tests to increase cell shrinkage at lower firing temperatures allowing production of dense electrolytes (along with lower density anodes) were completed. This was achieved by blending nickel oxide of different particle sizes for the anode substrate. Cells containing 60 and 65% w/w nickel oxide in the anode substrate were prepared with 10, 30, and 50% finer particle size nickel oxide substituted for the coarser particle size nickel oxide (six different cell types in total). These cells have been tested. The formulation selected for scale-up trials and long-term degradation study is 65% NiO with 10% finer particle size nickel oxide.

Figure 2-5 shows performance during the steady-state hold. The cell test has demonstrated a degradation rate of 0.21%/1000 hours (1.9 mV/1,000 hours) over 3070 hours, exceeding milestone 3 (Id) requirements.

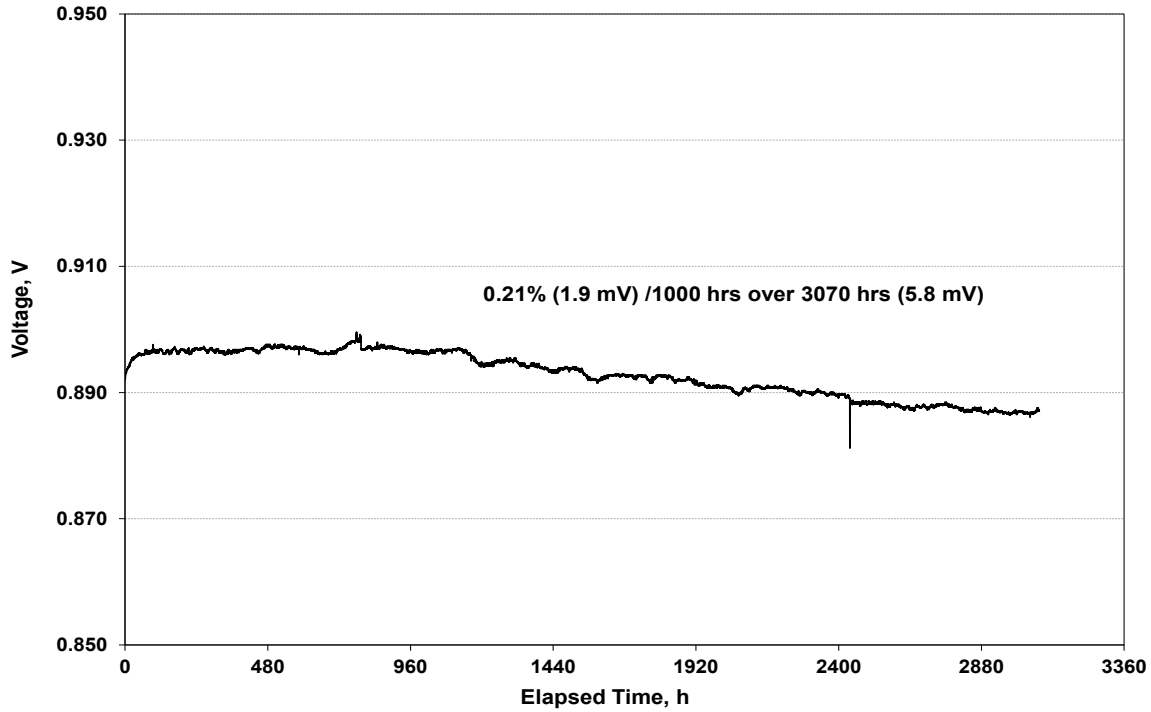

Figure 2-5. Steady State Performance of Thin Cell (286 µm, 5.17g/cm^3 density) GLOB 101991 at 0.5 A/cm^2, 50% Uf (hydrogen + 3% water) and 25% Uo (dry air)

Continued work to lower the sintering temperature of cells to less than 1,300°C. Seven tape formulations were prepared, and cells fired at 1,295°C followed by standard cell QC. The formulations that passed the standard cell QC were then electrochemically tested.

Cells were produced from all seven formulations with a 1,295°C firing temperature. Of these, two formulations (#5 and #7) showed the most promising initial QC (quality control) characteristics. Single cell tests have been initiated. The cell thickness was also reduced to 300 micron (nominal). Figure 2-6 and Figure 2-7 show the power curves and cell performance during a short term hold, respectively, for the cell evaluating Formulation 5. Figure 2-8 and Figure 2-9 show the results for the cell evaluating Formulation 7.

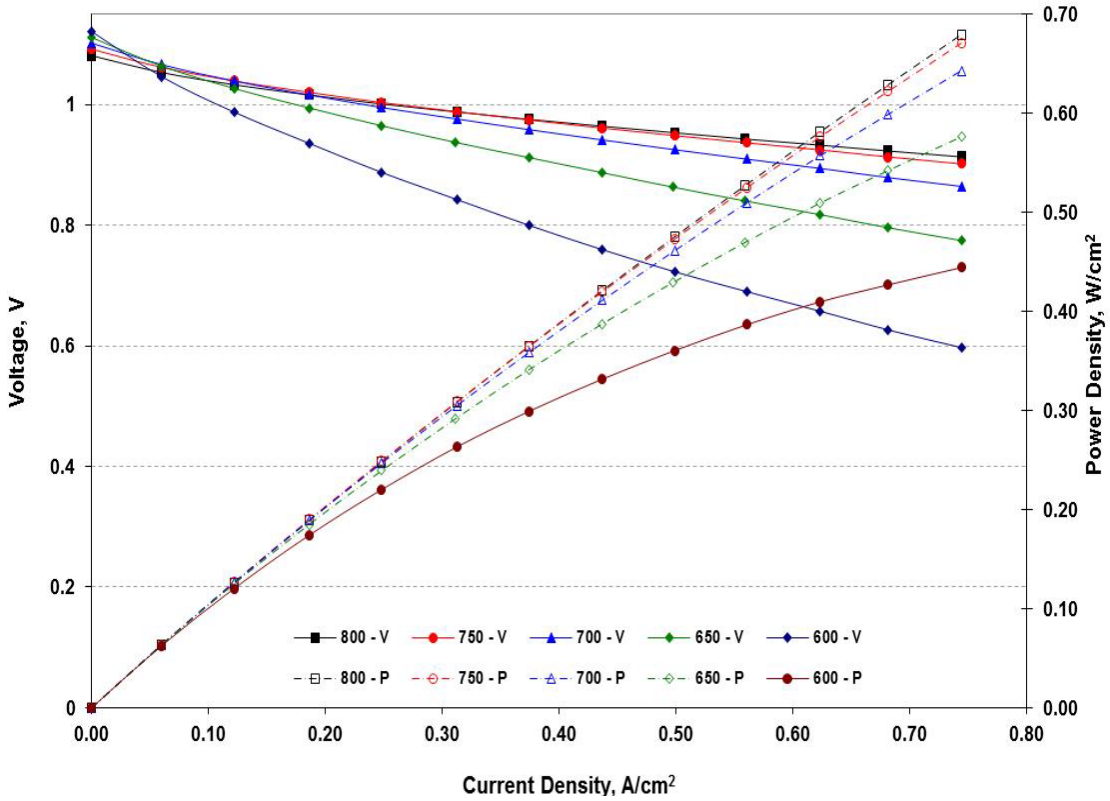

Figure 2-6 Power Curves of Cell Evaluating Formulation 5 in Operating Temperature Range of 600 – 800°C

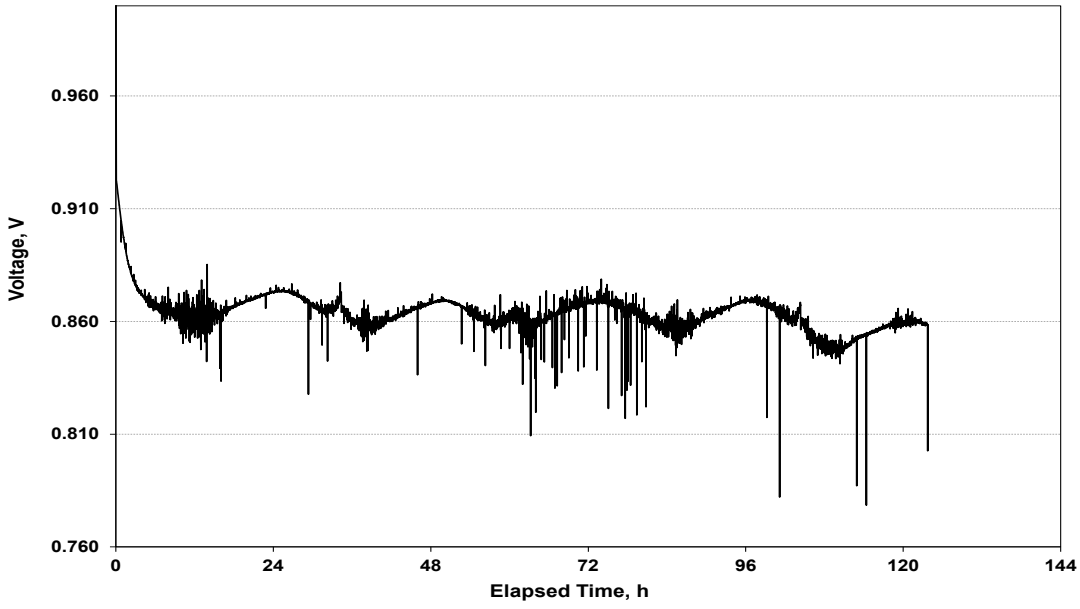

Figure 2-7 Short-term Hold (at 750 °C) Performance of Cell Evaluating Formulation 5

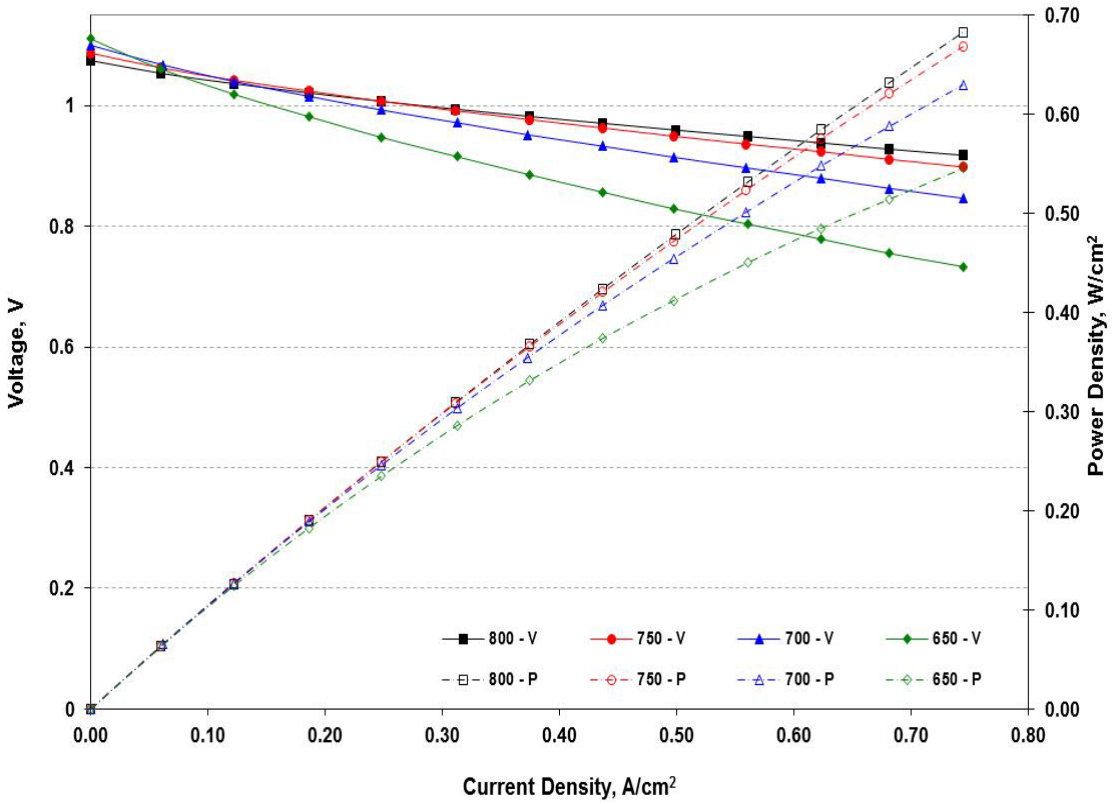

Figure 2-8 Power Curves of Cell Evaluating Formulation 7 in Operating Temperature Range of 600 – 800°C

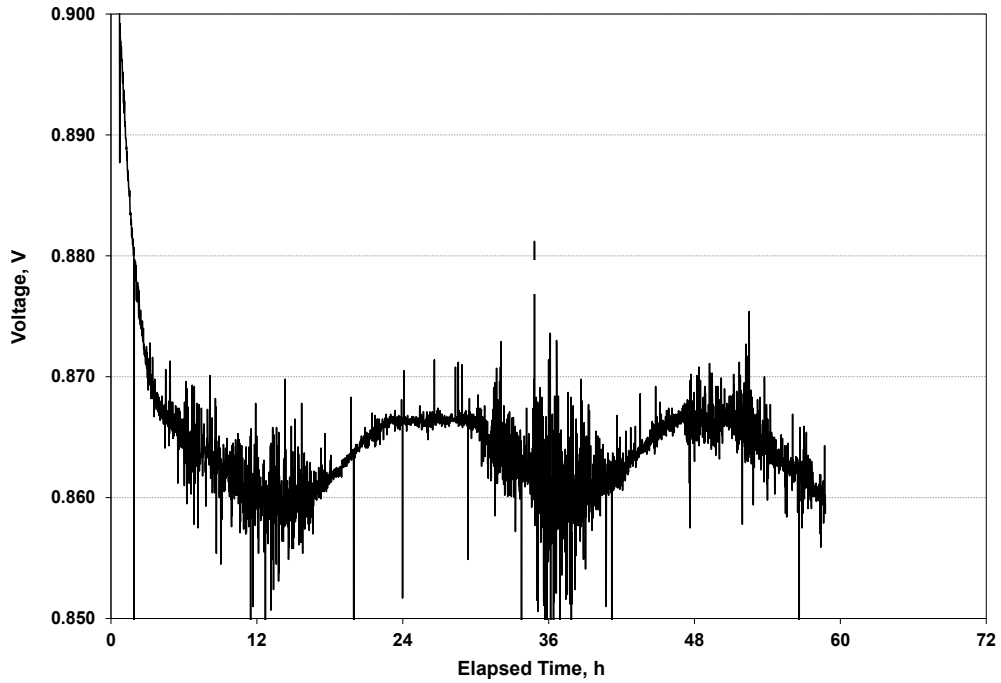

Figure 2-9 Short-term Hold (at 750 °C) Performance of Cell Evaluating Formulation 7

Both formulations showed performance that is interesting, though there is room for improvement. As reported previously, cells fired at higher temperatures have performance exceeding 880 mV at the short-term hold conditions. Based on observations and results for the initial seven formulations, additional 16 formulations of interest have been identified and new formulations used to produce cells, fired at both 1,250°C and 1,295°C. All that meet initial QC requirements (successfully sintered, appropriate density, acceptable leak rate) were electrochemically characterized.

From the cells produced using 1,295°C firing temperature, cells with Formulations #5 and #7 had shown the most promising initial QC characteristics. Single cell tests with both formulations have shown performance that is better than the current baseline cell technology. Figure 2-10 and Figure 2-11 show the power curves and cell performance during long term hold, respectively, for a repeat single cell test of Formulation #5 in a long term test facility.

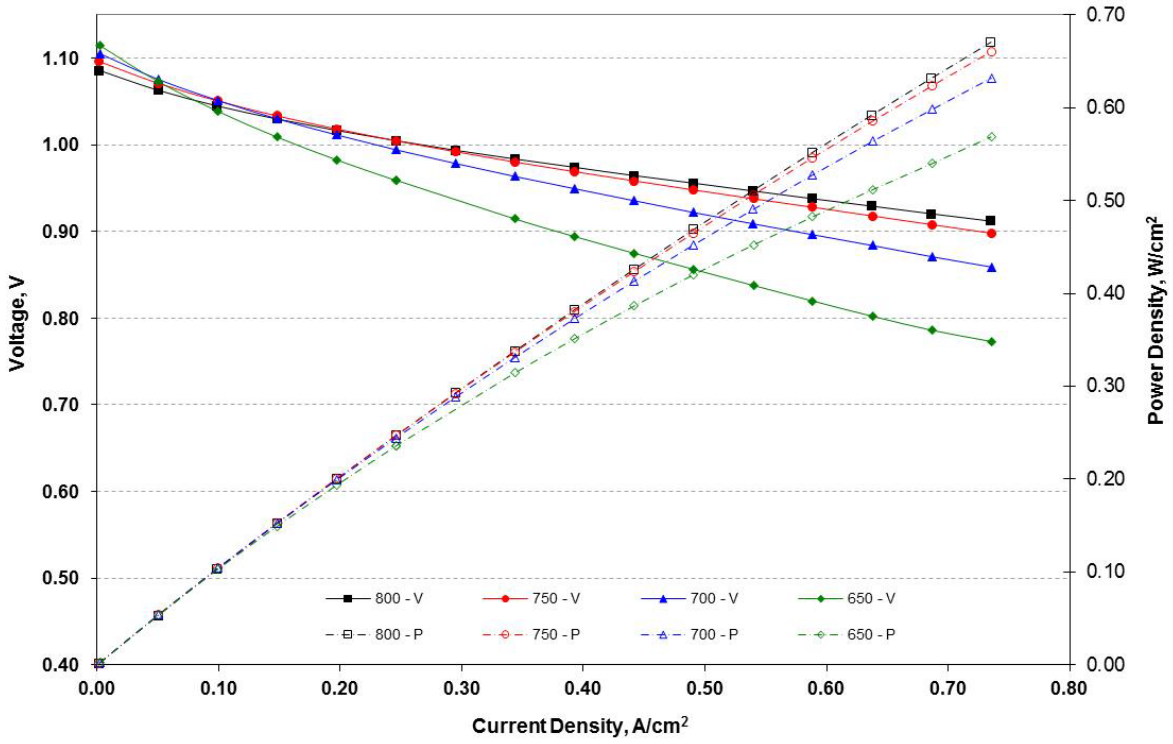

Figure 2-10 Power Curves for Cell Evaluating Formulation #5, 2nd cell (in operating temperature range of 650 - 800°C)

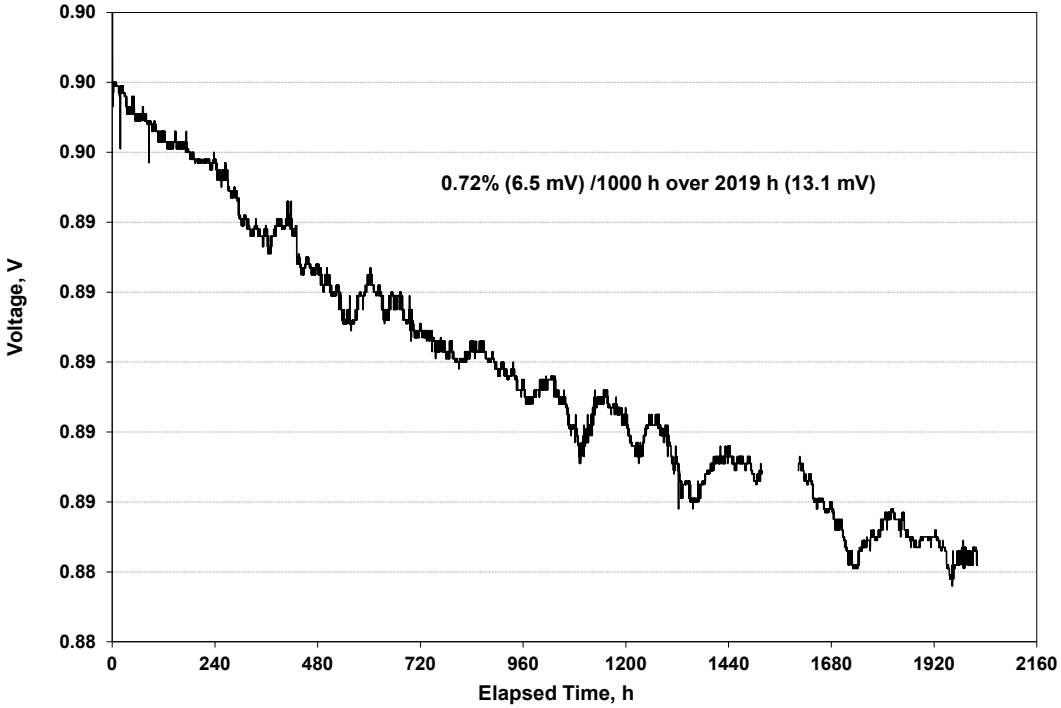

Figure 2-11 Performance of Cell Formulation #5, 2nd cell Long-Term Steady-State Test (at 750°C)

Table 2-1 summarizes QC measurements for the cells prepared using various formulations. All these cells were sintered at 1,295°C. Cell densities and leak rates were measured for an early evaluation of the cell formulations.

A cell made with Formulation #20 showed good density and low leak rate. Figure 2-12 shows power curves of the cell and Figure 2-13 shows a steady-state hold performance over 1000 hours. The cell demonstrated acceptable electrochemical performance, but the performance degradation rate is high. Figure 2-14 shows power curves of the cell with Formulation #24 and Figure 2-15 shows a short steady-state hold performance for the cell. This formulation features the highest level of sintering additives among all 24 formulations. As such, the test results will show the effect of additives on degradation rate.

At the current stage of developing new anode formulations, one key milestone in Q3, 2016 has been met with cell materials development as well as electrochemical testing. At least 11 new anode formulations show the promising results of co-sintering at less than $1,300^0$C. Three of these (Formulation #s 5, 20 and 24) were electrochemically tested in cells with anode thickness of ~ 300 μm. All showed acceptable electrochemical performance. Two have demonstrated stable performance over 1000 hours of steady-state testing, while the third has accumulated 330 hours of test time so far. All three continue to be tested. Cells with these anode formulations could be further scaled up for incorporation within the technology stacks.

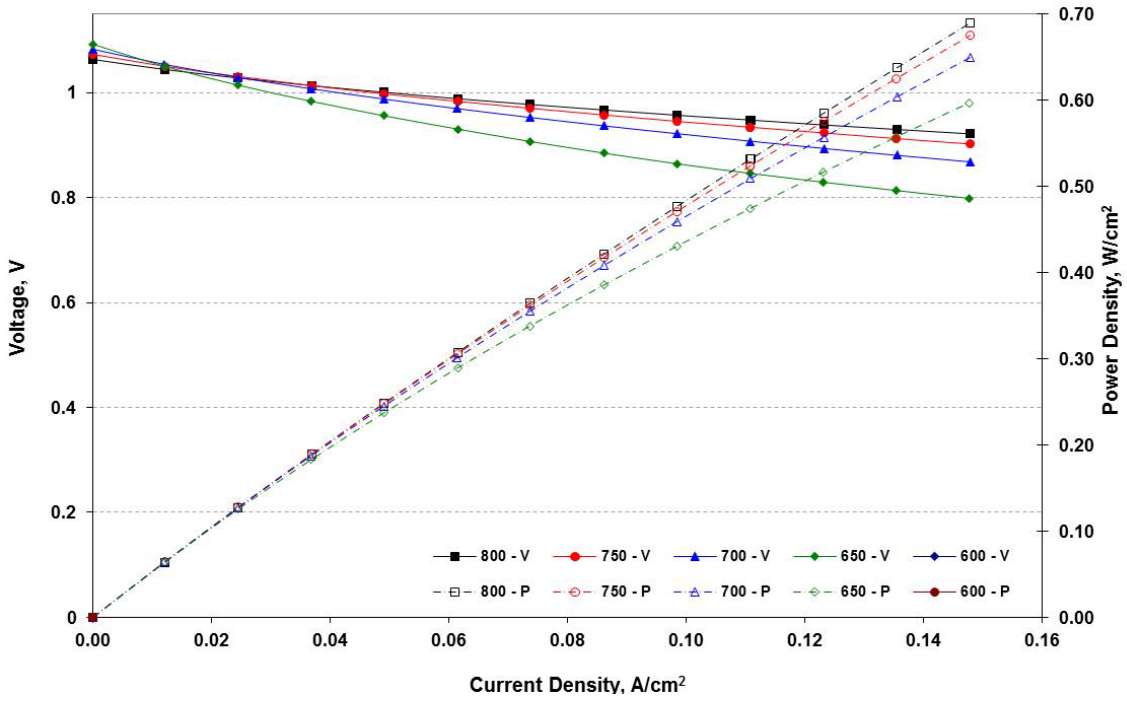

Figure 2-12 Power Curves for Cell Made Using Formulation #20 (in operating temperature range of 600 - 800°C)

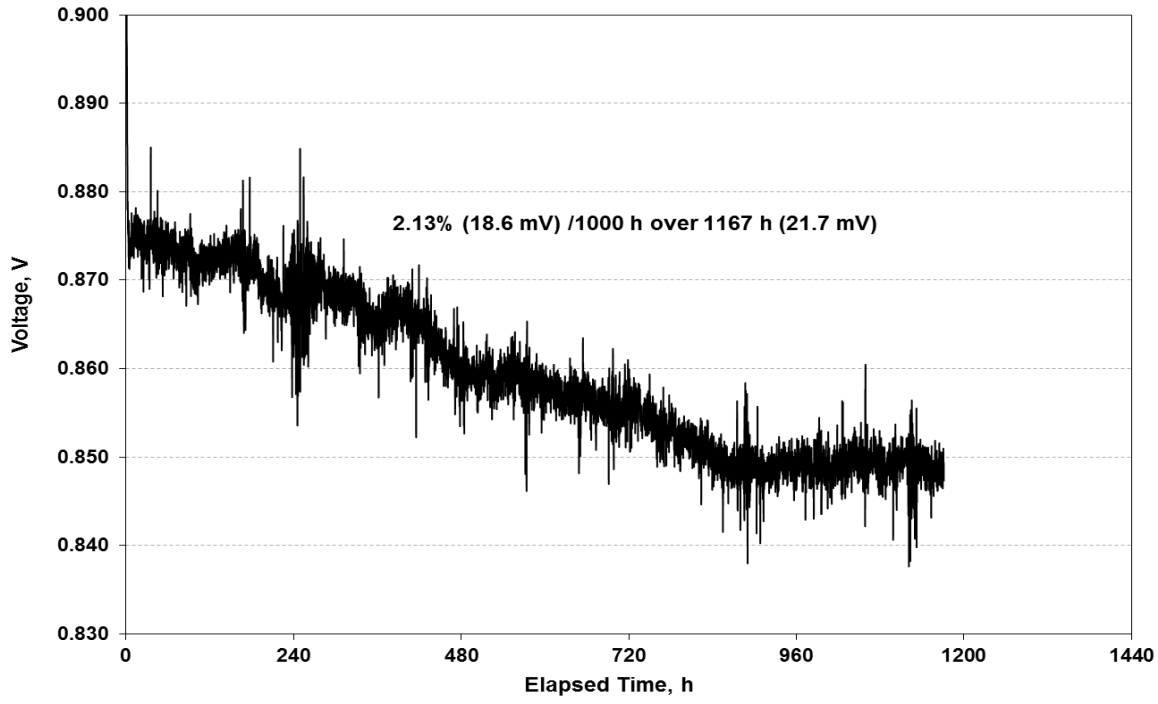

Figure 2-13 Performance of Cell Made Using Formulation #20 During Steady-state hold

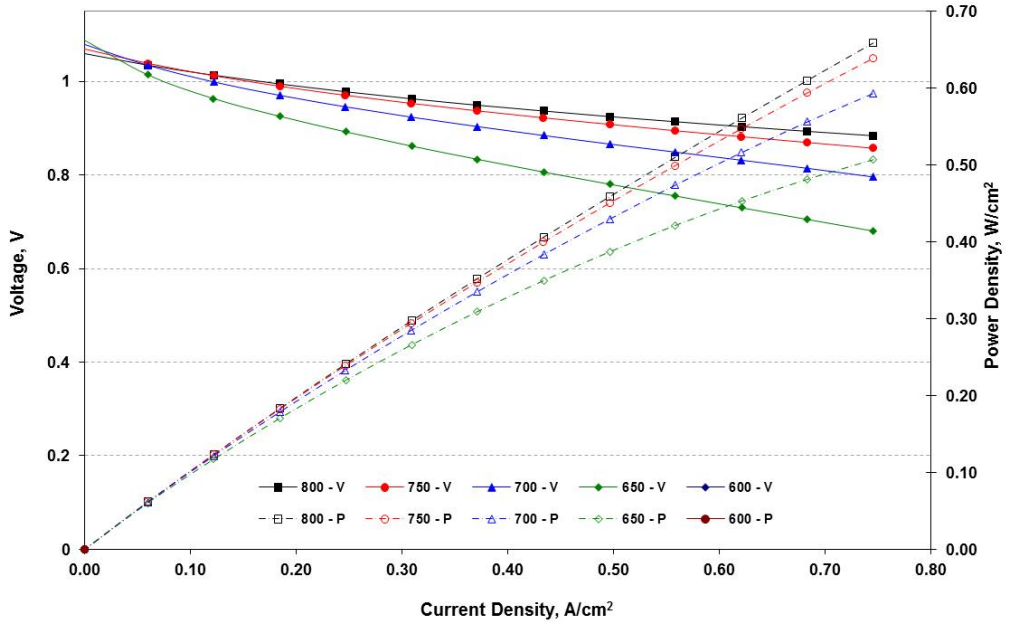

Figure 2-14 Power Curves for Cell Made Using Formulation #24 (in operating temperature range of 600 - 800°C)

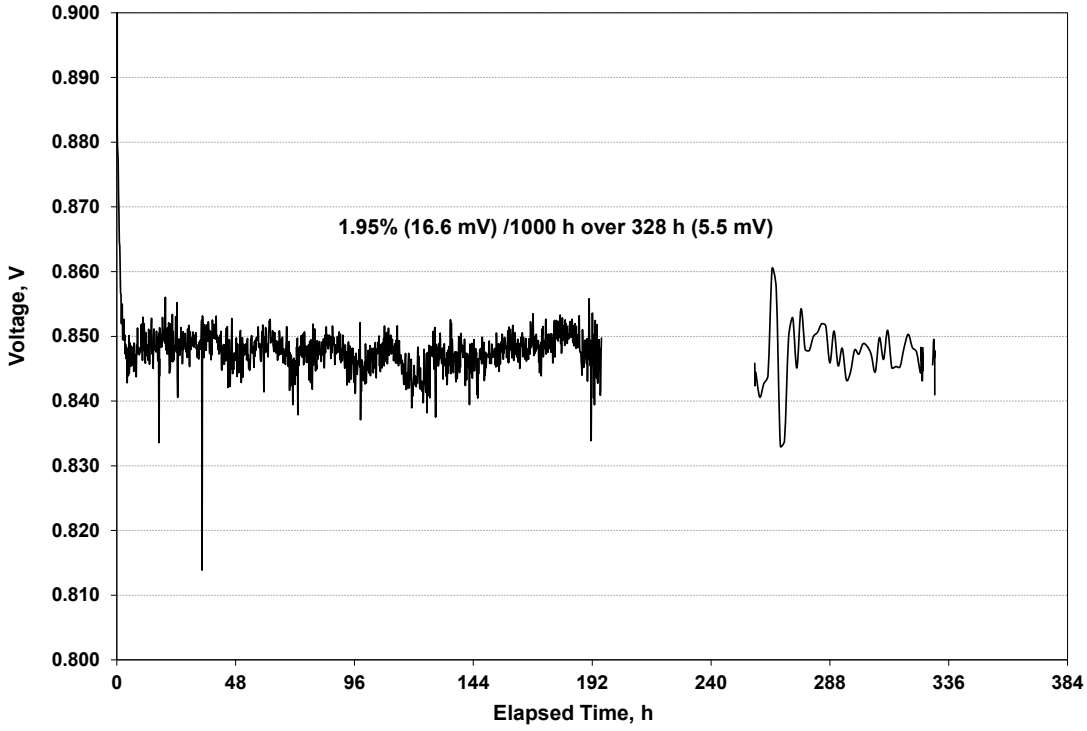

Figure 2-15 Performance of Cell Made Using Formulation #24 During Steady-state hold

Cells 1-7, 20 and 24 have been electrochemically tested and results discussed with cells 5 and 7 showing the most promise. Formulations 12, 13, and 21-23 have also been tested. Each cell ran power curves to 0.74 A/cm^2 at 800, 750, 700 and 650°C followed by a short steady-state hold at 0.5 A/cm^2 and 750°C to determine short-term stability. Results of the electrochemical testing are given in Figures 2-16 through 2-25.

Formulations 12 and 13 show the highest cell performance, while all cells show reasonable short-term stability.

Table 2-1 Cell QC for formulations 8-13 and 20-24 fired at 1295°C

Formulation No.	Shrinkage (%)	Thickness (um)	Density (g/cm3)	Relative Leak Rate
1	-	347	4.74	-
2	-	310	4.66	-
3	-	302	4.71	-
4	-	279	4.67	-
5	15.12	308	5.38	3
6	13.13	285	4.86	65
7	14.56	315	5.10	22
8	15.3	298	5.43	2
9	15.8	282	5.37	3
10	15.2	273	5.30	0
11	15.6	288	5.42	6
12	-	286	5.27	3
13	-	271	5.28	7
20	14.7	318	5.35	2
21	-	307	5.02	15
22	-	281	5.17	-
23	-	282	5.10	15
24	-	278	4.96	10

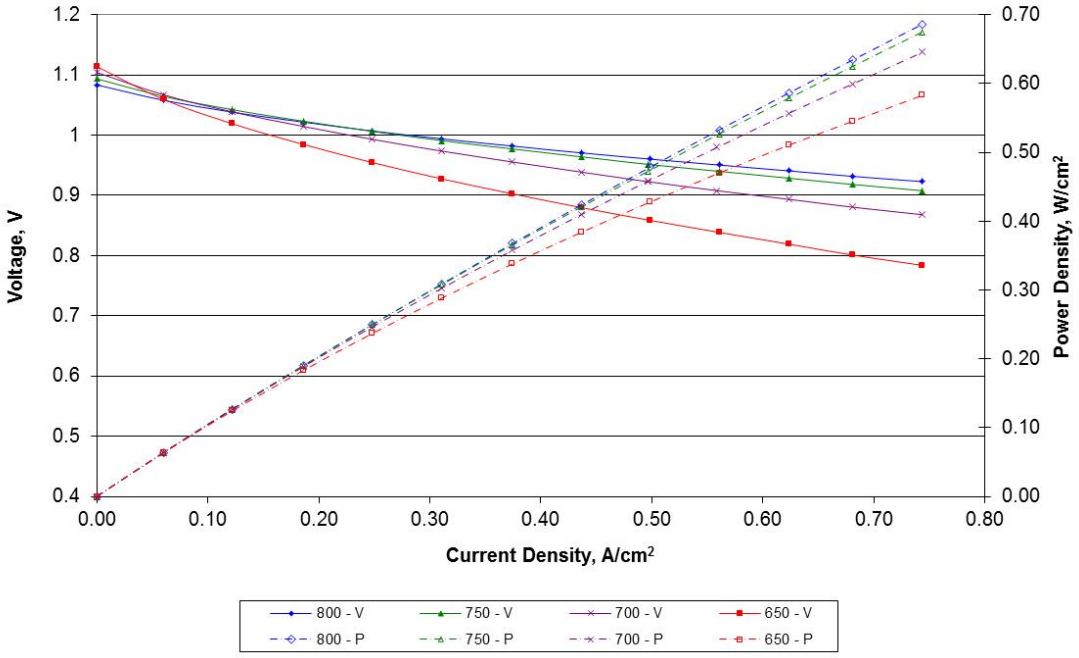

Figure 2-16 Power Curves for GLOB 5155 Cell Formulation 12 (1295°C fired)

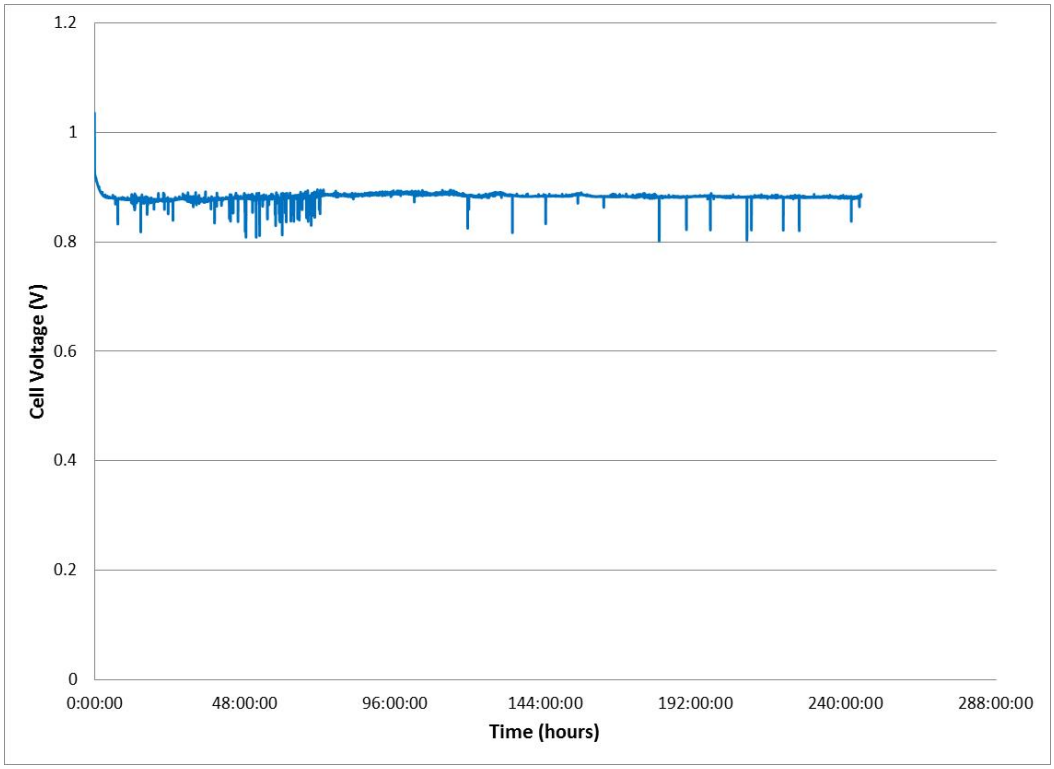

Figure 2-17 Cell Voltage against Time for GLOB 5155 Cell Formulation 12

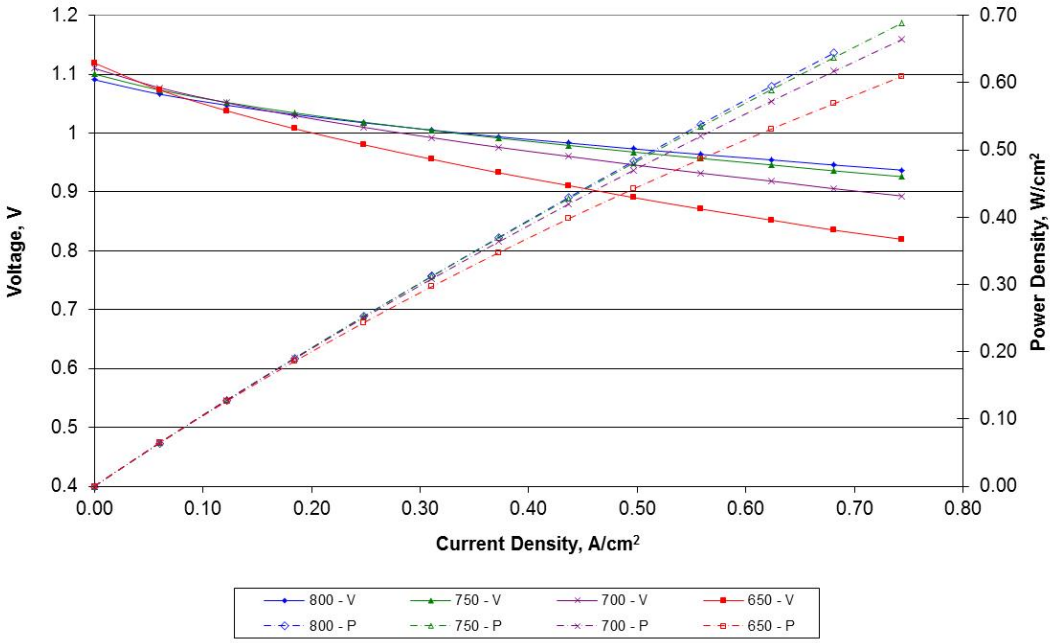

Figure 2-18 Power Curves for GLOB 5156 Cell Formulation 13 (1295°C fired)

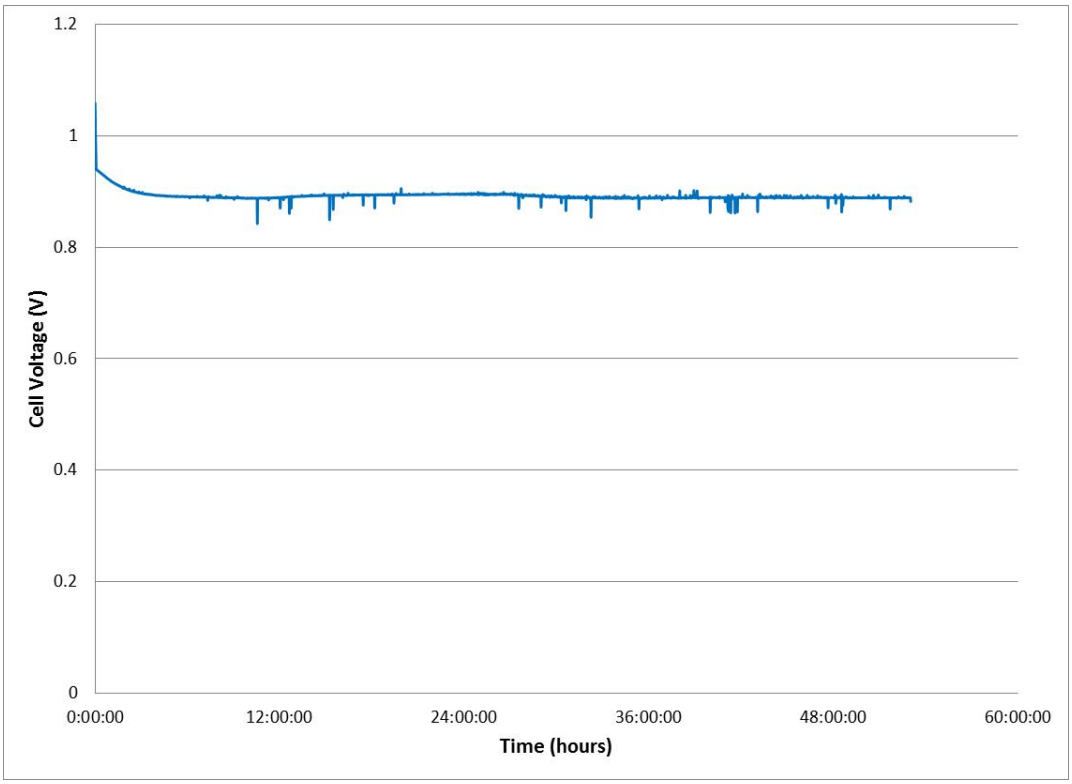

Figure 2-19 Cell Voltage against Time for GLOB 5156 Cell Formulation 13

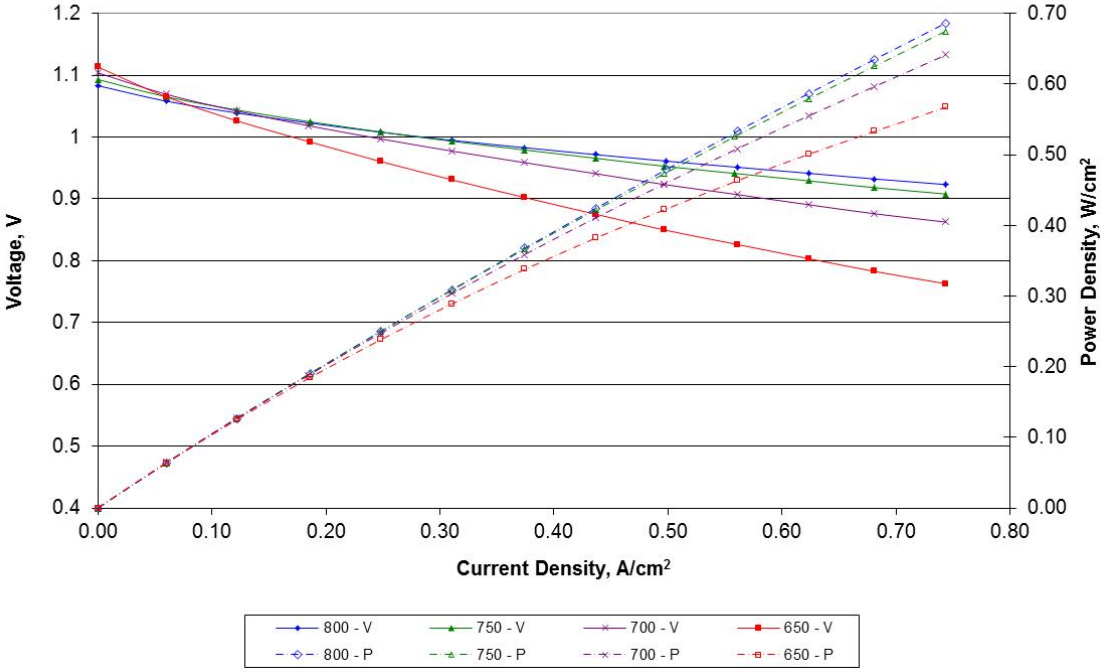

Figure 2-20 Power Curves for GLOB 5152 Cell Formulation 21 (1295°C fired)

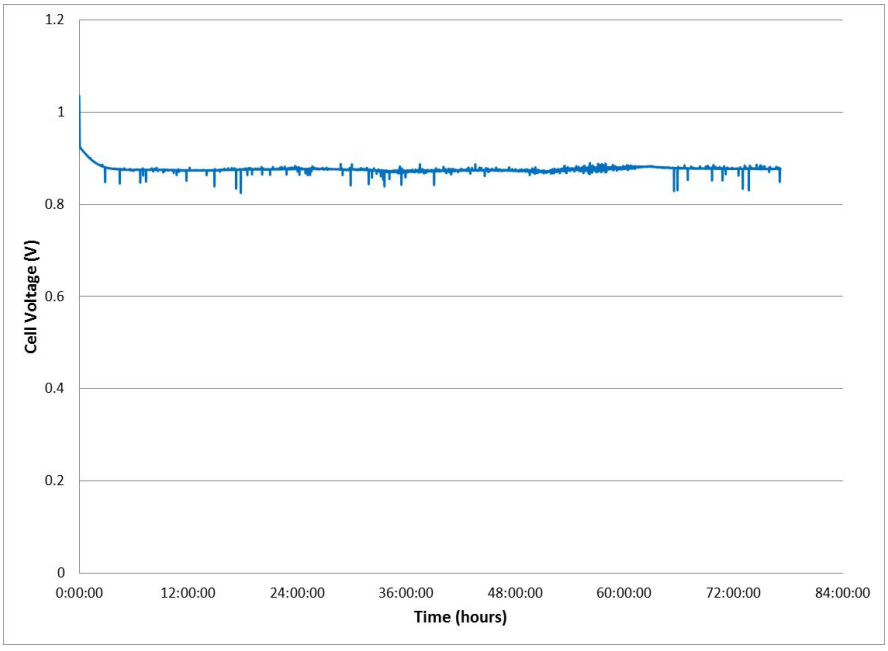

Figure 2-21 Cell Voltage against Time for GLOB 5152 Cell Formulation 21

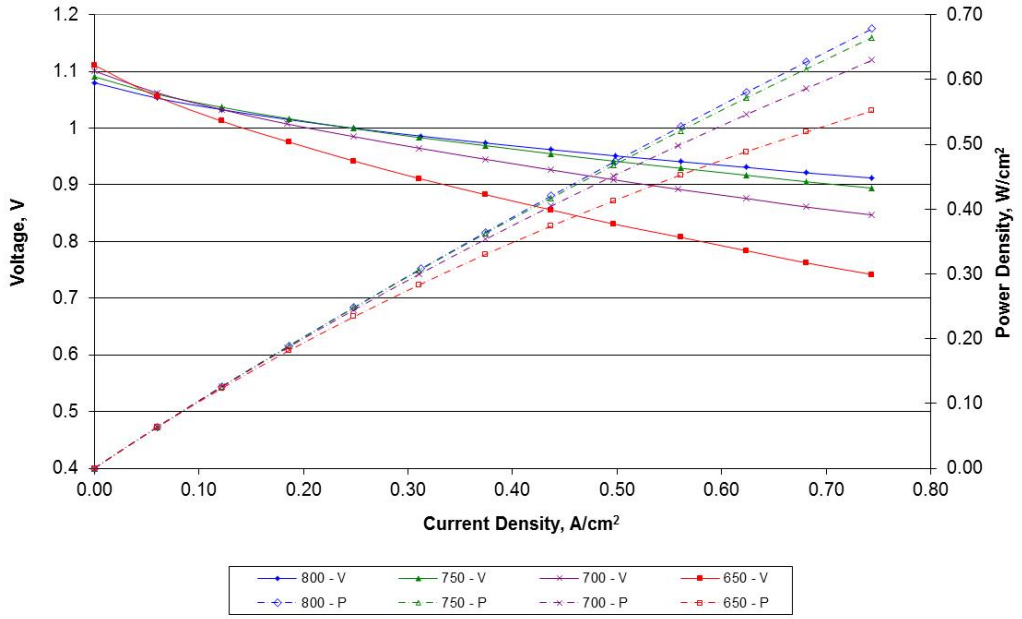

Figure 2-22 Power Curves for GLOB 5151 Cell Formulation 22 (1295°C fired)

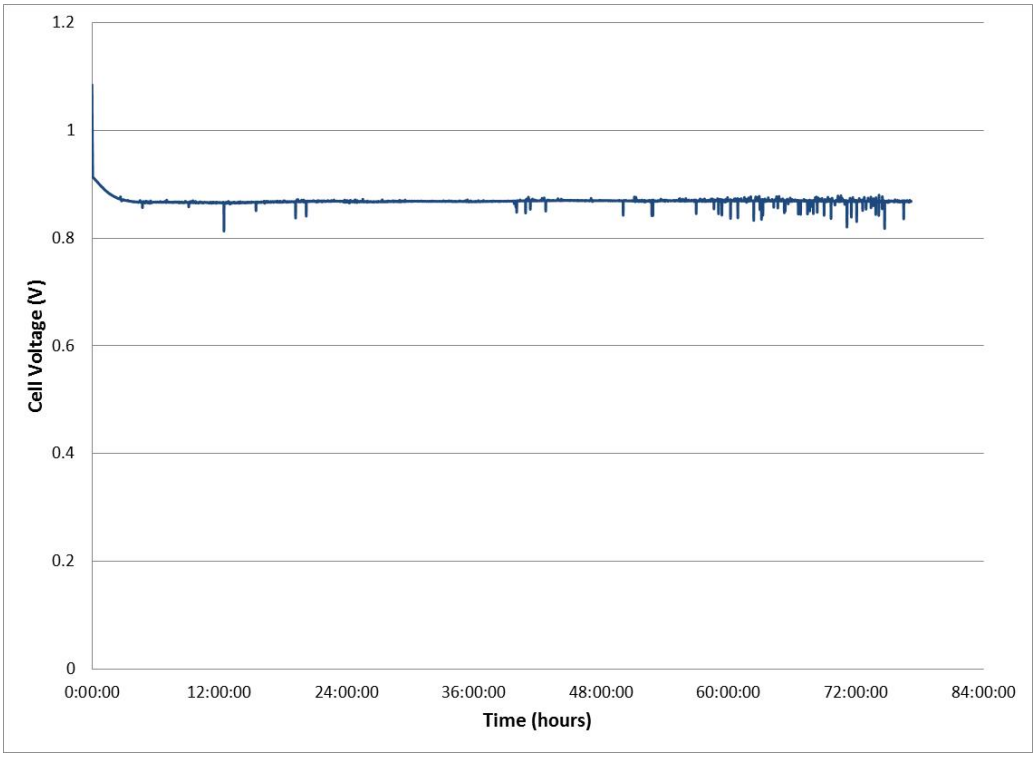

Figure 2-23 Cell Voltage against Time for GLOB 5151 Cell Formulation 22

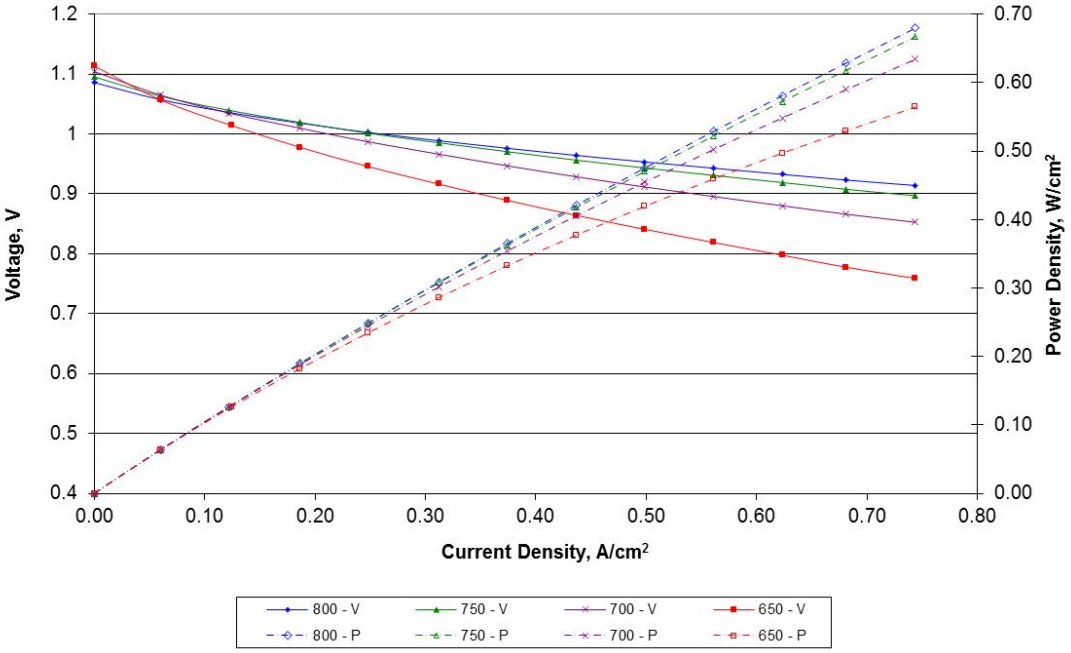

Figure 2-24 Power Curves for GLOB 5150 Cell Formulation 23 (1295°C fired)

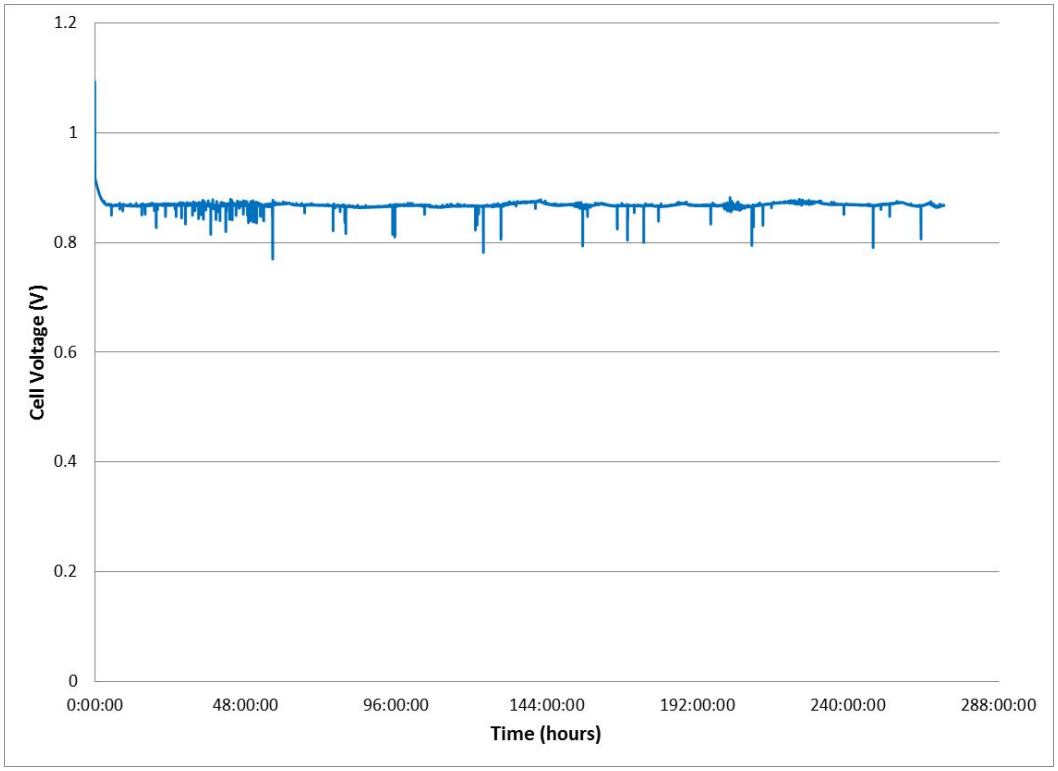

Figure 2-25 Cell Voltage against Time for GLOB 5150 Cell Formulation 23

Formulations 8-13 from Table **2-1** were also fired at an even lower temperature of 1250°C, with cell QC data summarized in Table 2-2 and Table 2-3. Of these, 4 cells fired at lower temperature of 1250°C were tested. These were formulations 9 and 11-13. Each cell ran power curves to 0.74 A/cm^2 at 800, 750, 700 and 650°C followed by a short steady-state hold at 0.5 A/cm^2 and 750°C to determine short-term stability. At that point the test was shut-down and autopsied and a new cell test installed. Longer-term testing of all of these formulations is beyond the scope of the current project.

Formulations 14-19 have low cell densities fired at 1,295°C and so were not selected for firing at 1250°C, however, formulations 20-23 were fired at 1,250°C.

Results of the electrochemical testing is given in Figures 2-26 through Figure 2-39.

Formulations 9 and 12 fired at 1,250°C show the highest cell performance with cell voltages of 848 and 817 mV respectively at 650°C and 0.74 A/cm^2. The cells also have good OCV values, 1.116 and 1.118 V respectively at 650°C with hydrogen and 3% humidity versus air indicating there may be room to further lower cell sintering temperature. However, while all cells show reasonable short-term stability, long term degradation and mechanical properties are important to study in the future to truly demonstrate feasibility for use in stacks and systems.

Table 2-2 Cell QC for formulations 8-24 fired at 1295°C

Formulation No.	Shrinkage (%)	Thickness (um)	Density (g/cm3)	Leak Rate
8	15.3	298	5.43	2
9	15.8	282	5.37	3
10	15.2	273	5.30	0
11	15.6	288	5.42	6
12	-	286	5.27	3
13	-	271	5.28	7
14	-	312	4.73	-
15	-	357	4.79	-
16	-	314	4.94	-
17	-	321	5.032	-
18	-	320	4.80	-
19	-	329	4.93	-
20	14.7	318	5.35	2
21	-	307	5.02	15
22	-	281	5.17	-
23	-	282	5.10	15
24	-	278	4.96	10

Table 2-3 Cell QC for formulations 8-13 fired at 1250°C

Formulation No.	Shrinkage (%)	Thickness (um)	Density (g/cm3)	Leak Rate
8	-	310	4.68	-
9	-	298	4.76	-
10	-	290	4.67	-
11	-	292	4.92	-
12	-	311	4.74	-
13	-	323	4.95	-

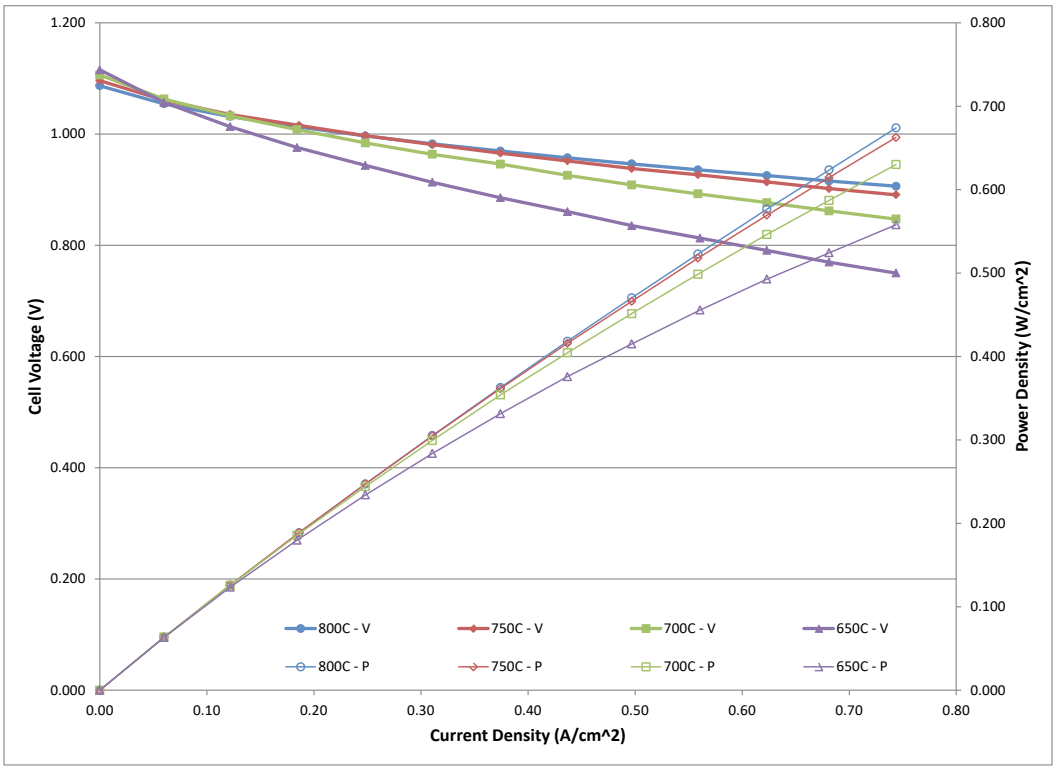

Figure 2-26 Power Curves for GLOB 5157 Cell Formulation 11 (1295°C fired)

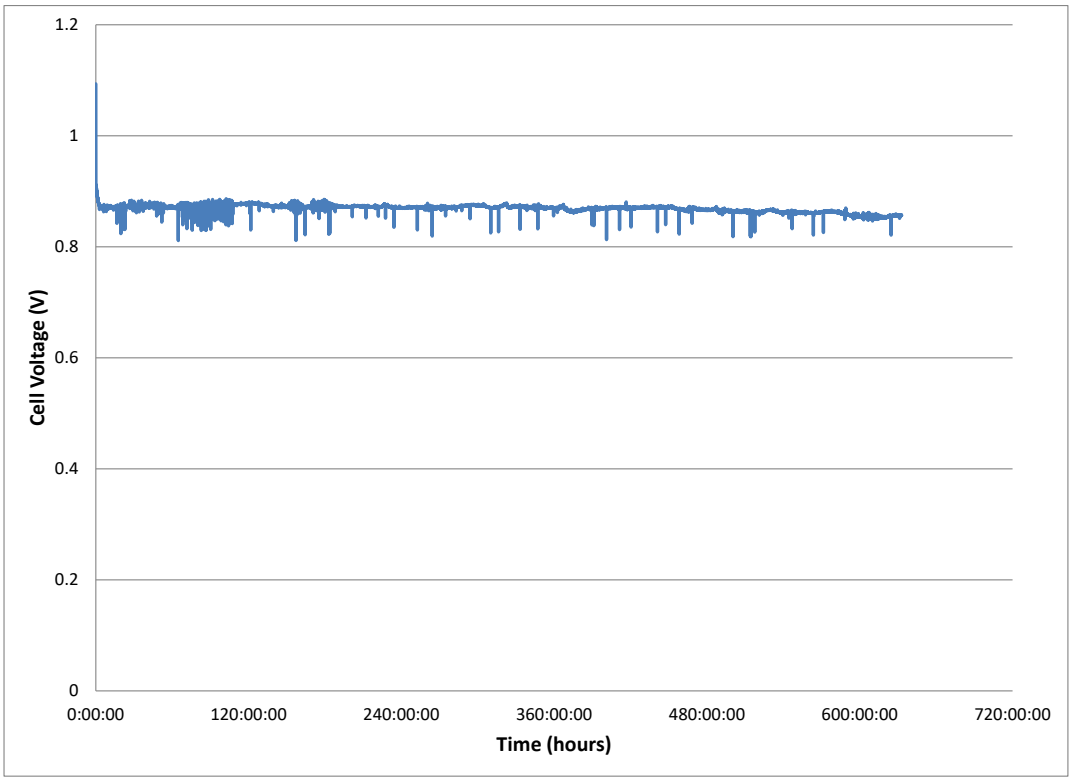

Figure 2-27 Cell Voltage against Time for GLOB 5157 Cell Formulation 11

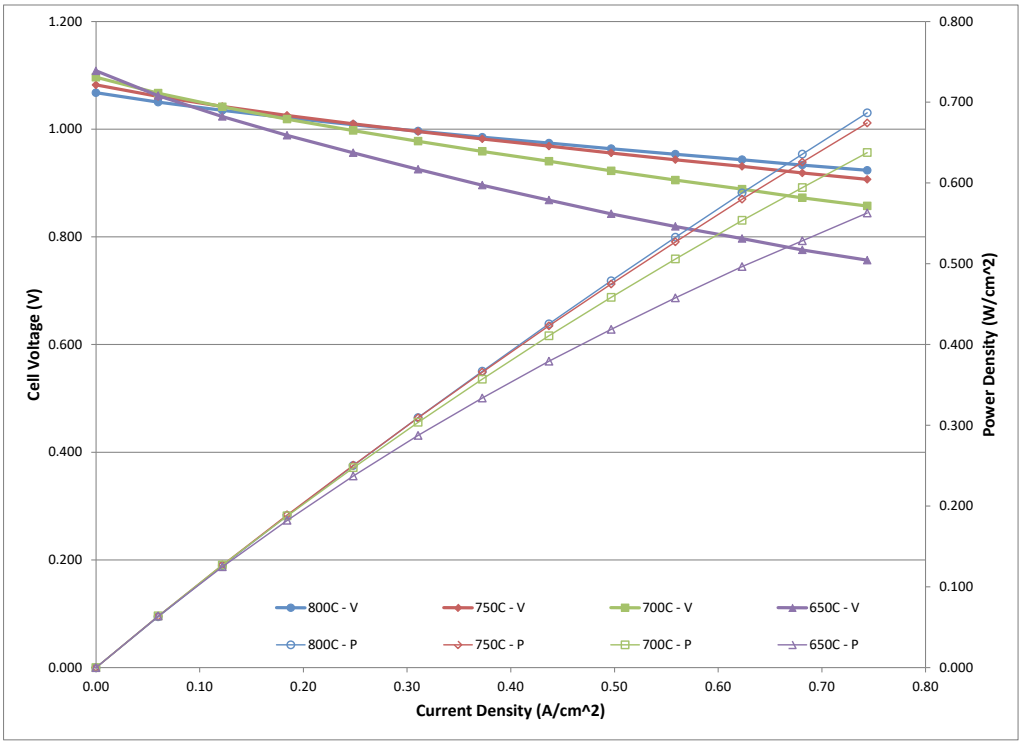

Figure 2-28 Power Curves for GLOB 5166 Cell Formulation 17 (1295°C fired)

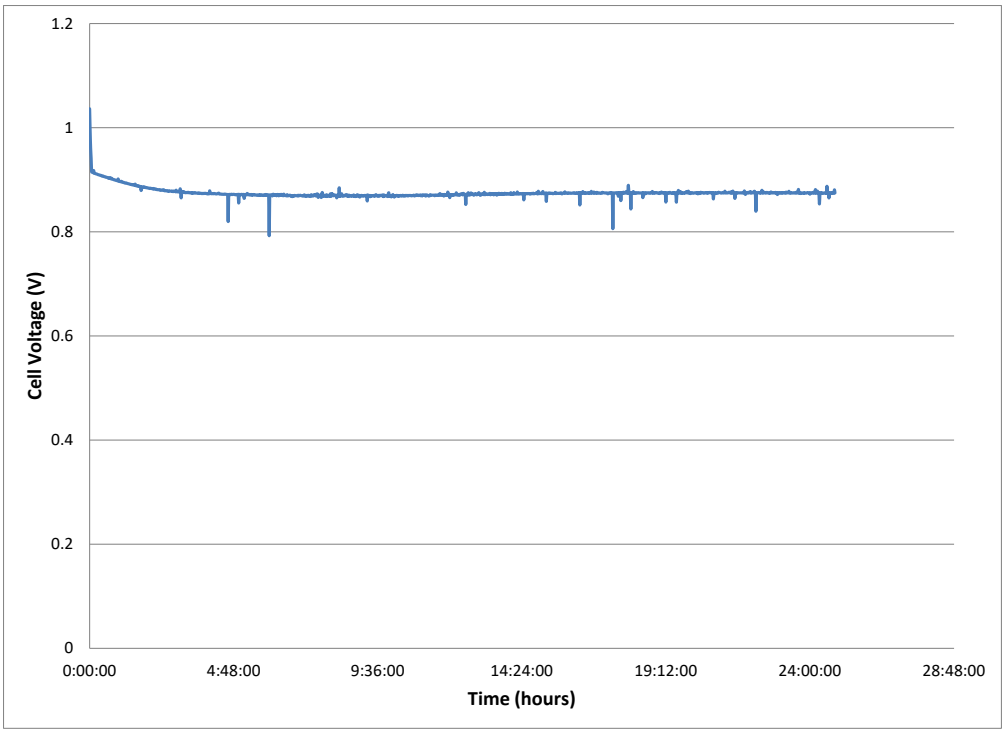

Figure 2-29 Cell Voltage against Time for GLOB 5166 Cell Formulation 17

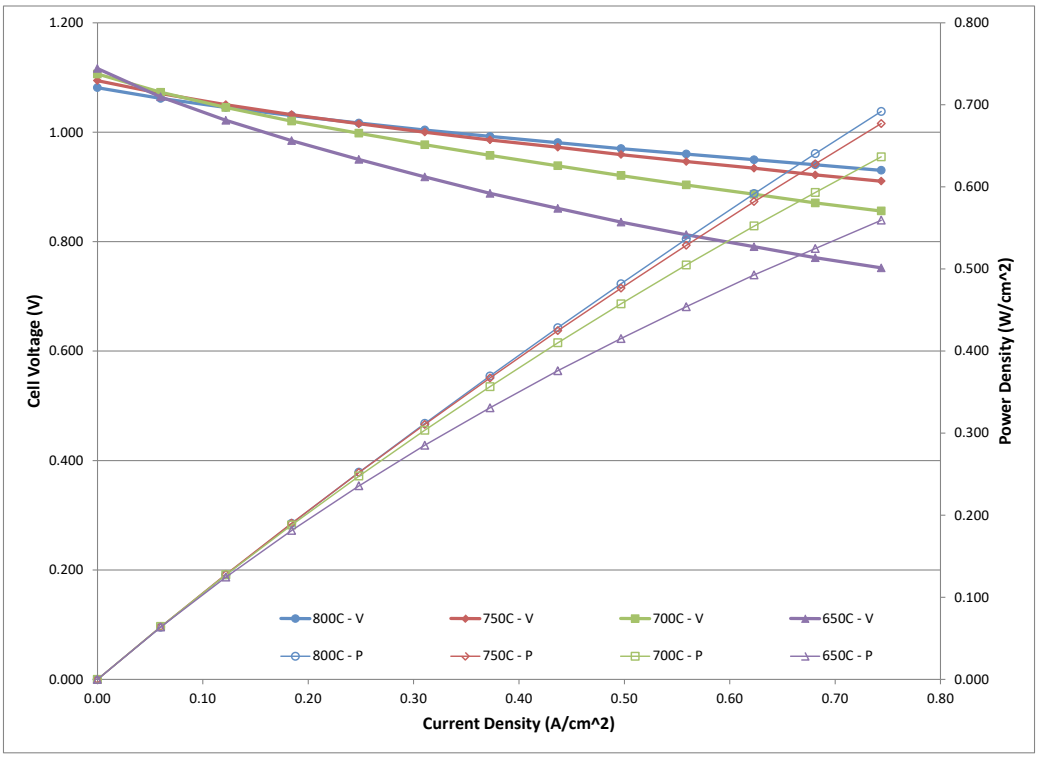

Figure 2-30 Power Curves for GLOB 5167 Cell Formulation 19 (1295°C fired)

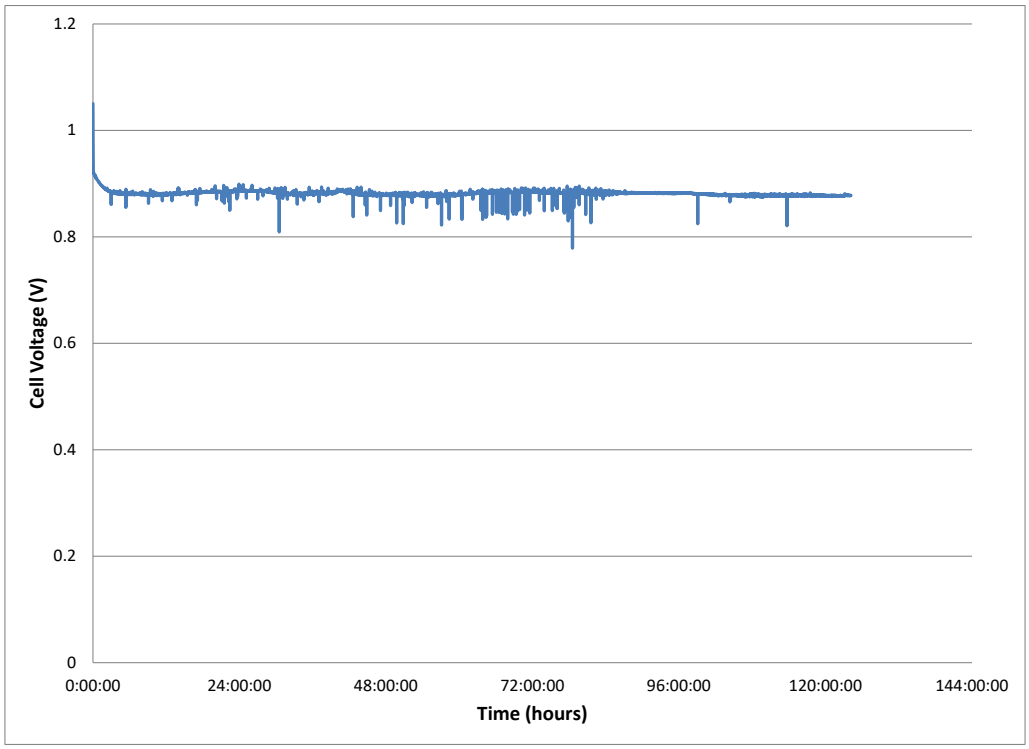

Figure 2-31 Cell Voltage against Time for GLOB 5167 Cell Formulation 19

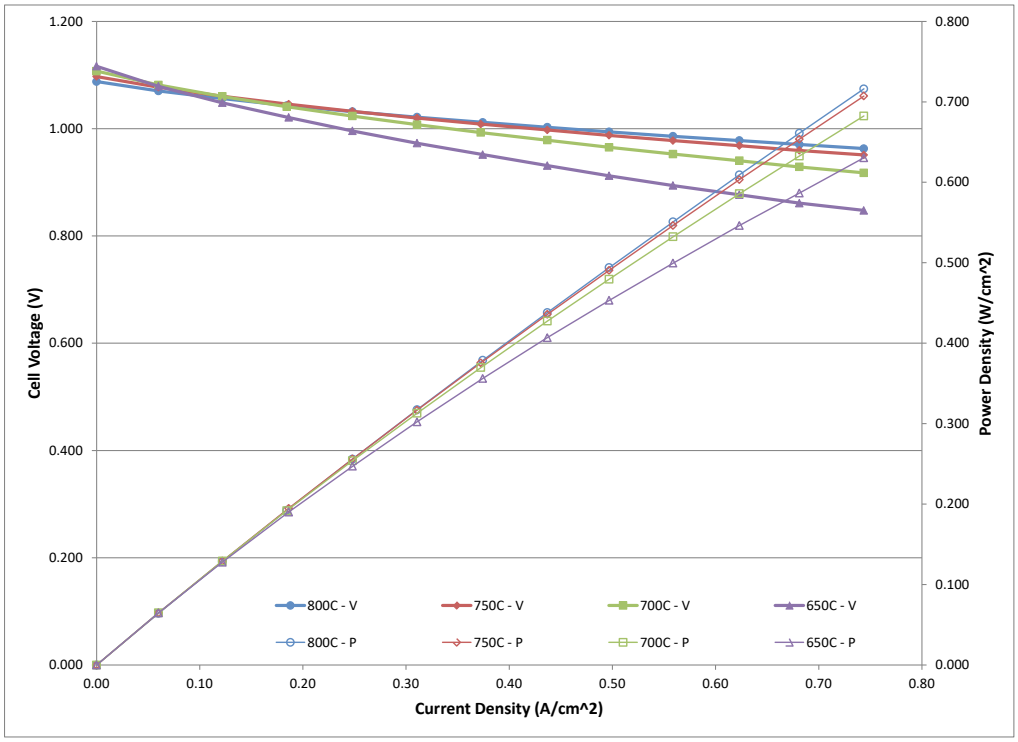

Figure 2-32 Power Curves for GLOB 5164 Cell Formulation 9 (1250°C fired)

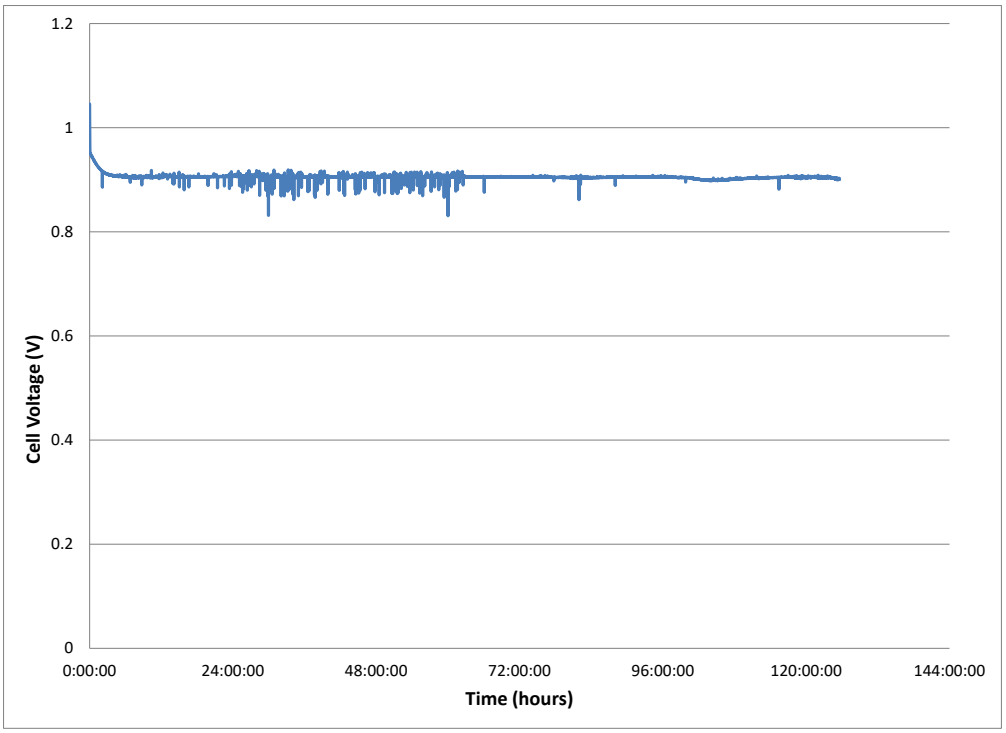

Figure 2-33 Cell Voltage against Time for GLOB 5164 Cell Formulation 9

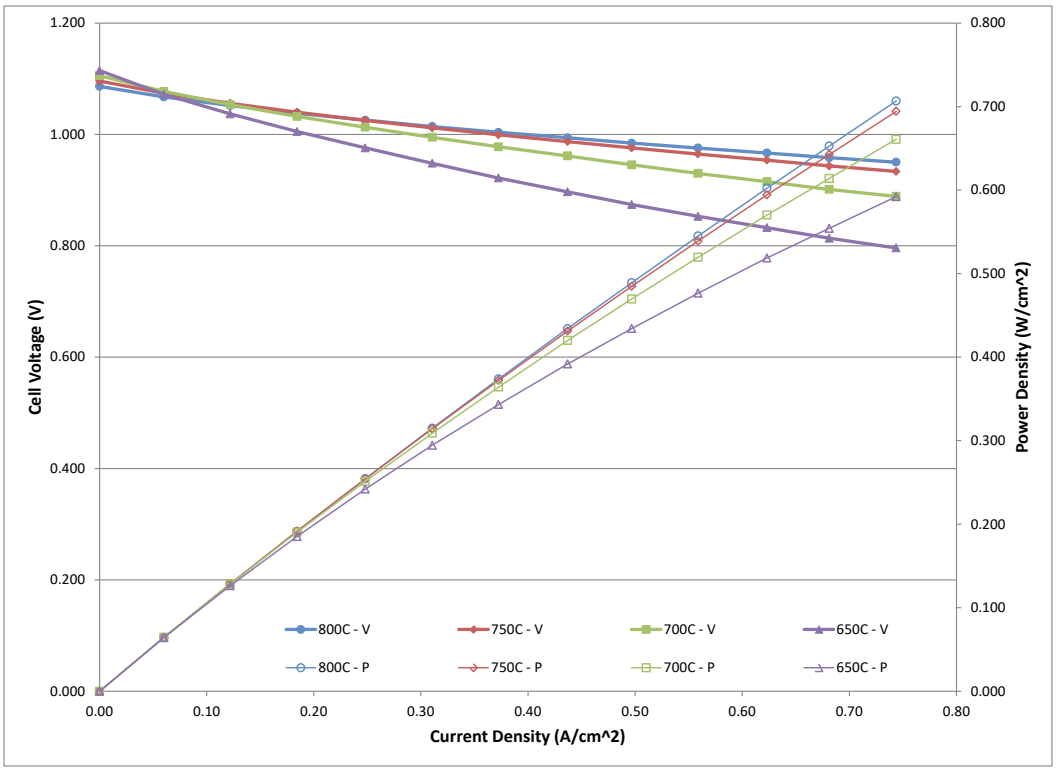

Figure 2-34 Power Curves for GLOB 5162 Cell Formulation 11 (1250°C fired)

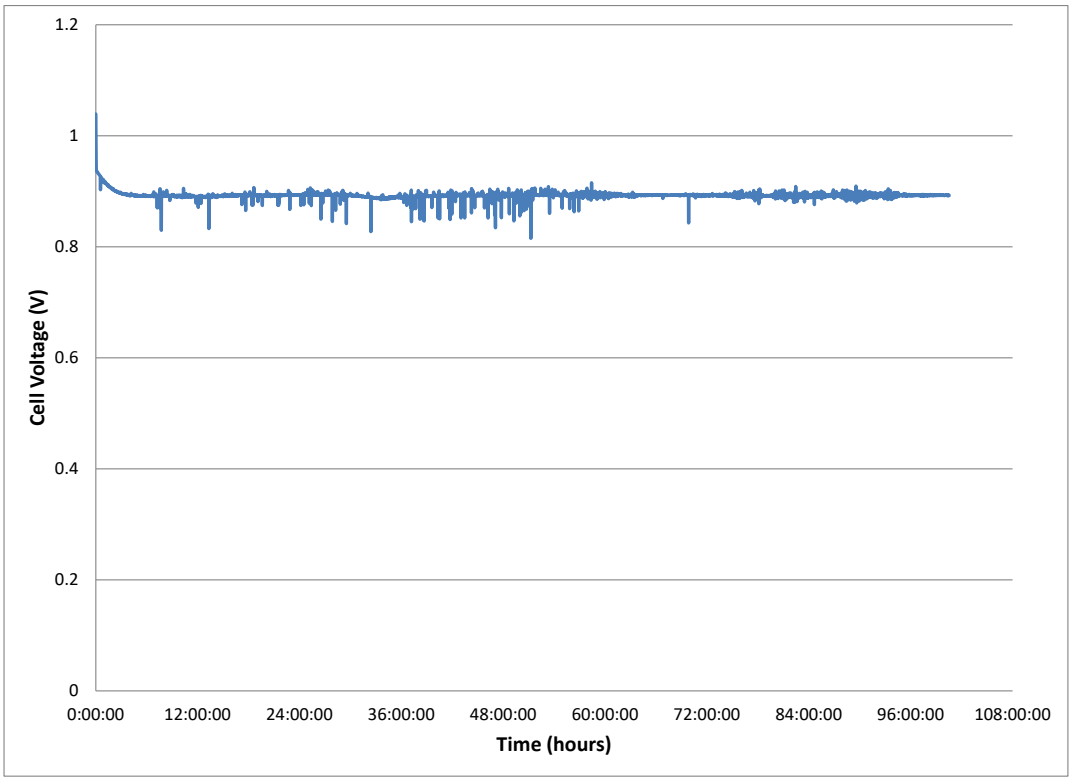

Figure 2-35 Cell Voltage against Time for GLOB 5162 Cell Formulation 11

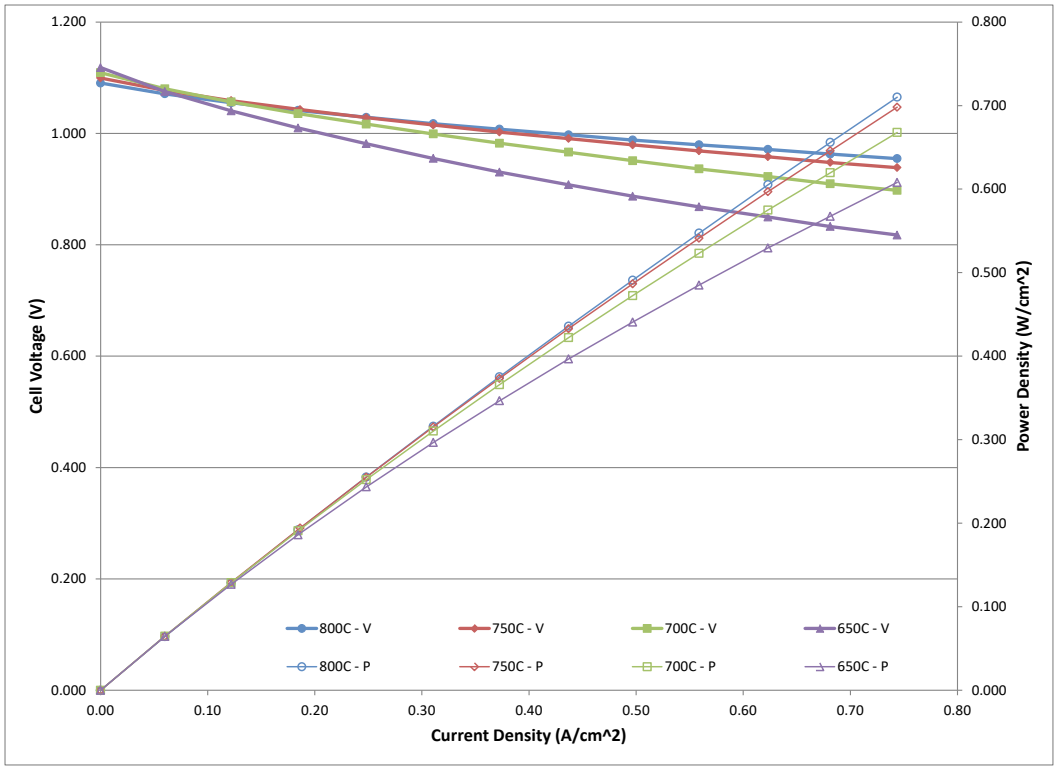

Figure 2-36 Power Curves for GLOB 5161 Cell Formulation 12 (1250°C fired)

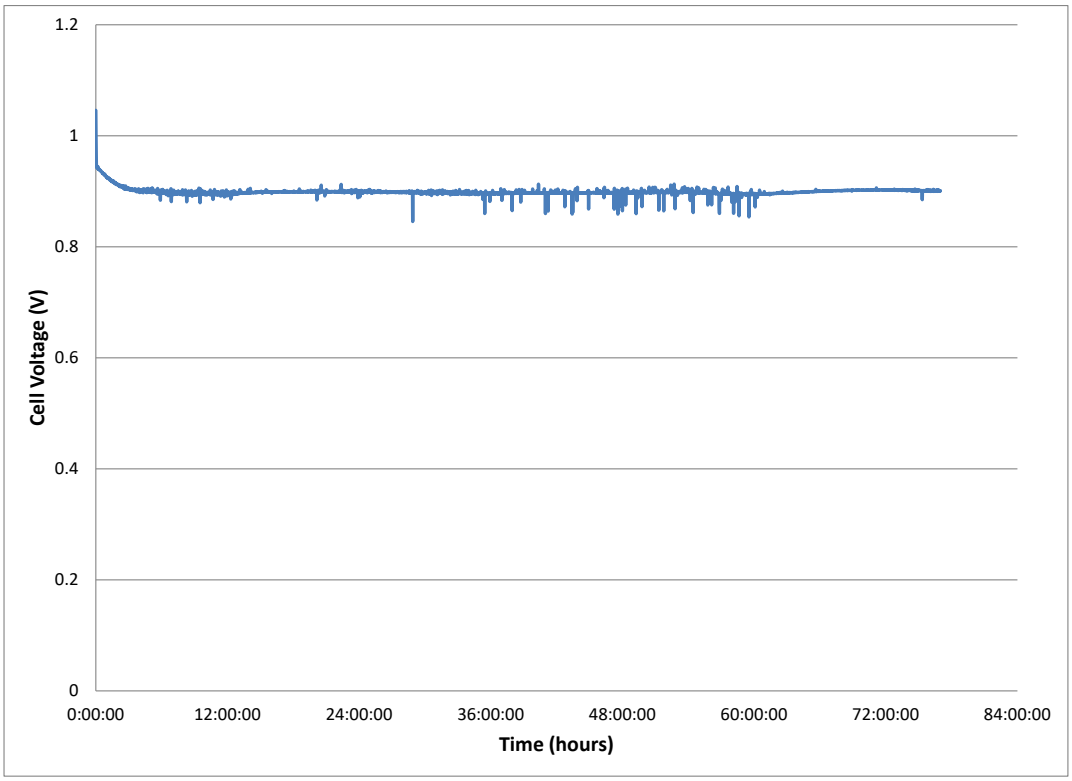

Figure 2-37 Cell Voltage against Time for GLOB 5161 Cell Formulation 12

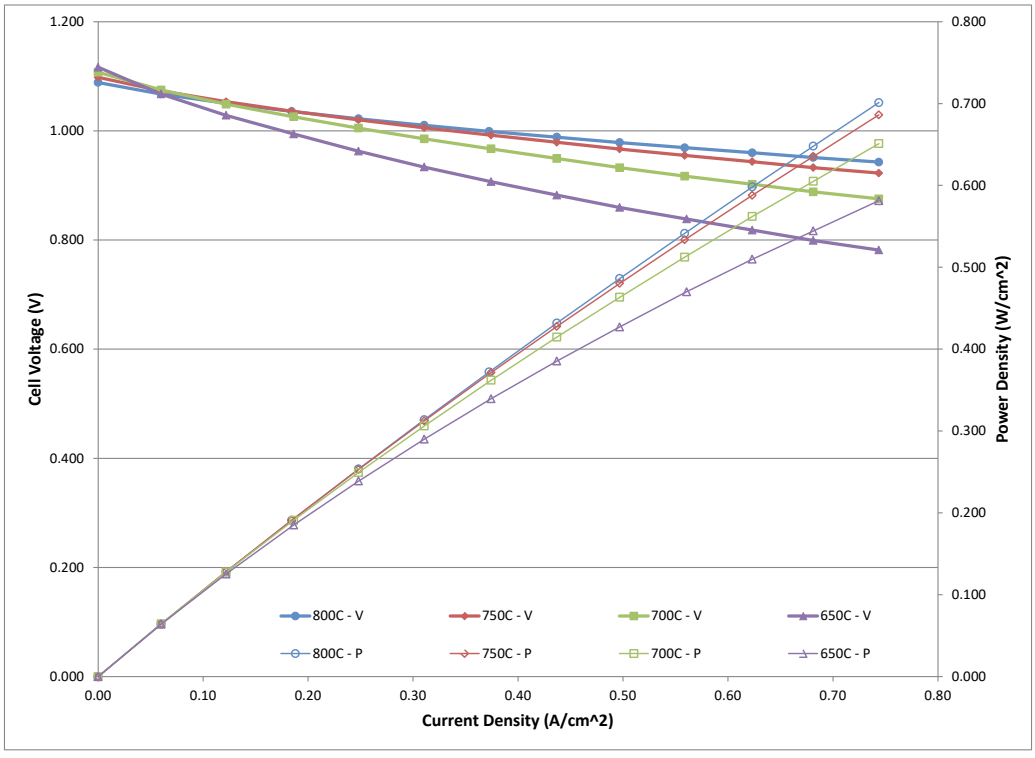

Figure 2-38 Power Curves for GLOB 5158 Cell Formulation 13 (1250°C fired)

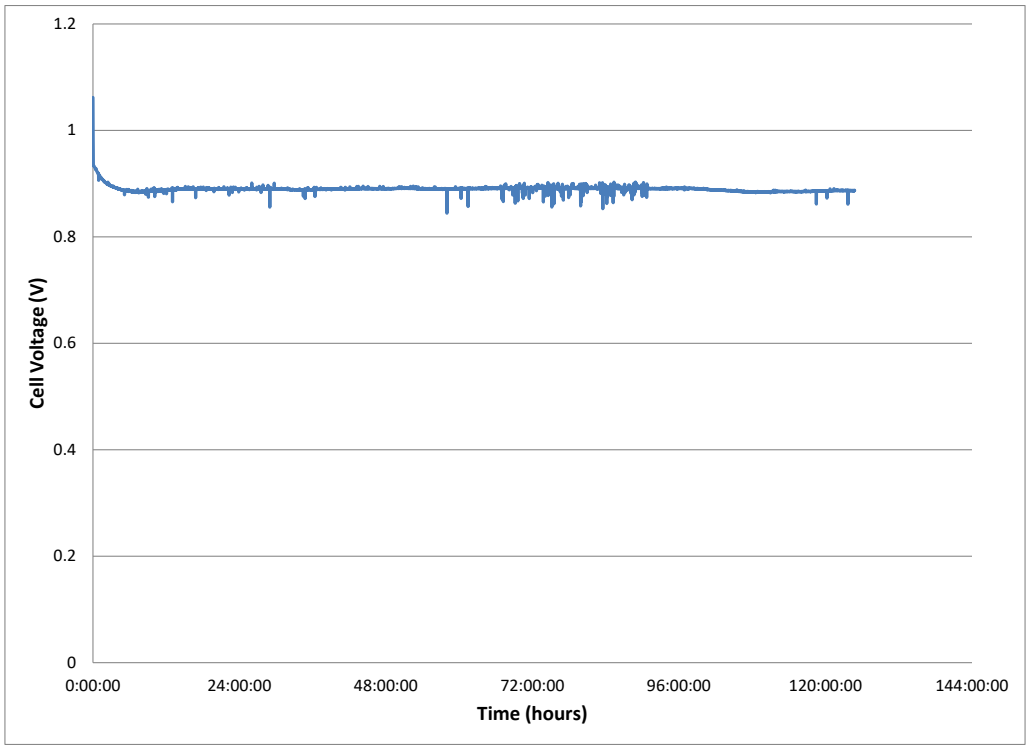

Figure 2-39 Cell Voltage against Time for GLOB 5158 Cell Formulation 13

Figure **2-40** shows power curves for GLOB 5168, cell formulation 16 fired at 1,295°C and Figure **2-41** shows a brief steady-state hold at 0.5 A/cm^2 for the same cell showing short-term stability. Figure **2-42** shows power curves for GLOB 5169, cell formulation 8 fired at 1,250°C and Figure **2-43** shows a brief steady-state hold at 0.5 A/cm^2 for the same cell showing short-term stability. These cells show good OCV values and high performance with formulation 8 having very good performance even at 650°C. Short-term stability is very good for both cells with high performance again for formulation 8 fired at 1,250°C (905mV at 0.5 A/cm^2, 50% Uf and 25% Uo). Longer term testing is required to determine the suitability of these cells for SOFC stacks. Finally, strength testing of most of the low temperature fired anodes was also completed.

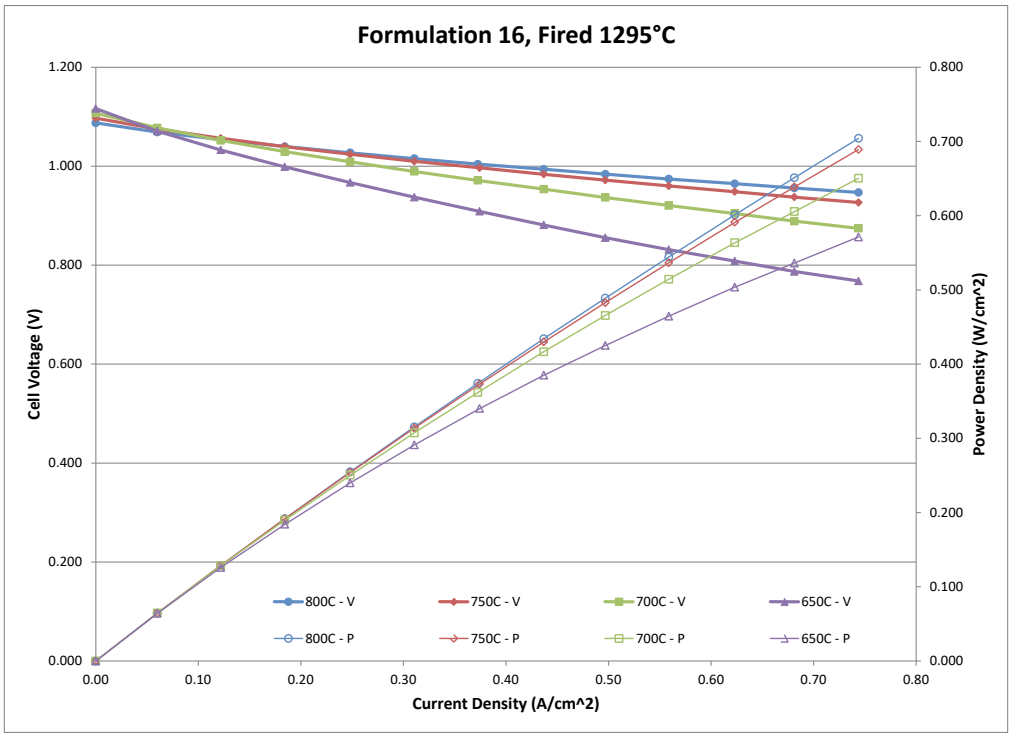

Figure 2-40 Power Curves for GLOB 5168 Formulation 16, 1295°C Fired.

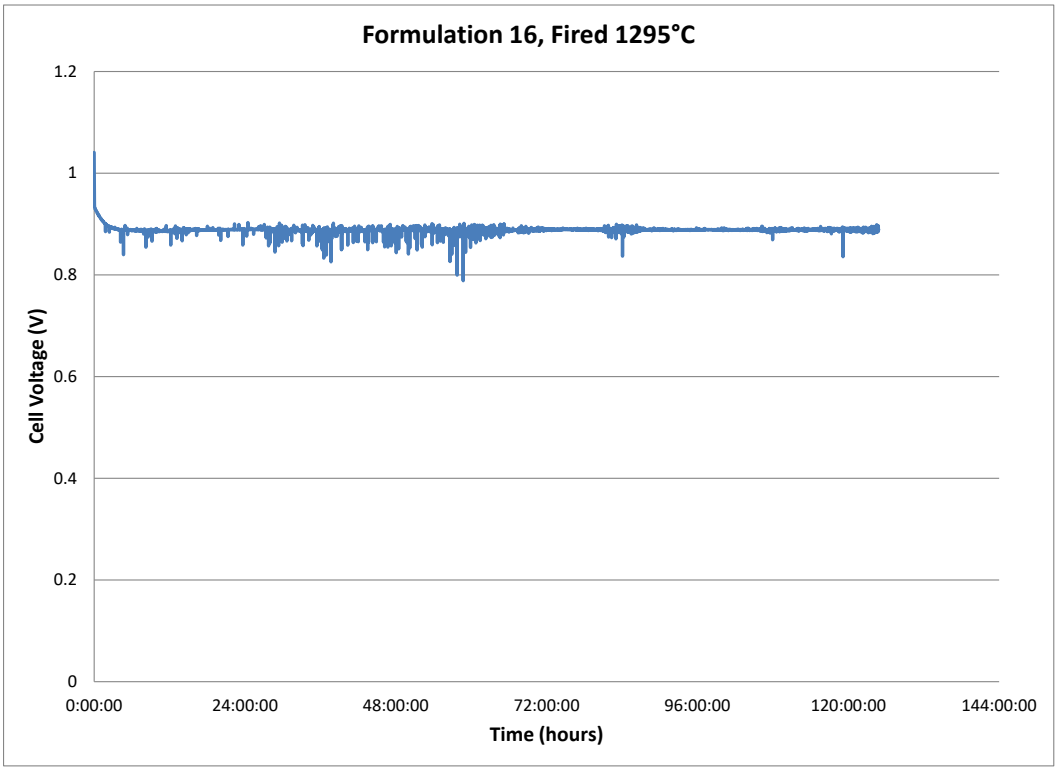

Figure 2-41 Steady-State Hold for GLOB 5168 Formulation 16, 1295°C Fired

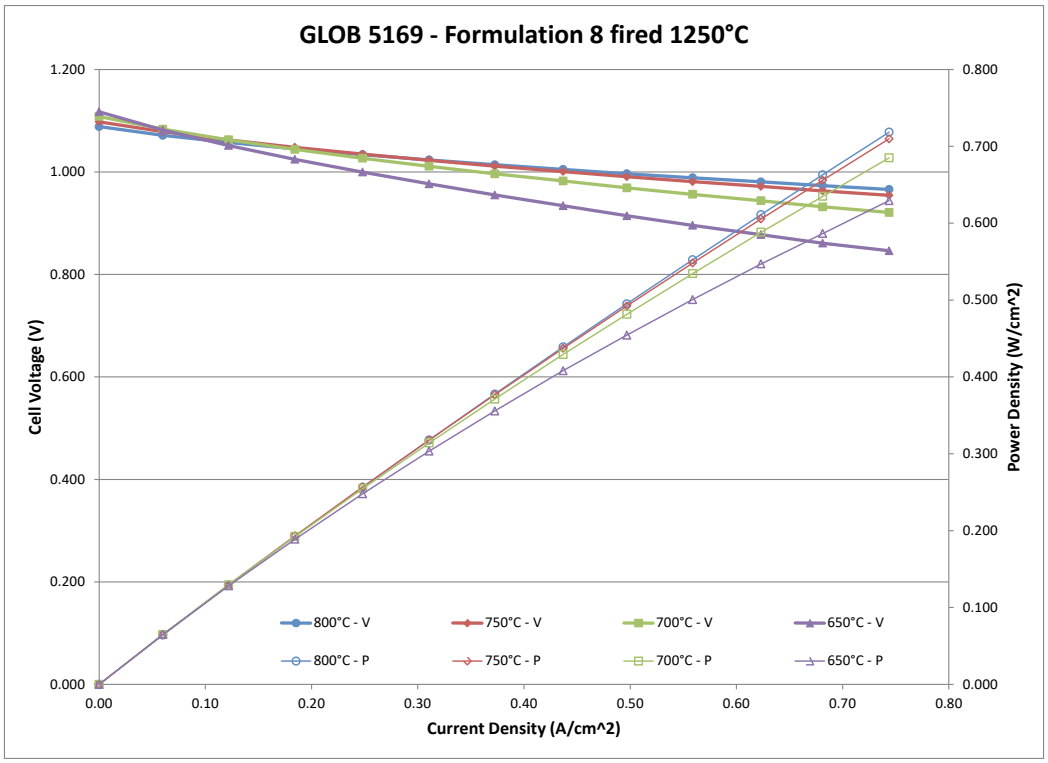

Figure 2-42 Power Curves for GLOB 5169 Formulation 8, 1250°C Fired

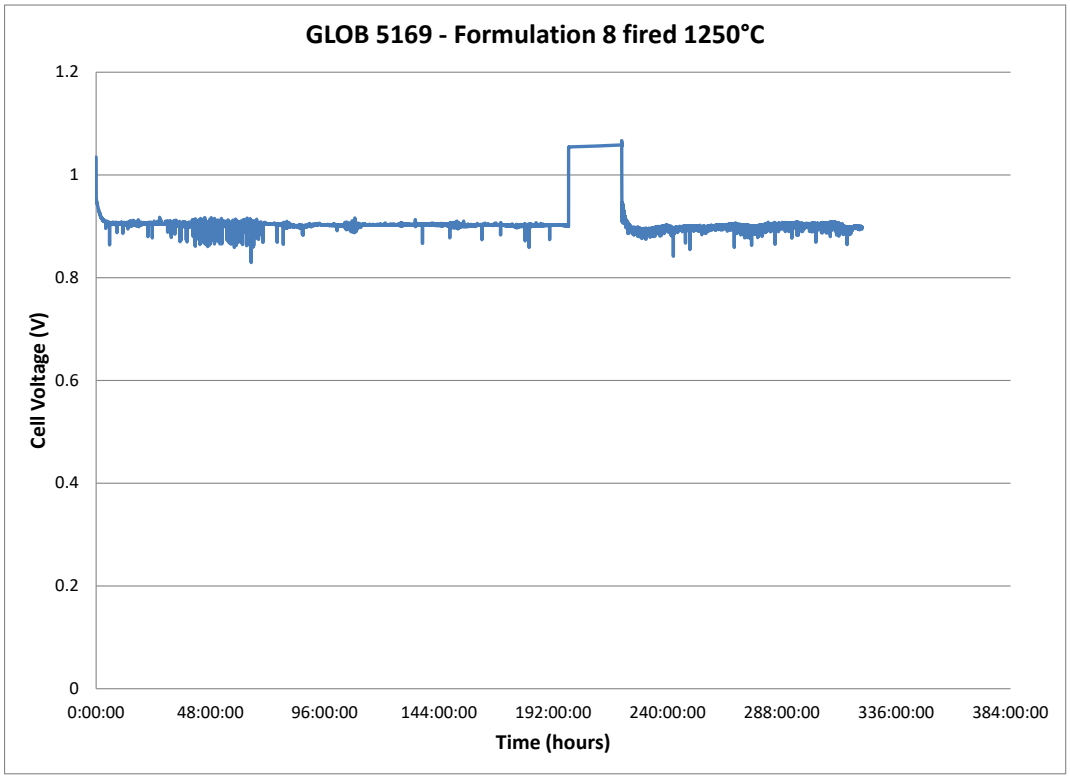

Figure 2-43 Steady-State Hold for GLOB 5169 Formulation 8, 1250°C Fired.

Biaxial flexural strength testing of 18 cell anode formulations all fired at 1295°C was completed. In addition a standard 57% NiO anode was also fired at normal firing temperatures and used as a comparison. Figure **2-44** shows results for all samples with 57% NiO in the anode substrate. Figure **2-45** and Figure **2-46** show the samples with 65% NiO in the anode substrate. The baseline anode, fired at standard sintering temperature, shows a flexural strength of 289 MPa while increasing the NiO content to 65% results in slightly lower strength values of 257 MPa at the same sintering temperature.

Figure **2-44** shows a Weibull plot of the biaxial flexural strength of various cell anode formulations (5 and 20 to 24) compared with a cell anode fired at standard temperature. All of these tests contain 57% NiO in the anode substrate, and all show improved strength fired at lower temperature with the exception of the last two (23 and 24) that are slightly lower. These formulations all have suitable strength for cells used in FuelCell Energy stacks.

Figure **2-45** shows a Weibull plot of the biaxial flexural strength of various cell anode formulations (8 to 13) compared with a cell anode fired at standard temperature. All of these tests contain 65% NiO in the anode substrate and all show lower strength when fired at lower temperature. However, with values around 200 MPa these are still likely adequate for the cell size and stack design proposed in this project.

Figure **2-46** shows a Weibull plot of the biaxial flexural strength of various cell anode formulations (14-19) compared with a cell anode fired at standard temperature. All of these tests contain 65% NiO in the anode substrate and all show significantly lower strength when fired at lower temperature indicating these additives do not compensate sufficiently for the higher NiO content to allow reduction of firing temperature to 1,295°C without lowering strength. These formulations have not been considered for further investigation.

A series of 24 formulations have been developed to successfully lower the sintering temperature of FuelCell Energy cells. These have been characterized by electrochemical and mechanical testing and the results show that 18 of the 24 formulations can be sintered at 1295°C or lower temperature. Furthermore, these cells produce equivalent or better short-term electrochemical performance than standard cells prior to this project, whilst maintaining sufficient mechanical strength for stack operation. It is recommended that long-term electrochemical stability be studied for these formulations in order to complete the development of a low temperature sintering cell since lifetime is also a key factor in the cost of an SOFC system.

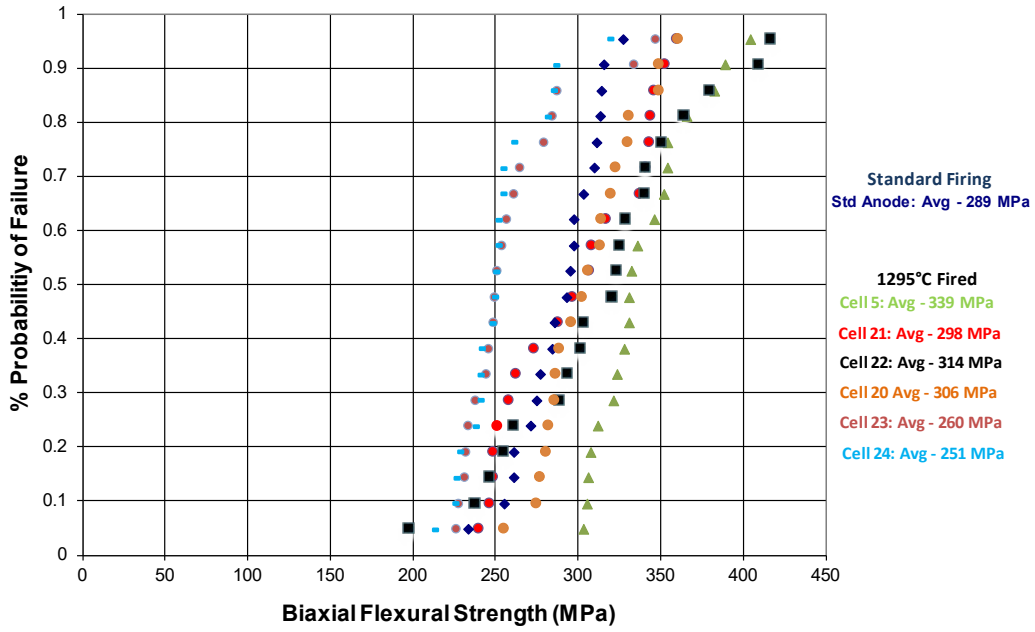

Figure 2-44 Weibull Plot Comparing Biaxial Flexural Strength Measurements for Various Cell Anode Formulations (all with 57% NiO in Anode Substrate, 1295°C Fired)

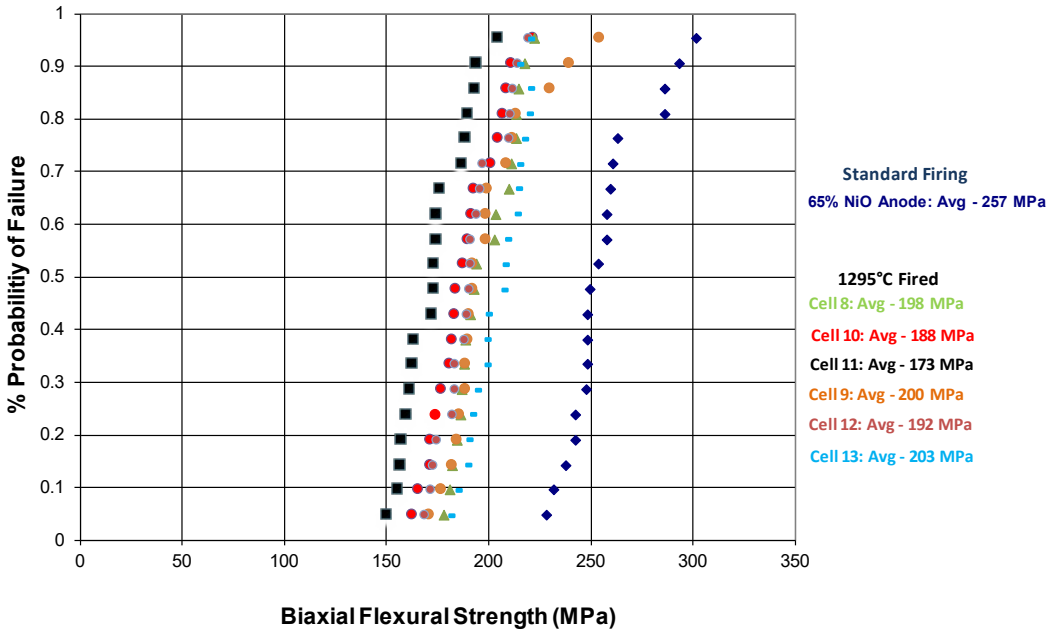

Figure 2-45 Weibull Plot Comparing Biaxial Flexural Strength Measurements for Various Cell Anode Formulations (all with 65% NiO in Anode Substrate, 1295°C Fired)

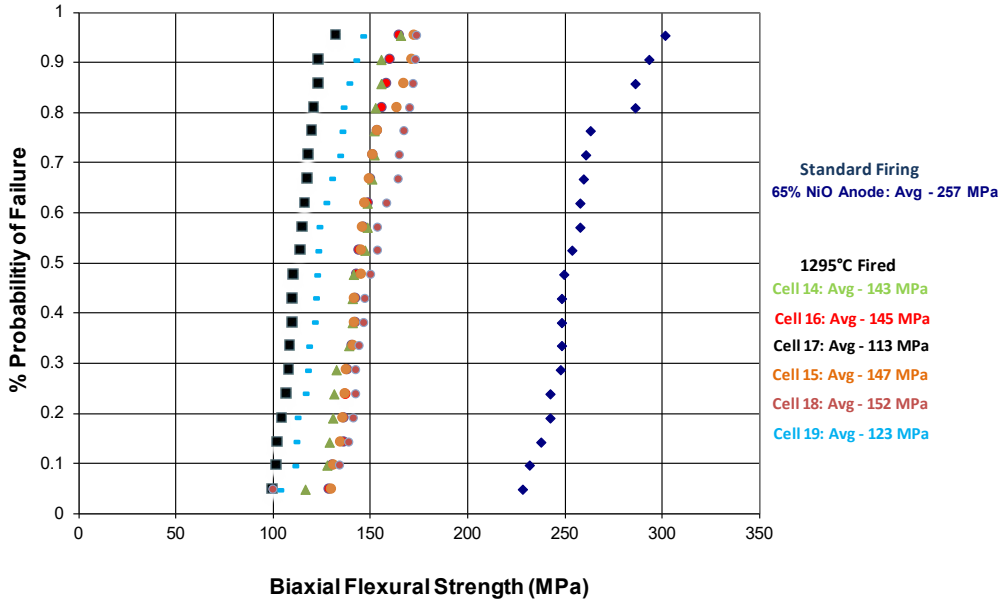

Figure 2-46 Weibull Plot Comparing Biaxial Flexural Strength Measurements for Final Cell Anode Formulations (all with 65% NiO in Anode Substrate, 1295°C Fired)

2.2 Task 2.2 Advanced Manufacturing Process Developments

This task will investigate the applicability and effectiveness of the advanced manufacturing processes in reduction of cost of the factory-produced SOFC cells. Three distinct cutting-edge technologies will be studied for their advantages and uniqueness in manufacturing of cell layers. With the input from cell manufacturing process development, a new baseline cell technology will be established.

2.2.1 Task 2.2.1 Roll-to-Roll Technology

Objective:

Evaluate roll-to-roll printing technology for cell layer printing

Approach:

Efforts will be made to work with equipment OEMs to demonstrate printing of functional layer pastes onto SOFC anode tapes at a lab scale. In parallel, a lab-scale roll printer will be used to support this research effort and could potentially be retrofitted with other roll print heads (e.g.: Rotary screen printing).

Lab scale processes will be evaluated using visual inspection, scanning electron microscopy, leak testing, and single cell testing of printed cells. After meeting cell performance and endurance criteria, the Roll-to-Roll process will be scaled up and a sufficient number of cells will be produced for assembly into the development stacks and 5-kW validation stack.

Results & Discussion:

A lab scale roll printer, previously in storage, was prepared for printing trials (Figure 2-47.). Baffles were inserted in the feed tray to reduce the print width from 610 mm (24”) for hand fed trials on

narrower tape. The variables on this device include roller speeds (print and backing rollers have independent speed control), squeegee positioning and pressure, roller pressure, and ink characteristics. These variables, including modifications to ink viscosity, were tried out in a first instance to identify where further focus should lie.

Figure 2-47. Lab Scale Roll Printer

Efforts were made to work with equipment OEMs to demonstrate printing of functional layer pastes onto SOFC anode tapes at a lab scale. In parallel, a lab-scale roll printer was used to support this research effort and the potential of retrofitting with other roll print heads (e.g.: Rotary screen printing) was explored.

Lab scale processes will be evaluated using visual inspection, scanning electron microscopy, leak testing, and single cell testing of printed cells. After meeting cell performance and endurance criteria, the Roll-to-Roll process will be scaled up and a sufficient number of cells will be produced for assembly into the development stacks and 5-kW validation stack.

Results & Discussion:

The roll printer discussed in the previous quarter was commissioned in the cell manufacturing clean room. Figure **2-48** shows the printer installed and set up for printing trials. Several trials have been executed with various rolls (different roll patterns for different paste transfer characteristics), different paste formulations (at this point primarily focussing on viscosity modifications) and different process conditions (roll pressure, roll gap, upper vs lower roll speed, etc.).

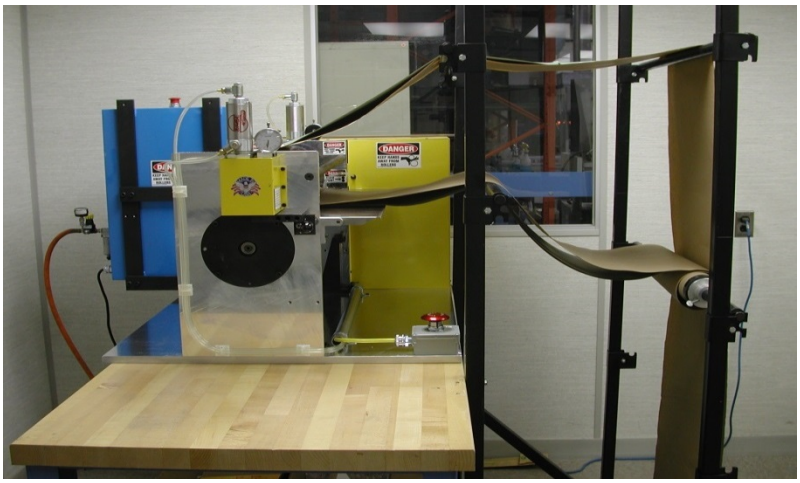

Figure 2-48 Roll printer installed and set up to run printing trials

The effort was in the exploratory stage, focused on understanding how process parameters affect the results. The results are generally promising, but further effort is required to get to the acceptable prints. Positive and negative features or attributes of the current status are summarized below.

Positives:

- Able to cleanly feed the anode support material, avoiding bunching and tears
- Able to deposit material with good coverage, generating appearance of 100% coverage
- SEM analysis of fired cells suggests that deposited material thickness is generally uniform and the material can be deposited in the thickness range of interest

Negatives:

- Although visually the coverage looks good, SEM cross sections after firing are showing many print gaps that are unacceptable (Figure 2-49)
- There are some indications of poor bonding between the layers in the fired cell (Figure 2-50)

Further work was undertaken to explore the process, including working with the machine supplier to improve the printing process.

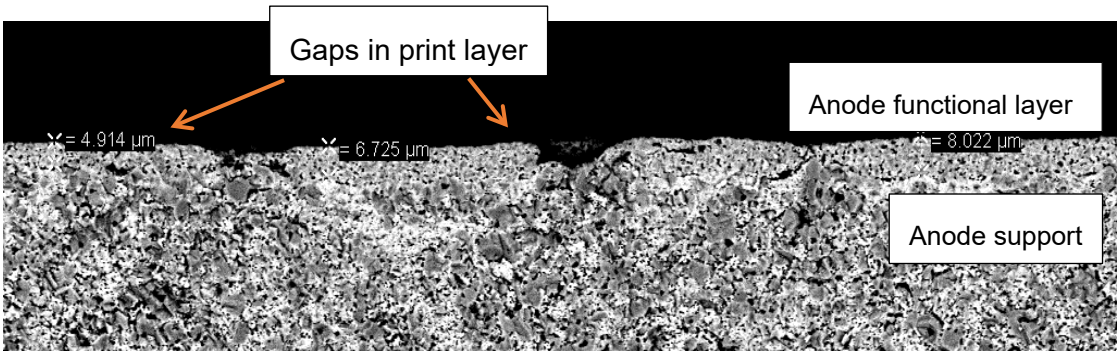

Figure 2-49 Roll printer trial for anode functional layer – examples of gaps in printed layer

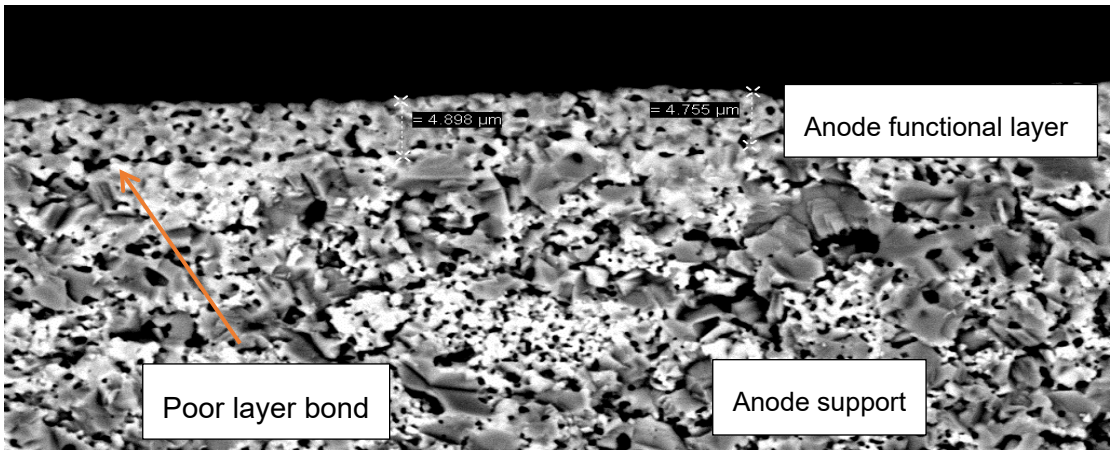

Figure 2-50 Roll printer trial for anode functional layer – example of poor layer bond in printed layer

The lab-scale roll-to-roll printing equipment (from Euclid Coating Systems) was commissioned and initial printing trials were conducted. Process parameters (roll patterns, speeds, pressure, print gap, paste formulation) were evaluated and values were found that enabled visually acceptable prints. Two main flaws were found in the print layers, when examined by SEM (scanning electron microscope):

1) Gaps in the printed layers with widths exceeding 20 microns
2) Delamination between the printed layer and the substrate after firing

Neither is acceptable in the anode functional layer or in the electrolyte. These are the cell layers that should benefit from roll-to-roll printing. Further attempts to improve roll-to-roll printing were carried out this quarter, but no significant improvement in printing was achieved.

In discussion with the roll printer supplier, nothing wrong was found with the approach taken. A general reformulation of the ink and the substrate surface was suggested to get the quality of printing required. The supplier's knowledge and understanding of the problems appeared excellent but did not provide a concrete path forward other than reformulation. Table 2-4 shows the variables that were explored and a summary of the results.

Table 2-4 Process Variables Evaluated and the Results

Variable	Range tested	Comments
Roll pattern	55 LPI, 180 LPI, 25 LPI Quad	Finest pattern printed best and is recommended pattern for print thickness
Print gap	0.000” to 0.012”	Note: Tape thickness of 0.012”. Slight compression on tape printed best.
Print pressure	10 psi to 80 psi	Higher was generally better, approaching the machine limits
Wiper blade pressure	10 psi to 30 psi	Higher was generally better until it caused blade distortion
Tape speed	10 to 50 (% machine speed)	Mostly a question of handle-ability with the present setup. 20% was manageable.
Print head speed	10 to 50 (% machine speed)	Differential speeds led to worse prints. Matching tape to print head speeds was best.
Paste viscosity	10,000 to 25,000 cP @ 0.3 rpm	Lowering viscosity changed the optimum parameters (above) but not the print quality
Resting time (reflow time)	0-5 minutes	No reflow was observed to occur. Reformulation could improve this.

The lab scale equipment being used is gravure printing, where the print head deposits material directly onto the substrate. There are alternatives, such as, offset printing, flexographic printing and rotary screen printing that are also roll-to-roll processes and will have different printing characteristics.

At this point, success of pure roll-to-roll printing seems unlikely within the scope of this program. Reformulation of the printing ink – which could imply reformulation of anode support, anode functional layer, electrolyte, etc. is too large a scope to complete within the time and budget of this program. Trials of alternative roll-to-roll processes are similarly out of reach. An approach showing more promise is an automated screen printing process that although not roll-to-roll, is a continuous automated process. Progress in this area is described in more detail below. Roll-to-roll printing need not be completely dismissed from future consideration, but it has become obvious that the scope of work required to successfully implement is larger than anticipated.

Project Milestone Id 4 is about demonstrating roll-to-roll technology development in single cells. As mentioned in earlier quarterly reports, print layers (cells) produced using the roll printer had flaws. The machine supplier’s recommendation was to consider material reformulation for the substrate and the printed inks. While reformulation may be a path to success in the longer term, it is not a viable path within the scope and timing of this project. Our conclusion is that without significant more effort than was anticipated within this program, roll-to-roll is not a viable approach.

A full process more suited to our materials and volumes has been identified and commissioned and is actively in use for cell production at this time. This alternate path has been funded under a separate IR&D effort. It consists of the installation and commissioning of an automated screen printing line from the printed circuit board industry. It meets many of the goals originally intended

for the roll-to-roll effort, and in some respects is more flexible (e.g.: It can handle both unfired and fired cells, and it can align and print patterns). The equipment (was described in the previous quarterly report) has been released for production for one of the cell printing layers where is has shown a reduction in cycle time of 66%, and a quality indistinguishable from our best human operator. Further reductions in process time are expected. No barriers are seen to extending the functionality to all printed cell layers in the future, pending validation trials. The equipment is in use for current deliverable stacks.

As reported last quarter, roll-to-roll cell processing was de-selected as a process for this program. More promising is some recent success in deploying automated screen printing to the cell manufacturing process under a separate effort. The plan is to use the same equipment to process cells in this program.

Current successes include the processing of more than 800 large area cells (550 cm^2 active area) for use in deliverable stacks. The process is being refined and is currently delivering cells in approximately half the time of the prior manual printing process. On initial deployment the process was delivering 2 to 4 bad prints per 100 cells, a little worse than the manual process it replaces. With refinement the defect count has been decreasing, and there have been no bad prints in the last 250 cells.

With appropriate tooling (parts holders and screens), it is anticipated that the same equipment will be usable on this program.

Figure 2-51 Installed Automated Cell Printing Line

Milestone 2.2.1 - Demonstrate Roll-to-Roll Technology Development in Single Cells

Previous quarterly reports have provided some highlights of FuelCell Energy internally funded development of an automated screen printing line for application of the functional layers of the fuel cell. While not directly responding to the original roll-to-roll development goals under task 1.2.1, the results are showing benefits directly in line with the original task goals. Print quality is improved, yield is improved, and processing time (both machine time and total labour) are down relative to the prior processes. The benefits are such that it is desired to extend the functionality to the CSA cells. The automated screen printing is currently deployed for all functional layers from the fired half-cell onwards (barrier layer, cathode, contact layer), and processes each 550 cm^2 cell individually.

For the smaller CSA cells (81 cm^2) it is desired to print multiple cells simultaneously in order to spread the machine and labour time over more active area, a method to ensure production costs are minimized. This presents a process challenge; the automated screen printing line is predicated on the use of machine vision to align the print screen to the parts to be printed, a process that only occurs once per load-and-print cycle. It is also designed to handle rectangular parts, not round ones. It is desired to retain the machine vision alignment functionality, which provides significant benefits to process flexibility and ease of transitioning between processes, but to use it in a way that allows for multiple parts to be printed in one setup.

The solution that was developed was a jig that provides mechanical alignment of the cells relative to a precision machined base plate. Vision targets are provided on the base plate to which the machine can align the print screen. The design allows for nine cells to be printed simultaneously for a total printed active area of 729 cm^2. With existing equipment it may be possible to extend this to sixteen cells for a printed active area of 1296 cm^2 per print cycle.

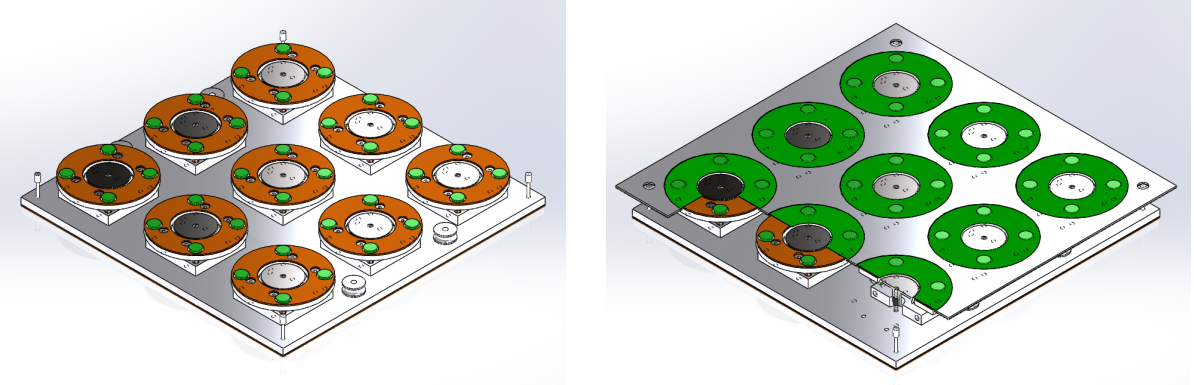

Figure 2-52 Automated cell printing nest empty (left) and with cells (right)

Figure **2-52** shows the multi-cell printing nest. To the left is the nest alone. The nine print locations are clearly visible; each consisting of a support table, a central floating alignment pin tapered to capture and mechanically center a cell, and four bellows suction cups that grab the cells and pull them down against the alignment pin and against the support table. At the four corners of the nest are pins with optical alignment features. These alignment features, as well as all nine floating alignment pins ride on precision dowel pins which are located in the main base plate. With careful machining these 4+9 features can be held to within 25 micron (0.001”) positional tolerance, which is more than sufficient for the printing.

The second challenge in automating the printing of these half cells is the part handling. If an operator has to manually load the cells, much of the labor benefit is lost. To the right of Figure

2-52 nine cells are shown in a carrier (front right corner cut away to show additional detail). This carrier loosely holds the cells and can travel through all the automated equipment (loader, conveyors, printer, buffer, and eventually, dryer).

For the automated print line, this setup will have the same behavior as a conventional rectangular cell (or printed circuit board, the industry of origin for the equipment), and should operate transparently. By including vision references in the cell nest, all the benefits of automatic alignment of the print screen to the parts is retained, eliminating much of the per-setup alignment effort that would otherwise be required. Since this tooling relies on mechanical centering of the cells, some of the intrinsic accuracy of print will be lost. However, as long as the cell ovality out of firing is not too severe (which in any case would present other process problems) it is believed that the print accuracy will be more than adequate. This is borne out by manual printing experience with similar annular cell geometry, where the process evolved to one of mechanically centering the cells on a floating alignment pin very similar to the one proposed here.

2.2.2 Task 2.2.2 Atomic Layer Deposition (ALD) Technology

Objective:

Investigate ALD for producing cell barrier layer

Approach:

The objective of this task is to produce thin, high performance Gadolinium Doped Ceria (GDC) barrier layer on anode supported YSZ substrate and to demonstrate the utility of this advanced manufacturing technique to produce reliable SOFCs with enhanced performance.

Initial experiments will establish the ALD process for depositing GDC on anode supported YSZ half cells. Process conditions and feed compositions will be tuned to achieve the desired Gd content and film thickness which will be characterized via wavelength dispersive x-ray fluorescence, SEM, and XRD. The scale-up of the ALD process, for testing in technology stacks including the ultimate 5kW stack, will be conducted.

Results & Discussion:

A series of experiments have been carried out in a research scale ALD reactor that has a horizontal configuration with a round cross section 50mm in diameter. The ALD process uses identical Gd and Ce precursors, named as tris-isopropylcyclopentadienyl gadolinium and cerium and represented as $Gd(iPrCp)_3$ and $Ce(iPrCp)_3$, respectively (Figure **2-53**). The precursors are highly reactive with water, which is used as the oxidant.

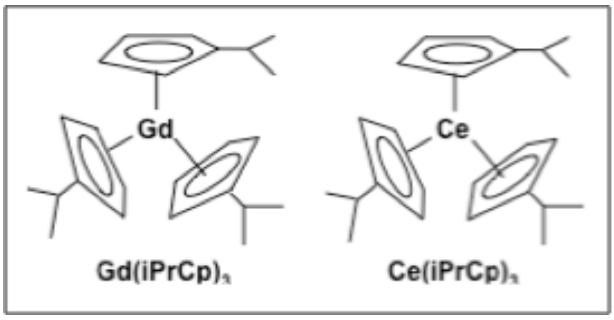

Figure 2-53 Gd and Ce precursors.

Based on previous work and literature processes for these and similar materials, a deposition temperature of 230°C has been used to carry out the process in the ALD temperature window. In this temperature region, the thickness of the film deposited in a single cycle should be invariant with temperature. Literature values for CeO_2 ALD via $Ce(iPrCp)_3$ are in the range of 0.3 – 0.5 Å/cycle). Deposition rates near this range have been obtained in a series of precursor dosing experiments on –OH terminated fused silica substrates. Thickness per cycle is measured by wavelength dispersive x-ray fluorescence (WD-XRF) with a Rigaku 3630 wafer analyzer using a Rhodium target operated at 40kV and 60mA. Deposition rates for Gd_2O_3 were similar to CeO_2.

The first set of samples to be coated with GDC are self-supporting YSZ discs for fabrication of symmetrical electrochemical cells. Anode supported button cells will follow, and finally bench scale anode supported YSZ. Uniformity on both sides of the symmetrical cell is critical for accurate electrochemical characterization. Visual uniformity was quite good across the front side of the substrates; however XRF revealed a significant difference in the coating thickness on the back side of the substrate. Additional experiments led to the conclusion that flow conditions in the reactor were non-uniform, leading to an uneven flux distribution, which results in an under-dosed condition on back side of the substrate. While these effects have not had a pronounced effect on previous work, the nature of the $Ce(iPrCp)_3$ and $Gd(iPrCp)_3$ leads to more interatomic reactions that are more difficult to compensate with large over-dosing. The uniformity is currently being corrected with a minor hardware change that adds a gas distribution baffle following similar approaches that have been used in rectangular cross section horizontal ALD reactors (ref. 1).The gas distribution baffle will adjust the flow velocity profile across the diameter of the reactor tube, and should result in acceptable uniformity.

The work has demonstrated the feasibility of depositing appropriate pre-cursors, but the challenges with uniformity require correction before proceeding to button cell trials. The focus of the next quarter will be in implementing and evaluating the effect of the distribution baffle and, assuming success, transitioning to the production of button cells for characterization.

Milestone 2.2.2 Complete Evaluation of ADL for Fabrication of Barrier Layer

Due: 29 Dec 2016

Status: This process has proven more difficult than anticipated to deploy, but good progress has been made. This quarter changes to equipment and to precursor materials were pursued but were not able to be implemented in time to answer the milestone question. While challenging, the process is showing some promise and the updated materials and equipment are now in place. The ALD work will be continued as planned into the next quarter.

Results & Discussion:

In the last report, we noted that uniformity of the GDC coating was less than desired (approximately 30% non-uniformity in Ce under the best conditions as measured by wavelength dispersive x-ray fluorescence (WD-XRF)). A brief modeling effort was undertaken to understand flow and concentration uniformity in the reactor. Flow is highly laminar (Reynolds number ~ 1, <<2400), and flow-based and diffusional effects were investigated on concentration within the gas stream. Modeling suggested that concentrations vary strongly across the flow field. Interestingly, uniformity of YSZ films (measured as Zirconia) was quite good (<10% non-uniformity by WD-XRF) under similar conditions. This suggests that the GDC precursors are more sensitive to particular flow dynamics within the reactor. In order to address the non-uniformity, system modifications were made to ensure improved mixing. Alternative cerium precursors have been identified which may also improve uniformity. Confirmation of the effects of improved mixing is commencing. Details of the modeling, mixing approach, and precursors are discussed below.

The ALD reactor is a 50mm diameter tube with a length of approximately 2 meters. Flow and concentration modeling were carried out with Comsol under pressure and flow conditions suitable for ALD and the reactor system. Flow was confirmed to be highly laminar. The original reactor configuration had two separate injection sites: one at the end and one at 90 degrees to the end, at approximately 70mm from the other injector. Flow from this configuration is shown in Figure 2-54. The overall flow is generally laminar and well established prior to the sample. The overall velocity is on the order of several meters per second. More detailed examination of the injector area showed the presence of recirculation cells (Figure **2-55**). These cells are considered to be non-desirable because they represent areas that may not be completely purged during the purge portion of the ALD cycle that is intended to separate the two reactants (i.e., the precursor and the water).

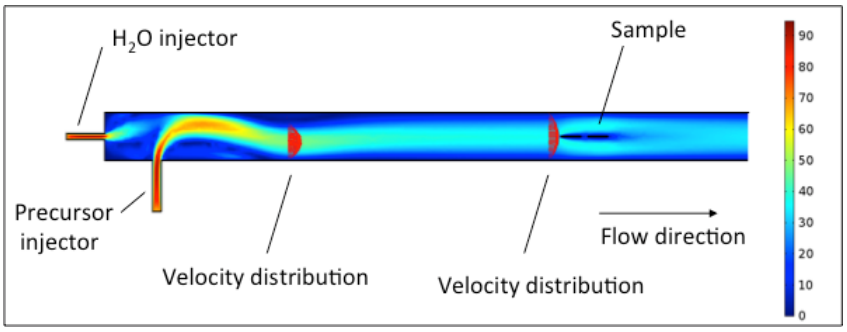

Figure 2-54 Modeled Flow Profile in the ALD Reactor Showing Gas Velocity

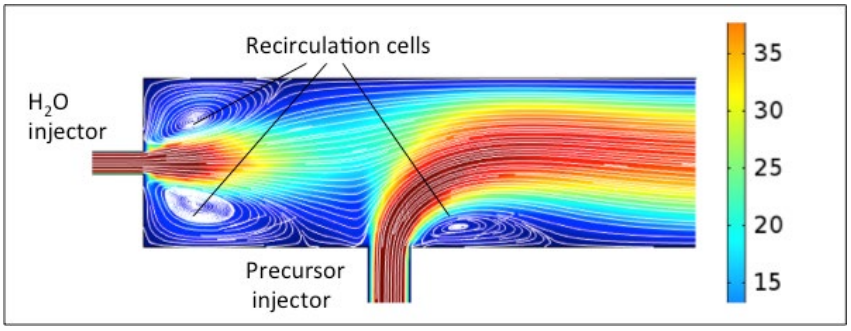

Figure 2-55 Modeled Velocity with Flow Paths in the Area of the Injectors

In order to overcome the recirculation cells for the end injector, a conical design was modeled. It was found that if the angle of the cone near the end injector is below 27 degrees, the recirculation cells are eliminated (Figure **2-56**).

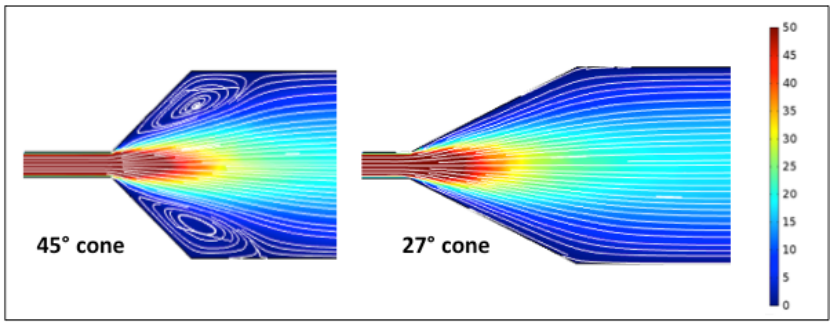

Figure 2-56 Modeled Velocity with Flow Paths in the area of the Injectors with Conical Geometry

Concentration in the reactor was also modeled. This provides considerable insight into the non-uniformity of the deposited film. Figure **2-57** shows concentration profiles with different inlet flows. (During the dosing process, a small purge flow is always present in each injector to prevent back streaming.) The low water purge (left) mode is most representative of the process. The effect of a higher water purge during precursor dose (right) exacerbates the effect. The dominant effect is that under strong laminar flow conditions, cross-diffusion is very limited. The net result is that the precursor dose of a vertically oriented sample would be non-uniform, with the upper part in a potentially under-dosed region. In principle, this could be overcome by longer dose times so that the entire sample has a saturated surface condition. In practice this is more difficult to implement, especially with precursors that may be more sensitive to gas phase interactions. An alternative is to introduce mixing.

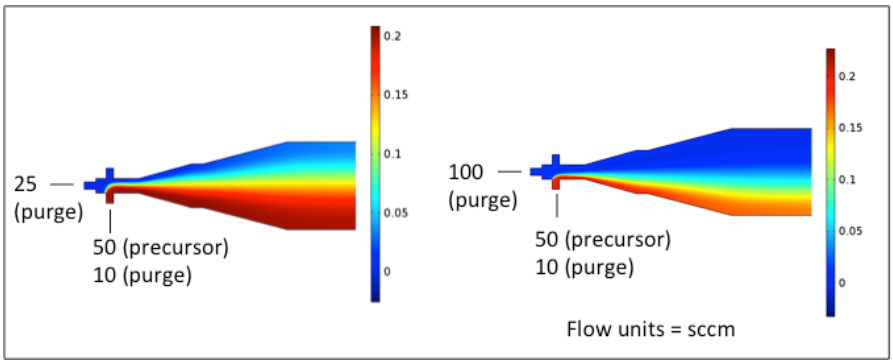

Figure 2-57 Modeled Concentration Profile with Different Proportions of Purge Flow during Precursor Dose

Although the injector area of ALD tools is often considered highly proprietary, mixing is viewed as critical (ref. 2) and there are references to static laminar flow mixers. The Gordon group at Harvard has reported using a Kenics brand mixer (ref. 3). A similar mixer (Figure **2-58**) from the same supplier has been obtained and implemented into a new reactor injector. The effectiveness of a static (non-moving) mixer has been modeled by others (ref. 4) and one example is seen in Figure **2-59**. Each helical segment of the mixer reverses the flow from left to right along the flow axis. As the flow passes each mixer element, the concentration uniformity across the flow front improves. At the same time as implementing mixing, the ALD system has been upgraded to a 75mm diameter to accommodate the required sample size. A schematic of the system is shown in Figure **2-60**.

Figure 2-58 Static Mixer (Cut Away View) [Ref. 5]. Each Blade Segment Reverses the Flow from Right to Left Along the Flow Axis

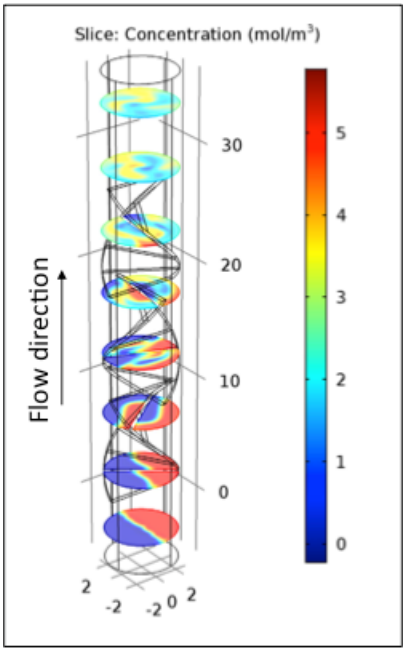

Figure 2-59 Modeled Concentration Profiles as a Function of Distance Along a Multiple Element Static Mixer. Modeling Published by Comsol, Inc.

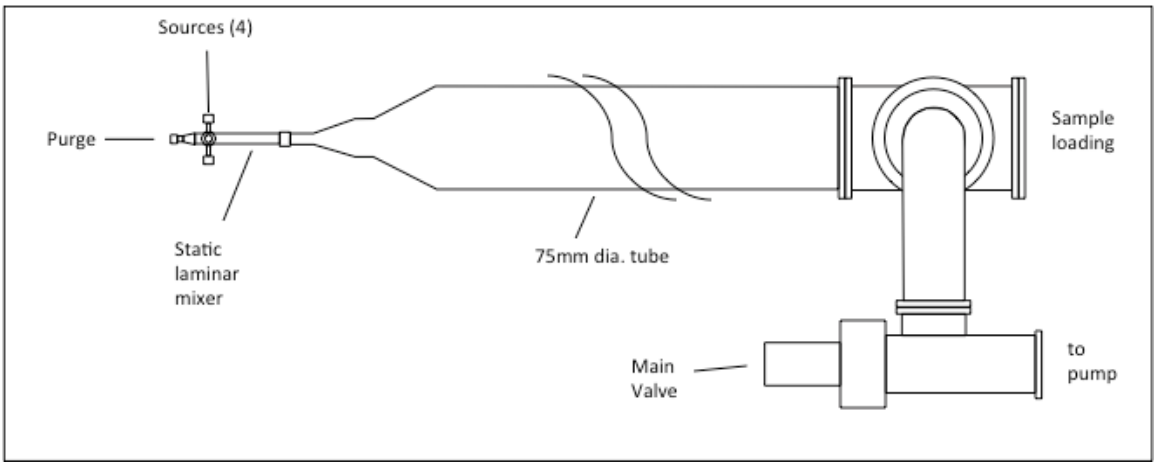

Figure 2-60 Schematic of Modified ALD System Hardware Incorporating Conical Geometries and Static Mixer

Precursor options for cerium have also been identified. A series of precursors are shown in Figure **2-61** along with their attributes; vapor pressure and sublimation temperatures are listed where known. Sublimation temperature provides a guide to volatility, with lower sublimation temperature indicating higher volatility. On the left is the currently used Ce precursor. The attributes of $Ce(iPrCp)_3$ include reasonable volatility, off the shelf commercial availability, and good reactivity with water. Water is a preferred co-reactant, as compared to oxygen plasma or ozone, which are more difficult to use. At the other end of the spectrum, β-diketonate sources like $Ce(thd)_4$ are highly stable, but have lower volatility and poor reactivity with water. Two alternative sources that have been reported as having higher volatility combined with reactivity with water are the mixed Cp – amidinate $Ce(iPrCp)_2$-amd and the alkoxide $Ce(mmp)_4$. Both are commercially available on a make-to-order basis and have been ordered for evaluation.

With the modeling guided ALD system modifications, and alternative Ce precursors as a backup, we believe that the project is well positioned to achieve uniform GDC layers via ALD as a novel barrier for solid oxide fuel cell electrolytes. Should the outcome prove successful, the concepts are readily scaled to larger samples and higher throughputs for manufacturing.

Class	cyclopentadienyl	cyclopentadienyl-amidinate	alkoxide	β-diketonate
Compound	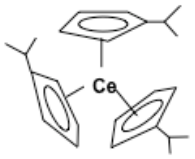 $Ce(iPrCp)_3$	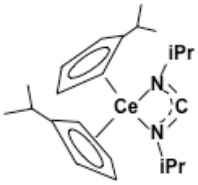 $Ce(iPrCp)_2$-amd	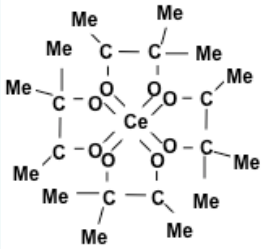 $Ce(mmp)_4$	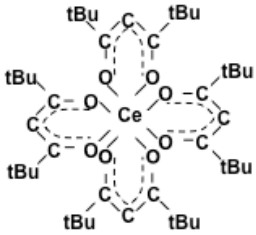 $Ce(thd)_4$
Valence	III	III	IV	IV
Vap. P	0.1Torr@157°C	0.7Torr@157°C		0.1Torr@187°C
Subl. T			120°C/0.8Torr	140°C/0.1Torr
H_2O reactive	yes	yes	yes	no

Figure 2-61 Precursor Options for Cerium in Order of Relative Stability from Left to Right

In the last reporting period, efforts to improve uniformity via modeling and reactor redesign were described. In the current reporting period, experiments were carried out to verify these improvements. The depositions were performed using a heteroleptic cerium precursor closely related to the homoleptic gadolinium precursor (Figure **2-62**). The cerium precursor has a vapor pressure approximately 1 order of magnitude higher than the homoleptic cerium analog of the gadolinium precursor. This allows a higher flux into the ALD process.

Uniformity of CeO_2 films deposited by ALD was characterized by UV-VIS spectrophotometry at approximately 5mm increments along a 50mm fused quartz substrate. The use of this substrate simplifies the reflection interferences observed in the UV-VIS spectra. A series of spectra are shown in Figure **2-63**. Literature values of refractive index (n) were used to convert the observed peak spacing to thickness with a model that allows n to vary with wavelength across the spectral region of interest (300-600nm). The calculated thickness is shown in Figure **2-64** as a function of distance. Uniformity was significantly improved, with approximately 10% peak to peak uniformity across a 40mm area. The previous best result was approximately 30%. There is an edge effect that is attributed to flow and a modest CVD component to the ALD process (see further discussion below). The uniform area is larger than the samples used for barrier performance characterization at this stage of the project.

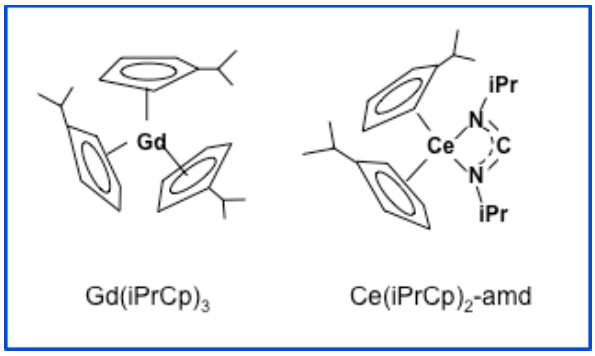

Figure 2-62 Gadolinium and Cerium precursors used in this reporting period.

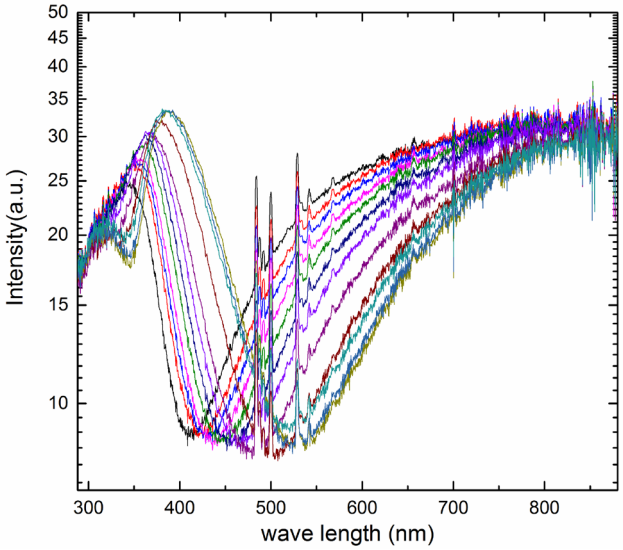

Figure 2-63 UV-VIS spectra taken at approximately 5mm increments along a 50mm substrate.

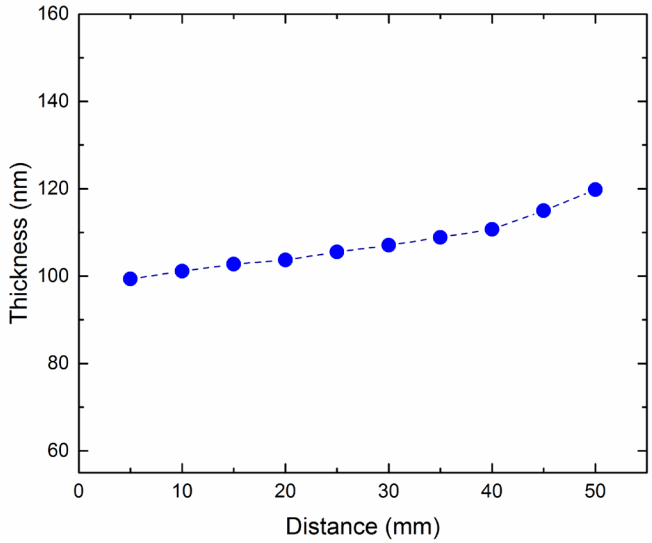

Figure 2-64 Variation of CeO_2 thickness as a function of distance along a 50mm substrate.

A number of runs were subsequently carried out on anode supported half cells with YSZ electrolyte and 8 samples were received. The deposition temperature was 240°C and the precursor dose and number of cycles were varied as shown in Table 2-6. The recipe included 1 cycle of Gd for every 3 cycles of Ce. In each case, two button cell size anode supported half cells were placed in the ALD reactor: one for electrochemical characterization and one for physical characterization.

Table 2-5 Sample number and run conditions.

Sample	# ALD Cycles	Dose time (s)
1	90	50 s
2	90 + 100	90@ 50 s + 100@ 30 s
3	200	10 s
4	400	5 s

Film thickness was characterized by x-ray fluorescence spectroscopy (XRF). Due to a peak overlap with Ce, Gd cannot be measured in a Gd-Ce film. Thicknesses for the films are expressed in nm (Table 2-7), not including the Gd component.

Table 2-6 Estimated thickness and growth rate per cycle for GDC deposited onto anode supported YSZ substrates from fused quartz monitor substrates.

Sample	Thickness (nm)	Growth rate / cycle (nm/cycle)
1	45	0.5
2	225	1.2
3	100	0.5
4	70	0.17

The growth rate per cycle suggests a chemical vapor deposition component to the ALD process. Typical ALD rates are on the order of 0.1-0.2 nm/cycle. In the case of sample 4, growth per cycle was limited by the duration of the dose step. Recent reports have suggested that this is the case for cerium and gadolinium ALD processes based on precursors containing cyclopentadienyl ligands. Deviations from an ideal ALD process are not unusual. The practical implication is that the CVD component will need to be addressed by flow and chamber design for a manufacturing process so that uniformity can be achieved over the desired area for a full scale cell.

X-ray diffraction (XRD) analysis of a monitor substrate (fused quartz) from sample 3 indicated that the films are crystalline at this deposition temperature with a slightly (220) preferred orientation (Figure **2-65**).

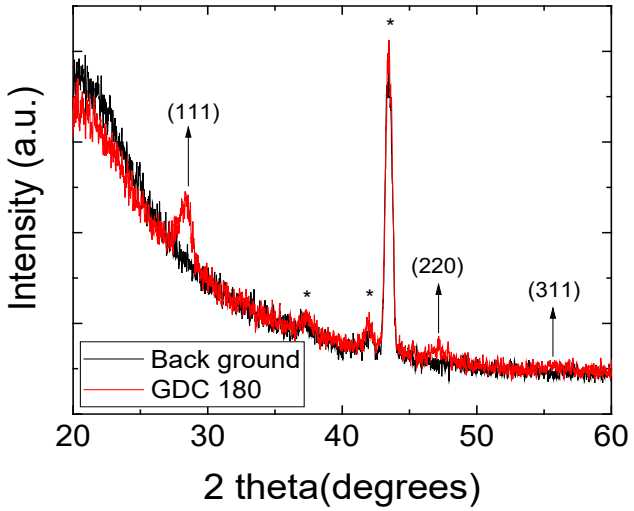

Figure 2-65 X-ray diffraction pattern from Sample 3 (GDC on fused quartz). CeO_2 peaks are indicated by (111), (220) and (311) reflections. The background peaks are from the XRD unit sample stage.

Figure 2-66 shows the electrochemical impedance spectra for three tested samples including a baseline cell with a 2 μm thick GDC barrier layer (screen printed), and samples 1 and 2. The measurements were done at 750°C with air flowing through the cathode and humidified hydrogen (3%) flowing through the anode (300 sccm each). The OCP impedance spectra are made of three arcs; one at high frequency range (10< kHz), one at medium frequency range (~100 Hz), and one at low frequency range (10> Hz). As observed, the medium and low frequency range arcs are rather similar in the baseline sample and the ALD processed ones, whereas the high frequency arc is much smaller in the baseline sample. It should be noted that these three cells have identical components except the GDC barrier layer. This figure also shows the impedance results for polarized cells (@ current density = 0.5A·cm^2). While the total polarization at 0.5A·cm^2 is 0.268 Ω·cm^2 for the baseline sample, it increases to 0.403 and 0.396 Ω·cm^2 for the ALD processed sample 1 and 2, respectively. Figure 2-67 demonstrates the polarization behavior of sample 1 vs the baseline. It is clear that performance of the ALD processed cell is more than 50% smaller than that of the baseline cell.

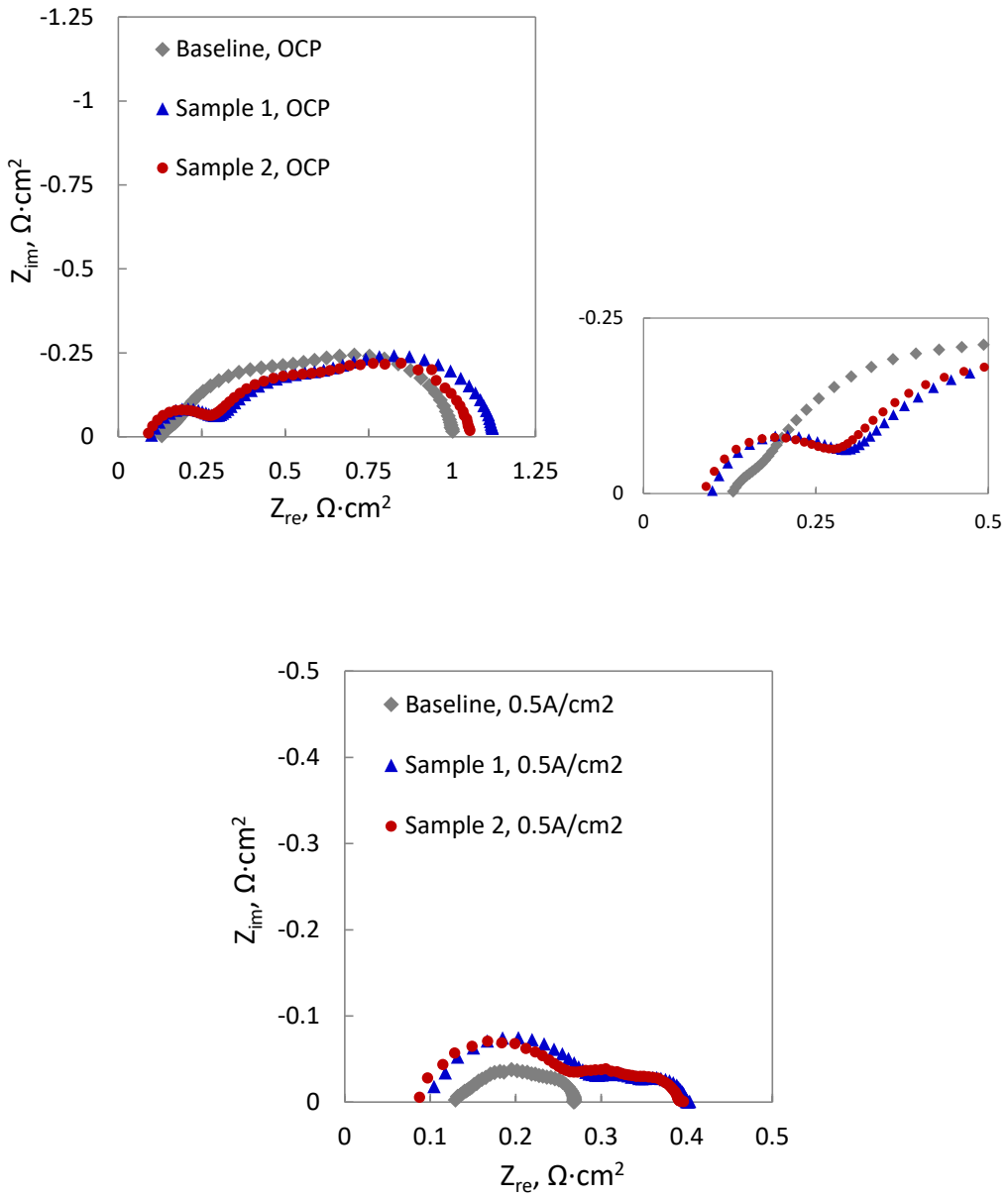

Figure 2-66 Electrochemical impedance spectra for three tested samples including a baseline cell, samples 1 and sample 2.

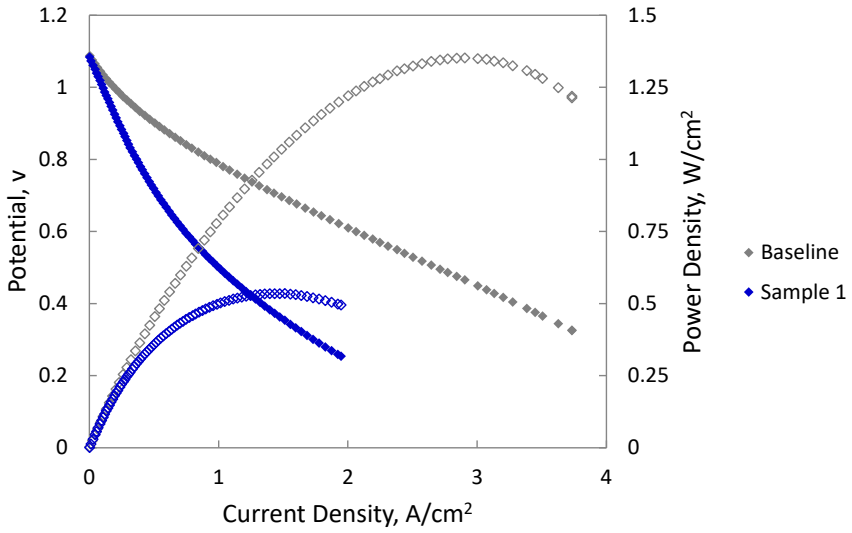

Figure 2-67 Voltage-current behavior of the baseline cell and sample 1.

The SEM micrograph of the baseline as well as sample 2 (cross sections) are shown in Figure 2-68. As indicated by the backscattered image of sample 2, a 200 nm thick barrier layer is observed which is in a good agreement with the thickness from the fused quartz monitor substrate (Table **2-7**). An EDS line scan revealed the inter-diffusion of Zr into the cathode and Sr into the electrolyte. This line scan result is illustrated in Figure 2-69. The inter-diffusion depth for Zr and Sr were estimated to be 1.5 and 0.5 μm, respectively. Figure 2-70 shows the plan view of sample 1 and 2 (GDC barrier layer on YSZ electrolyte). As observed, GDC forms slightly separated islands on the electrolyte surface. The SEM/EDS post-test analysis could explain the poor performance of the ALD processed cells comparing to the baseline. Although the barrier layer in baseline sample is not fully dense, but it is thick enough to prevent the inter-diffusion between the cathode and the electrolyte. On the other hand, the nano-sized barrier layer deposited by ALD could not prevent the inter-diffusion as it is very thin and does not appear to be fully dense. More samples will be processed and tested in order to see if a dense and effective barrier layer can be developed by ALD.

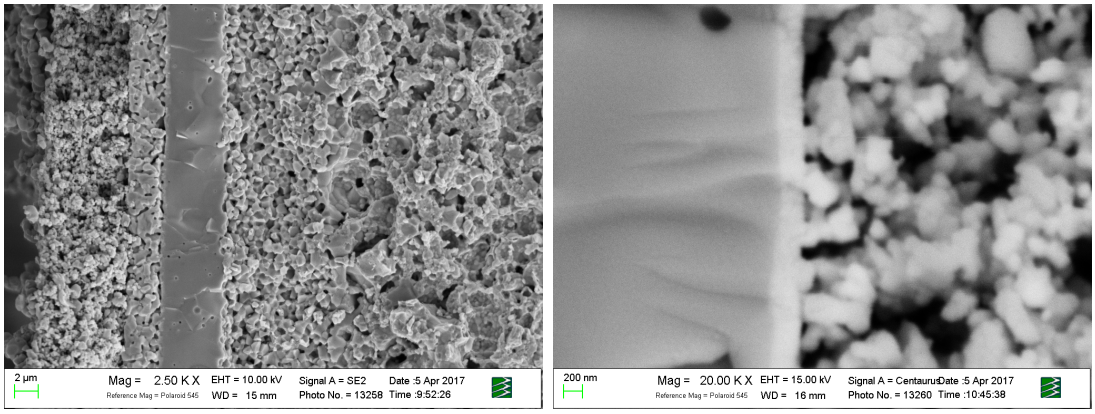

Figure 2-68 SEM micrographs (cross section) of the baseline cell (left) and sample 2 (right).

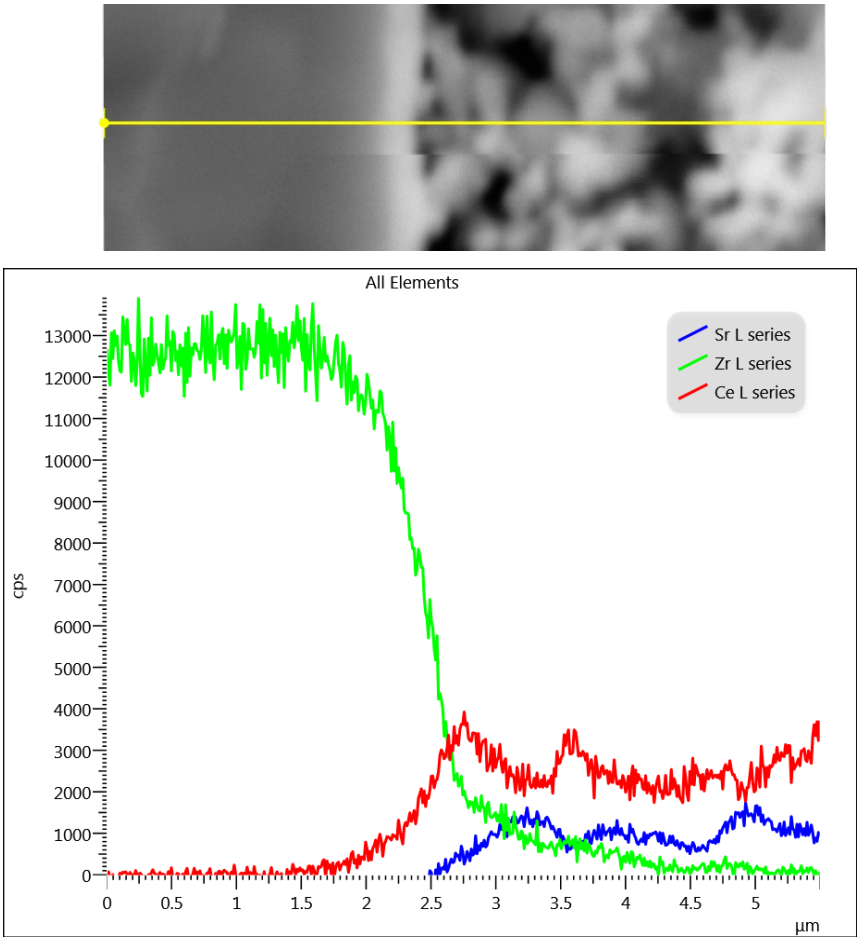

Figure 2-69 EDS line scan across the electrolyte-cathode interface for sample 2.

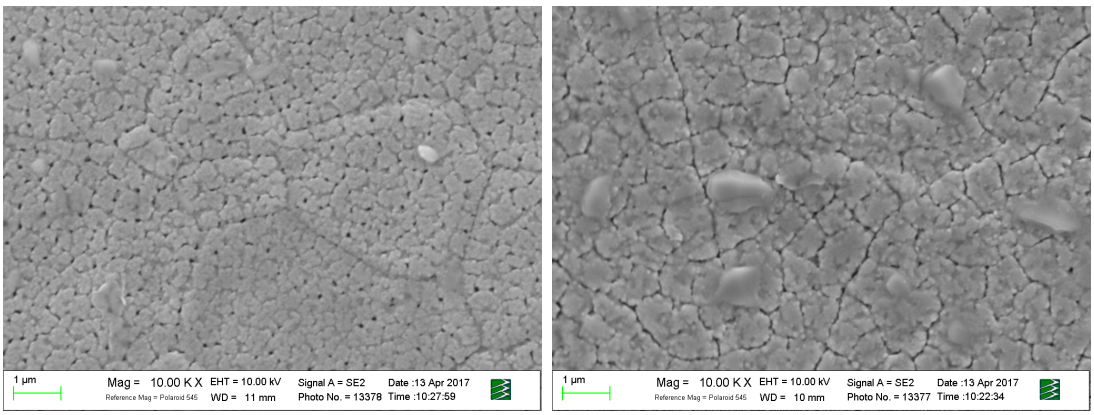

Figure 2-70 SEM micrographs (plan view) of sample 1 (left) and sample 2 (right).

In the current reporting period, results of for characterization and testing at FuelCell Energy were reviewed and additional barrier films were prepared and provided. To date, a number of samples have been provided to FCE as described in Table 2-7.

Table 2-7 GDC samples deposited on anode supported YSZ (2 samples each, one with additional Ni current collector on anode side of the sample).

Run number	Deposition temperature (°C)	# cycles	Ce dose time (sec)	Gd:Ce ratio in recipe	Approximate thickness (nm)
166	240	90	50	1:3	45
167	240	190	90@50;100@30	1:3	225
180	240	200	10	1:3	100
190	240	400	5	1:3	n.m.
204	350	550	10	1:4	130
207	350	550	10	1:4	130

Analysis of samples #166 (~40 nm thick) and #167 (~200 nm thick) revealed fine grain structure in the as-deposited condition (Figure 2-71 and Figure 2-72). This structure has a length size on the order of 100 nm and can be seen superimposed on the underlying grain structure of the YSZ electrolyte, which has a grain size on the order 1-5 µm. After subjecting the films to test conditions (750°C, 240 hr.), the grain boundaries showed much clearer definition and evidence of porosity, as shown in Figure 2-72. Another sample, #190, with a thickness similar sample 166 was deposited at a much lower growth rate by decreasing the precursor dose per cycle. It showed similar microstructure in the as-deposited condition and after test to the previous samples, as seen in Figure 2-73. Several runs were subsequently completed at a higher deposition temperature (350°C), which should improve crystalline quality of the film. Samples 204 and 207 were run under identical conditions (550 cycles, ~ 130nm) and with a recipe adjusted to yield 10mol% Gd_2O_3 content (4:1 ratio of Ce:Gd doses).

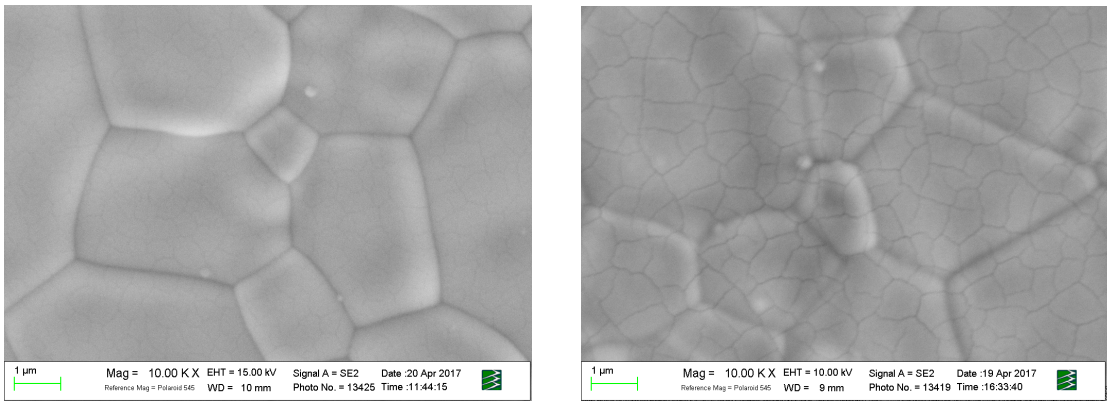

Figure 2-71 Top down SEM of GDC film as-deposited by ALD on anode supported YSZ. Sample 166 (left) with GDC film thickness ~40 nm and 167 (right) with GDC film thickness ~200 nm.

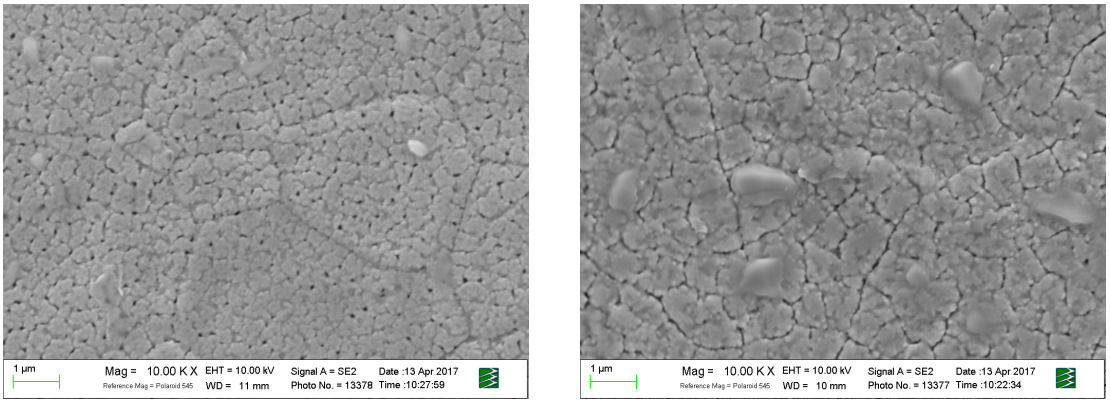

Figure 2-72 Top down SEM of GDC film deposited by ALD on anode supported YSZ and subjected to test conditions (750°C, 240 h). Sample 166 (left) with GDC film thickness ~40 nm and 167 (right) with GDC film thickness ~200 nm.

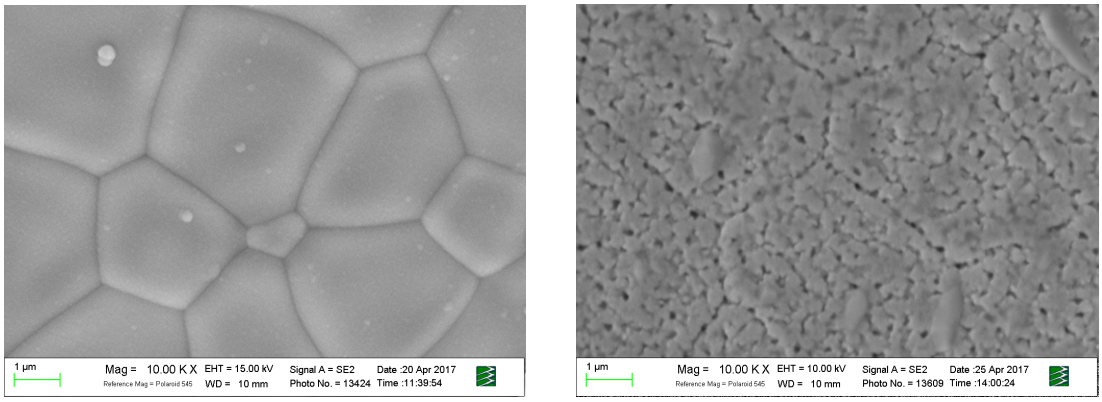

Figure 2-73 Top down SEM of GDC film #190 deposited by ALD on anode supported YSZ. Left image shows as-deposited film and right shows film subjected to test conditions (750°C, 240hr.)

The electrochemical impedance spectra (Nyquist and Bode plots) of the baseline cell (screen printed barrier layer), a cell with no barrier layer, and cells with ALD deposited barrier layers (166, 167, 190, and 207) are shown in Figure 2-74. Two important points should be noted from the impedance results in this figure. First, the electrochemical behavior of cells with ALD deposited barriers are very similar to the cell with no barrier and different from that with conventionally screen printed barrier layer. This simply implies that the interdiffusion of Zr and Sr at the electrolyte-cathode interface has not been mitigated by the ALD barrier layer. In addition, the major difference between the cell with conventional barrier layer and those with ALD barrier layer occurs in high frequency range (kHz) where interfacial charge transfer polarization is dominant. This again can confirm the detrimental effect of interfacial interdiffusion. Figure 2-75 shows the voltage-current plot at 750°C for the baseline cell, the cell with no barrier layer and samples 167 and 207. A significant performance drop is observed in the samples with ALD barrier layer, very similar to the sample with no barrier layer.

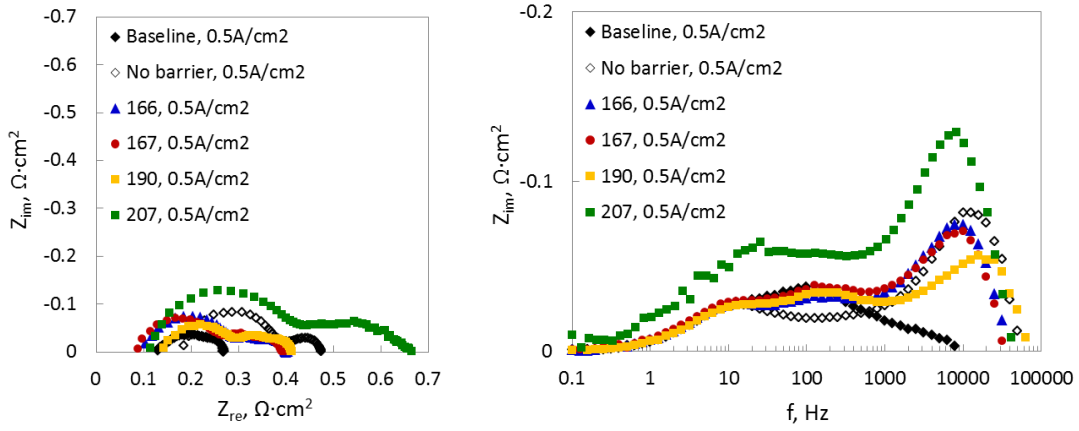

Figure 2-74 Nyquist (left) and Bode (right) electrochemical impedance plots at 750°C under current density of 0.5A/cm^2.

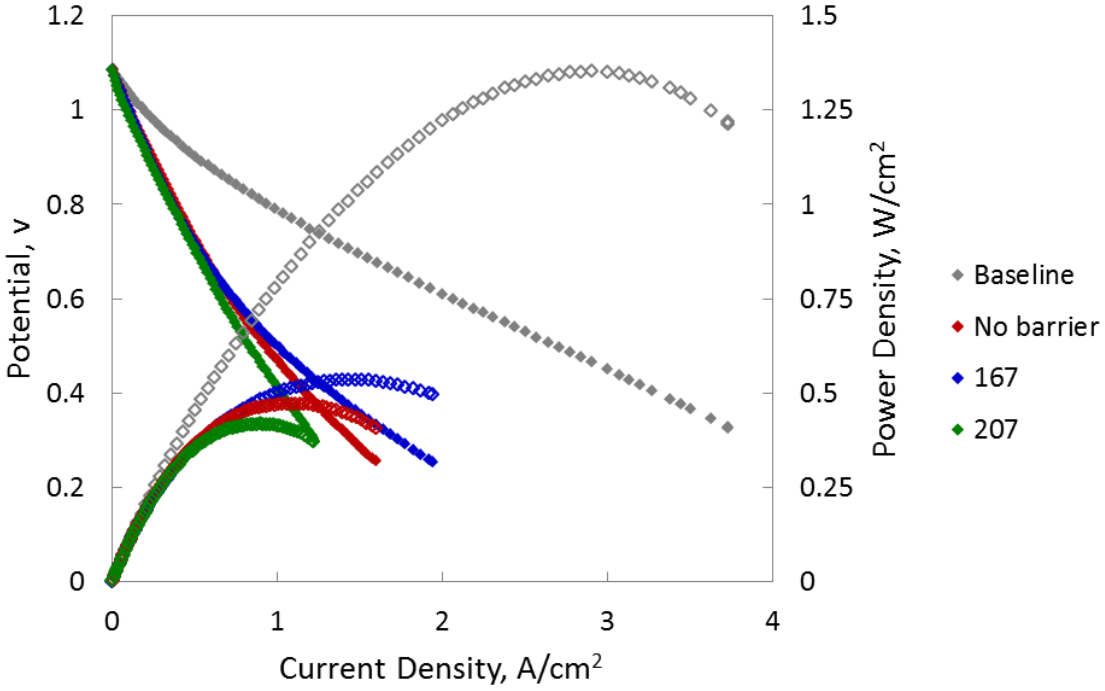

Figure 2-75 Voltage-current behavior of the tested cells at 750°C with humidified hydrogen as the fuel.

Work in the next period will focus on improving the physical properties and electrical behavior of the GDC films. Efforts will include evaluation of thicker films (~500nm) as well as strategies to densify the films and block diffusion through grain boundaries.

Milestone 2.2.2: Complete Evaluation of ADL for Fabrication of Barrier Layer

The milestone for the ADL work under this task is not completed as scheduled. The recommendation is to extend the work a further 5 months. Currently, three new samples are available for performance evaluation (button cells). The results from these tests will determine whether this innovative approach to application of the barrier layer is promising.

In the current reporting period, results of for characterization and testing at FuelCell Energy were reviewed and additional barrier films were prepared and provided. To date, 20 samples have been provided to FCE as listed in Table **2-9**.

In the current period, 8 samples were delivered (shaded in blue). All new samples were prepared further away from the reactor inlet where better film uniformity was discovered.

Table 2-8 GDC samples deposited on anode supported YSZ (2 samples each, one with additional Ni electrode on anode side of sample)

Run number	Deposition temperature (°C)	# cycles	Ce dose time (sec)	Gd:Ce ratio in recipe	Approximate thickness (nm)
166	240	90	50	1:3	45
167	240	190	90@50; 100@30	1:3	225
180	240	200	10	1:3	100
190	240	400	5	1:3	n.m.
204	350	550	10	1:4	130
207	350	550	10	1:4	130
231	350	5500	10	1:4	1000
241 (Co)	350	535	10	1:5	75
243	350	550	10	1:5	89
245 (Ti)	350	545	10	1:5	155

A thick sample was deposited for comparison (# 231) with previous thinner samples. Thickness and Gd:Ce ratio were estimated from quartz monitor samples grown prior to the thick sample. When applying the cathode, the GDC layer appeared to peel away from YSZ due to poor adhesion so no SEM or electrochemical data was measured.

A thinner sample (#243) was deposited with a modified Gd:Ce ratio to better target the 15 mol % Gd doping desired. The modified Gd:Ce ratio was also used in the doped samples (#241, 245). Thickness and Gd:Ce ratio were estimated from quartz monitor samples grown prior to the thick sample. Film thickness (89 nm) was determined from the Ce fraction of a quartz monitor sample located in a separate holder behind the electrolyte cells.

A Co doped (#241) film was deposited where Co was added to act as a sintering aid for GDC as shown by Nicholas et al. (Nicholas & De Jonge, 2007). The hypothesis was that Co should help prevent crack formation observed in previous samples during heat treatment. Target Co doping was 2 mol %. Co growth rate was measured at 1.0 Å/cycle from a quartz monitor sample. The thickness (75 nm) of the Co doped GDC layer was determined from the Ce fraction of a quartz monitor sample located in a separate holder behind the electrolyte cells. Co doping was confirmed from XRF and gave a Co thickness of 0.4 nm. The Co was distributed as 10 discrete layers spaced throughout the film thickness.

A Ti doped (#245) film was deposited. Ti has also been reported to act as a sintering aid for GDS as shown by Kuo et al. (Kuo & Su, 2012). A second hypothesis was that Ti may act as a grain boundary stuffing agent. Ti has low solubility in CeO2, and therefore should strongly segregate to the grain boundaries of the GDC layer. With regard to the grain boundary stuffing mechanism, Ti should also scavenge Zr that diffuses from YSZ to the electrode forming titanium zirconates, preventing Zr incorporation into the cathode. It should also form Sr titanates from migrating Sr from the cathode. Target Ti doping was 2 mol %. Ti growth rate was measured at 9.6 Å/cycle from a quartz monitor sample. The high growth rate is from the high reactor temperature used for GDC growth, which results in decomposition of the Ti precursor. The thickness (155 nm) of the Ti doped

GDC layer was determined from the Ce fraction of a quartz monitor sample located in a separate holder behind the electrolyte cells. Ti doping was confirmed from XRF and gave a Ti thickness of 2.1 nm. The Ti was distributed as 3 discrete layers spaced throughout the film thickness.

Figure **2-76** shows the SEM micrographs of samples 241, 243 and 245. These samples were pre-sintered at 850°C (the actual sintering temperature of the cathode). As observed, while the Co doped sample (241) has a very similar microstructure to the GDC (243), the Ti doped is largely different with much larger grain size. This type of microstructure is quite appealing because grain boundary is not only has a negative effect on electric conductivity of the GDC layer, but also facilitate the movement of Sr ions which is undesirable [Ref.. 6, 7].

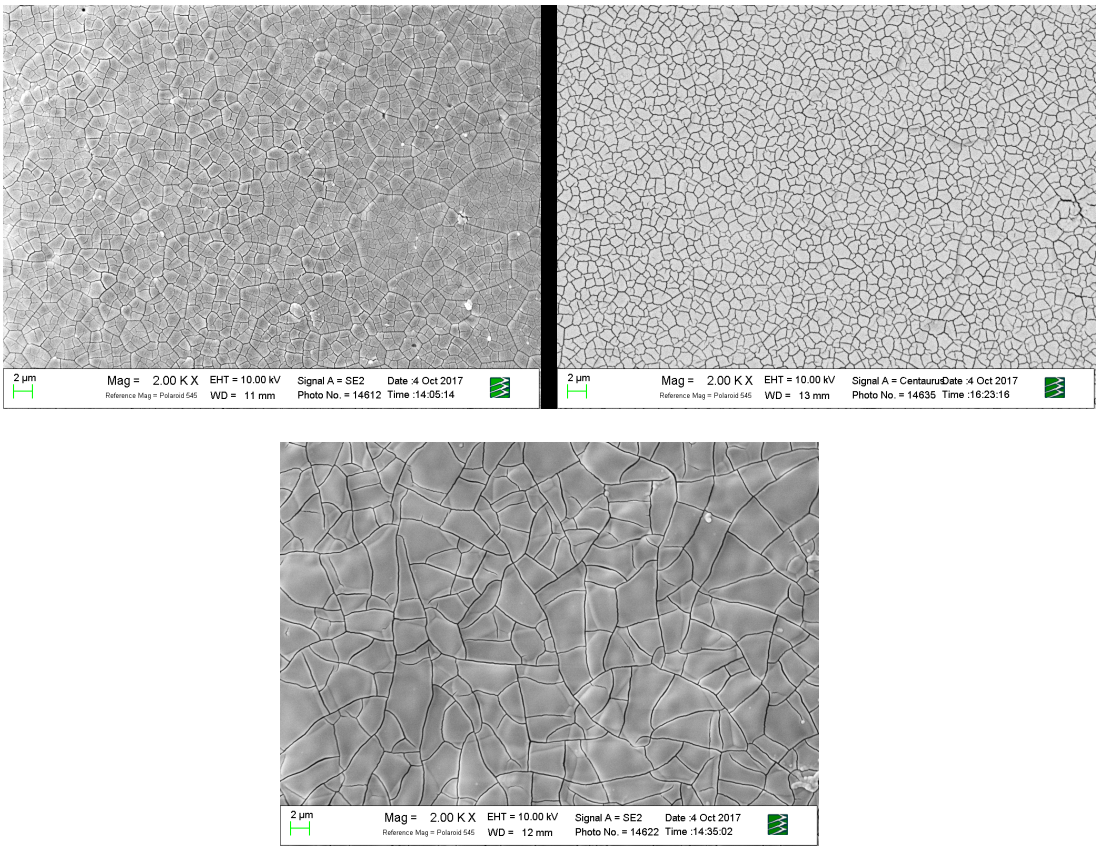

Figure 2-76 Plan view of the barrier layer: sample 241 and 243 (top left and right) and sample 245 (bottom)

The electrochemical impedance spectra (Nyquist and Bode plots) of the baseline cell (screen printed barrier layer), a cell with no barrier layer, and cells with ALD deposited barrier layers (167, 241, and 245) are shown in Figure 2-77. Two important points should be noted from the impedance results in this figure. First, the electrochemical behavior of cells with ALD deposited barriers are very similar to the cell with no barrier and different from that with conventionally screen printed barrier layer. This simply implies that the interdiffusion of Zr and Sr at the electrolyte-cathode interface has not been mitigated by the ALD barrier layer. In addition, the major difference between the cell with conventional barrier layer and those with ALD barrier layer occurs in high frequency range (kHz) where interfacial charge transfer polarization is dominant. This again can confirm the detrimental effect of interfacial interdiffusion. Figure 2-78 shows the voltage-current plot at 750°C for the baseline cell, the cell with no barrier layer and samples 167, 207, 241, and 245. A significant performance drop is observed in the samples with ALD barrier layer, very similar to the sample with no barrier layer, but samples 241 and 245 are greatly improved over previous efforts.

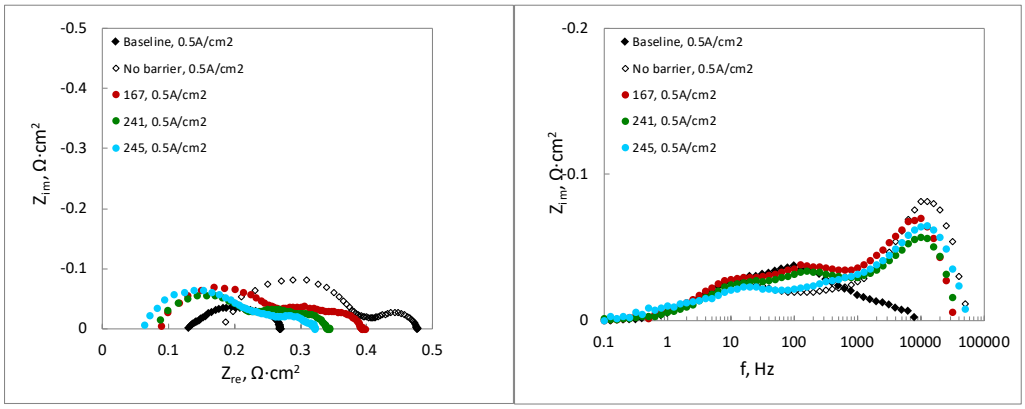

Figure 2-77 Nyquist (left) and Bode (right) electrochemical impedance plots at 750°C under current density of 0.5A/cm^2

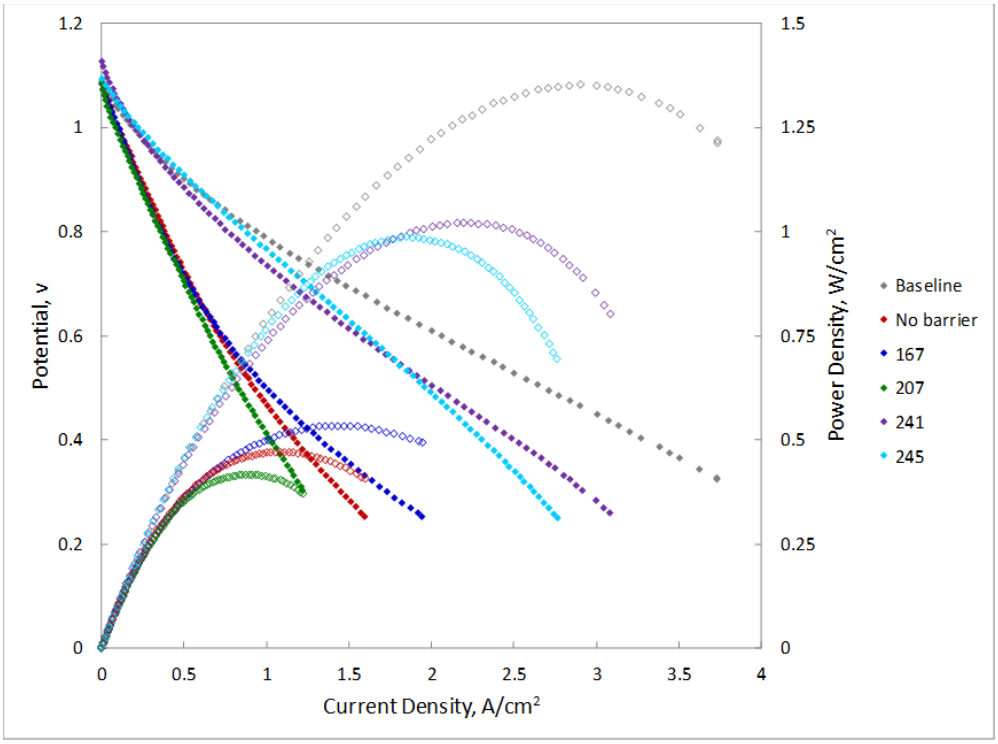

Figure 2-78 Voltage-current behavior of the tested cells at 750°C with humidified hydrogen as the fuel

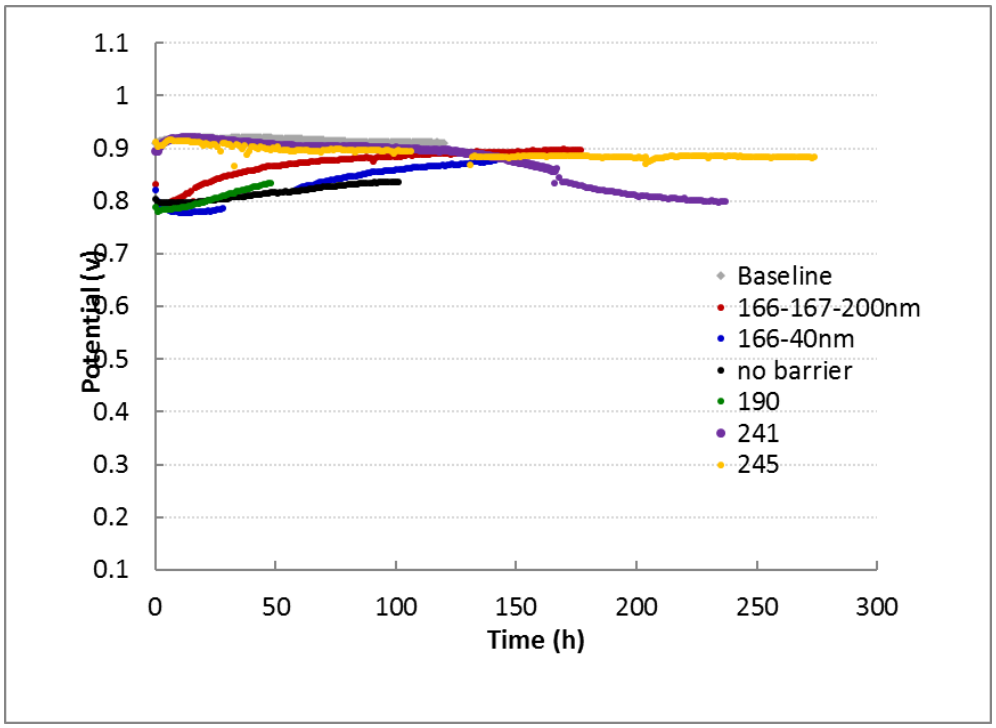

Figure 2-79 Degradation hold behavior of the tested cells at 750°C with humidified hydrogen as the fuel

Although significant progress has been made in the understanding and application of ALD to the task of applying the barrier layer, the results to date are not showing the necessary performance relative to the baseline. At this point the ALD process cannot be recommended for barrier layer application, and more fundamental development work is needed.

In the current reporting period, results of electrochemical testing at FuelCell Energy were reviewed. To date, a number of samples have been provided to FCE as described in Table **2-9**.

Table 2-9 GDC samples deposited on anode supported YSZ (2 samples each, one with additional Ni electrode on anode side of sample)

Run number	Deposition temperature (°C)	# cycles	Ce dose time (sec)	Gd:Ce ratio in recipe	Approximate thickness (nm)
166	240	90	50	1:3	45
167	240	190	90@50; 100@30	1:3	225
180	240	200	10	1:3	100
190	240	400	5	1:3	n.m.
204	350	550	10	1:4	130
207	350	550	10	1:4	130
231	350	5500	10	1:4	1000
241 (Co)	350	535	10	1:5	75
243	350	550	10	1:5	89
245 (Ti)	350	545	10	1:5	155
342	350	550	10	1:5	100
343	350	550	10	1:5	100

A thick sample was deposited for comparison (# 231) with previous thinner samples. Thickness and Gd:Ce ratio were estimated from quartz monitor samples grown prior to the thick sample. When applying the cathode, the GDC layer appeared to peel away from YSZ due to poor adhesion so no SEM or electrochemical data was measured.

A thinner sample (#243) was deposited with a modified Gd:Ce ratio to better target the 15 mol % Gd doping desired. The modified Gd:Ce ratio was also used in the doped samples (#241, 245). Thickness and Gd:Ce ratio were estimated from quartz monitor samples grown prior to the thick sample. Film thickness (89 nm) was determined from the Ce fraction of a quartz monitor sample located in a separate holder behind the electrolyte cells.

A Co doped (#241) film was deposited where Co was added to act as a sintering aid for GDC as shown by Nicholas et al. (Nicholas & De Jonge, 2007). The hypothesis was that Co should help prevent crack formation observed in previous samples during heat treatment. Target Co doping was 2 mol %. Co growth rate was measured at 1.0 Å/cycle from a quartz monitor sample. The thickness (75 nm) of the Co doped GDC layer was determined from the Ce fraction of a quartz monitor sample located in a separate holder behind the electrolyte cells. Co doping was

confirmed from XRF and gave a Co thickness of 0.4 nm. The Co was distributed as 10 discrete layers spaced throughout the film thickness.

A Ti doped (#245) film was deposited. Ti has also been reported to act as a sintering aid for GDC as shown by Kuo et al. (Kuo & Su, 2012). A second hypothesis was that Ti may act as a grain boundary stuffing agent. Ti has low solubility in CeO2, and therefore should strongly segregate to the grain boundaries of the GDC layer. With regard to the grain boundary stuffing mechanism, Ti should also scavenge Zr that diffuses from YSZ to the electrode forming titanium zirconates, preventing Zr incorporation into the cathode. It should also form Sr titanates from migrating Sr from the cathode. Target Ti doping was 2 mol %. Ti growth rate was measured at 9.6 Å/cycle from a quartz monitor sample. The high growth rate is from the high reactor temperature used for GDC growth, which results in decomposition of the Ti precursor. The thickness (155 nm) of the Ti doped GDC layer was determined from the Ce fraction of a quartz monitor sample located in a separate holder behind the electrolyte cells. Ti doping was confirmed from XRF and gave a Ti thickness of 2.1 nm. The Ti was distributed as 3 discrete layers spaced throughout the film thickness.

Figure 2-80 shows the SEM micrographs of samples 241, 243 and 245. These samples were pre-sintered at 850°C (the actual sintering temperature of the cathode). As observed, while the Co doped sample (241) has a very similar microstructure to the GDC (243), the Ti doped is largely different with much larger grain size. This type of microstructure is quite appealing because grain boundary not only has a negative effect on electric conductivity of the GDC layer, but also facilitate the movement of Sr ion which is undesirable.

More recent efforts have shown that rather than showing grain boundaries, the features seen are cracks in the film due to oxygen deficiency in the deposited film. As the film takes up oxygen, it contracts and this tension leads to the cracking seen. In order to counter this effect, a purge of oxygen is added to the ALD recipe after the water step. Replacing the water with ozone would also work, but requires modifications to the facility for safety. Samples 342 and 343 were delivered to FCE for testing using this modified recipe. Figure 2-81 is the surface of sample 343 showing that no cracks were resolvable.

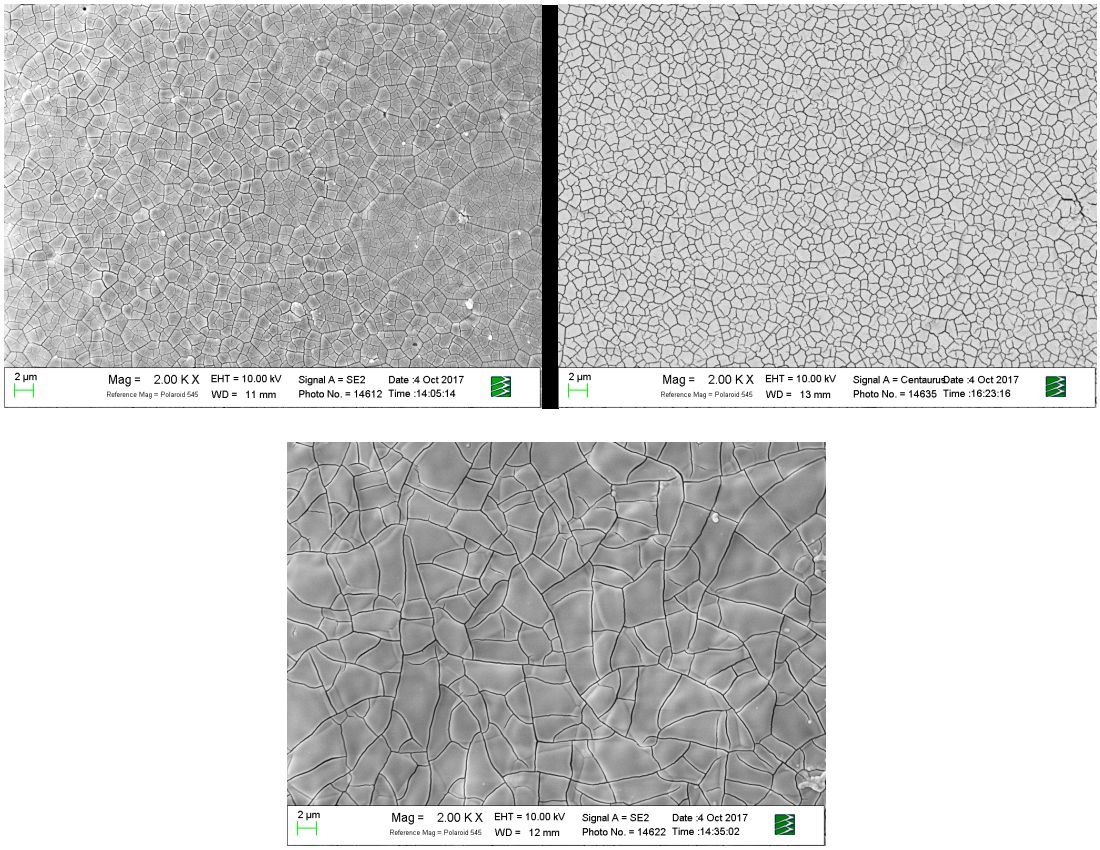

Figure 2-80 Plan view of the barrier layer: sample 241 (top left), sample 243 (top right), and sample 245 (bottom).

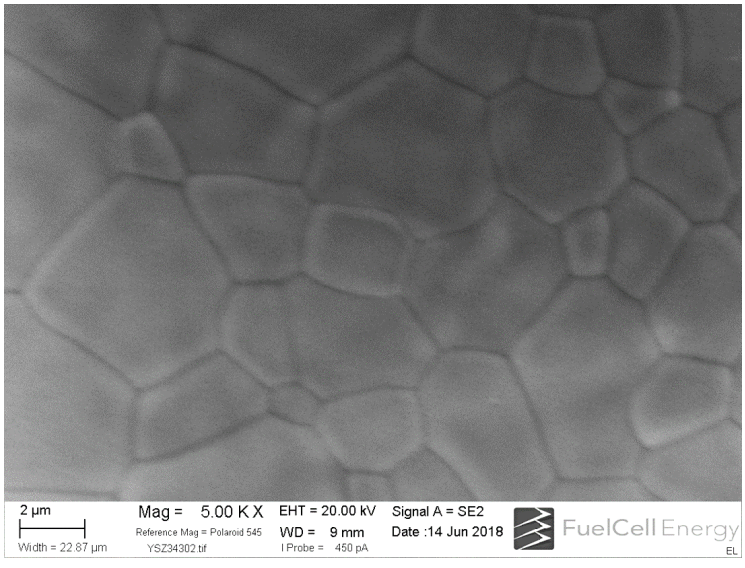

Figure 2-81. SEM micrograph of sample 343 in which no film cracks were resolvable.

The electrochemical impedance spectra (Nyquist and Bode plots) of the baseline cell (screen printed barrier layer), a cell with no barrier layer, and cells with ALD deposited barrier layers (167, 241, 245, and 343) are shown in Figure **2-82**. In prior reporting periods, it was shown that the electrochemical behavior of cells with ALD deposited barriers (167, 241, and 245) are very similar to the cell with no barrier and different from that with conventionally screen printed barrier layer. This simply implies that the interdiffusion of Zr and Sr at the electrolyte-cathode interface has not been mitigated by the ALD barrier layer in these samples. In addition, the major difference between the cell with conventional barrier layer and those with ALD barrier layer occurs in high frequency range (kHz) where interfacial charge transfer polarization is dominant. This again can confirm the detrimental effect of interfacial interdiffusion. Sample 343, however, is much improved. Figure **2-83** shows the voltage-current plot at 750°C for the baseline cell, the cell with no barrier layer and samples 167, 207, 241, 241, and 343. A significant performance drop is observed in the samples with ALD barrier layer that exhibit the cracking mentioned above, very similar to the sample with no barrier layer, but sample 343 showed greatly improved performance.

Figure **2-84** shows that results of galvanostatic hold testing @ 500 mA/cm^2 and 750 °C. Sample 343 shows improved performance over all other samples tested.

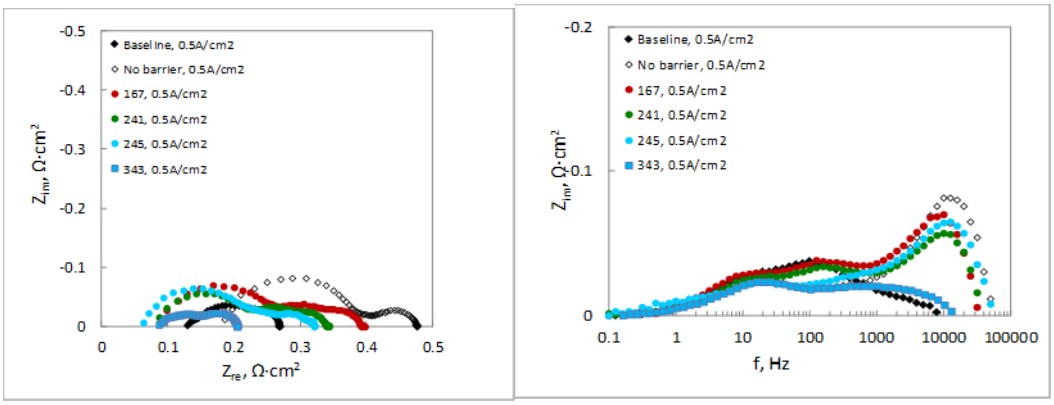

Figure 2-82 Nyquist (left) and Bode (right) electrochemical impedance plots at 750°C under current density of 0.5A/cm^2.

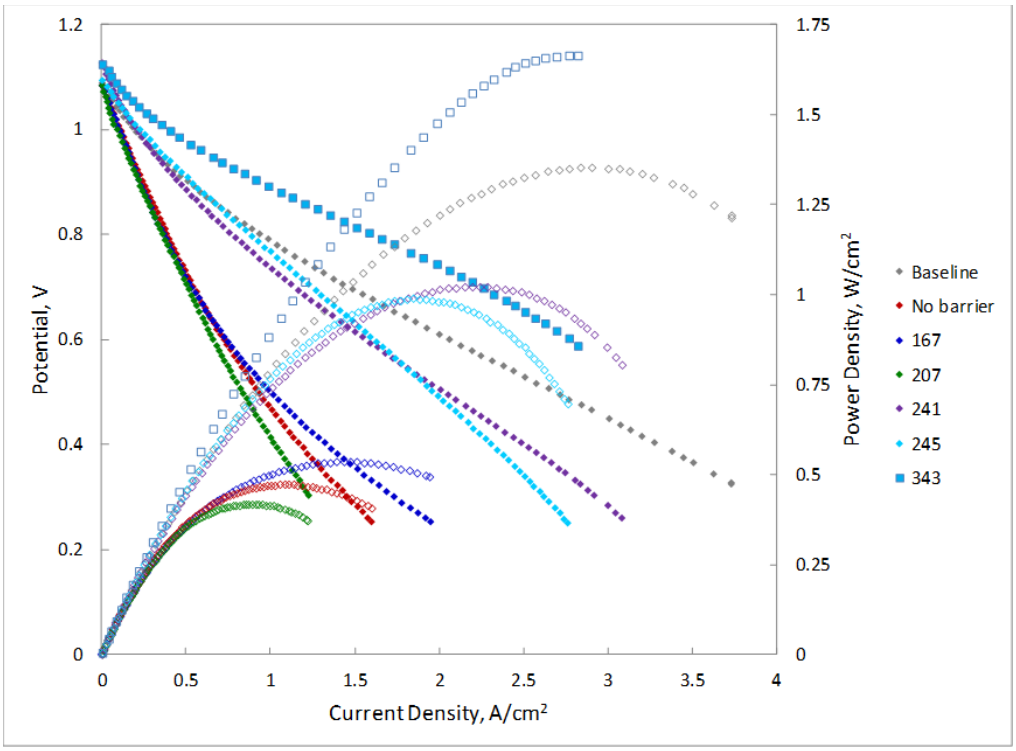

Figure 2-83 Voltage-current behavior of the tested cells at 750°C with humidified hydrogen as the fuel.

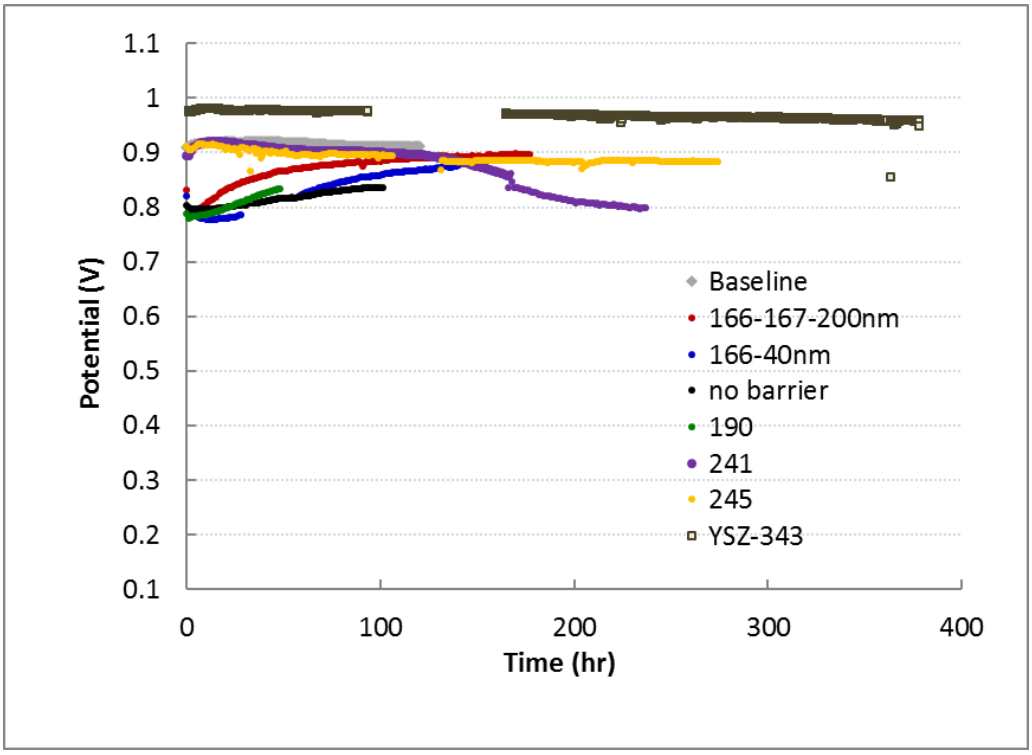

Figure 2-84 Voltage-current behavior of the tested cells at 750°C with humidified hydrogen as the fuel.

This task had previously been marked completed with less than favorable results for milestone 2.2.2 but due to results seen on another project, another attempt was made with the promising results described above.

2.2.3 Task 2.2.3 Reactive Spray Deposition Technology (RSDT)

Objective:

Demonstrate cost effective RSDT manufacturing of electrolyte

Approach:

The main objective of this task is to demonstrate the development of the RSDT deposition method for cost-effective manufacturing of dual-layer YSZ/GDC electrolyte on sintered anode supports. Components formed from the RSDT process will be evaluated via microstructure characterization as well as electrochemical cell testing. It will be verified that the innovative RSDT thin film deposition technology eliminates the need for high temperature sintering while providing an enhanced, more durable YSZ/GDC structure. The nanostructured coatings will be deposited using inexpensive precursor chemicals from solutions. The task includes studies on the optimization of the RSDT process through the key process parameters. The quality of deposited films will be examined through analytical methods such as SEM, XRD, etc. Electrochemical tests will be performed and compared to the baseline cell performance. The scale-up of the RSDT process for testing in technology stacks, including the ultimate 5kW stack, will be carried out.

Results & Discussion:

An important objective in SOFC material development is a low cost, rapid processing method that can be employed as one continuous process without the need for long sintering times at elevated temperatures. The current FCE/VPS cell fabrication process requires sintering steps both for the half-cell electrolyte and also for the screen printed cathode. Of significant concern are the reactions that can occur between materials that can lead to unwanted, high resistance secondary phases.

FCE and University of Connecticut (UConn) have been collaborating on applications of a transformational concept using RSDT to deposit thin films in an ARPA-E project. The innovative RSDT thin film deposition technology eliminates the need for high temperature sintering, while providing an enhanced, more durable cell structure. RSDT process is a cost-effective technique using a flame to deposit nanostructured coatings. Figure 2-85 shows a schematic of the RSDT apparatus (A) and a photograph of a lab scale unit (B).

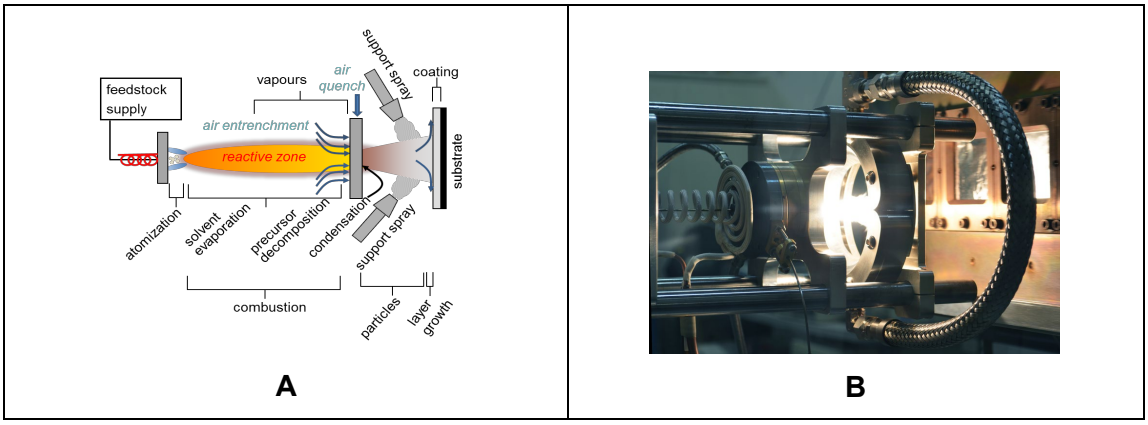

Figure 2-85 RSDT Setup

RSDT has the potential to address the project objectives by depositing thin films of appropriate material and form, porous or dense, without the requirement for further processing steps such as co-sintering. This is accomplished by atomizing solutions of appropriate precursors in a fuel-oxidant stream. Once ignited, the fine droplets of precursor solution vaporize and react to form the desired materials either in the gas-phase or as nano-scale particles as the resulting flame is impinged upon a substrate. Manipulation of a wide variety of parameters allows for a highly customizable deposition, and is what allows the single process to deposit all required SOFC materials, as either a dense or porous layer in the required sequence.

The objective of this work is to deposit gadolinium-doped ceria (GDC) with the composition $Ce_{0.9}Gd_{0.1}O_{2-\delta}$ as a diffusion-blocking layer on YSZ electrolyte. This work focuses on the evaluation of Reactive Spray Deposition Technology (RSDT) as a feasible technology for the deposition of a dense, thin (~0.5-1 µm) GDC layer without the need for the additional heating and sintering processes. The densification of the film happens due to the heat of the flame and surface diffusion during the deposition. The initial experiments were based off of previous work of Dr. Radenka Maric, in which a thin GDC film was deposited by RSDT using Gadolinium [III] 2-ethylhexanoate (Gd 2-ethex) and Cerium [III] 2-ethylhexanoate (Ce 2-ethex), dissolved in toluene, as precursors (Ref. 8,9,10,11).

Table 2-10 summarizes the parameters used for the GDC depositions performed to date for this project. All depositions use Gd 2-ethex (Strem) and Ce 2-ethex (Alfa Aesar) as precursors in roughly a 1:9 metal atomic ratio.

Table 2-10 RSDT Deposition Parameters

UConn sample ID#	Time (min)	Stand-off distance (cm)	Precursor Conc. (mM)	Solvent	Precursor Solution flow rate (mL/min)	Tip Oxygen flow rate (SLPM)	Substrate Temperature
979	120	11.8	1.0	Xylene+MeOH	2	1.5	not measured
999	110	9.84	1.0	Xylene+MeOH	3	4.8	~650-950 °C
1008	110	9.84	1.0	Xylene+MeOH	3	4.8	~800-1050 °C
1017	120	9.84	1.0	Toluene	2	3.78	~800-980 °C
1023	203	9.84	0.5	Toluene	2	3.78	~770-950 °C
1029	151	9.84	0.8	Toluene	2	3.78	~800-1000 °C
1042	120	9.84	1.0	Toluene	2	3.78	*
1051	83	8.57	1.0	Toluene	2	3.78	~800-1100 °C
1062	Failed	8.57	1.0	Toluene	2	3.78	**
1066	Failed	9.84	1.0	Toluene	2	3.78	*
1079	Failed	9.84	1.0	Toluene	2	3.78	*
1087	12	47.4	1.0	Toluene	20	20	~950 °C
II-009	11	34	1.0	Toluene	30	30	~950 °C

*The substrate temperature range was not measured, but it is expected to be the same as in #1042.

**The substrate temperature was not measured, but it is expected to be the same as in #1051.

An important focus in these experiments has been achieving a sufficiently high substrate temperature for GDC densification without causing the substrate to crack. Works by Movchan and Demchishin [Ref.12] and by Müller [Ref. 13] suggest that a critical temperature ratio, T1/Tm, where Tm is the melting point of the GDC film and T1 is the substrate temperature, is required to achieve a dense layer without microvoids. At this temperature, the diffusion of the surface GDC species balances the rate of microvoid formation by the deposited material. The diffusion of the surface species requires the species to have enough thermal energy to overcome an activation energy barrier; at higher temperature there will be greater surface diffusion. Additionally, at higher deposition rates, the rate of microvoid formation is expected to be higher. Therefore, it is observed that T1/Tm increases with increasing deposition rate. In GDC depositions by RSDT, the melting temperature of GDC has been estimated as the melting temperature of CeO_2, which is 2700 °C. For the RSDT-I depositions, the deposition rate is approximately 0.07 nm/s and for RSDT-II it can be estimated to be approximately 0.7 nm/s. From Müller's paper, the T1/Tm ratio required for densification can be estimated to be 0.22 for RSDT-I and 0.24 for RSDT-II. These correspond to substrate temperatures 594 °C and 648 °C respectively. In Dr. Maric's work, the substrate temperature was between 800 °C and 950 °C, which is comfortably above this critical temperature**.**

To achieve high enough substrate temperatures without damaging the substrate, the stand-off distance (the distance from the nozzle face to the substrate), precursor flow rate, substrate motion

pattern, and substrate mounting method were varied. Ultimately, it was determined that a relatively high precursor flow rate (20-30 mL/min), the use of a mask for mounting the substrate, along with a constant substrate position provide the best results. One of the as-prepared samples, #1087, has been characterized with top-down SEM, which suggests good density, and has been sent to FCE for performance testing. Because this sample is being used for testing, it was not possible to fracture it to perform SEM on the cross section; however, it is estimated that the thickness of the GDC layer is ~500 nm based on previous depositions. After performance testing, #1087 will be fractured for cross sectional characterization.

Depositions #979-1079 targeted a precursor flow rate of 2 mL/min to minimize the risk of damaging the substrates with a large flame. In depositions #979-1066 the substrate was moved in a raster pattern in front of the flame to ensure even coverage. #1079 failed before the raster could be used. #1087 and II-009 used a larger flame, such that it was not necessary to move the substrate in a raster pattern. In all depositions a heated stainless steel substrate holder was used with a temperature set point of 730 °C. In deposition #1051 the heated holder temperature oscillated between 726 and 737 °C, the variation is presumed to be due to the lower standoff distance of the flame and occurred during the rastering. In depositions #979-1062, the substrate was attached to the substrate holder using a ceramic adhesive, Resbond® 904 Zirconia. An example of this can be seen below in Figure 2-86. The adhesive was placed just around the edges of the substrate to adhere it to the substrate holder. In later depositions, different attachment methods were used.

Figure 2-86 Cracked Substrate, RSDT Deposition #1062 Trial 1

The #1087 sample was delivered to FCE where preliminary testing was positive. The OCV was stable and the sample performed well under load (0.7 V @ 2 A/cm2 and held @ 0.5 A/cm2 with a steady voltage of 0.927V), but broke before a full IV curve was taken. AC Impedance measurements show a very low ohmic loss of 0.15. This is indicative of adequate protection from the GDC barrier layer as zirconate phases are known to be highly resistive. Figure 2-87 shows the Impedance data and Figure 2-88 is an SEM micrograph of the tested cell cross section. The GDC layer is very thin and is not clearly evident in this image.

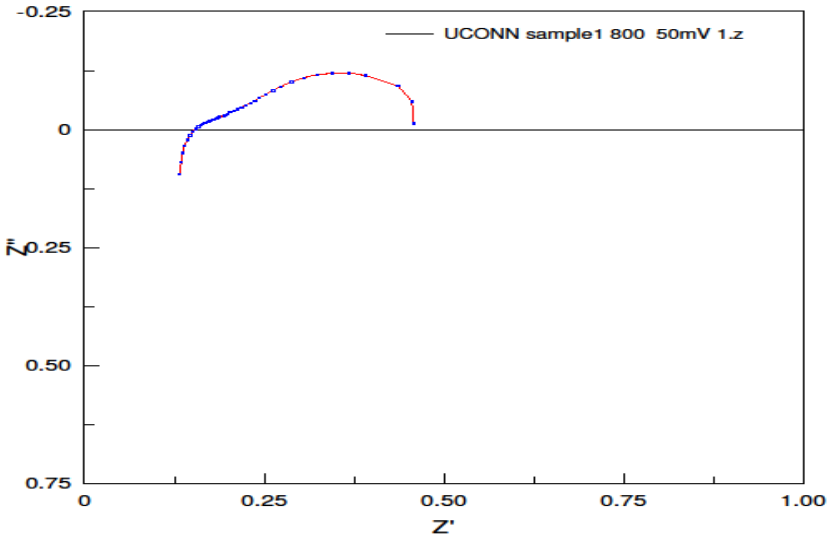

Figure 2-87 AC Impedance Curve of RSDT Tested Sample #1087

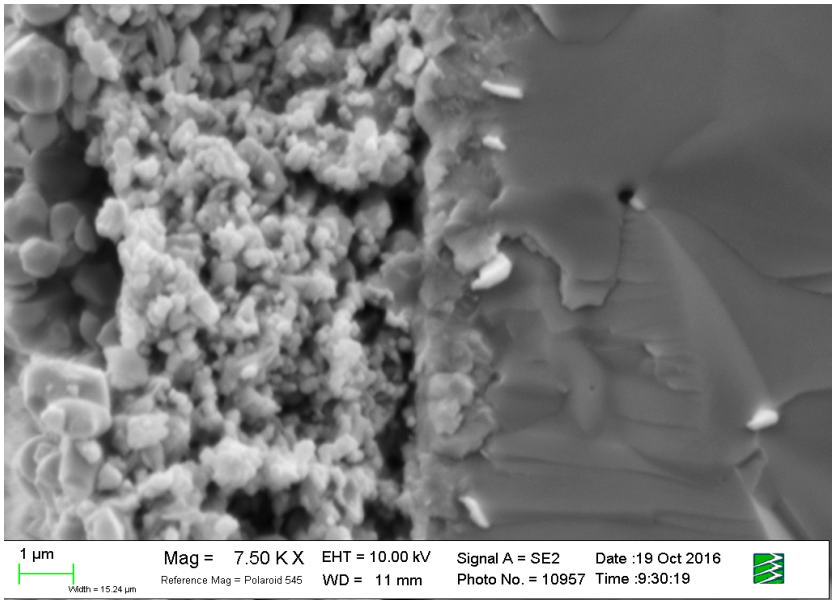

Figure 2-88 SEM Micrograph of RSDT Sample #1087

II-009 is the first deposition for this project that was performed on RSDT-II. The intention was to increase the deposition rate even further and allow for greater flexibility in precursor and tip oxygen flow rates. This deposition followed #1087, except with higher precursor and tip oxygen flow rates. The sample did not crack during the deposition. Figure 2-89 shows top-down and cross sectional SEM images. EDAX shows Gd/Ce atomic ratios ranging from 18%/82% to 13%/87%. The cross section shows that the GDC thickness is ~100nm. A different sample preparation method (potting and polishing) will be used to take more cross sectional images to verify these results. If it is desired to increase the GDC layer thickness, the substrate could be brought closer to the flame and/or the deposition time could be increased.

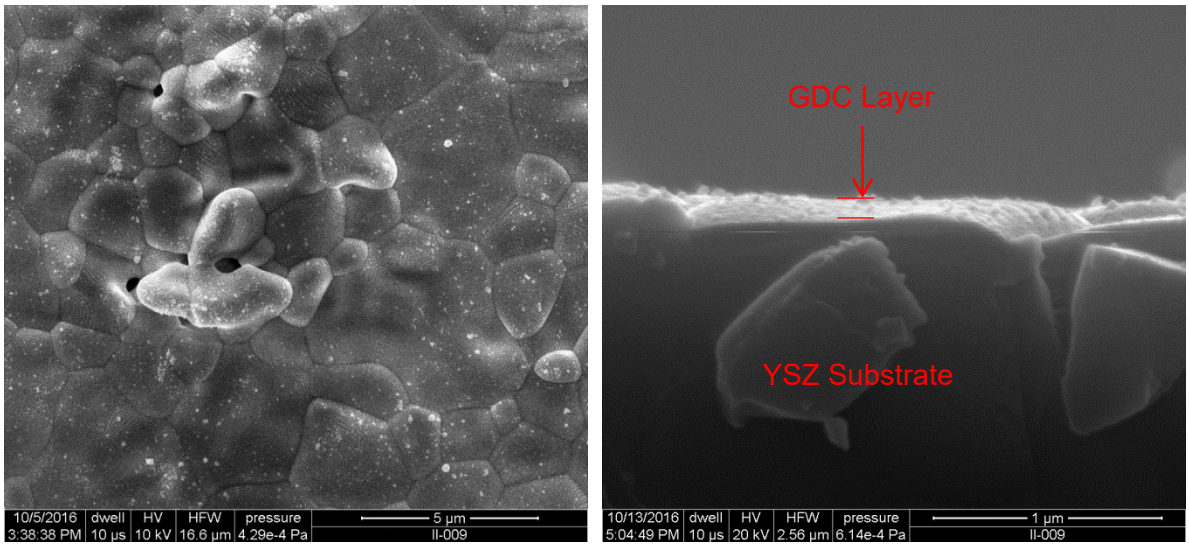

Figure 2-89 Top-down SEM images of two areas on II-009

The RSDT approach has demonstrated deposition of a dense GDC layer through optimization of the deposition conditions. The dense layer has been produced on both RSDT-I and RSDT-II (higher deposition rates). Both targeted a substrate temperature of 950°C. The stand-off distance is shorter in the RSDT-II setup, due to larger oxygen ports size which lower the gas velocity leading to a smaller flame despite the higher flow rates.

Further improvement in the yield and deposition rate will be possible by using RSDT-II with a precursor flow rate of 100 ml/min. The future work will focus on depositions on larger area cells, i.e. 5cmx5cm and 10cmx10cm. These cells will then be evaluated with electrochemical performance testing.

The Milestone Id 6 is about testing of a cell with RSDT coating and evaluation of the technique. Although the process is showing promise, the work has not yet progressed to the point of cell production for electrochemical testing. In the coming quarter the focus will be on producing a cell suitable for electrochemical testing in order to complete the evaluation of RSDT as a potential production process.

Milestone 2.2.2 Complete Evaluation of RSDT for Fabrication of Electrolyte Bi-Layer

Due: 29 Dec 2016

Status: This milestone is complete. The conclusion of the R&D activities is that the current state of RSDT technology does not warrant further pursuit for application in SFC fabrication. The technology is not ready from a physical parts perspective (using parts in real stacks) nor is it ready for detailed cost assessment, as too many fundamental feasibility questions remain unanswered.

This process has proven more difficult than anticipated to deploy. While good progress has been made, and the approach is of some technical interest, results to date do not support continued effort in the context of this program. No acceptable results (in terms of generating full size parts) have been demonstrated, and there is no reasonable expectation that the process will be able to deliver parts to this program. Therefore, in terms of evaluating the use of RSDT for fabrication of the electrolyte bi-layer, the recommendation is to consider RSDT as of possible future interest, but not suitably validated for consideration for physical parts or for cost modelling within this program. Of main concern is the higher than anticipated substrate temperature required for good

density in the GDC coating. Related to this is the problem with large temperature gradients encountered while rastering the flame across the substrate. Without a solution to this critical issue, it is difficult to scale up the process to larger parts.Table 2-11 summarizes the parameters used for the GDC depositions performed this quarter along with the successful depositions from last quarter (#1087 and #II-009). Samples #1134a and #1134b are repeats of #1087 and the samples were delivered to FCE for testing.

Table 2-11 RSDT Deposition Parameters

UConn sample ID#	Time (min)	Stand-off distance (cm)	Precursor Conc. (mM)	Solvent	Precursor Solution flow rate (mL/min)	Tip Oxygen flow rate (SLPM)	Substrate Temperature
1087	12	47.4	1.0	Toluene	20	20	~950 °C
II-009	11	34	1.0	Toluene	30	30	~950 °C
1134a	12	47.4	1.0	Toluene	20	20	~950 °C
1134b	12	47.4	1.0	Toluene	20	20	~950 °C
II-014	25	Impinging Flame	2.1	Toluene, DMF, EtOH	30	44	~850-900 °C
II-015	25	Impinging Flame	2.1	Toluene, DMF, EtOH	30	44	~700-800 °C
II-016	25	Impinging Flame	2.1	Toluene, DMF, EtOH	30	25	~575-700 °C

Additional investigation using RSDT for applying LSCF cathodes was performed. Depositions II-014, II-015, and II-016 are of $La_{0.6}Sr_{0.4}Co_{0.2}Fe_{0.8}O_{3-\delta}$ cathode using La and Fe acetylacetonates, Co acetate, and Sr 2-ethylhexanoate as precursors. Deposition parameters will be established using YSZ electrolyte as a substrate, then the process will be applied to the GDC bi-layer and this will then be tested as complete cells. Figure **2-90** shows the cells with LSCF coating while Figure 2-91 and Figure 2-92 show the SEM micrographs of the surface and cross section of II-016 respectively. Ultimately, button cells with LSCF will be delivered to FCE for testing followed by a 4cmx4cm cell to complete the study. RSDT does show promise for high performing cells at lowered cost and will be studied further in the future.

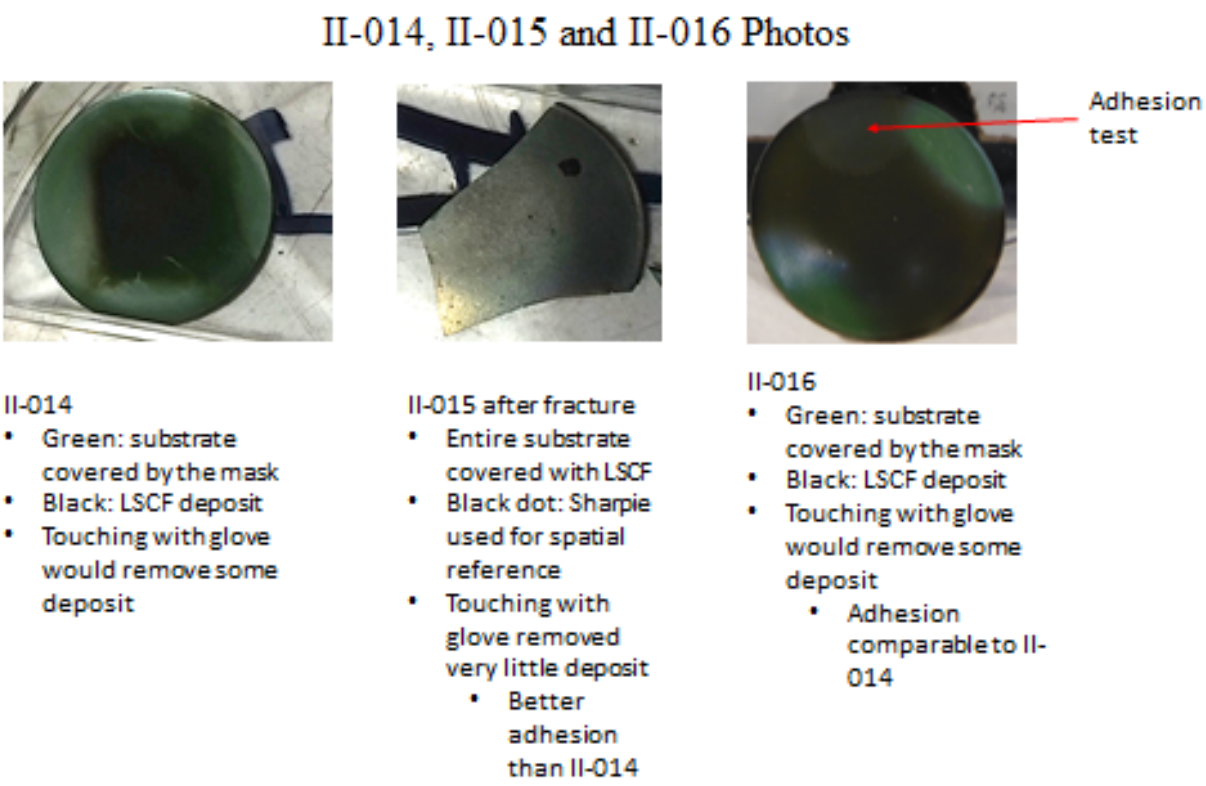

Figure 2-90 Photographs of Cells with RSDT Deposited Cathodes

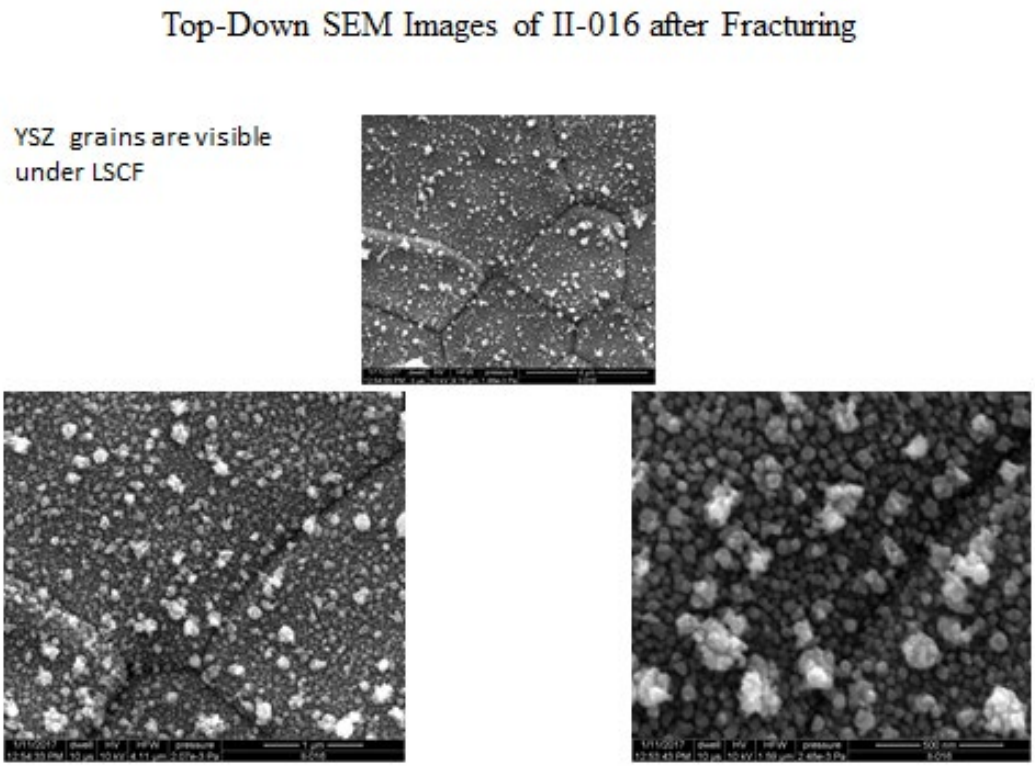

Figure 2-91 Plan view of RSDT deposited LSCF Cathode

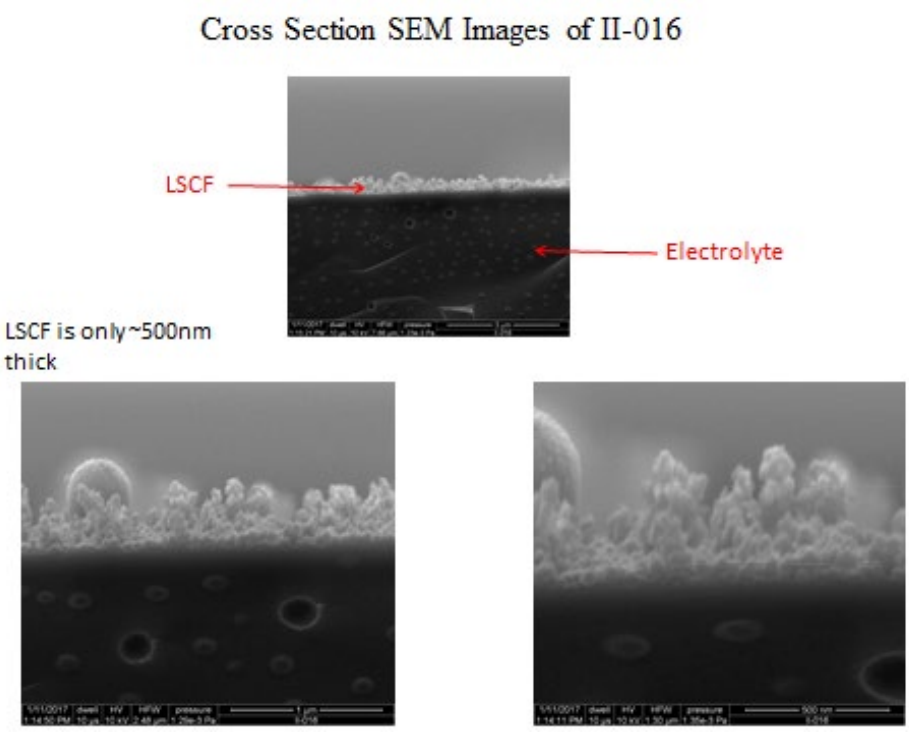

Figure 2-92 Cross Section of RSDT Applied LSCF Cathode

Attempts to coat a 5cm x 5cm ½ cell sample with GDC resulted in breakage due to the high thermal gradient of the RSDT flame. A plan to mitigate this problem with more consistent substrate heating is underway. Testing results of button cells coated with GDC and LSCF as well as LSCF without GDC is reported below.

GDC Depositions Using RSDT-I

GDC depositions were performed on RSDT-I, information about the individual depositions is included below.

#1134: This deposition was performed on two half-cells, one after another. The half-cells in this batch were notably cupped. #1134-1 was deposited for 12 minutes and had a powdery coating as can be seen in Figure 2-95. There is no clear reason why this occurred. Perhaps it was the result of the substrate cupping affecting the transport of particles from the flame. #1134-2 was deposited for 9 minutes and has a coating similar to #1087, evident both to the naked eye and in the plan view SEM image in Figure 2-94.

#1186 was performed on two half-cells, one after another. These half-cells were nicely flat and not cupped. #1186-1 was deposited for 12 minutes and #1186-2 was deposited for 8 minutes. Despite this difference in deposition time, there is no notable difference in the GDC films to the naked eye as can be seen in Figure 2-93.

#1197: Only one half-cell was coated in this deposition for 11 minutes. Instead of using the mask, a stainless steel mask with a ½" hole was used. This greatly simplified the substrate mounting process. The GDC film looked similar to the naked eye to that deposited in #1087.

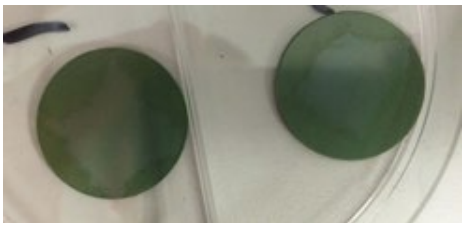

Figure 2-93 #1186-1 (left) and #1186-2 (right) after deposition. The GDC film can be seen toward the center of the cell.

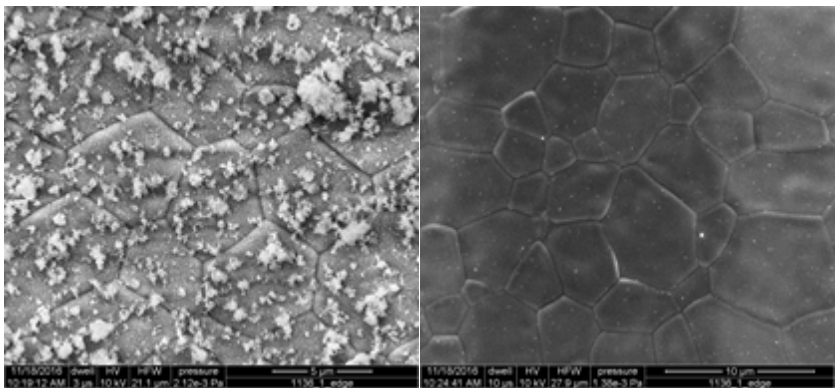

Figure 2-95 SEM image of powdery coating on #1134-1 (left) and the dense GDC coating on #1134-2 (right). In #1134-2, the GDC is transparent and the grains of YSZ are visible.

Figure 2-94 #1134-1 (left) and #1134-2 (right). The powdery coating is evident toward the edge of #1134-1.

GDC Depositions with RSDT-II

RSDT-II was used to attempt two GDC depositions on 5cmx5cm half-cells. The rationale behind using RSDT-II was that the flame in RSDT-II is larger than the flame in RSDT-I, which would allow for a more uniform substrate temperature on the larger samples,to ensure substrate does not crack due to thermal stress and that the GDC layer is dense. Both depositions used the same toluene-based precursor solution used in #1087 at a flow rate of 30mL/min and a tip oxygen flow rate of 40 SLPM. While the precursor to tip oxygen ratio for RSDT-I depositions is 1:1 [mL/min]:[SLPM], the ratio for RSDT-II is 3:4. This is due to the different nozzle geometry between RSDT-I and RSDT-II, in order to achieve a proper flame in RSDT-II.

The heated holder used in RSDT-I depositions could not be used for the RSDT-II depositions since the holder would exceed the maximum operating temperature of the heating elements. Therefore, achieving the desired substrate temperature for the RSDT-II GDC depositions relied solely on the heat from the flame.

II-019: In this deposition, the substrate was held between a stainless steel mask and frame. The mask was secured to the frame using through bolts with lock washers and finger tight nuts. The spring-like nature of the lock washers was intended to accommodate for the thermal expansion of the assembly. The substrate could freely expand in the length and width direction; the only force holding it in place was the friction between the substrate and mask and the substrate and substrate holder.

It was a particular concern that the substrate be brought to the deposition temperature, ~950°C, in a controlled manner in order to reduce the risk of cracking from thermal shock. In order to slowly increase the substrate temperature while maintaining spatial uniformity of substrate temperature, the substrate was brought to a blank toluene/propane (5:1 wt ratio) flame in a helical pattern centered about the axis of the flame. This resulted in an average temperature ramp rate of ~90°C/min, which was successfully used in RSDT-I depositions on the button cells. Despite these precautions, the substrate cracked when its temperature reached ~800°C, which coincided with the point at which the flame just began to impinge on the substrate. An attempt to mitigate the effect of thermal expansion during deposition, using a layer of stainless steel wool between the substrate and the frame, was made with **II-020**, however the substrate cracked at a lower temperature, 600 °C.

In previous work, the substrates were held in a furnace during deposition with a relatively small flame. This setup is being currently under implementation.

LSCF-6428 Cathode Depositions on RSDT-II

Initial trials for cathode depositions were performed with RSDT-II on alumina substrates and half-cells. The morphology of the alumina is similar to that of the YSZ electrolyte on the half-cell, as can be seen below in Figure 2-96. The alumina was determined to be a suitable analog for the YSZ for initial trials.

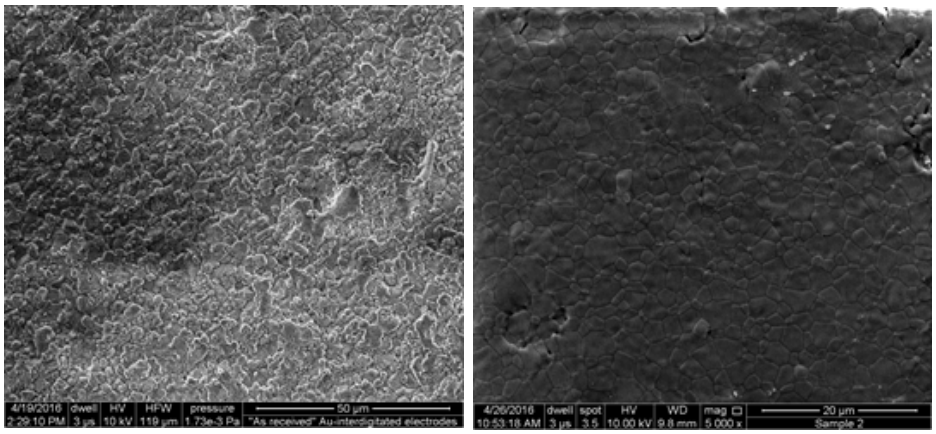

Figure 2-96 SEM comparison of the alumina substrate (left) and the YSZ electrolyte of the half-cell (right)

The approach to depositions focused on maintaining porosity suitable for the cathode while also achieving good adhesion and cohesion of the LSCF. It is well established that for similar deposition techniques, higher substrate temperatures lead to a denser deposited layer, while lower substrate temperatures lead to a more porous deposited layer. It was observed during the initial LSCF trials that substrate temperatures low enough to achieve a porous layer exhibited poor adhesion and cohesion. At higher substrate temperatures, the adhesion and cohesion were dramatically improved; however, these elevate temperatures resulted in the LSCF layer being too dense.

All initial LSCF trials were performed using a precursor solution of toluene (Fisher), dimethylformamide (Alfa Aesar), and ethanol (Fisher) with the respective weight ratios, 17.9:1:2.24. Cobalt (II) Acetylacetonate, Iron (III) Acetylacetonate, Strontium (II) Acetylacetonate Hydrate, and Lanthanum (III) Acetylacetonate Hydrate (Sigma) were used as precursors and were added to the solution in a metal ratio consistent with the intended $La_{0.6}Sr_{0.4}Co_{0.2}Fe_{0.8}O_{3-\delta}$ product composition. Prior to spraying, propane was added to the precursor solution in a 5:1 solution-to-propane mass ratio. Table **2-12** summarizes the parameters for the initial LSCF trials on RSDT-II.

Table 2-12 Initial LSCF trials on RSDT-II

Deposition	Total Precursor Conc. (mM)	Substrate	Substrate Temp (°C)	Precursor Flowrate (mL/min)	Tip Oxygen Flowrate (SLPM)	Deposition Time (min)
II-010	5	Al_2O_3	~450	30	22	24
II-011	5	Al_2O_3	~750-800	30	22	15
II-012-1	2	Al_2O_3	~750-800	30	22	9
II-012-2	2	Al_2O_3	~1000	30	44	7
II-013	2	Al_2O_3	~800-860	30	44	25
II-014	2	YSZ (half-cell)	~850-900	30	44	25
II-015	2	YSZ (half-cell)	~700-800	30	44	25
II-016	2	YSZ (half-cell)	~575-700	30	25	25
II-017	2	GDC	~600-800	30	25	27
II-018	2	GDC	N/A	30	25	26

In Table 2-12, the substrate "YSZ (half-cell)" refers to the YSZ electrolyte of the half-cells. "GDC" refers to a substrate which is a half-cell upon which a GDC layer had been deposited by RSDT-I (deposition #1186-2). Each LSCF initial trial is discussed in more detail below.

II-010: This was the initial trial for LSCF depositions. It was based off of LSCF depositions performed on RSDT-I, but with scaled up precursor and tip oxygen flow. The intended substrate temperature was 500°C, which was the temperature in the RSDT-I deposition. The setup of RSDT-II prevented the substrate from getting close enough to the flame such that the substrate temperature was ~450°C. Figure 2-97 and Figure 2-98 show a photograph and an SEM image of II-010. It is clear from these images that the LSCF adhesion and cohesion are poor and that there was insufficient LSCF collected on the substrate.

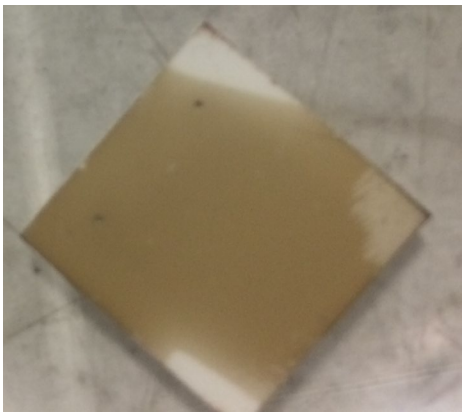

Figure 2-97 II-010 after deposition. The top and bottom corners show the shadows of the clamps used to hold the substrate to the holder. The right corner shoes there the LSCF layer is easily wiped away by a gloved finger.

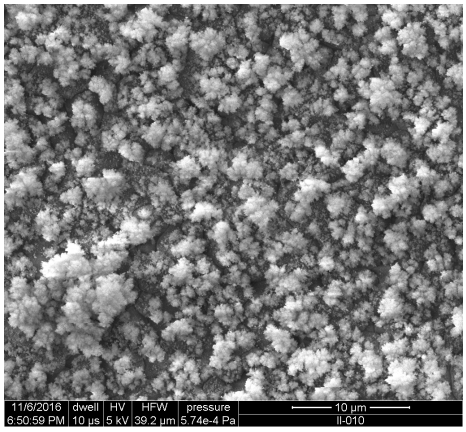

Figure 2-98 This SEM image of II-010 shows that the LSCF layer (white) is far too powdery and there is not enough material collected.

II-011: In this deposition, the substrate was positioned such that the flame just barely impinged on it. The substrate temperature was recorded to be between 750°C and 800°C. Despite this elevated temperature, which is markedly higher than that recorded for the RSDT-I deposition, the adhesion and cohesion of the LSCF are still poor, as seen in Figure 2-99 below. It is probable that the thermocouple used to measure the substrate temperature in II-011 read a temperature higher than the substrate temperature due to its positioning relative to the flame.

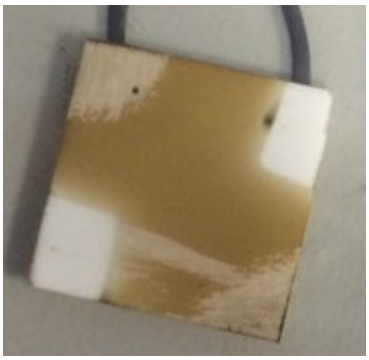

Figure 2-99 II-011 after deposition. The top-right and bottom-left corners show the shadow of the clamps used to hold the substrate to the substrate holder. The top-left and bottom-right corners show where the LSCF was wiped away with a gloved finger.

II-012: In order to improve adhesion and cohesion of the LSCF, the precursor concentration was decreased from 5mM to 2mM. A heated substrate holder was used with the holder set to 730°C as an additional measure to improve adhesion and cohesion. II-012 also investigated the impact of equivalence ratio (ER), where F is molar flow rate of fuel, O_{stoich} is the molar flow rate of oxygen required for complete combustion, and O_{actual} is the actual molar flow rate of oxygen.

$$ER = \left(\frac{F}{O_{actual}}\right) \Big/ \left(\frac{F}{O_{stoich}}\right)$$

With the conditions run for RSDT, decreasing the ER (running more fuel lean) tends to increase the flame temperature, which is what was observed in II-012. Decreasing ER from 2.5 to 1.3 increased the substrate temperature from ~750-800°C to ~1,000°C. This change in ER, and consequent increase in substrate temperature, had a notable impact on the deposited material, as seen in Figure 2-100.

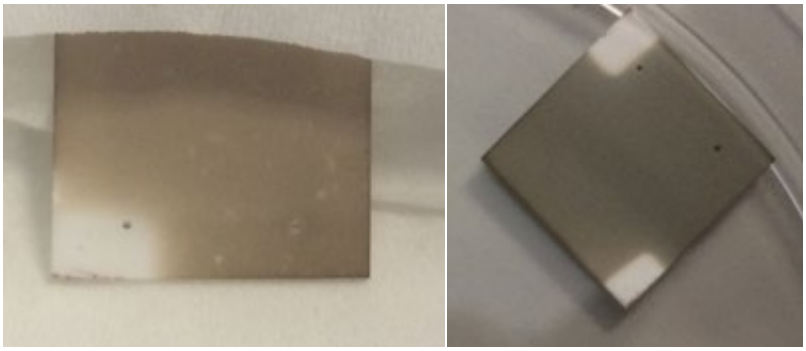

Figure 2-100 The impact of changing ER can be seen in the difference in LSCF color between II-012-1 (left) and II-012-2 (right). As in other samples, the white regions are shadows of the clamps use to hold the substrates.

Both II-012 samples show a marked improvement in LSCF adhesion and cohesion in comparison to II-010 and II-011. Little to no LSCF was be wiped away with a gloved finger in samples II-012. Despite the good adhesion/cohesion and evident coverage of the substrate, the SEM images do not clearly show any LSCF on the substrate surface, as seen in Figure 2-101. This may be the result of the densification of the LSCF due to high substrate temperature such that the LSCF conforms to the morphology of the underlying alumina.

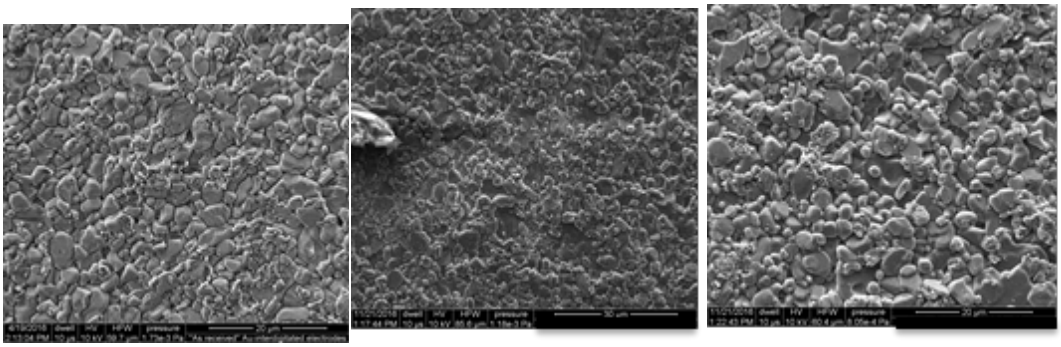

Figure 2-101 Comparison of SEM images of blank substrate (left), II-012-1 (center), and II-012-2 (right).

II-013: Because the LSCF layers in II-012 appear to be dense, it was decided to decrease the substrate temperature to 600°C to achieve a more porous layer. Achieving this substrate temperature was attempted by decreasing the heated substrate holder temperature to 300°C. Despite the lower heated holder set point, the substrate temperature was ~800-860°C. A photo of II-013 is shown in Figure 2-102. To the naked eye, it looks much like II-012-2, only darker due to a greater amount of LSCF deposited.

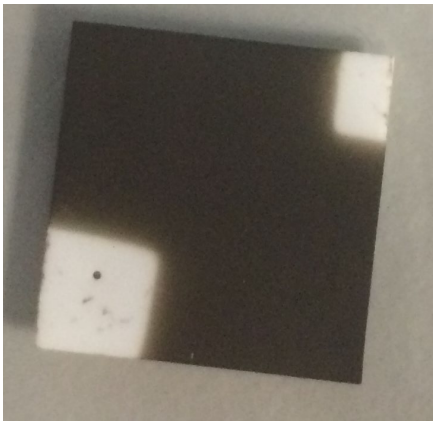

Figure 2-102 II-013 after deposition. As in other depositions, the white areas are the shadows of the clamps used to hold the substrate.

The adhesion and cohesion of II-013 are comparable to II-012. Figure 2-103 shows SEM images of II-013. There is evidence of LSCF collected on the substrate; however, it is clear that the substrate is damaged during the deposition, as gaps form between the alumina grains. Therefore, further LSCF trials will not be performed on alumina, rather on the half-cells.

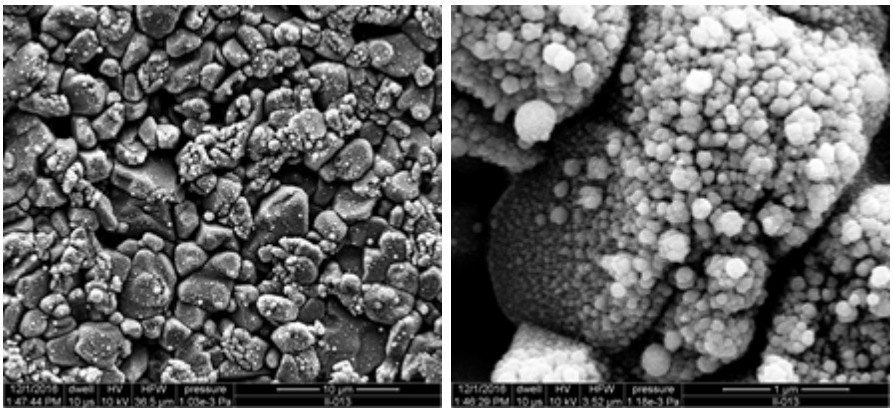

Figure 2-103 SEM images of II-013. Low magnification (left). High magnification (right)

II-014: This was the first LSFC trial done on an FCE half-cell. The heated holder was used, but was not heated. The substrate was held with a mask, unlike II-010 through II-013, which were held with clamps. This mask is described in the previous progress report. The substrate temperature was ~850-900°C. The adhesion was not as good as II-012 or II-013; some LSCF could be removed with a gloved finger. This was surprisingly since the substrate temperature of II-014 was relatively high. One possible cause for this was the use of a mask instead of clamps to hold the substrate to the substrate holder. Using a mask could have caused transport problems at the substrate surface preventing smaller, lighter LSCF particles from reaching the substrate and adhering. Figure 2-104 shows the expected black color of the LSCF. SEM was not performed on II-014.

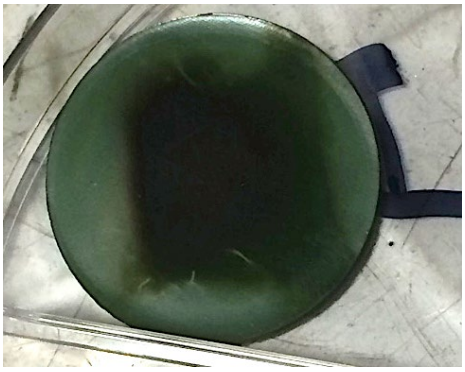

Figure 2-104 II-014 after deposition.

II-015: Because the mask was suspected of affecting the LSCF adhesion and cohesion in II-014, II-015 was performed with clamps holding the substrate in place. The substrate temperature was ~700-800°C. Figure 2-105 shows a picture of II-015 after it had been fractured to take SEM images of the cross section.

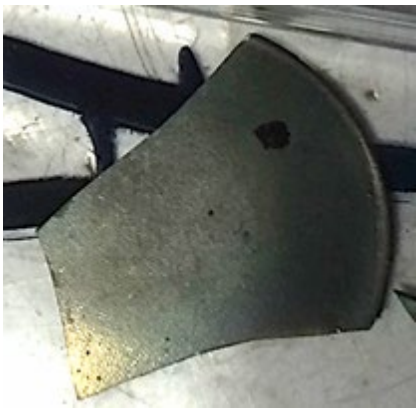

Figure 2-105 II-015 after fracturing for cross-section. The black dot is a Sharpie mark used for orientation during SEM.

The adhesion of II-015 was better than II-014 despite the decreased substrate temperature. This confirmed the suspicions that using the mask negatively impacted adhesion and cohesion of the LSCF. Figure 2-106 shows the plan view and cross-sectional SEM images of II-015, respectively. In both images, it is clear that the LSCF is too dense for a cathode. It is also apparent that the LSCF layer is too thin.

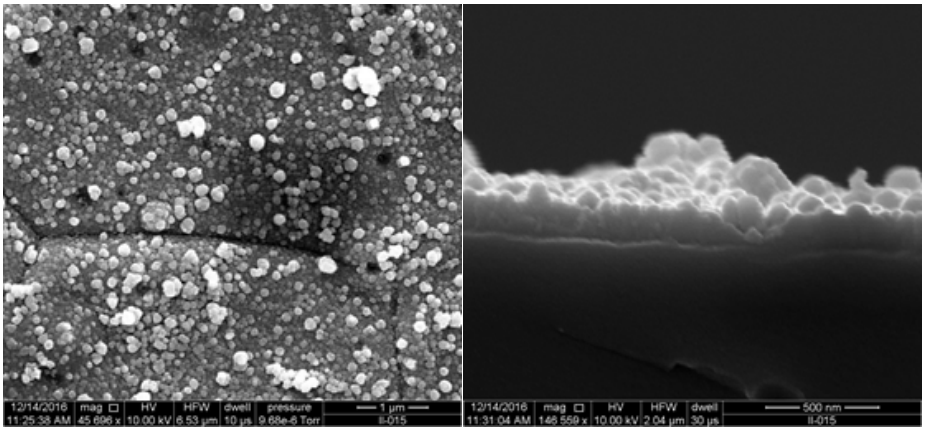

Figure 2-106 Plan view (left) and cross-sectional view (right) of II-015. In the plan view, the YSZ grains can be seen beneath the LSCF.

II-016: In II-016, the substrate was held with clamps as in II-015. The intent of II-016 was to have a lower substrate temperature in order to achieve porous LSCF. In order to achieve this drop in substrate temperature, the flame temperature was decreased by increasing the ER. To increase the ER, the tip oxygen flow was reduced from 44 SLPM to 25 SLPM. The substrate temperature was ~575-700°C. The adhesion/cohesion in II-016 was worse than II-015, which is consistent with the lower substrate temperature. The LSCF removed during the adhesion test is evident in Figure 2-107.

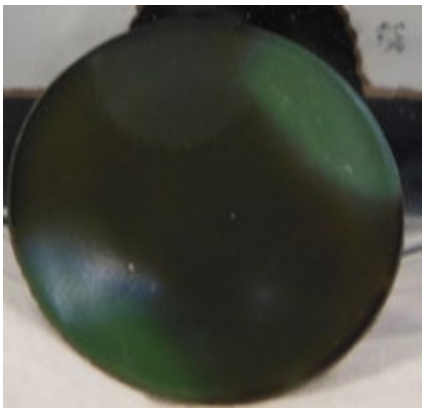

Figure 2-107 II-016 after adhesion test. The tested region can be seen in the 12 o'clock position of the substrate.

Figure 2-108 shows the plan view and cross-sectional images of II-016. It is clear in both images that the LSCF in II-016 is less dense and more powdery than the LSCF in II-015, which is consistent with the lower substrate temperature in II-016. However, the LSCF layer is still too thin.

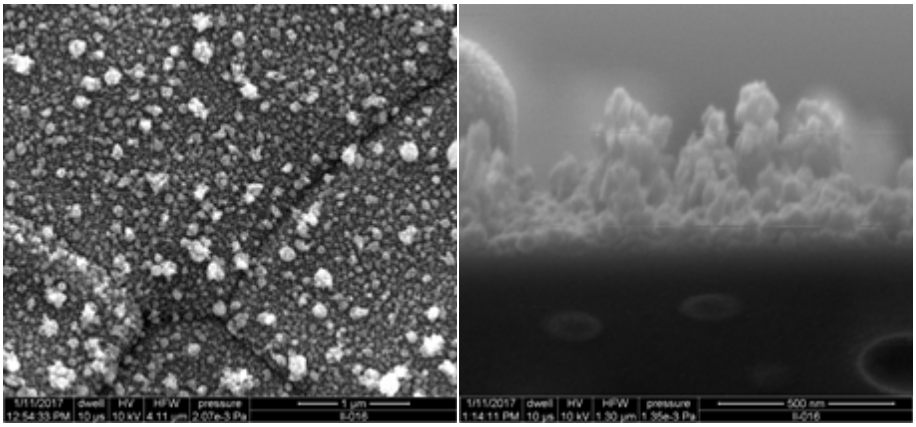

Figure 2-108 Plan view (left) and cross-sectional view (right) of II-016. In the plan view, the YSZ grains can be seen beneath the LSCF

II-017: This deposition was performed following II-016 with the intention of making a full cell sample to send for electrochemical testing. The substrate used was a half-cell with a GDC layer deposited on it with RSDT-I following #1087 (#1186-2), which is discussed in the previous progress report. Out of concern for the substrate cracking, the mask used in II-014 was used in II-017, despite the mass transport concerns. The substrate temperature was between ~600°C and ~800°C. The adhesion of II-017 was very poor as seen in Figure 2-109. This was attributed to mass transport problems introduced by the use of the mask. Because of this, different mask was used in II-018.

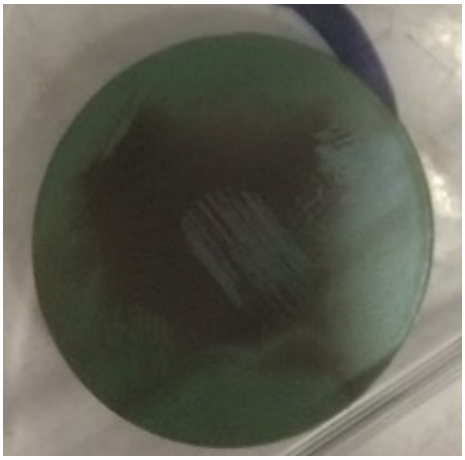

Figure 2-109 II-017 after testing for LSCF adhesion and cohesion. It is clear that LSCF was easily removed with a gloved finger at the center of the sample.

II-018: This deposition was performed to repeat II-017 with a different mask. The substrate used in II-017 was wiped clean with solvent and a Kimwipe and reused in II-018. The mask for II-018 consisted of a stainless steel frame with a 1/2" diameter hole. Fiberglass insulation was placed between the mask and the substrate to accommodate thermal expansion and prevent substrate cracking. The substrate temperature of II-018 was not measured due to the difficult in accurately measuring temperature without the thermocouple shadowing the substrate. Despite the use of the low-profile mask, the adhesion for II-018 was poor, as seen in Figure 2-110.

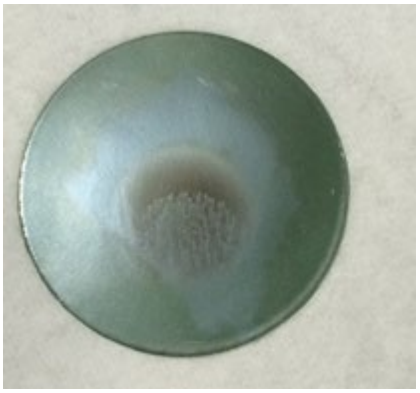

Figure 2-110 II-018 after testing for LSCF adhesion/cohesion. It is clear that the LSCF can easily be removed by a gloved finger.

LSCF Cathode Depositions on RSDT-I

Because of the poor adhesion and cohesion experienced in II-017 and II-018, which was notably worse than II-016, the plan of screen printing an LSCF layer on top of a RSDT LSCF layer was abandoned. Instead, a one-step RSDT process involving an LSCF slurry was used. This would not only achieve good adhesion and cohesion, but would avoid the need of screen printing an LSCF layer since this RSDT method alone would be able to achieve the desired cathode thickness. This alternative process was carried out on RSDT-I instead of RSDT-II.

LSCF Slurry Preparation and Spraying

The LSCF slurry was prepared using a LSCF-6428 nanopowder from CerPoTech. This was ball milled with equal volumes of DI Water and 2-Propanol (Fisher) with polyethylene glycol 400 (Sigma) to make a slurry concentrate. This slurry concentrate was then diluted in an equi-volume mixture of DI Water and 2-propanol with Nafion 5wt% solution. This diluted slurry was sprayed out of Nordson EFD 781S spray nozzles. These are referred to as secondary nozzles. An important property of the final slurry is the binder to support ratio (B/S ratio) which is defined by the following equation: $B/S_{ratio} = {(mass_{PEG} + mass_{Nafion})}/{mass_{LSCF}}$.

RSDT-I Flame

Two different approaches were taken with regards to the RSDT-I flame during the cathode depositions. One approach is to a use a blank flame (without precursors) consisting of xylenes and acetone (both from Fisher) in a 3:1 mass ratio, respectively. Another approach is to use a 2mM LSCF precursor solution similar to that used in the RSDT-II deposition described above. In both cases, propane is added to the solution in a 5:1 solution-to-propane mass ratio. In both cases the precursor/blank solution is sprayed at 4mL/min with a tip oxygen flowrate of 8 SLPM and the slurry is sprayed at a rate of 1.5mL/min.

It was hypothesized that spraying LSCF simultaneously from the secondary nozzles and from the flame would result in relatively large LSCF particles from the secondary nozzles being decorated with relatively small LSCF particles from the flame. This would increase the electrochemically active area of the cathode as compared with spraying LSCF from only the secondary nozzles.

Deposition Summary

Table 2-13 summarizes the parameters for the cathode depositions performed with RSDT-I.

Table 2-13 LSCF Depositions on RSDT-I

Deposition	Flame Contents	B/S ratio	Deposition Time (min)	Substrate Temp (°C)	Substrate(s)
1196	Blank	0.146	105	75 @ 83 min	#1186
1199	LSCF	0.148	85	80 @ 40 min	**#**1197
1213	Blank	Intended to repeat #1196 and #1199	82	77 @ 39 min	Half Cell
1229	LSCF	0.180	102	79 @ 66min	Half Cells

#1213 was intended to have the same B/S ratio as #1199 and #1196, so it is likely that the B/S ratio for #1213 is near 0.146 and 0.148. In #1229 an error in the slurry preparation resulted in the lower B/S ratio; it was intended to be approximately 0.148. One of the substrates used in #1196 had been used in II-017 and II-018. Since the LSCF adhesion in these depositions was so poor, #1186-2 was wiped clean with solvent and a Kim wipe prior to running #1196. Figure **2-111** shows #1186-2 after cleaning before #1196.

Figure 2-111 #1186-2 before being deposited in #1996. The small LSCF remnants from II-017 and II-018 occupy a circular area indicated by the red arrow.

Electrochemically Tested Samples

Six full cell samples have undergone electrochemical performance testing. Table **2-14** contains information about the six samples

Table 2-14 Samples sent to FCE for Testing

Sample Name	GDC Deposition	LSCF Deposition
FCE 1	#1186-2	#1196
FCE 2	#1186-1	#1196
FCE 3	#1197	#1199
FCE 4	N/A	#1213
FCE 5	N/A	#1229
FCE 6	N/A	#1229

Preliminary EDAX of FCE 2 showed zirconium diffusion through the GDC layer to the cathode after testing. This is likely due to the fact that the GDC is quite thin. This can easily be remedied by increasing deposition time if following the procedure of #1087. The newly proposed method using a furnace and a smaller flame will likely have higher collection efficiency than depositions based on #1087. Smaller flames tend to lead to higher collection efficiency. This higher collection efficiency can help in achieving a thicker GDC layer.

Figure 2-112 compares the performance of FCE 1-3 and FCE 5 with a cell with the standard FuelCell Energy cathode at 800 °C. As expected, FCE1 & 2 have very similar performance. FCE 3 has markedly better performance, which may be attributed to a greater active area on the cathode as a result of spraying LSCF from both the secondary nozzles and the flame. FCE 5 has no blocking GDC, but the deposited LSCF sees a maximum temperature of 860 °C as the glass sealing paste is cured briefly in testing. Any zirconate formation seems to be minor, at least initially.

Figure 2-113 gives the performance of FCE 1-3 at 750 °C and Figure Figure 2-114 shows Galvanostatic hold data at 500 mA/cm^2 for FCE 3 and briefly for FCE 5. The degradation over the short period tested looks very good. The failure of FCE 5 sample was not due to the coating.

Figure 2-115 shows an SEM micrograph of sample FCE 2. The GDC is too thin to be identified. EDAX line scans given in Figures Figure 2-116 and Figure 2-117 show diffusion of zirconia across the ceria barrier as well as a very faint ceria peak at the interface and further SEM work will be done.

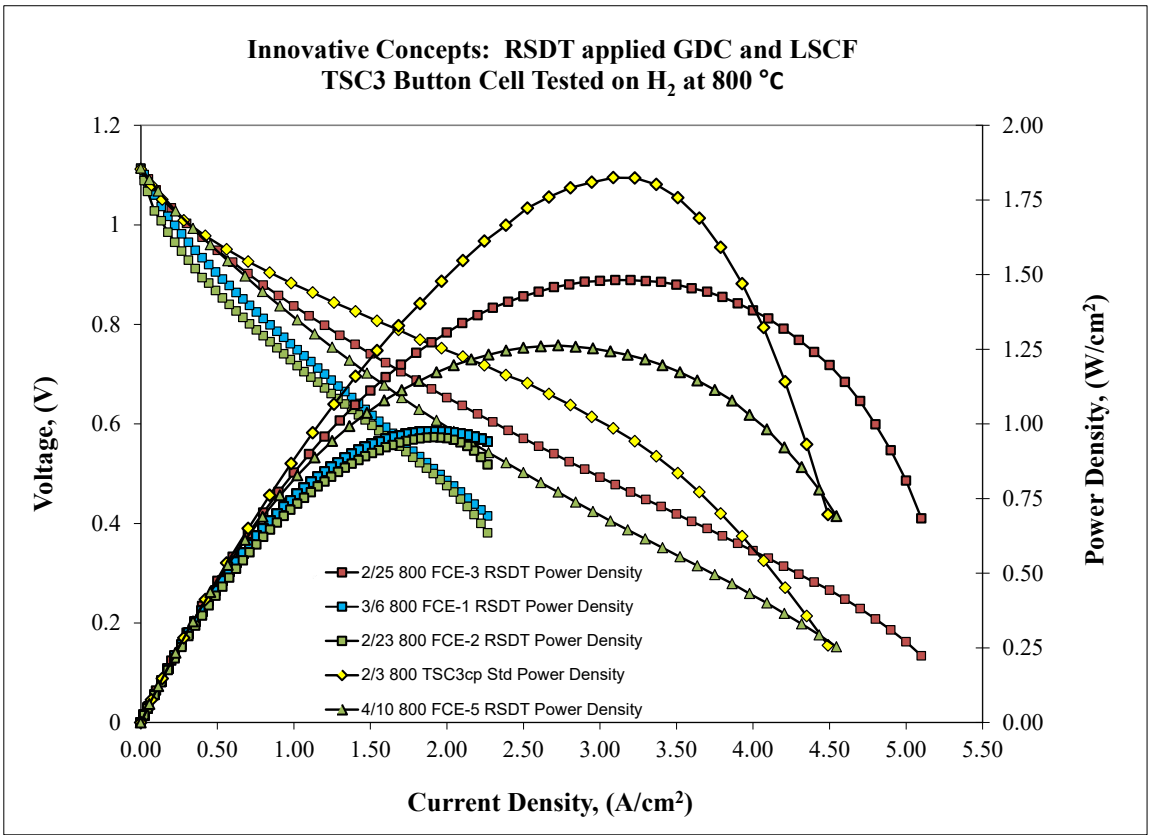

Figure 2-112 Button cell performance data at 800 °C

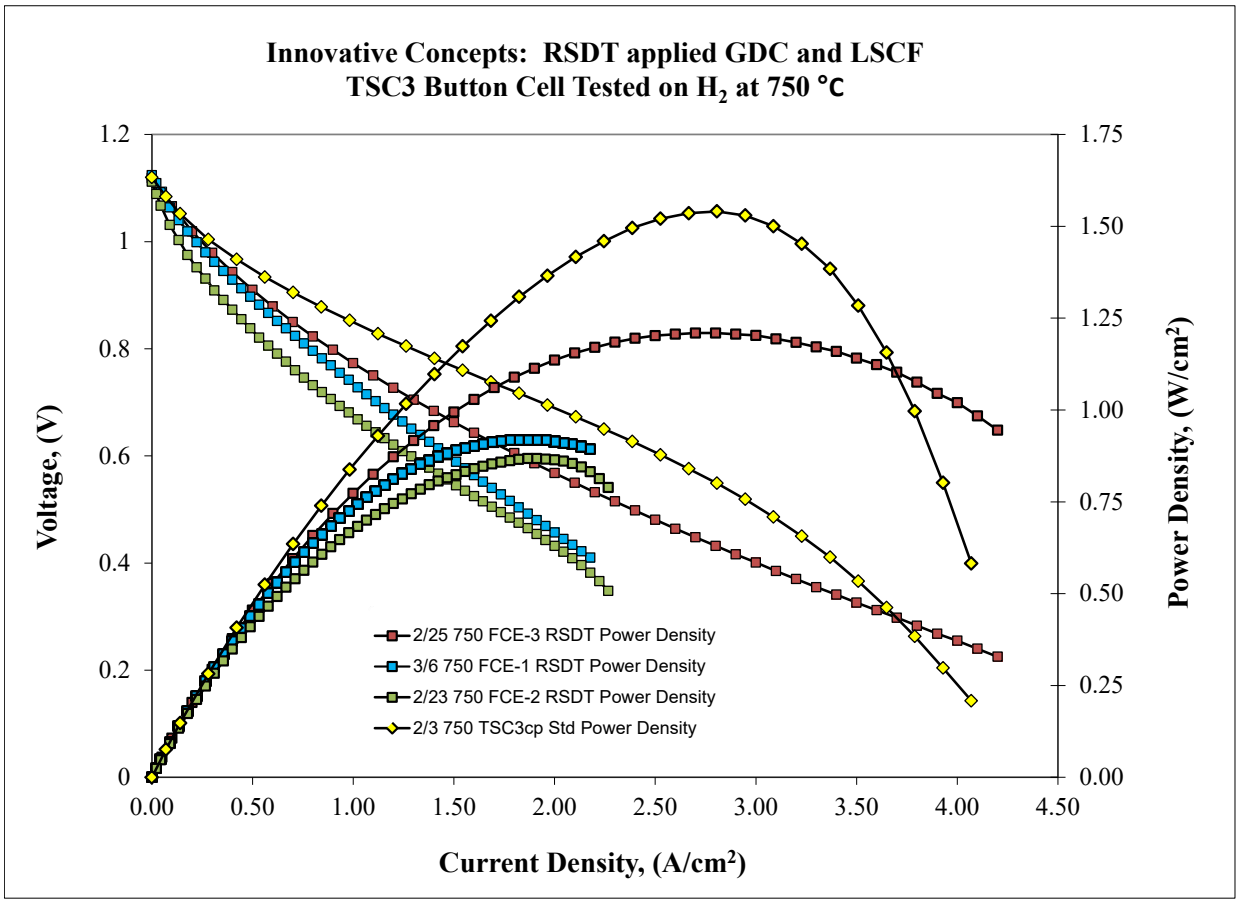

Figure 2-113 Button Cell Performance Data at 750 °C

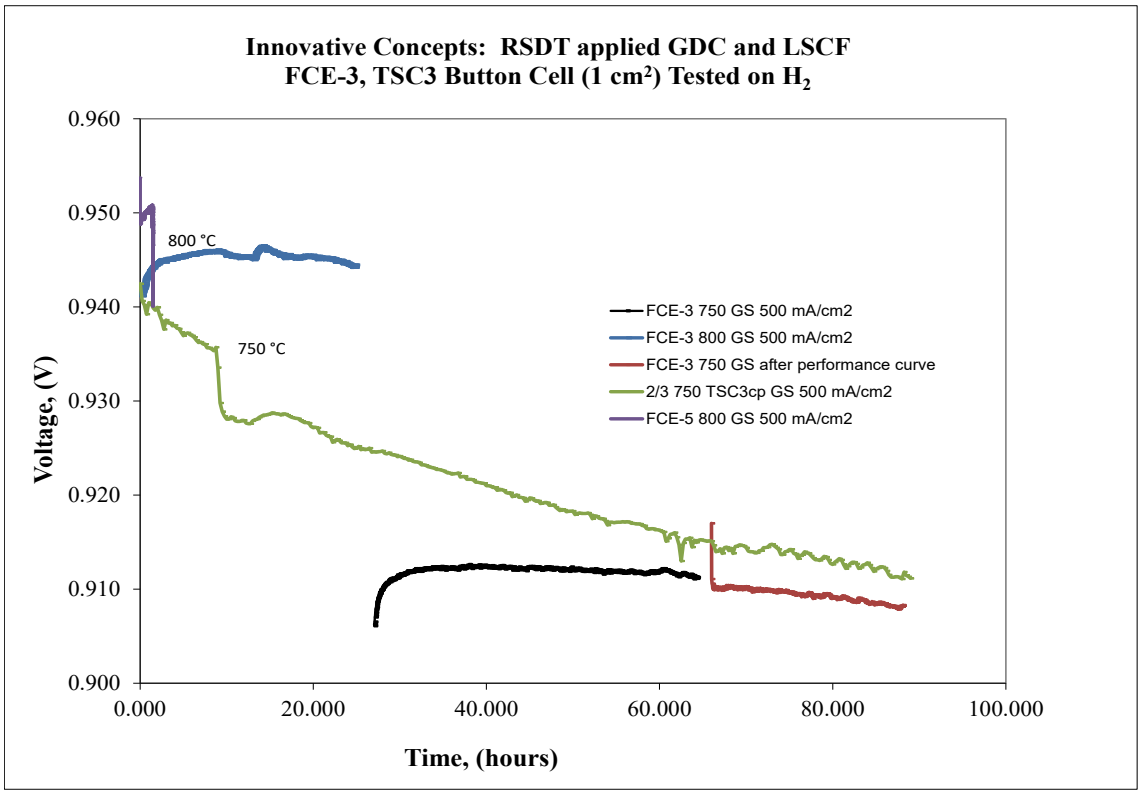

Figure 2-114 Button Cell Galvanostatic testing results.

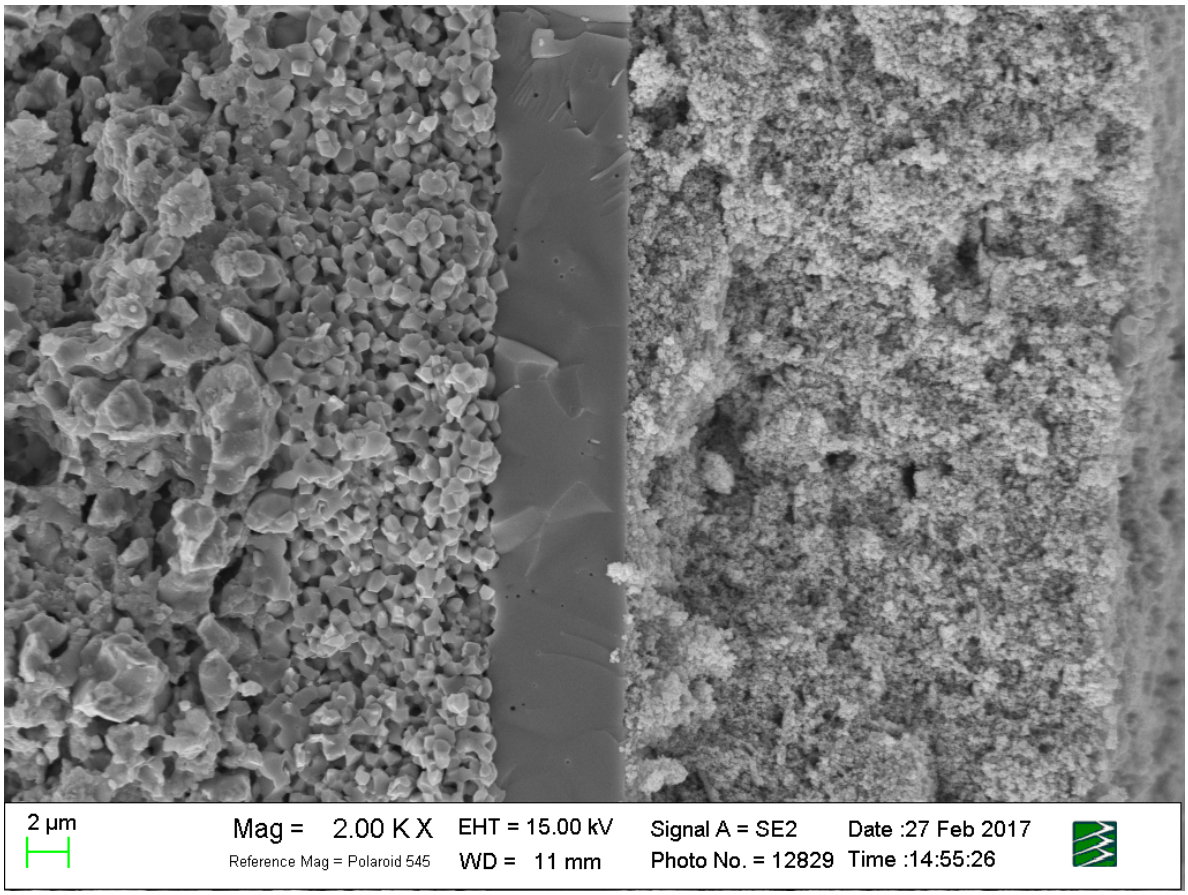

Figure 2-115 SEM Micrograph of tested sample FCE-2

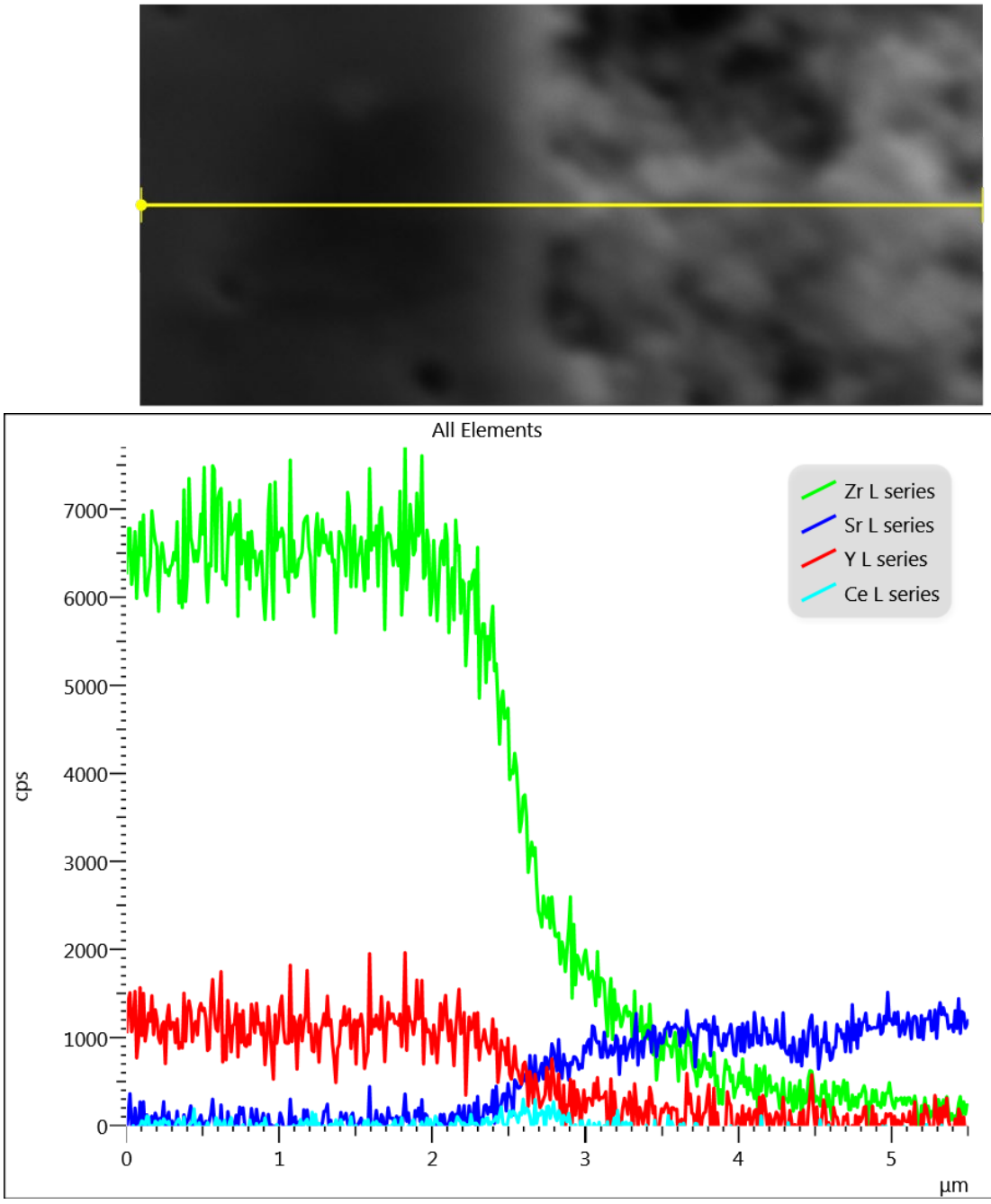

Figure 2-116 EDAX line scan of FCE-3 tested sample. Ceria peak is very small and significant diffusion of Zirconia is evident.

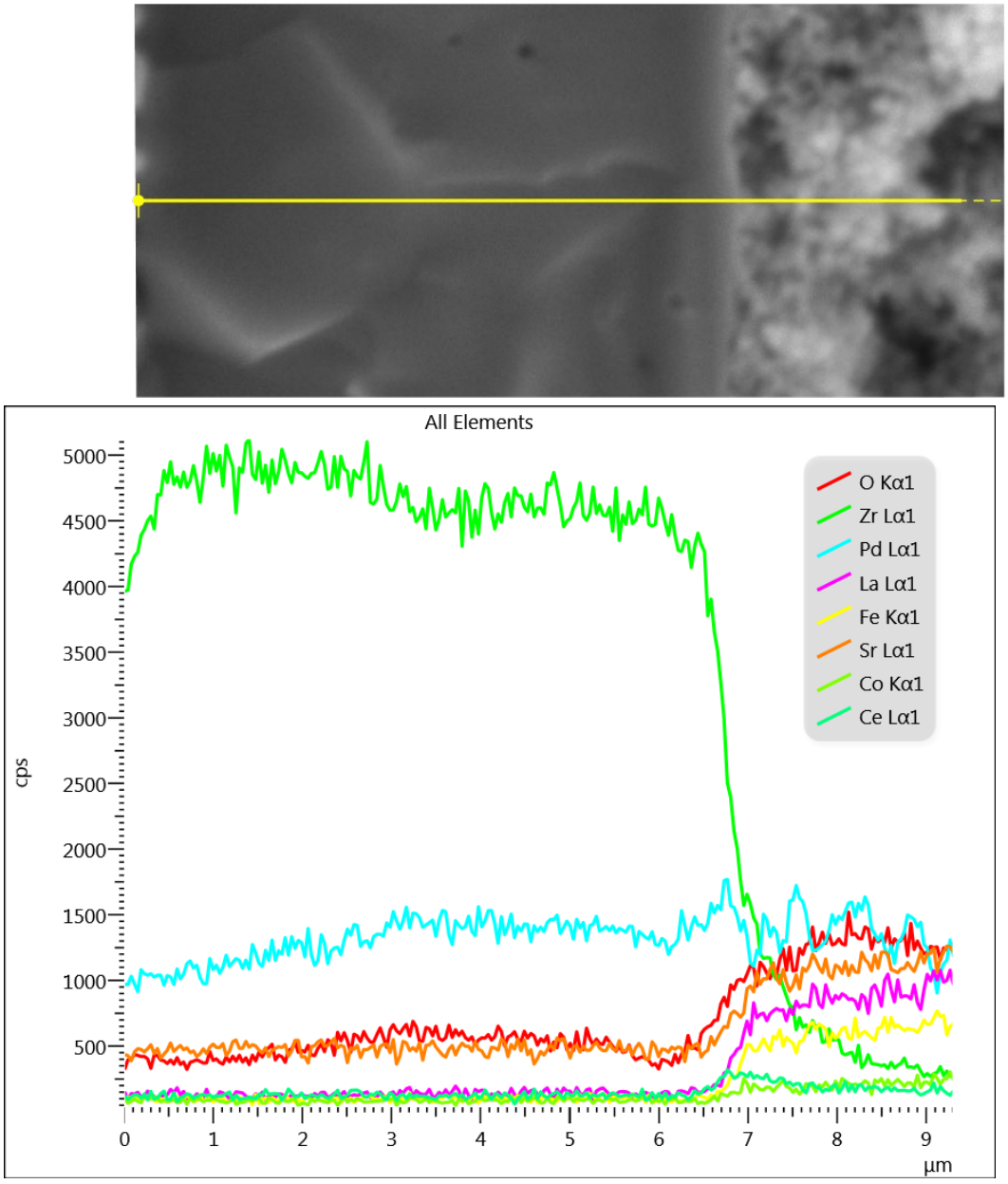

Figure 2-117 EDAX line scan of sample FCE2. Diffusion of Zirconia seen past the ceria barrier layer.

GDC Depositions on 5x5 Half Cells

GDC depositions were performed on 5x5 half cells in a manner similar to that used in a previous work. In this process, the substrates are held in a furnace to maintain uniform substrate temperature during the deposition process. Maintaining uniform substrate temperature both spatially and over time is paramount in preventing the substrate from cracking. Figure 2-118 shows setup of RSDT used with a furnace for SOFC depositions.

Figure 2-118 RSDT deposition with furnace, from left to right, side view of deposition, back view of furnace, metal mask holding substrate.

The RSDT/furnace setup used in the present work is similar; however, the main difference is that the flame in the current work is oriented vertically, depositing downward onto the substrate. This vertical orientation allows for the distinct advantage of not having to secure the substrate with a mask. This alleviates the concern of the mask limiting the thermal expansion of the substrate, which can lead to substrate cracking. Figure 2-119 shows a schematic representation of the most recent iteration of the vertical RSDT with furnace (abbreviated VRSDT).

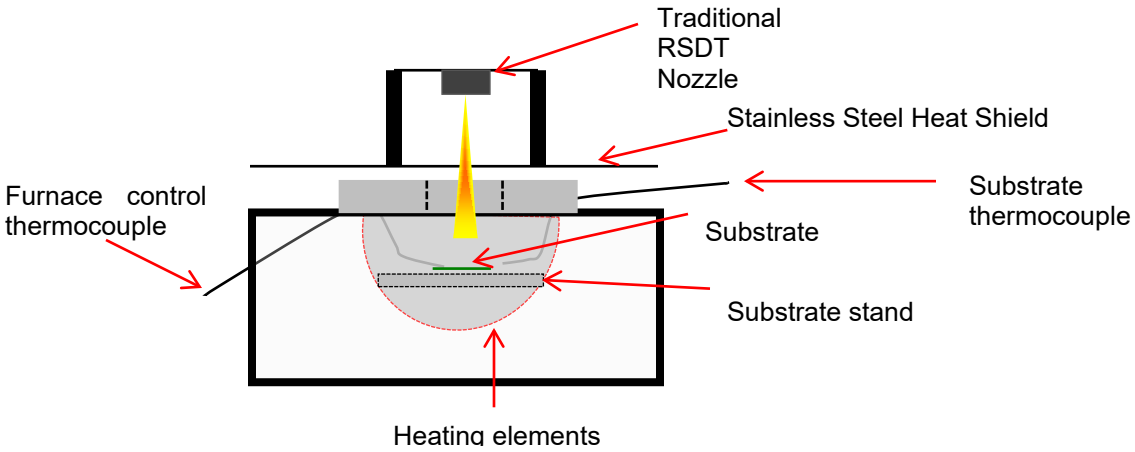

Figure 2-119 A schematic representation of VRSDT used in the present work.

The furnace is a CM 1000K Series with a Honeywell UDC 2500 power supply. The furnace was stationary and the nozzle was attached to the linear drives of RSDT traditionally used to raster the substrate. Figure 2-120 show photos of VRSDT and its components.

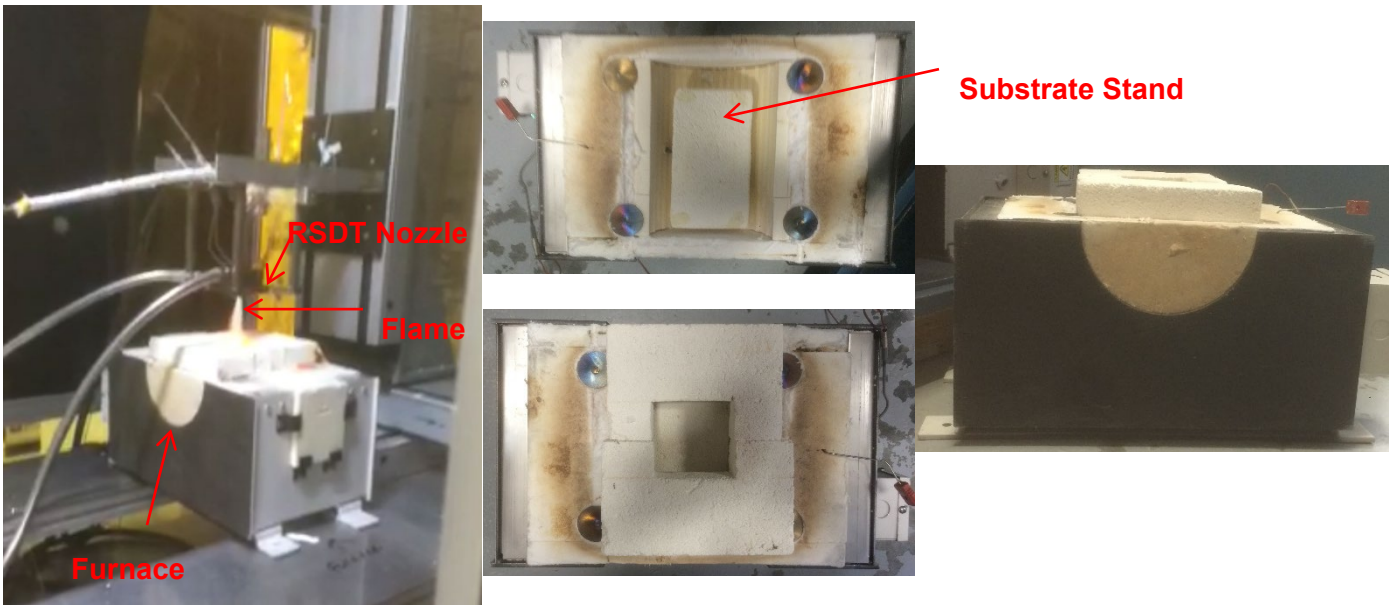

Figure 2-120 Left, VRSDT before the addition of the heat shield. Top center, top view of furnace without added insulation. Bottom center, top view of furnace with added insulation used during deposition. Right, side view of furnace with added insulation used during deposition.

A total of six depositions were performed on VRSDT and will be referred to as VRSDT-1 through VRSDT-6. Table 2-15 details important parameters for each deposition. All depositions used Cerium 2-ethylhexanoate and Gadolinium 2-ethylhexanoate as precursors with a total metal concentration of 1mM and have 17 wt% propane in the precursor solution. Prior to running the depositions, adiabatic flame temperature calculations were made using NASA CEARUN. It was intended that the flame temperature be approximately the desired substrate temperature to mitigate problems with cracking when the flame is rastered across the substrate. Calculations were performed for mixtures of methanol, ethanol, 2-propanol, acetone, and toluene with 17wt% propane. Based on these calculations and considerations of precursor and gas flowrates in the RSDT process, ethanol was chosen as the most favorable solvent, providing a calculated adiabatic flame temperature of 958 C at an equivalence ratio of 3.4 in oxygen.

Table 2-15 Deposition parameters for GDC on 5x5 half cells.

	Solvent	Precursor Flowrate (mL/min)	Furnace Setpoint (C)	Substrate Temp (C)	Swept area (cm^2)	Deposition Time (min)
VRSDT-1	**Ethanol**	**4**	**950**	**NR**	**59.1**	**93**
VRSDT-2	**Ethanol**	**4**	**1,050**	**NR**	**59.1**	**93**
VRSDT-3	**Ethanol**	**4**	**1,050**	**1010-1100**	**30.3**	**93**
VRSDT-4	**Ethanol**	**4**	**1,050**	**1010-1090**	**30.3**	**93**
VRSDT-5	**Toluene**	**4**	**1,050**	**1020-1040**	**30.3**	**92**
VRSDT-6	**Toluene**	**4**	**1,050**	**NR**	**30.0**	**45**

The temperature of the ethanol flame was measured to be ~1,000 C at ~1/2" from the flame tip.

VRSDT-1

The substrate temperature was not recorded during the deposition; however, with the furnace setpoint at 950 C and the flame temperature measured at ~1,000 C, it was expected that the substrate temperature would be ~950 C. In the absence of the flame, the inside of the furnace near the substrate measures ~850 C when the furnace is at the 950 C setpoint. Figure 2-121 shows a plan-view SEM image of VRSDT-1. The porous nature and poor adhesion of the GDC is indicative of insufficient substrate temperature.

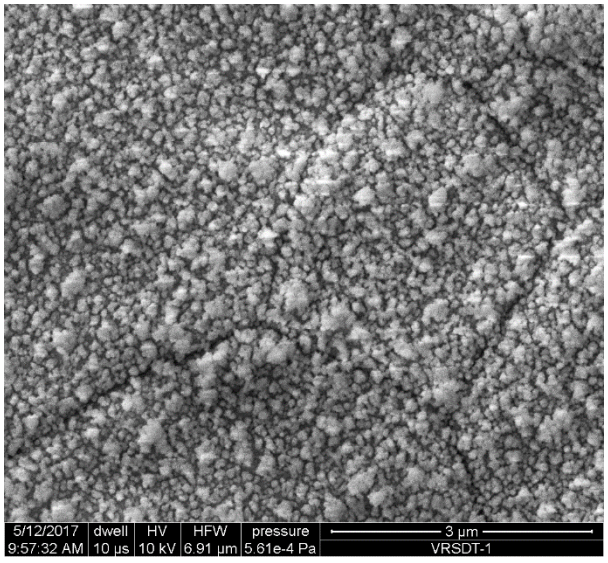

Figure 2-121. Plan-view SEM of VRSDT-1.

VRSDT-2

In an attempt to increase the substrate temperature, the furnace set point was increase to 1,050 C which increased the temperature at the substrate without the flame to ~980 C. Additionally, the flame was brought closer to the substrate. Because the furnace heating elements were too insulated, they burnt out during the deposition. Because of this, at 80 minutes, the temperature in the furnace was measured to be between 850 and 950 C. Expectedly, this low temperature led to a GDC layer with adhesion similar to that in VRSDT-1.

VRSDT-3

To avoid problems with burning out the furnace heating elements, design changes were made resulting in the setup show in Figure 2-119. All following depositions use this setup. In addition to changes in the furnace, a stainless steel heat shield was added (Figure 2-119) in order to reflect heat back into the furnace. This helps to maintain a uniform substrate temperature and decreases the load on the furnace. The raster area was also decreased in order to achieve a higher, more uniform substrate temperature. Throughout the deposition, the substrate temperature was measured to be 1,010-1,100 C. Due to thermocouple positioning, it is likely that the actual substrate temperature was lower. Despite this increased temperature, there are still islands of GDC present on the substrate as seen in Figure **2-122**.

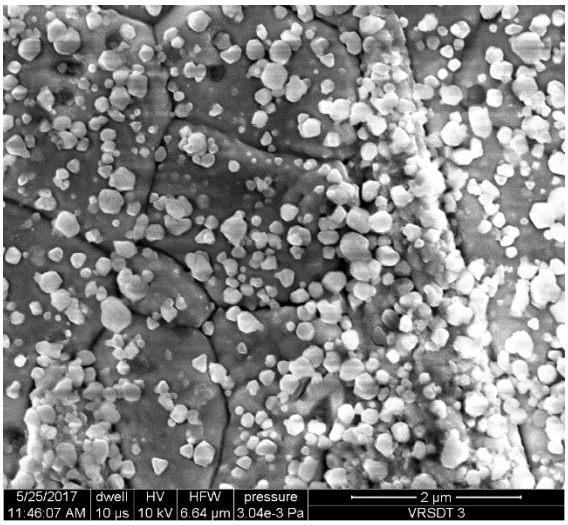

Figure 2-122 Plan-view SEM of VRSDT-3.

Figure 2-123 shows point EDAX results for VRSDT-3. From these results, it seems that there is a dense GDC layer in addition to the GDC islands.

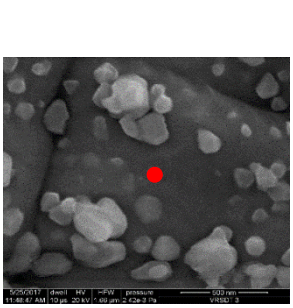

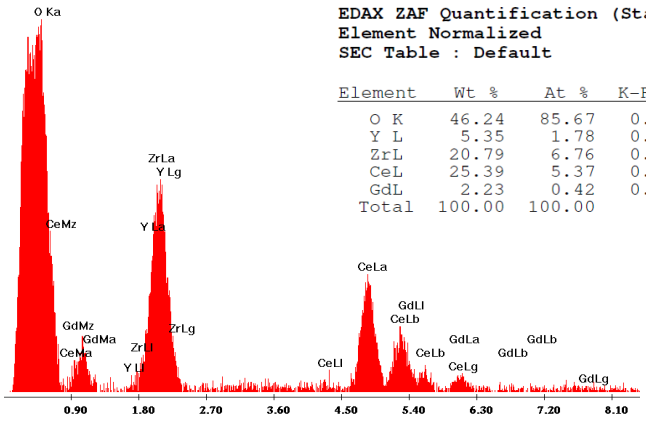

EDAX ZAF Quantification (Standardless)
Element Normalized
SEC Table : Default

Element	Wt %	At %	K-Ratio	Z	A	F
O K	46.24	85.67	0.1347	1.1241	0.2591	1.0001
Y L	5.35	1.78	0.0350	0.8843	0.7394	1.0011
ZrL	20.79	6.76	0.1438	0.8765	0.7879	1.0014
CeL	25.39	5.37	0.2142	0.8176	1.0304	1.0014
GdL	2.23	0.42	0.0178	0.7906	1.0122	1.0000
Total	100.00	100.00				

Figure 2-123 Point EDAX results from VRSDT-3. The red dot on the SEM image (left) approximates the point at which EDAX measurements were taken. The scale bar on the image is 500nm.

VRSDT-4

VRSDT-4 is a repeat of VRSDT-3. Similar substrate temperatures were recorded: 1010-1090 C. Figure **2-124** shows plan-view SEM of VRSDT-4, which looks very similar to VRSDT-3.

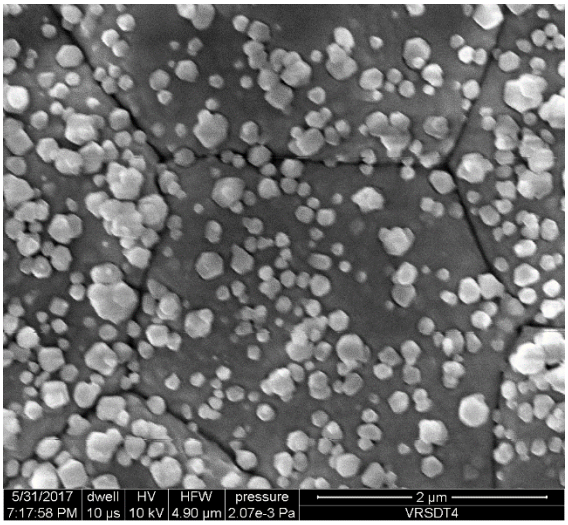

Figure 2-124 Plan-view SEM of VRSDT-4.

Figure **2-125** shows point EDAX results from the GDC islands and likely GDC dense layer of VRSDT-4, which suggest that both the islands and surrounding area contain GDC**.**

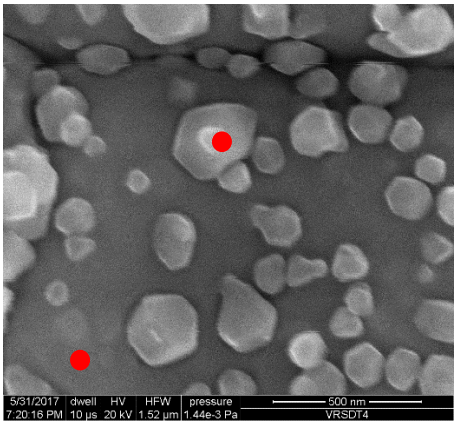

EDAX ZAF Quantification (Standardless)
Element Normalized
SEC Table : Default

Element	Wt %	At %	K-Ratio	Z	A	F
O K	34.37	78.82	0.0943	1.1636	0.2358	1.0001
AlK	0.07	0.09	0.0003	1.0814	0.3433	1.0041
SiK	0.19	0.25	0.0010	1.1123	0.4420	1.0074
Y L	5.33	2.20	0.0325	0.9183	0.6628	1.0013
ZrL	21.77	8.76	0.1417	0.9130	0.7118	1.0016
CeL	33.04	8.65	0.2852	0.8496	1.0131	1.0028
GdL	5.23	1.22	0.0427	0.8232	0.9917	1.0000
Total	100.00	100.00				

Figure 2-125. Left, plan-view SEM image showing where point EDAX was performed on the island (top) and surrounding area (bottom). Right, EDAX results for island (top) and surrounding area (bottom).

VRSDT 5

Research has shown solvents with lower enthalpy of combustion, such as ethanol, result in a bimodal distribution of particle sizes. This is consistent with the formation of a dense GDC layer and GDC islands observed in VRSDT-3 and VRSDT-4. Smaller particles will form a dense layer, while larger particles will form islands. In order to avoid this phenomenon, toluene was used as a solvent in VRSDT-5 and VRSDT-6 since it has a higher enthalpy of combustion. Stand-off distances needed to be adjusted from VRSDT-4 to VRSDT-5 to accommodate the difference in flame length. The substrate temperature was between 1,020 and 1,040 °C. Figure **2-126** shows plan-view SEM of VRSDT-5 along with plan-view SEM from prior work. The clear visibility of YSZ grains is indicative of a thin, dense GDC layer.

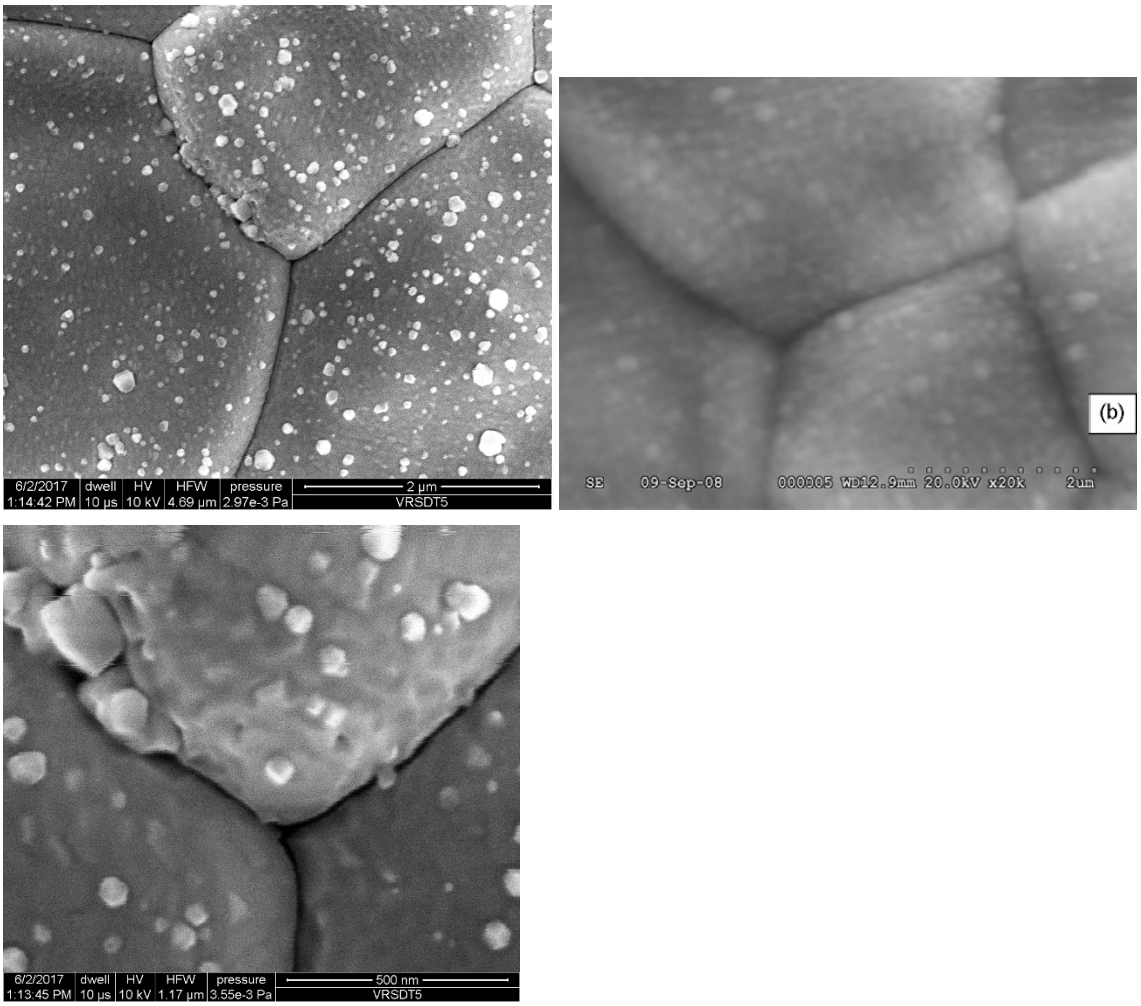

Figure 2-126 Upper left, plan-view SEM of VRSDT-5. Upper right plan-view SEM from prior work. Bottom, higher magnification plan-view image of VRSDT-5.

EDAX on VRSDT-5 shows peaks for cerium, but not for gadolinium. This is likely the result of the GDC layer being so thin such that the Gd X-Rays are not detected. The intended stoichiometry of the GDC has a Ce:Gd ratio of 9:1. Because of the significantly greater amount of Ce in the GDC layer, it is possible that the cerium is detected and the gadolinium is not. Figure **2-127** shows the EDAX spectrum, elemental analysis, and the area over which EDAX was measured for VRSDT-5.

EDAX ZAF Quantification (Standardless)
Element Normalized
SEC Table : Default

Element	Wt %	At %	K-Ratio	Z	A	F
O K	61.57	92.04	0.2384	1.0831	0.3575	1.0001
Al K	0.00	0.00	0.0000	1.0078	0.3990	1.0028
Si K	0.00	0.00	0.0000	1.0370	0.5189	1.0052
Y L	2.94	0.79	0.0193	0.8494	0.7730	1.0011
Zr L	12.16	3.19	0.0840	0.8393	0.8219	1.0015
Ce L	23.33	3.98	0.1950	0.7848	1.0648	1.0000
Gd L	0.00	0.00	0.0000	0.7573	1.0328	1.0000
Total	100.00	100.00				

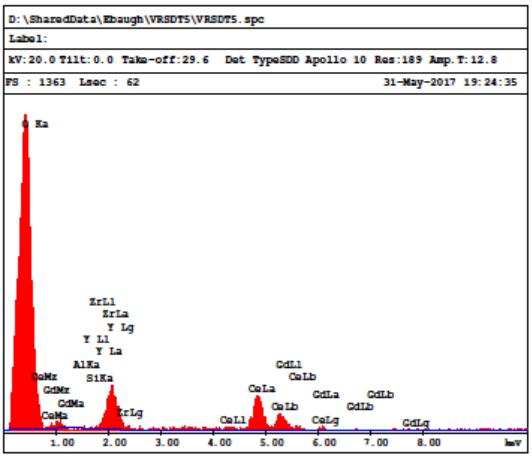

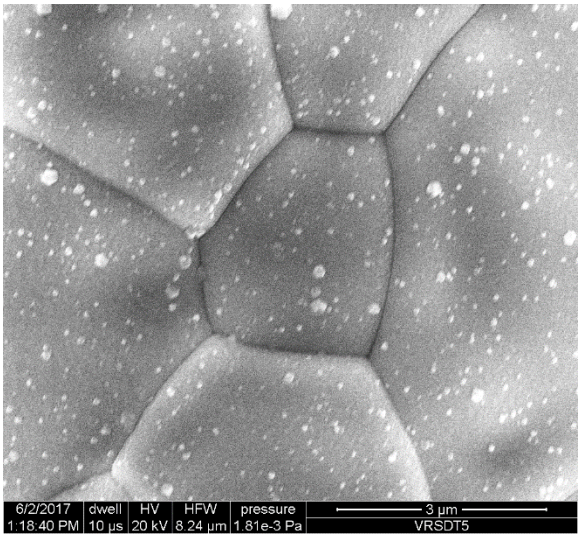

Figure 2-127 Top, EDAX results for VRSDT-5. Bottom, area over which EDAX was measured.

VRDST-6

VRSDT-6 was performed as a repeat of VRSDT-5 to produce a sample to fracture in order to view the cross section under SEM. The deposition duration was intended to be approximately 90 minutes long; however, problems with needle clogging limited the deposition duration to 45 minutes. Despite this, sufficient GDC material should have been deposited in 45 minutes to provide a representative thickness of the GDC layer that would have formed after 90 minutes. Figure **2-128** shows cross section SEM of VRSDT-6. In this image, the GDC is imperceptibly thin. If the GDC layer on VRSDT-5 is similarly thin, this could explain the absence of Gd peaks in the EDAX spectrum.

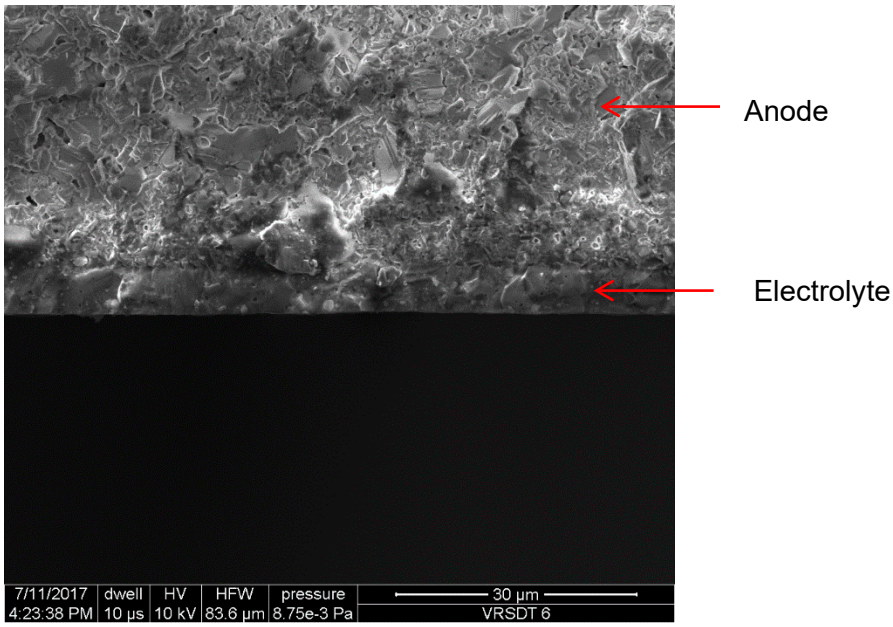

Figure 2-128 Cross section SEM of VRSDT 6

5x5 Cathode Coating

VRSDT-5 was coated with a LSCF cathode in the same manner as button cell samples FCE3 and FCE5-6. (A LSCF slurry was sprayed simultaneously with LSCF from the RSDT flame.) Adapting to the larger deposited area of the 5x5 substrate posed little difficulty because the substrate temperature is relatively low (~80C).

Milestone:

Milestone 2.2.3 Complete Evaluation of RSDT for Fabrication of Electrolyte Bi-Layer

Status: This milestone is complete. The conclusion of the R&D activities is that the current state of RSDT technology does not warrant further pursuit for application in SOFC fabrication. The technology is not ready from a physical parts perspective (using parts in real stacks) nor is it ready for detailed cost assessment, as too many fundamental feasibility questions remain unanswered.

3.0 Task 3.0 – Advanced Stack Architecture Design

The advanced stack development will focus on several design concepts and incorporation of the cells fabricated using the technologies in Task 2.0, with the objective of reducing the cost of the SOFC stack technology. The stack development task will investigate the thermal profile, flow management, and operating conditions / operating window as well as specific individual cell, seals, interconnects, and metallic component specifications and requirements. The most promising stack component advancements will be utilized to generate detailed stack/ component designs for implementation. These advancements will be utilized to deliver stacks for both innovation development tests and the 5-kW validation test.

The goal of this task is to develop a stack platform that intrinsically allows a 50% or greater cost reduction. The goal is to achieve that cost advantage without relying on fundamental breakthroughs in component technology, such as those being worked under Task 2. The stack architecture and component simplicity will deliver the cost advantages directly.

Costs are discussed in detail in Task 5. However, it is useful to review Figure 3-1, which shows the materials and labor contributions, at high volume projections, for the current stack. The plot illustrates the reason for the overall goal for this task. In order to significantly reduce stack costs, it is necessary to reduce stack materials (a category meaning all metal components) as well as cell costs. At lower production volumes, where less automation can be justified, labor costs also become important. Most of the stated objectives for this task reflect this cost distribution. Thin anode, thin interconnect, de-integrated manifolds, large cell count, lower seal area, etc. all reflect strategies to lower the material content of the stack. Exploration of U-flow is also related, indirectly, to reductions in stack material content. It is a thermal management strategy to improve temperature distribution, which is a key enabler for integration of thinner components.

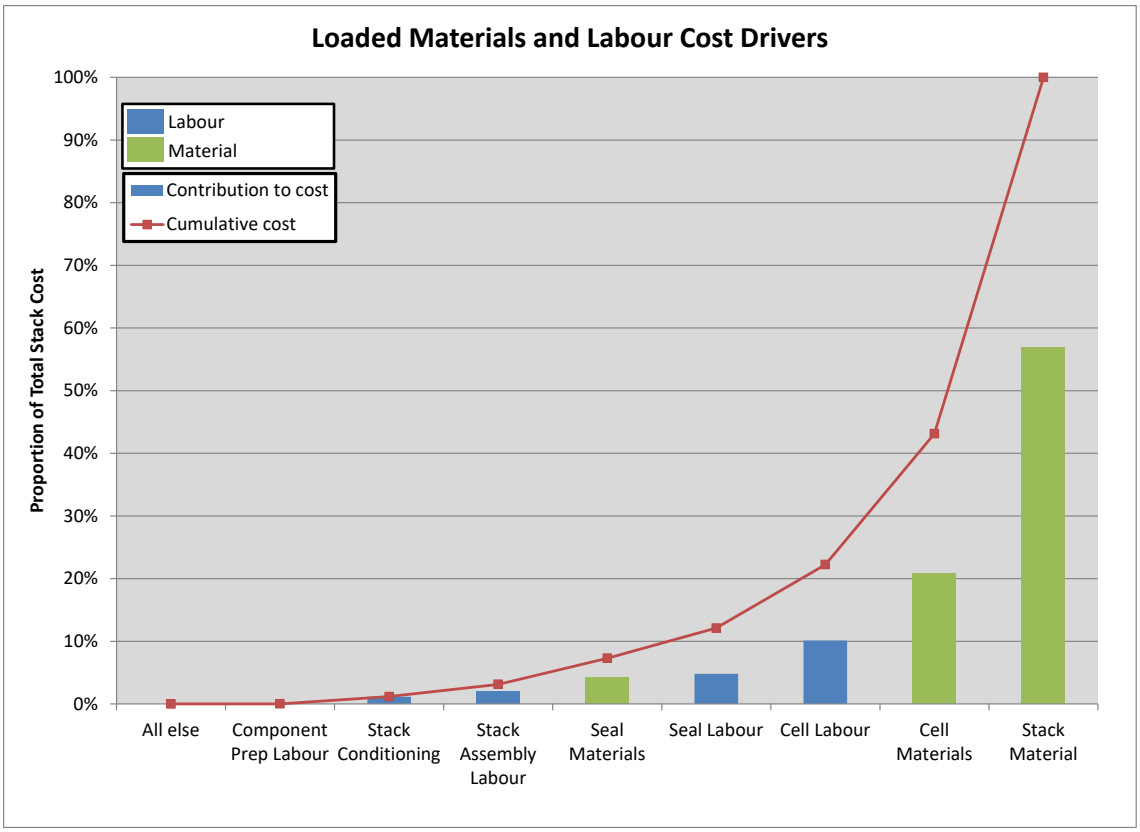

Figure 3-1. Stack (Conventional stack) Cost Breakdown at High Production Volume

It is not desirable to reduce the stack material content if this leads to poor performance or increase in assembly labor that overwhelm the costs, or if it drives system requirements that increase the cost of the overall system. So the overall design goal is to significantly reduce the stack costs, with a focus on reducing the material content of the stack, but with an interest in also lowering the labor involved and simplifying system integration.

Figure 3-2 shows a CAD version of the starting-point design. It has been designated the Compact SOFC Architecture (CSA) stack. This design is derived from a pre-existing stack that was originally developed by VPS for mobile applications. The stack incorporates many of the features corresponding to the goals targeted here, such as thin interconnects, thin cells (300 micron, 0.012”), de-integrated sheet metal manifolds and aggressive thermal design (U-flow). It has demonstrated roughly a 10x reduction in weight (material) per unit active area.

Detailed cost analysis for prototype level quantities showed that the stack was roughly cost neutral with the conventional larger area stack (LAS), but with a rebalance of costs towards more labor. i.e.: At a prototype level the 10x reduction in material content was offset by an increase in labor cost for the stack. The increase in labor cost of this stack, per kW produced, was due to the increased part count and the associated increase in part handling per kW.

The goal for this task is to retain the material content benefits of the lightweight stack while significantly reducing the labor. A major part of the design task will be to make the parts as large as possible while retaining the thermal conditions that enable simple and thin components to be successfully integrated. In addition, a priority will be placed on identifying where part processing may fit well with pre-existing mature production methods for which automated process equipment exists in the competitive market.

Subtasks will review this basic stack architecture with the focus on:

- design optimization to retain thin components and thermal management to the largest practical unit cell size (Subtask 3.1)
- thermal and stress analysis in support of the design (Subtask 3.2)
- identification of manufacturing processes that reduce the labor (Subtask 3.3)
- Development of a detailed cost model (Subtask 5.1) to guide the stack design.

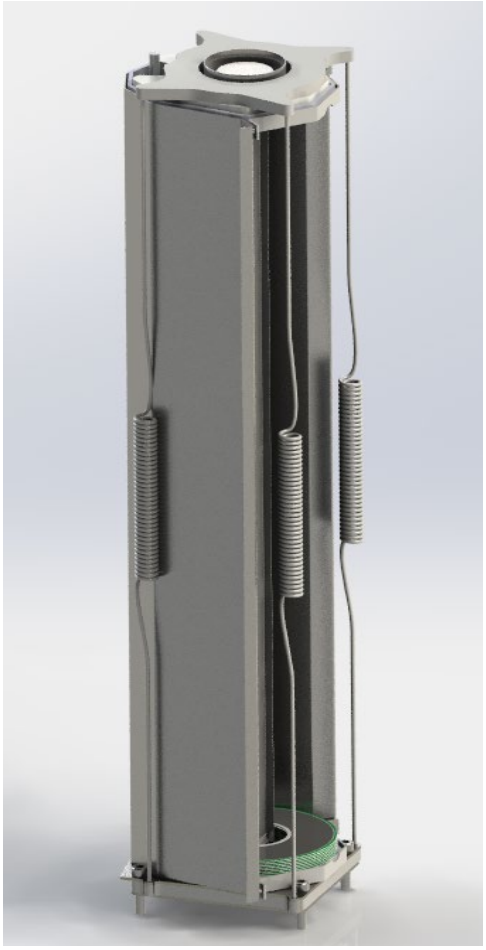

Figure 3-2 Conceptual Stack Layout

3.1 Task 3.1 Stack Components and Design

Objective:

- Develop innovative stack design enabling 50% or larger cost reduction

Approach:

In this subtask the design of the innovative stack concepts were developed in the following areas:

- De-integrated Manifold Stack Design: Implement the design concept to: 1) facilitate stack manufacturing, 2) to lower stack part count, 3) reduce the seal area, and 4) incorporate thin anode, interconnect, and flow fields. Reducing part count and simplifying design for assembly and manufacturing reliability will be the priority.
- Thin 0.45 mm Anode Scale-up: Utilize scaled thin 0.45 mm anode to diminish the raw materials usage and reduce anode concentration polarization.
- Thin Interconnect/Flow Field: Incorporate thin interconnect and flow fields within the stack.
- U-Flow Geometry: Implement the U-Flow geometry in either or both the cathode and anode sides of the stack with the purpose of lowering thermal gradients, reduction of hot spot areas, and ultimately a path to reduction of cathode air flow.
- Horizontal Stack: Develop stack design concepts with lower center of gravity amenable for large number of cells. Explore the horizontal orientation of stacks and provide a support

for the stack along the stacking direction (long axis) that protects the stacks during shipment and life.

- Hot Stack Swappability: Implement design concepts that will allow the change-over of the stack (or a group of stacks) during power production. This will reduce the O&M cost and result in higher availability of the entire system.

Results & Discussion:

The design for the innovative stack (the CSA design and its predecessors) involves a highly coupled interplay of conflicting requirements. Some examples include:

- Good thermal management tends to favor thicker components for improved conduction and increased surface (radiant surface) area of the stack per cell. However, cost improvements aiming at minimizing material content pushes towards thin components and minimizing unit-cell height.
- Non-repeat components (end plates, compression, manifolds, etc.) have costs that are largely or totally independent of cell count, so maximizing cells per stack is favored. However, flow distribution to the individual cell layers favors short stacks (in relation to manifold size.
- Compression system cost, and impact on system complexity and difficulty in system maintenance favor minimizing the number of components (or stacks) through larger cell area stacks. However, compression system forces (and associated complexity) rise proportionally to cell area, and compression plate stiffness favors spanning smaller distances, both of which favor small area cells for lower per-stack cost.
- Cell manufacturing is a major cost contributor and minimizing cell labor is important, favoring larger and thinner cells for less processing per unit active area. However cell yield during production and survivability in-stack favor higher thickness/size ratios meaning that smaller cells (for a given thickness) will tend to have higher yields.

The stack design requires a balance of competing factors. The goal of this program was to develop an innovative stack design that delivers the low cost at reasonable technological risk, and that is suitable for integration into sub-MW and MW level systems.

Starting with the pre-existing stack (5,017 cm^2 total active area) platform as a basis, the task was to increase its size (towards the large area stack of 66000 cm^2 total active area) while maintaining its material content advantage and improving its labor cost content. Two configurations were explored in progressive sizes, one with 11,200 cm^2 total active area and the other with 28,000 cm^2 total active area.

There are three design tradeoffs that tend to limit stack size when preserving the thin component benefits of the CSA approach.

1. As lateral dimensions increase, thermal management becomes more difficult
2. As cell count per stack increases, the column stability of the stack decreases and becomes a manufacturing problem
3. As cell size increases (at a given thickness), yield tends to decrease due to accumulation of sintering stresses

Relative to the smaller starting point stack, two design innovations were incorporated to allow for larger stacks. First, the gas inlets to each cell layer are located 120° angle apart (original design had ~10° separation). This helps distribute cooling effect from reforming load and cold inlet gases across a larger area of the cells. This is a path leading to larger active area per cell while avoiding thermal issues. Second, thinner seals are used. The stack goes through a consolidation phase during manufacturing, which is driven by seal consolidation and is a function of seal thickness. By making the seal thinner, the new stacks accommodate 350 cells with the same consolidation as

225 cells in the original stack. Managing consolidation was one of the challenges in this stack platform, but has been demonstrated with reasonable stability (no problems related to consolidation in 10 successive stacks built).

Preliminary thermal modeling of each stack was carried out to assess general feasibility (discussed under Section 3.2). Thermal model results for the smaller size stacks were favorable, so the focus shifted to the larger stack for more detailed modeling.

Figure 3-3 shows a comparison of stack cross sections. Some key observations from this comparison are:

- simplification of the unit cell design, due to decrease in number of parts per repeat layer from thirteen to five
- a significant reduction in seal volume per unit cell (and also per unit active area)
- simplification of the manifold structure
- increase in cell stacking density (350-cell CSA stack is shorter than 120-cell baseline LAS stack)

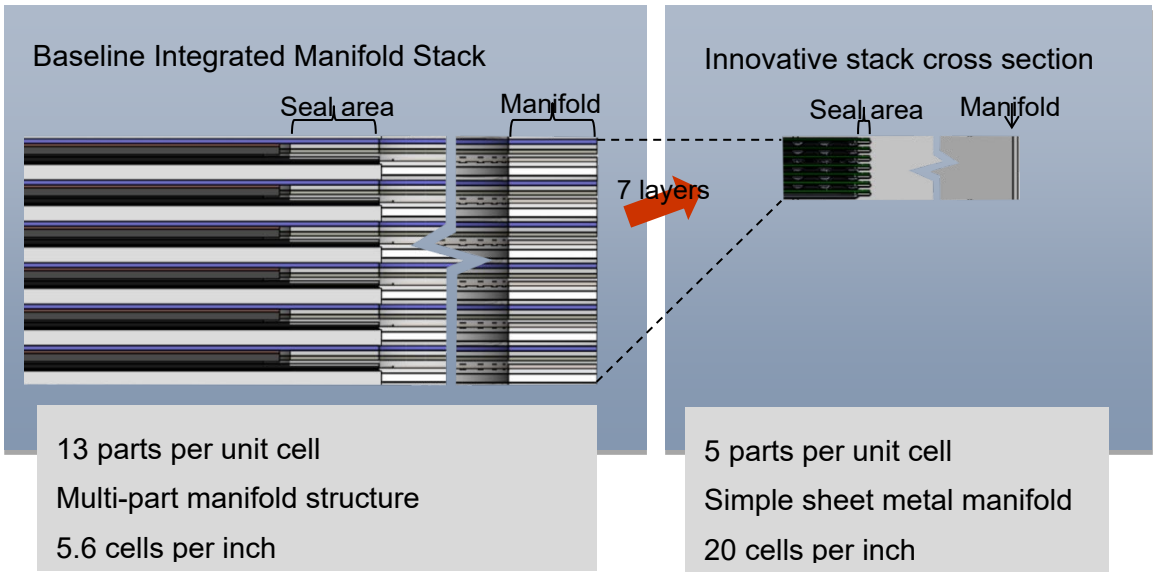

Figure 3-3 Same-Scale Comparison of Baseline and Innovative Stack Repeat Layers

The preliminary sizing exercise for the larger stack resulted in a cell size close to the diameter of a DVD (120 mm). In order to take advantage of processing technology from the CD/DVD manufacturing sector, size was adjusted so that the cell outer diameter exactly matched that of a DVD. Figure 3-4 shows a preliminary stack model based on this size. A DVD is also shown to provide a scale or comparison.

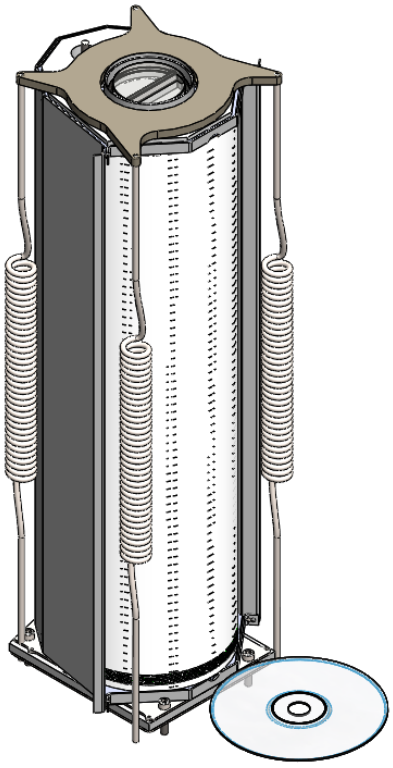

Figure 3-4 CSA Stack Model (Prelminary, DVD Disk is shown for Scale or comparison)

This stack design has a total active area ~40% that of the current 120-cell stack while occupying less than one tenth the volume and containing eighteen times less material. Part count and part complexity are greatly decreased per unit cell, cutting the number of distinct parts to less than half. These two factors lower the barriers to automation, since fewer steps of lower complexity need to be automated.

However the part count per kW does increase given the smaller cell size. This means that early automation is more important to reach reductions in labor costs for the stack. This is a design for which it is easier to transition to automated part handling and stack assembly, but it is also a design that requires automation in order to demonstrate the cost benefits. Past development in this area, as well as plans for the subsequent development are explored in more detail in Section 3.3.

Further refinement of preliminary stack design (compact SOFC architecture (CSA)) that retains the same general characteristics resulted in the following design parameters:

- 120 mm (4.7”) outer diameter cells
- 350 cells per stack
- 84 cm^2 active area per cell, 29,400 cm^2 total active area
- ~ 7 kWe power rating at nominal conditions (0.29 A/cm^2, 0.85 V/cell)
- 300 V normal operating voltage
- 480 mm tall x 150 mm deep x 127 mm wide (19” x 6” x 5”)
- 12 kg (26 lb) estimated total weight

The outer cell diameter remains 120 mm to match that of DVDs to retain the potential to use DVD manufacturing equipment (printers, dryers, part handlers, etc.). These characteristics are compared to the conventional LAS design in Table 3-1. The CSA stack has a little less than half the active area of the 120-cell Large Area Stack (LAS) design used in the most recent FCE DOE-sponsored demonstration program. Given that it operates using all the same materials as the larger stack, a baseline assumption of identical performance at identical conditions is taken (on a per-unit area basis).

The result is a stack electrical output that is 45% of the LAS stack, but with a tenth of the volume and a twentieth of the weight. Although volume and weight are not necessarily the major requirements for larger systems, there is a strong correlation with cost which is important. Reduced physical volume can offer significant reduction in packaging costs (insulation, support and framing, etc.). The reduced weight comes from lower material content in the stacks, which has a strong linkage to final cost.

Table 3-1 Comparison of Initial CSA Stack Design to conventional (LAS) design

Characteristic	Units	CSA	LAS	Ratio (CSA/LAS)
Total active area	cm^2	29,400	66,000	0.45x
Power at 0.85 V, 0.29 A/cm^2	W	7,230	16,269	0.45x
Weight	kg	12	250	0.05x
Volume	L	9.1	90.8	0.10x
Power density	W/L	795	179	4.44x
Specific power	W/kg	603	65	9.28x
Leak per unit active area (previously reported)	sccm/m^2 (cold)	28	1121	0.02x

Figure 3-5 shows a comparison of layouts for a 100 kW SOFC stack module based on the LAS stacks (i.e.: Representative of current hardware in test), and the CSA stack platform. The layout includes considerations for flow distribution to the stacks as well as gas pre-heat and fuel pre-reforming functionality. With a total of 20 stacks (compared to eight stacks constituting four stack towers for the LAS design), the CSA layout incorporates 12% additional power capacity into 4.7x less volume.

It has a cuboid envelope with only 35% of the surface area, which means approximately 3x less insulation thickness is required for the same heat loss. The layout includes oversized process tubes (compare to LAS layout) that have been designed to support 200 kW modules simply by incorporating two 100 kW modules. System voltage benefits also exist at this level. Both layouts arrange stacks in series (electrically) to increase output voltage. The LAS layout has two strings of four stacks arranged electrically in series for a nominal system voltage of 408 Vdc. The CSA layout has ten strings of two stacks arranged in series for a nominal system voltage of 596 Vdc . The latter is a good fit for solar inverter technology, while the former almost certainly requires a DC-DC boost stage, increasing costs and decreasing efficiency.

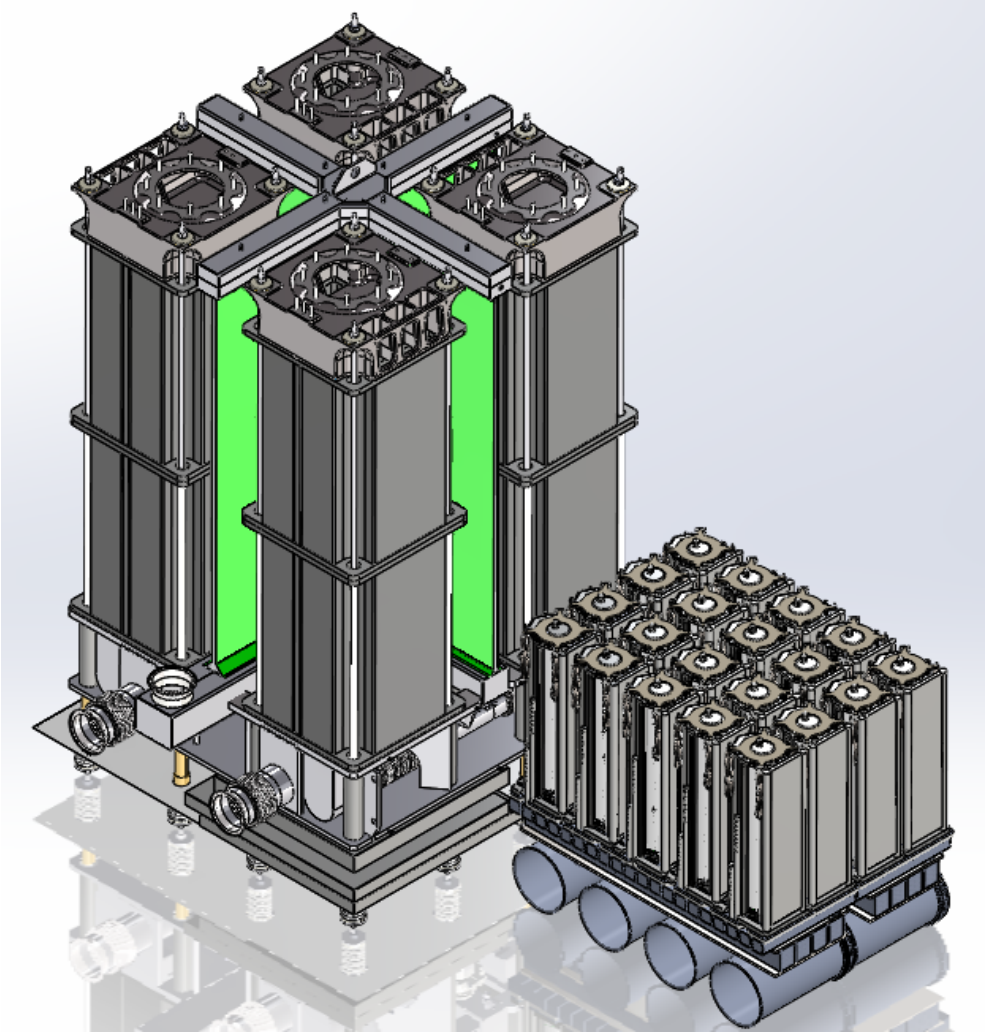

Figure 3-5 Comparison of conventional (LSA) stack layout to CSA Stack layout for 100 kW SOFC Module

A review of manufacturing tolerances and the need to guarantee minimum seal widths resulted in reduction of the active area by 4% to 81 cm^2. The reduction in active area leaves more room for seal around the perimeter of the cell. The general characteristics of the stack have evolved to:

- 120 mm outer diameter cells (4.7”)
- 350 cells per stack
- 81 cm^2 active area per cell, 28,350 cm^2 per stack
- 6.9 kWe power rating at nominal conditions (0.29 A/cm^2, 0.85 V/cell)
- 300 V normal operating voltage
- 480 mm tall x 150 mm deep x 127 mm wide (19” x 6” x 5”)
- 12 kg (26 lb) estimated total weight.

Detailed CFD design of the interconnect has led to a design with two oxidant inlets and two oxidant outlets. This change resulted in some changes to the outer manifolds and the compression system. Previously, the stack characteristics were compared to the conventional LAS (large area stack) design. Table 3-2 shows the updated comparison, modified to account for the reduction in active area per cell.

Table 3-2 Comparison of Interim CSA design to conventional (LAS) design

Measure	Units	CSA	LAS	Ratio
Total active area	cm^2	28,350	66,000	0.43x
Power at 0.85 V, 0.29 A/cm^2	W	6,990	16,269	0.43x
Weight	kg	12	250	0.05x
Volume	L	9.1	90.8	0.10x
Power density	W/L	768	179	4.29x
Specific power	W/kg	583	65	8.97x
Leak per unit active area (previously reported)	$sccm/m^2$ (cold)	29	1121	0.025x
System voltage (series stacks)	Vdc	596	408	1.46x

Although the reduction in cell active area penalizes the CSA stack design to some extent, the design retains a large advantage in W/kg, W/L and relative leak that present significant opportunity for simplification and cost reduction at the stack and system levels. Although there were further changes to the exterior of the stack, the basic comparison presented will remain relevant.

Further refinement of internal stack design resulted in a shift from having one air manifold to having two air manifolds on opposite sides of the stack in order to optimize the interconnect geometry. The external characteristics remained largely unchanged. This change is reflected as shown in Figure 3-6. The sheet metal manifolds (lower left and upper right in image) are simple brazements and are independent from the stack to allow differential thermal expansion.

The design change to the dual air manifolds lowered the pressure drop in the interconnect region. However this change also brought some stack level advantages including:

- The inlet air endotherm is spread across two opposing faces of the stack instead of being concentrated on one face
- The mechanical side forces on the stack are more balanced, there will be less tendency to bow the stack sideways due to manifold sealing forces
- The geometry lends itself better to manufacturing automation

A disadvantage of the dual manifold approach is a more significant packaging challenge which has driven some geometric complexity into the manifold design. There is no increase in part count (the previous manifold was made up of two half-manifolds), but the parts are more complex. As a result, there is a slight increase in manifold cost, in the long term, to manufacture the more complex manifold shape. However, this cost impact is not considered to be a significant.

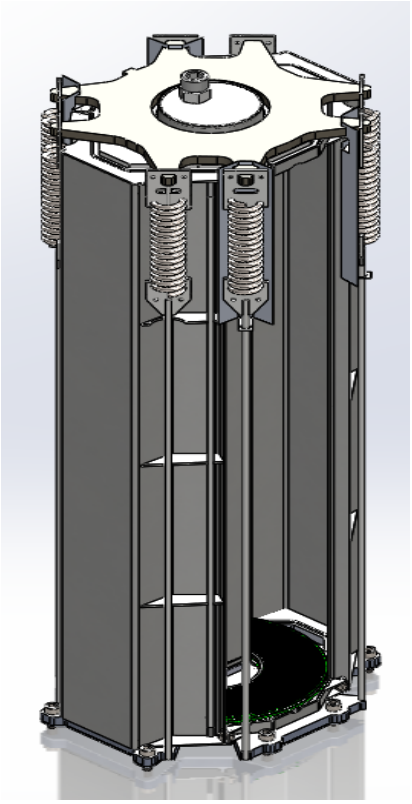

Figure 3-6 Stack Design Featuring Two Air-side Manifolds

The stack design varied slightly in response to the interconnect redesign (discussed in more detail in Section 3.2). The main impact on the stack is a slight lowering of the overall height from 19” to 17”.

The general characteristics of the stack design have matured to:

- 120 mm outer diameter cells (4.7”)
- 350 cells per stack
- 81 cm^2 active area per cell; 28,350 cm^2 per stack
- 6.9 kWe power rating at nominal conditions (0.29 A/cm^2, 0.85 V/cell)
- 300 V normal operating voltage
- 430 mm tall x 150 mm deep x 127 mm wide (17” x 6” x 5”)
- 12 kg (26 lb) estimated total weight.

Table 3-3 shows the updated comparison, modified to account for the reduction in the overall height from 19” to 17”.

Table 3-3 Comparison of Final CSA design to conventional (LAS) design

Measure	Units	CSA	LAS	Ratio
Total active area	cm^2	28,350	66,000	0.43x
Power at 0.85 V, 0.29 A/cm^2	W	6,990	16,269	0.43x
Weight	kg	12	250	0.05x
Volume	L	8.1	90.8	0.09x
Power density	W/L	858	179	4.29x
Specific power	W/kg	583	65	8.97x
Leak per unit active area (previously reported)	sccm/m^2 (cold)	29	1121	0.025x
System voltage (series stacks)	Vdc	596	408	1.46x

After the interconnect design change, the stack design passed an internal design review and was released for production. This did not preclude future design changes as experience accumulates, but it allowed release for production of the stack components.

Two main non-repeat components were released for production trials: external manifolds and their associated braze fixtures. Of the non-repeat stack components these were the longest lead items and are items where design iterations to improve manufacturability seem likely. Figure 3-7 shows an air manifold loaded into the planned braze fixture tooling.

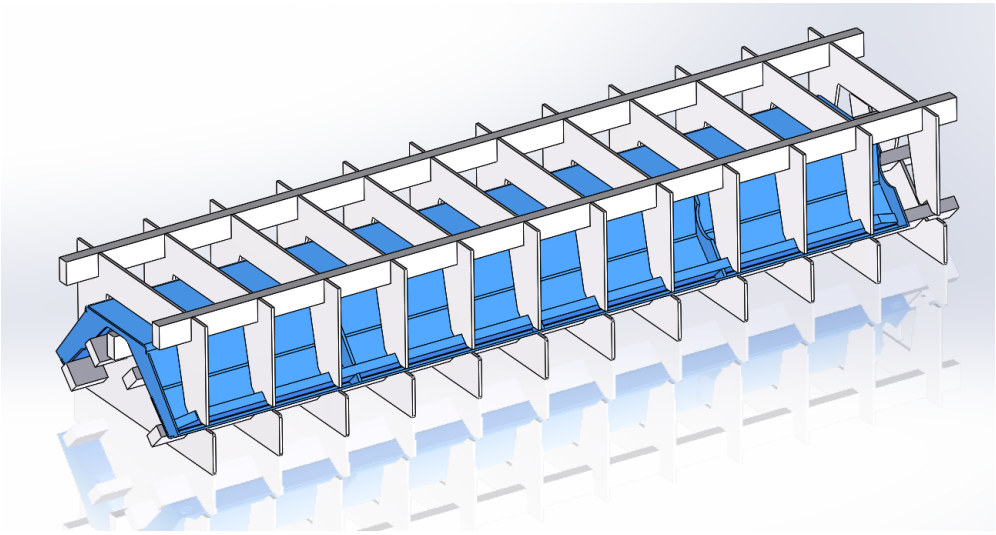

Figure 3-7 Example: Manifold (Blue) in Braze Fixture

Stack Compression Testing

When the second sub-assembly, the compression system, was released for production, this enabled creep testing of the high temperature spring system. High temperature springs were manufactured and heat treated in house. The spring holding hardware was procured and assembled (a brazement).

The test system principal maintained a constant force on the sub-assembly and monitored the change in the spring displacement over time when exposed to elevated temperatures of the operating environment (~750 °C). The test objective is to ensure the compressive force remained above established lower limits thresholds through EOL runtimes.

The springs were loaded into their associated hardware and two underwent creep testing. Creep test fixtures were built from available hardware and are shown in Figure 3-8.

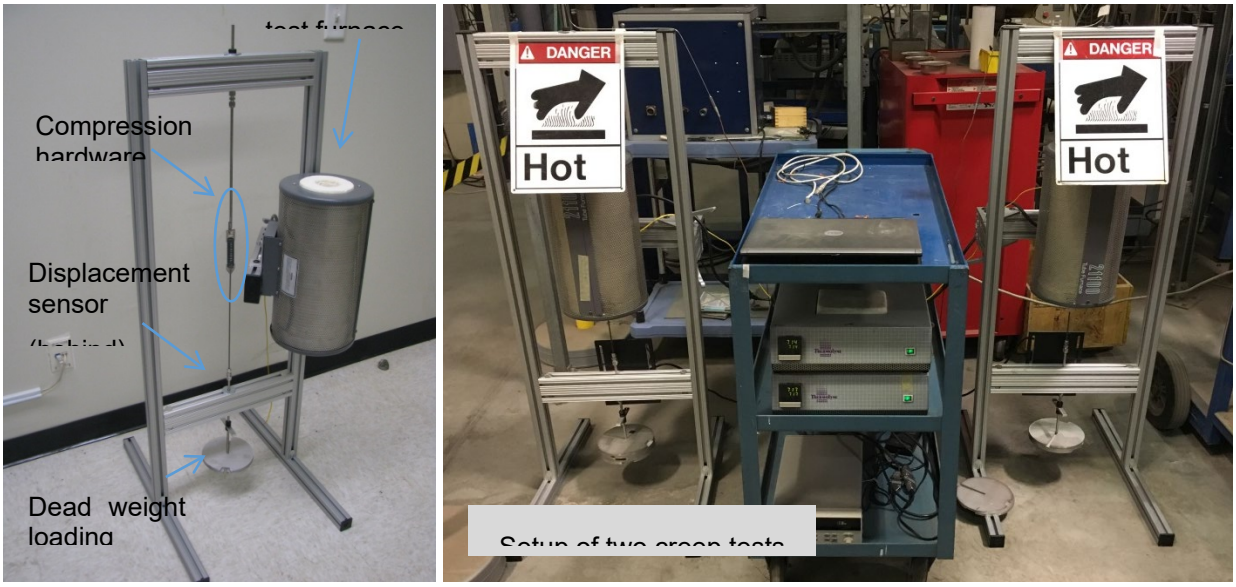

Figure 3-8 Creep Tester Setup for Compression Hardware Testing

The target behavior of the spring system in the stacks is for there to be an initial period of relatively high creep as the spring system beds together, followed by more moderate creep and progressive unloading of the stack. As the stack unloads, the stresses drop and the creep rate will diminish. Based on prior testing and considerations of scale, the design target is for the stack to be under 355 N (80 lbf) total top load after the initial bedding creep, and to drop to somewhere in the range of 45 N to 90 N (10 lbf to 20 lbf) top load by the end of life.

Figure 3-9 and Figure 3-10 show the initial test results through 1,400 hours on the two spring assemblies: Spring #2 and Spring #3. The spring systems creep test is performed at 750 °C, higher than the target operating temperature, estimated to be between 650 °C and 700 °C depending on the operating conditions. This increased temperature provides a measure of test acceleration. In both spring systems relatively rapid seating creep occurs, followed by more moderate creep rates.

The optical transducers that are being used to measure live displacement were problematic and make interpretation of the data somewhat difficult. The general characteristic of the reported creep is that of periods of little or no creep followed by step changes in displacement. It does not seem likely that these step changes are reflective of a real change in creep rate, but they have all occurred in the same direction, so they are hard to explain as simple sensor noise. At this point it is not clear if the step changes are artifacts of the measurement or real displacement that is

accumulating before being reported. If the displacement is real, then it is relatively rapid at an equivalent load of 80 lbf. For example, Spring #2 displaces 330 micron (0.013”) between hours 200 and 1000. Spring #3 displaces 130 micron (0.005”) between hours 200 and 800, but then makes a 130 micron (0.005”) step change. In both cases this works out to approximately 0.5mm per thousand hours. At 1000 hours, the load on Spring #2 was reduced to the equivalent of 215 N (48 lbf) and has shown no further creep over a period of 400 hours.

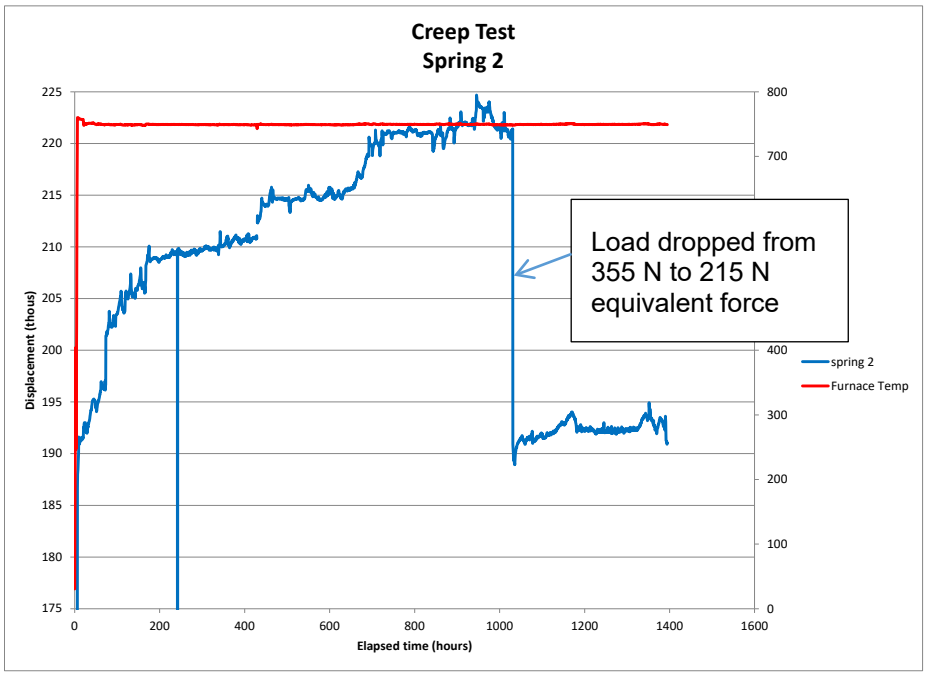

Figure 3-9 Creep Testing on Spring 2

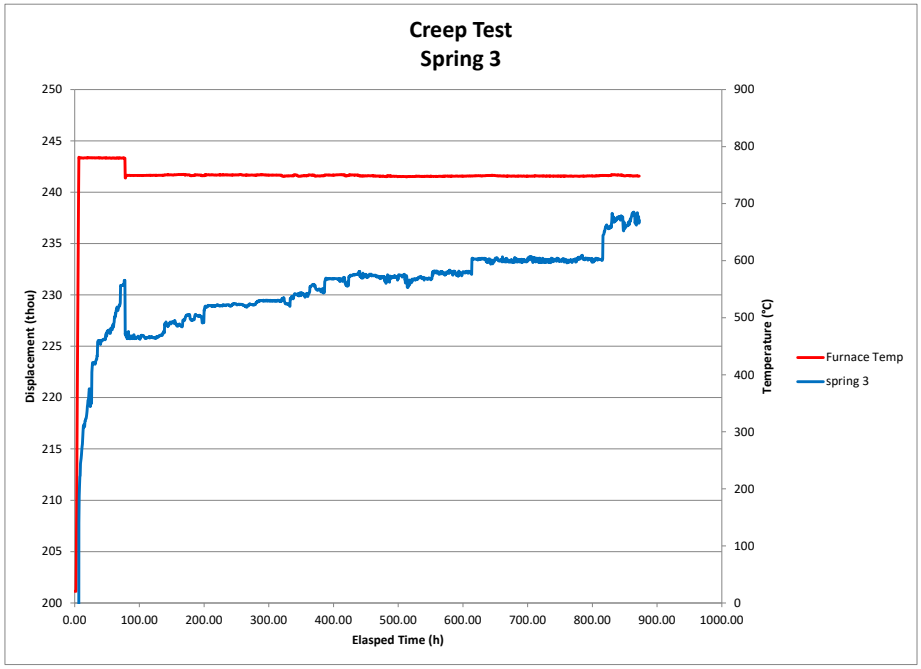

Figure 3-10 Creep Testing on spring 3

Figure 3-12 and Figure 3-13 show the full timeline of the tests for Spring #2 and Spring #3 respectively.

At the 3,000 hour mark, Spring #3 remained at 750 °C with a spring load corresponding to a stack compressive load of 355 N (80 lbf). Despite some noise in the measurement, it is obvious that creep of the spring occurred. A measured extension of approximately 0.56 mm (0.022 in) has occurred over a 3,050 hour hold, excluding the high rate of change over the first ~40 hours. The question this raises is: In a real stack where spring relaxation results in a lowering of compressive stresses, what does this measured displacement correspond to in terms of a reduction in compressive forces?

An approximate answer is derived from the data where the spring load was reduced from 355 N (80 lbf) to 215 N (48 lbf) stack equivalent load at elapsed time 1,031 hours. The corresponding displacement was 0.76 mm (0.030 in), giving an instantaneous stack equivalent spring constant of 184 N/mm (1,066 lbf/in). So the observed creep in Spring #3 of 0.56 mm corresponds to a drop in compressive load of ~ 100 N (23 lbf).

However, another observation of the testing on Spring #2 is that once the compressive load was reduced to 215 N, which is still well within the acceptable operating range of the stack, no further creep occurred over 2,500 hours of testing.

Therefore, although the creep rate at full compressive load is relatively quick, it is well within the acceptable range, and is displaying the self-limiting behavior that was desired. The test conditions for Spring #3 can be considered an accelerated test, the test conditions for Spring #2 approximates a mid-life condition

A check at the 5,500 hour mark found no additional displacement occurred for Spring #2 since the load was reduced after 1,031 hours. As Spring #2 reached 6,106 hours of operation on load, again with no further displacement observed, an unplanned test interruption due to a power failure required a test restart at that time. This event was used as an opportunity to increase the load to an intermediate equivalent stack load of 267 N (60lbf). The higher load did result in detectable creep, initially measured to be displacing at a rate equivalent to 226 micron/khr (0.009”/khr) corresponding to an unloading rate of 42 N/khr (9 lbf/khr). Figure 3-11 plots the observed creep rates for Spring #2 as a function of load with the target beginning of life and end of life loads marked.

A subsequent measurement after 6110 hours measured a detectable creep to be displacing at a rate equivalent to 138 micron/khr (0.005”/khr) corresponding to an unloading rate of 25 N/khr (5.7 lbf/khr). Another later check at 11,800 hours measured a detectable creep to be displacing at a rate equivalent to 112 micron/khr (0.004”/khr) corresponding to an unloading rate of 21 N/khr (4.6 lbf/khr). The overall unloading rate was observed to continue to decrease slightly after 14,100 hours of testing through to the end of the test. This is a favorable result, indicating that the rate of relaxation slows faster than previously reported. Spring #2 accumulated 17,472 hours (2 days short of 2 years) of test time over the life of the test.

As Spring #3 exceeded 5,000 hours at at 750 °C with a 355 N (80 lbf) spring load, the system was observed to have settled into a creep rate corresponding to roughly 76 micron/khr (0.003”/khr). The spring constant remained at 184 N/mm and the creep rate can be converted to an equivalent unloading rate of 14 N/khr (3 lbf/khr). Note, at about 3000 hours the laser displacement sensor was moved to re-center the measurement (i.e.: The step change in the graph can be ignored).

The creep rate for Spring #3 remained at roughly 76 micron/khr (0.003”/khr) and the spring rate remained at 184 N/mm with an equivalent unloading rate of 14 N/khr (3 lbf/khr) as measured at

6,800 hours, 9,100 hours, 11,300 hours, 13,600 hours through to the test end for Spring #3 at 16,944 hours (24 days short of 2 years).

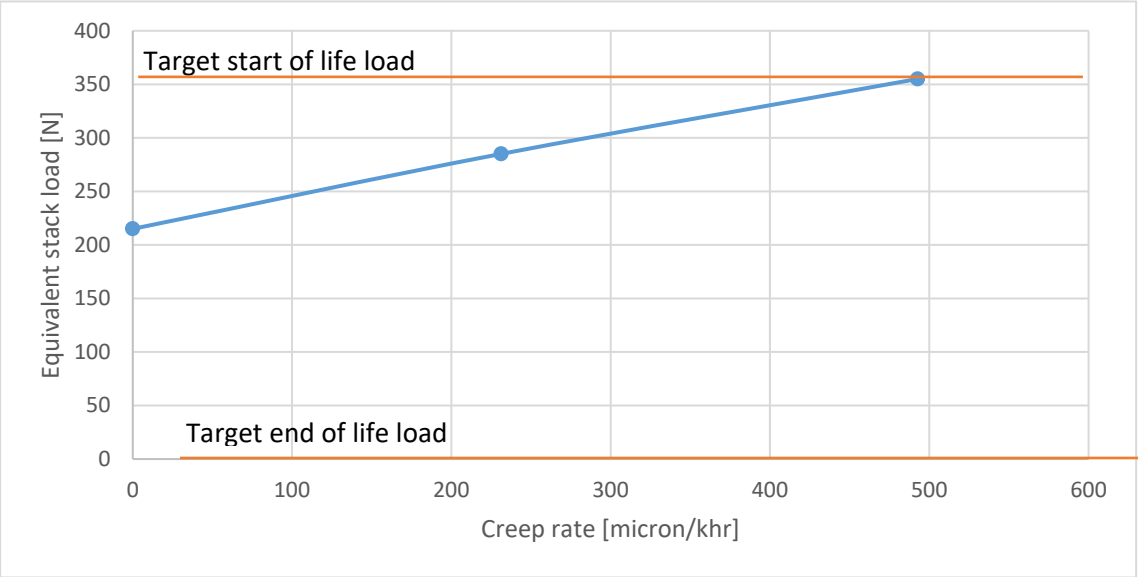

Figure 3-11 Creep response – Spring #2

There is some discrepancy with Spring #3 showing lower creep at higher load relative to Spring #2. While the cause is not certain, the hypothesis is that the heat treatment necessary for high creep strength may not have been adequately controlled for Spring #2 as is evidenced by the higher creep rate shown after 6,106 hours. The discrepancy between springs is somewhat concerning, and bears further investigation.

A larger three zone heat tube furnace has been commissioned for heat treating of the springs, and instrumented trials were carried out to ensure the process is now meeting the time and temperature targets for the full age hardening heat treatment.

Overall, the results remain positive, in that at the lower load of 215 N, which is well above the minimum target, Spring #2 showed stability over more than 5,000 hours. However it shows that even better performance may be achievable, as demonstrated on Spring #3.

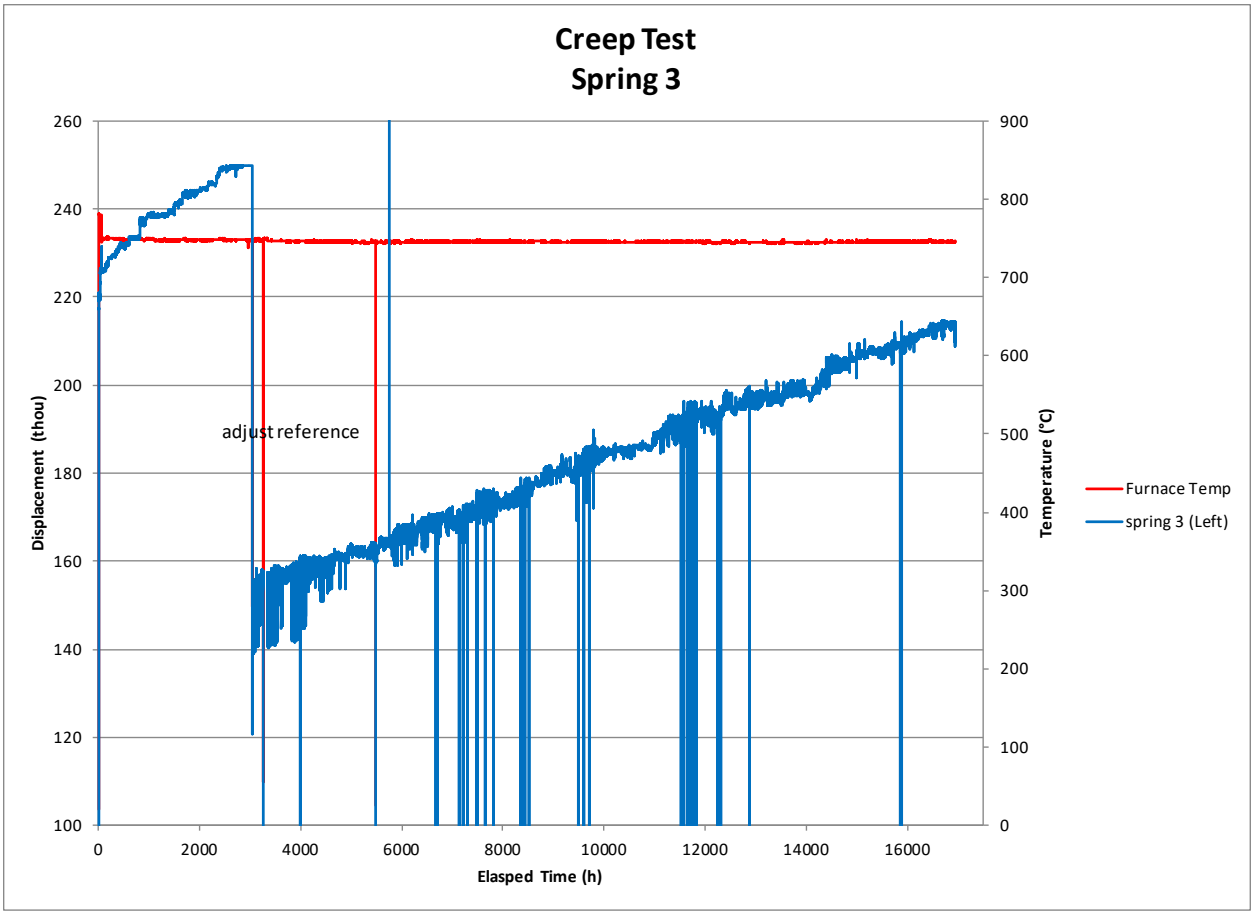

Figure 3-12 Creep test – Spring #3

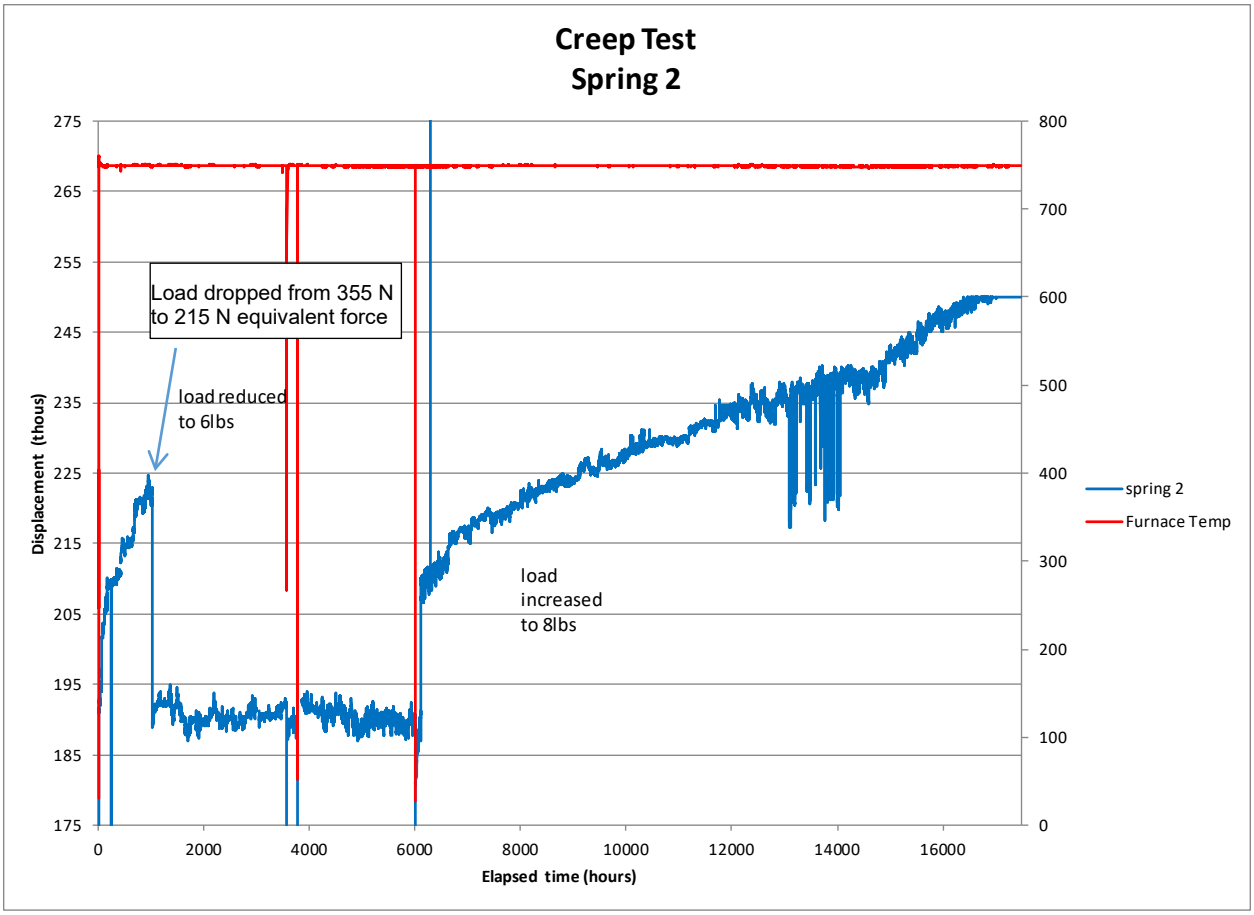

Figure 3-13 Creep test – Spring #2

The results for both springs show that after an initial bedding period in which relatively large displacement is possible, the springs settle into a relatively slow creep regime even at full load. As the compressive load decays due to the creep, the creep rate slows. Overall both tests show the long term viability of this hot spring design. As constant load tests, these tests somewhat exaggerate the relaxation that would be encountered in practice putting the results in a conservative light.

These results are very positive and demonstrate the feasibility of the (relatively) low cost hot springs proposed for the design. Subsequent efforts implemented extra finishing on the mating parts to reduce the initial bedding displacement without significant cost increase. While not necessary to the design, this added a level of predictability to the initial load vs time that is otherwise difficult to accurately predict.

The tests were terminated when a power interruption triggered a shutdown of both furnaces as well as the DAQ system. Given the length of the tests achieved and the linear response over the entire test period which met program requirements, these tests were considered complete at the test lifetime hours completed.

Some of the manufactured springs are shown in Figure 3-14.

Figure 3-14 Springs – as wound (top) and heat treated (bottom)

Long Lead Part Procurement

During the project, a period of time was focused on procurement of long lead parts, initial braze trials, and (primarily) procurement and commissioning of new manufacturing tooling for the CSA stack.

A progression of parts is shown in Figure 3-15 show the progress when Braze trials were started. The reinforcing bars, visible on the manifolds in the left of the image, proved difficult to braze, especially for the short manifolds. The short bars are not adequately supported by the braze fixtures. After a few trials, they were omitted and finished manifolds were produced (right of image). The finished manifolds were sandblasted. It should be noted that while the reinforcing bars are necessary for the full height manifold, they were incorporated into the short manifold design only to exercise the manufacturing process and are not required for functionality. More development will be required for the half-height and full height manifold brazing assemblies.

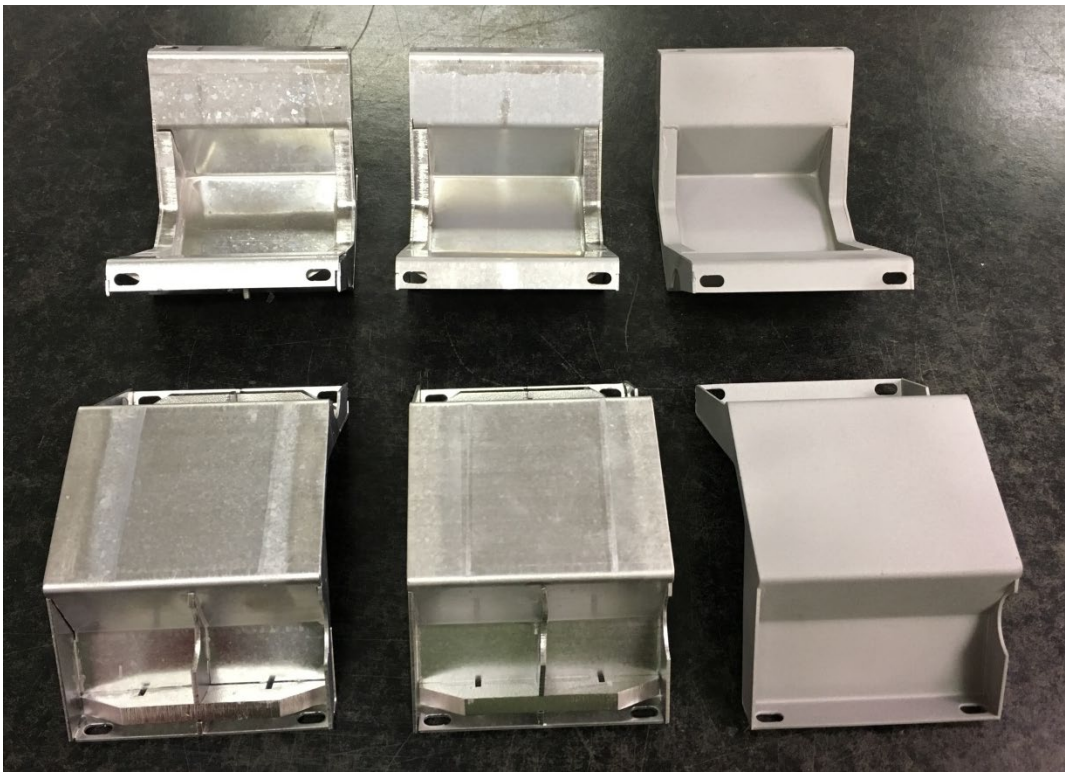

Figure 3-15 Manifold braze trials

External suppliers provided the hydro-formed interconnect and an expanded metal mesh that serves as an electrical contact media for the fuel electrode. When interconnects were received, the feedback from the supplier was there were no problems during manufacturing. This demonstrates that the multiple design iterations earlier in the program resulted in a manufacturable design. The parts were observed to stack tightly indicating excellent part-to-part consistency. An arrangement of contacts within a stack assembly is illustrated in Figure 3-16. Three different expanded metal mesh configurations are under consideration for the design. Figure 3-17 show these parts, as received from the vendor.

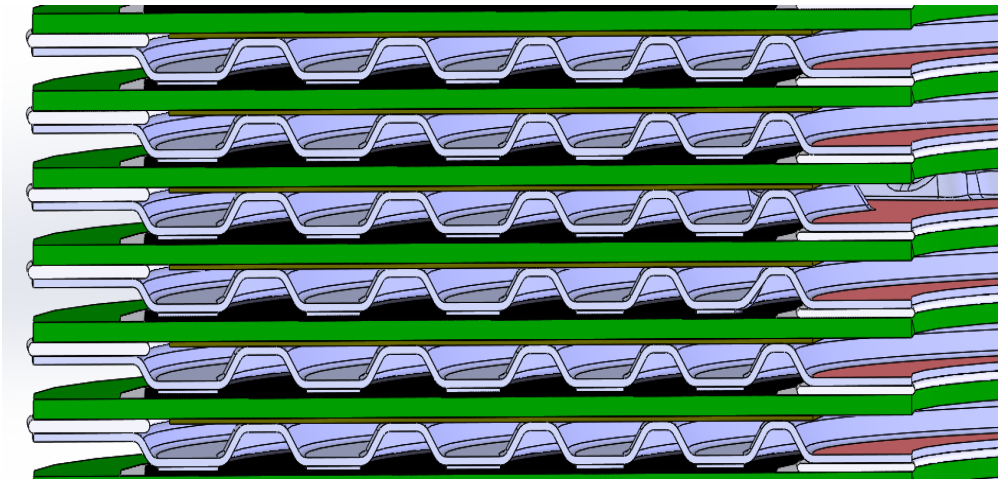

Figure 3-16 Illustration of arrangement of interconnects in stack assembly

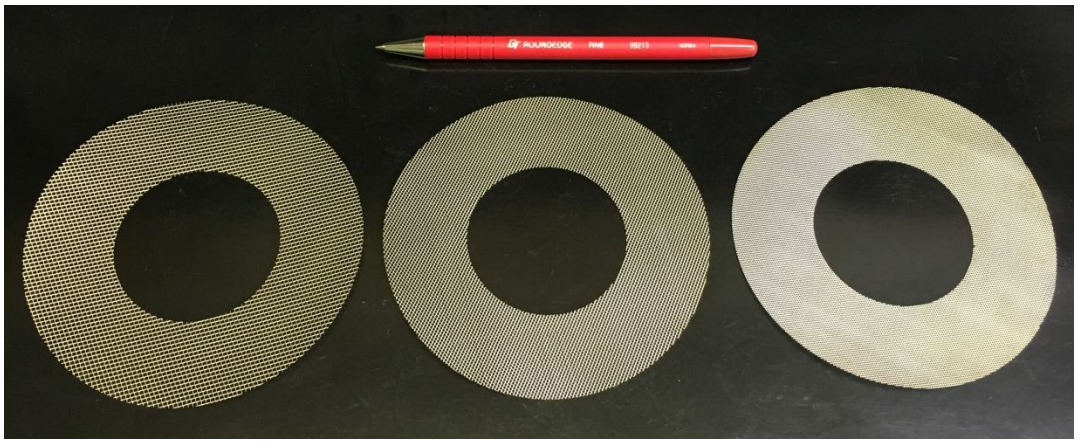

Figure 3-17 Expanded metal (Exmet) contact media

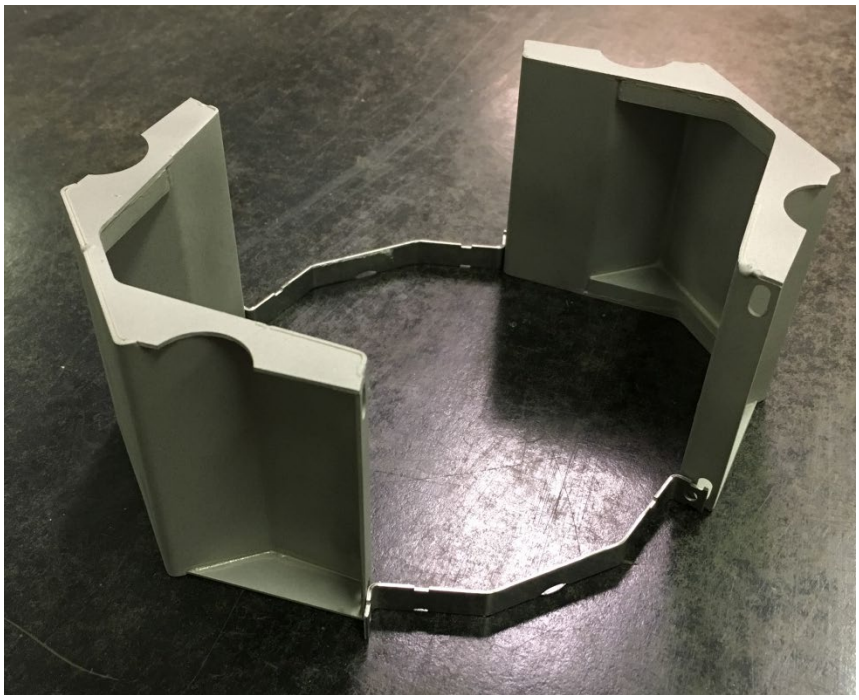

Figure 3-18 Manifolds and retaining clips

Figure 3-19 Internal manifold clips

Part procurement and manufacturing trials were conducted for both the external (oxidant) and internal (fuel manifolds). Figure 3-18 shows a layout of manifolds and retaining clips as they will be mounted on the stack (top retaining clips omitted). Figure 3-19 shows retaining clips used to locate and center the internal fuel manifold system.

In summary, the task focus was in receiving key long lead items and developing the tooling and processes for in-house processed parts. The effort progressed well, and the first off stack builds

were completed. Review of the in-house process development efforts continued during the task was executed.

Milestone 3.1.1 - Complete Advanced Stack Design

Milestone 3.1.1 required that the advanced stack design be complete by April 28 2017. In practice the last parts to be released for production were the stack base plate parts. These received some final adjustments to port and mounting hole locations that were completed on April 4th 2017, before the parts were released for production. This milestone was met successfully.

After the milestone was met, no further changes to the stack design were carried out other than minor geometric adjustments to some of the mounting hardware. Outstanding parts and components that make up the top and bottom end plate brazements were received along with the associated braze tooling. This culminated in the start of stack build trials.

An incremental component design change was implemented during the July to September, 2017 period to the top ceramic isolation plate for ease of manufacture in the short term and for cost reduction.

This part has two key functions: it mechanically distributes the compressive load onto the end of the stack, serving as dielectric isolation, thermally insulating the end of the stack and it provides locating and retention functionality between the compression plate and the stack end plate. In the earlier December 2016 design, this plate was cut from insulating ceramic sheet (alumina fiber reinforced composite insulation).

It was replaced by a cast ceramic component, made of an alumina cement with a calcium aluminate binder, reinforced by alumina fiber. The material is a modification to a commercially available alumina casting compound. The revised part has lower raw material cost and processing cost, uses less material overall, and provides better functionality than the part it replaces, simplifying some of its mating components. Figure 3-20 shows a comparison of the original (left) and revised isolation plate (right).

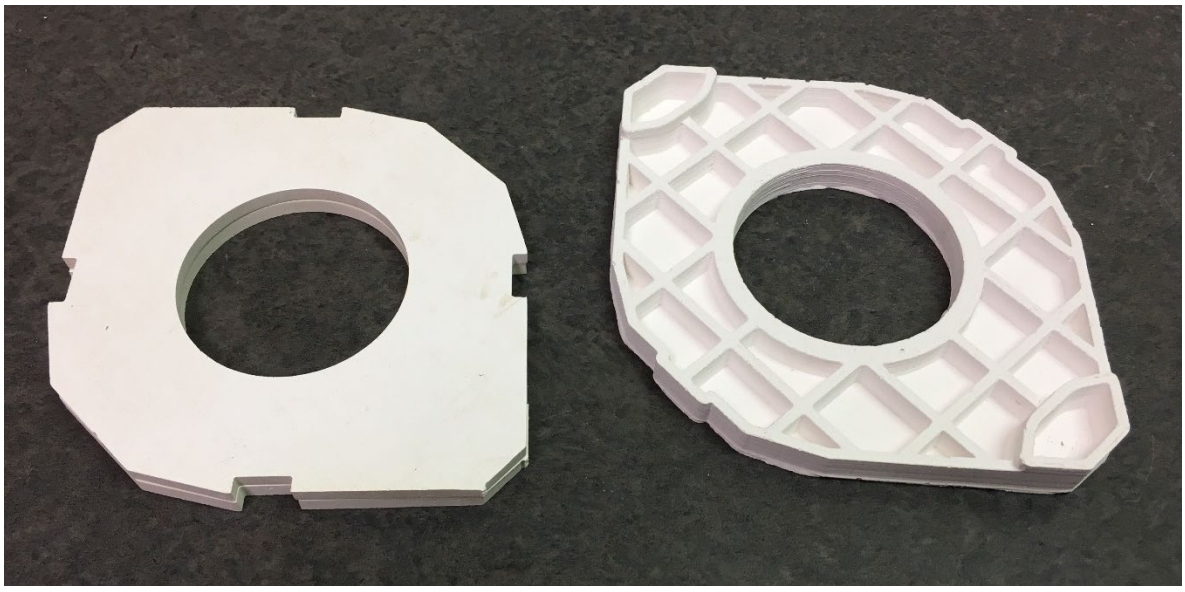

Figure 3-20 Comparison of original isolation plate (left) and revised plate (right)

The preparatory steps and build revealed some areas for improvement to the design which were carried out, including:

- Revision to the bottom compression plate to make installation of the compression system easier
- Revision to sub-components of the manifold brazements to improve self-fixturing features

These are relatively minor changes to the design; overall, the initial build went very smoothly and did not reveal any significant challenges.

In summary, two design revisions were identified:

1. Revision to the bottom compression plate to make installation of the compression system easier
2. Revision to sub-components of the manifold brazements to improve self-fixturing features

Neither revision impacts the final stack form and function but both improve the manufacturability characteristics. The alumina support bead improvement identified previously was implemented in the stacks built subsequently and delivered significant improvements in utilization performance (see Task 4.1 Technology Stacks Fabrication and Testing).

As reported below (see Task 4.1) changes to the fuel manifold (center post) were explored as an avenue to reducing fuel bypass flow, and increasing fuel utilization within the stack. The main focus in the stack design space is on understanding and resolving the lingering fuel bypass weakness whereby it was suspected that a portion of the inlet fuel was flowing directly to the fuel outlet without passing through the cell layers. This was leading to weaker fuel utilization performance than expected.

In general terms there are three interfaces between the internal fuel manifold (which defines the fuel inlet and fuel outlet cavities) and the stack. There is an interface between the bottom of the center post and the bottom plate of the stack, a second interface between the sides of the internal fuel manifold and the internal diameter of the cell and interconnect layers, and a third interface between the top of the fuel manifold and a ceramic sealing cap at the top of the stack. All three interfaces are sealed with an alumina based caulking material but differ in the details of their geometry.

A set of jigs was fabricated to test these three interfaces and to attempt to isolate root causes of the fuel bypass. Figure 3-21 shows the top (left) and bottom (right) view of the test jig with a fuel manifold installed. The sealing material is visible around the top insert (left) and up the sides (right).

Figure 3-21 Inner fuel manifold seal testing jig

With this jig, it was possible to pressurize the fuel inlet if the seals are well formed, since there is no flow through passage from inlet to outlet as there is in a normal stack. In addition there was sufficient access to rework seals in ways not possible in a real stack, and to apply more traditional low temperature sealants strategically to isolate different seal sections for testing.

This work identified two main sources of bypass leak:

1. The geometry of the top interface was such that there was a relatively high likelihood of vapor lock forming during application of the alumina caulking, leaving behind a cavity connecting fuel inlet to fuel outlet. At least one and in one case two cavities of this type were found in the first three of four samples prepared.
2. The geometry of the side interfaces was such that the amount of seal applied was not sufficient to guarantee a good seal. Manual application of additional seal material significantly reduced the measured bypass leak.

The first and larger problem was relatively simple to resolve once identified. In the left image (Figure 3-21) four cut-outs can be seen at 90° intervals around the central ceramic cap. These have been added above the location where vapor lock was forming cavities. They act as vents during the initial seal application. Once the seal is applied these four vents are back filled with additional seal material as shown above.

The second problem is one of geometry and access. For the shorter 45-cell stacks, it is possible to reach in and manually apply caulking where desired, but this becomes less feasible when considering a 17” tall 350-cell stack. For this reason, the center post is designed to be preloaded with caulking before it is inserted into the stack, after which the caulking is forced from the center post to form the sealing interface.

It was found that the amount of caulking pre-loaded in combination with the method of forcing it out of the center post was resulting in less than ideal sealing along the vertical interfaces. A more significant re-design was implemented to both increase the preload seal amount and to better control its behavior once in the stack. For the initial 45-cell stacks, manual touch-up of the vertical seals was used in an attempt to maximize the vertical seal performance.

There were two design revisions incorporated into the center post design to improve manufacturability and costs. The first is a change to the center post implementation, changing from a brazement of bent sheet metal parts from a conventional metal brake process, to a

brazement of sheet metal parts bent from the second revision which is photochemically etched blanks (Figure 3-22). This process has resulted in tighter tolerances and improved manufacturability, at lower cost. It is expected that the geometry will enable better seal structure between the fuel inlet and fuel outlet, improving on the previously reported fuel bypass challenge and thereby improving the overall stack performance.

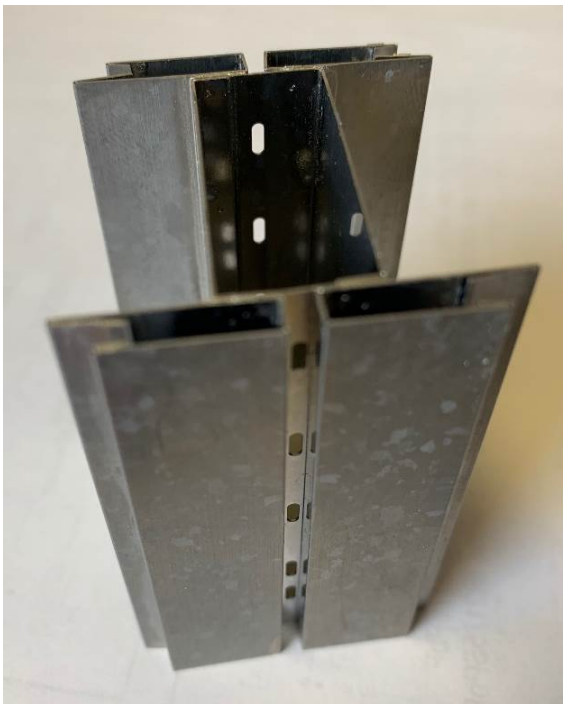

Figure 3-22 Revised center post made from photochemically etched pieces

A cast top isolation plate (providing both thermal and electrical isolation) has been through several iterations to improve manufacturability and tolerances. The current design is as shown in Figure 3-23.

Figure 3-23 Updated cast isolation part

The design has been produced and deployed and has provided significant benefit in the area of mitigating fuel bypass. While easier to manufacture and to install, it is also less expensive. It has also improved the fuel utilization performance and consistency. Three stacks have been built with the new center post (2 45-cell and one 150-cell) and all have shown stable operation at 80% fuel utilization during the conditioning tests.

3.2 Task 3.2 Modeling (CFD and FEA Analysis)

Objective:

- Optimize stack design using CFD and FEA tools in support of minimizing stack cost

Approach:

A proprietary user defined function (UDF), based on the Fluent CFD software, that emulates the electro-chemical reactions and thermal response of the SOFC, was utilized in the stack design activities. Detailed analyses was performed to quantify the thermal profile, current density map, contours of anode and cathode gas compositions, extent of Internal Reforming, and pressure maps within the stack.

Results & Discussion:

Figure 3-24 shows the flow configuration for the CSA stack design. The fuel manifolds are within the stack core while the oxidant manifolds are on the outside. The flow configuration is a pseudo counter-flow arrangement with two parallel flow paths per cell. The center port (fuel in/fuel out) is sized to ensure even distribution to all cell layers. Preliminary sizing of the center port is empirical, based on a comparison to the existing stacks, however more detailed modeling will be carried out to confirm size and flow distribution.

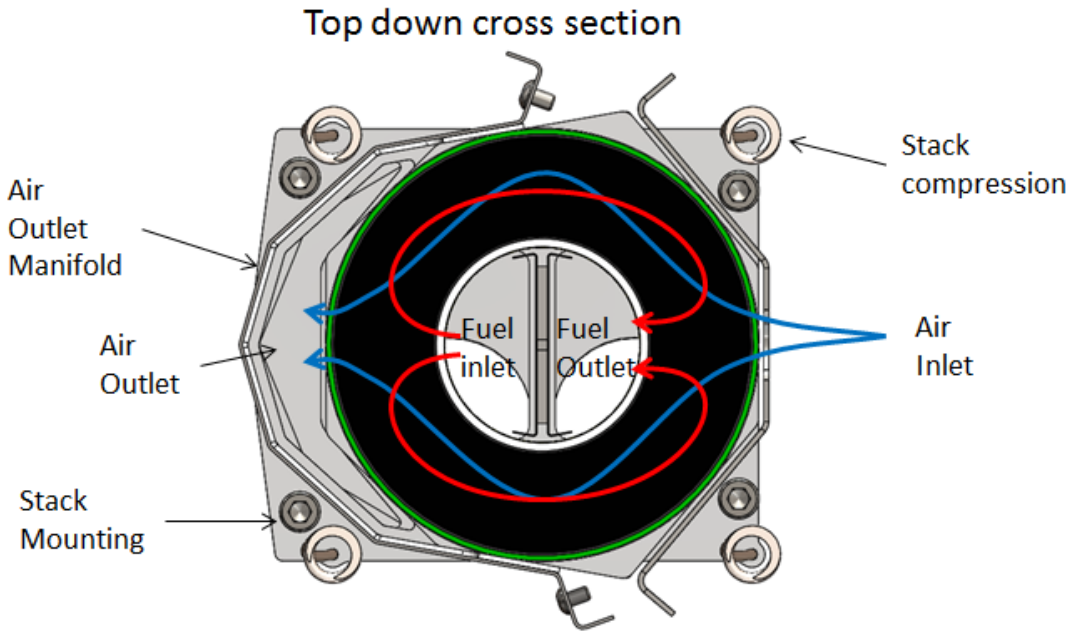

Figure 3-24 Flow Paths Through Stack

A unit cell model was assembled for thermal and flow modeling, consisting off a single repeat layer of the stack and simplified geometry representing the flow manifolds, as shown in Figure 3-25.

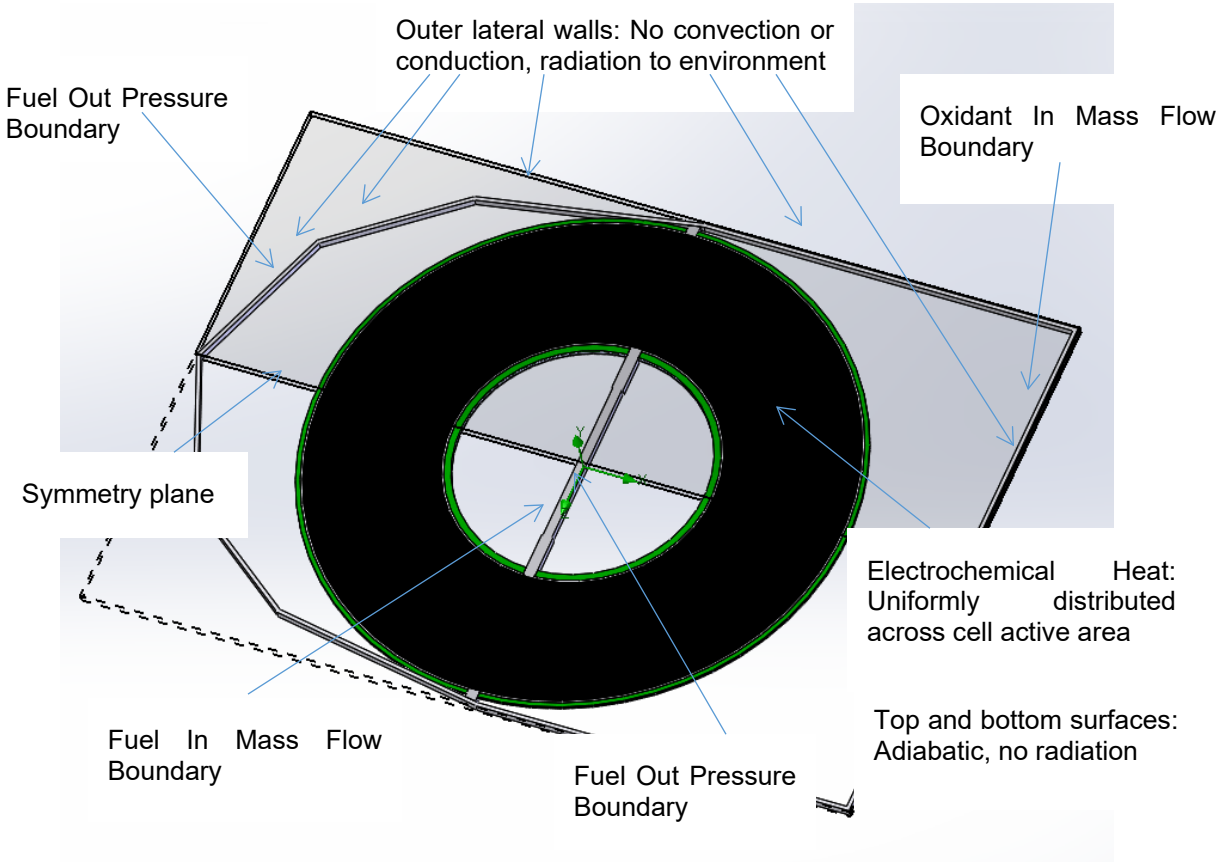

Figure 3-25 Unit Cell Model Boundary Conditions

Preliminary thermal modeling (Figure 3-26) was carried out which indicated operability for the cell size and component geometry, albeit approaching thermal limits. This preliminary modeling included the following characteristics:

- Full geometric detail of a single unit cell assembly (preliminary design)
- Fuel and oxidant streams representative of the average compositions encountered in, for example, the 50 kW SOFC demonstration unit
- Conduction through all components
- Radiation, internal and external. External radiation modeled as interacting with 650 °C environment.
- No heat transfer out from top or bottom of unit cell

Simplifications in the model included:

- Electrochemistry represented as a uniform heat load
- Reforming represented as a uniform heat load
- No mass transport (uniform compositions)

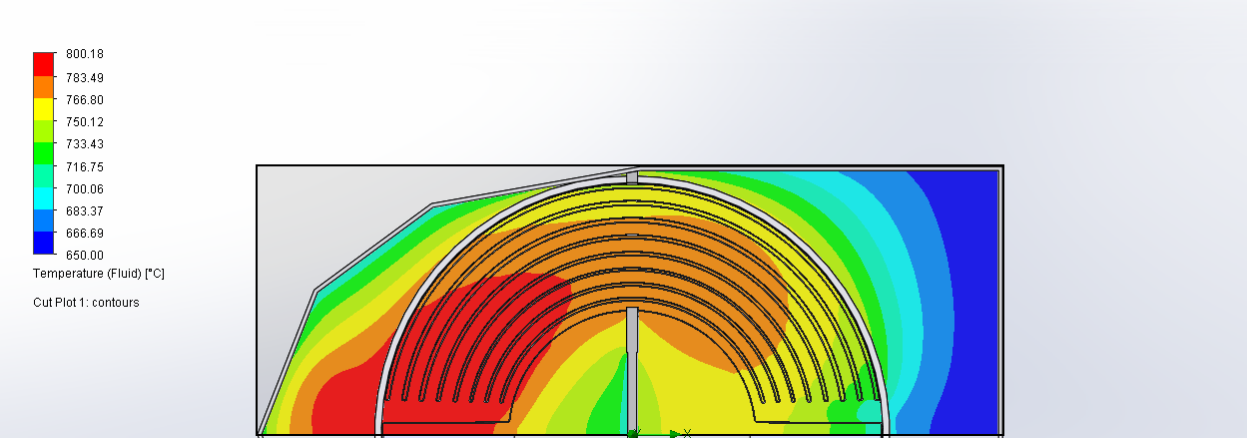

Figure 3-26 Unit Cell CFD Thermal Model (Preliminary)

Despite the simplifications, the model shows the operability in this configuration, and the layout was worthy of more detailed analysis. A bulk model was built for stack level thermal analysis, including details of the stack surroundings such as reforming panels and air inlet heat exchange (Figure 3-27) but has not yet been exercised. This model includes distributed reforming within the stack layers, and is set up to be representative of multiple stacks located within a single hot zone.

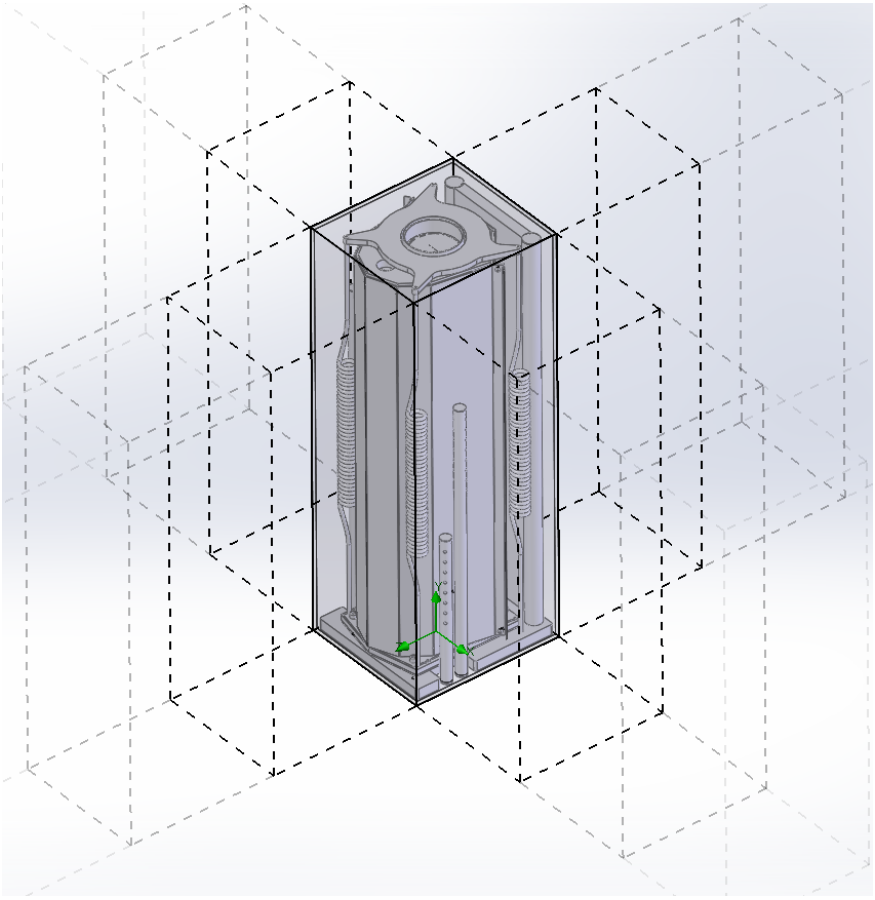

Figure 3-27 Unit Stack Thermal Model with Surroundings

Future modeling steps will include exercising the bulk stack model at different operating conditions as well as extending the unit cell model to include distributed reforming and detailed electrochemistry using a custom electrochemical UDF (User Defined Function) extension in Fluent.

High-level thermal models (for cell and stack) of the overall conceptual design (CSA stack) were presented initially. This was followed by the main modeling effort which supported the detailed design of the interconnect. The interconnect is a stamped metal component that fulfills many conflicting roles within the stack. It must:

- be manufacturable
- provide sufficient electrical contact area
- provide sufficient flow over the cell area on both fuel and air sides (for example the outer perimeter requires more flow because it represents a larger percentage of the total active area)
- have acceptable pressure drop
- have appropriate compliance to relieve cell stress.

While each of these features is apparent, achieving all simultaneously in a double-sided interconnect (oxidant passages are formed of fuel side ribs and vice versa) is a non-trivial exercise.

A two-domain CFD flow and thermal model developed for the unit cell operating at the projected system conditions is shown in Figure 3-28.

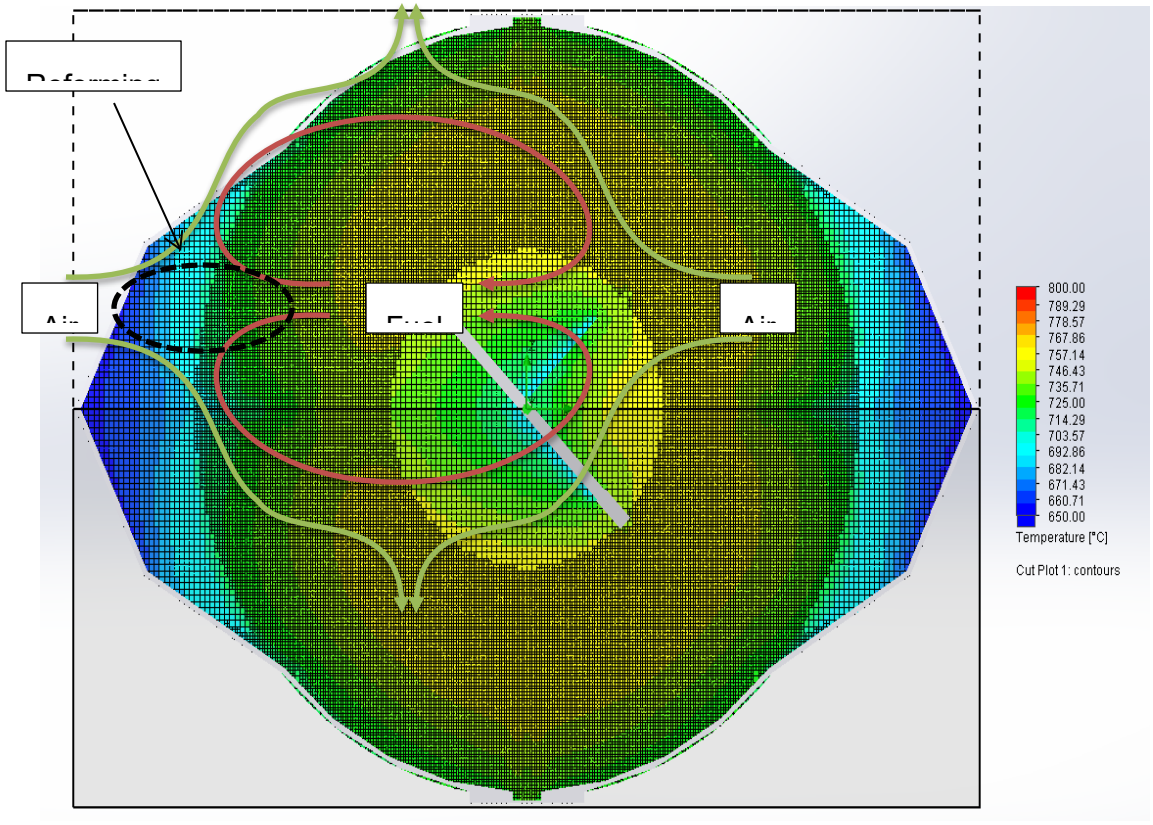

Figure 3-28 Thermal model of unit cell

As mentioned in Task 3.1, the unit cell design transitioned from a single inlet and single outlet oxidant flow configuration to a dual inlet and dual outlet oxidant flow configuration. This change

resulted from the requirements listed above and the realization, after comprehensive modeling, that the oxidant side pressure drop for the single path configuration was getting too large in order to meet the other technical requirements.

The interconnect is designed as a ribbed plate, which distributes fuel flow on one side and oxidant flow on the other side, while providing current conduction between cells. Prior work has demonstrated that for the interconnect to be reasonably manufacturable, the local rib formation should not exceed 15% strain. Also, based on empirical rules derived from past designs and testing, it was identified that to provide good electrical contact, the interconnect should contain at least 9 ribs. These two factors (15% strain limit and 9-rib requirement) coupled with a target wall angle and the target cell geometry, restrict the interconnect flow height to a maximum of 0.024" (0.61 mm). With 9 ribs, suitable contact density and 0.024" flow height, the air side pressure drop (dP) was exceeding 0.25 psid (in CFD analysis) at 40% air utilization which needed to be increased further to give acceptable flow distribution within the unit cell. It is desired to keep the dP below 0.15 psid at the unit cell level.

Compromising on rib density (for example an otherwise acceptable solution was found with 8 ribs) would penalize stack performance. Past testing suggests the penalty would be ~20 mV/cell (exceeding 2% in power output) given the respective geometries. Compromising on allowable strain would drive cost of the forming process (multi-stage forming) and/or might restrict material choice. Instead of compromising on the targets, a change in flow configuration was pursued. By dividing the oxidant flow in to two feed streams, the resulting flow in each channel is halved and the resulting flow distance is halved. This offered a lower dP without compromising the other interconnect characteristics.

Figure 3-29 shows the resulting interconnect design. This interconnect is the most aggressive design attempted by FuelCell Energy. Five prior designs of related geometry but smaller active area, were advanced to the stage of forming parts. One of these designs had a single rib at 14.9% local strain, the others had no ribs above 13% strain. In contrast, the final CSA design has six of nine ribs at 14.9% or 15% strain and no ribs below 13% strain.

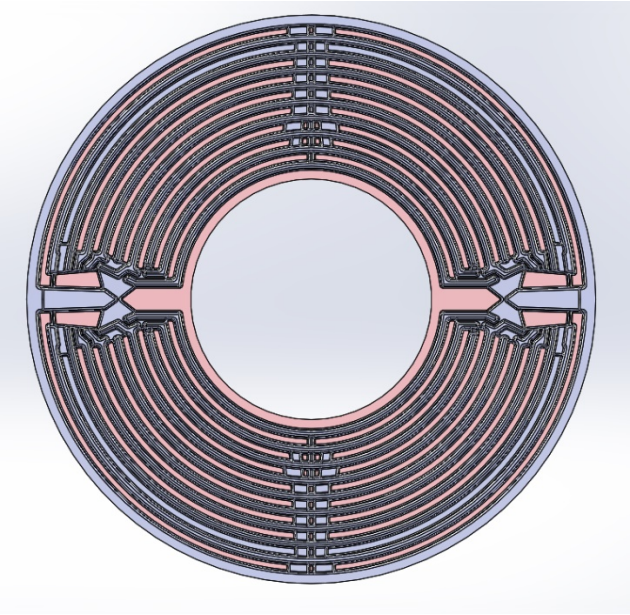

Figure 3-29 Overview of CSA Interconnect

A measure of interconnect design quality is the relative flow into each rib. In the ideal case, flow in each channel will be proportional to the active area supported by that channel. The concept of flow score is derived based on this. A flow score of 100% represents perfect distribution. A flow score above 100% means the channel gets more than its share of the flow. A score below 100% means the channel gets lower flow than ideal. The flow score estimated for each channel under three different conditions is shown in Table 3-4 Flow Score Summary for Different Conditions. The first column represents the target flow conditions under isothermal condition. The second and third columns show the flow scores once heat generation, reforming endotherm and radiant boundaries are added to the model (the third column is at a higher current density).

Table 3-4 Flow Score Summary for Different Conditions

	RELISS	RELISS w/ thermals	RELISS w/ thermals 0.4 A/cm2
Flow quality FUEL	102%	103%	103%
	99%	105%	101%
	99%	97%	94%
	100%	101%	100%
	100%	99%	98%
	99%	100%	101%
	99%	101%	102%
	102%	101%	103%
	100%	96%	98%
Flow quality OXIDANT	102%	110%	109%
	101%	102%	102%
	95%	96%	95%
	104%	102%	101%
	98%	97%	97%
	95%	94%	93%
	100%	100%	99%
	112%	112%	112%
	97%	96%	98%

As highlighted in the table, the minimal flow score on the fuel side is 94% and on the oxidant side is 93%. The fuel side flow is more critical than the air side flow due to typically higher utilizations. The fuel utilization of 68% and air utilization of 40% are representative of typical system design conditions which include anode recycle (system level fuel utilization of 85%). For a cell operating at 68% fuel utilization, having a flow score of 94% on one channel means that the channel has 72% effective utilization if current was evenly distributed across the cell.

In practice, there will be some intrinsic load balancing where flow-rich channels will tend to support more current and flow-lean channels will shed some current. It is desired to minimize this for best efficiency. For a cell operating at 40% air utilization, a 93% flow score means that the channel has 43% effective utilization, again assuming even current distribution across the cell. The thermal model results in Figure 3-28 show that despite a somewhat unconventional flow pattern (neither co-flow nor counter-flow nor cross flow), the modeled temperature distribution is reasonable.

Following on from the interconnect design effort, the detailed interconnect model was scaled into a simplified (porous media based) stack model which can be the basis for larger scale modelling. For example, it enables modeling of a full stack or a stack and its detailed environment in a way that would not be feasible if full interconnect detail was propagated across a 350-cell stack

assembly (e.g., even a relatively rough quarter domain CFD model of a single cell and interconnect layer has over a quarter million computational cells).

The porous media model, exercised at nominal conditions to validate the approach, is shown in Figure 3-30. This stack model will form the basis for upcoming hot module thermal/cfd design work.

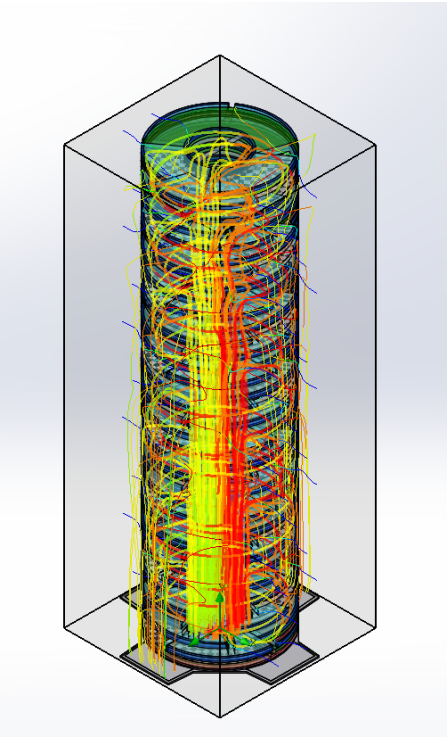

Figure 3-30 Porous Media Stack Model Exercised at Sample Conditions

Following from the unit cell and high level flow models the focus moved to development of a full electrochemical model for up to a full 350-cell stack. This involved translating the simplified Solidworks stack model into a Fluent model, with a specific effort in developing a meshing strategy that is simultaneously of sufficient quality to give good quality results, of appropriate structure to support the in-house UDF module that models the reforming and electrochemistry effects, while being simple enough that a 350-cell stack and its surrounding can be modelled in reasonable time and memory size.

The flow modelling effort was divided into two main strategies. At one level is a fully detailed model that captures the full geometric details of the unit cells, and is extendable across a small number of cells. At another level is a simplified stack geometry that should be representative, but does not capture the full internal geometric detail, thereby allowing a coarser meshing strategy. Both models need to be developed and to be calibrated for consistency.

Due to the nature of the very thin fluid channels of the interconnect (IC), and other thin repeating components, full geometry models require very high mesh density. Using conventional Fluent tools, the thin aspect ratios typically result in an excessive number of elements (tens to hundreds of millions per unit cell) to meet the recommended element quality standards recommended by the CFD software industry. Even then, the mesh quality and structure has proven problematic with respect to stability with the fuel cell and reforming UDF.

Efforts to use the Fluent software tools to mesh the full detailed unit cell model have shown those tools to be inadequate in providing a good quality model mesh that can succesfully interact with the electro-chemcial UDF within the CFD software interface. A different meshing tool (and method) was identified for unit-cell and short-stack full detailed electro-chemical modeling. Subsequent efforts in detailed evaluation at the unit-cell level were not successful. Therefore, another approach was required to validate the bulk flow version at reasonable 'short-stack' heights (<<350-cells).

Although success of the fully detailed geometry model remained elusive, efforts to develop a simplified stack model proceeded. In order to end up with a reasonably sized model for full stack modelling, a combination of three strategies were employed:

1) Model groups of cells as one repeat unit (i.e.: Model blocks of 10 or 25 cells as though they were a single repeat layer). This also required modification to the UDF to handle conditions representative of multiple cells.
2) Replace the detailed flow geometry with porous media flow bodies
3) Perform much of the mesh generation manually allowing the ultimate in mesh quality at the expense of increased manual labor to define the mesh

Simplified 350-cell model

Following initial exploration of a 125-cell model, a full stack (350-cell) simplified model was developed and numerically tested. The model is fully coupled (incorporates flow, thermal, electrochemical, and reforming calculations) and has been exercised under two loading conditions.

With respect to the early modeling results, the porous media bodies representing the flow passages were not dialed into representative DP conditions and as such the details of the flow results must be considered with caution. However, the general model stability and ability to run full electrochemistry shows that the meshing strategy is sound and that it can form the basis for further work this coming quarter.

The original SolidWorks CAD model has been rebuilt in ANSYS/Fluent and meshed, with a relatively modest mesh count of 4 million cells and max skewness of less than 0.35. The model was run at conditions of:

- 68% fuel utilization, 40% air utilization
- Reforming fuel composition of 6% CH_4, 44% H_2, 26% H_2O, and 23% N_2 which is representative of a simulated reformate gas used for in-house testing (N2 is used as a surrogate for CO_2 at the inlet). The overall composition is representative of a typical inlet composition for an anode recycle based system
- 0.29 A/cm^2 (24 A) – Representative of a typical operating point
- 0.49 A/cm^2 (40 A) – Representative of a more aggressive operating point

Figure 3-31 shows a view of the full stack model in which the air flow path lines are visible. Figure 3-32 shows cell surface species concentrations that result from coupled flow, thermal, reforming, and electrochemical reactions at the higher current density (0.49 A/cm^2). Some allowance needs be made for the relatively course meshing and the strategy of combining multiple cells (here 25) into repeat model units, both of which will tend to exaggerate local gradients. Nonetheless the results show the general operability of the model. Figure 3-33 shows the species driven reference Nernst voltage across each of the bulk cell models. Figure 3-34 shows the resultant wall

temperature profiles for the stack. In this first case the planned air pre-heat bodies are not in place in the model, and this is driving some overcooling of the stack base.

With the basic functionality and approach demonstrating feasibility, the next steps were to:

1) Tune the porous media body properties to match expectations (either to the full geometry Fluent model under development, or to the Solidworks Flow non-reacting flow results if the Fluent model is not deployed shortly)
2) Integrate further representation of the stack surroundings (e.g.: Air preheat) to get to a more representative thermal model
3) Use the resultant model to explore operating conditions to help guide stack testing and to guide stack module thermal design

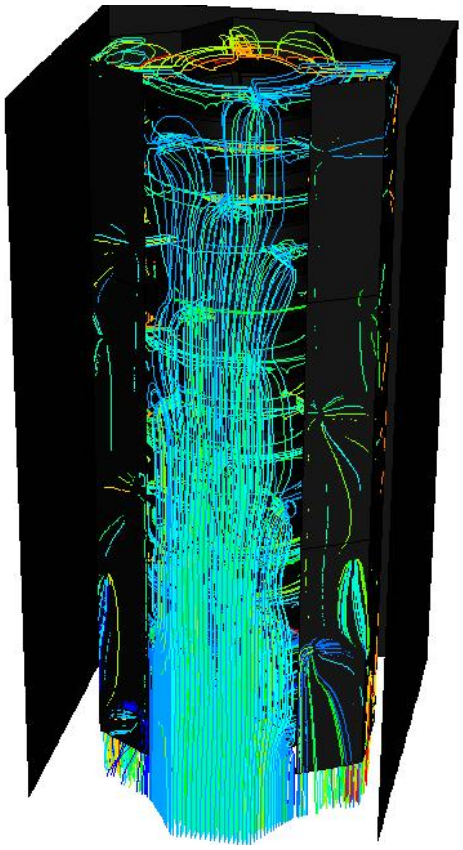

Figure 3-31 Full Stack Air Flow Path Lines

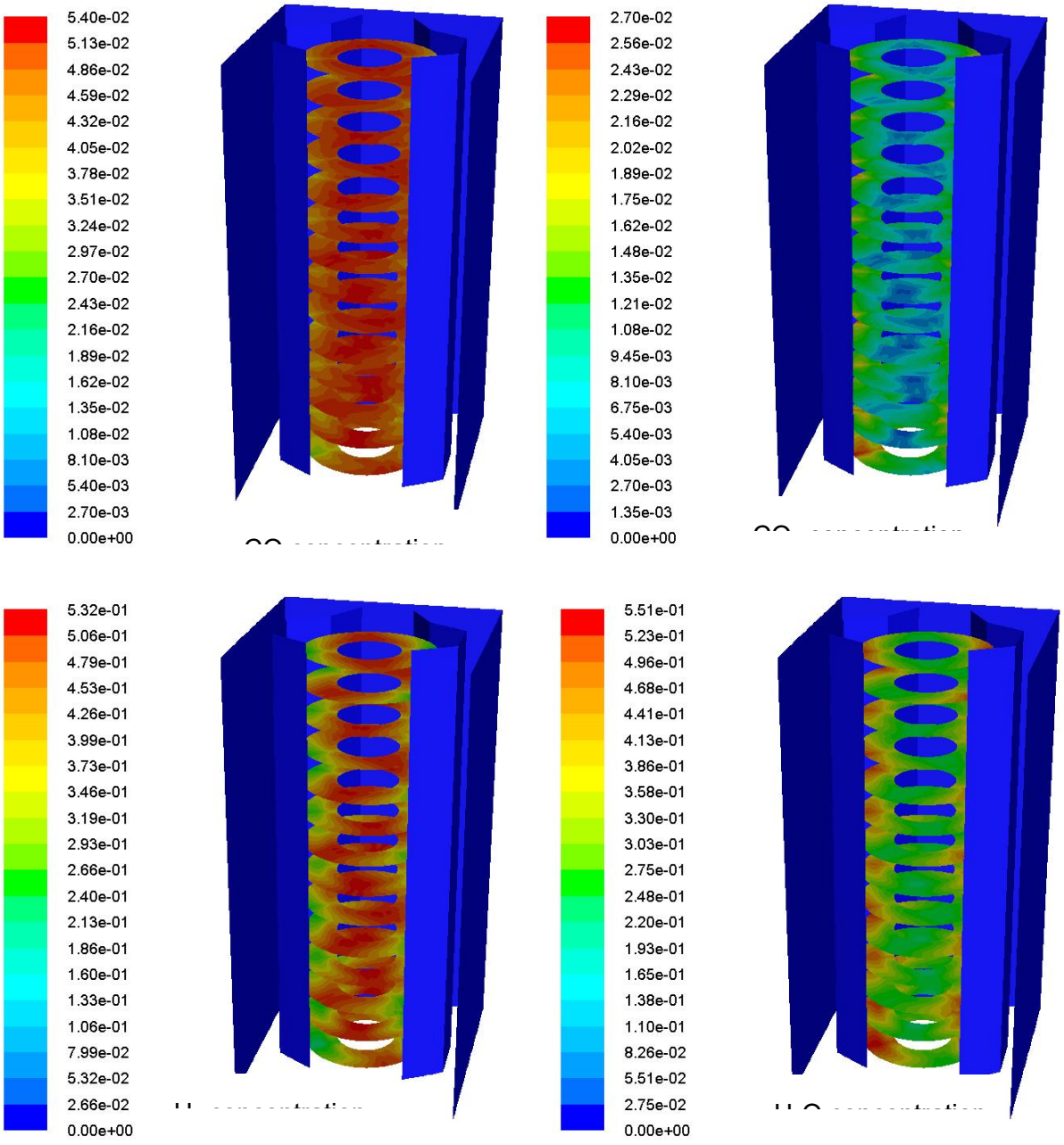

Figure 3-32 Full Stack Species Concentrations (0.49 A/cm^2)

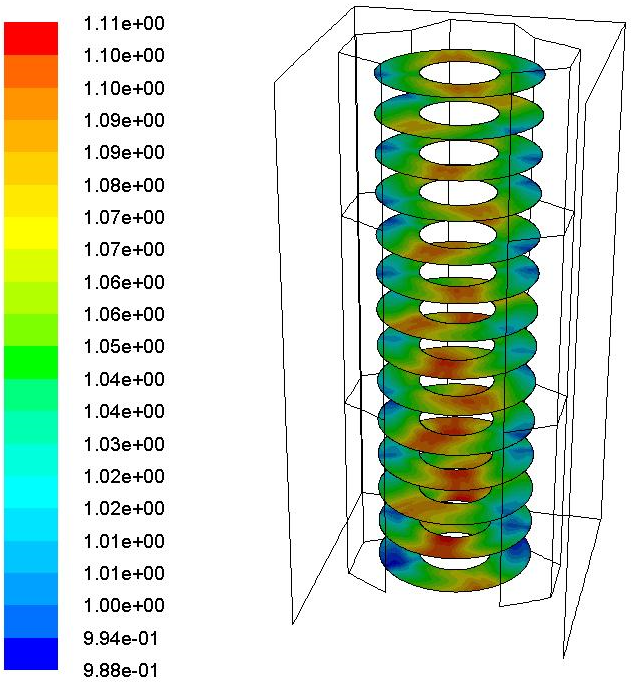

Figure 3-33 Cell Nernst Voltage Profiles (0.49 A/cm^2)

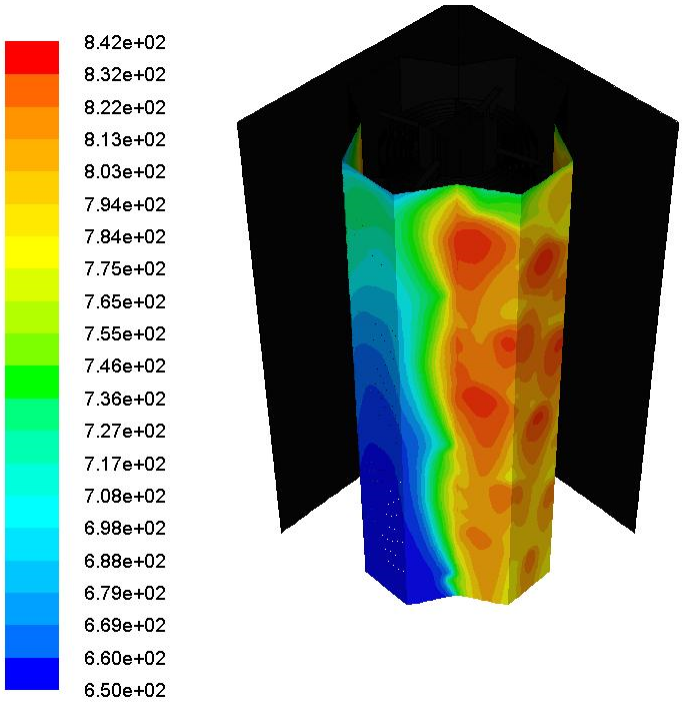

Figure 3-34 Stack Wall Temperature Profile (0.49 A/cm^2)

Due to the complexity of the stack (350 cells with relatively complex flow passages on both fuel and air layers), development of a meshing strategy has been crucial in getting to a manageable problem size with stable iteration properties.

The strategy involves simplifying the repeat unit flow geometry and representing it as a series of graded porous media bodies. A set of eight bodies is used on each of the fuel and oxidant sides, individually tailored to give a flow distribution matching that of the fully detailed geometric model. Cells were grouped together in sets of 25-cells, such that a full 350-cell stack is represented as 14 groups of 25-cells.

Each group of 25 cells has a single fuel electrode, a single electrolyte, and a single oxidant electrode, with electrochemical properties scaled to represent 25 cells worth of activity. The high local flows this combined electrode model generates causes stability problems in the solver, and a hybrid solution approach was adopted to address this. The hybrid solution has the following characteristics:

- Fully detailed and localized:
    - Current density
    - All electrochemically driven heating (net heat of reaction, resistive losses)
    - 1 cell worth of mass sources, positive and negative (H2, H2O, CO, CO2, O2)
    - Reforming reactions
    - Water gas shift reactions
- Uniformly distributed:
    - 24 cells worth of mass sources, positive and negative representative of the overall reaction

The result of this approach is that if there is a localized concentration of current, driven by the local temperature and concentration conditions, the corresponding local mass flux will be lower than reality since only $1/25^{th}$ of the flow will scale locally with current. i.e.: The model will tend to under-report the mass flux in those areas of highest heating – it is inherently conservative.

The stack model was exercised with reformate compositions derived from our 50 kW and 200 kW SOFC programs, consisting of 68% fuel utilization, 40% air utilization, 36% on-cell reforming. This is representative of a natural gas fired system running at 85% fuel utilization and using anode recycle to provide the steam necessary to support the reforming reaction. The model was run at open circuit, 0.29 A/cm^2, and 0.5 A/cm^2 conditions. Results of the modelling are presented below.

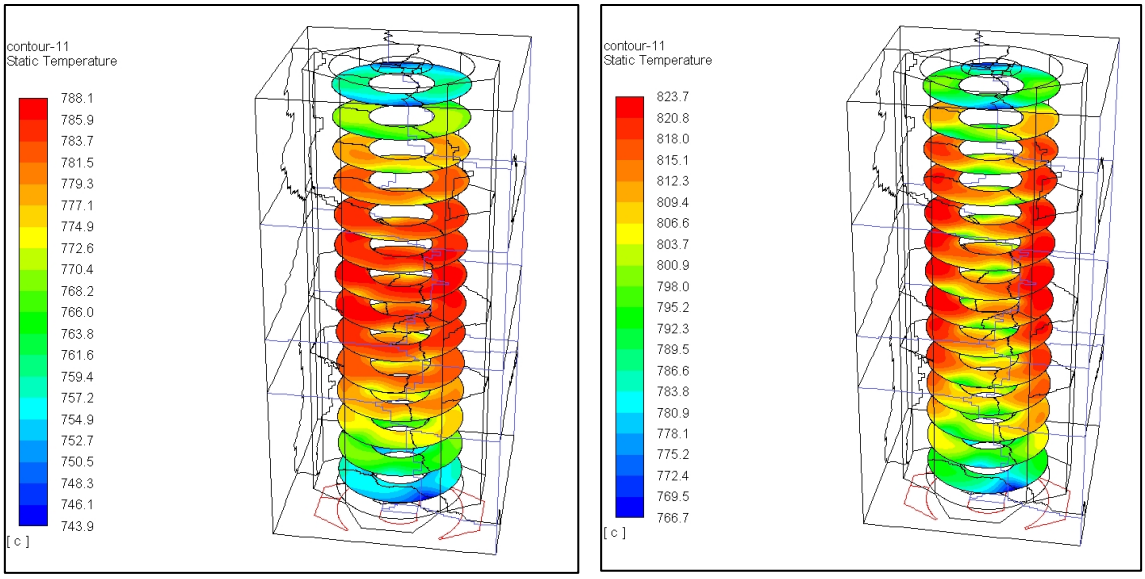

Figure 3-35 350-cell on-cell temperatures at 0.29 A/cm^2 (Left) and 0.5 A/cm^2 (Right)

Some of the results are illustrated in Figure 3-35 which show the on-cell temperature distribution at both 0.29 A/cm^2 (Left) and 0.5 A/cm^2 (Right) for the 14 sub-units that each represent 25 cells in the real stack. In both cases the inlet gas temperatures were set at an arbitrary 650 °C and the boundaries were set as radiant boundaries to a 650 °C environment. These are starting point boundary conditions from which real design conditions can be derived.

Figure 3-36 and Figure 3-37 show the average cell temperature and average cell voltage for each of the 14 sub-units at 0.29 A/cm^2, as well as the temperature distribution over the electrolyte for each sub-unit. Figure 3-38 and Figure 3-39 show the same data for the 0.5 A/cm^2 operating point.

The results are excellent. There is some tailing off of temperature towards the top (sub-unit 1) and bottom (sub-unit 14) of the stack, showing that insulation in these areas could benefit the temperature distribution. The top and bottom model boundaries for these results are the same radiation to 650 °C as the side wall boundary conditions. Overall the on-cell temperature range and overall stack temperature range are well controlled.

The 0.5 A/cm^2 condition in fuel cell mode is considered a limit condition, as it drives down the electrical efficiency of the stack quite significantly. The peak on-cell temperature difference at 0.5 A/cm^2 is just under 32 °C and shows up mid-way down the stack (sub-unit #8), and this is thought to be somewhat conservative due to the method of grouping 25 cells into a sub-group for modelling. At a more typical current density of 0.29 A/cm^2 the on-cell temperature difference is 15 °C and also occurs on sub-unit #8. There is some noise in the delta T results, probably a result of subtraction of two large numbers. It is prudent to consider these results as only accurate to the nearest 2 °C.

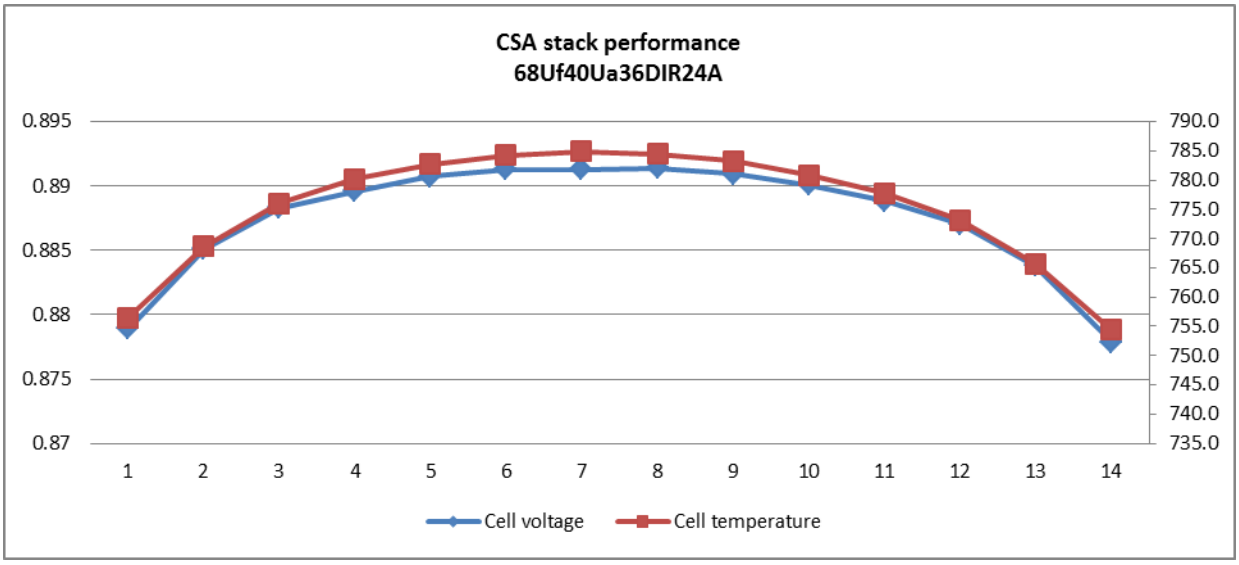

Figure 3-36 350-cell voltage and temperature distribution at 0.29 A/cm^2

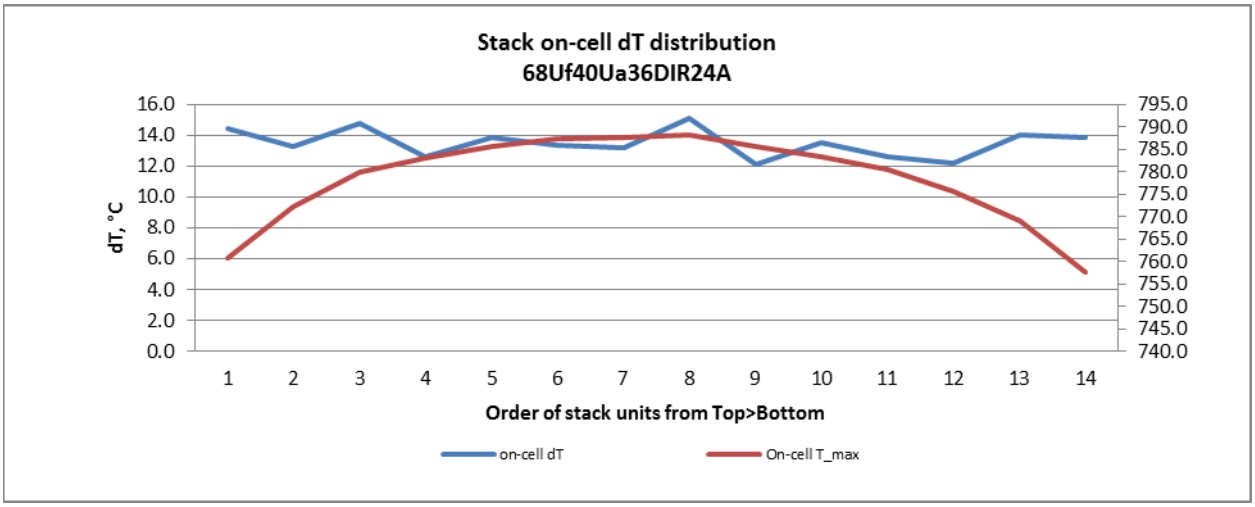

Figure 3-37 350-cell per cell delta T at 0.29 A/cm^2

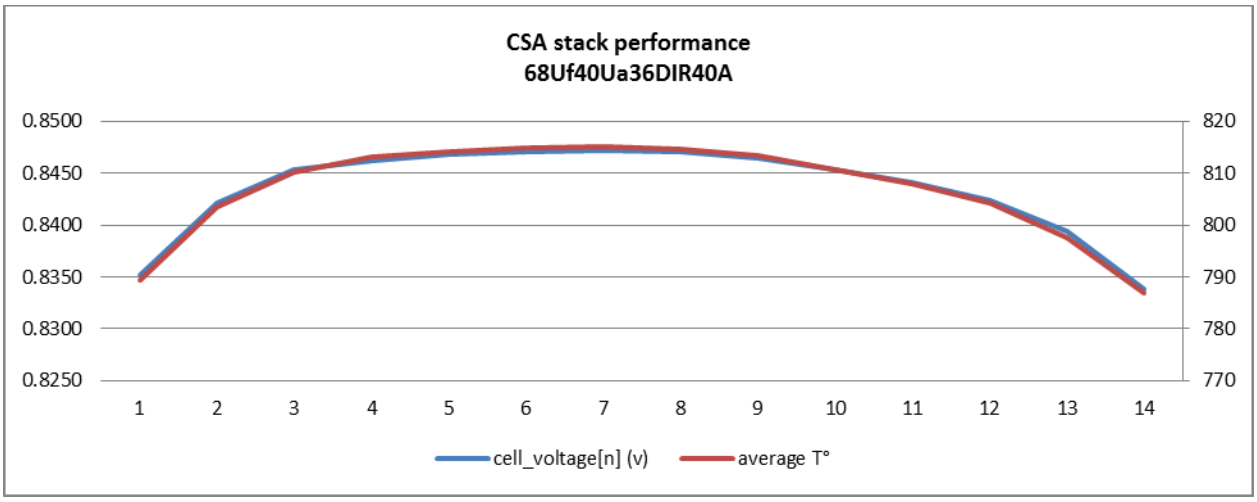

Figure 3-38 350-cell voltage and temperature distribution at 0.29 A/cm²

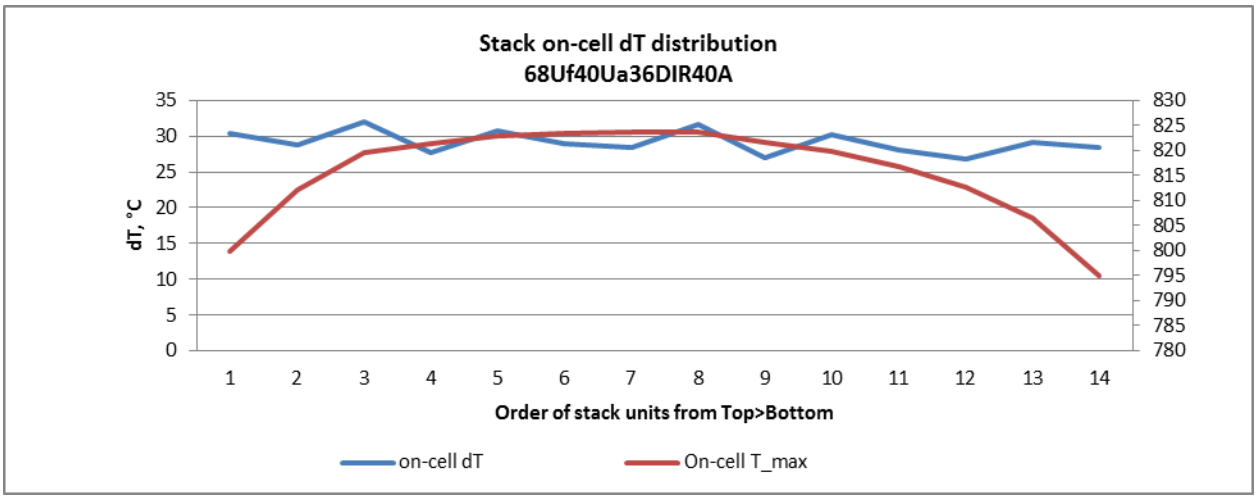

Figure 3-39 350-cell per cell delta T at 0.5 A/cm²

Figure 3-40 shows the current density distribution across each electrolyte layer. This is computed by the custom SOFC UDF within Fluent as a function of the local composition and temperature. The clocking strategy, as described in Task 3.2 Modeling (CFD and FEA Analysis), is clearly visible, where the peak current density on adjacent layers is rotated by virtue of the positioning of the gas inlet and outlet ports. This provides a measure of vertical heat transfer to moderate the on-cell temperature differences.

Figure 3-41 shows the molar fraction of methane in the gas streams. The reforming reaction is very fast, catalysed by the nickel in the anode support, and this is seen in the results where the methane concentration drops very quickly once exposed to the cell. The resulting reforming endotherm also occurs locally and is reflected in the temperature results presented above.

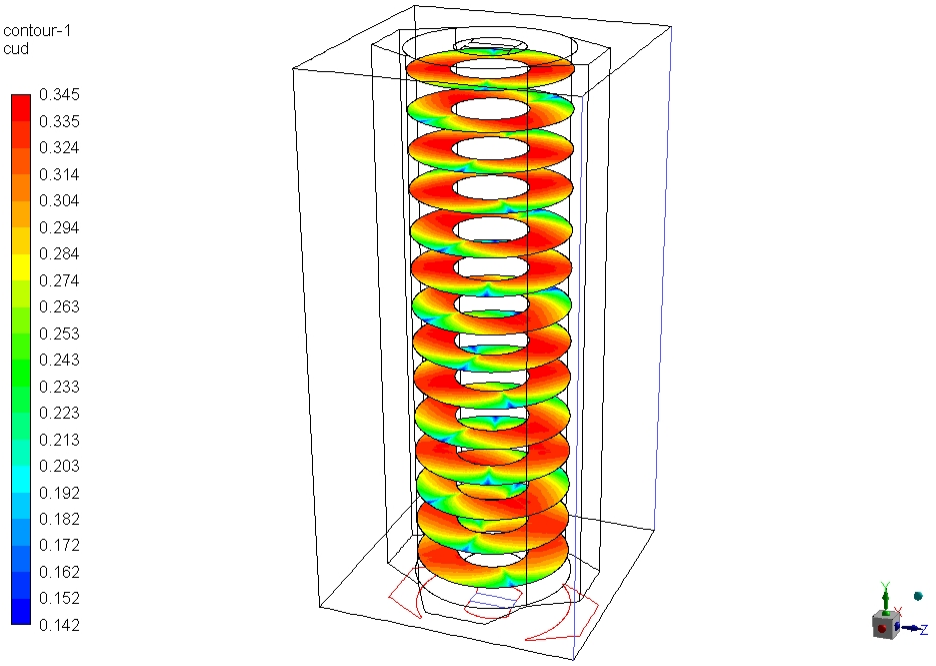

Figure 3-40 350-cell current density distribution at 0.29 A/cm^2 nominal [A/cm^2]

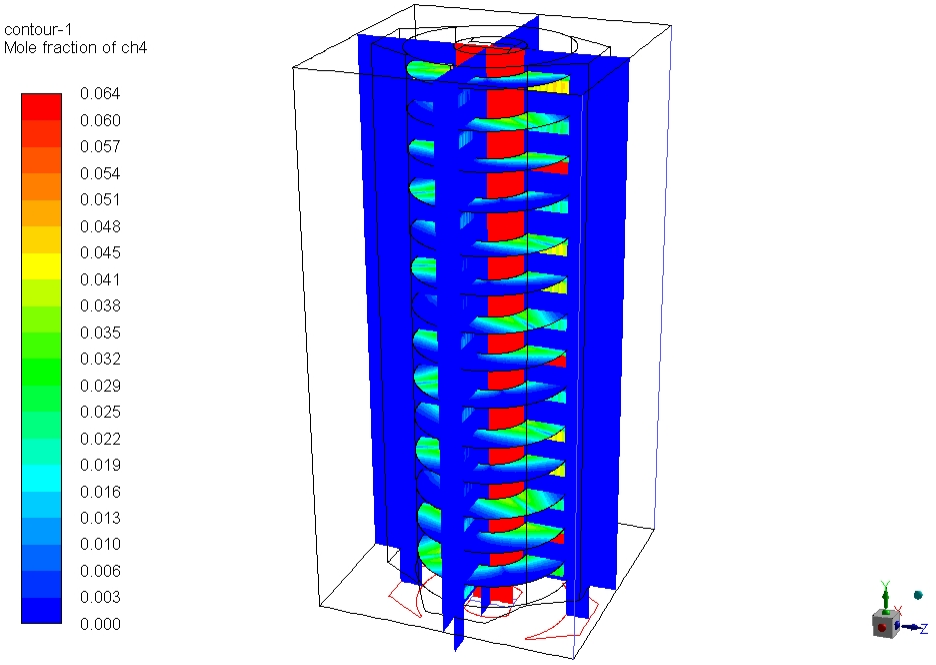

Figure 3-41 350-cell methane distribution at 0.29 A/cm^2 [mol % CH4]

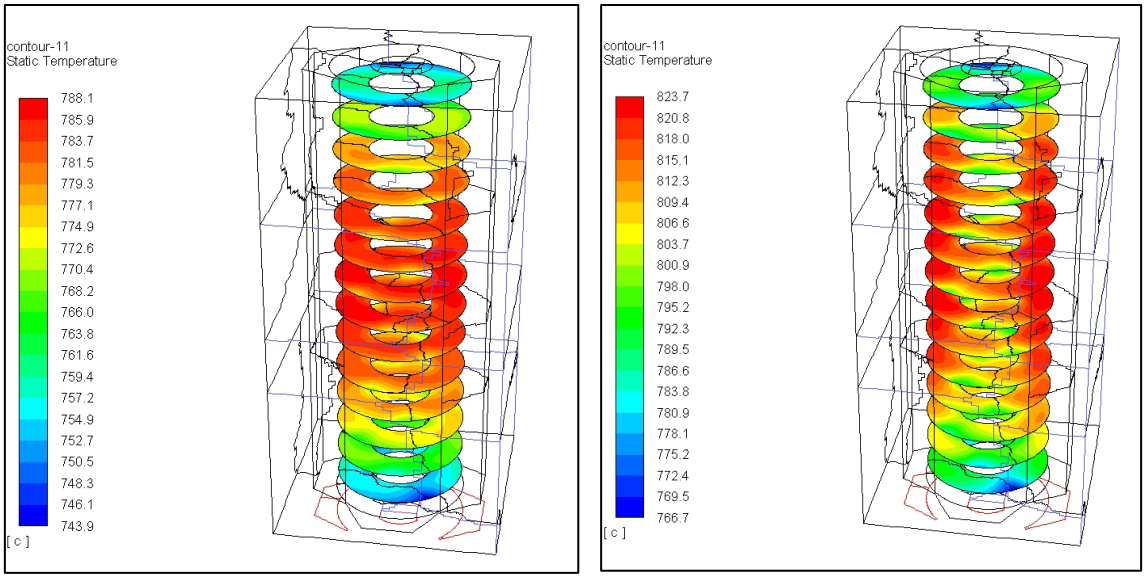

Figure 3-42 350-cell on-cell temperatures at 0.29 A/cm^2 (Left) and 0.5 A/cm^2 (Right)

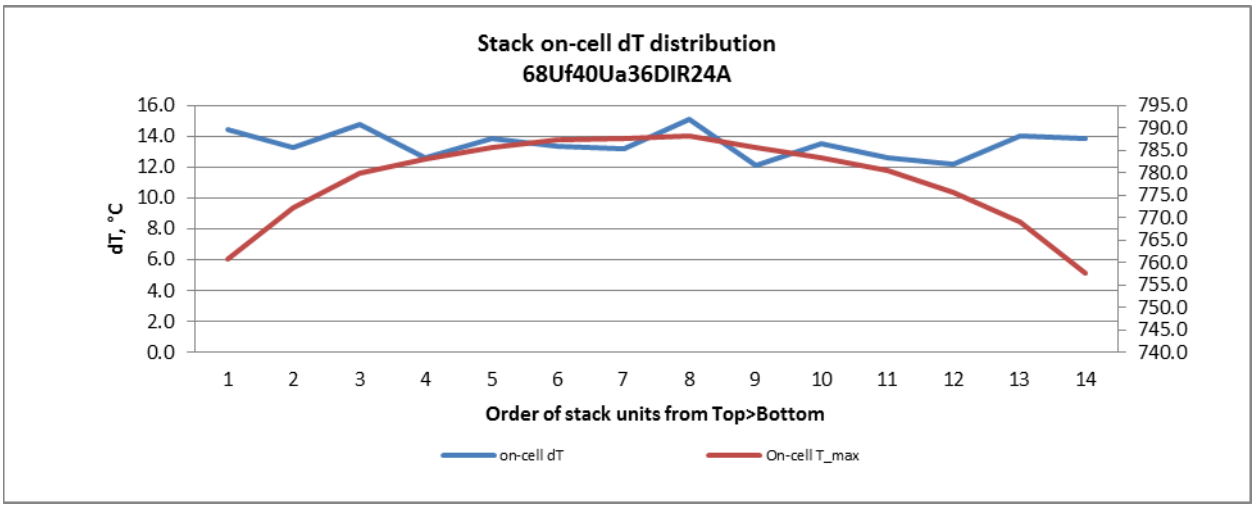

Figure 3-43 350-cell per cell delta T at 0.29 A/cm^2

These results made use of lumped porous media bodies to represent groups of cells, in order to build up a full stack model. The porous media flow properties had been fitted to unit cell modelling of the fully detailed geometry in order to match, with close fidelity, the flow distribution and pressure drop of the fully detailed cells.

On review, there was uncertainty in how best to capture the thermal properties of the unit cell in this lumped model, in particular the thermal conductivity. For example:

- In simplifying 25 layers down to a single lumped model should the model capture individual component thermal conductivities (the nature of the model produces localized heat at the lumped model electrodes), or pre-compute body average thermal conductivity and apply that across all components?
- Should a scaling factor be applied to the axial direction thermal conductivity in recognition that the clocking strategy will place hot spots near cooler spots vertically with much closer spacing that the lumped model allows?

These questions would best be answered by building a more detailed model that avoids lumped cells, and building it into a multi-cell model from which property data could be extracted to apply to the lumped model.

As a first assessment, a set of assumptions, of varying plausibility, were developed and exercised in the lumped stack model. From this were extracted on-cell temperature deltas (min to max temperature) for the different thermal conductivity assumptions. Figure 3-44 plots the observed thermal conductivities under six different assumptions as follows:

	Assumed conductivity	How it was applied
Case 8	Low thermal conductivity	Isotropic
Case 9	High thermal conductivity	Isotropic
Case 10	High thermal conductivity	Anisotropic
Case 11	High thermal conductivity	Anisotropic, increased axially
Case 12	Low thermal conductivity	Anisotropic, increased axially

The low vs high thermal conductivity reflect primarily on the assumed thermal conductivity into and through the cells. If the resistance to vertical (axial) heat flow is high so too are the cell temperature ranges. Likewise, if the axial conductivity is multiplied by a factor of 5, the on-cell temperature delta decreases significantly. The factor of 5 is very loosely based on the observation that by building a lumped model around units of 25 lumped cells, the effectiveness of clocking for thermal management is reduced significantly.

The results of this sensitivity exercise show that understanding conductivity is important to the overall fidelity of the model, and that low thermal conductivity in the z-direction is particularly problematic, while low thermal conductivity in the X-Y plane has relatively little effect.

In essence, the sensitivity study showed that within a range of reasonably plausible estimates of bulk thermal conductivity, the range of resulting temperatures was too large to ignore. A more systematic approach to determining equivalent bulk thermal conductivity was required in order to make practical use of the simplified lumped model.

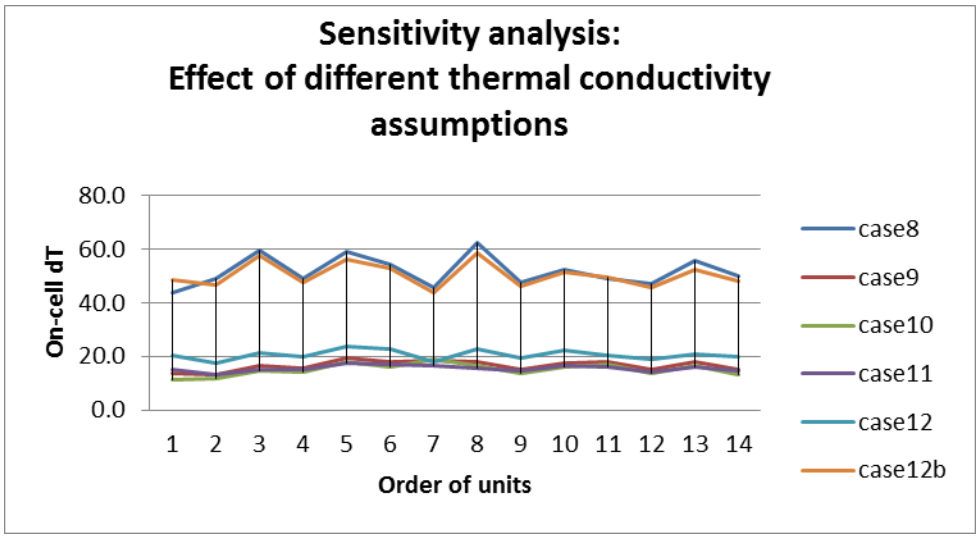

Figure 3-44 Effect of different thermal conductivity assumptions

In order to resolve open questions that used the lumped parameters, the focus shifted to the development of this more detailed model. Figure 3-45 shows preliminary results on a 5-cell stack built as 5 independent and clocked flow layers. This required a ground-up rebuild of the fluid model and meshing strategy. This model was run and extraction of equivalent thermal conductivities matching the full stack model was explored.

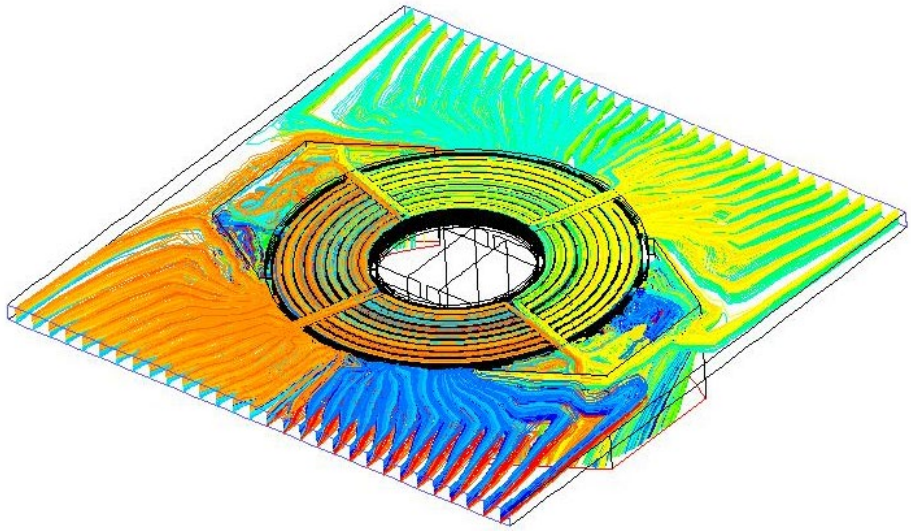

Figure 3-45 Model of 5 cell layers each represented as a detailed single layer

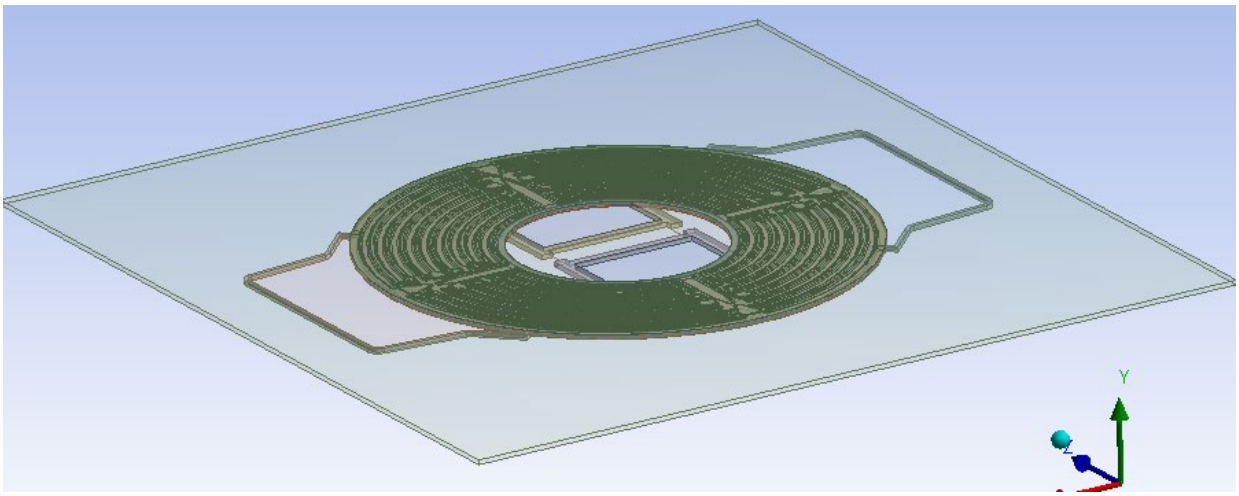

Figure 3-46 Full Geometry Single Unit Cell with Manifolds

While the above 5-cell model still uses porous media representation within the individual cell layers, a parallel effort is underway to develop a model that captures the full geometry detail while keeping the resultant mesh count at a usable size, and while meeting minimum mesh quality requirements. In this effort, as previously reported, due to the nature of the very thin fluid channels of the interconnect (IC), and other thin repeating components, full geometry models require very high mesh density.

Efforts were completed to identify an adequate meshing tool as a path towards successful unit-cell and short stack full detailed electro-chemical modeling. That tool was identified and has since been used to mesh the full geometry of a single unit cell (Figure 3-46) including fuel and oxidant manifolds. The resultant mesh (Figure 3-47) has sufficient quality metrics of skewness and orthogonal quality. The size of the file and number of elements,~21 million, is still quite large, and as of yet only represents a single repeat layer. This model was first given a test run in Fluent CFD with only energy turned on (no electrochemical, no radiation) and was successful operating on a machine with the largest capacity RAM.

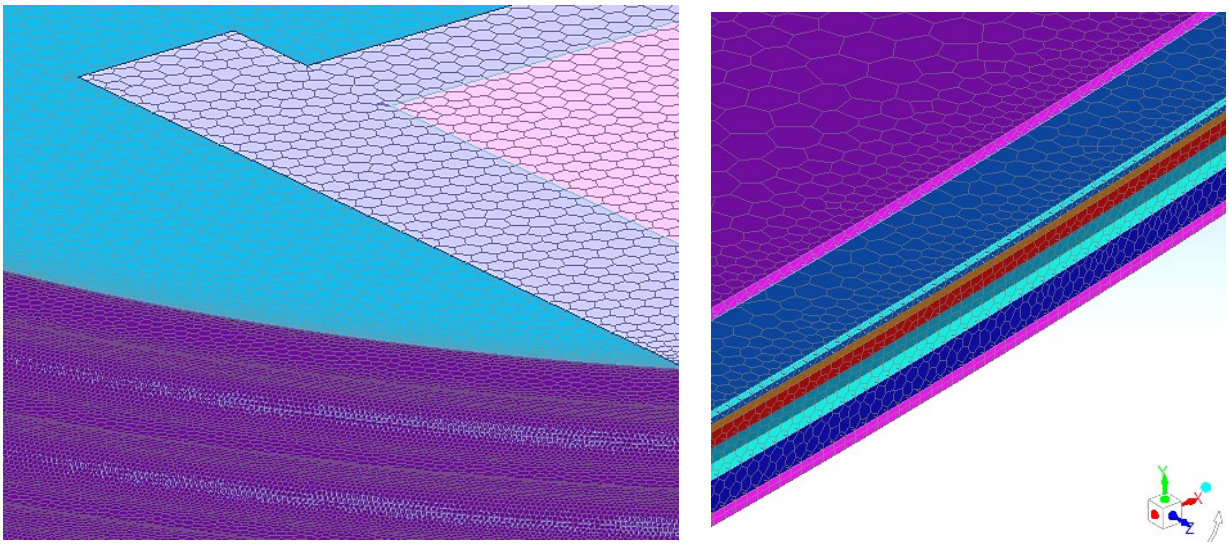

Figure 3-47 Full Geometry Single Unit Cell Resultant Mesh

Modelling efforts shifted to the development of a more detailed repeat layer model. The intent was to use the results of this more detailed model to validate and where necessary to adjust the full stack lumped model parameters to be more representative. Figure 3-48 shows preliminary results on a 5-cell stack built as 5 independent and clocked flow layers. This required a ground-up rebuild of the fluid model and meshing strategy.

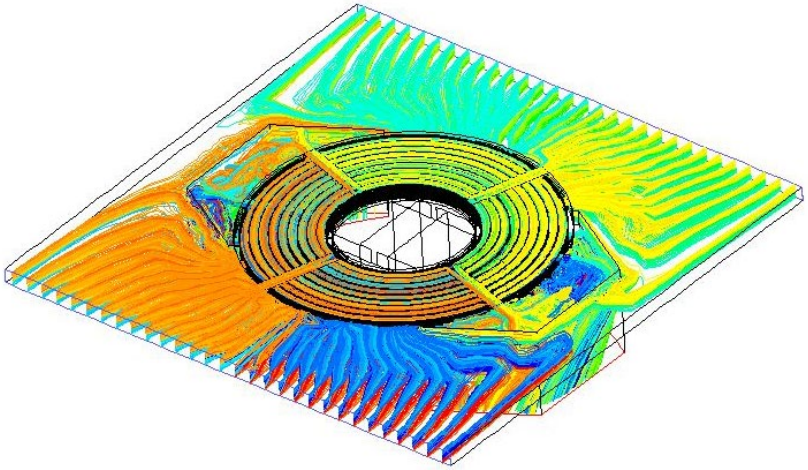

Figure 3-48 Model of 5 cell layers each represented as a detailed single layer

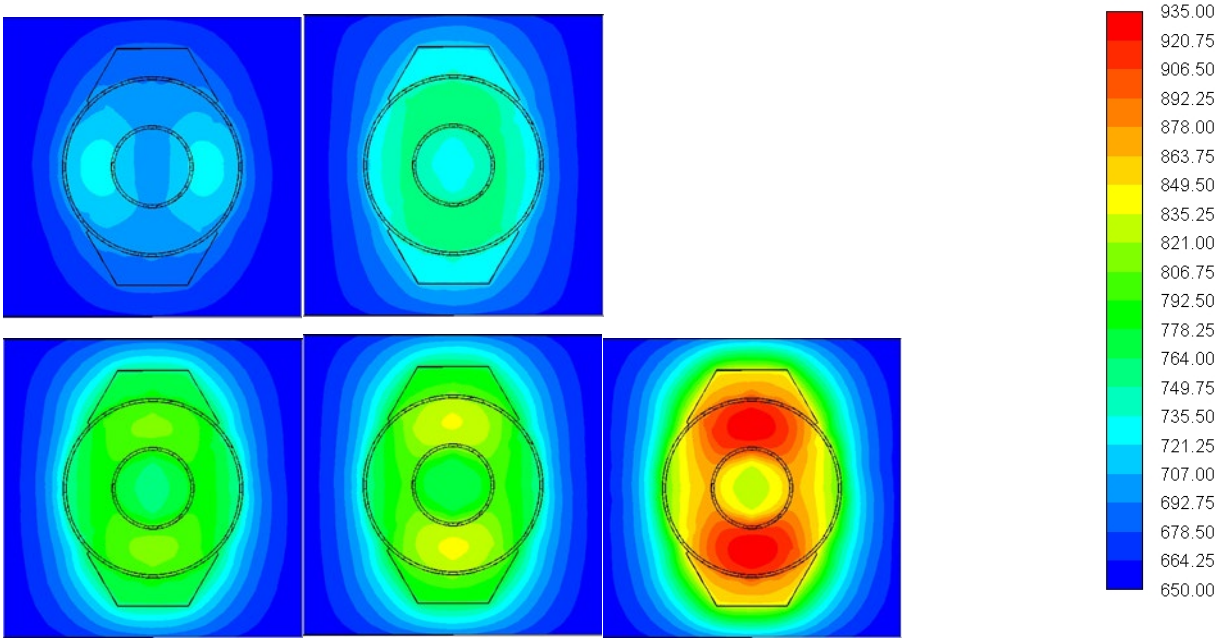

Figure 3-49 Comparison of model results at different conditions

(top row: 65% DIR, 36% DIR – bottom row: 25% DIR, 10% DIR, 0%DIR) All at 68% fuel utilization and 40% air utilization, 650 °C wall temperatures.

Figure 3-49 shows comparison data extracted from the 5-cell model comparing different levels of direct internal reforming (DIR). The test conditions span the range from 0% DIR, i.e., no reforming - all fuel in the form of hydrogen, to 65% DIR which is characteristic of a natural gas fired SOFC system with anode recycle where most of the reforming occurs in the stack. In these results the

perimeter boundary conditions are arbitrarily set at 650 °C, and the upper and lower boundaries are adiabatic. The intention is to simulate a set of 5 cells vertically centered in a tall stack. The information of primary relevance is the temperature range displayed, the absolute temperature is less important as it is largely set by boundary conditions. For example, it is not a surprise that at lower levels of reforming, with all else held constant, that the peak temperature is higher. In practice, additional cooling is required at lower levels of reforming, by increasing air flow or by reducing the cathode inlet temperature.

The main observation is that all conditions with reforming are relatively low delta T, showing that the stack should be capable of operating at a range of internal reforming levels. This is, incidentally, a fully coupled model so that the current distribution and cell voltages vary according to the different localized conditions of flow, temperature, and composition.

The one condition of some concern is the pure hydrogen case (0% DIR). It shows a substantial temperature gradient across the stack, and this intuitively makes sense. The hydrogen is entering the cell in the top and bottom relative to the image, leading to the highest current density in these areas. The primary cooling mechanisms are the sensible heating of gases and radiation to the surroundings, which are both maximized to the left and right of the image. This raises the question – What would happen if the fuel flow direction were inverted such that the hydrogen rich areas corresponded with the areas of better cooling? The results are shown in Figure 3-50. Again, the focus is on temperature difference across the cell and it is apparent that the inverted flow case (right image) has much lower on-cell temperature range.

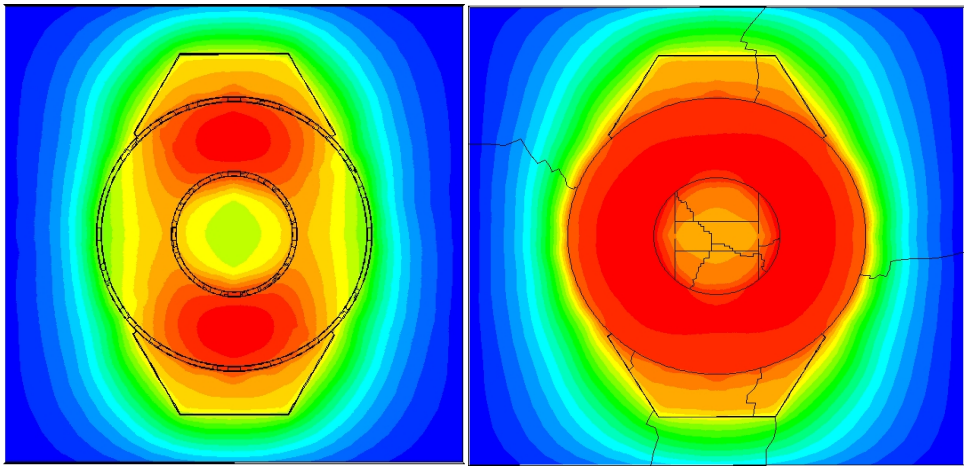

Figure 3-50 Comparison of model results with different flow directions

The modelling suggests that for a natural gas fired system, or any system with moderate to high levels of internal reforming, the default flow configuration yields good thermal results. However if the stack were to be deployed for operation with straight hydrogen, there would be advantage to inverting the fuel flow direction. This is a minor change to the stack requiring only an adjustment to the base plate to redirect fuel flow.

The above results all display the temperature of the center cell in the group of five. As previously described, the stack uses a strategy of clocking layers relative to their neighbors in order to more evenly distribute the heat across the plane of the cell. Figure 3-51 and Figure 3-52 show the methane concentration at each of the five cell layers (where the clocking strategy is clearly visible) and the resulting temperature distribution across each of the five cells respectively. These results are for the 36% DIR case, with the temperature scale zoomed in to more clearly show the temperature distribution. The similarity in temperature distribution on all layers, despite

significantly different local cooling distribution, demonstrates that the strategy of thermal blending between layers is effective.

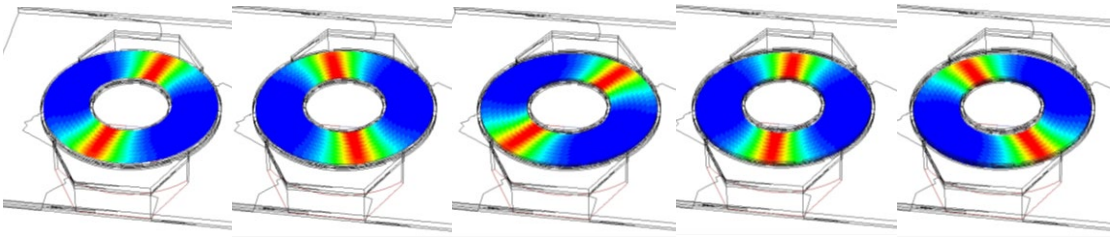

Figure 3-51 Methane concentration at each cell layer

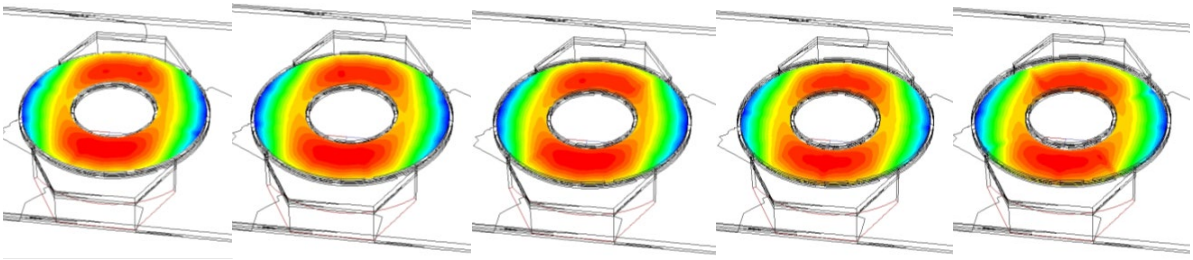

Figure 3-52 Temperature distribution at each cell layer

In summary, the five-cell stack model has been exercised over a range of conditions and provided some early evaluation of the operability envelope of the stack.

3.3 Task 3.3 Stack Manufacturing Process Development

Objective:

- Review and deploy (where warranted) volume manufacturing processes for stack and stack component production and QC

Approach:

For the new stack architecture, manufacturing process development considered high volume methodologies from the outset. With the chosen Design for Manufacturing and Assembly (DFMA) approach, the number of unit cell components was minimized for cost, simplicity, and overall reliability. Additionally, process development and programming for the execution of the stack build itself and follow-on final stack assembly, firing, and conditioning made up work in this area. With key input from cell manufacturing and the new advanced stack architecture, new geometries were expected, and manufacturing QC tools were updated for alignment. It is believed that an additional step reduction in cost could be attained by matching a form factor for which entire, high-volume robotic factories have already been designed and commercialized.

For seal manufacturing, high volume near net shape manufacturing techniques such as dispensing are preferred and was explored. VPS' alumina and glass sealing technologies were both be considered for implementation using VPS' existing automated dispenser equipment.

Results & Discussion:

One of the characteristics of the CSA design approach is that the component size and the simplicity of the unit cell lend themselves to relatively simple automation. Low cost (relatively) and existing commercial solutions (from other industries such as printed circuit board (PCB)

manufacturing) can be used for the CSA design. Automation of several key steps has already been demonstrated on the precursor stack design. Three of these processes are discussed.

Figure 3-53 shows an automated work cell that is capable of measuring the key dimensions of cells with no operator intervention other than loading the cells into the machine (in batches of up to 300 cells) and removing the cells from the machine after QC. The cells are automatically sorted by dimensional criteria. Only those cells that pass QC move to subsequent processes. All data is simultaneously recorded for future reference or further analysis. Of the cell QC steps, two processes have not been automated; leak testing and weighing. Weighing is used as a cross check of cell density which can be an indicator of drift in the firing process.

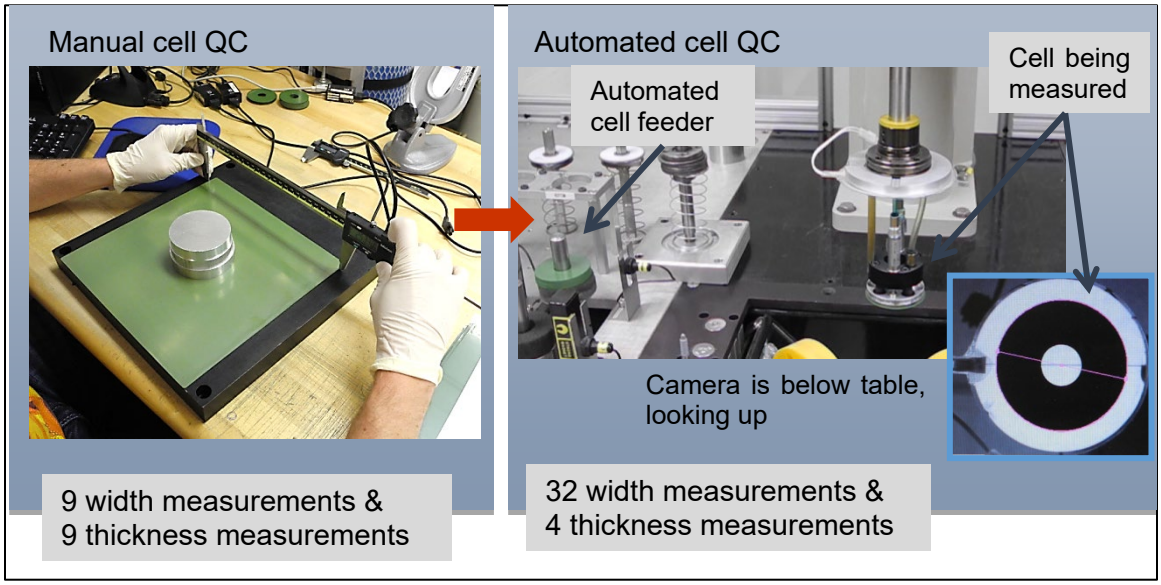

Figure 3-53 Automated Cell Measurements

Automated cell leak testing was an area of development for this project. It was a manual process and is relatively slow (~45 seconds per cell) in order to get stable and repeatable measurements. Efforts involved integration of automated leak testing in the measurement work cell, so that leak testing does not add manual labor, as well as shortening the leak test cycle time.

In addition, the work cell required general re-work to accommodate the larger component size in the CSA stack. No significant problems are anticipated due to the larger component sizes, as their weights and dimensions fall within the capabilities of the existing robot.

Figure 3-54 shows the setup for automated spot welding of the fuel-side electrical contact grid onto the interconnect. This capability is built into the work cell used for cell QC (previously discussed), and allows for unattended spot welding in batches of 150 parts, limited only by the size of the finished part accumulator. The spot welding process includes machine vision alignment of the interconnect to the contact grid, as well as visual plausibility checks that reject parts not matching an expected profile (e.g.: If a part was loaded upside-down).

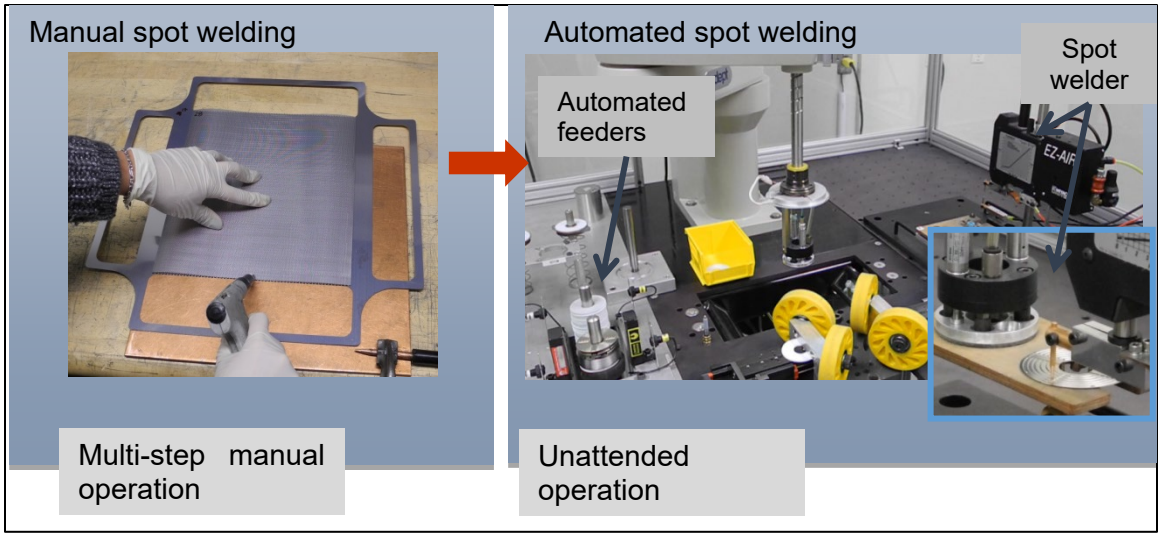

Figure 3-54 Automated Spot Welding

The spot welding process is currently followed by a manual leak check. A goal of the current effort is to integrate leak testing capability into this work cell to provide both cell leak check (discussed above) and interconnect leak check after spot weld.

Figure 3-55 shows the automated stack build setup (built into the same work cell as that for QC and spot welding) that is currently used to build the 225 cell stacks. The process uses machine vision to locate and orient parts and assemble them in a firing fixture. The process uses machine vision to check plausibility on components (e.g. to identify and reject parts that may have been loaded upside down), and runs without operator interventions other than loading parts into feeders before the build, and installing the final fixture before removing the stack from the assembly cell.

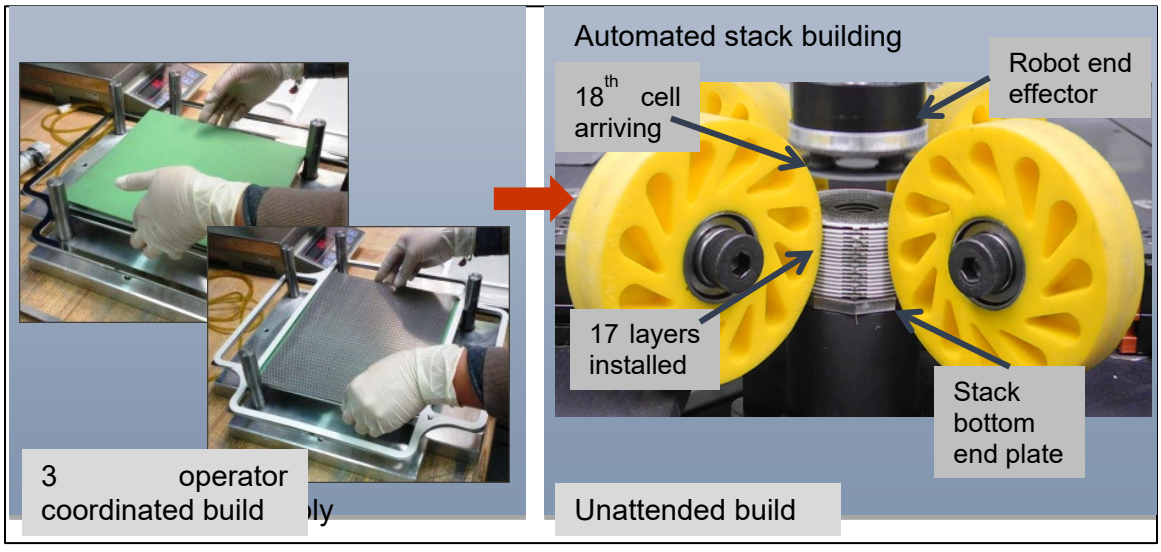

Figure 3-55 Automated Stack Build

Automated screen printing was reviewed in more detail, including initiating discussions with ASM regarding its DEK line of automated screen printers (Figure 3-56). These highly flexible printers (available from several vendors with similar capabilities) are very optimized and price competitive, designed for easy integration into larger production lines with standardized upstream and downstream communication to linked processes. The standard size of these printers is larger than

would be required for the CSA design, but it is unlikely that a customized smaller machine would be available for a lower price, simply due to the level of competition in the PCB (printed circuit board) manufacturing equipment area. Discussion with ASM/DEK revealed that at sufficient production volume they would design a full process optimized for cell manufacturing, and that they have successfully completed similar projects for solar cell printing lines.

In addition to the printing machine; part feeders, loaders and dryers from the PCB industry were reviewed, and all seem near drop-in capable for handling SOFC cells from FCE (LAS or CSA). It is likely that part carriers would be required due to variations in cell size and in the case of CSA cells because they are round. Printed circuit boards are generally rectangular and of precise width, and part-handling in various processes (printing, transport, feeding, drying) relies on this. Carriers to handle special cases are well known in the industry.

Figure 3-56 DEK Horizon 03i printer

Overall, a review of technical capability and suitability of printed circuit board manufacturing equipment has been almost universally positive. The processes appear well suited to SOFC cell manufacturing and, following the work done for solar cell production, can be adapted to much higher throughput when volumes justify customized equipment. ASM-AE, the division of ASM that specializes in alternative energy, has published claims of up to 3,600 wafers printed per hour in

their *Eclipse* solar cell metallization line[1] (in a relatively compact line volume) which includes part feeders and process steps such as printing, drying, inspection and finished-part stacking. The printed circuit board printers run at a slower rate of 10 to 20 seconds per part, depending on the specifics of the print requirements. Printing trials are planned at ASM to verify part handling and printing using FCE (VPS) cells and printing pastes.

Discussions with ASM/DEK with respect to the potential acquisition of an automated screen printer from the printed circuit board industry led to an opportunity that arose to purchase a similar automated screen printer (used) along with various support equipment. The equipment was purchased, installed, commissioned and trialed and shows great promise for CSA cell production.

The equipment purchase and subsequent commissioning was funded directly by FuelCell Energy, separate from this project. However, the equipment capabilities align well with the goals of this program, and will provide information for the cost exercise. Figure 3-57 shows the newly acquired equipment installed in a cleanroom at FuelCell Energy.

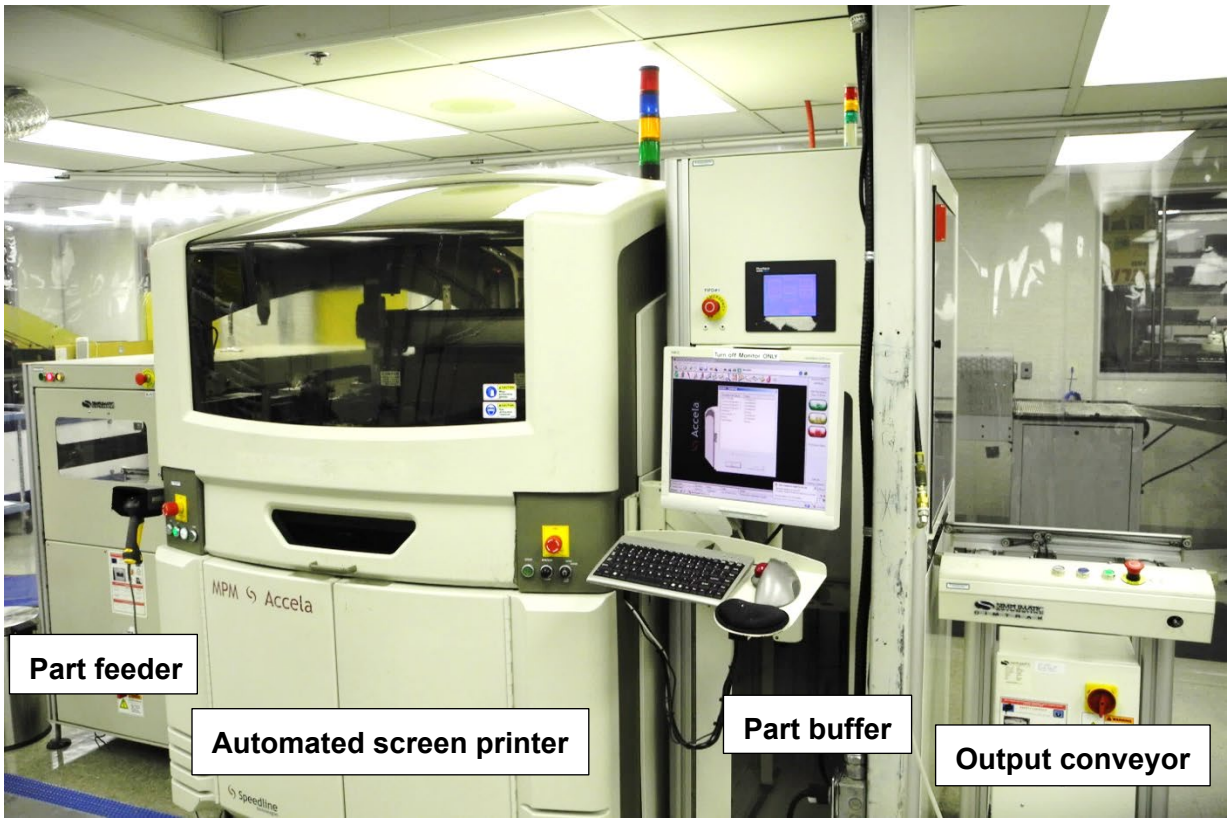

Figure 3-57 Installed Automated Cell Printing Line

The printer line has been commissioned for the current baseline 550 cm^2 cells. The equipment comes from the printed circuit board industry and consists of the following equipment:

Part feeder: Accepts a stack of cells and automatically feeds the cells to the printer on demand.

[1] http://www.asm-ae.com/addmindms/download.aspx?domid=10&d_id=856cea39-354a-4345-b39c-c6c45d14cdc8&fdl=0

Automated screen printer: Uses machine vision to position and align the incoming cells relative to the print screen, and executes a print cycle. Uses the same process as the current manual screen printing, but with a higher level of process control and without operator intervention after the initial setup

Part buffer: Accepts and holds printed cells separately to prevent damage to the printed layer. Not strictly necessary in this installation, but allows the line to run unattended for periods of time between operator unloading of the cells

Output conveyor: A convenience item to make it easy for the operator to accept the printed cells for transfer to a dryer.

For a complete line, it would be ideal to add an inline dryer. These are available and would be acquired when production volumes justify.

The line has been demonstrated with the current baseline cells, and has been implemented using carriers for the cells. It is anticipated that the carrier solution would apply equally to the CSA cells and that nine cells could be loaded and printed simultaneously. With nine cells per carrier the part feeder would hold over 1,400 cells. Without optimization, the line has demonstrated a timing of 22 seconds/carrier (per print layer), which corresponds to almost 1,500 CSA cells printed per hour (29 kW/hr) with minimal operator intervention. To achieve this rate in practice would require the installation of multiple print lines, since the cells require multiple print layers. In the current installation, the line processes different print layers sequentially and the actual throughput is reduced proportionally.

Although funded separately from this Innovative SOFC program and implemented specifically to help the baseline stack production, the capabilities of this production line form a strong basis for the cell costing portion of the current program. The line is composed entirely of off-the-shelf equipment from the printed circuit board industry and can easily be extended and replicated when production volumes are required.

For the detailed design of the interconnect CFD studies showed the flow distribution quality across the unit cell and estimates were made of the local strain of formation for the stamped part. The flow distribution on both oxidant and fuel side were shown to meet requirements, as well as having sufficient electrical contact area, sufficient compliance, and acceptable pressure drop. These characteristics came at the cost of more aggressive forming (local strain) than prior demonstrated designs.

During manufacturing trials of the proposed design, the increase of the local strain of formation proved problematic, resulting in several further design iterations. Figure 3-58 and Figure 3-59 show areas of the form that failed during forming. The first trials had rib forms with a strain of 17.9%[2]. For the second revision the rib strain was reduced to 16.3%, but failed in a similar manner and at a similar location.

[2] In the last report this was expressed as 15% strain. The calculation is an approximation and depends on the reference end points. In discussion with the supplier, they suggested the best approximation starts and ends at the tangency points to the formed ribs, which are the numbers reported here. In prior reports the strains were reported as calculated to the center points of adjacent ribs.

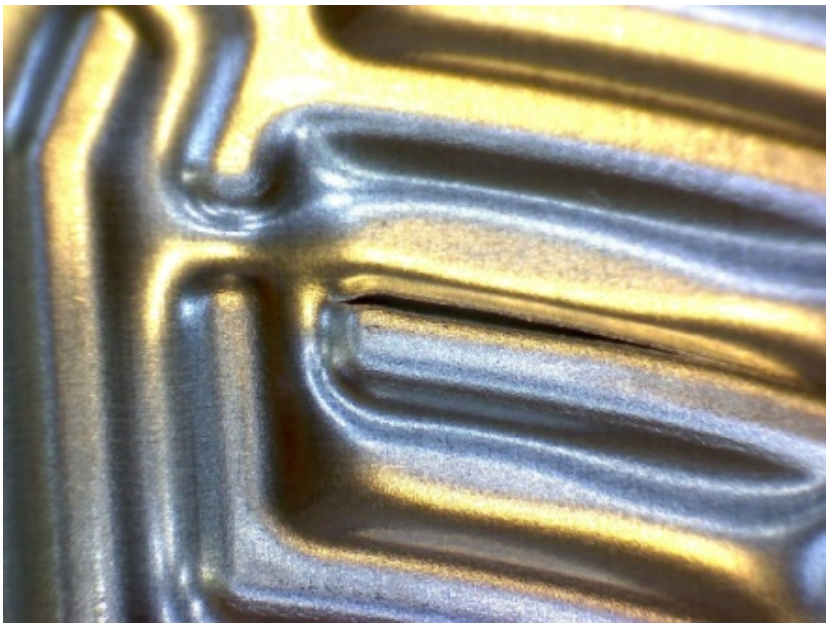

Figure 3-58 Cracks in First Design Revision

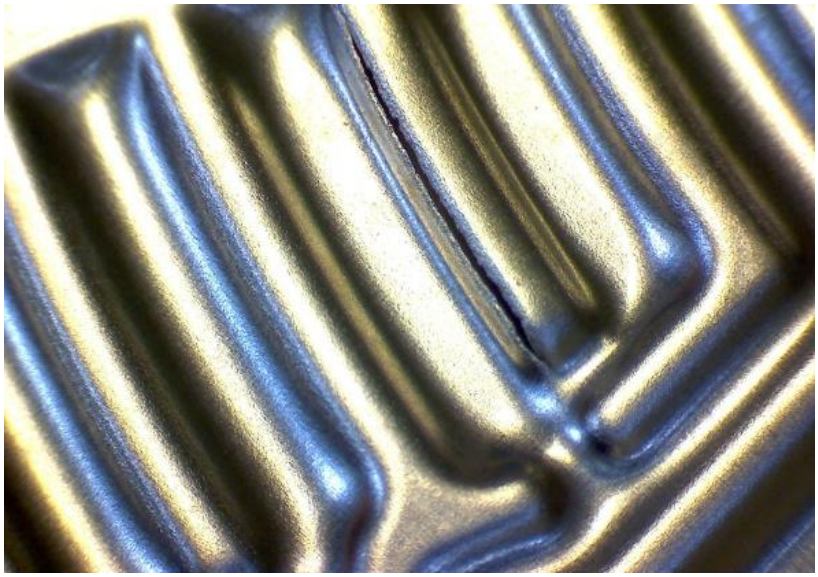

Figure 3-59 Cracks in Second Design Revision

These results caused concerns. Although the target strains were higher than past designs, it was somewhat surprizing to see failures even at a relatively low 16.3% theoretical strain. The strain in this case is reported as the average strain across the local formed rib, whereas the failure location is constrained to a particular bend where the local strains may be higher.

These results prompted new characterization tests of candidate materials. The characterization testing showed that the target forming strain was such that the material failed if the bend was parallel to the material rolling direction (mill direction) but did not fail if the ribs were perpendicular to the material rolling direction (see Figure 3-60).

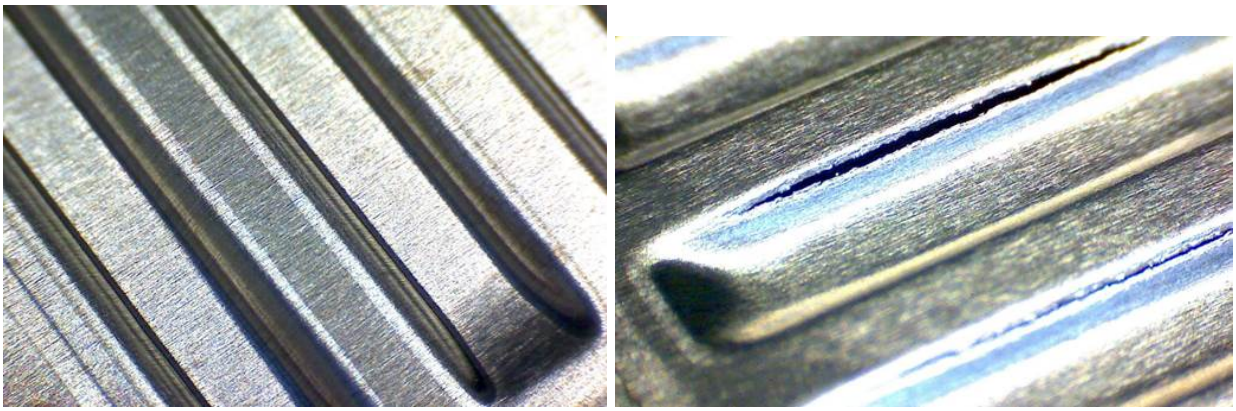

Figure 3-60 Comparison of Ribs Perpendicular (left) and Parallel (right) to Material Rolling

In an annular design the material is formed in all directions and so must be formable in all orientations relative to the material rolling direction. As is well established, the materials suitable to SOFC interconnect applications is restricted to a handful of alloys, primarily of the family of ferritic steels. Two candidate materials were tested this way and showed the same failure mode, despite being of different composition and from different suppliers.

Strategically it is desired to avoid tying the design to a particular alloy or supplier (and in any case the two lead materials were the only materials tested, and both failed). Therefore the preferred path forward became a further reduction in rib strains.

Additional trials were carried out to identify a forming limit that was workable, resulting in a suggestion of 14.6% rib strain or less as a reasonable design target. It was desired to operate somewhat away from the absolute strain limit to provide a robust process for material variations across and between melts. Figure 3-61 shows a trial form at 14.6% rib strain, oriented parallel to the material rolling direction and capturing some of the detail of the annular interconnect.

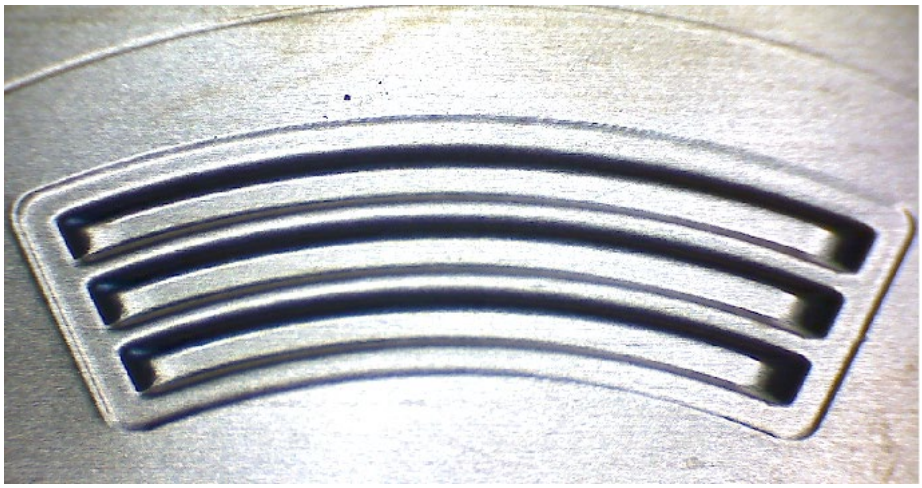

Figure 3-61 Forming Trial at 14.6% Rib Strain

The interconnect design was modified to fall within the 14.6% rib strain. The main solution path was to lower the rib height (other paths, such as lowering rib density were unacceptable for their impacts on performance). This resulted in higher pressure drop for a given flow was accommodated by the design. No change in the overall stack characteristics were identified other than a slight decrease in overall height.

Other manufacturing developments

In parallel with the interconnect development, other stack manufacturing processes progressed. Half-cell manufacturing trials (half-cell = anode support, anode functional layer, and electrolyte) were successfully carried out. The first two cells are shown in Figure 3-62, inserted into a DVD tray for a sense of scale. These cells are ~330 micron in thickness exceeding the program target of 450 micron.

Figure 3-62 Initial Fired Half-Cells in a DVD Tray

Designs were also completed on several of the manufacturing tools, including the robot end effector (Figure 3-63). The end effector incorporates both vacuum and magnetic pickup technologies in a lightweight structure. It is used by the robot within the stack assembly work cells to handle cells, interconnects, end plates, and contact materials for the purposes of automated inspection, automated leak testing, and automated stack builds.

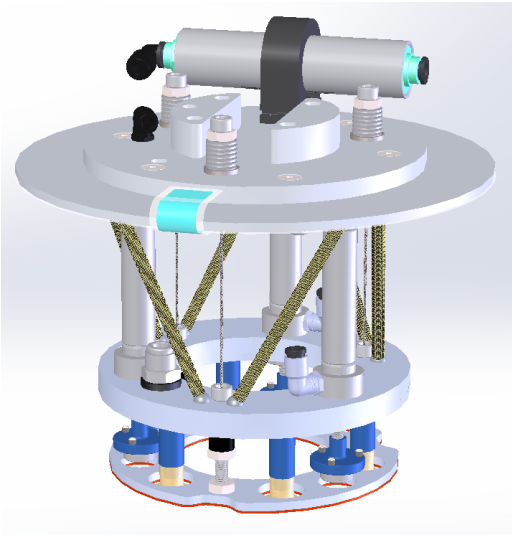

Figure 3-63 Robot End Effector

Leak testing fixtures for both cells and interconnects are designed (Figure 3-64) and were incorporated into the robot work cell, where it will be loaded by the robot, and tested with an automated leak tester (e.g.: http://zaxisinc.com/leak-testers/i-kit-leak-tester/).

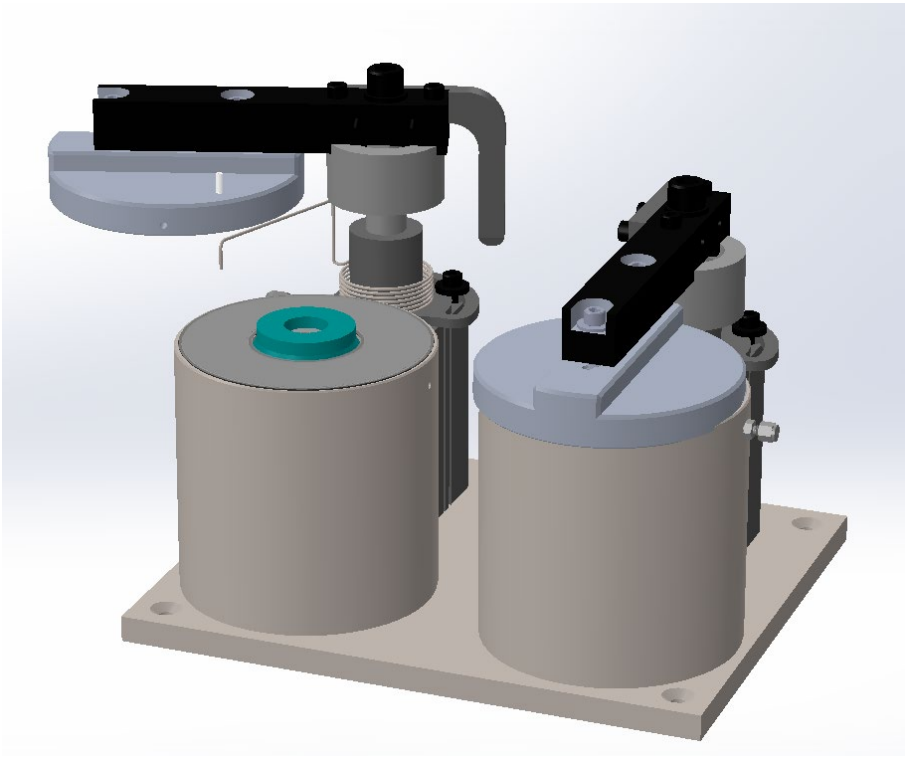

Figure 3-64 Automated Leak Test Fixture

The stack firing jig was designed (see Figure 3-65). It is a multi-function device that supports the stack during the build process as cells and interconnects are added in the automated work cell. It then serves as a transport jig to move that stack from the work cell to a firing furnace. Finally it supports and guides the stack through the glass-ceramic seal firing process, during which there is significant stack consolidation.

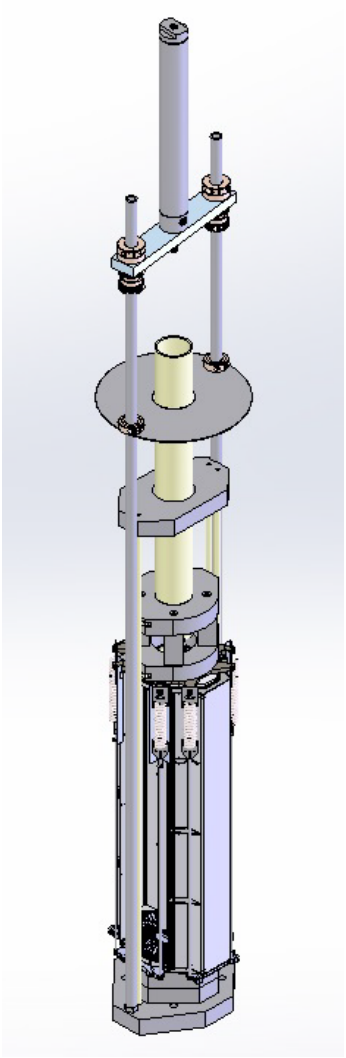

Figure 3-65 Stack Firing Jig

This equipment forms the basis for the automated manufacturing cell. The remaining equipment was designed and a fixture fabrication was completed. This design work included work on part feeders, integration of the firing jig into the automated work cell, spot welding tooling, and screen printing fixtures and screens.

During the forming trials discussed previously for the hydro-formed interconnects, strain rate limits were exceeded. Many years of effort goes into identifying suitable materials for the SOFC interconnect so there is a strong desire to match the process to known materials. Trials were carried out on three candidate materials and although there were slight differences in behavior, all were being pushed to the point of failure. Based on the forming trial results, an interconnect redesign was undertaken to reduce the forming strain.

A maximum local forming strain target of 14.6% was identified and a revised interconnect was developed that did not exceed that strain at any point. Geometry representative of the expected interconnect was developed and trialed on three candidate materials. Some typical results are shown in Figure 3-66.

Cross sections were taken to check form quality and to check for signs of excessive local thinning. Figure 3-67 shows a series of ribs that were checked. The upper material is 0.005” Sanergy HT, below that is 0.004” SS441, below that is 0.004” SS444. Some local thinning is evident at the rib root on all samples, but nothing beyond expectations or prior experience.

With these successful forming trials there was good confidence in the revised (low strain) interconnect design and it was released for production.

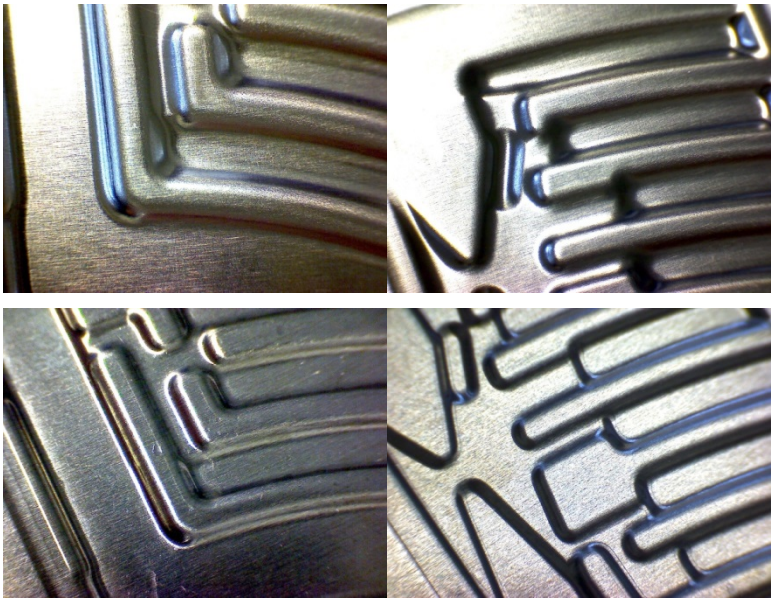

Figure 3-66 Forming Trials on SS441 (top row) and Sanergy HT (bottom row)

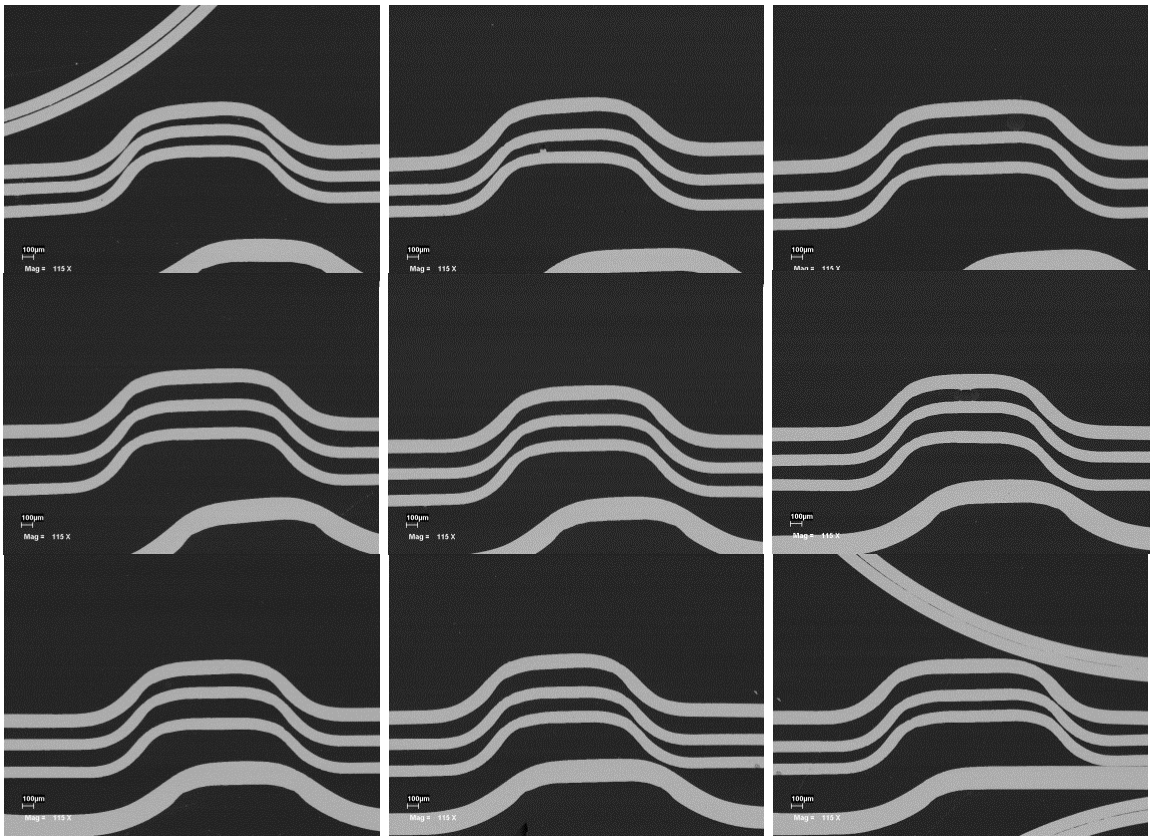

Figure 3-67 Cross Sections of Formed Samples

Dispensing

The glass seal formulations for stencil printing were handed off to the production team for trials and were completed with mixed results. One formulation has shown particular interest (#13), with good printing and green seal characteristics. Firing trials showed promise, but also some challenges. The fired seals formed well, but showed signs of inconsistency which is of concern for the stack design. Glass ceramic seals such as these have the benefit of no leak if properly formed, unlike compressive seals; but, if they do not form properly the leak local to the malformed area can be relatively large, compressive seals tend to be more forgiving in this aspect.

Given the observed weakness, two alternate paths were initiated. First, a dispensed glass seal process was deployed (Figure 3-68). This process has been used with good success by FuelCell Energy in the past. The hope was to replace it with a stencil printing process which, if fully developed, could offer faster processing, slightly better material usage, and better green state dimensional control. The fall-back dispending process was commissioned and successfully deployed for production of stack GT060248-0001. It is anticipated that dispensing will continue to be the prime seal application method until the stencil printing process is shown to yield sufficient consistency.

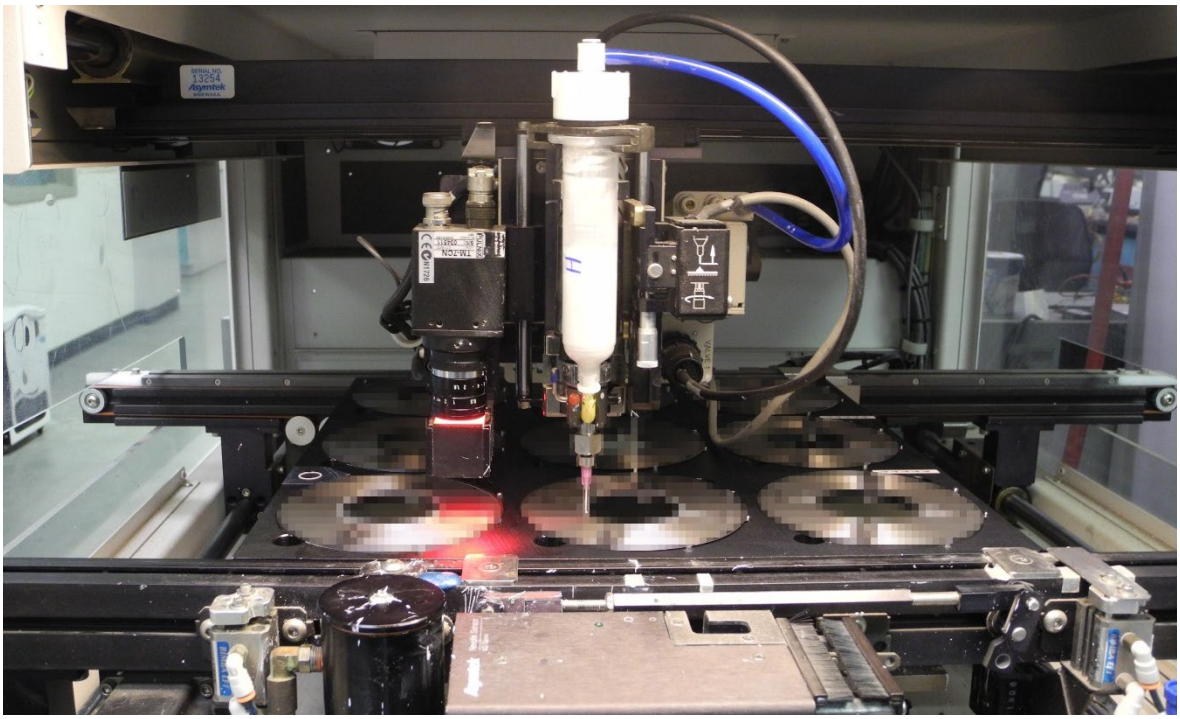

Figure 3-68 Automated vision guided seal dispensing

The second avenue pursued was to commission Heraeus to develop a stencil printing paste formulation for better characteristics. Heraeus has proven highly capable in past paste development efforts and provide the paste formulation used in the dispensing process.

A paste development effort was initiated with Heraeus, with a goal to develop a stencil printing paste for the glass seals with favorable characteristics. After development trials, Heraeus delivered two candidate materials designated 79 and 80, which were tested at FCE.

Both pastes had excellent printing characteristics, flowing well during the print process and releasing cleanly from the stencil. These characteristics are somewhat difficult to achieve given the high solids loading target and relatively high print height (0.016”) of the dried seal. Figure 3-69 shows an example seal stencil for the printing process. Bridges are required to hold the center of the stencil in place. One of the challenges with stencil printing of seals in this geometry is guaranteeing that the gaps from the printing process full close during seal processing.

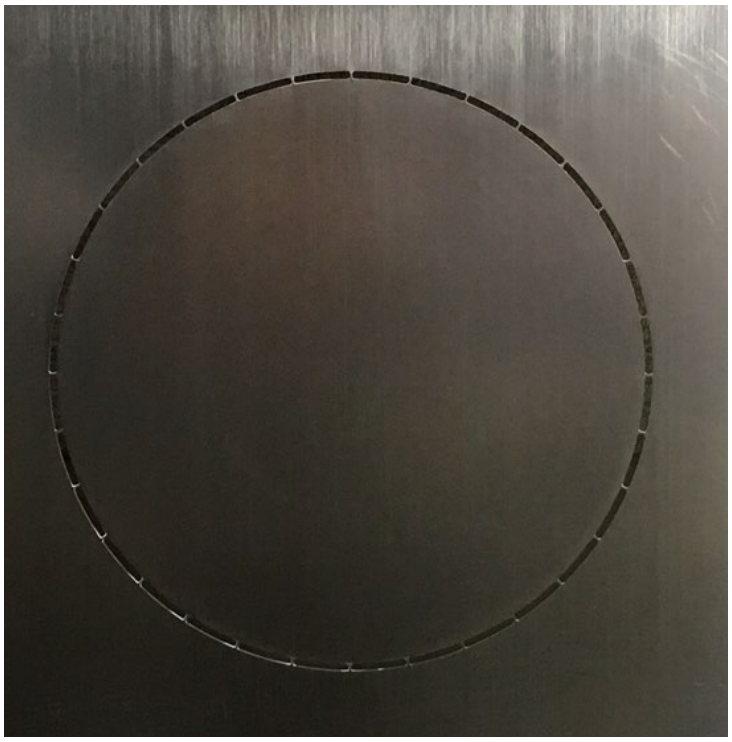

Figure 3-69 Seal stencil

Both pastes had weaknesses in practice and further iteration was pursued. Paste 79 showed a particular tendency to form uncontrolled peaks after the print/dry cycle (Figure 3-70), raising concerns that this would trigger cell breakage. In practice this proved to be the case as highlights (red ovals) in Figure 3-71. In the same figure the blue ovals show some examples of the appearance of the outer seal edge in the areas where the bridges in the stencil were located. From the outside, all the gaps appeared to close fully. The samples were then pulled apart so that the seals could be further examined. Figure 3-72 shows a typical view, all the original gaps have comfortably been closed.

In summary, Paste 79 printed well and closed the print gaps properly, but did not print smoothly enough and caused some local cell breakage. Any cell breakage is unacceptable. It was slightly weaker before firing than the dispensed seal.

Figure 3-70 Paste 79 after dispense and dry

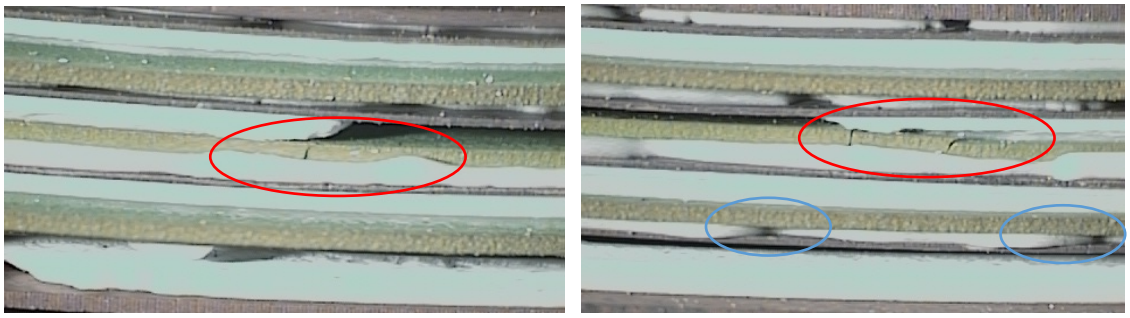

Figure 3-71 Paste 79 sample assemblies

Figure 3-72 Paste 79 after firing

Paste 80 showed a much better smoothness after print/dry than Paste 79, but still not nearly the uniformity expected (Figure 3-73). No cracked cells were found in the build trials (Figure 3-74), but this process needs to be consistent over hundreds of cells, so the absence of broken cells in a 6-cell trial is not sufficient to be considered a success. As with paste 79, the learning was that the post print/dry uniformity must be better. While there were no cracked cells, the samples gave the appearance of having gaps remaining in the seal ring (blue circles, same figure). This was confirmed when the samples were opened (Figure 3-75) where it can be seen that the gaps did not adequately fill.

In summary, Paste 80 printed well, was smoother than Paste 79 but not smooth enough. It did not break any cells on the small sample size, but it also did not properly close the gaps in the seal. It was significantly weaker before firing, leading to part handling difficulties.

Figure 3-73 Paste 80 after dispense and dry

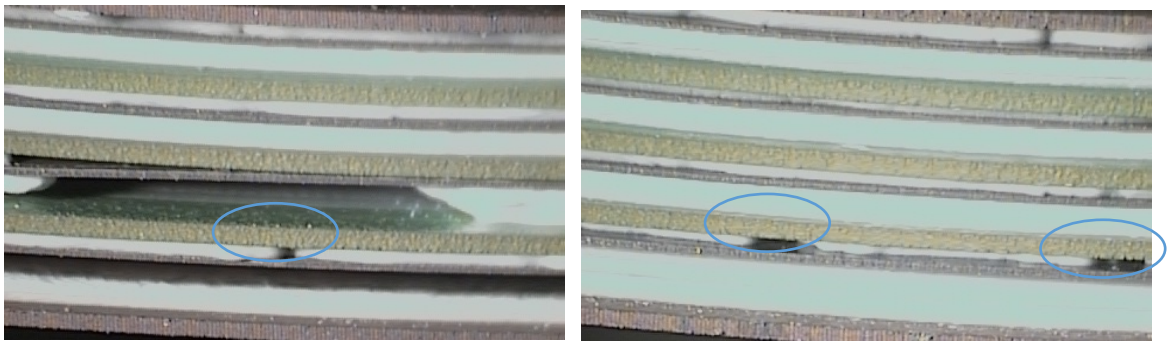

Figure 3-74 Paste 80 sample assemblies

Figure 3-75 Paste 80 after firing

Feedback has been given to Heraeus and they are running another paste iteration with a focus on having a smooth surface after drying (Heraeus confirmed that they saw similar peaks in their processing trials), and on improved handle-ability after drying but before firing. Revised samples will be evaluated as per the above.

Stenciling

Another area of development was stencil printed seals. Whereas SOFC seal application at FuelCell Energy has focussed on dispensed seals, this project hopes to deploy stencil printed seals. Stencil printing has advantages of speed (being by nature an area print process rather than a point print process), ease of automation (vision guided automated stencil printing equipment is highly developed and in use at FuelCell Energy), and is anticipated to yield improved quality (specifically in the form of accurate height control).

Figure 3-76 shows an example stencil printed seal. The damaged areas are due to handling and are not characteristic of the printing process itself. The intended behavior was that during the glass firing process, during which the glass is heated to a fluid state and compressed, that the 0.4 mm (0.015”) gaps between seal sections would be bridges. Note that these bridges are an inevitable consequence of using stencil printing technology. The bridging elements support the inner portion of the stencil.

The post-firing results were not as hoped, and the gaps in the seal did not reliably close. Closer inspection of the material reveals that although there was more than enough growth in the width direction, there was little or no growth in the direction that would bridge the gaps. In retrospect it may be obvious that the seal is preferentially growing perpendicular to the larger dimension of each seal body.

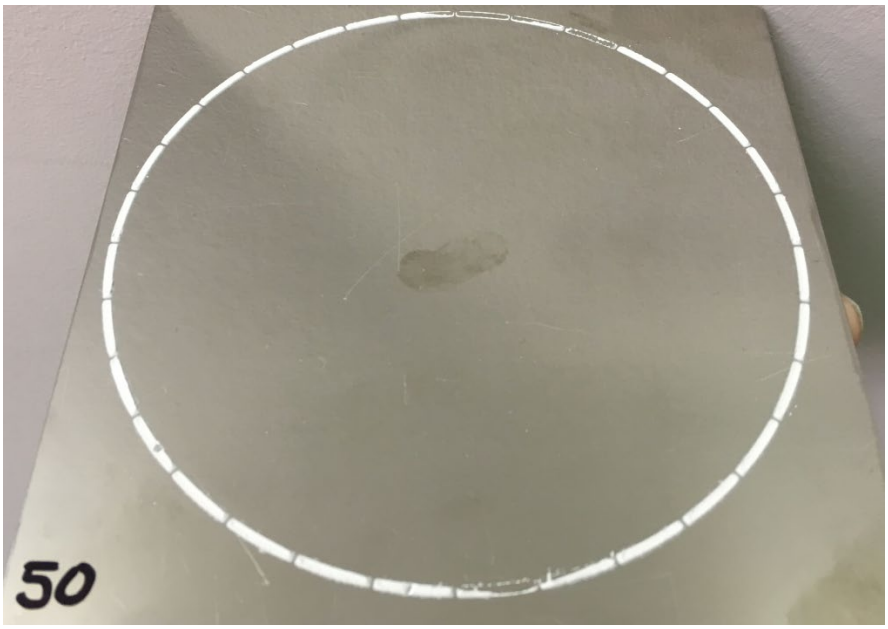

Figure 3-76 As dispensed seal (missing areas due to handling, not printing)

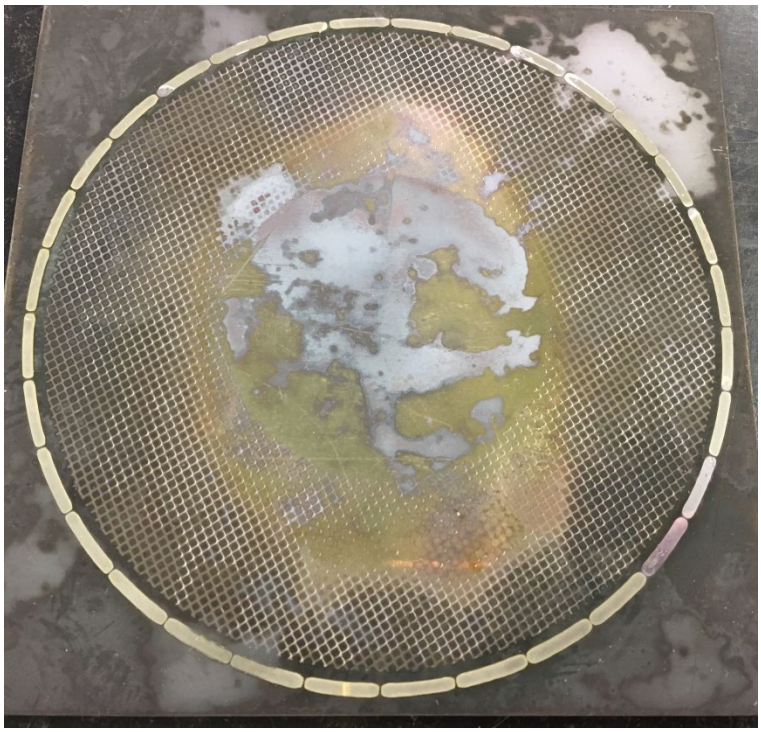

Figure 3-77 Dispensed seal after firing

Work continued to revise the stencil geometry to improve this behavior through two main strategies:

1. A stepped stencil will be used, such that the seal will be deposited as a complete ring to half its depth and will only have gaps in the upper half.
2. The stencil opening geometry was reworked to reduce the dominant direction effect or to re-orient the dominant direction to help close gaps.

Figure 3-78 shows the stencil geometry that was prepared for trial:

- Left: Re-orientation of bridges such that gaps are closer to aligned with the dominant opening dimension
- Center: Pairing of bridges such that the spacing between pairs is small so that seal growth during firing will tend to occur in the annular direction
- Right: Largely similar to the first trials except the bridging elements only extend to half the stencil depth (which is true of the other two geometries as well)

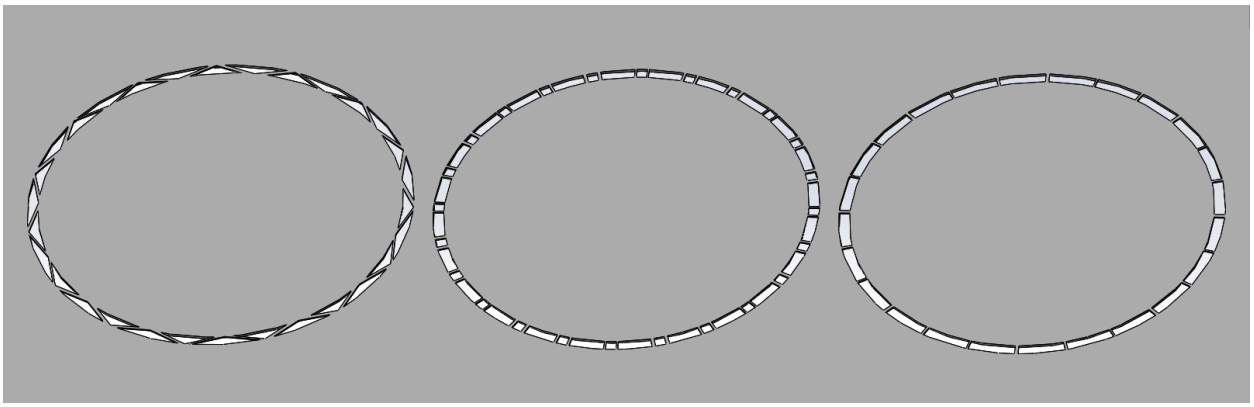

Figure 3-78 Revised stencil geometries for seal trials

The undercut stencil was received and trialed, and while it performed as desired, it revealed further weaknesses in the process, specifically with the formulation of the organic printing vehicle of the seal. Initial variations in the organic vehicle formulation struggled to balance ease of printing with stability during drying. Figure 3-79 shows a typical example of a formulation modified for ease of printing, which did not have sufficient stability during drying and spread significantly instead of maintaining shape. This led to an effort to reformulate the organics for characteristics more suited to stencil printing, with some success.

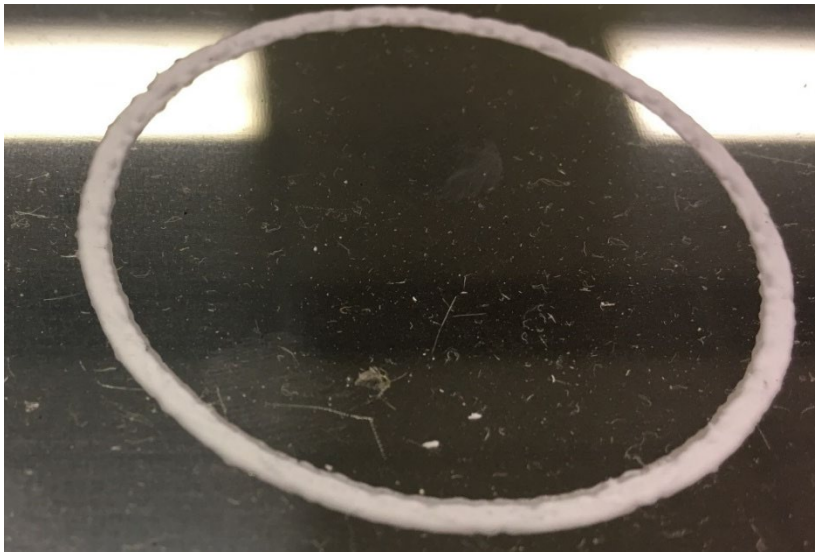

Figure 3-79 Example of slumping seal (after drying)

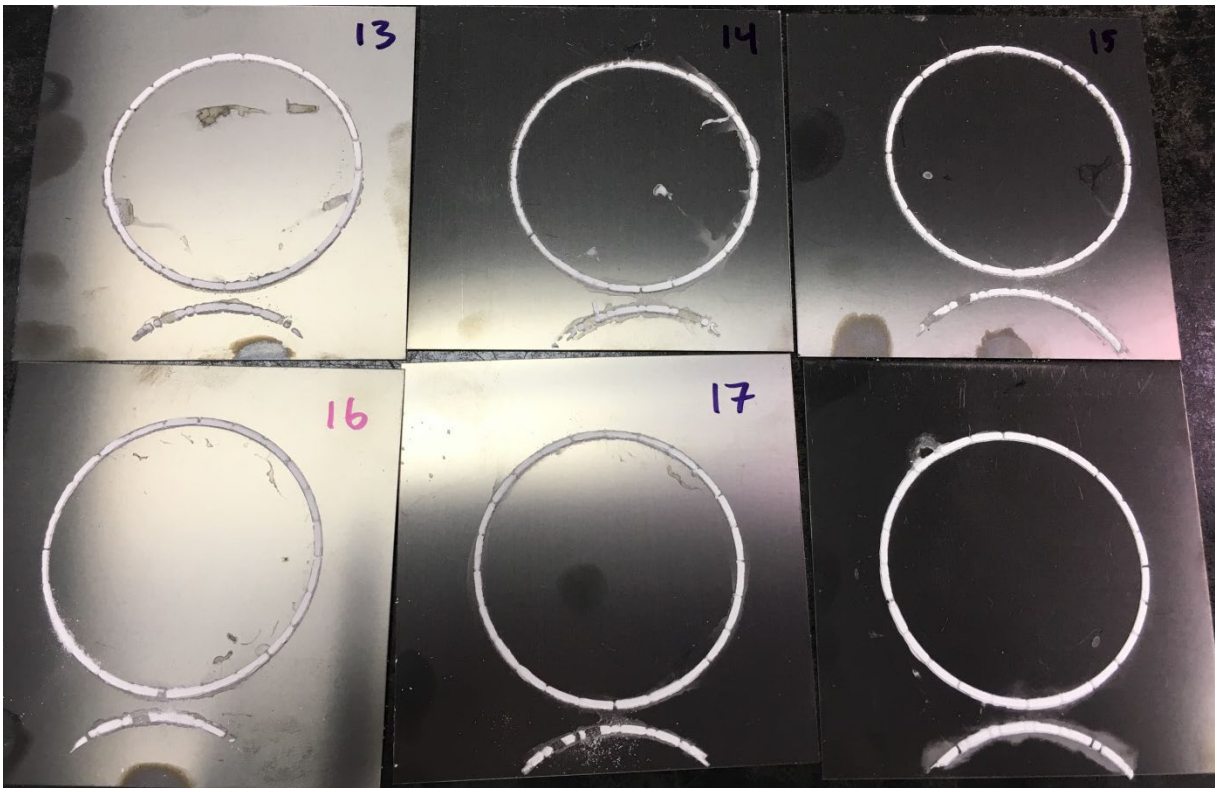

Figure 3-80 Seal formulation trials

Figure 3-81 Example of good seal height control (after drying)

Figure 3-80 shows some of the seal formulation trials, after drying. The six formulations shown were all relatively easy to print, i.e., not overly sticky nor runny, filled the stencil channels, and released easily after printing, yet held their shape on drying (the samples are shown in their dried state). Figure 3-81 shows a close-up of one of these formations after drying. Although there is room for further improvement, these samples are showing clean release and excellent retention of printed height after drying. This latter characteristic is of great benefit as it allows the stencil height to control the dried seal height directly. Control of the dried seal height is critical to successful formation of the finished seals in the stack without gaps or overflow. On a full height stack (350 cells), there are 702 individual printed glass-ceramic seals, so consistency and reliability is of great importance.

The seal related efforts were then focussed primarily on development of alternate seal formulations for improved printing characteristics. At this point, the seals were hand printed for reasons of ease of iteration. The most promising formulations (#13, #15, and #17) were released to the production team for trials on production equipment. These trials were completed during Q3, 2017, however; design development continues.

Internal Manufacturing Equipment

An automated work cell was refitted for the CSA stack production, and for some of the sub-assembly and quality control steps. Figure 3-82 shows the work cell that formed the basis of this program. All the tooling was replaced with tooling adapted to the CSA design. Figure 3-83 shows the work cell layout.

Figure 3-82 Automated Stack Build Work Cell (Original)

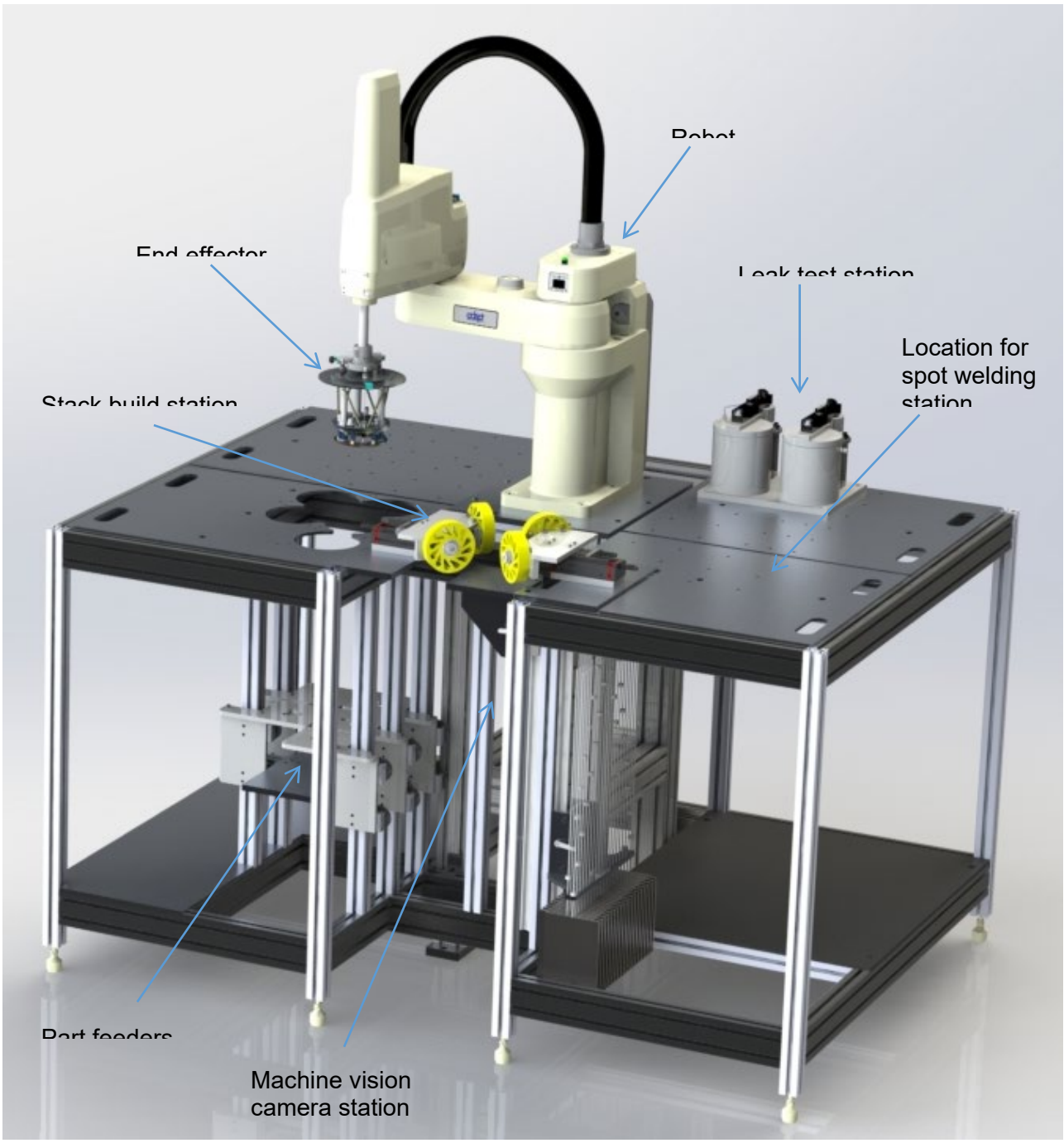

Figure 3-83 Planned Work Cell Layout

Much of the tooling was designed and hardware ordered and received. The cell and interconnect leak testing tooling was completed with hardware in-house and assembled as shown (Figure 3-84). The end-effector components and stack firing jig were ordered and received. The work cell was operational as of the end of Q1 2017.

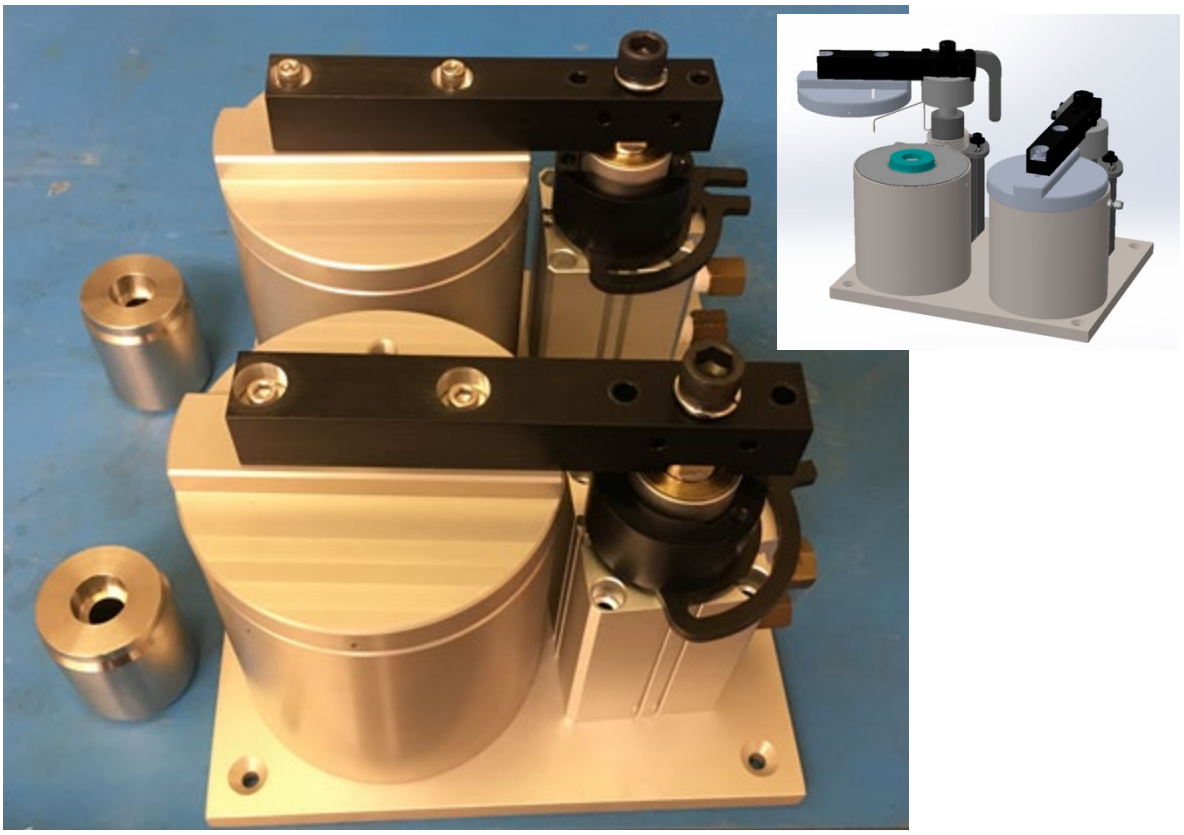

Figure 3-84 Cell and Interconnect Leak Test Tooling in Progress

The main focus of the stack manufacturing process development was in the robot work cell. This work cell, as described in previous reports, fulfils several key functions including:

- Dimensional QC
- Spot welding
- Leak testing of components
- Stack builds

This is both a validation of the approaches to automating these steps, and a way to achieve higher tolerances, at higher speeds, than equivalent manual processes are capable of achieving. At higher volumes the processes would be individually deployed to specialized work cells, but for current volumes all processes can be incorporated into a single generic work cell.

A key tool for automated handling of the parts is the robot end effector. It must be capable of picking up cells (non-magnetic), interconnects, electrical contact media (highly porous) as well as end plates. It is ideally light (for rapid movement), stiff (to prevent vibration or other uncontrolled displacement), and yielding (in case of collision with other workspace elements, especially during the development phase).

Figure 3-85 shows the design that was developed. It is a tensegrity structure, using six carbon fiber rods as the compressive members and three spring tensioned cables as the tensile members. This provides a stiff yet lightweight structure (sub 1 kg) with the functionality to provide magnetic or vacuum based-part pickup. A degree of collision protection is provided by the spring tensioned cables which can release the compression members in the event of impacts with solid objects in all directions except straight down. The table height is set such that the end effector cannot impact the table top at the limit of robot travel, reducing the likelihood of collisions in the downward direction.

Figure 3-85 Robot end effector

A subtle but important feature of the end effector design is that it is completely hidden from an upwards facing camera when a cell or interconnect is in its grasp. Figure 3-86 shows the view of the upwards facing camera when the end effector is holding a cell at the bottom end of the tolerance limit, with the cell purposely off center. Even under these limit conditions, the structure of the end effector is completely masked. This enables optical dimensional measurements and related measures (e.g.: Centroid of part) to be determined without interference from the end effector structure. Figure 3-87 shows the CAD model of the planned robot work cell layout.

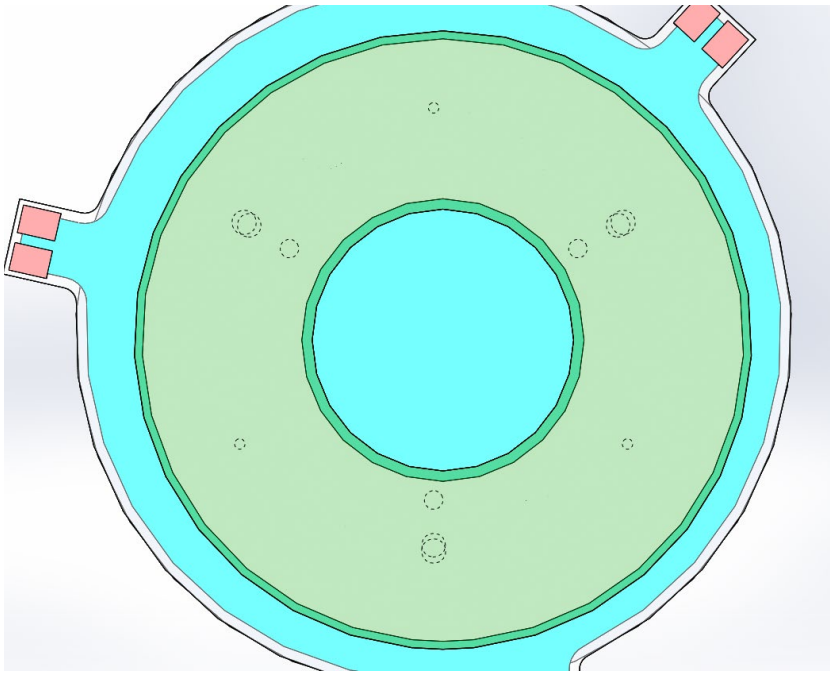

Figure 3-86 Camera view of end effector holding a cell

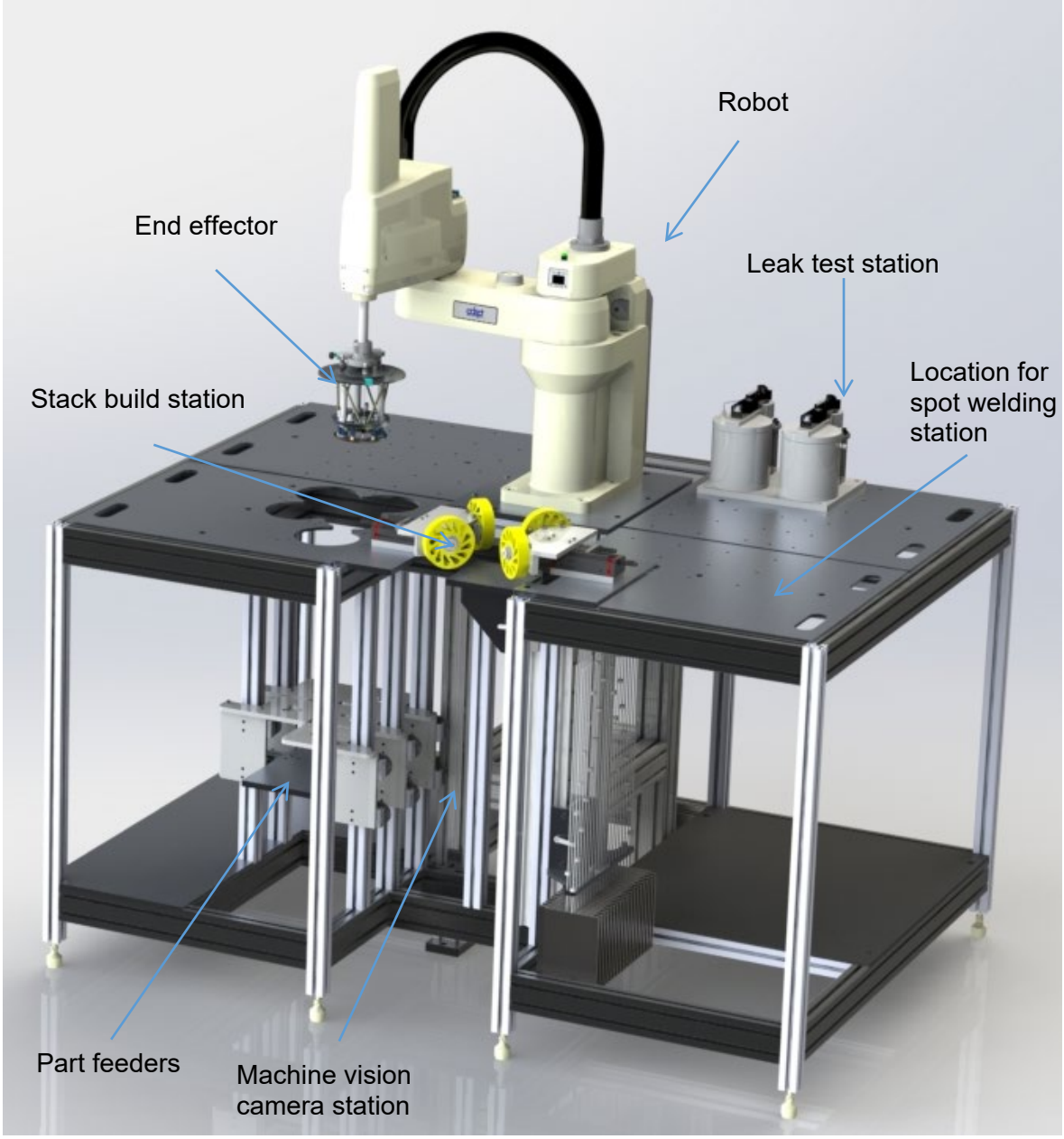

Figure 3-87 Robot work cell CAD layout

Figure 3-88 shows the largely completed automated work cell. To the left and right of the work cell are the controlling user interface and the spot welding control unit respectively. The left third of the work cell is dedicated to part feeding and receiving, with five independent bi-directional part feeding channels, each capable of handling upwards of 500 parts. The central area of the work cell contains the upwards facing camera used for part measurement, QC and part positioning, as well as the counterweighted stack build platform. In the right third will be the spot welding station (in place) and the cell and interconnect leak testing station (not yet installed).

Figure 3-89 shows a close-up of the bi-directional part feeders. Each can operate in a feed mode in which the top part is automatically advanced to the top position each time a part is removed until there are no parts left, or in receive mode in which the top part is automatically lowered to make room for a new part until the feeder is full. An example usage scenario would

be a cell QC step, where one feeder is feeding cells into a QC process, and two feeders are receiving pass and fail cells respectively.

The right of Figure 3-89 shows the action of a custom magnetic part fanner. This has the effect of separating the top metallic component off a stack and spacing it away from the rest of the parts. This makes for an easier and more reliable pickup by the robot.

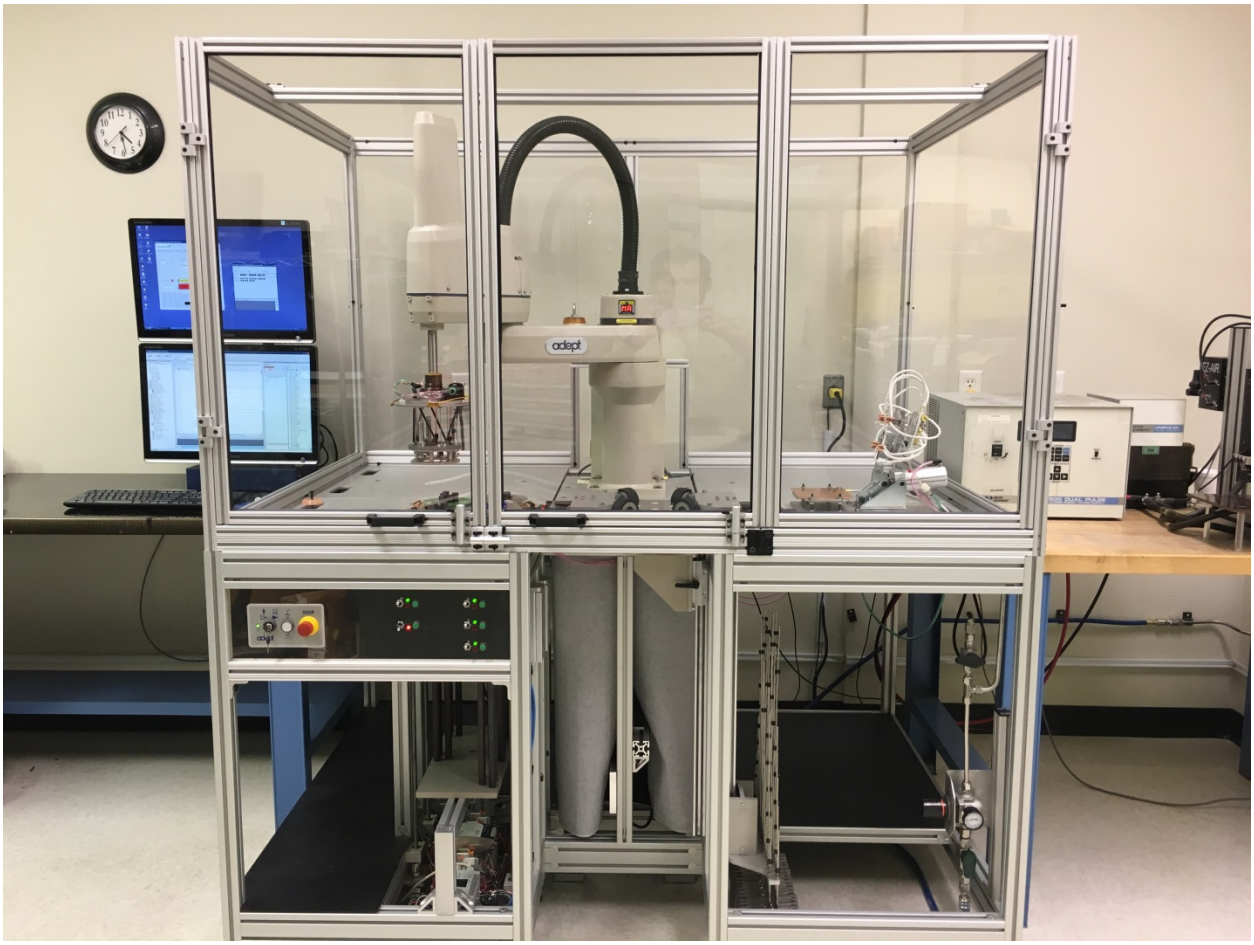

Figure 3-88 Automated work cell

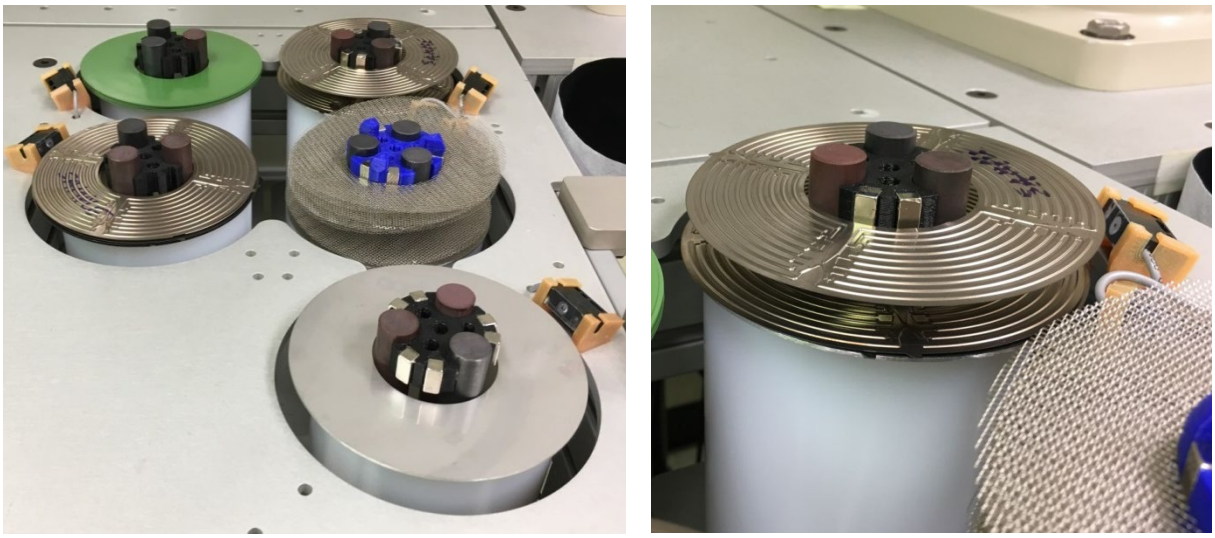

Figure 3-89 Part feeders and part fanners

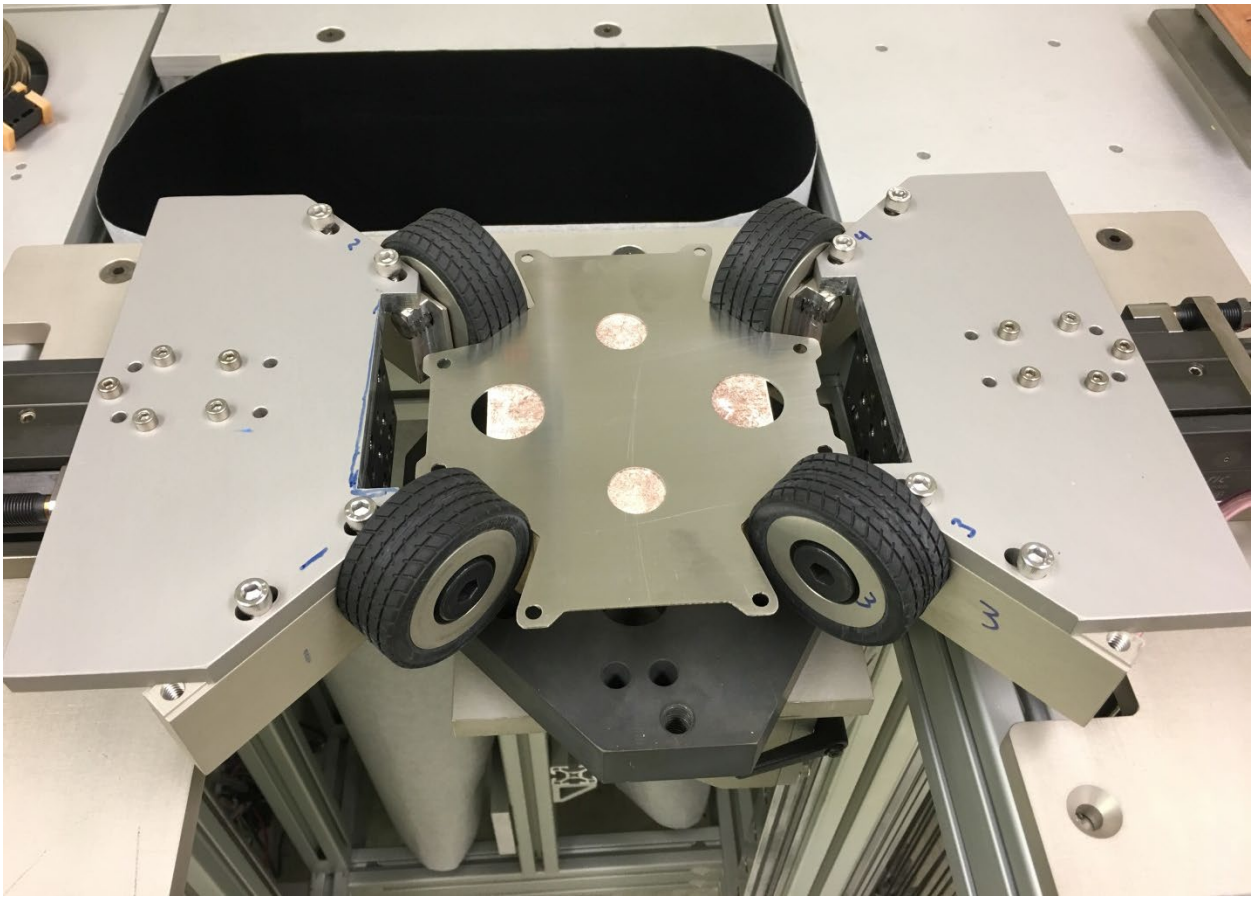

Figure 3-90 Stack build platform and camera tunnel

Figure 3-90 shows a top down view of the center section of the work cell. In the foreground is the stack build stage onto which the stack will be built. It the background is the camera tunnel, isolated from ambient light to provide more even illumination for the machine vision system.

Figure 3-91 shows the right side of the work cell with the multi-point spot welding station in the foreground. A leak testing station will be located towards the back of this work area. The multi-point welding station is a new development that allows up to 12 spot welds to be generated, individually, in a single setup. This provides significant process time savings relative to a typical single point spot welding process. Without optimization the setup has demonstrated completion of 12 welds in 4.8 seconds (not including load and unload time)

Figure 3-92 shows the station closed and executing. The robot end effector is visible in the background, waiting for the weld cycle completion before retrieving the finished part.

A code framework for the work cell has been developed including the UI and fundamental software tools (interconnect position and orientation detection, metal mesh center finding, cell, interconnect, and mesh pick and place, spot weld cycle execution, etc). The more complex processes (stack build, cell QC) were developed from these building blocks.

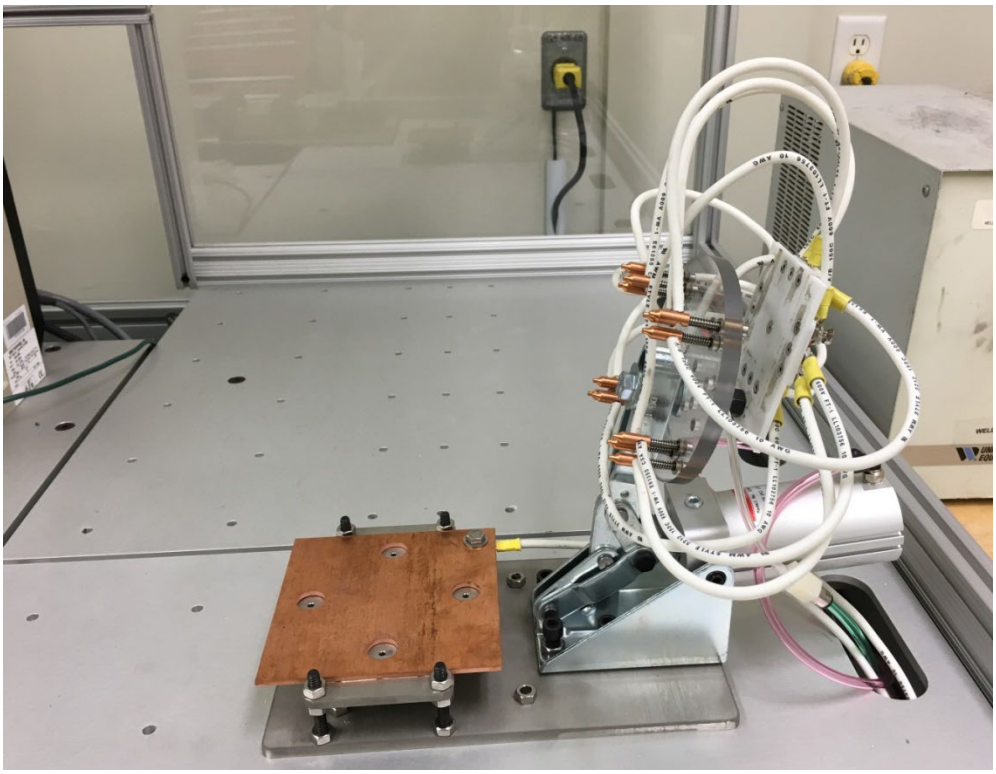

Figure 3-91 Multi-point spot welding station (open)

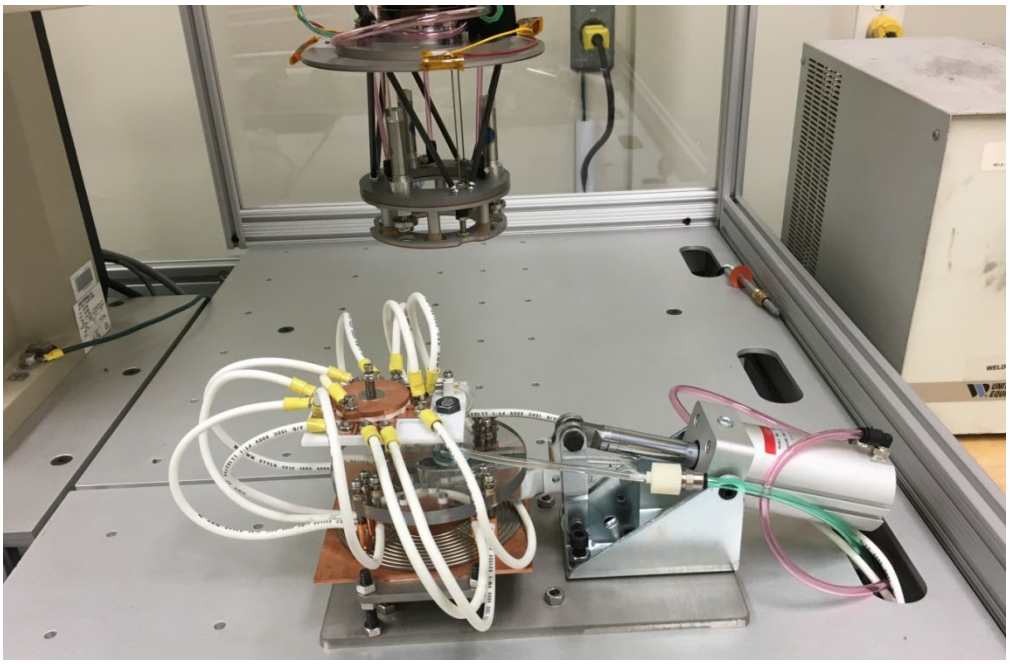

Figure 3-92 Multi-point spot welding station (closed, with part)

As previously reported, the work cell serves as a test and demonstration platform to prove different manufacturing steps, and is also crucial to accurate building of the final stack. It performs five separate process steps as follows:

- Cell measuring (id, od, and thickness)
- Cell leak checking
- Interconnect spot welding
- Interconnect leak checking
- Stack building

These are process steps that have previously been done manually and for which time studies have shown to be the larger labour cost drivers (for other stack platforms). The CSA stack development focussed immediately on automating these key steps, and other than a few initial manual proof of concept trials, all part processing has occurred through the automated work cell. In addition to validating these labor saving processes, the automated stack build has also proven to be more adaptable to different design configurations and more accurate than the best of prior manual processes.

The main progress in the automated work cell was the addition of error checking and recovery procedures. In particular, all processes now benefit from feed error recovery. If any component miss-feeds, the robot will enter a recovery process up to five times, trying to reset and re-feed the part. If it fails too many times the process will stop and display an alarm message to the operator. As we transition towards unattended operation with larger part quantities this sort of error checking is very useful, especially as final tuning of the feeders occurs, for example. The work cell is not fully error proofed, but the additional code has made some operations more robust.

Gauge R&R studies on the original leak test tooling revealed a lack of repeatability. A wholesale re-design was carried out and installed as shown in Figure 3-93. Gauge R&R review of the new tooling is completed. Marking technology and a marking ink that survives cell processing in a readable form was found through trials with multiple vendors. A cell marking station was installed in the robot work cell (Figure 3-94), enabling cells to be directly serialized rather than relying on travellers with each cell. This has improved traceability going forward.

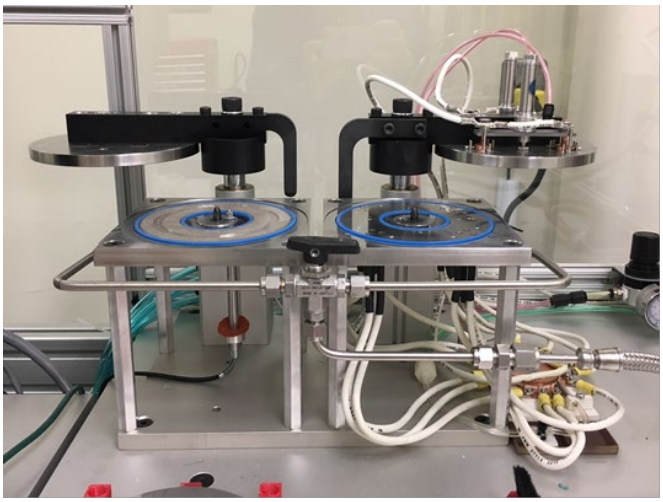

Figure 3-93 Revised leak test fixtures

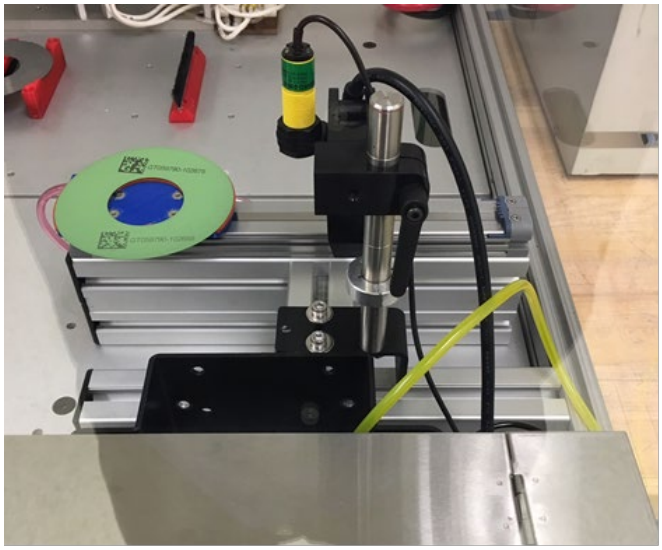

Figure 3-94 New cell ID marking station

A fairly significant change was implemented in the cell manufacturing area. Up to this point the stacks have been using the so-called HiPoD cell technology. A relatively new development of a cell showing vastly improved electrolysis performance and a slight improvement in fuel cell operation as compared to the baseline cells that have been used in prior FuelCell Energy SOFC stacks. While the HiPoD cells have been performing well in general testing, and were seen as the next baseline cell technology, there have been manufacturing issues in the attempts to scale production to supply the CSA stack. The root of these problems, which manifested as difficulties in controlling size, flatness, and to some extent the leak rate, have been traced to instabilities in the precursor slurry from which the tape-cast anode support is produced.

CSA cell production has been redirected to the baseline TSC3 materials which have proven stability. Initial results, including a 45-cell stack build showed promise. Cell dimensions have been more stable, cell flatness and yield through firing has been better, and cell leak rate is significantly lowered.

The combination of improved cell dimensional control and decreased cell leak rate was illustrated in a 45-cell stack GT060248-0010 which demonstrated a leak rate of 5.4 sccm He at 0.5 psid (cold) after cell reduction, as compared to a previous best of 81 sccm He at 0.5 psid (cold) in previous best with stack GT060248-0009, and prior stacks on the order of 300 sccm and higher under the same conditions.

The addition of a cell marking station was discussed above. This station within the robot work cell allows the printing of a temperature tolerant id onto the cell with the intent to have this as part of the QC process to provide improved cell traceability. Before commissioning the device, which involves loading inks into the supply system and print head, testing was carried out to evaluate the possible impact of the commercial ink on the cell performance and lifetime. As an exaggerated test, a single cell was coated with ink such that 100% of the cell surface was coated, applied by brushing in a thicker layer than would occur during printing. The resulting cell was under test for 2,335 hours and showed no signs of low performance or abnormal degradation (Figure 3-95).

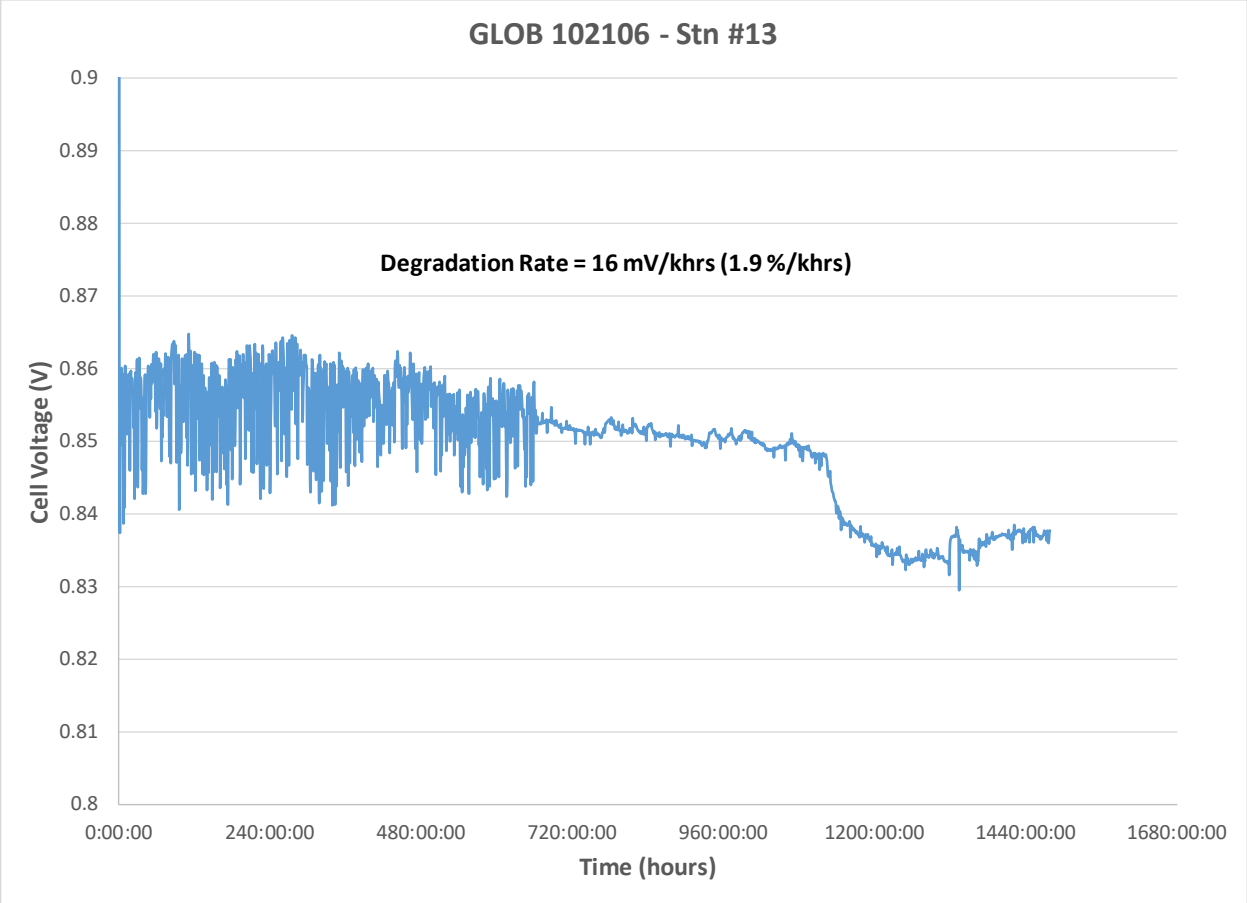

Figure 3-95 Glob102106 Single Cell with 100% ink coverage on Anode Support

The initial voltage noise was eventually traced to an exhaust line which had allowed water buildup and was resulting in pressure spikes at the cell impacting performance. Once that was fixed, the voltage trace stabilized until 1,123 hours elapsed. At that time a heat tape failed on, overheating the humidifier and increasing the on-cell humidity. This was detected and corrected at hour 1,250, at which point the cell voltage started to recover. Prior to the heat tape failure the degradation rate was approximately 7.8 mV/khr (0.9% /khr).

Figure 3-96 shows a cell sample printed by the vendor showing two examples of text printing and two examples of 14x14 DataMatrix codes. At that size a single DataMatrix combined with the single alphanumeric identifier amount to coverage of approximately 2.5% of the cell surface. At 100% cell surface coverage the trial cell with a voltage degradation of 7.8 mV/khr is higher than normal (normal expectation is something on the order of 2 mV/khr at these conditions), but not so high as to indicate clear materials issues. There could be ink related degradation, or this could be a slightly weaker cell than average, coupled with some off-design conditions for the first 640 hours that manifest as higher degradation. SEM/EDX analysis of the proprietary ink show no materials of concern.

While the degradation results do not provide absolute clarity, they do show that any effect is small enough that the marking does not impact short to mid-term operation. This gave confidence to start marking a subset of cells, with much lower ink coverage, and to trace them through subsequent stack builds to assess comparative performance and degradation of marked and unmarked cells in the same stack. Testing confirms there is no significant impact of cell marking on stack performance.

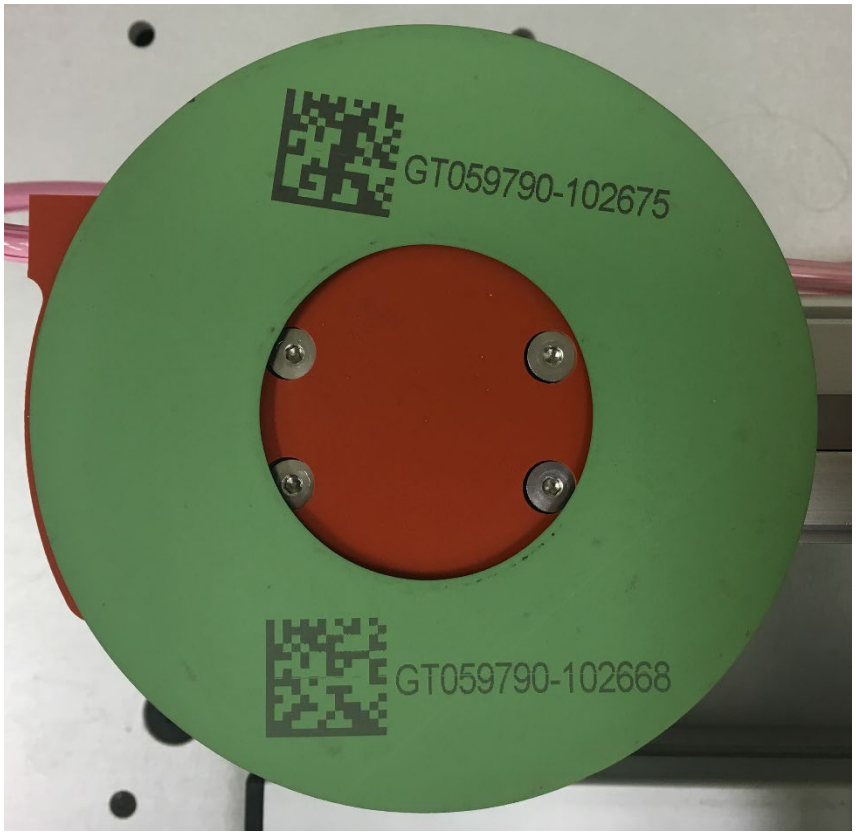

Figure 3-96 Cell marking sample (Printed by vendor)

There was a strong focus on developing the manufacturing strategies and equipment to support the stack build and to demonstrate the path to significant cost reductions at high volumes. From the initial braze trials to the various work cell stations, significant progress has been made.

4.0 **Task 4.0 – Technology Stacks Validation Tests**

4.1 Task 4.1 Technology Stacks Fabrication and Testing

Objective:

- Test stacks in support of design and cost reduction activities

Approach:

Fuel cell stack fabrication, assembly and testing was conducted to validate the new stack architecture and to refine and optimize design parameters and electrochemical and thermal performance. The activities in this task included fabrication and testing of a number of technology stacks of various sizes to prove the stack design and to study and confirm the effect of stack components and manufacturing process. Technology stacks included 1) short stacks, 2) half height stacks and 3) full height stacks. The lessons learned were passed on to Subtask 4.2 to demonstrate stable stack operation and confidence for a successful 5 kW deliverable test.

Results & Discussion:

The general stack design approach anticipated in this program is derived from a pre-existing stack design originally developed for mobile applications but showing promise as a robust and low-cost stack design. Initial test conditions have focused on fuel compositions other than coal based or natural gas-fired system compositions. In order to explore and demonstrate SECA-like conditions on this low material content stack, stack GT059072-0012 was built and tested.

The stack (Figure 4-1) has the following characteristics:

- 225 cells – 300 micron (nominal) cell thickness
- Thin interconnect
- 22.3 cm^2 active area per cell
- Glass-ceramic seals between fuel and oxidant
- Fully integrated compression system
- De-integrated manifold

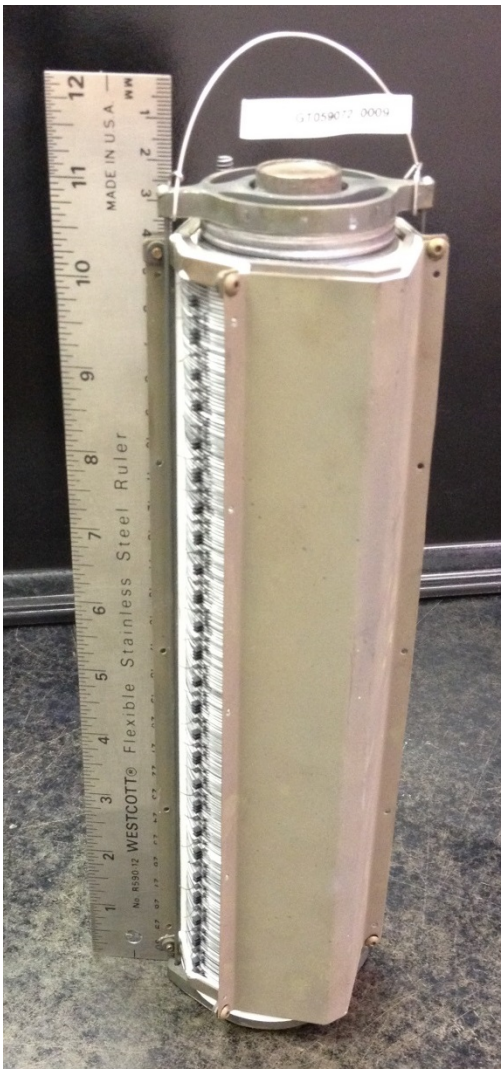

Figure 4-1 Full Height HPD Stack

Stack GT059072-0012 has completed TC0 (before thermal cycle) and TC1 (after thermal cycle) characterization periods. TC0 consisted of fuel utilization test at 5 Amps (0.224 A/cm^2) and 6.5 amps (0.291 A/cm^2) with fuel composition of 55% H_2 and 45% N_2 (mole% dry basis) with 3% humidity. Figure 4-2 shows the test results.

The stack was able to run at 75% fuel utilization. Testing at 80% fuel utilization was attempted. However, cell voltages were decreasing and the attempt was aborted. Air utilization test was also conducted showing no issues up to 65%.

This is very similar to the test protocol that is carried out on the LAS stacks delivered for the past and present DOE programs, except that the LAS stacks do not attempt fuel utilization beyond 75% nor air utilization beyond 13% during conditioning.

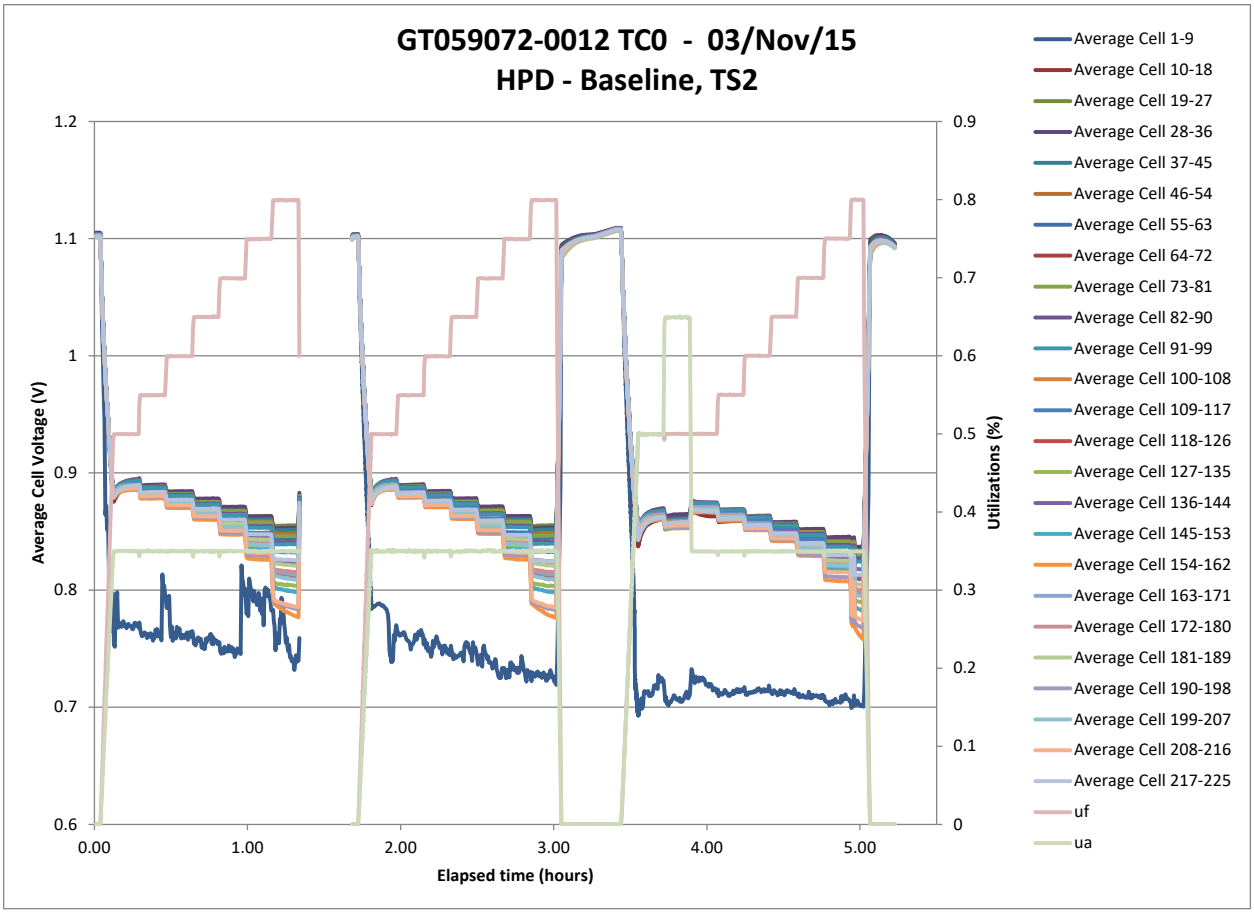

Figure 4-2 Stack GT059072-0012 Performance During TC0 Characterization Period

Due to the dense spacing of the cells (1.1 mm/cell or 22 cells/inch) in the stack, voltage leads are attached only to every 9th cell, resulting in 25 cells groups. Cell group 1 (cells 1-9) is at the bottom of the stack and is significantly lower than any other cell group. This is a new problem not seen on prior stacks of this design.

Upon review, a substitution of material in the brazed base plate has impacted the electrical contact. EDX has shown that the current plate was manufactured with weaker alloy than the one in the design specifications. Visual inspection of an end plate from the same braze run revealed some surface distortions (sagging) and this is believed to the source of the low cell voltage. Prior to TC1 characterization, additional voltage leads were added to cell group 1. They allow further problem isolation with a hand-held meter. With additional measurements across individual cell layers, the performance loss was found to occur entirely in the first cell layer (unit cell directly on end plate).

Although this low performing cell is a concern, as it is experiencing significant thermal stress, it did not appear to degrade over the TC0 and TC1 periods. The decision was made to continue testing with risk.

A brief TC0 hold was conducted at 68% fuel utilization using the 'VPS gas replacement' fuel gas composition[3], consisting of 6.4% methane, 44.2% hydrogen, 23.4% nitrogen and 26% steam. Figure 4-3 shows the test results. This gas composition corresponds to 37% in-stack reforming level. Due to test stand flow and preheater limits, the test was not run at the traditional (LAS stacks) 15% air utilization, but was run at 40% and 65% air utilizations instead.

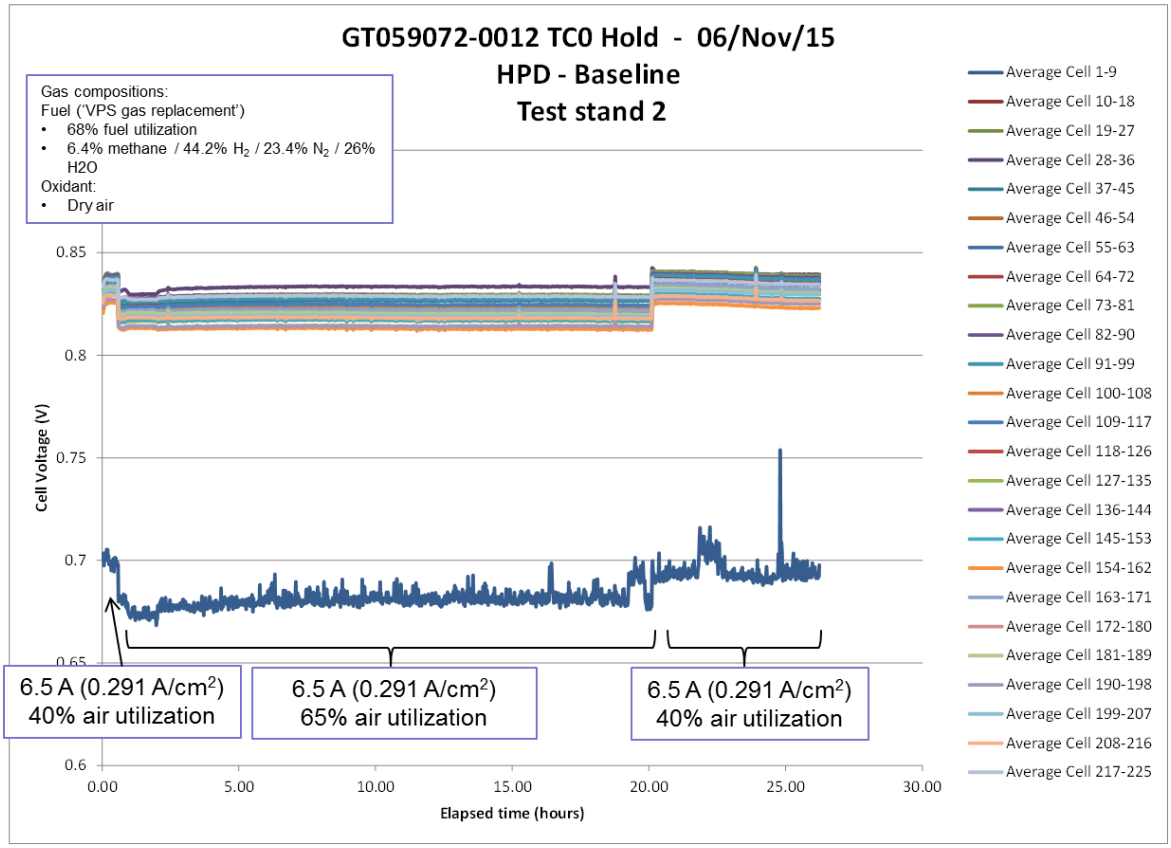

Figure 4-3 Stack GT059072-0012 TC0 Hold

The stack was leak tested prior to TC1 period. A helium leak rate of 31.7 sccm @ 0.5 psi was found which is consistent with prior stacks of this type.

These stacks incorporate glass ceramic seals and have significantly lower leak rate than the LAS stacks, even when normalized per unit active area. This is the reason to leak test using helium. Comparison to LAS stack requires conversion to equivalent air leak as well as a normalizing per unit active area. Prior empirical testing has suggested that helium leak testing of these stacks will show a leak approximately 2.3x higher than that when leak tested on air (when reported as sccm). A leak comparison is shown in Table 4-21. The stack has a leak rate (cold) that is about 2.5% of the larger stack on a per active area basis.

[3] This composition is used in VPS testing as a surrogate for natural gas fired system conditions (e.g. 50 kW SECA demonstration system). It is used here because it is the same condition under which conventional LAS stacks are evaluated during development.

Table 4-1 Leak rate comparison

Stack	Helium leak		Air leak	Stack active area	Leak per unit active area
GT059072-0012	31.7 sccm		13.8 sccm (est)	0.5 m^2	28 sccm/m^2
Best LAS stack delivered to 50 kW test	N/A		7.4 slpm (total fuel leak)	6.6 m^2	1121 sccm/m^2

Utilization testing was repeated during TC1 period (Figure 4-4) with 80% fuel utilization excluded. Performance was similar to TC0 period, a verification that no significant damage occurred during the thermal cycle. There was concern that the bottom cell would not survive thermal cycle, but its behavior is also consistent with the TC0 results.

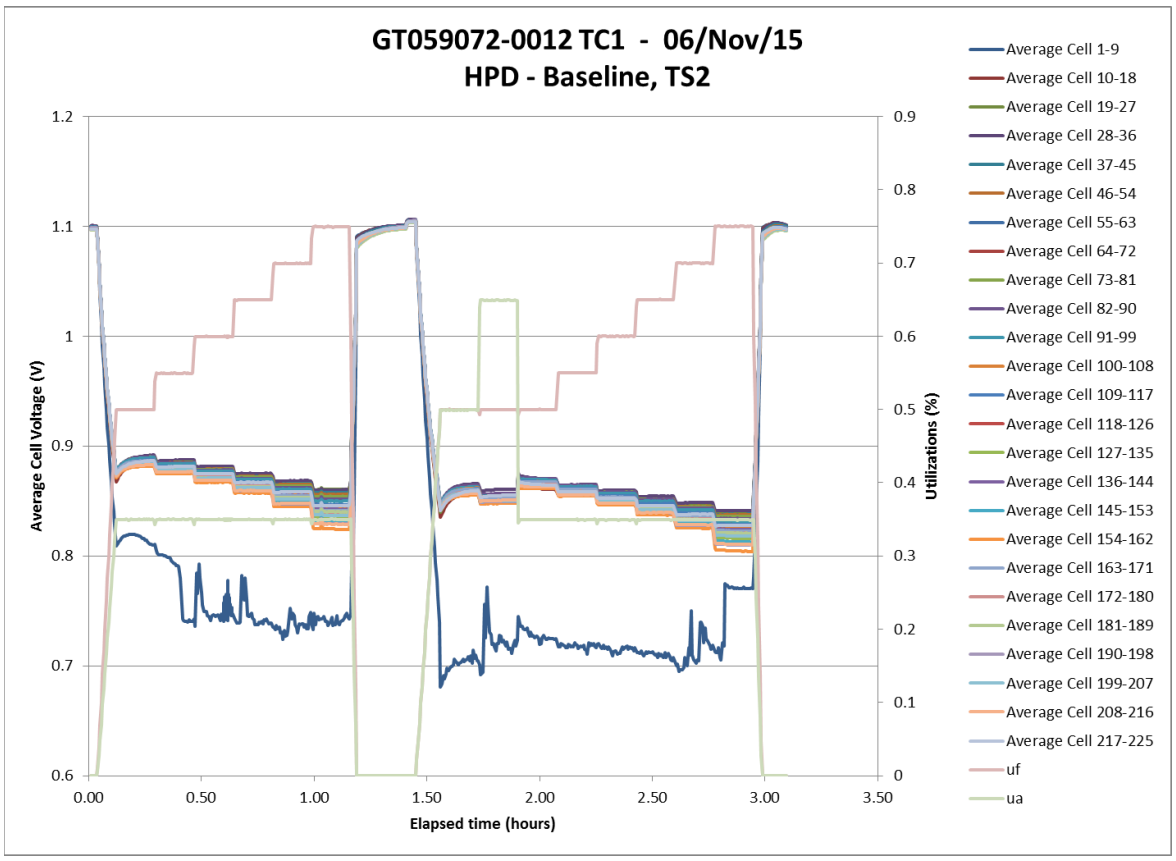

Figure 4-4 Stack GT059072-0012 Fuel Utilization Testing

The TC1 hold (Figure 4-5) is ongoing with an accumulated run time of over 1500 hours using the same flows and current density as used on the large area stacks, with the exception of air utilization which is set at 40% instead of the 15% (as mentioned above). The current density is also matched to large area stacks at 0.291 A/cm^2. Under these conditions the stack is generating 1.2 kW while weighing 2.2 kg, indicating the power to weight ratio of 545 W/kg.

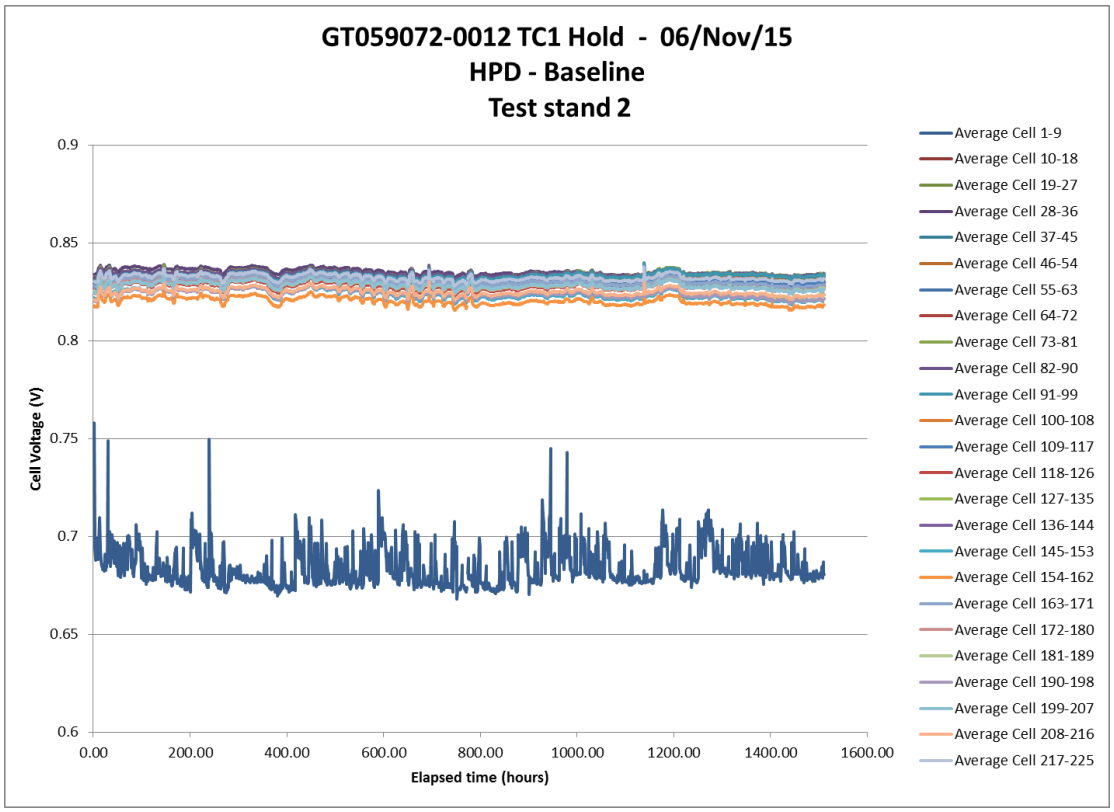

Figure 4-5 Stack GT059072-0012 TC1 hold at SECA Conditions

Cell group 1 voltage appears to be low (and with measurement noise) and is degrading with time. With the exception of the lower air flow, stack GT059072-0012 was tested at conditions identical to those for the larger area stacks, with the purpose of providing a direct comparison of performance and degradation.

The average degradation at this point was 1.8 mV/1,000 hr or 0.21%/1000 hr. Figure 4-6 shows the degradation rates for individual cell groups. The degradation trend was relatively even across the stack, with no outliers or indications of problem areas within the stack. The average cell voltage is lower than a typical LAS stack by about 40 mV/cell at these conditions. Part of the performance difference can be attributable to the shift in Nernst potential at the higher air utilizations:

$$dV = \frac{RT}{nF} \ln\left(\frac{\sqrt{PO_2}}{\sqrt{PO_2}}\right),$$

where the ratio of oxygen partial pressures reflects the outlet oxygen concentration of the conditions being compared. This calculation suggests a 6 mV drop in cell voltage is attributable to higher air utilization. This left 34 mV of performance loss to be explained. Some of this was thought to be a result of relatively wide rib spacing in the interconnect that is increasing the resistive losses in the unit cells. Part of the design effort in this project involved identifying causes and recover from this performance difference. The first step was to incorporate higher rib density into the interconnect.

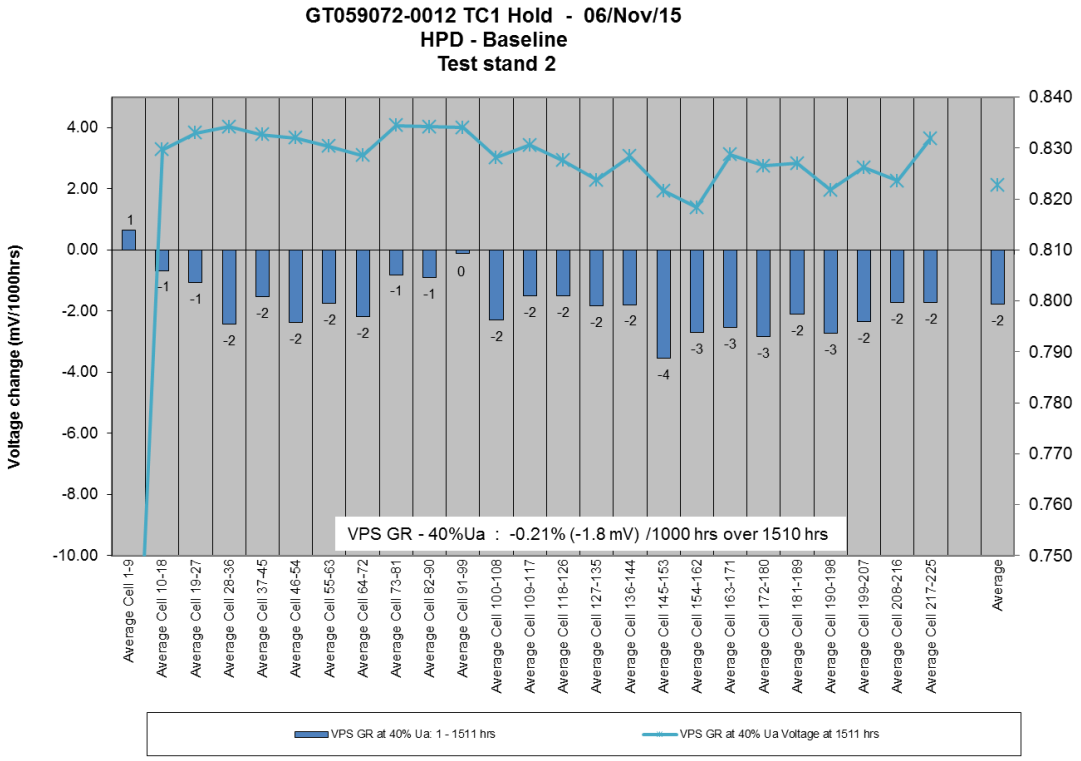

Figure 4-6 Stack GT059072-0012 Individual Cell Group Degradation Rates during TC1 Hold

Testing of Stack GT059072-0012 continued through 3,000 hours of operation. Though, it is a 225-cell stack of design similar to the CSA stack, the design is of a previous generation and the cells have a smaller active area. Figure 4-1 shows the test results. The operating conditions have been selected to match those used when testing LAS (stacks) and reporting on degradation rates.

After the 1,500 hours of operation the range of individual cell voltages for the stack started to increase, with the lowest cells degrading faster than the higher performing cells. This is thought to be due to a thermal-viscous phenomenon. A hotter area is generated at approximately 75% of the height of the stacks due to a combination of thermal and flow effects. In the hot spot the gas temperatures increase, increasing the local viscosity and decreasing local flow, suppressing local voltage. Less flow and lower voltage both contribute to more local heating, driving even less flow. The phenomenon is prevented from running away thermally by conduction vertically through the stack and by thermal coupling with the environment.

Evidence for this theory of thermal-viscous driven degradation comes from several observations on a prior stack as well as this one. For example, Figure 4-8 shows the degradation rates for individual cell group average voltages in the stack along the height of the stack (cells are numbered bottom to top). Figure 4-9 shows temperature trends including in-stack temperatures for Cells 1, 75, 150 and 225. The highest temperatures are in cell 150. Despite being the hottest region, the cell voltage graph shows that this region of the stack started as and remained the lowest performance section of the stack. Normally performance would improve with increased temperature (although the gain is moderate with this cell technology in the 700 °C to 800 °C range). The low performance suggests that the cause is thermally driven reductions in local flow resulting in higher effective utilizations at the hot cells relative to the cooler cells.

The average performance degradation rate over the test period to 3835 hours at VPS GR operating conditions (and 40% Ua) increased to 0.55%/1000 h (4.6 mV/1000 h). The problematic end cell (end plate material substitution error discussed in the previous quarterly report) continued to operate at a low but stable voltage. In Figure 4-8 the red bars show the voltage response over the last 1,000 hours of testing. Compared to the degradation over the whole test period (blue bars), the cooler cells have progressively less degradation, which is consistent if they are getting progressively more flow as the temperature difference between the hottest and coolest cells increases with time.

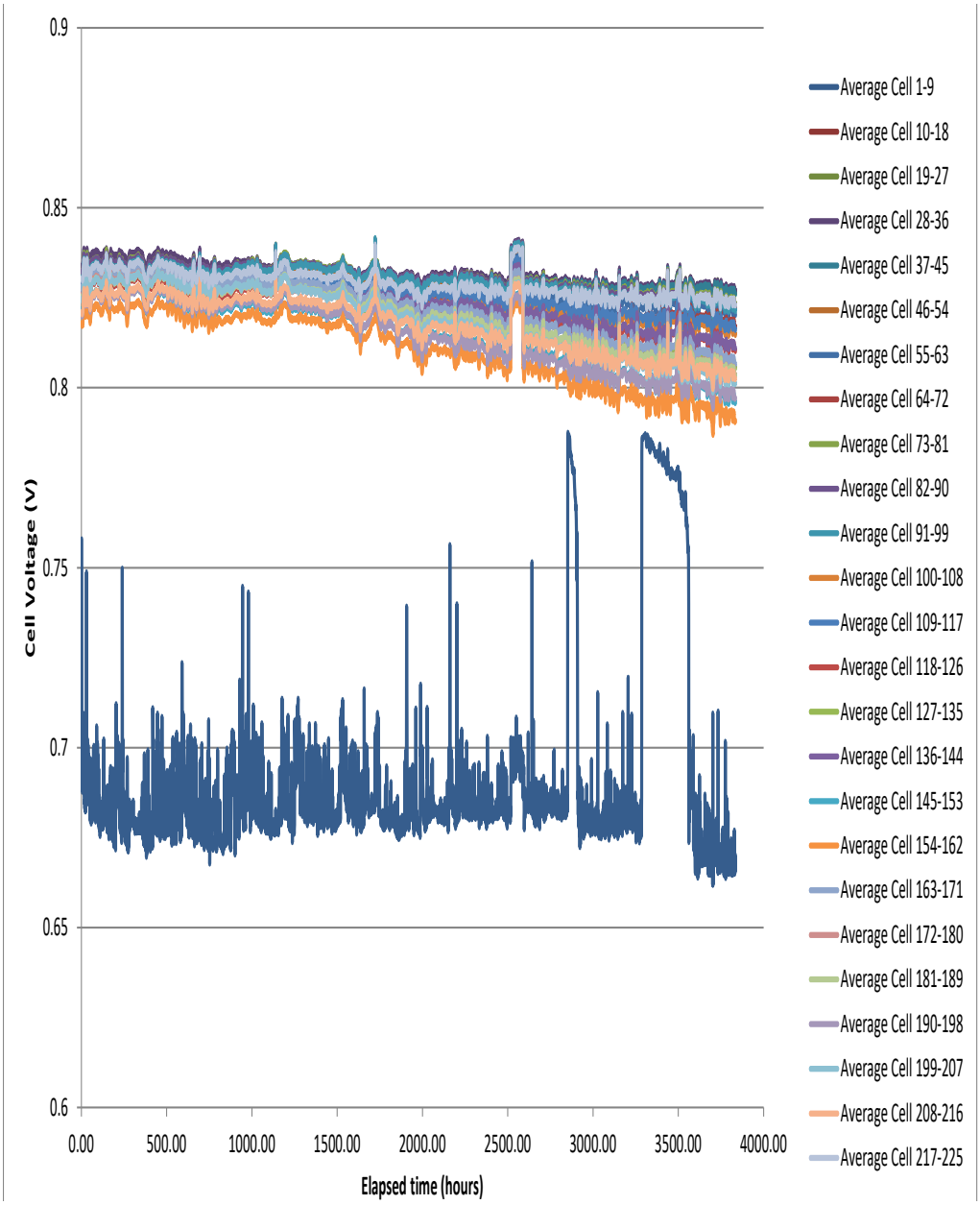

Figure 4-7 Stack GT059072-0012 Performance during TC1 Hold

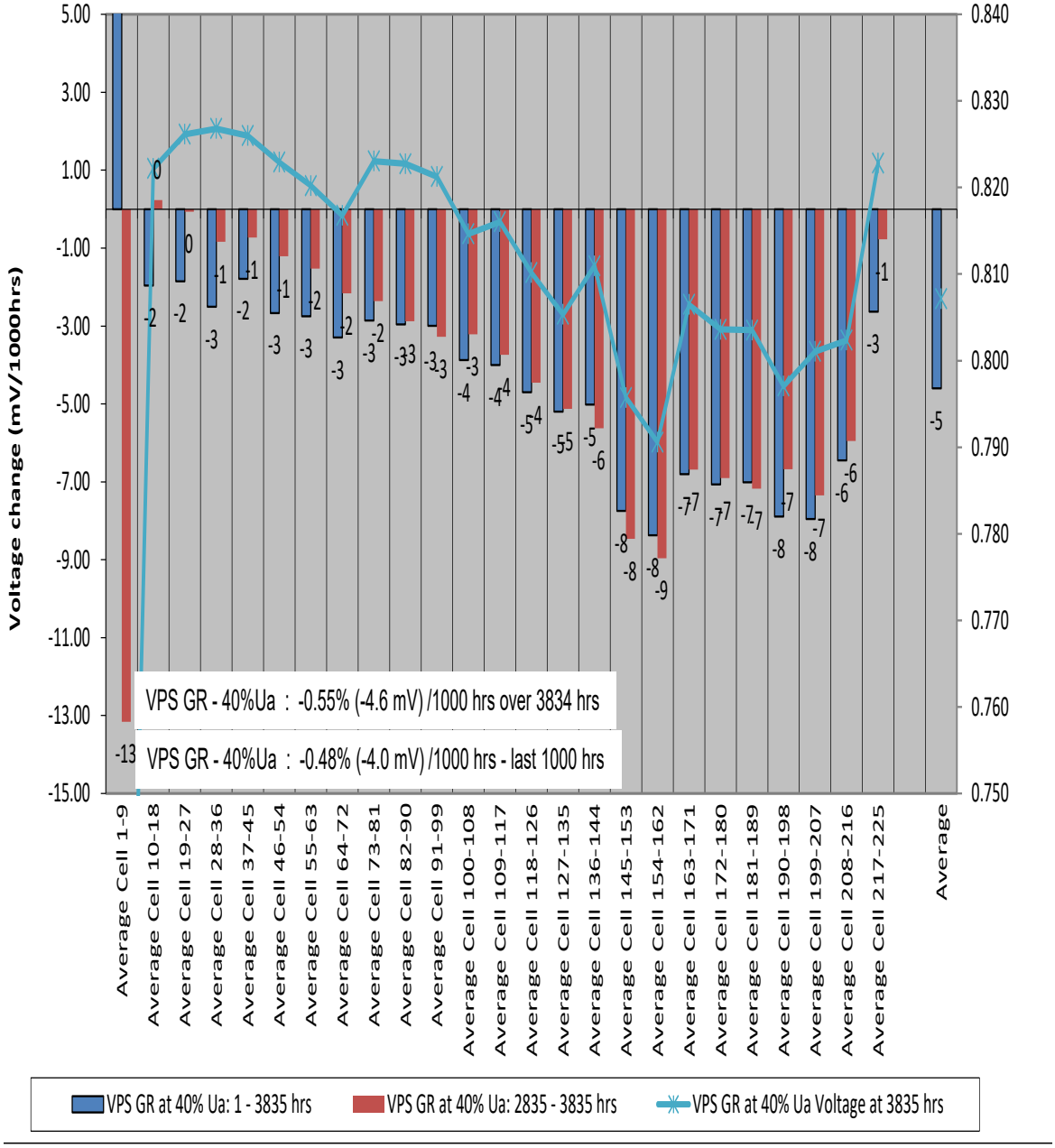

Figure 4-8 Stack GT059072-0012 Individual Cell Degradation Rates

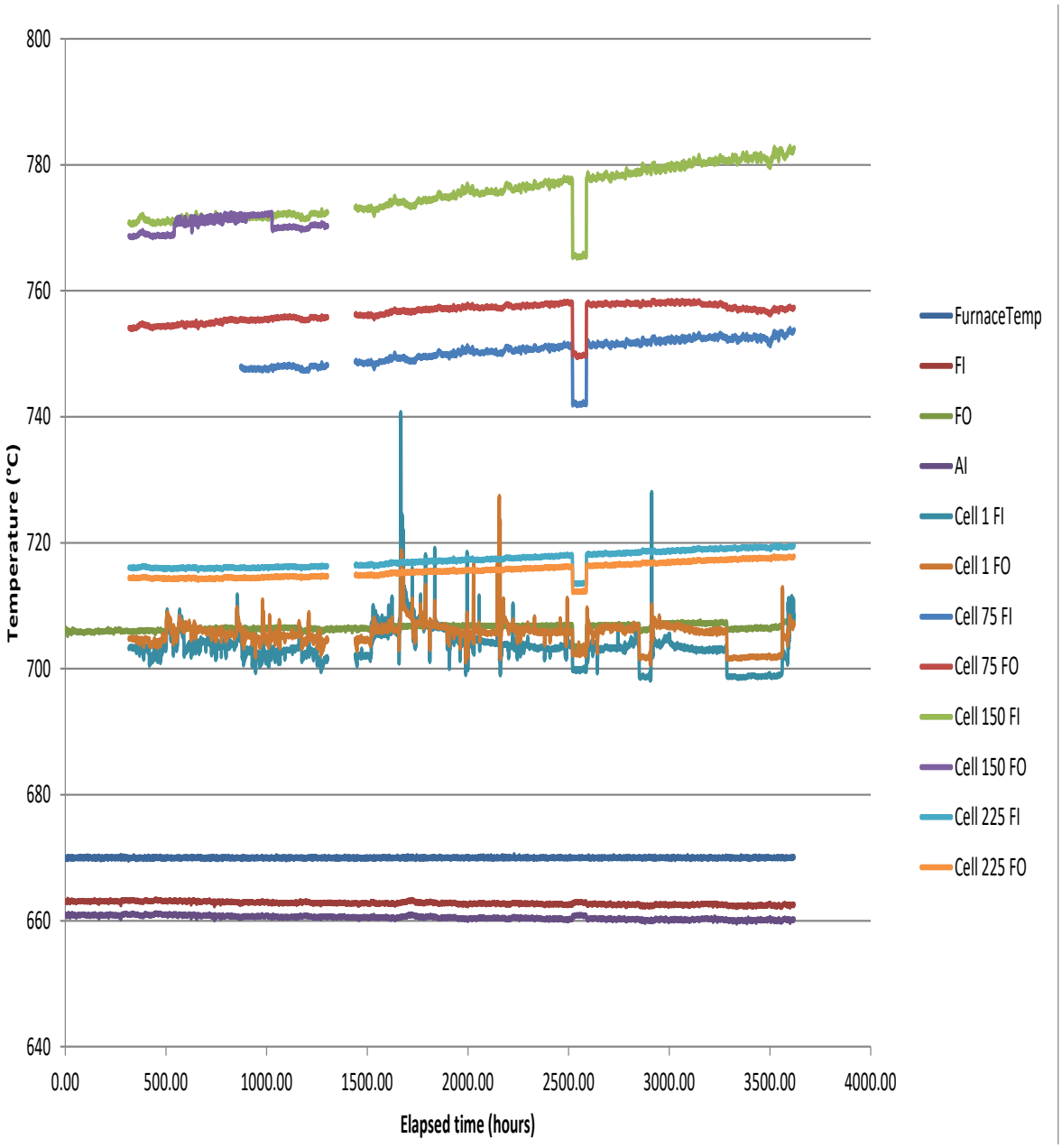

Figure 4-9 Stack GT059072-0012 Temperatures

At ~2,500 hours, the current was lowered for a period such that the average cell voltage matched the start of test. This reduced the temperature difference between hottest and coldest cell to almost the same as at the start of test, and the performance distribution across the stack also closely resembled that at the start of test. This seems to be consistent with the idea that the main driver of voltage distribution and of degradation is temperature distribution across the stack in the stacking direction. This is therefore a key area for improvement in the CSA stack.

Finally, it should be noted that this degradation rate is not out of line with what would be expected from a conventional LAS (stack) running under the same conditions. It is not as good as the best LAS results, but is in line with the average results of production stacks. If the degradation of the CSA stacks is dominated by thermal-viscous effects and if the above changes successfully moderate those effects, the result should be reduced degradation.

Testing of Stack GT059072-0012 continued through 5,000 hours of operation. Though the stack it is a 225-cell stack of design similar to the CSA stack, the design is of a previous generation and the cells have a smaller active area. The performance degradation rate at 5,000 hours was 6 mV/1,000 hr/cell, which is comparable to that demonstrated in the more conventional LAS (stacks) operating at similar conditions.

The individual cell-group performance degradation rate profile for the 5098-h period (at VPS GR system representative conditions) is shown in Figure 4-10. The secondary Y-axis represents average cell voltage for individual cell groups in the stack (at the end of 5098-h period). Cells are numbered from the bottom of stack to the top. Two primary observations from this chart are that the degradation rate tends to increase along the stack height, and that two cell groups (Cells 145-153 and Cells 154-1620 had noticeably higher degradation rates than their neighbor groups.

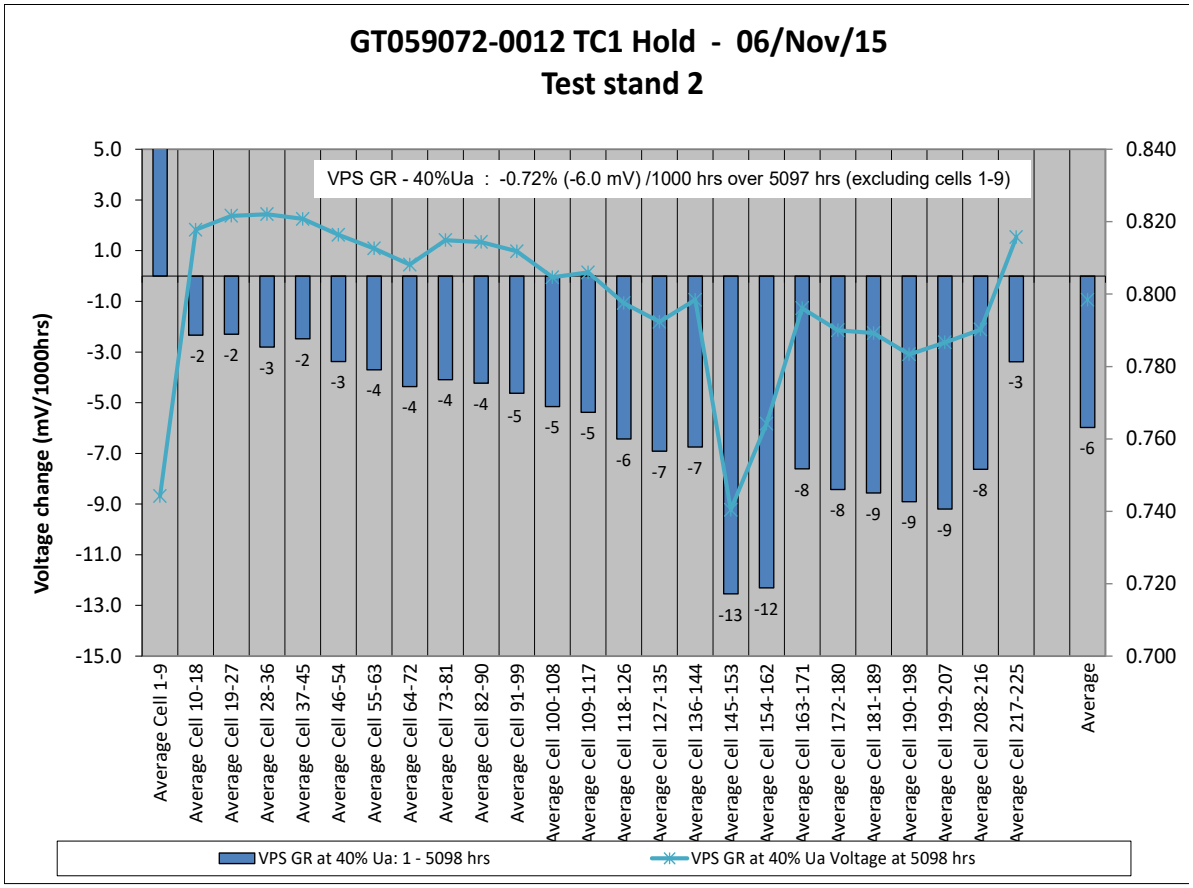

Figure 4-10 Stack GT059072-0012 Individual Cell Group Degradation Rate Profile

Figure 4-11 shows in-stack temperatures measured at several points during the progress of the test. The thermocouples must be ~0.005" to fit into the stack and are prone to failure. By the end of the test, three of the eight thermocouples had stopped working. Nonetheless, a general temperature profile is visible with the hottest area at about two-thirds of the height of the stack. Some increase in temperature was expected as the stack degrades, but it is clear that there was a developing problem around Cell 150 by the end of the test. The cell temperature rose nearly as much in the last 100 hours of operation (9°C rise) as in the prior 2,000 hours (11°C rise).

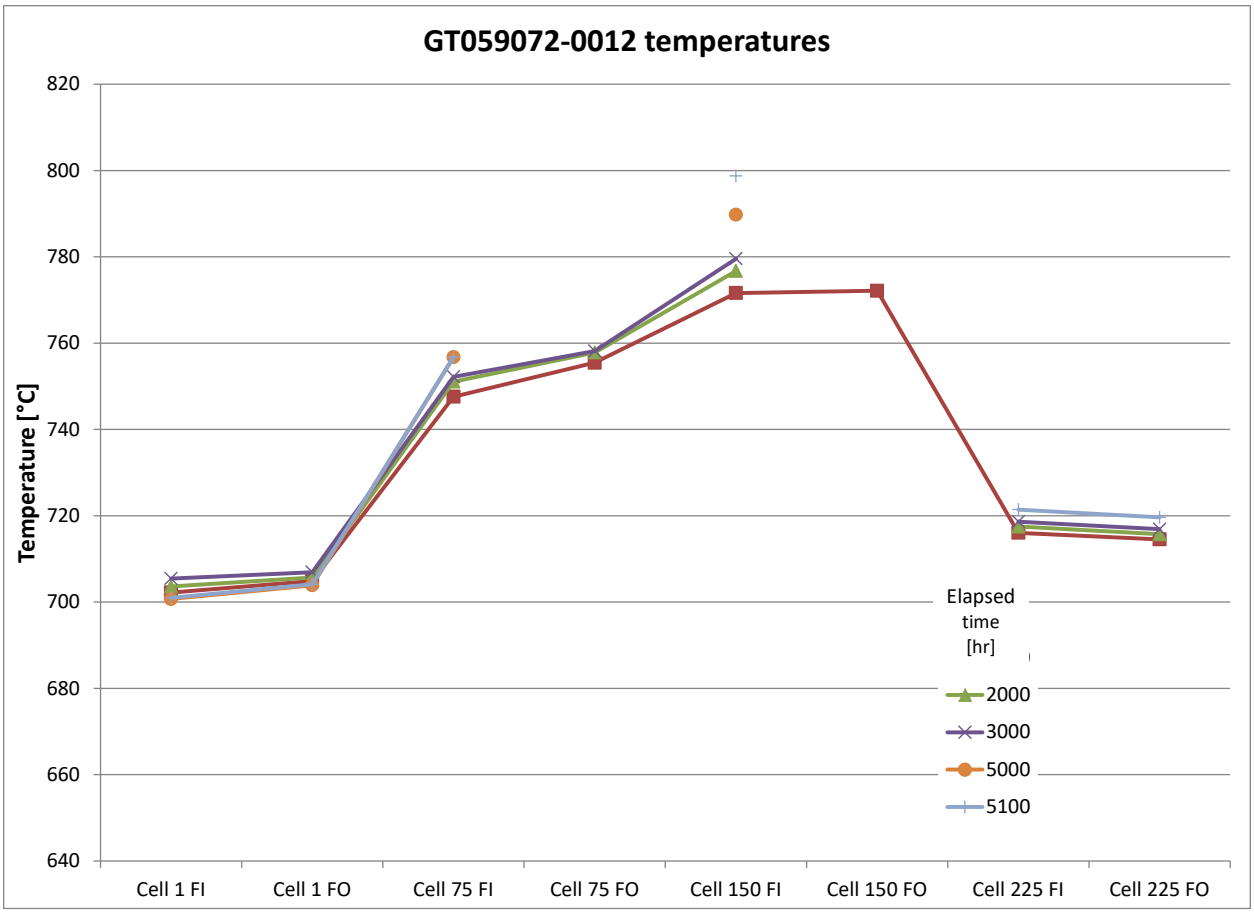

Figure 4-11 Stack GT059072-0012 In-Stack Temperatures During the Test

It is a known problem with this particular stack design that the (vertical) fuel manifolds are undersized for the stack height, leading to progressively less flow to cells located higher up in the stack. This leads to cells operating at progressively higher utilization and result in more heat generation and less convective cooling for higher cells. Heat rejection through the top of the stack counters the temperature effect to some extent for the top cells. Overall, it is typical with this stack design to observe the hottest location somewhere between two-thirds and three-quarters of the height of the stack. The CSA design is expected to address this weakness by increasing the size of the fuel manifold in proportion to the active area fed, and by re-configuring the stack to locate the oxidant inlet to the sides of the stack versus to the bottom of the stack, for more even distribution of oxidant convective cooling.

Shortly after 5,000 hours, voltage of a cell group (Cells 145-153) started dropping and the stack was shut down for assessment. The cold leak rate of the stack was found to be 1.6 slpm He at 0.5 psid, roughly two orders of magnitude larger than what would be considered normal for this stack. The combination of the high leak rate, the drop in cell voltage and the increase in temperature suggested that there was damage (possibly a cracked cell) within the group of cells from Cell 145 to Cell 162.

Post-test examination of the stack was conducted to assess the damage and to see if a root cause can be determined. Every cell layer was examined and crack initiations were found on Cells 1, 146, 154 and 162. As already mentioned in a prior report, there was a supply error related to one component of the base plate that resulted in damage and poor performance of Cell 1. The focus

was therefore placed on the other three cell layers that were damaged later in test and may be the cause of the cell performance drop that led to the termination of the test.

Figure 4-12 shows SEM sections of Cells 146 and 154 and a top-view of Cell 154 showing the cell cracks and delamination (delamination is suspected to occur after cracks). No other signs of damage or problems were observed through the rest of the stack. Figure 4-13 shows a typical interconnect from the stack displaying a 3 to 4 micron oxide layer that is well adhered and relatively non-porous. Figure 4-14 shows a potted cross section through the seals, interconnects and cells, typical of what was found in the stack. Everything looks normal, suitable to continue operation for a long period.

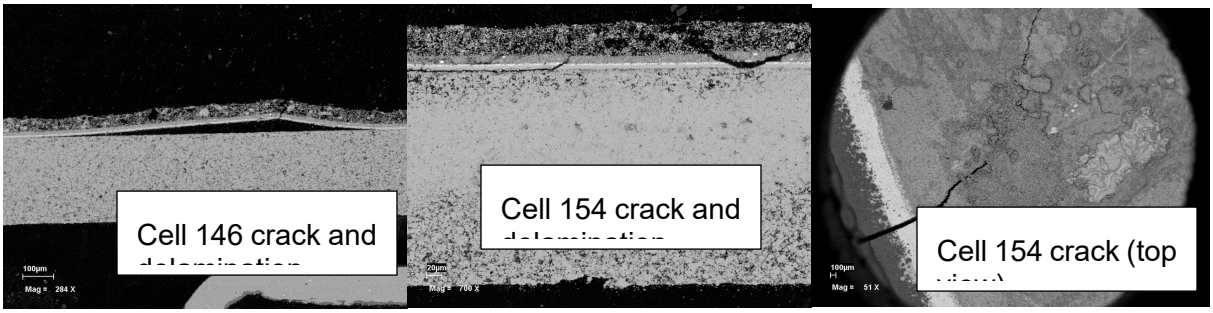

Figure 4-12 SEM Images Showing Cell Damage Found During Post-test Examination of Stack GT059072-0012

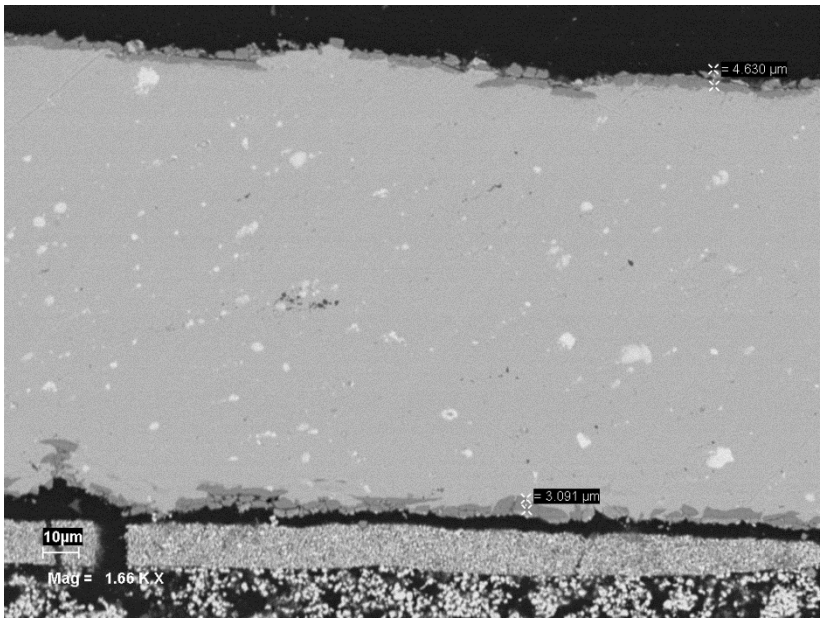

Figure 4-13 Interconnect Oxidation Observed in Stack GT059072-0012

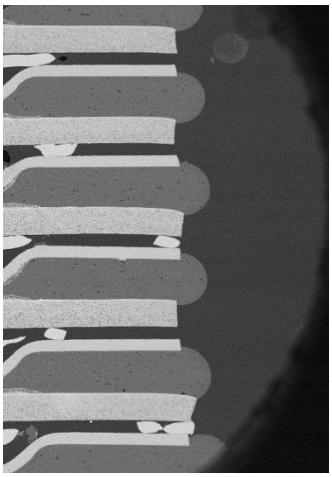

Figure 4-14 Seals, Interconnects and Cells (Cells 208-216) During Post-test Examination of Stack GT059072-0012

It is believed that the failure was due to local cracking at the outer edge of the cell, which progressed radially inwards by up to 3 mm by the time the test was ended. The cracks were perpendicular to the cell edge, characteristic of a hoop stress related failure. Furthermore, the cells that failed are relatively tightly grouped in the hottest region of the stack, but are not adjacent to each other, suggesting that the failures did not directly cascade from one cell to the other. In fact, careful observations of cell layers adjacent to the failed cells revealed no signs of damage.

The working hypothesis of the cell failure cause is as follows:

1) This was the first sustained operation at these conditions for this stack design. Conditions, in particular the temperatures (distribution) in the hottest area of the stack, were such that they led the cells to stress conditions overlapping the probability distribution of their fracture strength. As a result, three of the cells in this area of the stack that encompasses an estimated 50 cells (~Cell 140 to Cell 190) failed from thermal stress.
2) The direct mechanism driving the failure (conjectured) is the difference between the in-cell temperature (approaching 800 °C) and the temperature of the outer edge of the cell (radiating to a furnace at 670 °C) which puts the edge of the cell in tension.
3) When that local tension on the cell edge exceeded the tensile strength of the edge (which is reinforced by the glass ceramic seal and its bond to the metal interconnect), a crack was initiated.
4) With a crack initiation, further crack growth was easy. The gas leak across the crack could lead to both localized high temperatures and to material stability issues, especially oxidation of the anode functional layer, further leading to delamination and damage propagation.
5) The progression of damage was slow enough such that three separate crack initiations occurred before the test was shut down. Temperatures continued to rise over this period, thereby increasing the hoop stresses in the cell edges.

Paths addressing the hypothesized causes of the failure and current status in CSA stack:

1) Reconfigure the stack flow such that the oxidant flows into the cell edges and out the bottom of the stack, rather than vice versa. In the current flow configuration, the hottest location on the cell is adjacent to the coolest edges.
2) Increase the relative size of the fuel manifold to reduce the extent of flow maldistribution (vertically) that results in higher temperatures in the upper central area of the stack.

3) Reconfigure the unit cell flow such that there is improved temperature distribution across the cell.
4) (potentially) Add a gas porous radiant barrier adjacent to the cell edges to reduce their thermal coupling to the environment.

Although increasing cell strength is of a potential interest, it is not seen as a key path forward. The focus should be on designing the stack and the operating conditions to allow the cell to operate effectively, rather than on adding yet more requirements to the cell. It is not believed that there is any fundamental materials issue driving the result. Two stacks of this design have demonstrated over a year of operation, although at more moderate operating conditions.

A first trial stack was built in late September, 2017 consisting of:

- 45-cell stack
- Fully representative of a real stack with the exception of using metal (non-functional) cells instead of real cells, due to availability
- Fully representative of all build steps (automated QC, automated build, cell and interconnect printing, etc).

Figure 4-15 Stack GT060248-0001 (45-cell CSA)

Figure 4-15 shows the completed stack beside a pen for a sense of scale. It has 45 cells of an active area of 82 cm^2 each, for a total stack active area of 3690 cm^2, and would equate to a 900 W fuel cell stack at a modest 0.29 A/cm^2 and 0.85 V/cell.

Approximately 40% of the height and 60% of the weight of this stack is taken up by end plates. As discussed in previous quarterly updates, this is just the first of three stack sizes that were built with the CSA design, stacks with 150-cells and 350-cells in this project. At the larger stack sizes

(larger cell counts) the weight, volume, and cost of the end plates will be spread over more cells, lowering their relative importance.

By and large, the processes proved robust and the stack build proceeded as intended. A few areas needing further refinement or adjustment were identified as follows:

- A counterweight arrangement that maintains stack compression during the build process was incorrectly calibrated, leading to progressively higher stack compression during the build. This has been fixed.
- Additional error-proofing of the automated work cell would be beneficial to overall process stability, although no problems arose specifically during the stack build.
- Better tooling and geometry is needed to make installation of the compression system easier and more repeatable.

Three technology stacks were built and two were tested electrochemically. The stacks have the designations GT060248-0002 through GT0060248-0004. They will be discussed sequentially below. All three share the following characteristics:

- 81 cm^2 active area cells
- 45 cells/stack
- Full CSA design as previously reported (i.e.: No simplifications or omissions)
- Fully automated stack build

Stack GT060248-0002

Stack GT060248-0002 was the first electrochemically active CSA stack produced[4]. In the interest of getting to electrochemical testing, significantly out-of-tolerance cells were used. Due to the nature of the design, this large deviation introduced leak paths into the stack. The risk of added leakage was balanced against waiting for in-spec cells to be produced and the decision was made to go ahead.

During the stack build it was observed that several cells were cracked. The stack was disassembled and closely examined, some imperfections in the dispensed seal structure were corrected, and the process was repeated. After several such iterations two determinations were made:

1. An alumina paste filler material was being used to provide mechanical support in key areas of the structure. Its interface with the cell was proving very problematic. Very fine manual retouching of all interface surfaces was required to enable a build without breaking cells.
2. No matter how good the alumina fill was made, compressing the stack to the design load of 80 lbf resulted in cracked cells. Dropping the compressive load to 20 lbf was enough, in combination with the retouched alumina fill, to build without breaking any cells.

In the interest of getting to testing, this further compromise was accepted and the stack was built and fired. It was then installed into the test stand (Figure 4-16 and Figure 4-17)

[4] The first stack produced, serial GT060248-0001, was made with metal dummy cells to validate the overall stack assembly process.

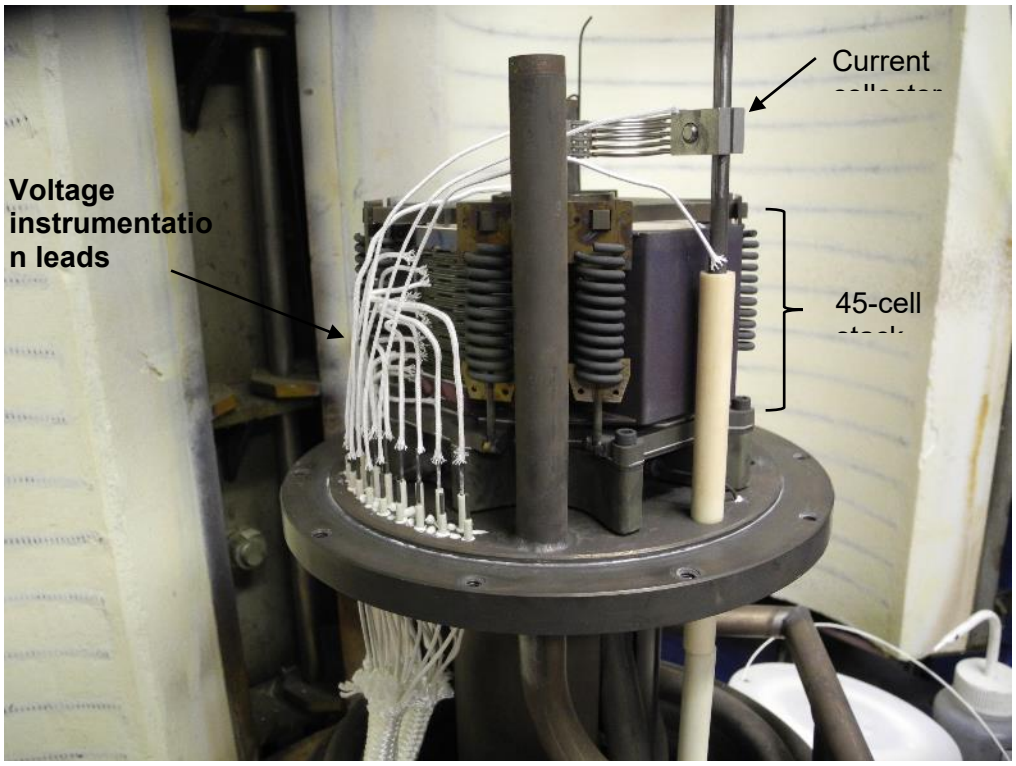

Figure 4-16 GT060248-0002 in test stand, left side

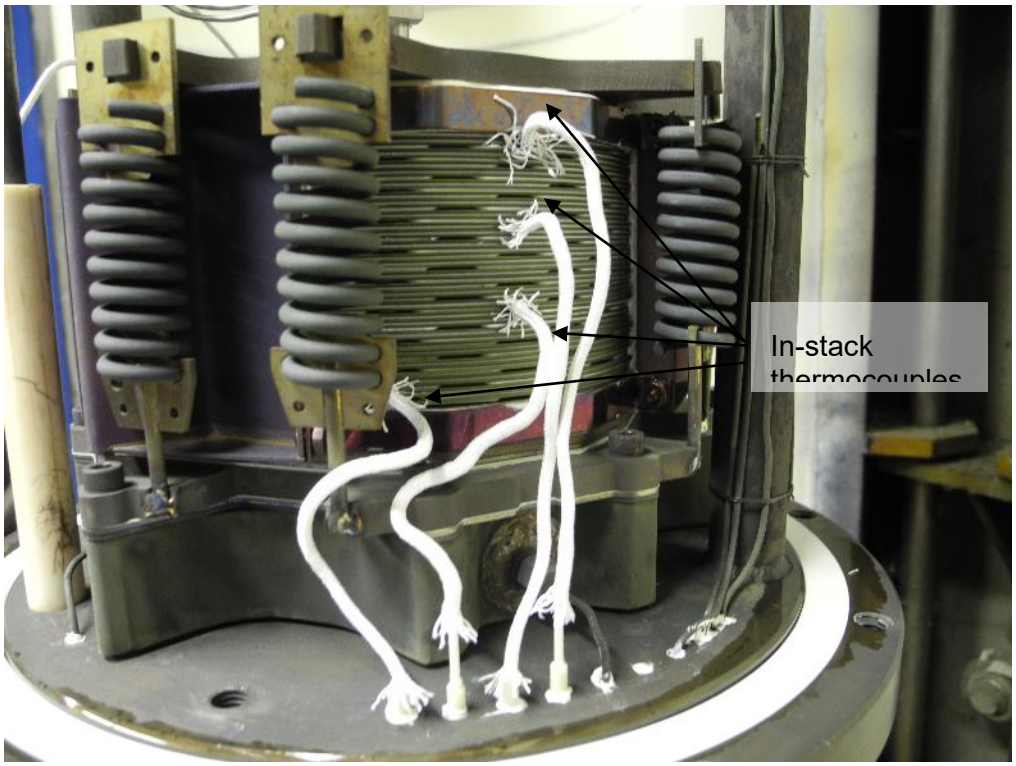

Figure 4-17 GT060248-0002 in test stand, right side

On the initial heat-up a problem was detected, the cell voltages did not rise as expected as the stack reached operating temperature. This was diagnosed as an apparent short somewhere between layer 32 and layer 35 to ground (layer 1). The immediate cause was not apparent. The stack was cooled to prevent further damage and for closer inspection.

On inspection the suspected short was confirmed to be present, but the location was uncertain. It was suspected to be between layer 32 and the metal center-post, which is itself electrically bonded to the base of the stack. This area was inaccessible without destroying the stack. In the absence of better options an energy pulse from a spot welder was used to vaporize the short path. While a high risk process, in this case it appeared to work and the stack was restarted.

This time the stack showed no signs of short on heating and ran through reductions normally. As a first stack this showed some positives: Despite oversized cells and the related problems, there were no broken cells. Temperatures were a little bit high, but that was expected from the leak path caused by the oversized cells, and while high enough to indicate leakage, they were reasonable to continue testing. The overall design was working.

Testing then proceeded to characterization and in particular to utilization testing. This immediately revealed weakness in the stack. Cell voltages were low relative to what we know they can be, and performance was dropping quickly as fuel utilization was increased to 60%. We'd expect to be able to maintain strong performance to higher utilization. A similar but less severe weakness was observed in air utilization testing. Figure 4-18 shows the cell voltages and how they responded to utilization. Due to the high cell density, voltages are monitored in sets of 5 cells.

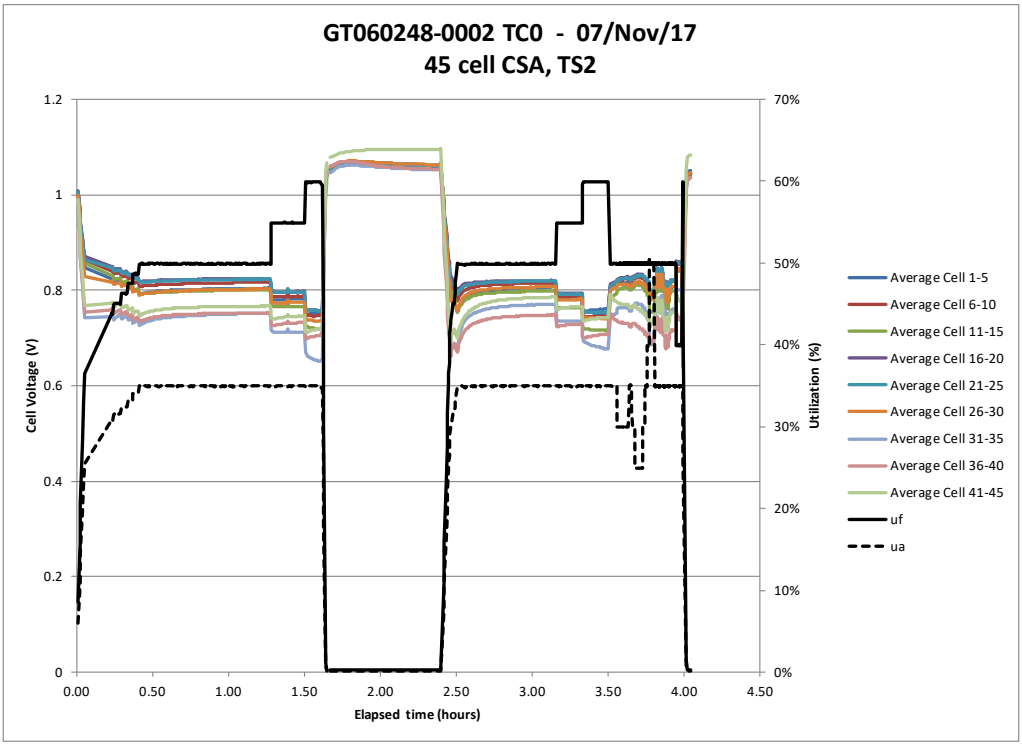

Figure 4-18 GT060248-0002 TC0 utilization exploration

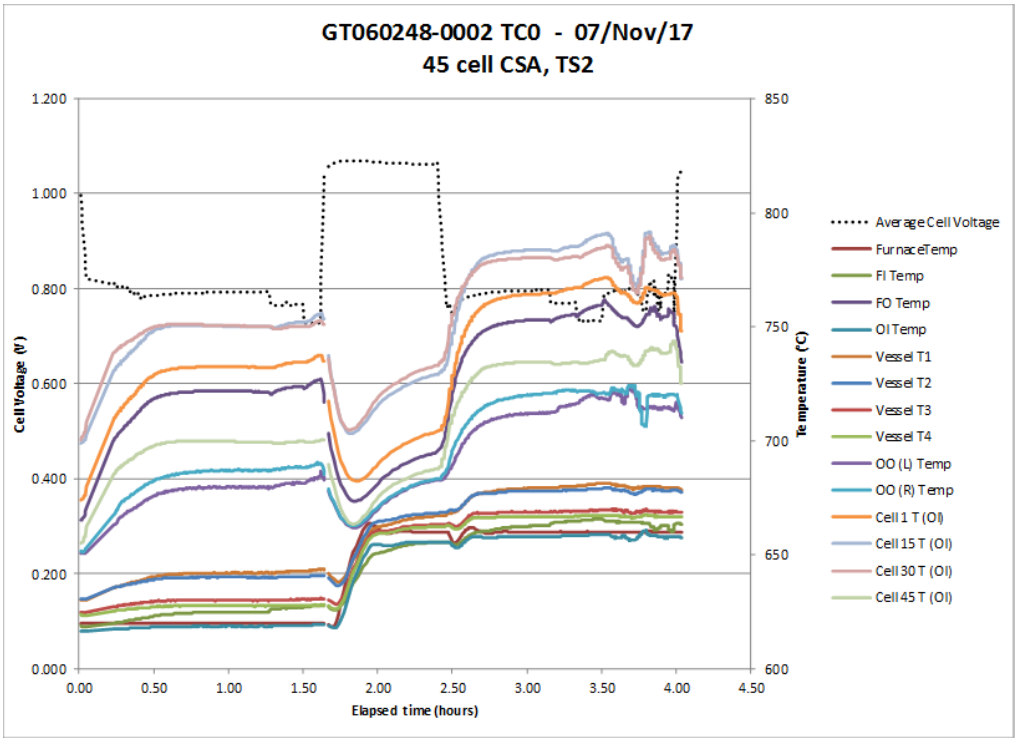

Figure 4-19 GT060248-0002 TC0 temperatures

Figure 4-19 shows the temperatures over the same period, and there are some points of interest therein: First the stack to furnace temperature difference is relatively high, which can be at least partially attributed to the oversized cells and the resulting leak path around the cell perimeters. The temperature difference between layer 30 and layer 45 exceeds 50 °C across a distance of less than 20 mm (0.75in). This indicates that the test environment is overcooling the top (and bottom) of the stack relative to an ideal conditions, or stated differently, shows that the high volumetric power density of this stack limits the ability to reject heat off the sides. Adjustment to the design of the surroundings can alleviate some of this (add insulation above stack, redirect cold inlet air flow to enter nearer the center of the stack).

Although these results show some areas for improvement in the stack surroundings, they also a first confirmation and validation of the robustness of the stack design. Despite these high temperature differences it is clear that this has not caused cells to crack, and this is due to the ability of the individual layers to dissipate thermal stress away from the cells. It is surprising to some that at some conditions the air temperature around the stack reached 680 °C yet this did not result cell cracking or other problems despite cell temperatures at the same conditions reaching 790 °C. This temperature is measured ~10 mm (0.4”) into the stack.

The stack was subsequently thermal cycled as part of the initial characterization, with no indications of problems. Reduction and open circuit voltages were normal, confirming that neither the initial operation nor the thermal cycle had caused any cell breakage. Utilization exercises showed similar performance and temperatures as the prior thermal cycle.

The stack was then switched into electrolysis operation, with explorations reaching towards a EERE project DE-EE0006961 target of 250 g/hr hydrogen production at -2 A/cm^2. This is a very aggressive target both thermally and electrochemically. The stack was only pushed to -0.6 A/cm^2 before aborting. The cell performance and thermal conditions were getting too severe for comfort (Figure 4-20).

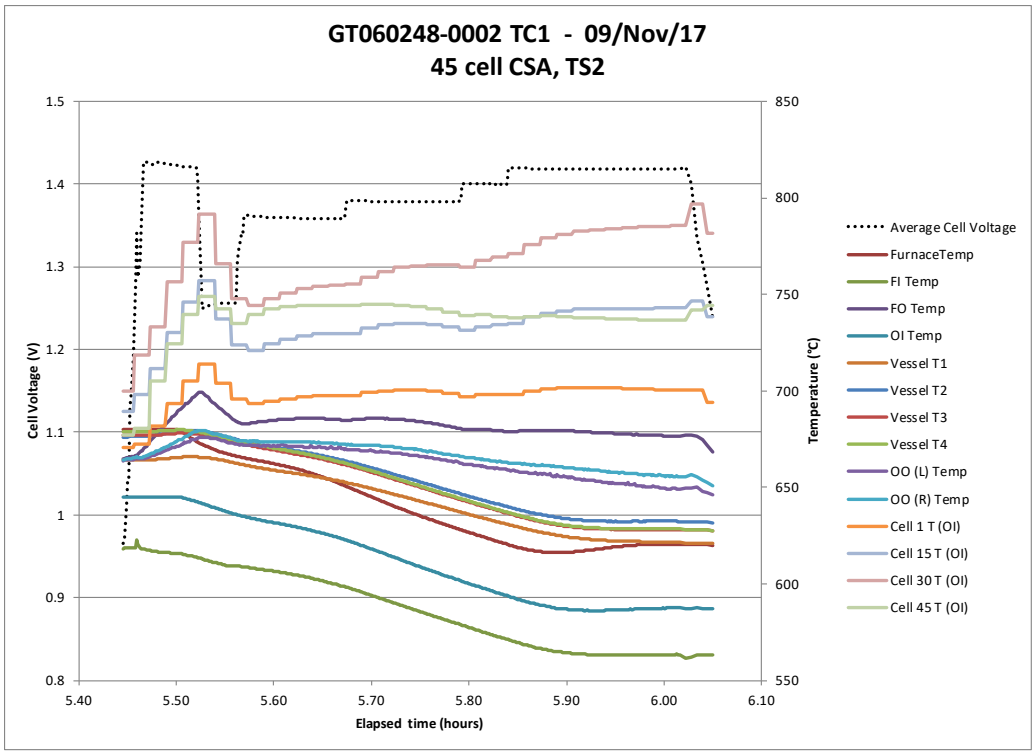

Figure 4-20 GT060248-0002 TC1 high current electrolysis

At this point the stack was shut down for autopsy. With oversized cells and their associated leak, a clear utilization weakness, lower than desired compressive load to prevent cell breakage during firing, and a short that had to be burned out on initial heat-up, it seemed reasonable to focus on getting a second stack into test and to autopsy this first stack for learnings.

Despite efforts, the location of the initial short was not found, and the working assumption is that the center post lightly touched an interconnect. A local dielectric coating of the center post planned for larger stacks (with larger standoff voltages) had been thought to be optional for these short stacks, but with this result the dielectric coating will now be used for all stacks.

By and large the stack looked clean on autopsy, however clear indications of cell damage were seen on several layers, all occurring at the fuel out locations on the affected cells. Figure 4-21 shows a typical example. The cell break occurred on disassembly, not during operation. The damage of interest is indicated by the local discoloration of the cell (dark grey areas). In the same image the impact of the oversized cells is obvious by the wide band of oxidized cell (green band) outboard of the seal.

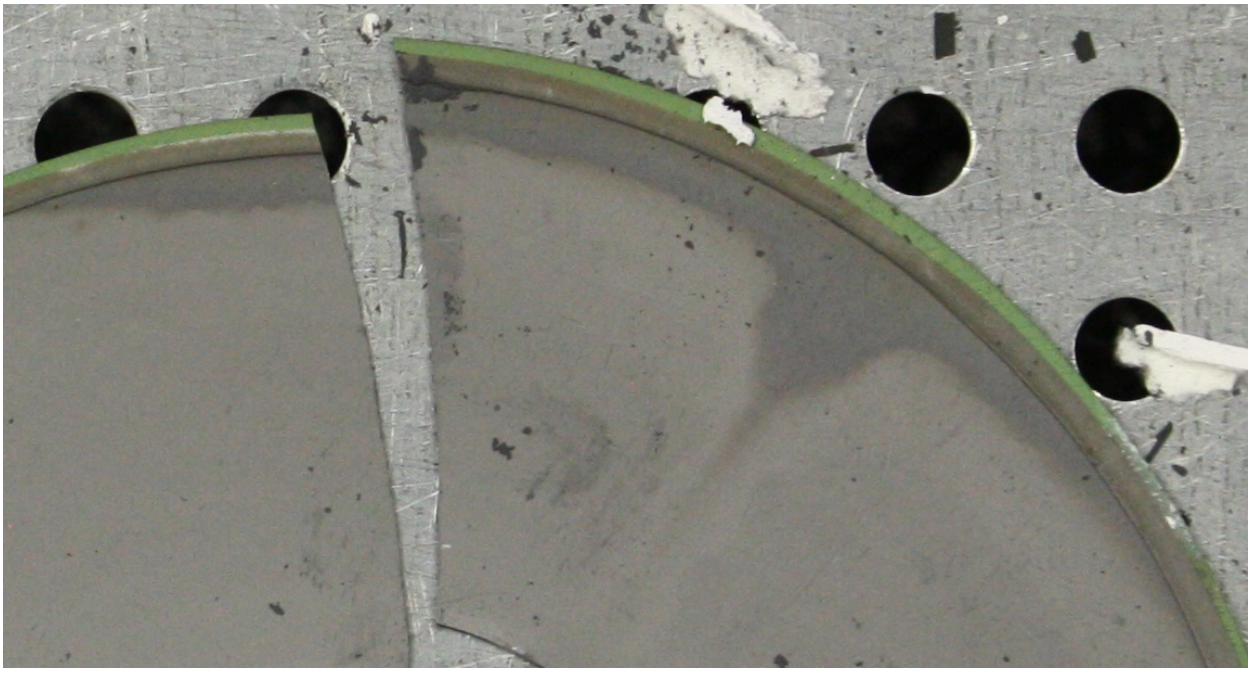

Figure 4-21 GT060248-0002 evidence of cell damage

SEM micrographs of the cell surface at the air electrode (Figure 4-22) and of a cell cross section (Figure 4-23) revealed damage right through the electrolyte, through the fuel cell AFL, reaching down into the cell support. Given the nature of the damage it is believed to have occurred at the end of testing during the higher current electrolysis operation. At that point, the thermal conditions were aggressive, the combination of higher current and poor utilization performance was stressing the cells, and the lower compressive load may have contributed to poorer electrical contact quality and therefore higher localized heating.

The damage appeared to be concentrated in the areas where the metal interconnect ribs contact the cell, furthering the idea that the damage was related to local current density. In all cases the damaged areas were primarily towards the outer edge of the cell where the conditions were likely aggravated by the leak at the cell edge.

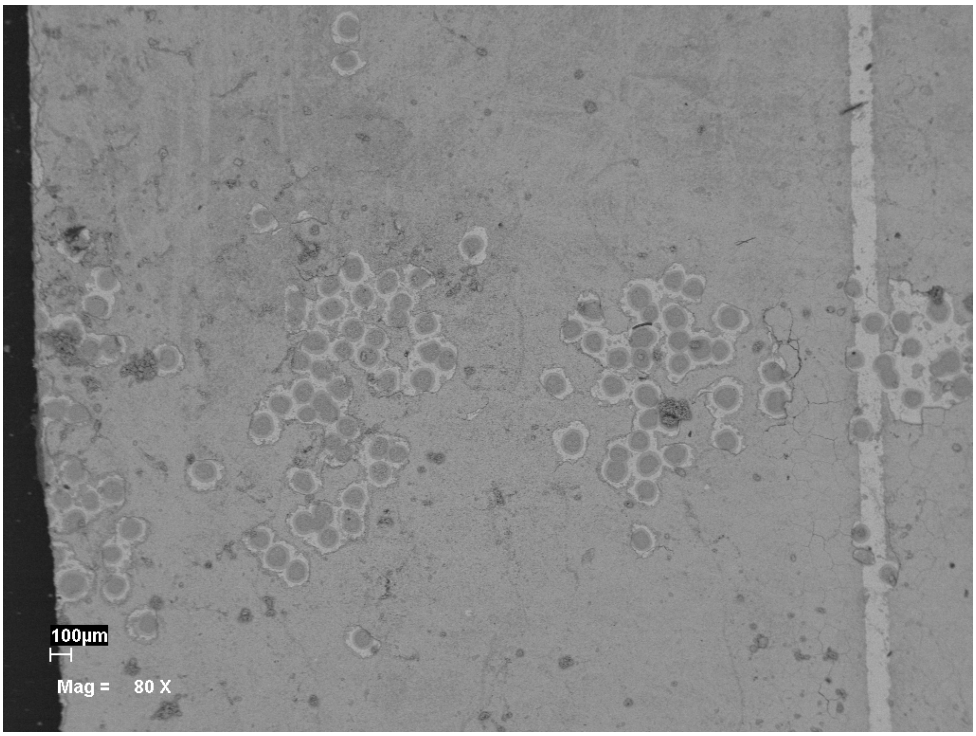

Figure 4-22 GT060248-0002 Close-up of damage on air electrode side

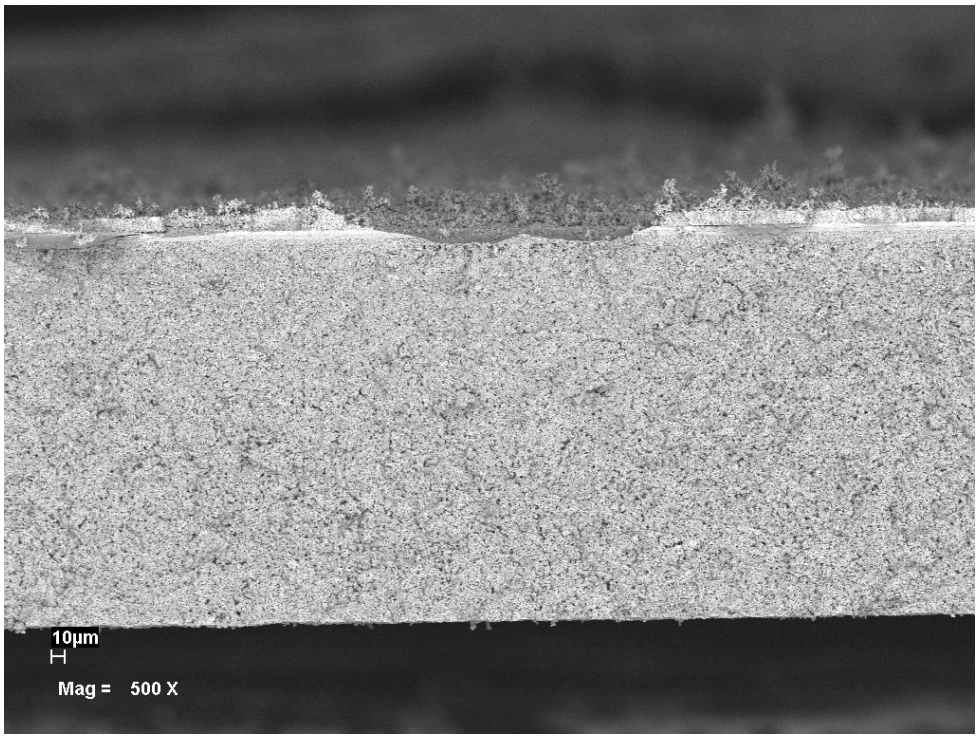

Figure 4-23 GT060248-0002 cross section through damaged cell

In summary, stack GT060248-0002 was the first electrochemically active stack of the CSA design, built and tested with some known compromises in the interest of getting some stack testing results and test experience. The stack showed robustness to aggressive conditions and also some clear weakness in utilization performance and possibly in terms of electrical contact, although the latter effect is largely masked by the weak utilization performance and is hard to quantify. It highlighted strategies for the subsequent stack as follows:

1. Use on-size cells
2. Apply localized dielectric coating to center post
3. Change the details of the seal design to allow higher compressive load (more detail to follow)
4. Adjust center post sealing strategy to reduce potential fuel bypass

Stack GT060248-0003

The subsequent stack was built with all of the suggested changes. In GT060248-0002, described above, the sealing structure was composed of a glass-ceramic seal forming the seal between the interconnect and the cell, and a backing support, composed of an unbounded alumina support structure (Figure 4-24).

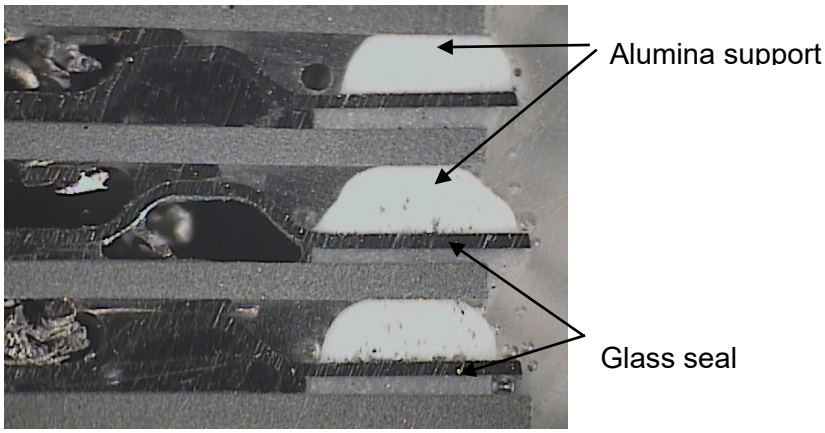

Figure 4-24 GT060248-0002 seal and seal support

Through further experimentation it was determined that the cause of the cell cracking that prevented reaching the design load of 80 lbf was the interface between the alumina support and the cell. Detailed attempts to make the alumina support as smooth and as cell-friendly as possible where not sufficient to enable the full design load. While the design load is itself open to adjustment, the 20 lbf that was achieved was deemed too low and the process too temperamental. Since the interface between the cell and the glass-ceramic seal was not showing any problems, a revised support structure was developed that consists of a partial height alumina support overlaid with a thin glass-ceramic seal layer. In this way the non-bonded structure was maintained (critical to the stress relieving nature of the stack), while simultaneously avoiding direct alumina support to cell interfaces. Trial builds showed a repeated ability to load to 80 lbf top load without breaking cells, and this is the way in which stack GT060248-0003 was built.

An explanation of why 20 lbf top load during initial firing is deemed too low while 20 lbf top load is seen as an acceptable end-of life stack compression (as discussed in Task 3.1 under Stack Compression Testing). The difference is due to the contribution of the dead weight of the stack itself. In the planned full height stack the weight of the repeat layers would be on the order of 20 lbf. When the design targets a compressive load, this is the effective load on the top cells. The

compressive load on the bottom cells will be 20 lbf higher. If, as was the case in the prior stack, the cells are on the verge of being damaged at 20 lbf, then there is no path to a full height stack. Thus the focus on higher top load even at this stage.

Another path to solution would be to reformulate the alumina support structure, for example to increase its compliance, such that it no longer broke cells. This is a valid approach, and may in the longer term be favored. In the immediate term the layered support structure was deemed the fastest way to a solution.

The stack was cycled through a similar test protocol as the previous, including utilization testing, thermal cycle, then further utilization testing. The stack showed some clear differences, and some disappointing similarities to GT060248-0002. The main difference was a roughly 40 °C reduction in in-stack temperatures at otherwise identical conditions, which were attributed primarily to the elimination of the cell edge leak by using on-sized cells. The performance was again stable through the thermal cycle. However the utilization performance was disappointingly similar. The efforts to improve the sealing between the center post and the stack core did not appear to have significantly impacted the utilization results.

Despite the utilization weakness, the improved thermal characteristics of the stack gave confidence to attempt a high current electrolysis operation towards a deliverable for EERE project DE-EE0006961.

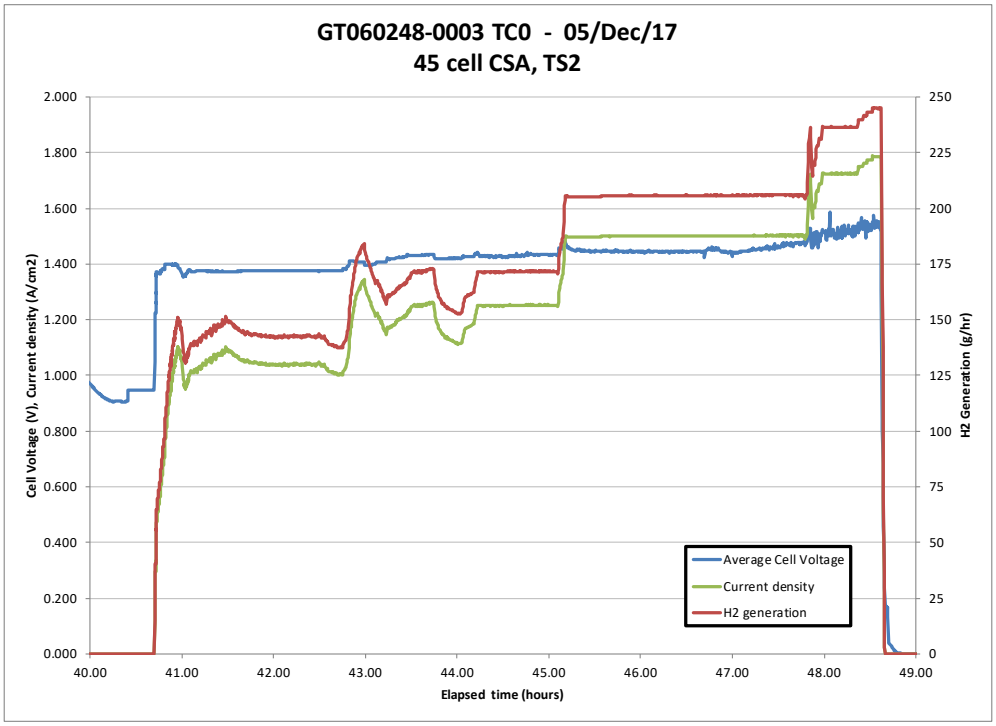

Figure 4-25 GT060248-0003 High current electrolysis operation

Figure 4-25 provides a summary of the electrolysis testing which included 7.5 hours of electrolysis at greater than -1 A/cm^2, and a peak current density of -1.8 A/cm^2. The temperatures and voltages were stable during the test period (other than on condition changes). At the end of the test the stack was absorbing 10 kWe and producing 245 g/h of hydrogen, with a stack power density of 2.8 kWe/kg.

Unfortunately, in an attempt to close to the project target of 250 g/hr, the final push on the stack triggered a cascading failure, ending further testing.

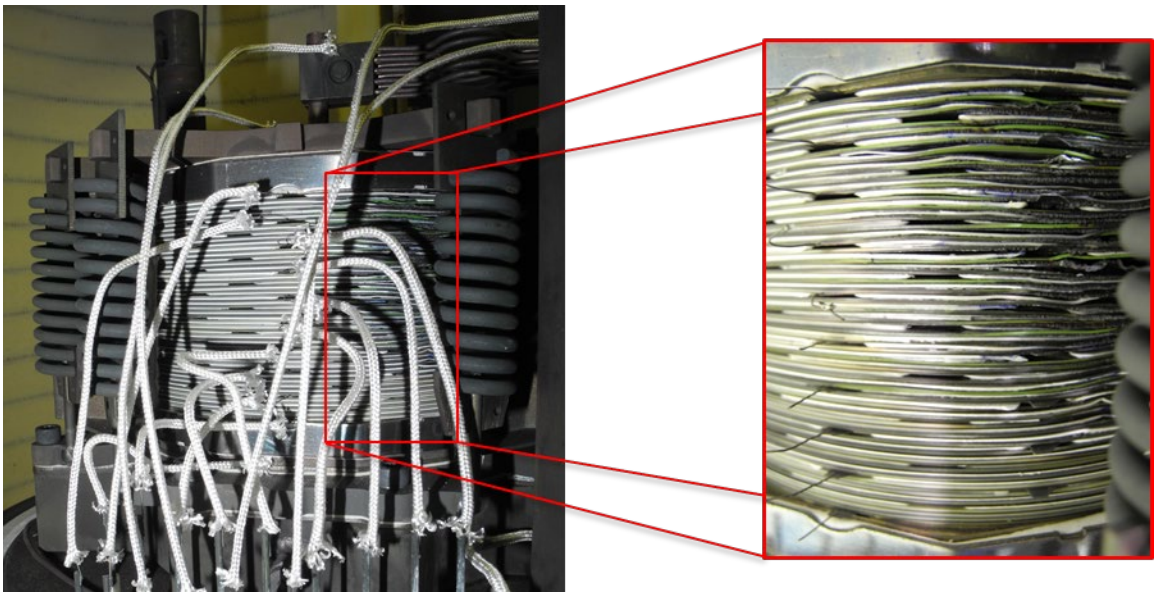

Figure 4-26 GT060248-0003 After failure

Figure 4-26 shows the appearance of the stack after the failure where it is obvious that combustion occurred within and around the stack. Once combustion started the localized heating was enough to cascade the failure down the stack over a period of 2.5 minutes.

At that point in the test the indicated steam utilization was 37%. It is suspected that at the conditions the bubbler humidifier system is not keeping up to demand and that the actual utilization was substantially higher. Equipment is being commissioned to validate actual delivered steam at test conditions. Suffice to say that the steam utilization was most likely in the same range where utilization weakness was observed.

In summary, stack GT060248-0003, the second electrochemically active stack of the CSA design, was built with fixes intended to address weaknesses observed in the previous stack, with partial success. On the positive side the stack was able to run much harder, primarily due to better thermal conditions within the stack attributed to cell dimensions within design targets. The utilization performance was still weak. Despite this the stack was able to run aggressive electrolysis conditions with 3x higher hydrogen production than the prior stack with apparent stability, although ultimately the stack was driven to the point of failure when it was pushed harder.

The key question was why the utilization performance remained weak. Since the increased attention to the center-post sealing had not yielded good results, it led to a search for other potential causes. In reviewing some of the development samples for the layered support, a suspect area was identified. Figure 4-27 shows the suspected fuel bypass path (highlighted in red). Although relatively small at roughly 0.5mm square (0.020” square), this path occurs in some form at four locations on each layer. Multiple by the number of layers (45) and this may be a significant contributor to the fuel bypass.

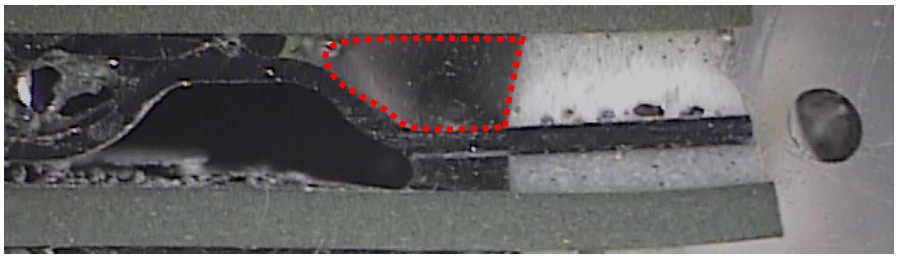

Figure 4-27 Layered support and suspected fuel bypass path

To address this bypass path, the layered support structure has been extended to fill that gap as much as possible. This solution was deployed in stack GT060248-0004.

Stack GT060248-0004

Stack GT060248-0004 was built in mid-December. It differed from the prior stack in two key aspects:

1. The layered support was adjusted to fill the suspected bypass path
2. An adjustment was made to the interface between the bottom plate of the stack and the stack core

This second adjustment was an attempt to improve an observed voltage loss between the bottom interconnect and the end plate. It was not a critical loss, amounting to 0.855 V of resistive loss at -1.5 A/cm^2 in GT060248-0003. It was mostly noticeable as being significantly larger than (for example) the loss between the top interconnect and the top plate which under the same conditions was 0.031 V.

In what was considered to be a minor change, the bottom interface was made to mimic the top interface with the hope of re-creating the low loss connection. The only negative of the adjustment, which proved critical, was that it eliminated the bellows-like stress relieving structure in that first interface. It was thought that the design would tolerate a single non-stress relieved layer, with subsequent layers providing the necessary compliance.

This was not successful. There was complete failure of the seal between the bottom end plate and the first interconnect. Two attempts were made to repair and replace this seal with progressively more material added to handle any stresses, and at each step the seal failed after firing. The stresses on cool down from seal firing were sufficient to break any reasonable attempt at this geometry. The compliant structure is clearly required on all layers.

A final attempt was made to disassemble and rebuild the interface similar to the prior stack, but catastrophic damage was done to the stack in the disassembly attempt.

In the end stack GT060248-0004 was unsuccessful and could not be tested. Samples have been submitted for sectioning so that the effectiveness of the change to the layered support can be evaluated visually.

The plan forward was to build GT060248-0005 with the revised support layered support identical to GT060248-0004, but with the bottom interface the same as stacks GT060248-0002 and GT060248-0003. For now the electrical loss at the bottom end will be tolerated, and improvement to this interface will be addressed at a later time.

Three technology stacks were then built and were tested electrochemically. The stacks have the designations GT060248-0005 through GT060248-0007. They are discussed sequentially below. All three share the following characteristics:

- 81 cm^2 active area cells
- 45 cells/stack
- Full CSA design as previously reported (i.e.: No simplifications or omissions)
- Fully automated stack build

Stack GT060248-0005

Stack GT060248-0005 was built with one primary objective: to improve the utilization performance. The stack was built and funded under parallel project DE-EE0007646 which focusses on electrolysis. The results are shared here as they have relevance to the overall CSA stack progress.

As discussed above, the stacks were showing a weakness in utilization performance that was thought to be evidence of fuel bypass – the flow of fuel directly from inlet to outlet without passing through the cell layers. Effort was focussed on improving the sealing of the internal fuel manifold against the stack and elimination of an unintended bypass opening. Stack GT060248-0005 showed a step improvement in fuel utilization. Figure 4-28 shows the TC0 (first heat-up) qualification test sequence showing utilization performance up to 75% fuel utilization, comparable to that of prior stacks at 55% fuel utilization. This supported the conjecture that the earlier stacks had been limited by fuel bypass flow.

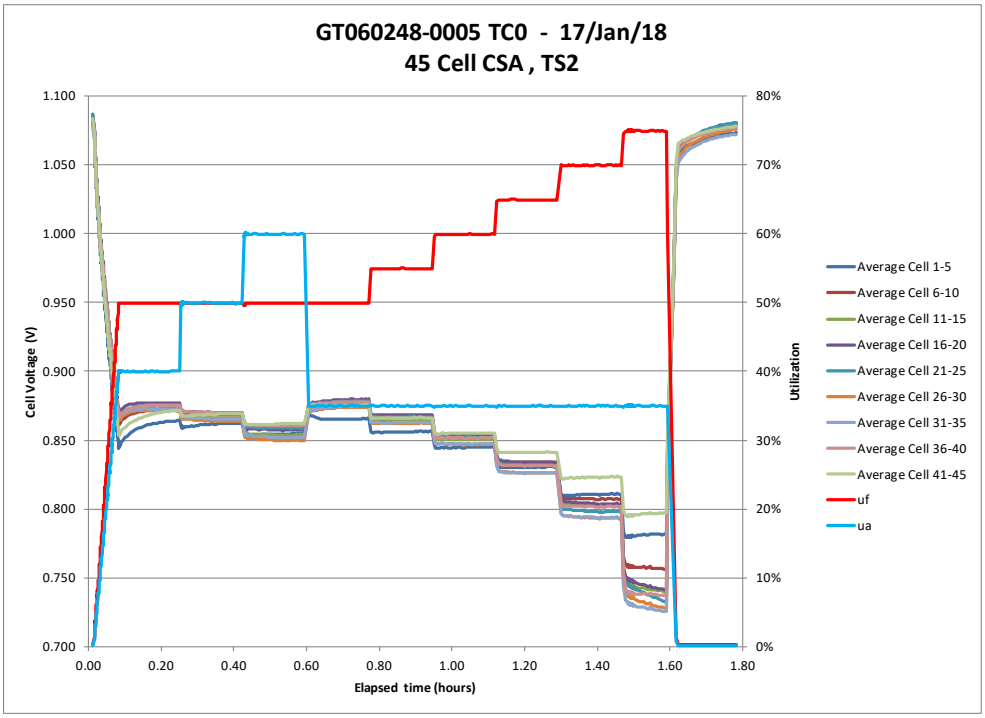

Figure 4-28. GT060248-0005 TC0 utilization performance

While much more robust in utilization tests, the performance was still not quite at the level expected. In addition the leak rate of this stack was approximately 4x higher than prior stacks. In retrospect the increased leak rate has been attributed to using expired organics in the glass seal paste after a mix-up with the supplier delayed delivery of new materials. While not noticed at the time, when new paste was received prior to stack GT060248-0007 the application characteristics were markedly different, and the leak rate and utilization performance improved dramatically (see discussion of GT060248-0007 below).

The stack was tested for a limited time (~300 hours) under various electrolysis and fuel cell conditions for project DE-EE0007646. While giving some initial characterization results, the relatively high leak rate limited its performance and the stack was replaced with GT060248-0006.

Stack GT060248-0006

Stack GT060248-0006 was built with the intention of being a direct repeat of GT060248-0005. It was hoped that the higher leak in that stack was simply coincidental and that a repeat would show the lower leak rates observed in prior stacks. This did not occur, and GT060248-0006 had a leak rate similar to GT060248-0005. This has subsequently been attributed to out of date organics in the glass seal paste.

This stack was also built under project DE-EE0007646, and despite the leak rate, successfully ran that program's 1,000 hour, -1 A/cm^2 electrolysis test demonstrating better than 97% LHV efficiency and no degradation over the initial 1000 hours.

Even though the stack was less than ideal, it began to demonstrate the robustness and reliability of this new platform.

Stack GT060248-0007

Stack GT060248-0007 was built under this program, and is identical to the prior two stacks except with new glass seal paste. The new organics behaved substantially better during the application process, and the results carried into the stack performance.

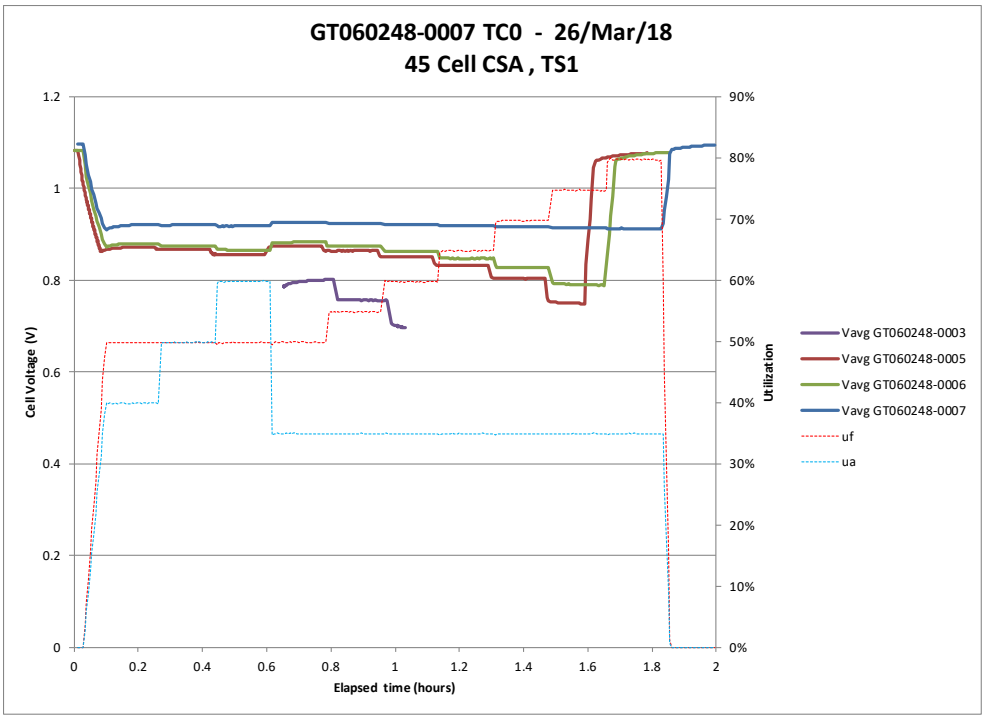

Figure 4-29. GT060248-0003, 5, 6, 7 TC0 utilization performance

Figure 4-29 compares the utilization performance of the last four stacks. GT060248-0003 only has limited results due to significant weaknesses, and is shown by the purple trace at 50%, 55%, and 60% fuel utilization. Stacks GT06248-0005 and -0006 show progressively better performance, reaching 75% utilization. Stack GT0602418-0007, which combines the improvements to the fuel manifold sealing with the new batch of glass seal paste, shows a significant improvement in utilization (blue trace) with solid and stable performance at 80% fuel utilization, the maximum that was tested.

The leak rate before reduction was 0.02 sccm He/cm^2 at 0.5 psid, approximately ten times lower than that observed in the previous two stacks, and ten times lower than a typical baseline technology LAS stack. This is the lowest leak rate on a CSA Stack observed at this point in time in this study.

The stack was subsequently put into a fuel cell hold at the following conditions:

- 65% fuel utilization, 40% air utilization
- 55% hydrogen / 45% nitrogen (dry percentages)
- 3% humidity
- 0.25 A/cm^2
- 750 °C nominal

These conditions are historically standard surrogate conditions for natural gas, providing similar voltage and degradation rates (if thermals are managed) in a simpler test, but without the beneficial reforming endotherm.

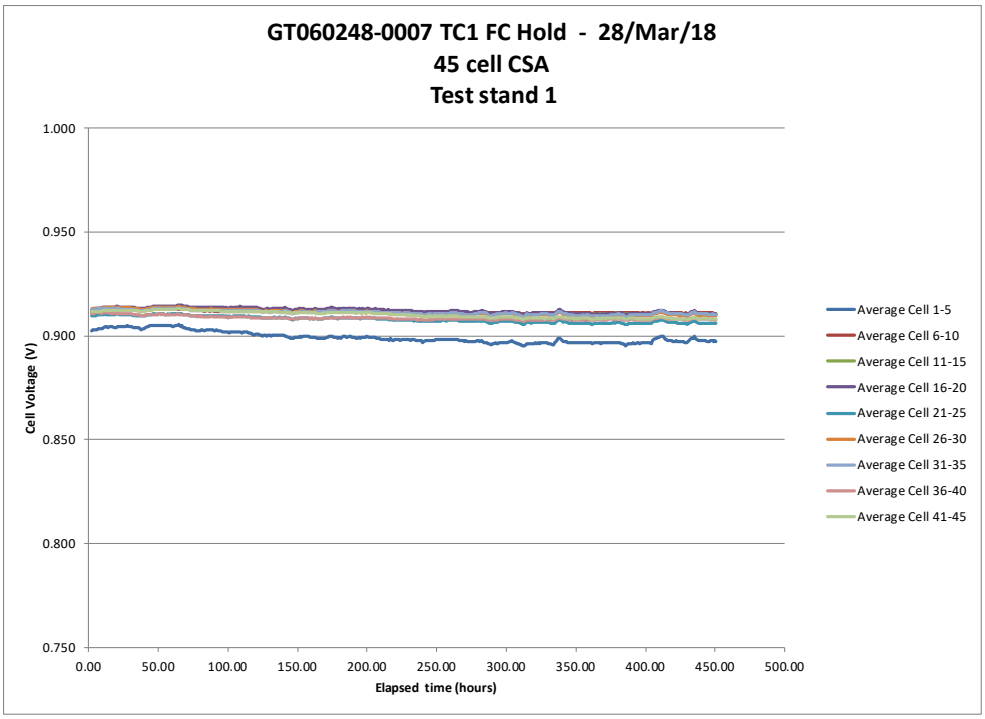

Figure 4-30. GT060248-0007 fuel cell hold

Figure 4-30 shows the test results with a little over 450 hours elapsed and a 1% /khr degradation rate overall. There is a general slowing trend in degradation after a 250 hr settling period. The bottom cell group is slightly out of the pack, but noticeable primarily because of the very low voltage spread overall. The total voltage spread is only 13 mV at 450 hours.

Both the tight voltage spread and the overall voltage (better than 0.900 V at these conditions) were considered positive results. They demonstrate that the CSA platform is delivering excellent flow uniformity to the cells (vertically) and excellent flow distribution across the cells (in plane).

Two stacks were build (GT060248-0008, and GT060248-0009) and used for commissioning of test stands 24 and 7. A calibration error was found in a mass flow controller in test stand number 2, which negates the very positive utilization results achieved on stack GT060248-0007 reported last quarter and requires new analysis of the degradation testing of that stack which was executed for most of this quarter.

The calibration error of the hydrogen mass flow controller resulted in a much higher flow than indicated. Estimates put the actual flow somewhat more than twice set-point and feedback. The MFC had been calibrated just prior to installation and was reported well within specifications. The device was returned to the calibration service and an as-received calibration report was requested. The calibration service reports that the MFC was flowing approximately 11 slpm more hydrogen than indicated across the full calibration range. They did not find any mechanical problems and reported that they have never encountered this problem before.

It was previously reported that the challenge with achieving high fuel utilization had been resolved through a redesign of the center-post top and of the dispensed alumina support beads on each layer. This allowed the focus to shift to commissioning additional test stands and accumulating degradation data. With this revised understanding that the utilization results were in fact an artifact of a mass flow controller error, focus shifted back to resolving the fuel utilization issues.

Figure 4-31 shows the average cell voltage across different utilization at the end of thermal cycle 3 (with original hydrogen controller) as compared to the start of thermal cycle 4 when the hydrogen MFC was replaced. The erroneous MFC was detected by attempting to drive the stack to failure through starvation and achieving an indicated fuel utilization of 105%. Upon restart with a replacement mass flow controller the stack showed weakness at 75% utilization, which is more in-line with prior stack -0006. Based on the as-received information from the calibration service the approximate utilization at 105% indicated was closer to 39%, and the approximate utilization at 65% indicated (where degradation testing was carried out) was closer to 32%.

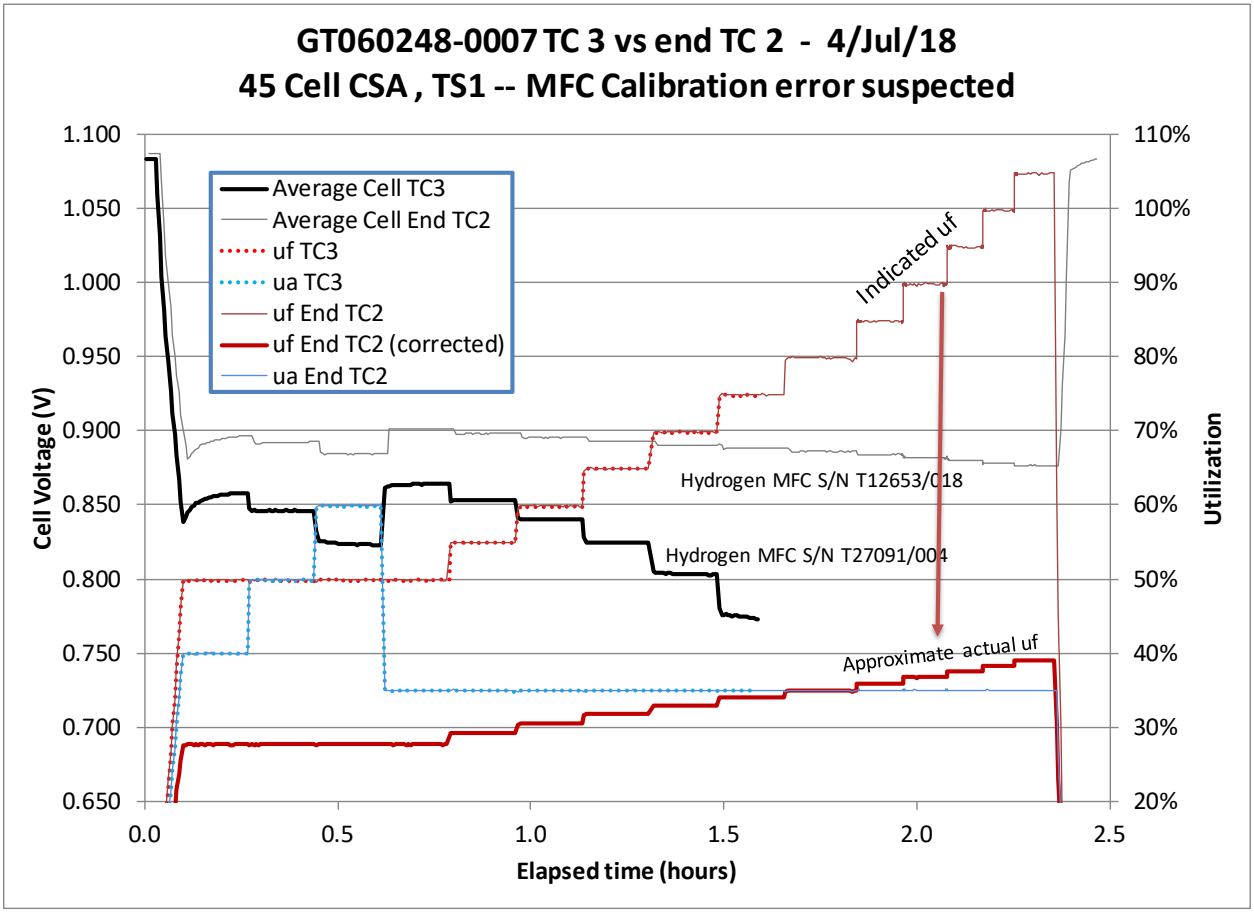

Figure 4-31: MFC flow error

Previous efforts have shown that short of starvation or introduction of unsustainable thermal conditions, that degradation is largely independent of utilization. Notwithstanding the low utilization resulting from the fuel bypass, the voltage show a tight grouping (less than 25 mV difference in average cell voltage across the stack) and degradation rates of 6.0 mV/khr and 5.5 mV/khr at 0.25 A/cm^2 and 0.29 A/cm^2 respectively (Figure 4-32). For two 1,000 hr duration tests this is in-line with results on the prior LAS stacks.

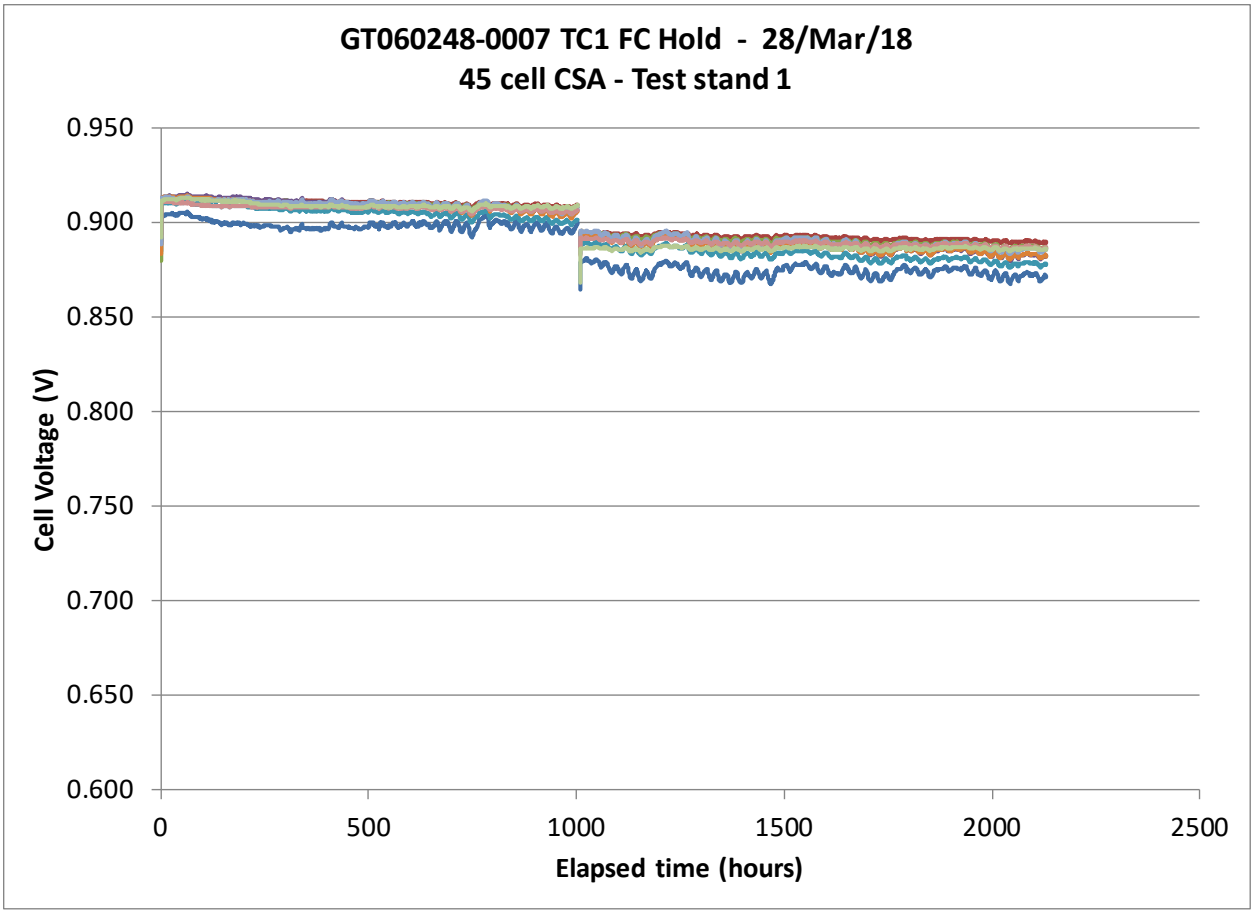

Figure 4-32: GT060248-0007 degradation testing (~32% fuel utilization), hydrogen/nitrogen + 3% steam, 0.25 A/cm^2 (0-1000 hours) and 0.29 A/cm^2 (1000-2100 hours).

Subsequent to the discovery of the mass flow controller error, the stack was switched to a reforming condition for further fuel cell mode degradation testing. A further 300 hours of testing was carried out at conditions of:

- 60% stack fuel utilization
  - Noting that with the suspected fuel bypass the effective utilization at the cells would be higher
  - Due to performance limits this is lower than the typical 68% fuel utilization run on larger stacks
- 35% stack air utilization
- 0.29 A/cm^2 (23.5 A)
- 37% direct internal reforming (DIR)
- Recycle ratio of 67%

These conditions correspond roughly to an equivalent system condition (including recycle) of 82% system utilization and 20% of the reforming done external to the stack, and to typical test conditions reported for the large area stack (LAS) platform.

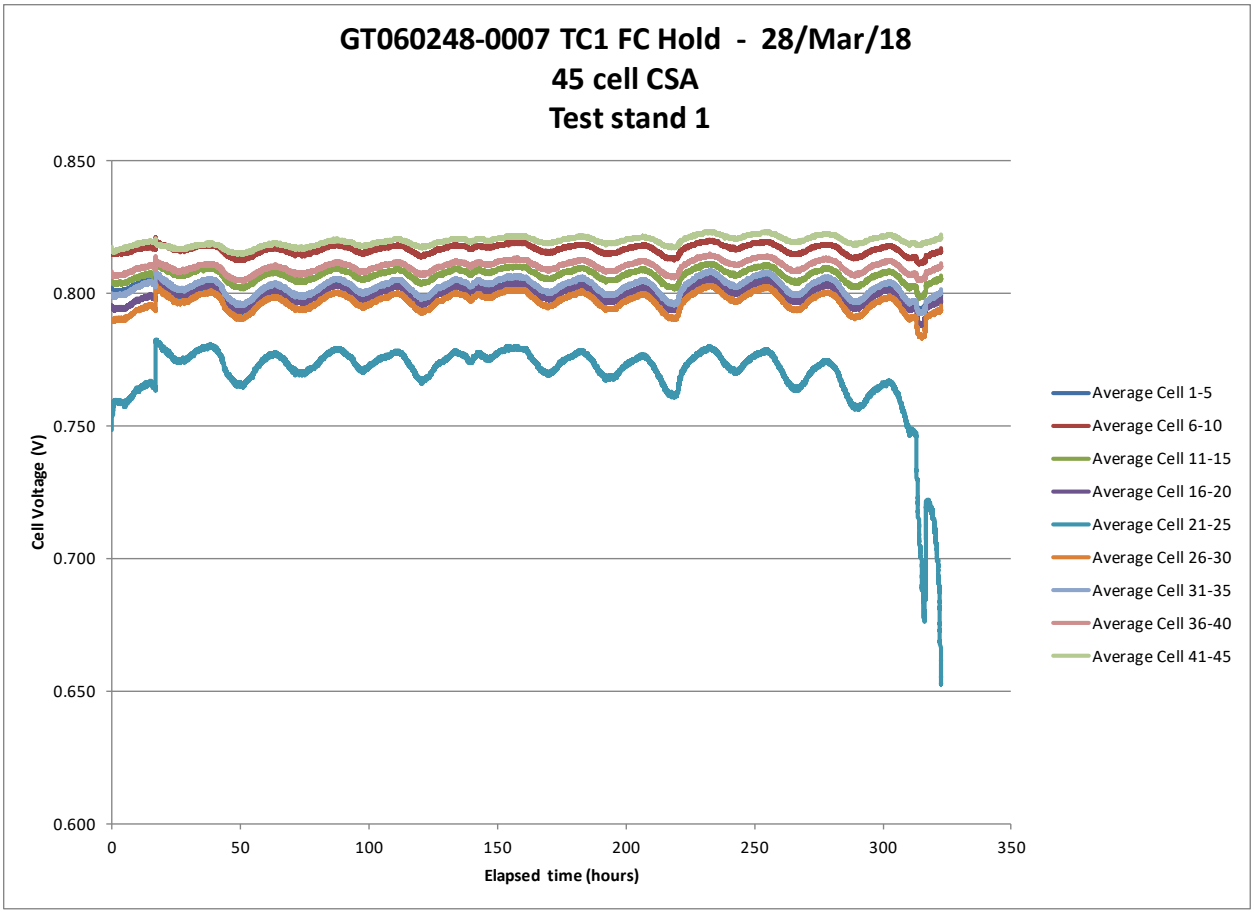

Figure 4-33: GT060248-0007 degradation testing on reformate. 60% fuel utilization, 35% air utilization, 37% DIR, 0.29 A/cm^2

The stack showed stable operation for ~300 hours with a net slight appreciation in performance. The apparent oscillations in the voltage, shown in Figure 4-33, are due to the effects of ambient temperature variation on fuel/air flow rates during a 24-hr cycle. A weak cell grouping in the center of the stack dropped suddenly after 312 hours, hitting a preset voltage limit at 0.65 V/cell and ending the test.

A review of Figure 4-34 reveals that the cell grouping that triggered the end of test was noticeably weaker than the balance of the stack on utilization. The intent with the more modest 60% fuel utilization operating point was to avoid pushing the stack to the point where local starvation was causing damage, but the operating point was clearly not conservative enough. Overall the stack was operated for over 2,500 hours.

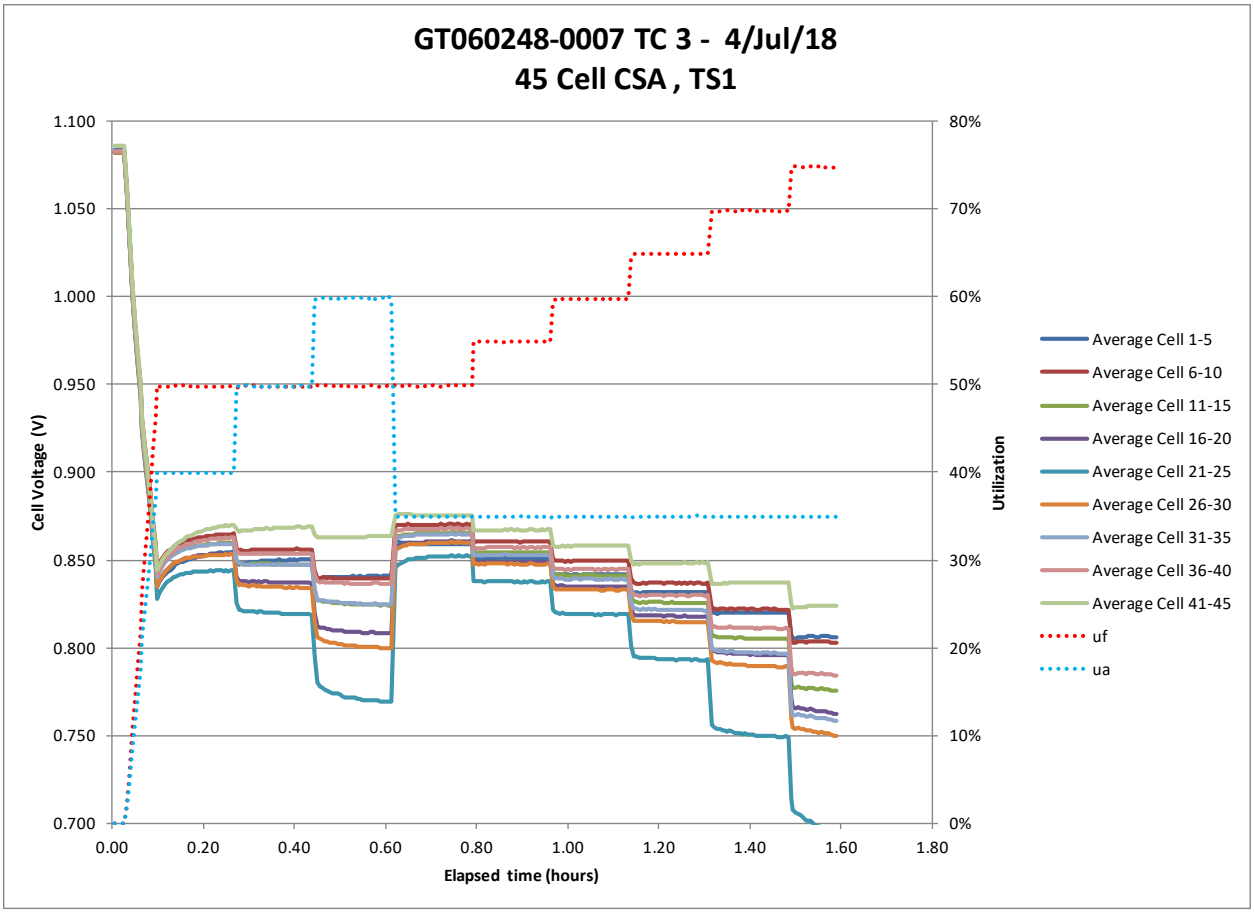

Figure 4-34: GT060248-0007 TC3 utilization testing (before reforming hold)

The stack was removed and autopsied with a particular focus on identifying potential bypass flow areas on the fuel side including a careful review of the weak section that failed the stack (Cells 21-25). This stack incorporated a change to the design and application of a dispensed alumina support layer on each interconnect. The intent was to reduce the potential for fuel bypass, and with the initial results it was thought that this change was successful. However, the test result indicates that this change was not sufficient to resolve the fuel bypass. Further actions to resolve bypass will be discussed below, after reviewing the two stack builds this quarter.

Two test stands were in need of commissioning, identified as test stand #7 and test stand #24. In addition, it was desired to replicate stack -0007 and demonstrate process repeatability. To expedite next stack fabrication and testing, stack -0008 was built using cells from inventory that were undersized (below design target) with the result that the effective sealing width was reduced. The as-built leak rate was higher than typical at 371 sccm helium at 0.5 psid, as compared to stack -0007 at 48 sccm helium at 0.5 psid. Figure 4-35 shows the utilization results with the stack showing weakness at 65% fuel utilization and unstable operation (steady voltage decrease) at 70% fuel utilization. This was also the first test in stand 24.

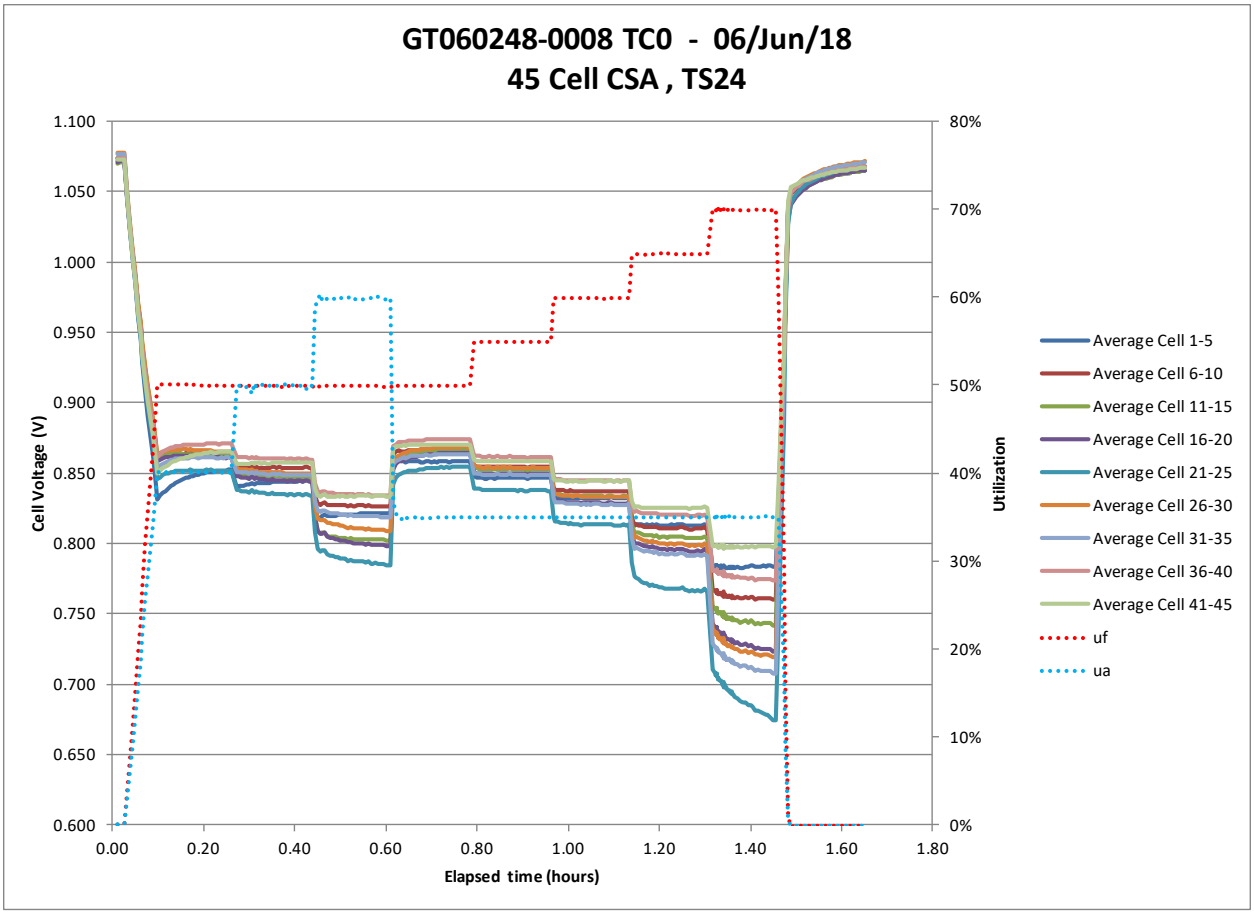

Figure 4-35: GT060248-0008 TC0 utilization test

The results on stack GT060248-0008 were sufficient for commissioning, but the high leak rate and poor utilization performance were not satisfactory. At the time the understanding was still that stack -0007 had run up to 80% utilization and remained a strong performer under those conditions; the mass flow controller error had not yet been discovered. This stack was subsequently used to commission stand #7.

Stack GT060248-0009 was built in another attempt to replicate the results of stack #7, this time using a subset of cells produced over the last year, hand selected to have the best dimensions. These cells encompass several process adjustments and were leftover from prior builds. The aim was to build another stack for commissioning and to replicate the performance of stack #7, and these cells provided the quickest path to getting cells within the target dimensions.

While the initial leak rate of 38 sccm helium at 0.5 psid was back in the expected range, the utilization performance was again quite weak (Figure 4-36). This result triggered further concern about the results reported for -0007, and ultimately led to the discovery of the mass flow controller problem with that test. So, while these stacks showed a substantial improvement over the earlier stacks in terms of fuel utilization and fuel bypass reduction, they did not perform to the level expected. It wss expected that these stacks should operate well at 80% fuel utilization or higher, giving good operational margin down to in-system design points closer to 65% or 70% fuel utilization.

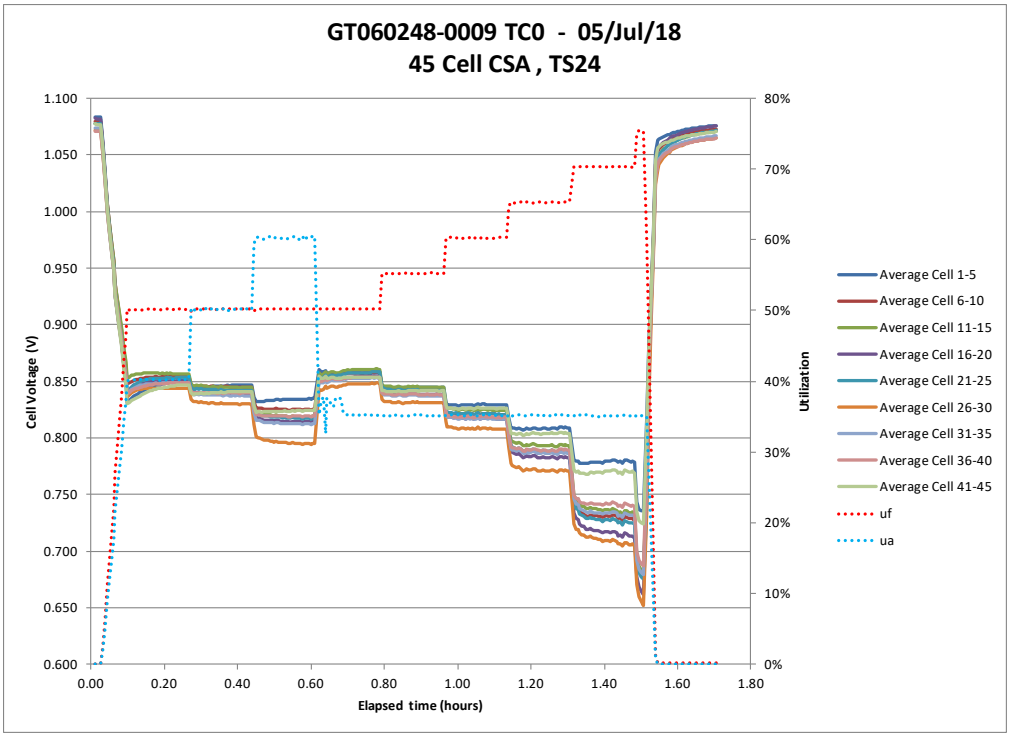

Figure 4-36: GT060248-0009 TC0 utilization test

The focus shifted back to resolving the issues related to the fuel bypass. There are three distinct areas of possible fuel bypass.

1. Top of center post and its seal to the top end plate
2. Bottom of center post and its seal to the bottom end plate
3. Vertical walls of center post and their seal to the inner edges of the interconnects and cells

Figure 4-37: GT060248 centerpost top (left) and bottom (right) interfaces

All three areas are sealed with a high solids loading alumina caulk (FCE proprietary). While this caulk is far from hermetic, the final structure is similar to the tape cast seals used (for example) in the LAS designs and is known to perform well enough to enable high utilizations, especially when the total sealed perimeter is small relative to the total active area as occurs in this stack. The CSA stack has approximately 25x less alumina seal length per unit active area as the LAS platform, and where it occurs is only between fuel inlet and fuel outlet or between air inlet and air outlet.

With this in mind, the search target was to identify areas where the caulked seal does not interface properly between components; leaving inadequate material or in the worst case direct openings through which flow can bypass. There is confidence that the top cap seal geometry is robust, and so the focus remained on the bottom and vertical seals.

To aide in isolating the root cause and to develop solutions, a dummy stack core was built that replicates the stack interfacing geometry, but that eliminates cells and glass-ceramic seals. The resulting stack core would hermetically separate fuel and air sides, and would be robust to multiple re-builds and thermal cycles. A subtle design change to the bottom of the center post was introduced to eliminate one possible gap at the base interface. This change and possibly others were evaluated in the dummy stack. The dummy stack enabled each of the three fuel bypass areas to be evaluated separately, which helped isolate where further development is needed.

A 40-cell stack was built, stack GT060248-0010. The cell count was reduced from 45 cells to 40 cells as a result of a simultaneous increase in cell thickness from 300 micron to 350 micron, and the desire to fit with the same pre-existing fuel and air manifolds which constrain the allowable total stack height.

The leak rate on this stack was better than 10x lower than the best prior stack, and it was hoped this would translate into stronger fuel utilization performance. This was not the case and the stack had utilization performance comparable to recent CSA stacks with stable operation at 65% fuel utilization and an unstable group of cells at 70% fuel utilization (Figure 4-38).

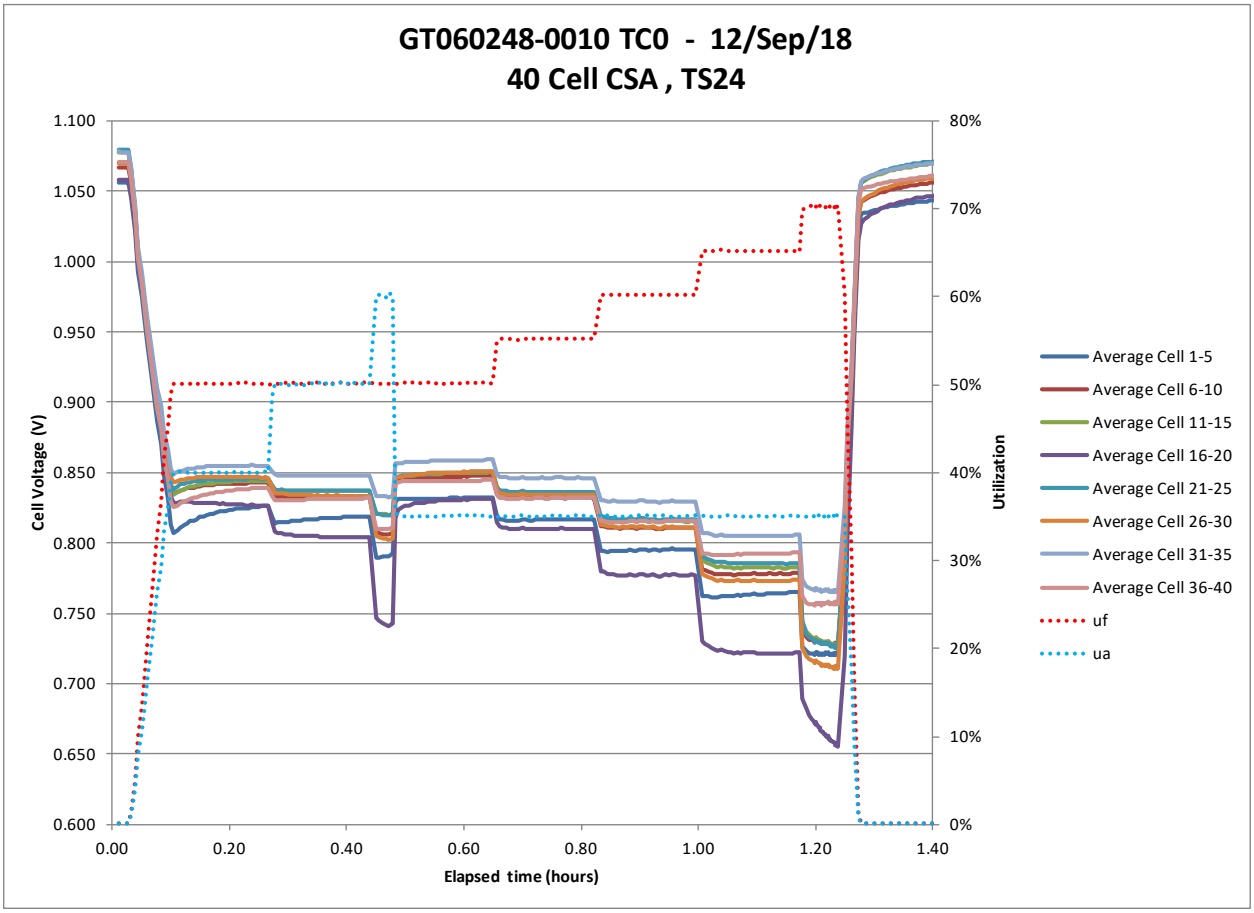

Figure 4-38 GT060248-0010 Utilization test – TSC3 cells

Also of note in this stack is the distinct groupings at OCV (far left and right of Figure 4-38) that is not normally observed, tabulated below:

Cell group	Cell type	OCV characteristic
1-5	3 print AFL	Low
6-10	3 print AFL	Mid
11-15	2 print AFL	High
16-20	3 print AFL	Low
21-25	2 print AFL	High
26-30	3 print AFL	Mid
31-35	2 print AFL	High
36-40	3 print AFL	Mid

As part of the process development cells had been produced with either two or three prints to build up the anode functional layer. Two is generally preferred, for the lower cost processing, but it was thought that a three layer AFL might provide a more uniform surface on which to print the electrolyte and therefore be a path to an improved leak rate.

No difference was discernable through the standard QC steps (dimensional and leak checks), but it seems like there is a difference in the stack. Interestingly, and with no explanation at this time, the results are opposite expectations. A better sealed cell would tend to have higher open circuit voltage by virtue of purer reactants (less depletion from leak and combustion) and also by virtue of lower temperature (again from less combustion). Both effects are minor at low leak rates, but this stack showed the lower OCVs on the three print AFL cells. The cause is not known at this time.

End effects can come into play, so the lower OCV in cells 1-5 might be explained by that. However the notably low OCV in grouping 16-20 is not so easily dismissed, especially when the utilization test (Figure 4-38) is considered. Cell group 16-20 was substantially weaker than the balance of the stack.

The test stand into which this stack was first installed had been configured for electrolysis testing, and an initial attempt was made to hold the stack in electrolysis mode. This was motivated partially by the fact that the TSC3 cells at 350 micron thickness had not been previously testing in a stack in electrolysis. The performance is shown in Figure 4-39. Again cell group 16-20 proved problematic, degrading substantially over a period of less than two days. At this point it was suspected that there was significant damage within that grouping of cells and the stack was shut down with the intent of performing an autopsy.

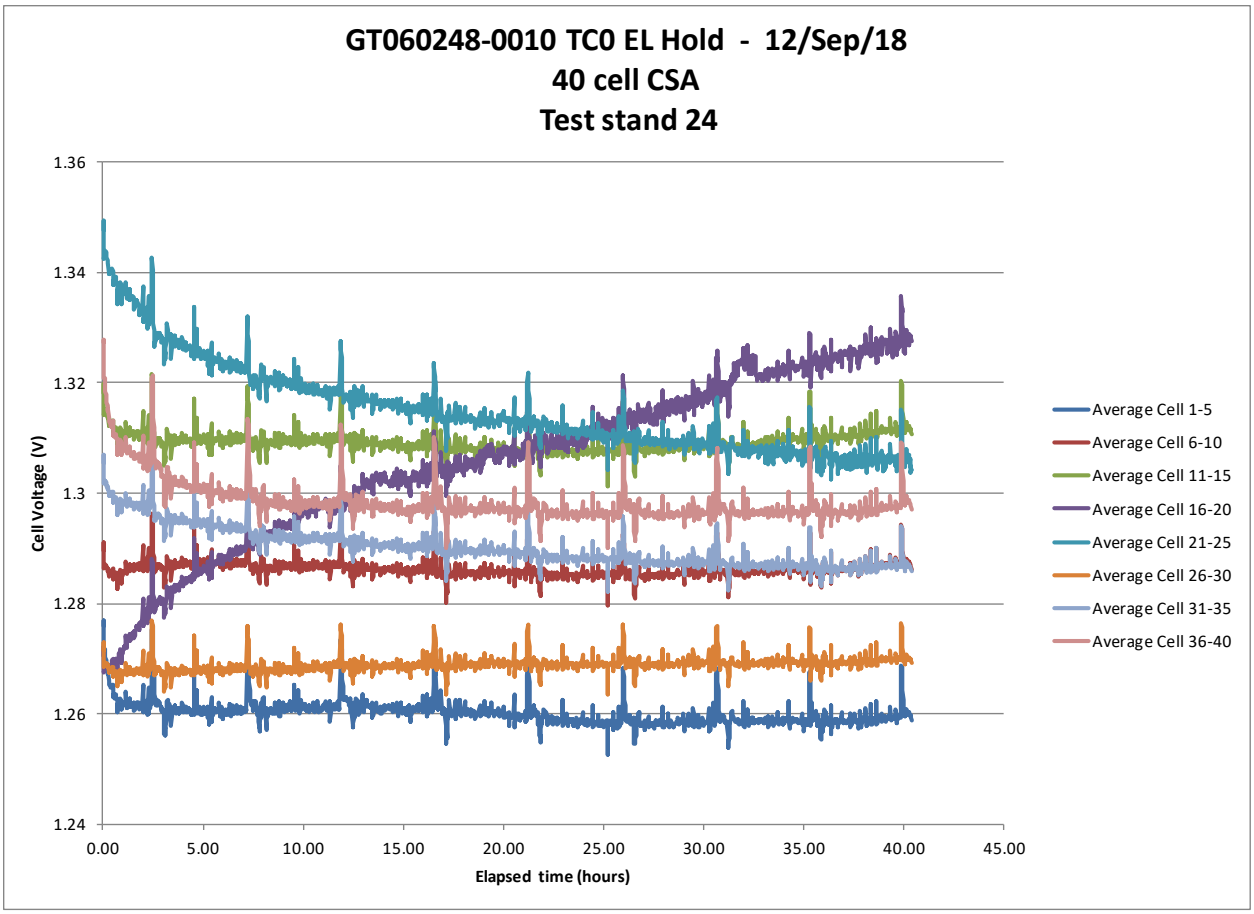

Figure 4-39 GT060248-0010 TC0 electrolysis hold

However a post test leak test showed a leak rate of only 5.4 sccm He and 0.5 psid, still substantially better than any prior CSA stacks, so the stack was re-installed for TC1 and fuel cell testing. While difficult, it is possible to connect voltage leads on every cell layer (unit cell layer height of 1.2 mm). With the foreknowledge that group 16-20 was weak, every cell layer in that grouping was instrument prior to the second heat-up.

The TC1 utilization testing with additional instrumentation revealed that cell 20 in particular was causing the majority of the losses in group 16-20, and that cell 18 was similarly weak although not as sensitive to utilization increases. These two cells also have the lowest of the measured open circuit voltages. Low OCV indicated either electrical leakage or gas leakage and combustion. Of the cell grouping 16-20, only cell 16 is not abnormally low compared to the other stack layers (Figure 4-40).

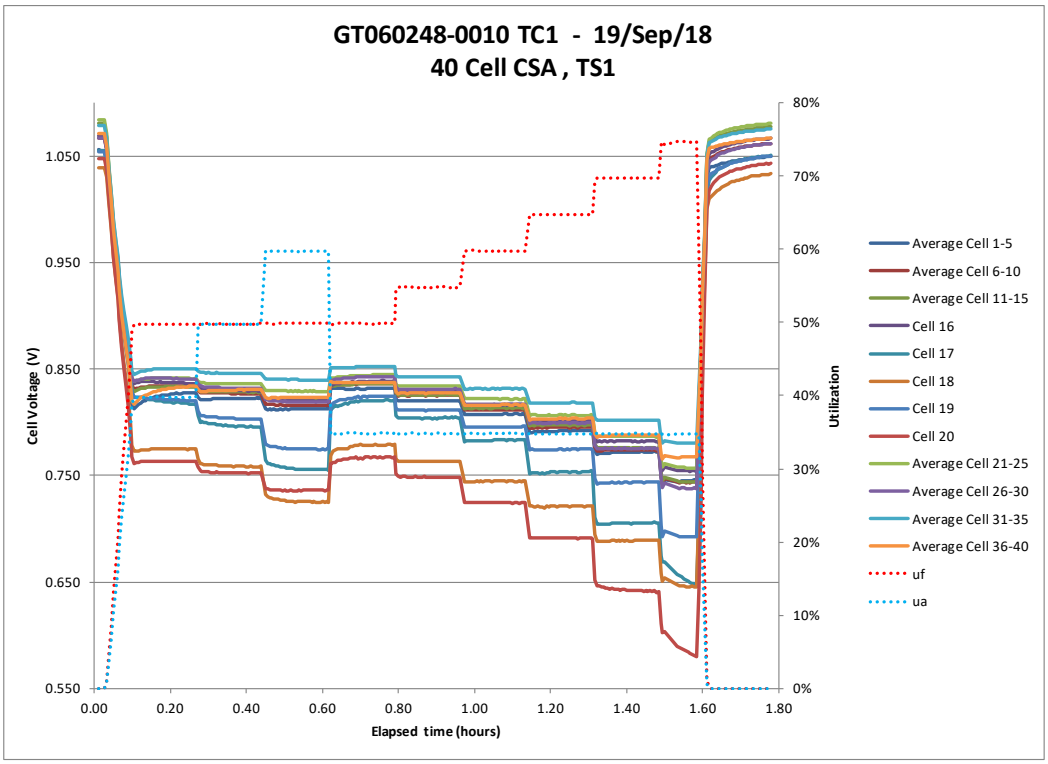

Figure 4-40 GT060248-0010 TC1 utilization testing

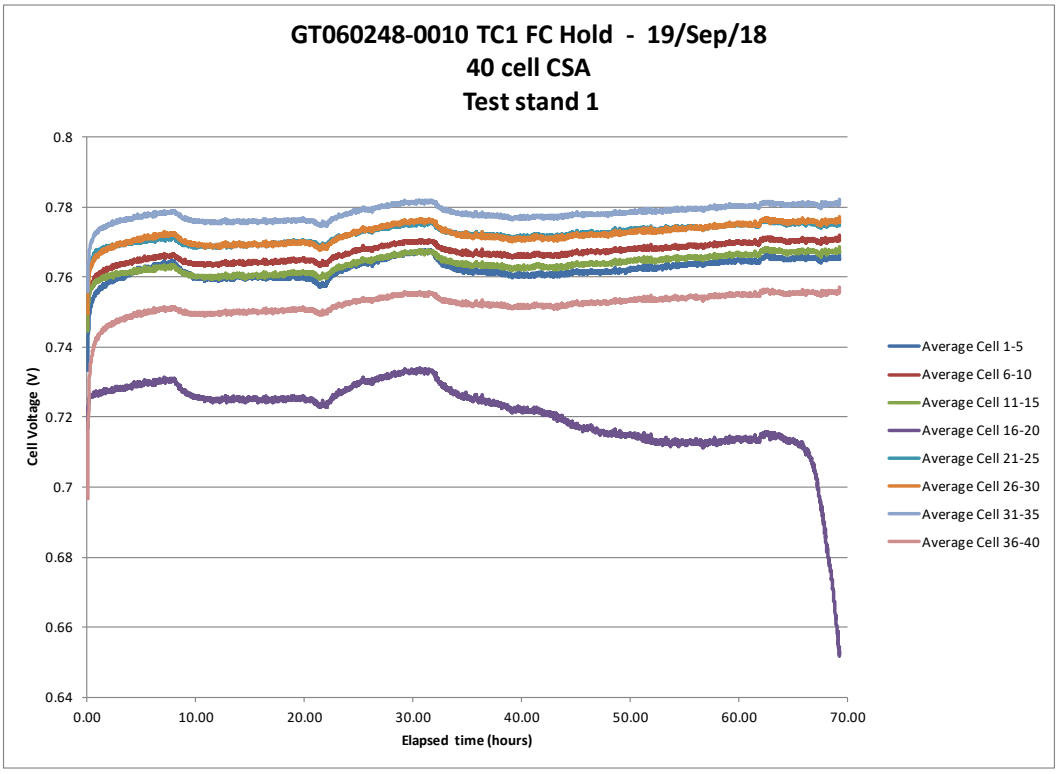

Figure 4-41 GT060248-0010 TC1 reforming hold

The stack was then transitioned into a reforming fuel cell hold with conditions of 0.29 A/cm^2, 60% fuel utilization, 40% air utilization, and 70% on-cell reforming. Due to a limitation in the test stand, it is not possible to simultaneously record the added voltage channels while maintaining low voltage protection. Low voltage protection triggers safe conditions for the stack on the event of a cell voltage channel dropping below a pre-set threshold. So for this fuel cell hold only the block voltages are recorded live.

Under these conditions cell group 16-20 started substantially low and stayed low for the duration of the test. Degradation of this group was higher than the other groups but gave some appearance of stabilizing after 50 hours. At this point in time a manual measure of cell 20 showed it was operating at 0.580 V. At 65 hours elapsed cell group 16-20 started to collapse and just before 70 hours the cell group 16-20 voltage dropped to 0.650 V/cell and triggered an automatic unload of the stack.

Stack GT060248-0010 was the first CSA stack built with the baseline TSC3 cells rather than the newest HiPoD cells. This strategic move was made due to better processing stability of the TSC3 as compared to the HiPoD. While this was generally observed to be the case in the production of the cells for this stack build, the results on this stack raise some concerns. While most of the stack operated reasonably, it was clear that there were individual cells that failed in ways not previously observed in the CSA stack. The OCV discrepancy also points to some quality issues in these cells still to be resolved.

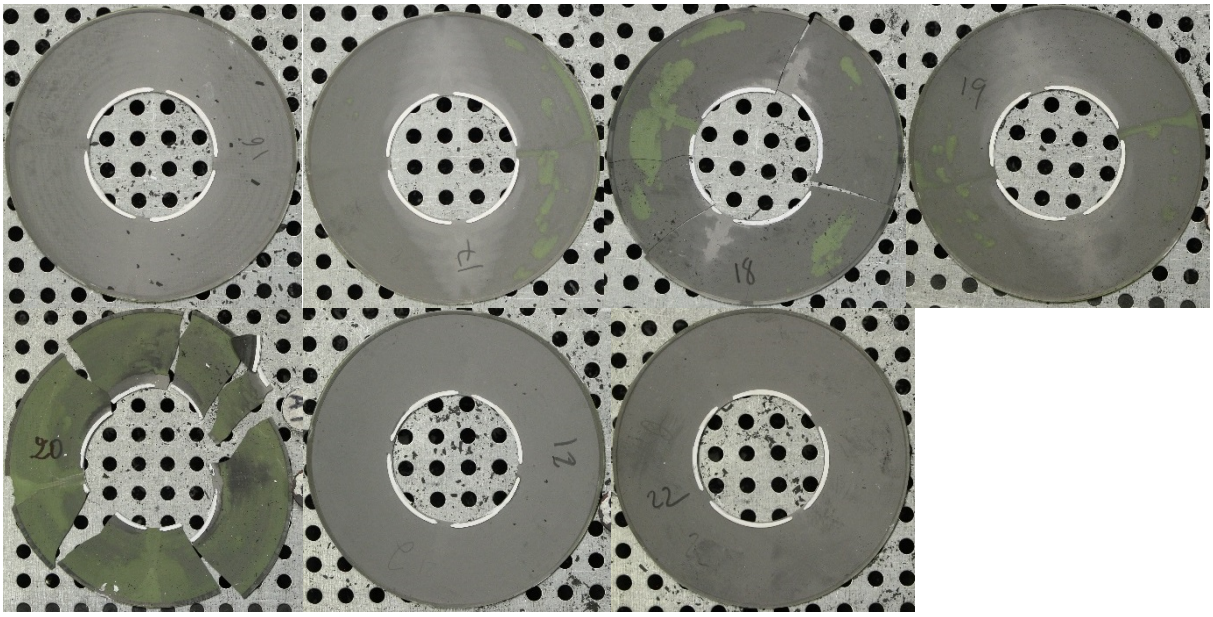

Figure 4-42 GT060248-0010 Cells 16-22 oxidation patterns

(Broken cells are a result of the autopsy process and were not broken during operation)

The performance observations were not consistent with stack level problems. The fuel utilization weakness previously observed is still present and is a stack level issue being pursued as described in Task 3 and Task 4. However the combination of a low leak rate, the OCV discrepancies and fact that much of the stack ran well, but the overall stack was constrained by just a couple of individual cells shows that there are unit cell level problems beyond the stack utilization weakness.

Upon autopsy it was observed that approximately 50% of the cells showed signs of anode re-oxidation through the electrolyte, and that while many of these were small and localized, cell 20

was almost completely re-oxidized and cell 18 was the second most oxidized cell in the stack. A sampling of the cells around cells 18 and 20 is shown in Figure 4-42. There was good correspondence between observed re-oxidation and observed cell performance in the stack.

It should be noted that due to a test fault, the reducing gas flow normally intended to protect the cell anodes during cool-down was significantly lower than intended. As a consequence it is likely that the re-oxidation patterns observed are larger than they would otherwise have been. In effect the flow fault has amplified the visual evidence of the cell faults, serendipitously making them easier to identify. The location of the re-oxidation patterns, away from the edges and manifesting as individual spots, shows that they are not due to any seal faults, and can only be the result of holes through the electrolyte.

As a result of these findings, the manufacturing team has been made aware of the results, an additional visual QC inspection has been implemented, and efforts are underway to improve the sensitivity of the cell leak tester. At this point multiple root causes were identified including some form of contamination that occurred during the switch from HiPoD back to TSC3 cells. This sort of re-oxidation pattern has not been previously seen with the TSC3 material system.

The transition away from HiPod cells and back to TSC3 cells was reported as were the results on the first CSA stack build with the TSC3 cells. As a reminder Figure 4-43 shows the utilization testing of GT060248-00010 with notable aspect being the wide voltage spread at OCV (indicative of leak) and the still weak utilization performance that although stronger than prior stack due to the improvements to the center post sealing, were still not at the level expected.

Stack GT060248-0010 incorporated all the flow bypass improvements, and the relatively poor utilization performance was a disappointment. During autopsy signs of through-cell leak were observed. In parallel, visual assessment at the half cell level revealed many surface flaws. Microscopy work was able to demonstrate that at least some of the visible surface flaws corresponded with holes through the electrolyte. As a consequence a visual QC step was added to the cell production process, sorting cells at the half-cell stage.

Stack GT060248-0011 was built with visually sorted cells, but was in all other ways identical to GT060248-0010. The difference is significant (Figure 4-44).

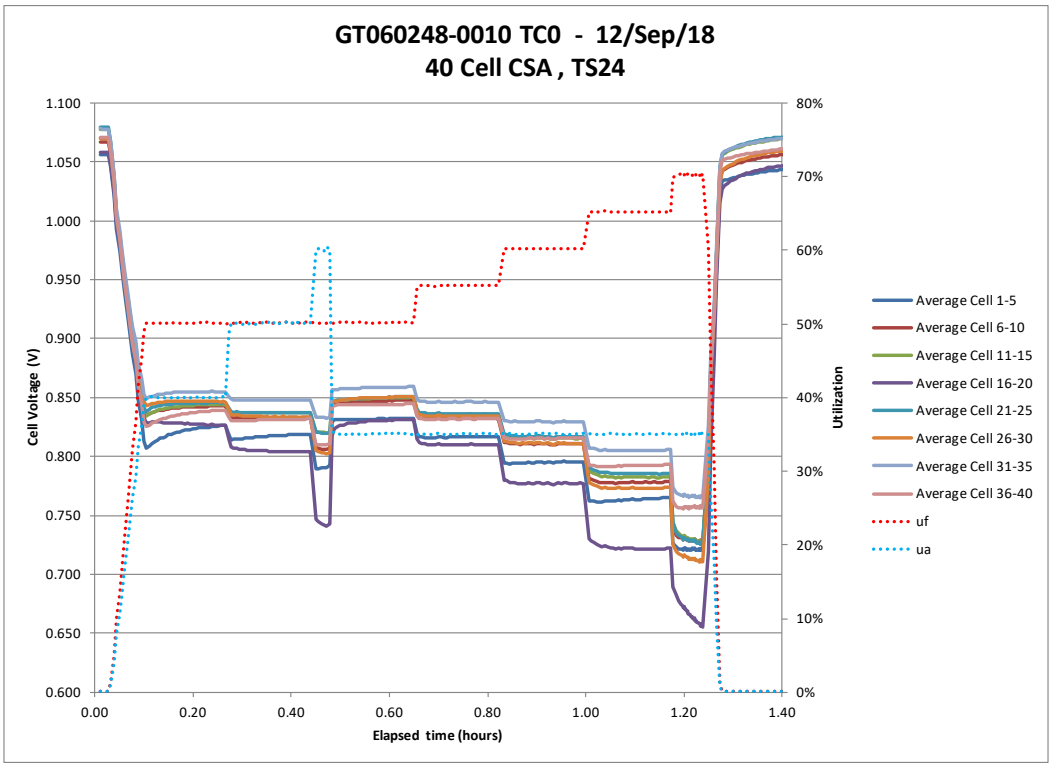

Figure 4-43 GT060248-0010 Utilization Test

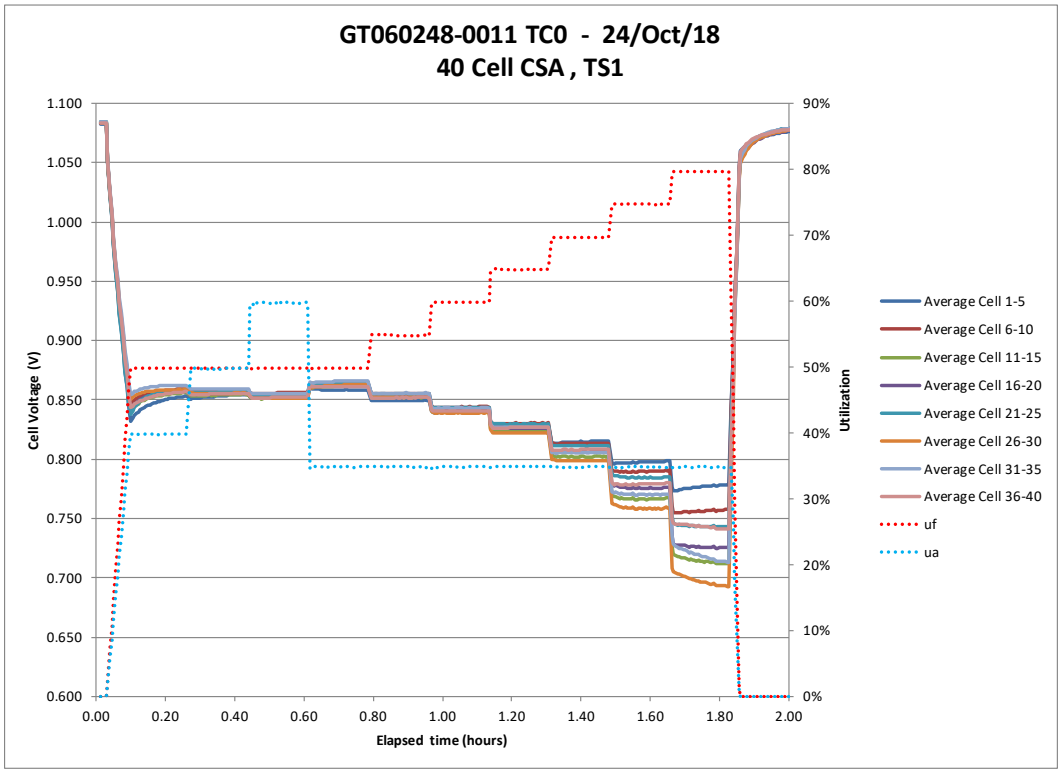

Figure 4-44 GT060248-0011 Utilization Test

GT060248-0011 had higher OCV, the OCV of the lowest cell group had higher OCV than the highest cell group on stack GT060248-0010, and much tighter OCV spread. These are signs of lower cross leak. In addition the stack operated stably at 80% utilization, as compared to weak results at 70% in the previous stack. The average voltage at 80% utilization was comparable to the average voltage at 70% utilization in the previous stack. These results demonstrate that the visual QC had significant benefit and that the observed flaws were negatively impacting cell performance.

Amid the positives of GT060248-0011, remain some areas for concern. The rapid increase in voltage spread at 75% utilization and 80% utilization shows that although the stack was operable at these higher utilizations, that there was still weakness. It is observed that the voltage cell group 31-35 was degrading during the 10 minutes at 80% utilization, indicating a weakness in that layer.

The stack was subsequently put into a reforming fuel cell hold at conditions of 68% fuel utilization, 40% air utilization, 0.29 A/cm^2, 37% DIR, corresponding to recent FCE SOFC system operating targets, with the exception of higher air utilization (40% vs 20% in system). The stack held for 160 hours before being manually interrupted when cell grouping 31-35 started to drop out (Figure 4-45). A review of the data shows that this group had in fact been dropping the whole time and only accelerated at the end. All cells were dropping somewhat faster than might be expected, although often stacks experience a settling-in period over the first 200 hours.

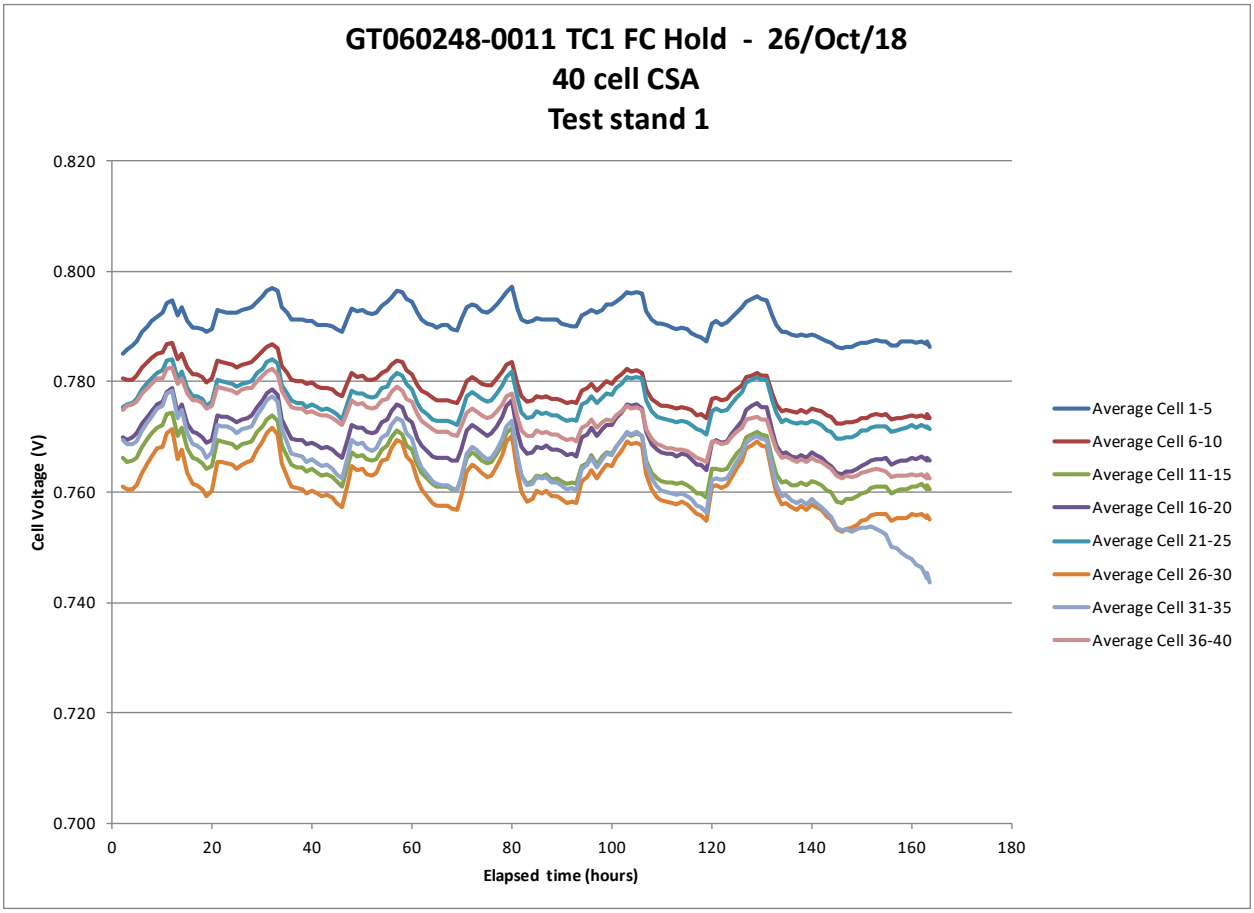

Figure 4-45 GT060248-0011 Reforming hold

Nonetheless, having seen the results on the previous stack, and with a cell group showing weakness, it was deemed prudent to remove the stack for autopsy, rather than run to the point of catastrophic failure.

Figure 4-42 above showed anodes of cells 16-22 of stack GT060248-0010. These cells are from the cell grouping that caused the end of test and the takeaway was the inconsistent but frequent findings of anode re-oxidation localized internal to the cell (away from any seals) demonstrated holes through the electrolyte.

Figure 4-46 shows the cells of note from the grouping 31-35 in stack GT060248-0011, the grouping that led to the end of test. The dropping voltage of that group was traced to cell 34 (left) which at the point of autopsy had severe re-oxidation and signs of cracking during operation. There is a question of which came first, the re-oxidation or the cracking, but clearly some of the observed cracking was caused by redox stresses. The main question was whether the redox was the result of some pre-established but smaller crack, or from more electrolyte leakage as evidenced in the previous stack.

Figure 4-46 GT060248-0011 Cells 34-36 oxidation patterns

A pre-existing crack could be a cell problem, but it could also be the result of a malformed seal, or from thermal stresses due to the stack thermo-mechanical design and the operating point. It is therefore of importance to assess the likelihood of one cause versus the others when looking to solutions.

An examination of cells 35 and 36 suggests that problems remain with the cell electrolyte. While not to the same extent as the previous stack, there is clear mottling of the anodes, localized and away from seal edges. These darker spots are indicative of shifting oxidation levels in the nickel, i.e.: of localize electrolyte leakage. So, while cell visual QC and sorting has significantly improved the stack performance, it seems clear that weaknesses remain. This sort of pattern was seen throughout the stack to various extents on difference cells.

The autopsy results triggered a review and rethink about the observed performance. Keeping in mind that due to spacing constraints that voltage monitoring is in groups of 5 cells, if there is one weaker cell in a group of 5, that weakness will be somewhat masked. It is observed that the voltage spread starts to increase at 70% fuel utilization, and that in particular the cell group 31-35 went from one of the stronger groups at 65% utilization to one of the weaker groups at 70% utilization. An operating theory for the results on GT060248-0011 is as follows:

- The cells continue to suffer from some electrolyte inconsistencies and internal leaks that are small enough not to be observed via impact on OCV and utilization performance (as

compared to stack GT060248-0010), but are large enough to show up as re-oxidation on the cells after operation.

- While at first glance looking relatively strong at 70% uf, a closer examination suggests some weakness in layer 31-35 primarily evidenced by the larger drop in voltage at that utilization step. As a consequence, running the stack at 68% utilization was operating much closer to the operating limit than was intended.
- When operating close to a utilization operating limit, the result is localized depletion of the fuel stream, leading to an increased risk or re-oxidation in areas where small electrolyte leaks are present.
- Re-oxidation of the anode results in significant volume change in the underlying structure and can damage the electrolyte. As such, a runaway condition can occur where localized re-oxidation causes electrolyte damage, which causes more leak, causing more damage, etc.
- It is theorized that cell 34 happened to have the worst combination of flow distribution and internal cell leak, leading to runaway damage when operating near the operating limit, causing the cell group to drop out after 160 hours.

So the root cause was surmised to be a combination of current cell quality limits and operation of the stack too close to its operating limits. This does not preclude the possibility that there remain stack and cell level flow mal-distribution effects, and this must be kept in mind as cell quality improved. In the meantime the approach to enable continued stack testing and development, is to operate at lower effective utilizations, giving time for the cell process to improve.

A 145-cell stack was built and tested for 1,000 hours this quarter, results are reported in Task 4.2.

4.2 Task 4.2 5-kW Stack Fabrication and Tests

Objective:

- Fabrication and testing of 5 kW demonstration stacks

Approach:

This task involved the design and fabrication of a 5 kW stack to verify the key design features of the low-cost anode, new cell components fabrication processes and, above all, the innovative stack architecture design. The goal was to demonstrate stable stack operation in a thermally self-sustaining environment for more than 1,000 hours with ≤1% degradation per thousand hours. The results of the 5 kW stack test and its performance is utilized for the Factory Cost Analysis under Task 5. The experimentally observed stack performance at NOC is used in the denominator for the calculation of cost ($/kWdc).

Milestones:

Milestone 4.3, Complete >1,000 hrs. Tests of the 5 kW Stack with <1% per 1,000 hrs.

Results & Discussion:

Initial trial builds were delayed due to challenges sourcing some of the end plate components. After braze development trials for the end plate brazements, stack build trials began in September, 2017. A no-cost time extension was requested and subsequently approved, to allow the stack design and process be demonstrated at the full stack level.

The path to the 5 kW demonstration became:

- Initiate production of TSC3 cells for CSA
- As soon as cells are available, start stack scale-up and use this as an opportunity to evaluate if taller stacks perform better in utilization
- In parallel, continue improving fuel bypass weakness and incorporate into demonstration stacks when available

A scale-up effort to production quantities was completed for a 340-cell stack. The transition back to TSC3 cells has not been as smooth as anticipated, with the first stack exposing some cell weaknesses that need to be resolved. At this time the production team is still stabilizing the TSC3 cell production process for the CSA stack and starting to build inventory towards the 340-cell build.

Prior to the 340-cell stack, three 150-cell stacks were built. This first-of larger cell-count CSA stack was built to exercise the manufacturing processes and equipment. It was built and funded under the separate project *DE-EE0007646 Modular SOEC System for Efficient H2 Production at High Current Density*. The build process went extremely smoothly, although the increased part count stressed some of the in-house part processing steps (primarily cell production).

Figure 4-47 shows the stack, GT060247-0001, just after the automated stack build process in the work cell. Figure 4-48 shows the stack after manifold install and installed into test stand #24. A Sharpie™ marker is in the photo to give a sense of scale. The stack is a little over 7” tall.

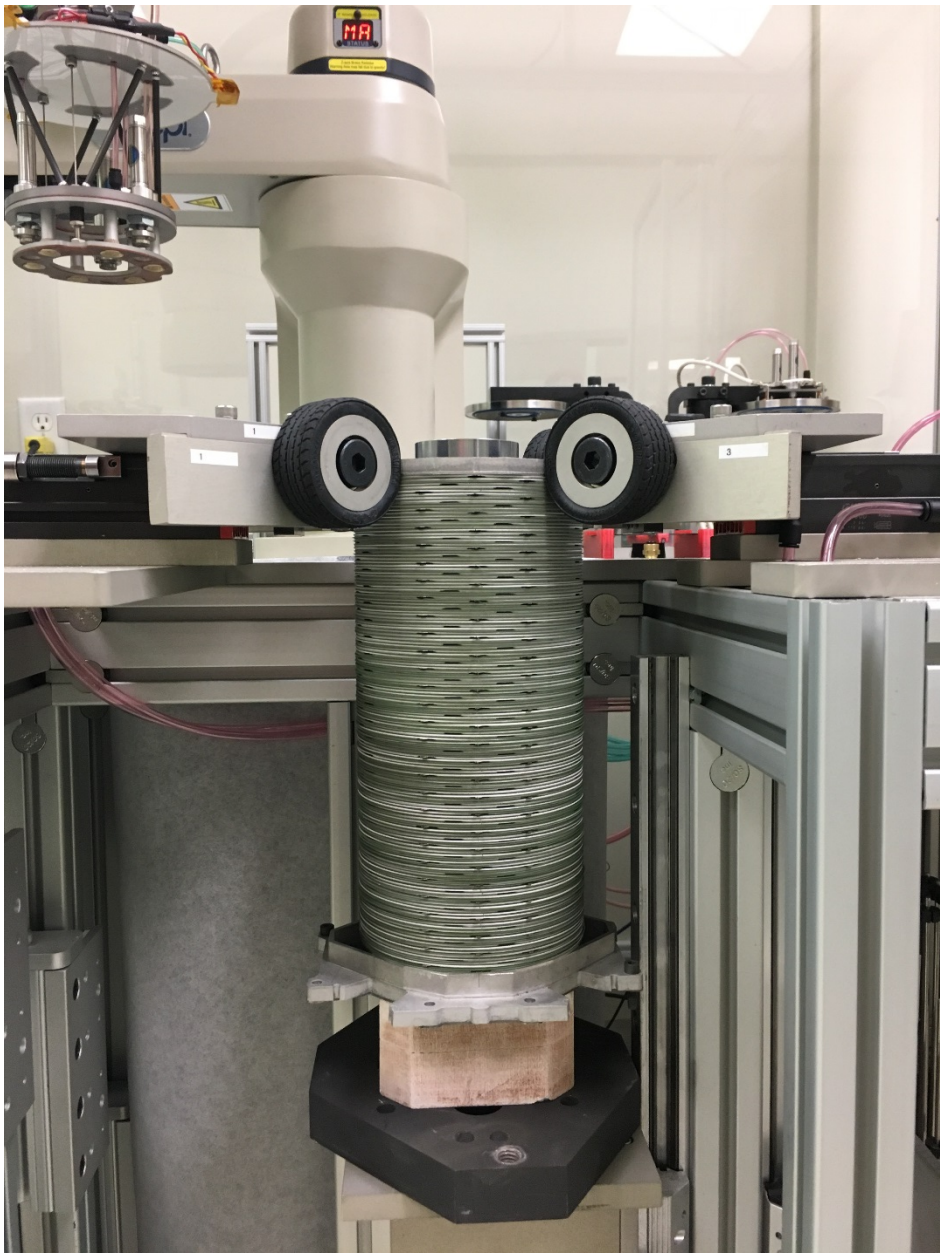

Figure 4-47 GT060247-0001 140-cell stack just after automated build

Figure 4-48 GT060247-0001 140-cell stack in test stand with Sharpie™ for Scale

This stack build is an important step towards full height stack builds (nominally 350 cells), and gave confidence in the build and firing process of the full stack. Unfortunately a failure in the test stand terminated the stack test early when liquid water was injected into the stack at 550 °C.

Due to continued challenges with cell yield, insufficient cells have been available for a full stack scale up. A second 150-cell stack, GT060247-0002, (145-cell in practice due to slightly thicker cells) was built and was subsequently operated for more than 1,000 hours on a natural gas, hydrogen, steam, and nitrogen blend, simulating an in-system gas composition (

Figure 4-49).

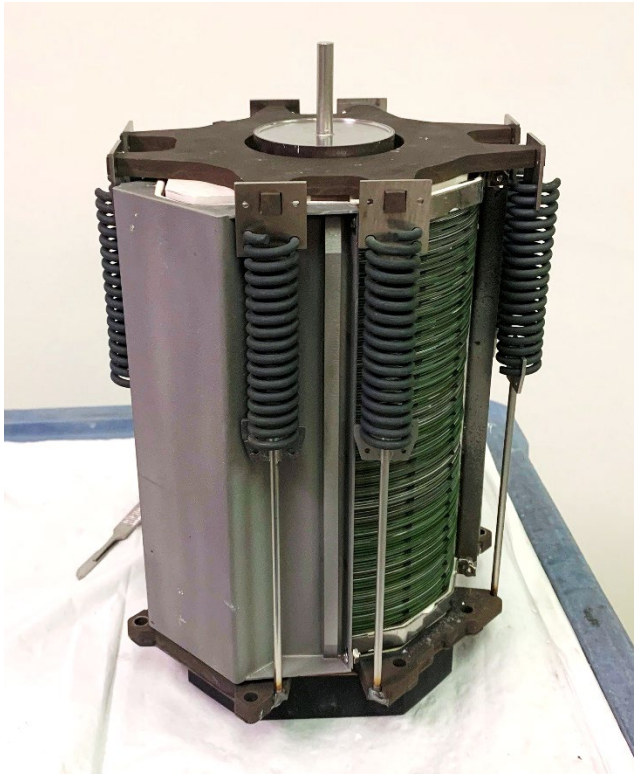

Figure 4-49 145-cell stack GT060247-0002

The stack was exposed to several unplanned test interruptions early in testing, including several where fuel flow was stopped while still on electrical load, a particularly harsh form of interruption. These test stand failures were eventually traced to failing solenoid drivers which, when too many were active simultaneously, were overheating and causing seemingly random failures of adjacent drivers.

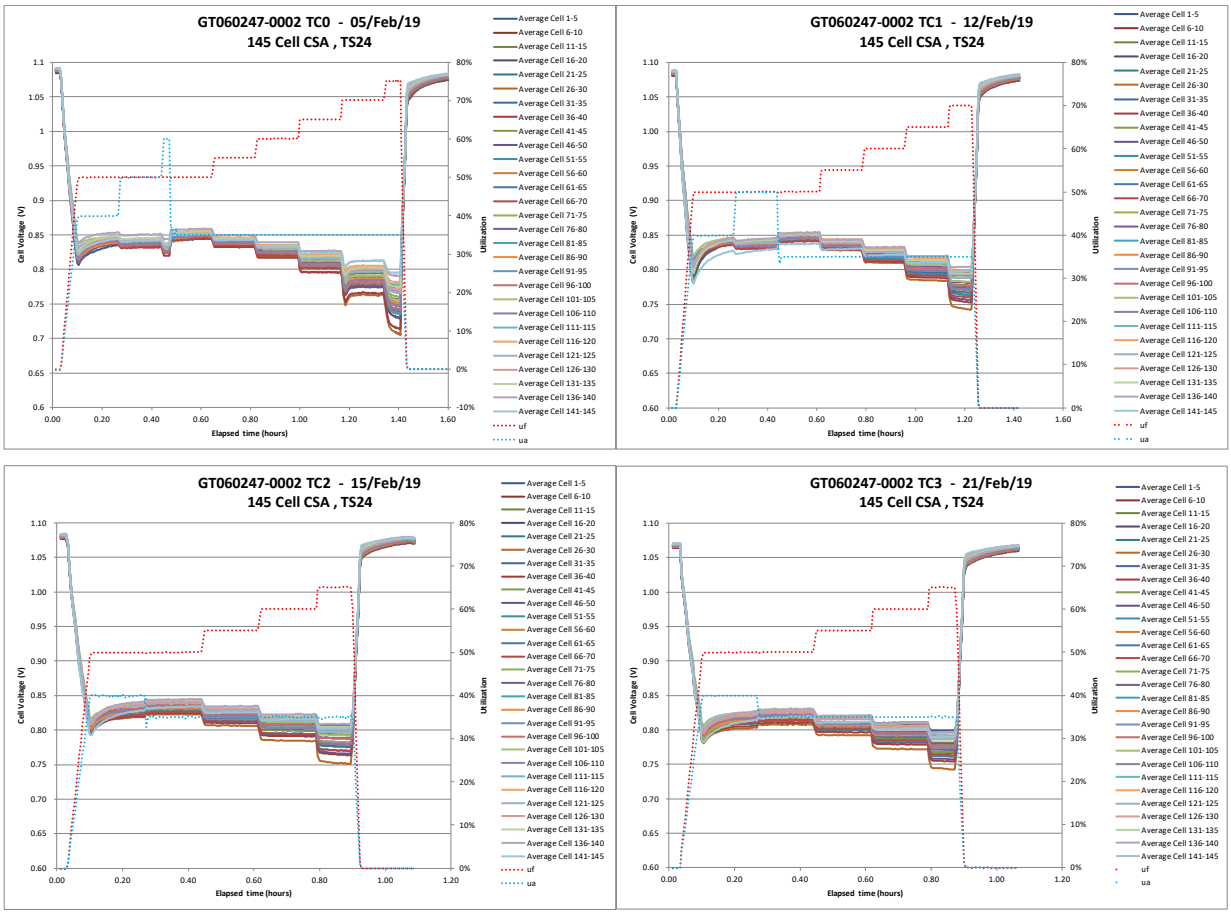

Figure 4-50 GT060247-0002 First three thermal cycles utilization testing

Figure 4-50 shows the utilization performance after the initial heat up, and for the three subsequent thermal cycles, each taken in an attempt to repair the test stand, but only the last having successfully eliminated the unplanned interruptions. Some damage to the stack is evident as the fuel utilization performance gets progressively weaker. At 65% fuel utilization, what started as an average cell voltage of 810 mV dropped to an average cell voltage of 777 mV by the third thermal cycle.

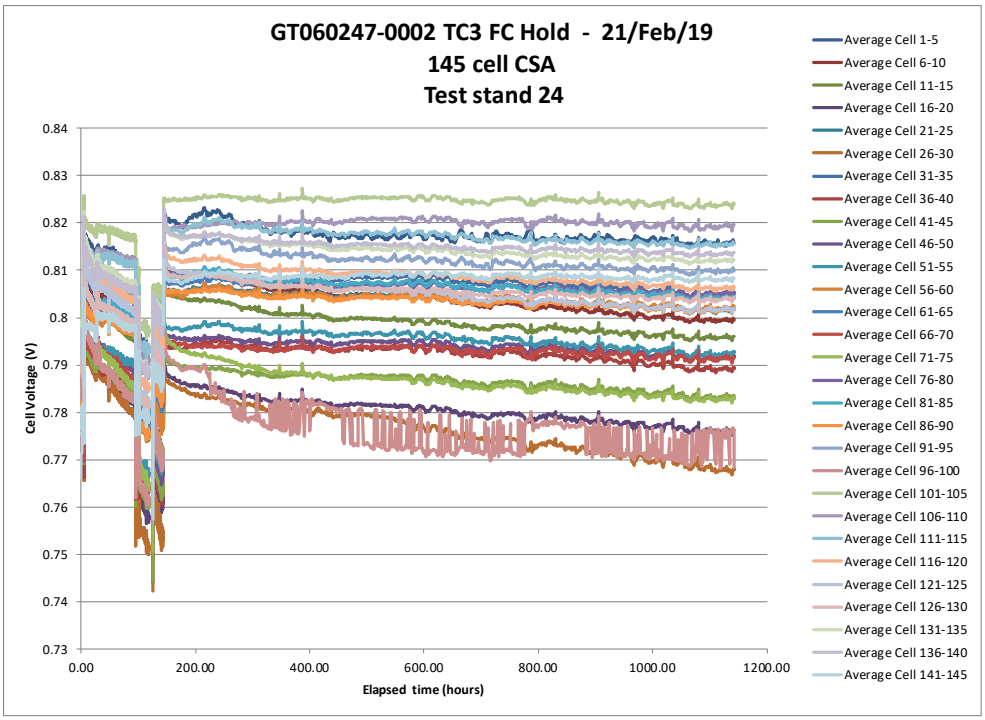

Figure 4-51 GT060247-0002 Fuel Cell Hold on Simulated Reformate

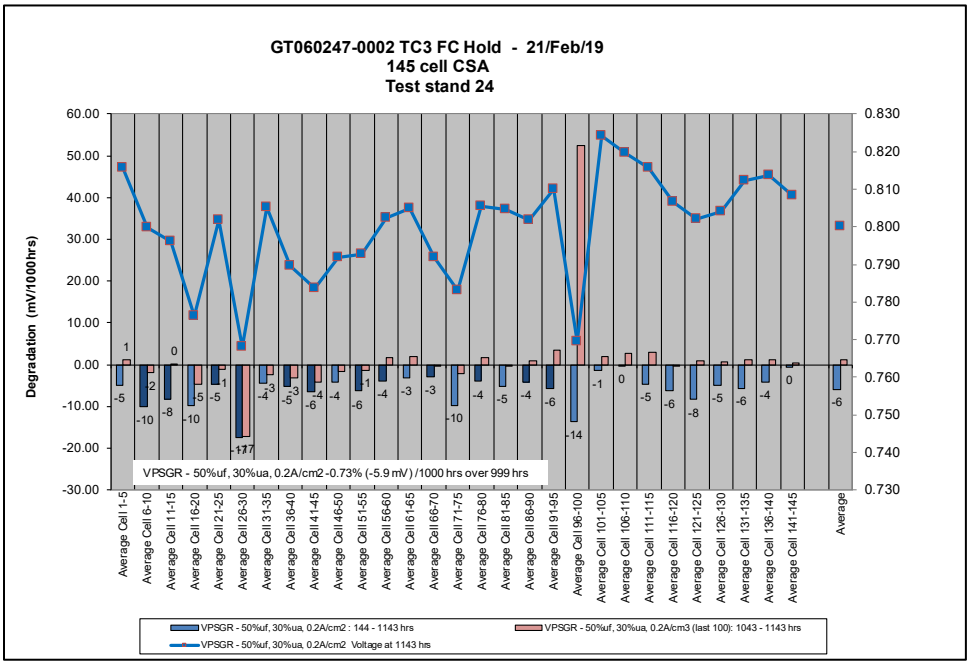

Figure 4-52 GT060247-0002 Degradation Rate by Cell Position

Figure 4-51 shows the cell voltages over an 1143 hour period operating on a simulated system reformate composition. The first 140 hours were spent assessing various operating points before settling on a final condition and holding for 1,000 hours. The operating point selected consisted of a simulated system reformate, including anode recycle and a pre-reformer. The composition was as follows:

Species	Percentage	Dry percentage
Natural Gas	6%	9%
Hydrogen (H_2 + CO surrogate)	44%	60%
Nitrogen (CO_2 surrogate)	23%	32%
Steam	26%	n/a

The operating point was chosen as representative of a possible system condition (variations on the level of within system pre-reforming can affect the composition), at a current density that would yield the 5 kW target power in a full sized stack, at a reduced fuel utilization of 50% in recognition of the damage and reduction in fuel utilization performance after the test interruptions and three thermal cycles.

Figure 4-52 shows the linear fit degradation as a function of cell position for the 1000 hour hold at the above conditions. Of note are:

1. The average cell degradation for the period was 5.9 mV/khr or 0.7% /khr[5].
2. The degradation was relatively uniform across the stack from bottom (cell 1) to top (cell 145)
3. Cells 96-100 were noisy, typically an indication of a broken cell
4. Cells 26-30 had noticeably higher degradation rate of 17 mV/khr

This stack, despite some test stand problems and the resulting damage to the stack, demonstrated the program targets with the exception of the output power, illustrating the potential of this technology direction. Following efforts focused on scaling to full sized (350-cell) stacks for the final demonstration.

The 145-cell stack GT060247-0002 was the first successful test of scaling up of the CSA stack after the first stack test was interrupted in a test stand failure. It demonstrated the performance required to meet this program's 5 kW goal once scaled to 350 cells, although with lower cell performance than was expected.

Subsequently a 45-cell parametric stack was built (GT060248-0013) which led to the discovery of one of the reasons for the low performance. Stack GT060248-0013 mixed two interconnect materials, about half were made from Sanergy HT base material, and the other half were made with SS441. There was no expectation of a difference, and this was seen as an opportunity to validate the replacement material (SS441) in preparation for using it in larger stacks.

However, testing showed a significant difference as can be seen in Figure 4-53. The blue traces represent the cell layers with SS441 interconnects. The pink traces the cell layers using the Sanergy HT material. At most conditions only the weakest of the SS441 layers was weaker than the strongest of the Sanergy HT layers. These results led to the discovery that a batch of interconnects had been manufactured upside down, putting the coatings on the incorrect sides.

This error has negatively affected performance where the inverted interconnects were used. This at least partially explains the lower than expected performance in stack GT060247-0002 reported.

[5] Evaluated against a starting voltage of 0.8 V/cell under load.

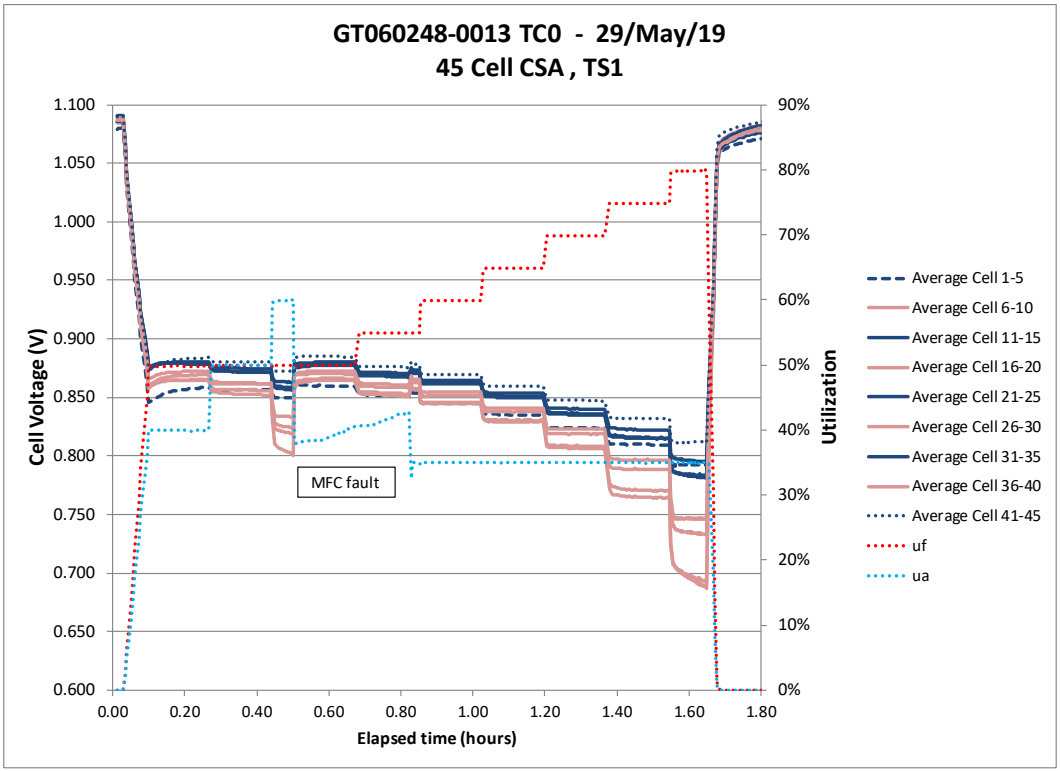

Figure 4-53 Utilization testing of parametric stack GT060248-0013

While built and tested under a separate program (DE-EE0007646 *Modular SOEC System for Efficient H2 Production at High Current Density*), the 150-cell stack, GT060247-0003, is of some relevance as it has demonstrated good stability over 1,800 hours of electrolysis operation, showing that the progression towards larger stacks followed an effective strategy to a successful conclusion (Figure 4-54).

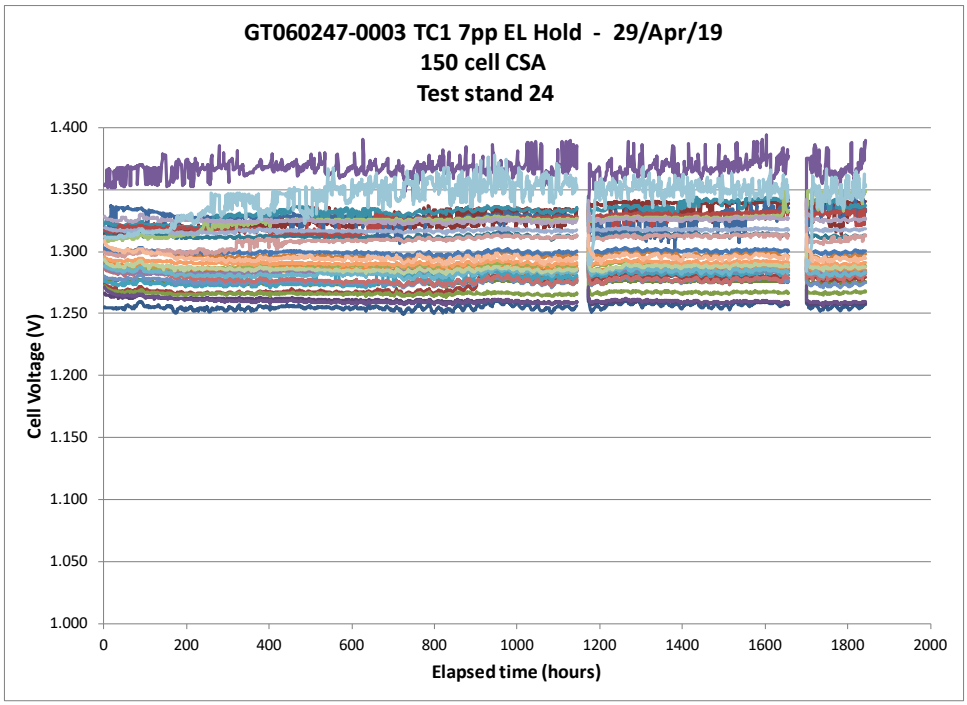

Figure 4-54 Electrolysis hold on stack GT060247-0003

The first full height CSA stack was built and tested in fuel cell mode, at greater than 5 kW. Due to the cells being slightly thicker than target there was a risk that a full 350 cell stack would have been too tall for the manifolds. With a desire to have a multiple of 10 cells for ease of instrumentation, the cell count was reduced to 340 cells for this build.

This was an opportunity to validate the production processes for the full height stack and in particular for the automated stack build. The only hiccup was with the cell feeding mechanism which had trouble dealing with the full weight of 340 cells. A fix has been implemented, but in the meantime the operator would reload the cell feeder part way through the build.

In order to exercise the process the stack was disassembled and rebuilt twice more, for a total of three builds. All three builds went smoothly, with no anomalies other than the cell feeder limitation. Each build completed in 52 minutes, it took longer to carefully disassemble the stacks manually than to rebuild in the automated work cell.

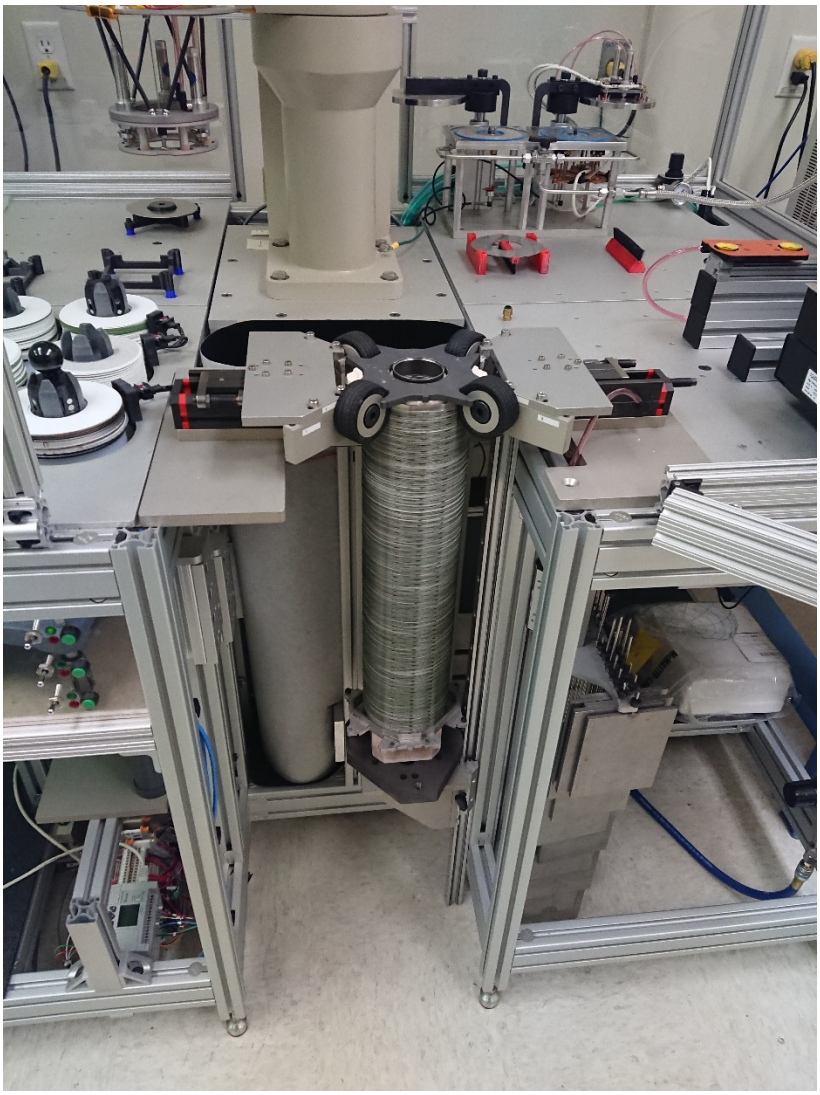

Figure 4-55 First full height CSA stack build

Figure 4-55 shows the stack core in the build table after the automated build. Figure 4-56 shows the stack installed into the test stand. The integrated (hot) compression springs are visible towards the top, as is the compliant current collection connection. One of the air manifolds is visible towards the front right, the second manifold is behind the stack.

Figure 4-56 First full height CSA stack installed into test stand

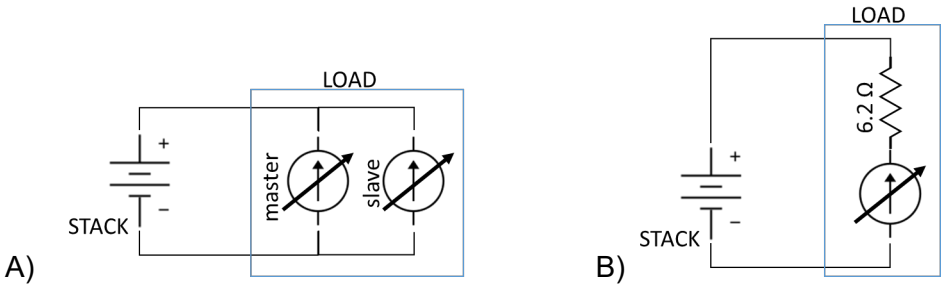

Figure 4-57 Load bank configurations

Testing of this stack, GT060081-0001, presented some initial difficulties. The test stand had been retrofitted with dual 4 kW Dynaload load banks arranged in a master/stave configuration (Figure 4-57A). This configuration had been commissioned and tested on previous stacks. However this was its first time running with a full height stack. Although rated at 400 Vdc, the slave load bank failed on initial connection to this stack (OCV ~ 370 Vdc). Since stack voltage is the only difference compared to prior tests, an internal insulation failure of some sort was suspected. The stack ran fully shorted through the load bank for approximately 40 seconds, with ~ 90A (1.11 A/cm^2) and ~0V total stack voltage.

The load bank did not recover from the failure and has been sent out for service. The remaining load bank (the original master) continued to operate normally but is power limited to 4 kW and so could not support the 5 kW program target. In order to achieve 5 kW, an old load bank (Torkel 840) was recommissioned and configured as a constant resistance load (Figure 4-57B). In this way the Torkel could dissipate ~2 kW at full current, while the original Dynaload could remain under test stand control. With this configuration the test was able to proceed at > 5 kW.

The test conditions are as follows:

- 18 A (0.222 A/cm^2)
- 50% fuel utilization, 35% air utilization
- Simulated reformate:
    - 8.6 dry% Natural gas (desulfurized)
    - 59.8 dry% Hydrogen (H2 & CO surrogate)
    - 31.6 dry% Nitrogen (CO2 surrogate)
    - 26% humidity

  This is representative of an anode recycle system with recycle sufficient to ensure water independence)
- Corresponding to:
    - 37% stack level internal reforming
    - 100% system level internal reforming

The resultant cell voltages are as shown in Figure 4-58. General observations include:

- The voltage distribution is tight, within 20 mV average cell voltage top to bottom. This is indicative of good vertical flow distribution, validating the manifold sizing and configuration for the full height stack. This also validates the thermal design and the ability of the stack to present similar thermal conditions top-to-bottom.
- Operation is stable, all cells are responding roughly the same with time. This suggests a good overall build with no localized differences that might lead to different degradation characteristics

- The cells appreciated in voltage over the first ~550 hours. While the cause of this is unclear, the shorting event previously described may have contributed to this behavior. While shorted and running at around 90 A, there would have been insufficient fuel present to react with the transported oxygen ions which would therefore begin to oxidize the anode functional layer and anode support of the fuel cells. i.e.: This would have been a short term but aggressive redox event. It is suspected that at least some of the cell appreciation is a slow recovery from this redox event.

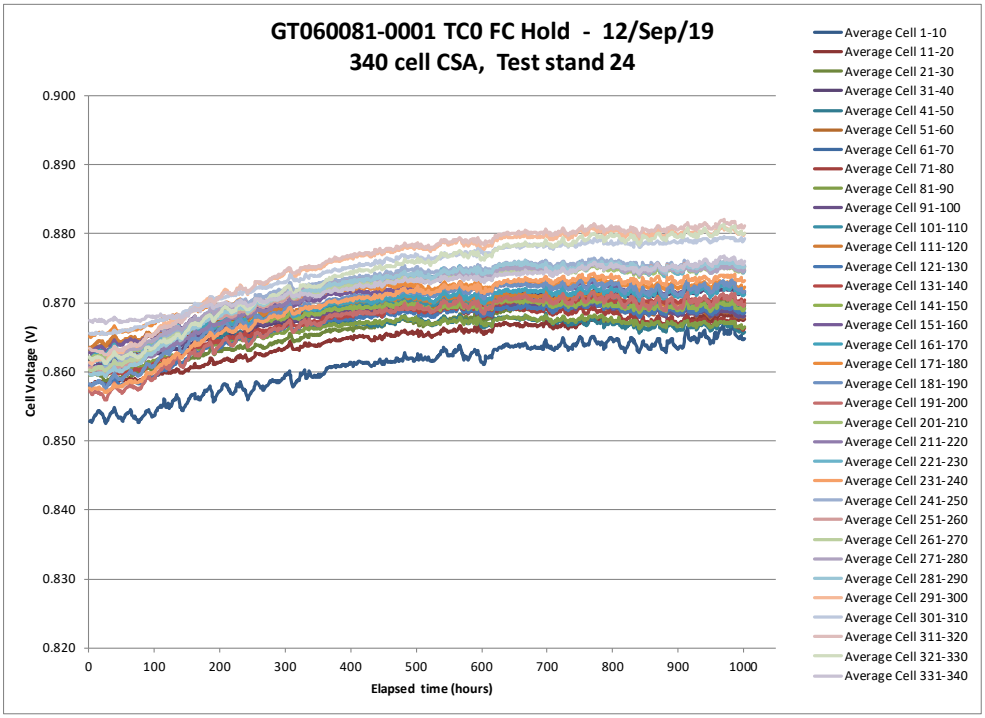

Figure 4-58 GT060081-0001 Fuel cell degradation test

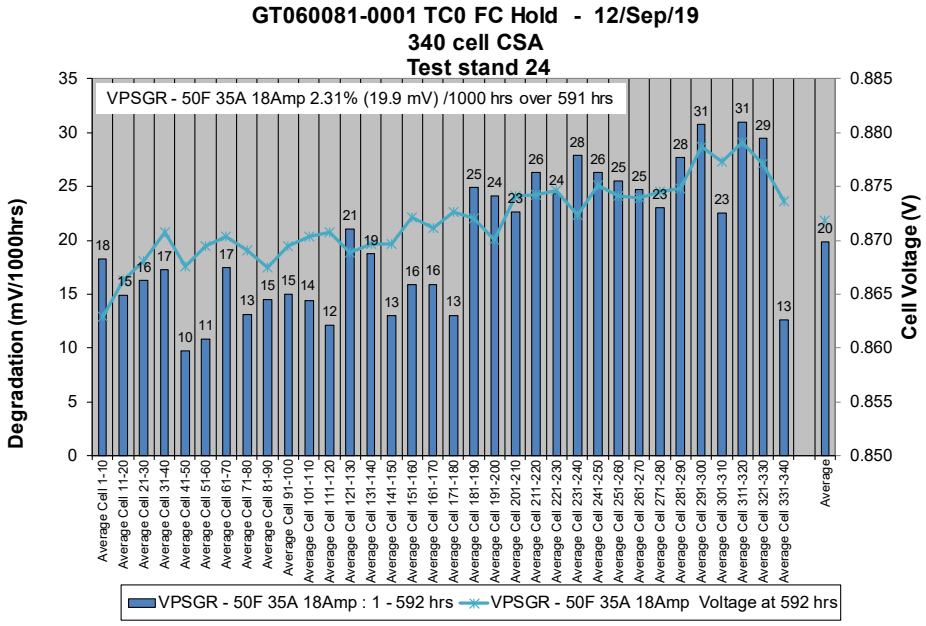

Figure 4-59 GT060081-0001 Degradation by cell position, 0 to 591 hours

Figure 4-59 shows the same data replotted as average linear fit degradation rate over the first 591 hours. Positive values indicate an increase in performance over the hold. This graph shows the overall uniformity of the stack. There is a slight trend towards higher voltages with cell number, and a slight trend towards more voltage recovery with cell number. There is a correlation here with cell thickness, which were ordered from thickest (400 micron) to thinnest (290 micron) through the stack height. Generally thinner cells will show somewhat better performance, and are less robust to redox, so these results are in alignment with the cell thickness and the shorting event, however it is difficult to determine if there is truly a causal relationship between these events and results.

Figure 4-60 shows the cell-by-cell degradation profile for the full test period. Again all cells show improvement with general uniformity across the stack in both voltage change (bars) and end of period voltage (line). Although there were many challenges getting to this point, it is encouraging that the first full height stack build is showing uniform and stable operation over this 1,000 hour hold, despite some test stand problems at the start.

Figure 4-61 shows an overview of the full height CSA stack test under simulated reformate powered fuel cell operation. The stack has completed 1,000 hours of testing with an overall improvement in performance, driven largely by a sharp recovery over the first 500-600 hours followed by relatively flat performance over the balance of the 1,000 hour hold. The stack maintained > 5 kW for the full 1,000 hour hold, with a stack voltage between 293 V and 297 V.

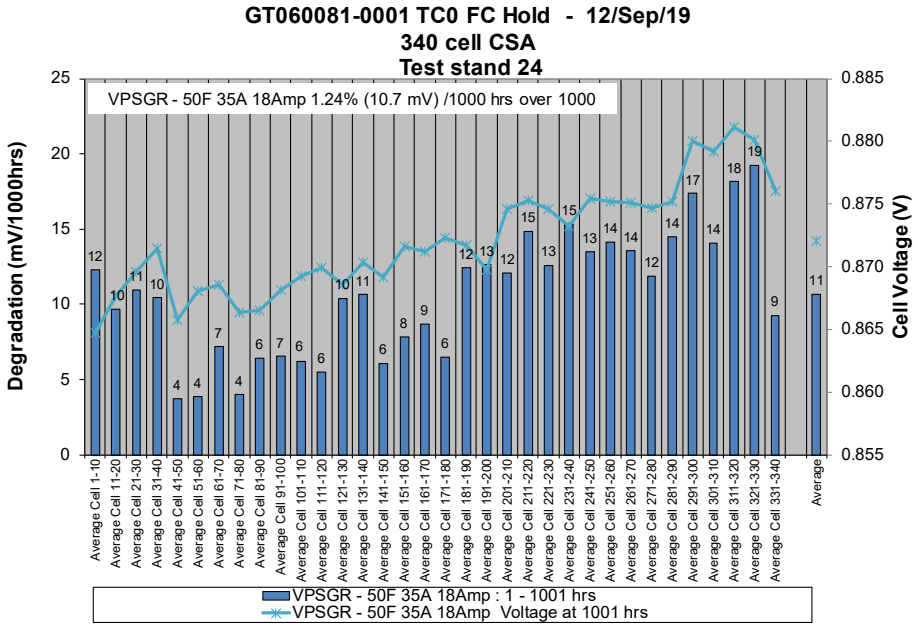

Figure 4-60 GT060081-0001 Full period degradation by cell position

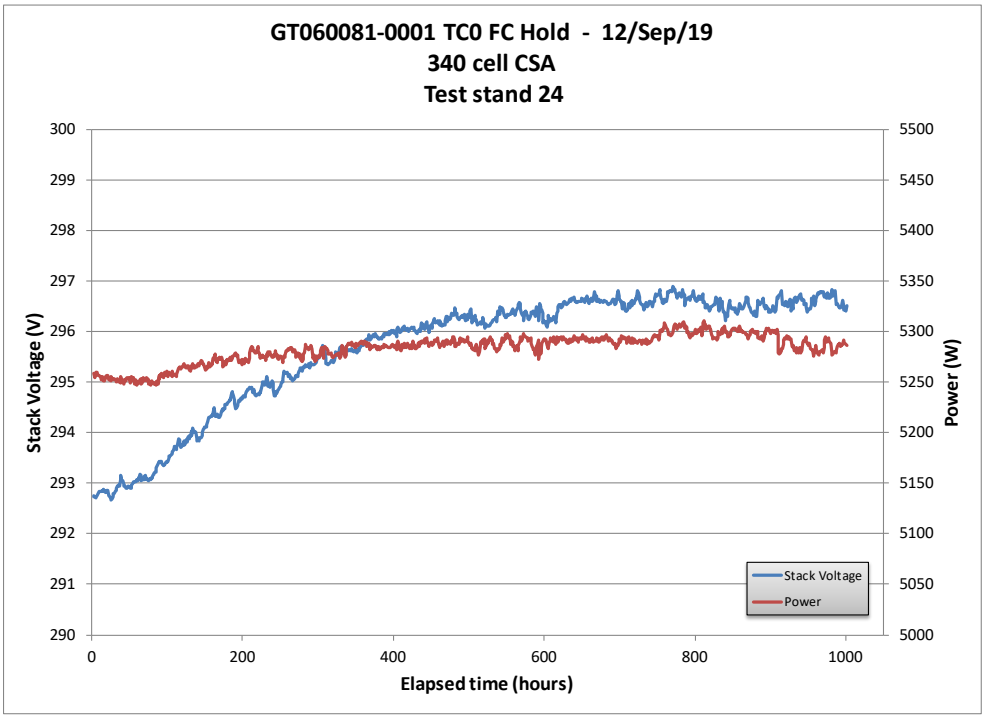

Figure 4-61 5 kW Innovative SOFC demonstration test

The testing continued and the stack accumulated in excess of 1,700 hours of operation on load. Figure 4-62 shows an overview of this testing. As previously reported all cells appreciated in voltage over the first 1,000 hours. This is somewhat atypical and is likely due to slow recovery from the shorting event that occurred on an initial loading event, when a load bank failed.

In general there is a tight grouping of cell voltages over the entire period and generally stable operation. However there are also signs of degradation in parts of the stack starting around 1,000 hours elapsed. Figure 4-63 shows the same test results replotted as linear fit degradation by cell position, from bottom (cells 1-10) to top (cells 331-340). The degradation is plotted for the full period (blue bars) and for the last 750 hours (red bars).

Over the entire hold, the stack averaged a 3 mV/cell/khr improvement. The weakest cells (Cells 71-80) degraded a modest 6 mV/khr or approximately 0.7% /khr. However it is evident in the degradation distribution that the lower third of the stack is degrading faster than the rest of the stack. The behavior is qualitatively similar in the last 750 hours of operation, with the majority of the stack degrading at 2 to 6 mV/khr and the lower third degrading much faster with the same weakest cell grouping degrading at a relatively high 19 mV/khr.

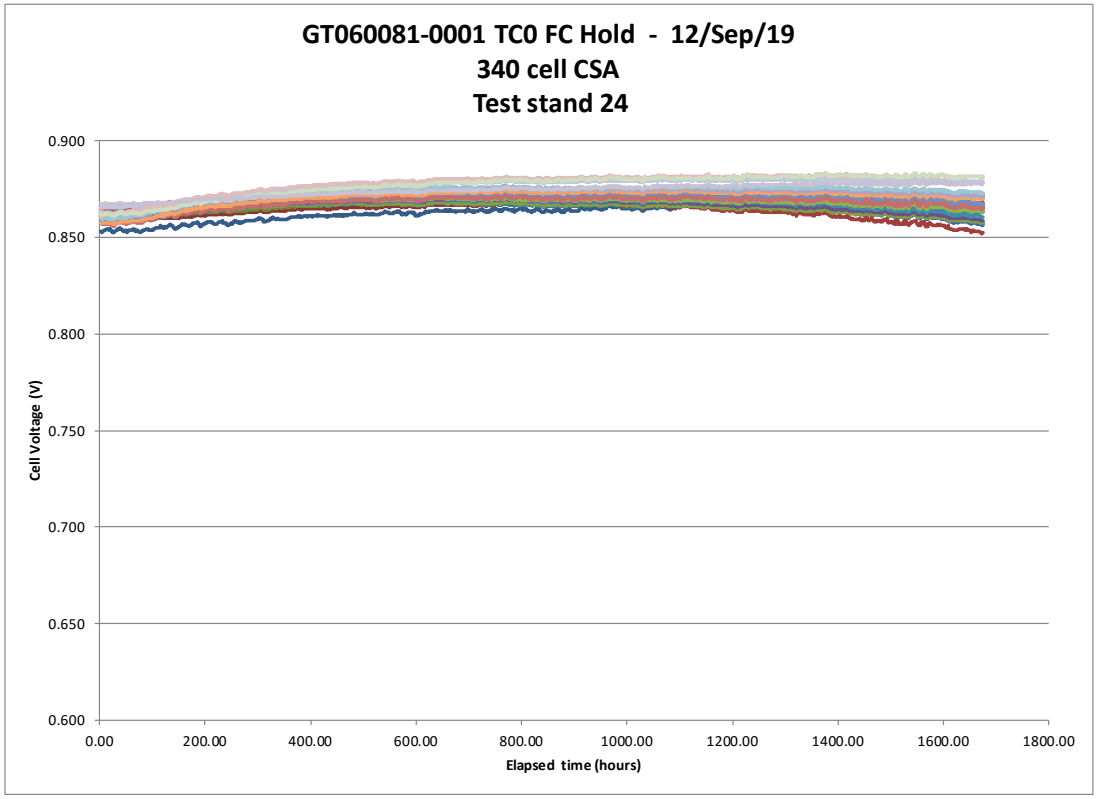

Figure 4-62 340-cell stack GT060081-0001 5 kW reforming hold

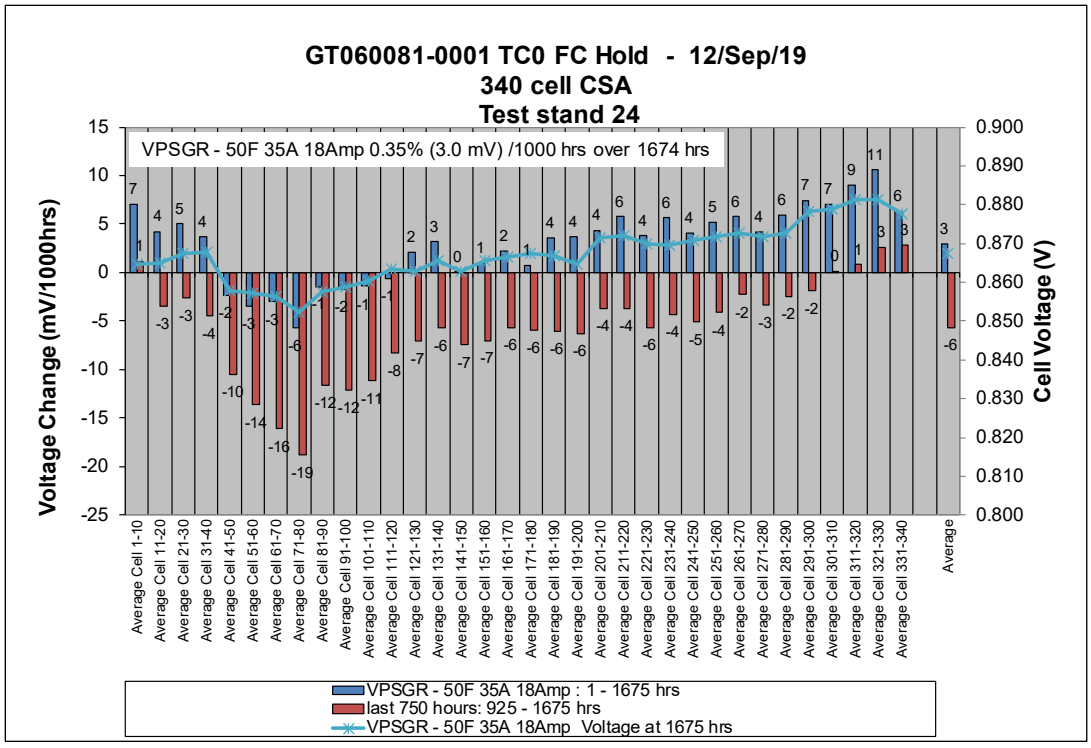

Figure 4-63 Stack GT060081-0001 Degradation by Cell Position and Time

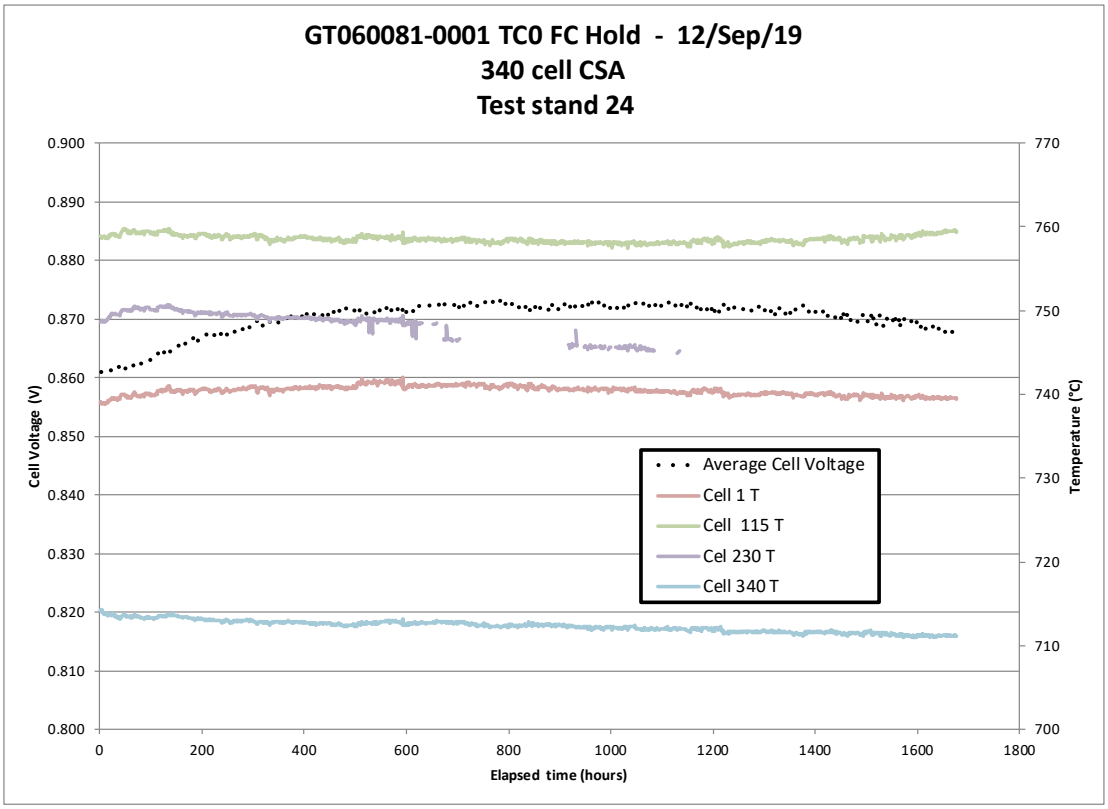

Figure 4-64 Stack GT060081-0001 In-stack Temperatures

Figure 4-64 plots four in-stack thermocouples through the height of the stack over the same time period. While three of the four thermocouples show a slight cooling of the stack with time, the thermocouple located within the section of the stack that is degrading faster is both the highest temperature, and starts to increase in temperature at around 1,200 hours elapsed.

Temperature is only an indirect measure of what is happening in the stack, however some tentative conclusions can be drawn. First, the hottest part of the stack is in the region that ended up degrading the fastest, and this is true right from the start of the test. This suggests that the cause of the higher temperatures in that section of the stack may be related to the higher degradation in that section. The relatively modest temperature difference (~10 °C) shouldn't in itself cause significantly higher degradation.

Figure 4-65 replots the cell voltage data, showing the voltage profile in the stack every 100 hours of operation. This graph illustrates that while the voltage distribution was relatively even at the start of test, it progressively improved over time, with roughly twice the improvement towards the top of the stack around cells 71-80. In addition cells 71-80 and neighboring cells started to degrade much sooner than the cells at the top of the stack, and were degrading faster than the top of the stack.

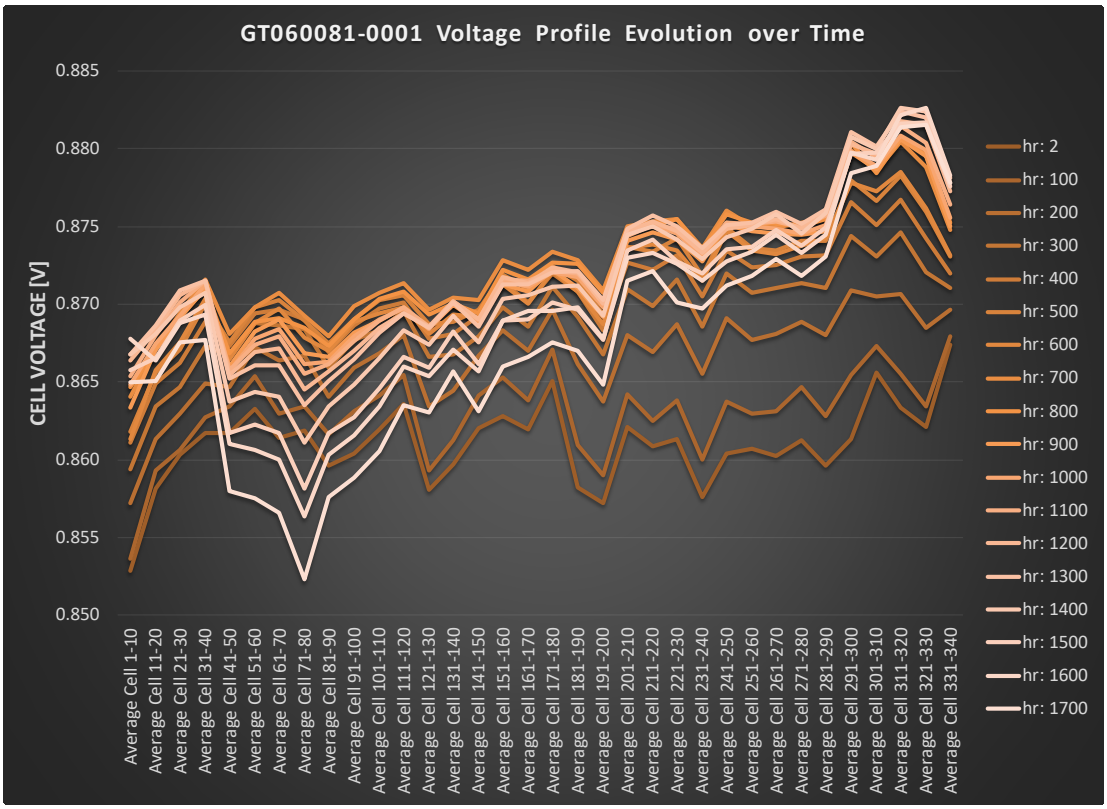

Figure 4-65 Stack GT060081-0001 Voltage Profile Evolution with Time

These voltage results, together with the temperature data, suggest that while the stack started with roughly even performance, implying roughly even electrochemically induced heating, that there were external factors making the bottom third of the stack hotter, and that the bottom third of the stack degraded sooner and more rapidly, perhaps as a result of those external factors.

Figure 4-66 shows a flow model of the original air inlet flow (with which the above testing was carried out) on the left, and a revised inlet flow geometry on the right. The flow lines for the original layout show a significant portion of the inlet flow is travelling towards the top of the stack.

This might explain the observed temperature and degradation behavior. With the relatively cold inlet air travelling primarily towards the top of the stack the result will be additional cooling towards the top of the stack. This would explain why the in-stack thermocouple shows the higher temperature in the lower third of the stack. Noting that the in stack thermocouples are point measures, and that the closest thermocouple (layer 115) is relatively far from the layers showing the highest degradation (Cells 71-80), it seems plausible that the temperatures were even higher than indicated in the lower cells. The profiles of performance and degradation are also consistent with a thermal or flow effect in that they are relatively smooth from the bottom to the top of stack. In contrast, degradation attributable to cell, seal, or interconnect manufacturing would tend to be distributed randomly.

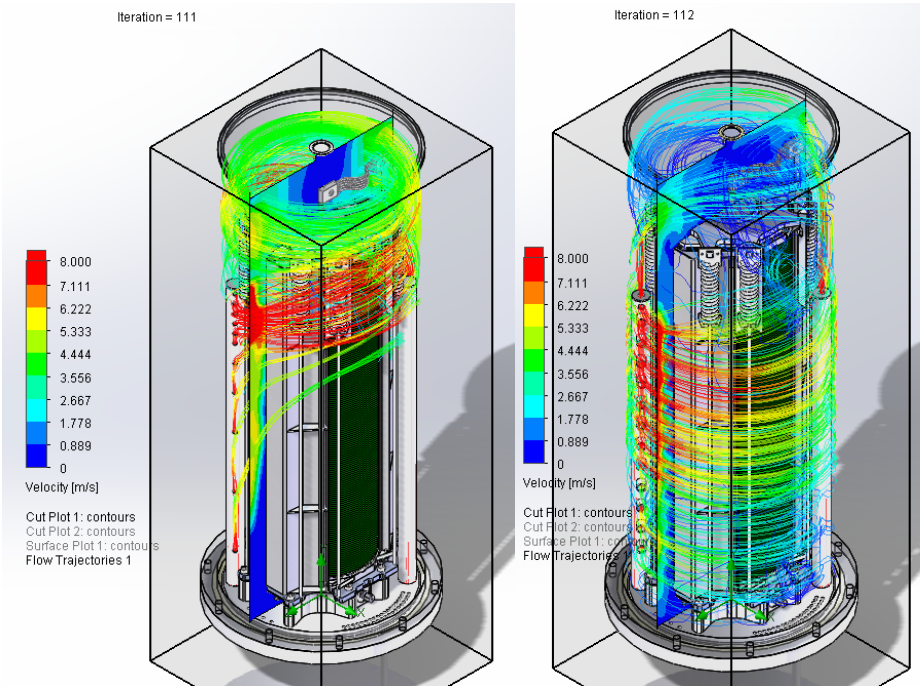

Figure 4-66 Air inlet flow distribution. Original (Left) – Improved (Right)

A working theory is therefore as follows:

- Due to inlet air flow favoring the top of the stack there resulted a hot region of the stack around cells 71-80.
- The local temperature in cells 71-80 is unknown, but might be expected to be somewhat above that measured at cell 115, perhaps on the order of 780 °C
- Likewise the local temperatures towards the top of the stack might be expected to be somewhat lower than that measured at cell 230, perhaps on the order of 730 °C
- Viscosity sensitivity to temperature may favor more flow through the cooler cells and less flow through the warmer cells, aggravating the temperature differential.
    - There are some signs this may be happening as the in-stack thermocouples are generally dropping in temperature with the exception of cell 115, whose temperature begins to rise again after initially dropping.
    - This could represent flow moving away from cell 71-80, initially providing more cooling flow to cell 115, but then as cell 71-80 got progressively hotter, the heat starts to affect cell 115 directly.
    - Of course the alternate explanation is that as voltage performance increases the internal heating decreases, and vice versa. So it is hard to say with certainty whether the temperature is a result of the voltage, or if the voltage is a result of the

temperature. However, given that the voltage was relatively constant at the start of test, whereas there are signs suggesting a variation in temperature at the same time, there are reasons to believe that the trigger was the temperature difference.

- Increasing local temperatures drive decreasing local flows, reducing the cooling while simultaneously making the cells work harder (and generate more heat), leading to a slow runaway condition, which is what we observe as the degradation accelerates, as does the voltage and temperature spread, towards the end of the test.

A revised gas inlet distribution tube was fabricated and testing restarted at 1,674 hours with the new distribution tube in place to evaluate the impact on temperatures and performance. At the same time the thermocouple in cell 230 was replaced since it failed part way through testing.

Stack GT060081-0001 was the first full height CSA stack built. It validated the manufacturing processes, and exceeded the final program performance and degradation milestones. It has showed relatively good stability over the 2,000+ hours of testing and performance and degradation profiles across the stack that illustrate a good uniformity across the 340 repeat units (cells, interconnects, and seals) within the stack.

A review of the air inlet flow patterns has highlighted a weakness in the component design external to the stack. A new air inlet design that better manages the inlet air flow has been designed and will be under test shortly as we continue to evaluate this stack. Improved air distribution will not reverse existing degradation but should improve the temperature distribution across the stack, and should present better conditions for the next stack to be installed.

A summary of the progression of stacks developed and/or used as reference to advance and validate the CSA design is presented in Table 4-222 below.

Table-4-2 Summary of SOFC Stacks Developed and/or Referenced

Stack ID	Time Period	No. of Cells	Hours	Objective	Notes
LAS	--	--	--	Baseline Performance	Performance and Cost Reference
GT059072-0012	Q4 2015	225	5,098		
GT060248-0001	Q3 2017	45	0	1st CSA Trial Build	Confirmed Assembly Build
GT060248-0002	Q4 2017	45	6	1st CSA Electrochemical Test	Ended after Electrolysis Mode Test
GT060248-0003	Q4 2017	45	48	2nd Electrochemical Test	Failed in Electrolysis Mode
GT060248-0004	Q4 2018	45	0	Layered Support Filled, Core – Bottom Plate Adjustment	Seal Failure
GT060248-0005	Q1 2018	45	300	Improve Uf Performance	Ended due to high leak rate
GT060248-0006	Q1 2018	45	>1,000	Repeat of 0005 Test	Ended due to high leak rate
GT060248-0007	Q1 2018	45	>2,500	0005 w/new glass seal paste	
GT060248-0008	Q2 2018	45	<2	Repeat of 0007 Test	
GT060248-0009	Q2 2018	45	<2	Repeat of 0007 Test	Discovered H_2 MFC Error
GT060248-0010	Q3 2018	40	<2	Used TSC3 Cells	
GT060248-0011	Q4 2018	40	160	Used visually sorted cells	Ended due to cell leak
GT060247-0001	Q1 2019	140	<1	Automated Build	Test Stand Failure
GT060247-0002	Q1 2019	145	1,143	Repeat 0001	Test Stand Errors at Start Up
GT060248-0013	Q2 2019	45	<2	Check Build	Discovered Interconnect error
GT060247-0003	Q2 2019	150	1,800	Larger Stack Build	Reference from other program
GT060081-0001	Q3 2019	340	>2,000	Automated Build for 5 kW	

With this test completed, stack GT060081-0001 met the final technical milestone for the program. Beyond meeting the bare milestones, this stack has also demonstrated that the manufacturing methods and equipment are capable and that the design achieves the intended thermal and flow distribution across the stack. The summary of milestones for the project is presented in Table 4-23.

Table 4-3 Milestone Summary

Id.	Task /Subtask No.	Milestone Description	Planned Completion	Actual Completion	Verification Method
1	1.1	Updated Project Management Plan	10/30/15	11/27/15	Project Management File
2	1.1	Project Kickoff Meeting	11/16/15	12/3/15	Presentation File
3	2.1	Verify <0.45 mm Anode Thickness in 1000 hours Tests	3/31/16	3/20/16	Report
4	2.2.1	Demonstrate Role-to-Role Technology Development in Single Cells	9/28/16	9/28/16	Report
5	2.2.2	Complete Evaluation of ADL for Fabrication of Barrier Layer	12/29/16	12/29/17	Report
6	2.2.3	Complete Evaluation of RSDT for Fabrication of Electrolyte Bi-Layer	8/28/16	12/29/17	Report
7	3.1.1	Complete Advanced Stack Design	4/28/17	4/4/17	Report
8	4.3	Complete >1000 hrs. Tests of the 5 kW Stack with <1% per 1000 hrs. Degradation	9/20/17	10/30/19	Final Report
9	5.2	Complete Validation of SOFC Stack Cost Reduction	9/29/17	9/30/19	Report

5.0 Task 5.0 – Advanced Stack Factory Cost

5.1 Task 5.1 Cost Analysis

Objective:

- Perform cost analysis based on factory cost model, including full considerations of capital and overhead costs

Approach:

The cost estimate is to include the following fixed and variable cost elements: Equipment and Plant Depreciation, Tooling Amortization, Equipment Maintenance, Utilities, Indirect Labor, Cost of Capital, Manufactured Materials, Purchased Materials, Fabrication Labor, Assembly Labor, and Indirect Materials. It will not include: Research and Development, Sales and Marketing, General and Administration, Warranty, and Taxes.

Results & Discussion:

Given acceptable life and performance (efficiency), factory cost is the barrier to commercialization. It is often attractive and convenient to project costs to some anticipated future volume and date assuming commercial success. This leads to the so called “Technology Valley of Death” where large investments are required in the medium term, at a net loss, before product volumes are sufficient to reduce costs and overheads to reach profitability. It is interesting and in a tight capital market, necessary, to make the valley of death as narrow (in time) and shallow as possible. Part of the scope for this task was to identify and justify a reasonable yearly production rate to support the cost projections. It is in the interest of the effort to identify pathways to that yearly production rate that minimize the size and duration of the technology valley of death. Pathways to reducing costs at lower volumes are particularly attractive since they favorably impact the cost to get to market at lower volumes and the time to reach profitability.

Previous solid oxide technology cost studies provided by FCE pertained to Pre-Commercial Internal (PCI) and Large Area Stack (LAS) platforms. The base PCI stack has an internal manifold and utilizes 12.5 cm x 12.5 cm cells. For LAS stack, 1.0 mm (before 2011) and 0.6 mm (2011 and after) thick planar SOFC-TSC3 cells with an active area of 550 cm^2 active area were utilized.

For this new SOFC stack Factory Cost study, the focus is on the light weight and power dense next generation CSA stack platform. This platform uses annular shaped SOFC-TSC3 cells, and includes integrated stack manifolds and compression. The CSA stack cell is a 0.30 mm annular anode-supported SOFC-TSC3 (Tape cast, Screen print, Co-fired, third generation) cell with a 120 mm outer diameter and an 81 cm2 active area. Each stack is comprised of 350 cells and outputs a stack power of 8.46 kW DC at 298 mW/cm2 nominal power density.

As inputs to the estimate, DOE has provided guidance on costing methodology, as well as a revised set of raw materials cost data for Year 2011 which is utilized as a basis for the cost of the materials for SOFC production. Notably, the reference DOE cost target is $225/kW AC (2011 USD). The CSA-SOFC Factory Cost Estimate in the report is also evaluated in Year 2011 so that it can be easily compared to the LAS-SOFC Factory Cost Estimate which was previously provided by FCE.

The denominator for the calculation of cost ($/kW) was the net AC power of the fuel cell system based upon the experimentally-observed stack performance at NOC determined under Subtask 4.2. The cost estimate established and fully justified a reasonable estimate of the size and number of systems that must be manufactured per year to support the cost goal.

5.2 Task 5.2 Factory Cost Report

Objective:

- Prepare a Factory Cost Report

Approach:

A Factory Cost Report was prepared upon completion of the cost analysis, including the results of the cost estimation and cost sensitivity analysis.

Results & Discussion:

A Factory Cost Report has been prepared as a separate document entitled "Topical Report CSA Stack Factory Cost Estimate". It is based on an amalgamation of past SECA cost models from prior DoE programs, which were built on a prior generation PCI stack platform, combined with recent internal models developed specifically for the CSA stack platform, but with a focus on much lower volumes than the SECA cost model. Also included are the results from cost sensitivity analysis to the contribution of individual components, rates, etc. and an examination of how the uncertainty or variability of a cost element contributes to the uncertainty or variability of the overall cost.

The report presents the Factory Cost Estimate for the Compact Solid Oxide Architecture (CSA) stack at a high volume production rate of 1000 MW per year. FCE initiated and developed this new stack platform as well as this cost estimate under DOE supported cooperative agreement DE-FE0026093 for *Innovative SOFC Technologies*.

In a recent Q4 2019 quarterly report under DE-FE0026199 (SOFC Prototype System Test), it was reported an updated Large Area Stack cost of $5,316 (Year 2011 USD), which translates to 270 $/kW DC at a high volume production rate of 1,000 MW per year. The CSA Stack Factory Cost Estimate, forecasts a CSA stack cost of $889 (Year 2011 USD) which translates to 105 $/kW DC at the same 1,000 MW/year high volume production.

This significant 61% cost improvement for the CSA stack compared to the Large Area Stack is reported at the same operational power density of 298 mW/cm^2. Additionally, if the Net AC to Gross DC ratio is equal to x1.272, which is the same as that for LAS-SOFC stack, the converted CSA Stack cost at $/kW AC will be $83/kW AC which is significantly lower than the DOE cost target of $225/kW AC (2011 USD). The reduction of $/kW AC from $/kW DC is due to the presence of a bottoming cycle and thus greater overall power generation within the combined system. This CSA stack achievement is realized via the minimization of stack material content, simplified unit cell design and design for automation and assembly.

Regarding cost sensitivity, the analyses identified that cell materials represent the largest proportion of stack cost at 28.5 %. It is followed by cell fabrication which accounts for 28.5% of stack cost. Repeat stack components (all the components of a repeat unit excluding the cell), which are mostly procured, represent 20% of stack cost. The remaining 23% is distributed to interconnect assembly, stack assembly (which includes stack outgoing QC), compression components, non-repeat components (which includes cast components and center post materials), component material preparation.

The top 5 contributors to overall stack cost are identified to be:

1) labor rate - 2.23%
2) nickel oxide price - 1.23%
3) zirconia price - 1.14%
4) electricity rate - 0.73%
5) nickel contact fabrication – 0.70%

The cost of the overall stack is influenced by the uncertainty of the cost assumption of each component. To determine the relative strength of the influence of the uncertainty, all input variables were identified and their values were adjusted lower and higher than a baseline setting for every variable - one at a time. The effect of adjustment to the stack cost was observed and expressed in cost per kW.

The top three cost drivers for 5 categories of cost sensitivity that exceeded an established threshold for each category are listed in Table 5-1 below:

Table 5-1 Summary of Cost Sensitvity Cost Drivers

Category	1st Cost Driver		2nd Cost Driver		3rd Cost Driver	
General Input Parameters	cell fabricator and stack assembler labor rate	2.23%	electricity rate	0.73%	overhead rate	0.63%
Cell Raw Materials	nickel oxide	1.23%	zirconia	1.14%	glass powder	0.50%
Stack Component Raw Materials	stainless steel	0.68%	nickel	0.25%	Ni-Cr Alloy	0.12%
Vendor Fabrications	nickel contact fabrication	0.70%	small part stamping	0.45%	interconnect stamping	0.21%
Equipment	co-firing and ironing tunnel kilns	0.43%	small part stamping	0.45%	interconnect stamping	0.21%

The Factory Cost Report was presented to DOE and the NETL project manager.

CONCLUSION

- A Compact SOFC Architecture (CSA) stack was designed toward the development of a stack platform that offers 50% or greater stack cost reduction. The CSA stack design is derived from a pre-existing stack (5,017 cm^2 total active area) originally developed for mobile applications that incorporates thin cells, thin interconnects, more cells/stack, de-integrated sheet metal manifolds and a U-flow configuration.
- The CSA design development effort focused on increasing cell size by evaluating configurations with 11,200 and 28,000 cm^2 total active area (current large area stack (LAS) has 66,000 cm^2 total active area). The target design employs thinner seals. Thermal modeling results based on a simplified unit cell model were favorable verifying operability for the cell size. The cell size is comparable with the size of a DVD (disc) which affords manufacturability benefits. A full stack model was developed for more detailed analysis of the design.
- A preliminary review of factory costs, based on pre-existing cost models for the precursor stack, was carried out at prototype quantities. The review showed that the CSA stack offers the opportunity to reduce the stack material content by an order of magnitude.
- A thin (~0.3 mm) low-cost anode cell design was developed and evaluated. Cells containing 60 and 65% w/w nickel oxide in the anode substrate were prepared with 10, 30, and 50% finer particle size nickel oxide powder substituted for the coarse particle size nickel oxide and tested. A formulation was selected for scale-up trials and long-term degradation study. Long-term test of the 10 cm x 10 cm cell with 0.286 mm thickness accumulated over 3000 h demonstrating an average performance degradation rate of 0.21%/1000 h (at 0.5 A/cm^2), which met (and exceeded) one of the project milestones.
- The Compact SOFC Architecture (CSA) stack design featuring 350 cells with 84 cm2 cell active area was developed to validate that the design offers 50% or greater stack cost reduction. A layout for the 100 kW SOFC module containing 20 stacks was generated which included design considerations for feed gas (fuel and oxidant) flow distribution to and exhaust collection from the stacks as well as the gas preheating and fuel pre-reforming capabilities. The electrical configuration for the module is based on 10 strings of series-connected stack pairs, providing a (nominal) module voltage of 596 Vdc.
- The detailed design of the interconnect was performed. The unit cell now features a flow configuration with two inlets and two outlets for the oxidant side (instead of one each considered previously). This design approach limits the increase in the cell cathode-side pressure drop, while still providing a good flow distribution. The design condition of 40% oxidant (air) utilization was used while ensuring good thermal management in the stack.
- An automated screen printing option, as a part of the stack manufacturing process development, was explored for cell component production. An automated screen printer along with supporting equipment was purchased, installed and commissioned. The test trials conducted showed great promise. The printer line has been commissioned for the 550 cm^2 (active area) baseline cells (baseline stack production). The production line will provided needed component design information and cell cost data (applied to CSA stack production).

  The spring creep tests show the long term viability of the hot spring design. As constant load tests, these tests somewhat exaggerate the relaxation that would be encountered in practice. The Spring #2 testing, accumulated over a period of 2 years (less 2 days), between hours 1,031 and 6,110 indicated further relaxation will not occur below a load of

215 N (48 lbf). Spring #3 testing occurred over a period of two years (less 24 days) at 750 °C with a spring load corresponding to a stack compressive load of 355 N (80 lbf).

Together, the results show that after an initial bedding period in which relatively large displacement is possible, the springs settle into a relatively slow creep regime even at full load. As the compressive load decays due to the creep, the creep rate slows. These loads are well above the minimum design load for the stack which is predicted to be between 45 and 90 N (10 and 20 lbf).

- Testing of the 225-cell stack (22.3 cm^2 cell active area), built with the design features of the CSA stack, was conducted through 5,000 h at 291 mA/cm^2, 68% fuel utilization, 36% in-stack reforming level and 40% (higher than the typical 20%) air utilization, demonstrating an average performance degradation rate of 0.72%/1,000h. This first-ever test of this stack platform at these test conditions showed a degradation rate in-line with what would be expected from the baseline large area stack.
- The 225-cell stack test was terminated as three cells started to drop in performance around 5,000-hour mark. These cells were located in the hottest part of the stack and seemed to be affected by high in-cell temperature gradients. The rest of the stack was normal, suggesting that the magnitude of the operating temperatures was not the problem (only the gradient in the vicinity of the failed cells).

  Overall, this is seen to be a positive result, giving confidence in the operability of this stack design at these conditions. Also, it shows that despite an order of magnitude reduction in material content and a simplification to the structure, there are no indications of compromised stack capability. Based on the results of the test, several improvements (including oxidant flow configuration and fuel manifold sizing) were planned for the CSA stack design to improve the thermal conditions within and around the stack.
- Efforts in fabrication of cells using a Roll-to-Roll process have not been successful in production of flawless cells. In place of continued development efforts of the Roll-to-Roll process, automated screen printing was explored for cell component production. Initial results showed a 67% reduction in cycle time per print while meeting all quality requirements.
- Development of detailed electrochemical models (coupled CFD, thermal, reforming and electrochemistry models) continues, with promising results at the simplified full stack level. A full 350-cell stack model has been built and has shown good convergence and stability. Some work remains to tune the model to better represent the physical characteristics of the stack.
- Development and evaluation of thin (~0.3 mm) low-cost anode cells continued. Eleven formulations were trialed with a 1,295°C firing temperature. The results of cell testing suggested that a sintering temperature below 1,300 °C (the project target) is feasible, with several candidate material approaches. Subsequent preparation of several sub-1,300 °C fired cell candidates demonstrated good performance and as far as tested, good degradation results. The question of commercial levels of stability (i.e.: Multi-year stability) remains challenging. The overall goal of demonstrating feasibility of low temperature firing has been met. Some candidate materials were prepared for sub 1,250 °C firing trials.
- Evaluation of the low temperature fired cells with a focus on mechanical strength, had most, but not all trialed formulations showing sufficient strength. The development of low firing temperature cells is concluded under this program with several candidates identified.

- Exploration of Atomic Layer Deposition (ALD) for the air electrode barrier layer showed some promise but was more challenging than originally anticipated. Equipment upgrades were hoped to lead to better success. The program could not meet the ALD milestone decision date so an extension of one quarter was requested to complete evaluation. The results from investigating the application of ALD process for fabrication of GDC barrier layer as an alternative to screen printing did not show any improvements that were originally sought. The ALD barrier layers seem to be not as effective as screen printed layers. It is felt more lab scale development work is needed before the process can be considered for demonstration at the stack level.
- Reaction Spray Deposition Technology (RSDT) for electrolyte deposition has been very challenged in this program. While it may offer potential in the future, the recommendation is it to de-scope further work in this in this area for the program. Progress was made in achieving uniform and dense coatings by both RSDT (and ALD) cell layer deposition methods. Preliminary button cell testing of RSDT coated electrolyte has shown promise. However, more lab scale development work is needed before the process can be considered for demonstration at the stack level.
- Cell and stack production processes progressed to the point of stack production with the first 45-cell stack successfully built in the automated work cell. While the intention of this work cell is primarily for development and demonstration of production processes, it has nevertheless demonstrated commercially relevant production rates of 4 MW/shift/yr to 12 MW/shift/yr equivalent throughputs for different production steps. This provides a strong basis for the development of the factory cost model. It has demonstrated the key process steps such that deployment into a real factory environment could be done with confidence.
- Three full scale CSA stacks consisting of 45-cells each with an active area of approximately 81 cm^2 were fabricated and tested. Two stacks were built and tested under parallel project DE-EE0007646. One of the stacks has been operating over 1000 hours at -1 A/cm^2 in electrolysis mode, showing no degradation. A third stack built based on the lessons learned from the previous stacks has achieved the lowest leak rate yet observed (~10x better than the Fuelcell Energy Large Area Stack (LAS)), as well as excellent voltage and excellent utilization performance. This stack has displayed less than 1% /khr degradation over the first 450 hours of operation.
- A previously built stack GT060248-0007 under this program has operated over 2,500 hours at various conditions including reforming conditions with degradation rates similar to prior technology LAS stacks. A critical problem was found with the hydrogen mass flow controller used in GT060248-0007 testing which resulted in the stack being fed 11 slpm more hydrogen than indicated, meaning that the initial degradation testing ran at 32% utilization rather than the target 65% utilization. The previously reported very good stack performance results at high utilization were not reproducible when the mass flow controller error was corrected. While better than initial stacks, more work was needed to improve fuel utilization.
- The transition from HiPoD cells to the older but more stable TSC3 cells has been implemented. The transition was not as fast as originally thought, with some challenges dialing in the process parameters to meet the requirements for the CSA cell. A first stack was built with the TSC3 cells (stack GT060248-0010) and had by far the lowest leak rate of any stack built to date. However it also highlighted varying quality in the TSC3 cells that resulted in an early termination of stack testing. A characteristic of larger cell-count stacks is a requirement for confidence in the individual cells, and that is the focus of

current efforts. Additional visual QC was implemented and improvements were implemented for the cell leak tester.

- Two CSA stacks were built, limited by cell availability. The reversion to the TSC3 cell technology from the HiPoD cells has brought some extra stability to the cell production process but throughput and quality remain challenges. A 45 cell stack was built for this project and it showed significant improvement to utilization performance as a result of improvements to the center post sealing and the addition of a visual QC step in cell production to eliminate cells with obvious electrolyte flaws. The 45 cell stack (GT060248-0011) ran 160 hours of fuel cell operation on simulated reformate before being manually interrupted and autopsied.

  Posttest analysis revealed continued cell weakness and that the selected operating point was too close to the operational limit of the stack. Moving forward required a more conservative operating point (especially in terms of fuel utilization) until stack performance can be improved. Indications are that those improvements will come from improvements to the cell electrolyte, but do not preclude that there may be some underlying flow mal-distribution also contributing to the weakness that will need to be addressed.

- A 145-cell stack was built and, after addressing some test stand problems, was successfully operated for 1,000 hours on a system representative reformate composition, with a degradation of less than 1% /khr, meeting the final program metrics with the exception of stack size (power output of 5 kW). The stack demonstrated a significant scale up from the prior 45-cell stacks and represents a good step towards full height (350-cell) stacks.

- Final activities for the project were the build and test of a full height 350-cell CSA stack and demonstration of both the manufacturing approach and the overall stack design capability, as well as the completion of the factory cost model. These two activities complete the final milestones for the project and close it on a positive note.

  Stack GT060081-0001, with 340 cells, validated the manufacturing processes and exceeded the final program performance and degradation milestones. It has showed relatively good stability over the 1,700 hours of testing to date and the performance and degradation profiles across the stack that illustrate a good uniformity across the 340 repeat units (cells, interconnects, and seals) within the stack.

- The CSA-SOFC stack Factory Cost Estimate using TSC3 cell technology projected to Year 2011 is $ 889 per stack achieved at an annual production level of about 1 GWe. This is equivalent to 105 $/kW DC or 83 $/kW AC which exceeds the DOE target of < 225 $/kW for Year 2011. The power density of the stack is assumed to be at 298 mW/cm2.

- This stack cost result can be compared against the updated LAS-SOFC stack block Factory Cost Estimate provided in DE-FE0026199, Here, a 120-cell LAS stack cost of $5,316 (Year 2011 USD) was reported which translates to 270 $/kW DC or 212 $/kW AC. Thus, this indicates that the next generation CSA stack platform for SOFC is significantly offers a 61% cost improvement.

REFERENCES

1. K.-E. Elers, T. Blomberg, M. Peussa, B. Aitchison, S. Haukka, and S. Marcus, “Film Uniformity in Atomic Layer Depostion,” Chem. Vap. Deposition 12 (2006) 13-24.
2. K.-E. Elers, T. Blomberg, M. Peussa, B. Aitchison, S. Haukka, and S. Marcus, “Film Uniformity in Atomic Layer Depostion,” Chem. Vap. Deposition 12 (2006) 13-24.
3. D.M. Haussmann, E. Kim, J. Becker, and R.G. Gordon, “Atomic Layer Deposition of Hafnium and Zirconium Oxides Using Metal Amide Precursors,” Chem. Mater. 14 (2002) 4350-4358.
4. www.comsol.com/model/download/319961/models.chem.laminar_static_mixer.pdf
5. www.chemineer.com/products/kenics/km-mixers.html
6. Kuo, Y.-L., & Su, Y.-M. (2012). Sintering behavior and electrical properties of gadolinia-doped ceria modified by addition of silicon oxide and titanium oxide. Micro & Nano Letters, 7, 472-475.
7. Nicholas, J., & De Jonge, L. (2007). Prediction and Evaluation of Sintering Aids for Cerium Gadolinium Oxide. Solid State Ionics, 178, 1187-1194.
8. R. Nédélec, et al., Surface & Coatings Technology 205 (2011) 3999-4004
9. R. Maric, et al., Journal of Power Sources 195 (2010) 8198-8201
10. R. Maric et al., ECS Transactions 35 (2011) 473-481
11. R. Maric et al., Journal of Thermal Spray Technology 20 (2011) 696-718
12. B. Movchan et al., The Physics of Metals and Metallography 28 (1969) 653
13. K-H Müller, Journal of Applied Physics 58 (1985) 2573-2576
14. H. Ghezel-Ayagh, “Progress in SOFC Technology Development at FuelCell Energy”, 20th Annual Solid Oxide Fuel Cell (SOFC) Project Review Meeting, Washington, DC, April 30, 2019
15. H. Ghezel-Ayagh, “SOFC Development Update at FuelCell Energy”, 19th Annual Solid Oxide Fuel Cell (SOFC) Project Review Meeting, Washington, DC, June 13, 2018
16. H. Ghezel-Ayagh and B. P. Borglum, “(Invited) Review of Progress in Solid Oxide Fuel Cell at FuelCell Energy”, Electrochemical Society Transactions, 232nd ECS Meeting, volume 80 (9), October 1-5, 2017, pp. 47-56.
17. H. Ghezel-Ayagh and B. P. Borglum, “Review of Progress in Solid Oxide Fuel Cells at FuelCell Energy”, Electrochemical Society Transactions, 15th International Symposium on Solid Oxide Fuel Cells (SOFC-XV), Vol. 78 (1), 2017, pp. 77-86.
18. Y. Cheng, R. J. Gorte, J. M. Vohs, K. Huang, J. E. Barton, H. Ghezel-Ayagh, “Cost-Effective Manufacturing and Morphological Stabilization of Nanostructured Cathodes for Commercial Solid Oxide Fuel Cells”, 18th Annual Solid Oxide Fuel Cell (SOFC) Project Review Meeting, Pittsburgh, PA. .June 12-14, 2017.
19. H. Ghezel-Ayagh, “Advances in SOFC Power System Development”, 17th Annual Solid Oxide Fuel Cell (SOFC) Project Review Meeting, Pittsburgh, PA, July 19-21, 2016.
20. J. Roeder, A. Zeberoff, P. Van Buskirk, A. Torabi, J. Barton, C. Willman, H. Ghezel-Ayagh, and K. Huang, ” Behavior of $La_{0.6}$ $Sr_{0.4}$ $Co_{0.2}Fe_{0.2}O_{3-\delta}$ Cathode Powders Surface Modified by Atomic Layer Deposition for Solid Oxide Fuel Cells”, Electrochemical Society Transactions, Volume 75 (6), 2016, pp. 195-202.
21. A. Torabi, J. Barton, C. Willman, H. Ghezel-Ayagh, E. Tang, and M. Pastula, ”Development of Solid Oxide Fuel Cells at Versa Power Systems & FuelCell Energy”, Electrochemical Society Transactions, 229th ECS Meeting, Volume 72 (7), 2016, pp. 3-9.

LIST OF ACRONYMS

AFL	Anode Functional Layer
AI	Air In
AO	Air Out
ASR	Area Specific (cell) Resistance
BOL	Beginning of Life
BOP	Balance of Plant
CC	Current Collection (DC)
CFD	Computational Fluid Dynamics
CFL	Cathode Functional Layer
CSA	Compact SOFC Architecture
CTE	Coefficient of Thermal Expansion
DC	Direct Current
DIR	Direct Internal Reforming, meaning in-stack reforming
DOE	United States Department of Energy
EOL	End of Life
FCE	FuelCell Energy, Inc.
FEA	Finite Element Analysis
FI	Fuel In
FO	Fuel Out
HHV	Higher Heating Value
I	Electrical Current
IC	Interconnect or separator plate
IIR	Indirect Internal Reforming, meaning in-stack, between-cell, reforming
LHV	Lower Heating Value
MDU	Module Demonstration Unit
NETL	National Energy Technology Laboratory
Ni/YSZ	Nickel – Yttria-Stabilized Zirconia
NOC	Normal Operation Condition
OCV	Open Circuit Voltage
PFD	Process Flow Diagram
P&ID	Piping & Instrumentation Diagram
PNNL	Pacific Northwest National Laboratory
Redox	Reduction - oxidation

SECA	Solid State Energy Conversion Alliance
SLPM, Slpm	Standard liter per minute (at conditions of 1 atm and 70°F (21.1°C))
SOFC	Solid Oxide Fuel Cell
TSC	Tape casting Screen-printing Cofiring
Ua, U_o, UtO	Air (Oxygen) Utilization
Uf, UtF	Fuel Utilization
USA	United States of America
VFD	Variable Frequency Drive
VPS	Versa Power Systems Ltd.